

X-ray crystallography has long been a vital method for studying the structure of proteins and other macromolecules. As the importance of proteins continues to grow, in fields from biochemistry and biophysics to pharmaceutical development and biotechnology, many researchers have found that a knowledge of X-ray diffraction is an indispensable tool. In this new edition of his essential work, Dr. Jan Drenth, recognized internationally for his numerous contributions to crystallographic research, has provided an up-to-date and technically rigorous introduction to the subject.

*Principles of Protein X-Ray Crystallography* provides the theoretical background necessary to understand how the structure of proteins is determined at atomic resolution. It is intended to serve as an introduction for graduate students, postdoctoral researchers, and established scientists who want to use protein crystallography in their own endeavours, or need to understand the subject in order to critically evaluate the literature. New additions to the book include a section on twinning, an additional chapter on crystal growth and a discussion of single-wavelength anomalous dispersion (SAD).

#### Reviews:

"The new edition... will bring important and significant, and timely, coverage of twinning and of SAD phasing."

—Professor John Holmwell,  
Department of Chemistry, University of Manchester

"a complete and up to date... single source of theory."

—Duncan McIvor, President, ActiveSight

#### About the Author:

Dr. Jan Drenth is a Professor Emeritus at the Laboratory of Biophysical Chemistry at the University of Groningen, The Netherlands.

Contributing author Dr. Jeroen R. Meesters is a Senior Research Assistant at the Institute of Biochemistry, University of Lübeck, Germany.

Life Sciences



springer.com

Drenth



Principles of Protein X-Ray Crystallography

Third Edition



# Principles of Protein X-Ray Crystallography

Third Edition



Jan Drenth

 Springer

# Principles of Protein X-Ray Crystallography

Jan Drenth

# Principles of Protein X-Ray Crystallography

---

**Third Edition**

With Major Contribution from

Jeroen Mesters

*University of Lübeck, Germany*

 Springer

Jan Drenth  
Laboratory of Biophysical Chemistry  
University of Groningen  
Nyenborgh 4  
9747 AG Groningen  
The Netherlands  
j.drenth@rug.nl

*Cover illustration:* Courtesy of Adrian R. Ferré-D'Amaré and Stephen K. Burley, The Rockefeller University. The four- $\alpha$ -helix bundle moiety of transcription factor Max. Reproduced with permission from *Nature* 363:38–45 (1993).

Library of Congress Control Number: 2006926449

ISBN-10: 0-387-33334-7

e-ISBN-10: 0-387-33746-6

ISBN-13: 978-0-387-33334-2

e-ISBN-13: 978-0-387-33746-3

Printed on acid-free paper.

© 2007, 1999, 1994 Springer Science+Business Media, LLC

All rights reserved. This work may not be translated or copied in whole or in part without the written permission of the publisher (Springer Science+Business Media, LLC, 233 Spring Street, New York, NY 10013, USA), except for brief excerpts in connection with reviews or scholarly analysis. Use in connection with any form of information storage and retrieval, electronic adaptation, computer software, or by similar or dissimilar methodology now known or hereafter developed is forbidden.

The use in this publication of trade names, trademarks, service marks, and similar terms, even if they are not identified as such, is not to be taken as an expression of opinion as to whether or not they are subject to proprietary rights.

9 8 7 6 5 4 3 2 1

springer.com

# Preface to the Third Edition

In the 7 years since the publication of the previous edition, protein X-ray crystallography has made rapid progress. This was, to a large extent, triggered by the sudden growth of interest in structural genomics. Impressive technological advances facilitated this development. It required updating Chapter 2 on Sources and Detectors.

It is no longer an exception to collect a full dataset in a few minutes and to solve the structure in hours. However, one bottleneck remains and that is the growth of quality crystals. Although accelerated by robotic systems, it is still a trial-and-error process. For the benefit of the novice in crystallization, a chapter on “Practical Protein Crystallization” written by Dr. Jeroen R. Mesters has been added.

Another addition is a section on single-wavelength anomalous diffraction. This technique has gained much popularity in recent years, especially in the high-throughput field. Also SHELXD, a dual-space direct method for substructure determination, equally useful as SnB, has now been added to Chapter 11 on Direct Methods.

We are indebted to many colleagues who in some way or another assisted us in the preparation of this edition. Among them are Thomas Barends, Zbigniew Dauter, Rolf Hilgenfeld, Ankie Terwisscha van Scheltinga, Bram Schierbeek, George Sheldrick, and Simon Tulloch. Jan Drenth is especially grateful to Bauke Dijkstra for the generous hospitality in his laboratory.

Jeroen Mesters  
Jan Drenth

# Preface to the Second Edition

Since the publication of the previous edition in 1994, X-ray crystallography of proteins has advanced by improvements in existing techniques and by addition of new techniques. Examples are, for instance, MAD, which has developed into an important method for phase determination. Least squares as a technique for refinement is gradually being replaced by the formalism of maximum likelihood. With several new sections, the book has been updated, and I hope it will be as well received as the previous edition.

In the preparation of this second edition, I was greatly assisted by experts who commented on relevant subjects. I acknowledge the contributions of Jan Pieter Abrahams, Eleanor Dodson, Elspeth Garman, Eric de La Fortelle, Keith Moffat, Garib Murshudov, Jorge Navaza, Randy Read, Willem Schaafsma, George Sheldrick, Johan Turkenburg, Gert Vriend, Charles Weeks, and my colleagues in the Groningen Laboratory.

I am especially grateful to Bauke Dijkstra for the generous hospitality in his laboratory.

Jan Drenth

# Preface to the First Edition

Macromolecules are the principal nonaqueous components of living cells. Among the macromolecules (proteins, nucleic acids, and carbohydrates), proteins are the largest group. Enzymes are the most diverse class of proteins because nearly every chemical reaction in a cell requires a specific enzyme. To understand cellular processes, knowledge of the three-dimensional structure of enzymes and other macromolecules is vital. Two techniques are widely used for the structural determination of macromolecules at atomic resolution: X-ray diffraction of crystals and nuclear magnetic resonance (NMR). While NMR does not require crystals and provides more detailed information on the dynamics of the molecule in question, it can be used only for biopolymers with a molecular weight of less than 30,000. X-ray crystallography can be applied to compounds with molecular weight up to at least  $10^6$ . For many proteins, the difference is decisive in favor of X-ray diffraction.

The pioneering work by Perutz and Kendrew on the structure of hemoglobin and myoglobin in the 1950s led to a slow but steady increase in the number of proteins whose structure was determined using X-ray diffraction. The introduction of sophisticated computer hardware and software dramatically reduced the time required to determine a structure while increasing the accuracy of the results. In recent years, recombinant DNA technology has further stimulated interest in protein structure determination. A protein that was difficult to isolate in sufficient quantities from its natural source can often be produced in arbitrarily large amounts using expression of its cloned gene in a microorganism. Also, a protein modified by site-directed mutagenesis of its gene can be created for scientific investigation and industrial application. Here, X-ray diffraction plays a crucial role in guiding the molecular biologist to the best amino acid positions for modification. Moreover, it is often important to learn what effect a change in a protein's sequence will have on its three-dimensional structure. Chemical and pharmaceutical companies have

become very active in the field of protein structure determination because of their interest in protein and drug design.

This book presents the principles of the X-ray diffraction method. Although I will discuss *protein* X-ray crystallography exclusively, the same techniques can in principle be applied to other types of macro-molecules and macromolecular complexes. The book is intended to serve both as a textbook for the student learning crystallography, and as a reference for the practicing scientist. It presupposes a familiarity with mathematics at the level of upper level undergraduates in chemistry and biology, and is designed for the researcher in cell and molecular biology, biochemistry, or biophysics who has a need to understand the basis for crystallographic determination of a protein structure.

I would like to thank the many colleagues who have read the manuscript and have given valuable comments, especially Aafje Vos, Shekhar and Sharmila Mande, Boris Strokopytov, and Risto Lapatto.

Jan Drenth



# Contents

Preface to the Third Edition	v
Preface to the Second Edition	vi
Preface to the First Edition	vii
Chapter 1	
Crystallizing a Protein	1
1.1 Introduction	1
1.2 Principles of Protein Crystallization	1
1.3 Crystallization Techniques	4
1.4 Crystallization of Lysozyme	8
1.5 A Preliminary Note on Crystals	9
1.6 Preparation for an X-ray Diffraction Experiment	11
1.7 Cryocooling	15
1.8 Notes	17
Summary	20
Chapter 2	
X-ray Sources and Detectors	21
2.1 Introduction	21
2.2 X-ray Sources	21
2.3 Monochromators	30
2.4 Introduction to Cameras and Detectors	31
2.5 Detectors	33
2.6 The Rotation (Oscillation) Instrument	38
Summary	43

Chapter 3	
Crystals	45
3.1	Introduction 45
3.2	Symmetry 49
3.3	Possible Symmetry for Protein Crystals 56
3.4	Coordinate Triplets: General and Special Positions 56
3.5	Asymmetric Unit 57
3.6	Point Groups 58
3.7	Crystal Systems 58
3.8	Radiation Damage 60
3.9	Characterization of the Crystals 61
	Summary 63
Chapter 4	
Theory of X-ray Diffraction by a Crystal	64
4.1	Introduction 64
4.2	Waves and Their Addition 65
4.3	A System of Two Electrons 68
4.4	Scattering by an Atom 71
4.5	Scattering by a Unit Cell 73
4.6	Scattering by a Crystal 74
4.7	Diffraction Conditions 76
4.8	Reciprocal Lattice and Ewald Construction 77
4.9	The Temperature Factor 81
4.10	Calculation of the Electron Density $\rho(x y z)$ 84
4.11	Comparison of $\mathbf{F}(h k l)$ and $\mathbf{F}(\bar{h} \bar{k} \bar{l})$ 90
4.12	Symmetry in the Diffraction Pattern 91
4.13	Integral Reflection Conditions for Centered Lattices 95
4.14	Intensity Diffracted by a Crystal 96
4.15	Scattering by a Plane of Atoms 103
4.16	Choice of Wavelength, Size of Unit Cell, and Correction of the Diffracted Intensity 105
	Summary 107
Chapter 5	
Average Reflection Intensity and Distribution of Structure Factor Data	109
5.1	Introduction 109
5.2	Average Intensity; Wilson Plots 111
5.3	The Distribution of Structure Factors $\mathbf{F}$ and Structure Factor Amplitudes $ F $ 114
5.4	Crystal Twinning 116
	Summary 118
Chapter 6	
Special Forms of the Structure Factor	119

6.1	Introduction	119
6.2	The Unitary Structure Factor	119
6.3	The Normalized Structure Factor	120
	Summary	122
Chapter 7		
The Solution of the Phase Problem by the Isomorphous Replacement Method		123
7.1	Introduction	123
7.2	The Patterson Function	124
7.3	The Isomorphous Replacement Method	133
7.4	Effect of Heavy Atoms on X-ray Intensities	139
7.5	Determination of the Heavy Atom Parameters from Centrosymmetric Projections	142
7.6	Parameters of Heavy Atoms Derived from Acentric Reflections	144
7.7	The Difference Fourier Summation	146
7.8	Anomalous Scattering	148
7.9	The Anomalous Patterson Summation	152
7.10	One Common Origin for All Derivatives	154
7.11	Refinement of the Heavy Atom Parameters Using Preliminary Protein Phase Angles	157
7.12	Protein Phase Angles	160
7.13	The Remaining Error in the Best Fourier Map	167
7.14	The Single Isomorphous Replacement Method	170
	Summary	171
Chapter 8		
Phase Improvement		172
8.1	Introduction	172
8.2	The OMIT Map With and Without Sim Weighting	173
8.3	Solvent Flattening	179
8.4	Noncrystallographic Symmetry and Molecular Averaging	185
8.5	Histogram Matching	187
8.6	wARP: Weighted Averaging of Multiple-Refined Dummy Atomic Models	190
8.7	Further Considerations Concerning Density Modification	192
	Summary	193
Chapter 9		
Anomalous Scattering in the Determination of the Protein Phase Angles and the Absolute Configuration		194
9.1	Introduction	194
9.2	Protein Phase Angle Determination with Anomalous Scattering	194
9.3	Improvement of Protein Phase Angles with Anomalous Scattering	196
9.4	The Determination of the Absolute Configuration	198
9.5	Multiple- and Single-Wavelength Anomalous Diffraction (MAD and SAD)	199
	Summary	209

Contents	xiii
Chapter 10	
Molecular Replacement	210
10.1 Introduction	210
10.2 The Rotation Function	211
10.3 The Translation Function	217
Summary	230
Chapter 11	
Direct Methods	231
11.1 Introduction	231
11.2 Shake-and-Bake	231
11.3 SHELXD	236
11.4 The Principle of Maximum Entropy	238
Summary	240
Chapter 12	
Laue Diffraction	241
12.1 Introduction	241
12.2 The Accessible Region of Reciprocal Space	242
12.3 The Multiple Problem	243
12.4 Unscrambling of Multiple Intensities	244
12.5 The Spatial Overlap Problem	245
12.6 Wavelength Normalization	245
Summary	246
Chapter 13	
Refinement of the Model Structure	248
13.1 Introduction	248
13.2 The Mathematics of Refinement	251
13.3 The Principle of the Fast Fourier Transform Method	262
13.4 Specific Refinement Methods	264
Summary	278
Chapter 14	
The Combination of Phase Information	279
14.1 Introduction	279
14.2 Phase Information from Isomorphous Replacement	280
14.3 Phase Information from Anomalous Scattering	282
14.4 Phase Information from Partial Structure Data, Solvent Flattening, and Molecular Averaging	283
14.5 Phase Information from SAD	284
Summary	284
Chapter 15	
Checking for Gross Errors and Estimating the Accuracy of the Structural Model	285
15.1 Introduction	285

15.2	<i>R</i> -Factors	285
15.3	The Ramachandran Plot	287
15.4	Stereochemistry Check	287
15.5	The 3D–1D Profile Method	288
15.6	Quantitative Estimation of the Coordinate Error in the Final Model	292
	Summary	296
Chapter 16		
Practical Protein Crystallization		297
16.1	Introduction	297
16.2	Gene Cloning and Expression	298
16.3	Protein Purification	299
16.4	Protein Crystallization	302
	Summary	303
Appendix 1		
A Compilation of Equations for Calculating Electron Density Maps		305
Appendix 2		
A Compilation of Reliability Indexes		308
Appendix 3		
The Variation in the Intensity of X-ray Radiation		314
References		316
Index		326

# Chapter 1

## Crystallizing a Protein

### 1.1. Introduction

Students new to the protein X-ray crystallography laboratory might understandably be confused when colleagues discuss Fouriers and Pattersons or molecular replacement and molecular dynamics refinement. However, they understand immediately that the first requirement for protein structure determination is to grow suitable crystals. Without crystals there can be no X-ray structure determination of a protein! In this chapter, we discuss the principles of protein crystal growth, and as an exercise, we give the recipe for crystallizing the enzyme lysozyme. We will also generate an X-ray diffraction picture of a lysozyme crystal. This will provide an introduction to X-ray diffraction. The chapter concludes with a discussion of the problems encountered.

### 1.2. Principles of Protein Crystallization

Obtaining suitable single crystals is the least understood step in the X-ray structural analysis of a protein. The science of protein crystallization is an underdeveloped area, although interest is growing, spurred especially by microgravity experiments in space flights (Kundrot et al., 2001; McPherson et al., 1995). Protein crystallization is mainly a trial-and-error procedure in which the protein is slowly precipitated from its solution. The presence of impurities, crystallization nuclei, and other unknown factors play a role in this process. As a general rule, however, the purer the protein, the better the chances to grow crystals. The purity requirements of the protein crystallographer are different and more stringent than the requirements of the biochemist, who would be satisfied if, for example, the catalytic activity of an enzyme is sufficiently high. On the other hand, in order to achieve protein

crystallization, not only should other compounds be absent, but all molecules of the protein should have the same surface properties, especially the same charge distribution on their surface, as this influences the packing of the molecules in the crystal. Mass spectrometry is a valuable tool in protein crystallization (i.e., in checking the expression of recombinant protein, the purity of a preparation, heavy atom derivatives, and the nature of protein constructs (Cohen, 1996; Potier et al., 2000)).

The crystallization of proteins involves four important steps:

1. The purity of the protein is determined. If it is not extremely pure, further purification will generally be necessary to achieve crystallization.
2. The protein is dissolved in a suitable solvent from which it must be precipitated by a salt or an organic compound. The solvent is usually a water–buffer solution, sometimes with an organic solvent such as 2-methyl-2,4-pentanediol (MPD) added. Normally, the precipitant solution is also added, but only to such a concentration that a precipitate does not yet develop. Membrane proteins, which are insoluble in a water–buffer or a water–organic solvent, require a detergent also.
3. The solution is brought to supersaturation. In this step, small aggregates are formed, which are the nuclei for crystal growth. For the crystallization of small molecules, which is understood much better than the crystallization of proteins, the spontaneous formation of nuclei requires a supply of surface tension energy. Once the energy barrier has been passed, crystal growth begins. The energy barrier is easier to overcome at a higher level of supersaturation. Therefore, spontaneous formation of nuclei is best achieved at a high supersaturation. We assume that this is also true for the crystallization of proteins. Formation of nuclei can be studied as a function of supersaturation and other parameters by a number of techniques, including light scattering, fluorescence depolarization, and electron microscopy.
4. Once nuclei have formed, actual crystal growth can begin. As for low-molecular-weight compounds, the attachment of new molecules to the surface of a growing crystal occurs at steps on the surface. This is because the binding energy is larger at such positions than if the molecule attaches to a flat surface. These steps are either created by defects in the crystalline order or occur at nuclei formed randomly on the surface.

Theory tells us that the best crystals grow by reducing the supersaturation to a lower level; maintaining a high supersaturation would result in the formation of too many nuclei and, therefore, too many small crystals (Figure 1.1). Also, crystals should grow slowly to reach a maximum degree of order in their structure. In practice, however, this fundamental rule is not always obeyed. The easiest way to change the degree of supersaturation is by changing the temperature or the concentration of the precipitating agent.

Precipitation of the protein can be achieved by the addition of a salt, polyethyleneglycol (PEG), or an organic solvent. As a precipitating agent a salt acts in two ways (salting out). Its ions screen electric charges on the surface of the protein molecules, thereby weakening the repulsive forces between the molecules.

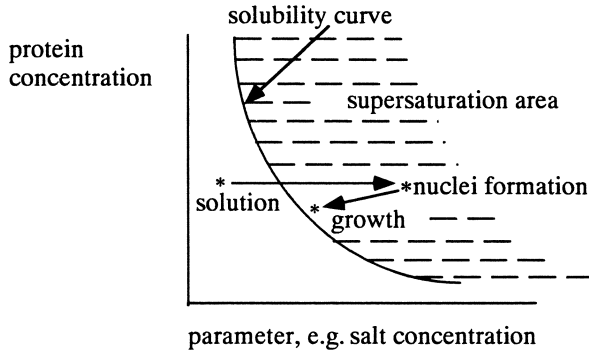


Figure 1.1. A typical solubility curve for a protein, as a function of the salt concentration or another parameter. For best results, the crystals should be grown at a lower level of supersaturation than is required for formation of nuclei.

In addition, part of the water is immobilized and not available to the protein because of the generation of a hydration layer around the salt ions. The most popular salt is ammonium sulfate. Its advantages are that it is highly soluble and is not harmful to most proteins even in a high concentration.

Polyethyleneglycol has a high affinity for water and can immobilize water just as salt does. Moreover, it affects protein solubility in a different way. PEG molecules cannot approach the protein molecular surface closer than the radius of the PEG molecule, and a layer that is inaccessible for the center of the PEG molecules surrounds the protein molecules. If the protein molecules aggregate, these layers partly overlap and the inaccessible region becomes smaller. As a result, the accessible region becomes larger. There is more space available for the PEG molecules, their entropy increases (at the expense of some protein entropy), and the free energy of the system decreases. This situation with aggregated protein molecules is, therefore, the most favorable in the presence of PEG.

The most common organic solvent for protein crystallization is MPD. Organic solvents have an electrostatic effect. They lower the dielectric constant of the medium. Electric forces become stronger. This compresses the electric double layer of ions around the protein molecules. The molecules can approach each other much closer and, if in a favorable orientation, they can aggregate.

Some proteins are poorly soluble in water but do dissolve if a small amount of salt (much smaller than for salting out) is added. By removing the salt, the protein precipitates. This “salting in” effect is explained as the result of a competition between charged groups on the protein molecular surface and the ions in the solution. In the absence of solvent ions, the protein molecules are not surrounded by an ionic double layer and can aggregate by Coulomb attraction between opposite charges on different protein molecules. If a small amount of ions is added, a double layer forms around the protein molecules. These layers do not penetrate and repel each other.

Other methods to decrease the protein solubility are changing the pH of the solution or the temperature.



To summarize, the usual procedure for crystallizing a protein is as follows:

1. Check the purity carefully.
- 2a. Slowly increase the concentration of the precipitant, such as PEG, salt, or an organic solvent; or
- 2b. Change the pH or the temperature.

In practice, the amount of protein available for crystallization experiments is often very small. To determine the best crystallization conditions, it is usually necessary to carry out a great number of experiments; hence, a minimum amount of protein should be used per experiment. A single protein crystal of reasonable size ( $0.2 \times 0.2 \times 0.2 \text{ mm} = 0.008 \text{ mm}^3$ ) weighs approximately  $10 \mu\text{g}$ . Therefore,  $1 \text{ mg}$  of purified protein is sufficient to perform about 100 crystallization experiments.

Membrane proteins are insoluble in water and notoriously difficult to crystallize. The conventional strategy is to use detergents to solubilize them in an aqueous solution and then follow one of the procedures for water-soluble proteins (Michel, 1990; Sowadski, 1994). Landau and Rosenbusch (1996) introduced a new method that could be promising for the crystallization of membrane proteins. They applied lipidic cubic phases as crystallization matrices for a variety of compounds. Lipidic cubic phases are liquid crystals with a cubic symmetry. They can be formed in a mixture of lipids and water (Lindblom and Rilfors, 1989). Several types of lipidic cubic phases exist. Landau et al. (1997) succeeded in growing well-ordered crystals of the membrane protein bacteriorhodopsin in a certain type of lipidic cubic phase (see also Gouaux, 1998). It remains to be seen whether this method will be successful in the crystallization of more membrane proteins.

## 1.3. Crystallization Techniques

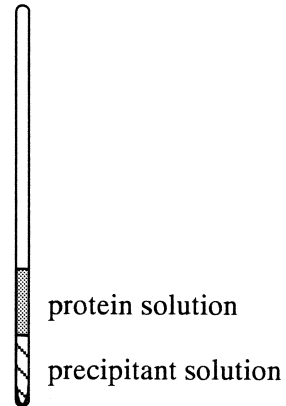
### 1.3.1. Batch Crystallization

This is the oldest and simplest method for protein crystallization. The principle is that the precipitating reagent is instantaneously added to a protein solution, suddenly bringing the solution to a state of high supersaturation. With luck, crystals grow gradually from the supersaturated solution without further processing. An automated system for microbatch crystallization has been designed by Chayen et al. (1990, 1992). In their microbatch method, they grew protein crystals in  $1\text{--}2\text{-}\mu\text{l}$  drops containing the protein and the precipitant. The drops are suspended in an oil (e.g., paraffin oil). The oil acts as a sealant to prevent evaporation. It does not interfere with the common precipitants, but it does interfere with organic compounds that dissolve in the oil (Chayen, 1997; see also Chayen, 1998).

### 1.3.2. Liquid–Liquid Diffusion

In this method, the protein solution and the solution containing the precipitant are layered on top of each other in a small-bore capillary; a melting-point capillary

Figure 1.2. Liquid–liquid diffusion in a melting-point capillary. If the precipitant solution is the denser one, it forms the lower layer.



can conveniently be used (Figure 1.2). The lower layer is the solution with higher density (e.g., a concentrated ammonium sulfate or PEG solution). If an organic solvent such as MPD is used as precipitant, it forms the upper layer. For a 1:1 mixture, the concentration of the precipitant should be two times its desired final concentration. The two solutions ( $\sim 5 \mu\text{l}$  of each) are introduced into the capillary with a syringe needle, beginning with the lower one. Spinning in a simple swing-out centrifuge removes air bubbles. The upper layer is added and a sharp boundary is formed between the two layers. They gradually diffuse into each other.

García-Ruiz and Moreno (1994) have developed the technique of liquid–liquid diffusion further to the acupuncture method. The protein solution is sucked up into narrow tubes by capillary force; one end of each tube is closed. Next, the open end is pushed into a gel contained in a small vessel. The gel keeps the tubes in a vertical position, and the protein solution is in contact with the gel. The solution with the precipitating agent is then poured over the gel, and the whole setup is kept in a closed box to avoid evaporation. The diffusion time of the precipitating agent through the gel and the capillary can be controlled by the penetration depth of the capillary in the gel. A range of supersaturations is created in the protein solution—high at the bottom and low at the top of the capillary. This can be used as additional information in screening the best crystallization conditions.

### 1.3.3. Vapor Diffusion

#### 1.3.3.1. The Hanging Drop Method

In this method, drops are prepared on a siliconized microscope glass cover slip by mixing 3–10  $\mu\text{l}$  of protein solution with the same volume of precipitant solution. The slip is placed upside down over a depression in a tray; the depression is partly filled with the required precipitant solution ( $\sim 1 \text{ ml}$ ). The chamber is sealed by applying oil or grease to the circumference of the depression before the cover slip is put into place (Figure 1.3).

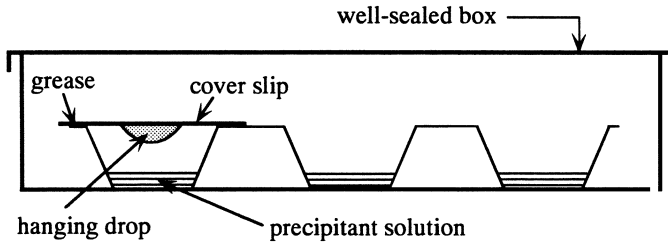


Figure 1.3. The hanging drop method of protein crystallization. Using a tray with depressions, the protein solution is suspended as a drop from a glass cover slip above the precipitant solution in a sealed depression. The glass slip is siliconized to prevent spreading of the drop. Equilibrium is reached by diffusion of vapor from the drop to the precipitating solution or vice versa. All of the depressions in the tray can, of course, be used.

#### 1.3.3.2. The Sitting Drop Method

If the protein solution has a low surface tension, it tends to spread out over the cover slip in the hanging drop method. In such cases, the sitting drop method is preferable. A schematic diagram of a sitting drop vessel is shown in Figure 1.4.

#### 1.3.4. Dialysis

As with the other methods for achieving protein crystallization, many variations of dialysis techniques exist. The advantage of dialysis is that the precipitating solution can be easily changed. For moderate amounts of protein solution (more than 0.1 ml), dialysis tubes can be used, as shown in Figure 1.5a. The dialysis membrane is attached to a tube by means of a rubber ring. The membrane should be rinsed extensively with water before use or, preferably, boiled in water for about 10 min. For microliter amounts of protein solution, one can use either a thick-walled microcapillary (Zeppezauer method) or a plexiglass “button” covered with a dialysis membrane (Figure 1.5b). The disadvantage of the button is that a protein crystal in the button cannot be observed with a polarizing microscope.

Another microdialysis procedure is illustrated in Figure 1.6. Five microliters of protein solution is injected into a capillary, which is covered by a dialysis

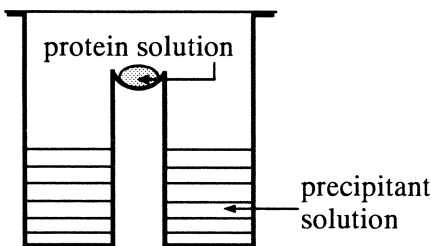


Figure 1.4. The sitting drop method for performing protein crystallization.

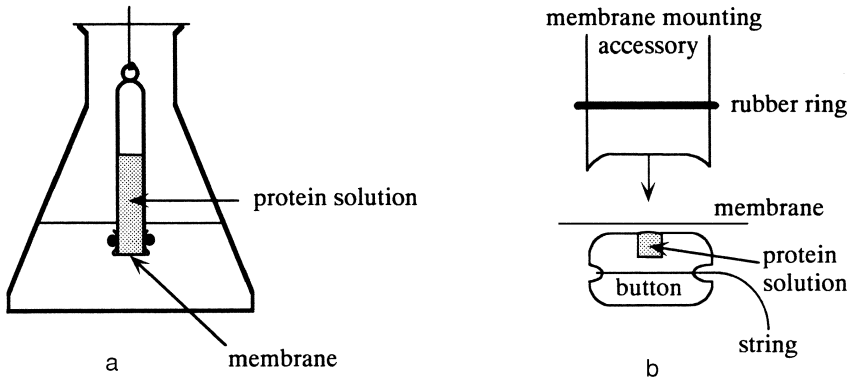


Figure 1.5. Protein crystallization by dialysis. If a relatively large amount of protein is available, dialysis can be performed as in (a). Smaller amounts can be crystallized in a button (b).

membrane. The membrane can be fastened with a piece of tubing. The protein solution is spun down in a simple centrifuge and the capillary closed with modeling clay. The capillary is then placed in an Eppendorf tube containing the dialysis solution.

### 1.3.5. Final Remarks

Crystallization of a protein is a multiparameter problem in which the parameters are varied in the search for optimal crystallization conditions. The most common parameters that are changed include protein concentration, the nature and

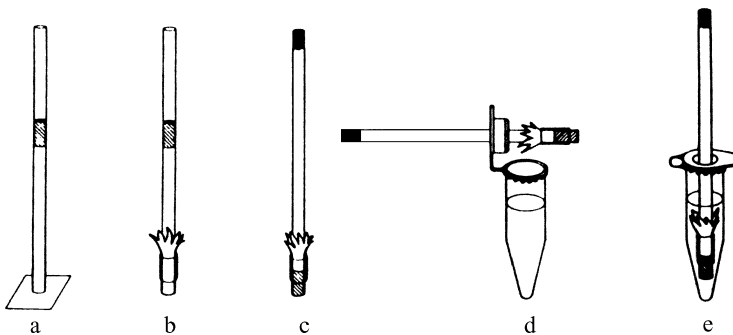


Figure 1.6. Protein crystallization by microdialysis procedure. In (a) and (b), the protein solution is still somewhere in the capillary. In (c), it has been spun to the bottom of the tube and is in contact with the membrane. In (d) and (e), the capillary is mounted in an Eppendorf tube containing dialysis solution.

concentration of the precipitant, pH, and temperature. Specific additives that affect the crystallization can also be added in low concentration.<sup>1</sup>

Because a prediction of the best crystallization conditions is not possible, a huge number of different conditions is screened for obtaining high-quality crystals in a reasonable time. The screening technique is called sparse matrix sampling (Jancarik and Kim, 1991). The time pressure exerted by high-throughput structural genomics requires speed and efficiency in scanning the enormous number of crystallization conditions. The solution is by automation of the process. Robots replace the laborious manual operations.

Crystallization screens can be homemade or obtained commercially. Suppliers of screens and other useful gadgets for crystallization are, for instance; Hampton Research,<sup>2</sup> Molecular Dimensions,<sup>3</sup> and Jena Bioscience.<sup>4</sup>

## 1.4. Crystallization of Lysozyme

After learning the principles of protein crystallization, it is time to do a crystallization experiment. The most convenient protein to start with is hen egg white lysozyme. It can be obtained commercially in pure form, is relatively inexpensive, and can be used immediately for a crystallization experiment. In addition to native lysozyme, a heavy atom derivative of the protein will be crystallized, because the determination of a protein structure sometimes requires X-ray diffraction patterns of crystals of the native protein as well as of one or more heavy-atom-containing derivatives. In this experiment, the mercury-containing reagent *p*-chloromercuriphenyl sulfonate (PCMS) is used. The steps are as follows:

1. Prepare a sodium acetate buffer solution of pH 4.7 by dissolving
  - a. 1.361 g of sodium acetate in 50 ml water (purified by reverse osmosis or double distillation).
  - b. 0.572 ml glacial acetic acid in 50 ml water. The acetic acid solution is added to the salt solution until the pH reaches 4.7.
2. Prepare a precipitant solution of sodium chloride
  - a. for the native crystals by preparing 30 ml of 10% (w/v) NaCl in the sodium acetate buffer;
  - b. for the derivative crystals by dissolving 0.041 g of the sodium salt of PCMS in 5 ml of the precipitant solution prepared in 2a.

---

**Warning!** Heavy atom reagents can be very toxic or radioactive. Handle them with care and wear gloves. Discard excess reagent and solution in a special container.

---

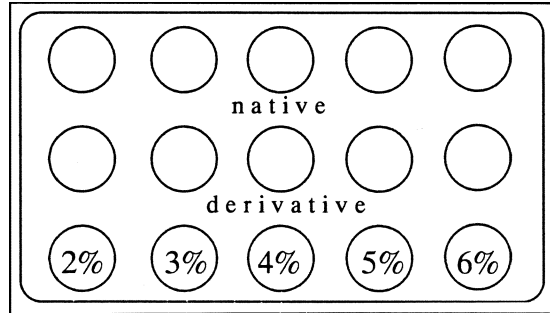
<sup>1</sup> Protein crystallization is extensively discussed in Ducruix and Giegé (1999) and in McPherson (1999).

<sup>2</sup> Hampton Research, <http://www.hamptonresearch.com>

<sup>3</sup> Molecular Dimensions Ltd, [www.moleculardimensions.com](http://www.moleculardimensions.com)

<sup>4</sup> Jena Bioscience GmbH, <http://www.jenabioscience.com>

Figure 1.7. A tray for the crystallization of lysozyme. Five experiments each for the native protein and for the heavy atom derivative can be performed with increasing concentrations of the precipitant solution: 2–6% NaCl.



3. Dissolve the native lysozyme in the acetate buffer to a concentration of 50 mg/ml (e.g., 10 mg in 200  $\mu$ l). The heavy atom derivative is less soluble and its concentration should be only 15 mg/ml in the same buffer. To remove insoluble particles the solutions are centrifuged at 10,000 rpm and 4°C for 10 min prior to setting up the crystallization experiments.
4. Take one or two trays for the native and for the derivative protein, with at least  $5 \times 3$  depressions in each (Figure 1.7). The crystallization experiments are performed with five concentrations of the precipitant solution: 2%, 3%, 4%, 5%, and 6% NaCl and two replicates per condition. Use the extra row of depressions to label the experimental conditions. Fill each depression with 1 ml of the precipitant solution at the required concentration. Prepare the hanging drops on the siliconized side of microscope cover slips: Pipette 10  $\mu$ l of the enzyme solution onto a cover slip and mix with 10  $\mu$ l of the precipitant solution. Brush a film of immersion oil around each depression on the surface of the tray to seal (Figure 1.3).

The lysozyme crystals will grow in a day or so and you will probably be anxious to see how your crystals will diffract X-rays. However, we will first consider some general features about crystals.

## 1.5. A Preliminary Note on Crystals

Crystals occur in a great variety of shapes and colors and naturally grown crystals have been used as gems since prehistoric times. Their flat faces reflect the regular packing of the molecules, atoms, or ions in the crystal. Crystals are distinguished from amorphous substances by their flat faces and by their anisotropy: Some of their physical properties are dependent on the direction of measurement in the crystal. For some properties, crystals might be isotropic, but usually not for all of them. You can easily observe the anisotropy of the lysozyme crystals that you have just grown by examining them between crossed polarizers in a polarizing microscope. They display beautiful colors because the crystals are birefringent: They have two different refraction indexes. If you rotate the microscope

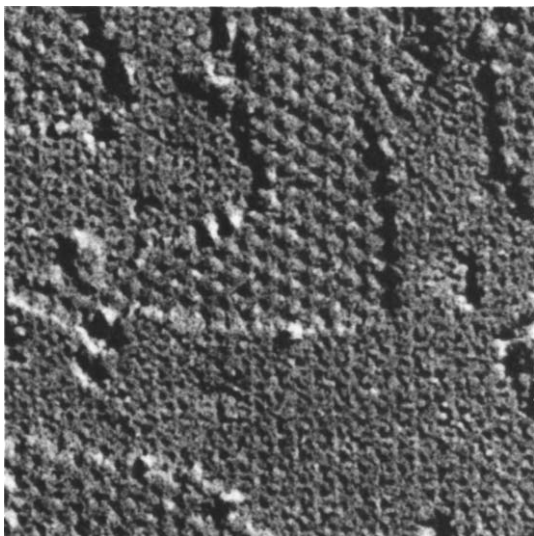


Figure 1.8. An electron micrograph of a crystal face of the oxygen-transporting protein hemocyanin from *Panulirus interruptus*. The molecular weight of this protein is 450,000; magnification: 250,000 $\times$ . (Courtesy of E.F.J. van Bruggen.)

platform holding the crystals, they will become completely dark at a certain position and every  $90^\circ$  away from it; thus, extinction occurs four times in a complete revolution.

The flat faces and anisotropy of crystals reflect their regular packing of molecules, atoms, or ions. This regular arrangement cannot be observed with the naked eye or with a light microscope because the particles are too small, but it can be visualized with an electron microscope (Figure 1.8). If the resolution of the microscope were high enough, the atomic structure inside the large protein molecules could be observed. Unfortunately, this is not possible because biological substances can be observed in an electron microscope with a resolution of only 10–20 Å due to limitations in specimen preparation. Although atomic resolution cannot be reached in this way, electron micrographs of crystals show convincingly the regular packing of molecules in the crystals. It is because of this regular arrangement that the crystals diffract X-rays.

Before starting the X-ray diffraction experiment, it can be illuminating to demonstrate diffraction with visible light and a grating. The principle is the same, the only difference being that the grating is two dimensional and the crystal is three dimensional. Take a laser pointer as light source and ask an electron microscopist for one of the copper grids on which specimens are mounted. In a dark room you will see a beautiful pattern of diffraction spots. Rotation of the grid causes the pattern to rotate with it. If you can borrow grids with different spacings, the pattern from the grid with larger spacings will have the diffraction spots closer together: Here you observe “reciprocity” between the diffraction pattern and the grid. Alternatively, you can perform the experiment with transparent woven fabric. Note that stretching the fabric horizontally causes the diffraction pattern to shrink horizontally.

## 1.6. Preparation for an X-ray Diffraction Experiment

You should now perform the real X-ray diffraction experiment using one of the crystals you have just grown. However, you should be aware of an important difference between crystals of small molecules and crystals of a protein. In protein crystals, the spherical or egg-shaped molecules are loosely packed with large solvent-filled holes and channels, which normally occupy 40–60% of the crystal volume. This is an advantage for the reaction of the protein with small reagent molecules; they can diffuse through these channels and reach reactive sites on all protein molecules in the crystal. However, the high solvent content causes problems in handling the crystals because loss of solvent destabilizes the crystals. Therefore, protein crystals should always be kept in their mother liquor, in the saturated vapor of their mother liquor, or at a sufficiently low temperature to prevent evaporation of the solvent.

For the collection of X-ray data at or near room temperature, the crystal is inserted into a thin-walled capillary of borosilicate glass or quartz. The classical procedure for this operation is shown in Figure 1.9. For beginners, this can be a rather frustrating method mainly due to the fragility of the glass capillary. Alternative methods have some advantages but also disadvantages—for instance, using a thin-walled polyester tube instead of the glass tube (Kalinin et al., 2005; Kalinin and Thorne, 2005). This material is strong but allows some evaporation

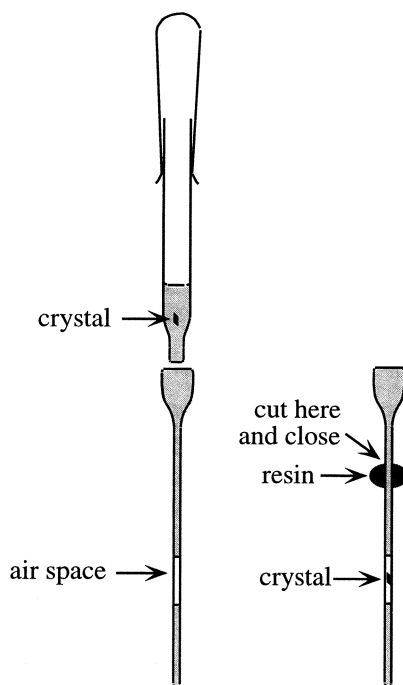


Figure 1.9. Mounting a protein crystal in a glass capillary between layers of its mother liquor.



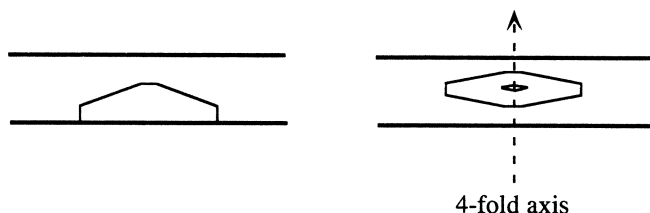


Figure 1.10. Two perpendicular views of a lysozyme crystal mounted in a capillary. The size of the crystal is 0.2–0.5 mm.

of the solvent. In another method, the crystal is lifted from the solution in which it has grown with a small loop made from a thin fiber (Teng, 1990). Surface tension keeps the crystal in a thin liquid layer spanning the loop. The loop with the crystal is inserted into the capillary that contains some mother liquor at its closed end. The crystal can be removed from the loop to the glass wall by gentle touching. A small amount of mother liquor is inserted, leaving the crystal in an air space between two liquid layers. Finally, the capillary is closed. This can be done with a resin that can be melted using a soldering iron. Although this method is more convenient than the classical procedure, the chance that the crystal dries before it is protected by the mother liquor on both sides is rather high (Basavappa et al., 2003; Mac Sweeney and D’Arcy, 2003). For your first data collection, the crystal will be mounted in a glass capillary. You can choose either the classical (Figure 1.10) or the loop technique.

---

**Warning!** The human body should not be exposed to X-rays because of their damaging effect on tissues

---

The crystal in its capillary is attached to a goniometer head (Figure 1.11). This gadget has two perpendicular arcs, allowing rotation of the crystal along two perpendicular axes. For further adjustment and centering, the upper part of the goniometer head can be moved along two perpendicular sledges. After preadjustment under a microscope, the goniometer head is screwed on to an area detector. At this point, you need the assistance of a colleague with experience in handling the area detector.

Be sure that the crystal is in the X-ray beam path and adjust it with its four-fold symmetry axis along the direction of the X-ray beam. Observe the X-ray pattern with the crystal oscillating over a tiny angle (e.g.,  $0.15^\circ$ ). You will see reflection spots arranged in circles (Figure 1.12a). These circles can be regarded as the intersection of a series of parallel planes with a sphere (Figure 1.13). Try to adjust the orientation of the crystal such that the planes are perpendicular to the X-ray beam. The inner circle will then disappear and the others will be concentric around the beam, which is hidden by the beamstop. From this position oscillate the crystal over a  $3^\circ$  range; many more reflections appear on the screen. The inner circle appears again and you observe that the plane to which it corresponds has



Figure 1.11. A goniometer head.

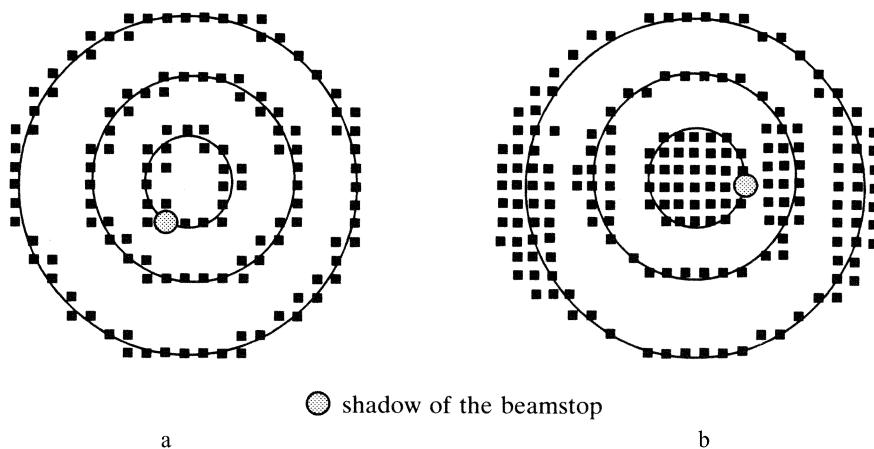


Figure 1.12. (a) A schematic representation of the diffraction pattern of a stationary lysozyme crystal. The diffraction spots are arranged in circles. The innermost circle passes through the origin, which is behind the beamstop. The latter prevents the strong primary beam to reach and damage the detector. (b) A  $3^\circ$  oscillation picture of the same lysozyme crystal.

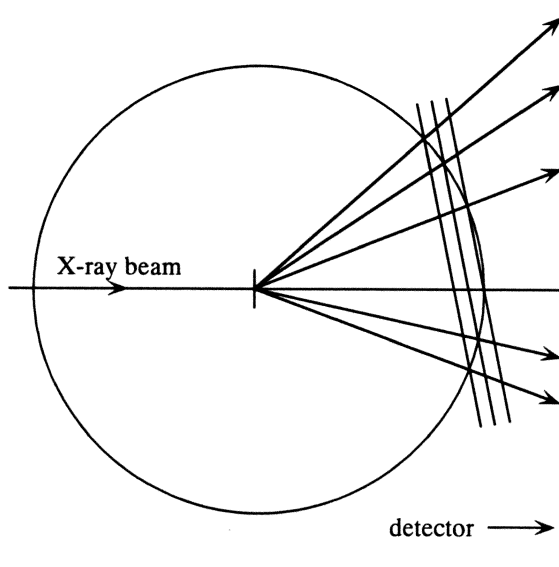


Figure 1.13. Diagrammatic representation of the generation of an X-ray diffraction pattern. The circles shown in Figure 1.12a can be regarded as the intersection of a series of parallel planes with a sphere. The planes are part of a lattice composed of diffraction spots. However, diffraction occurs only if the spots are on, or pass through, the surface of the sphere. The planes are determined by the lysozyme crystal and the sphere is determined by the wavelength of the X-ray radiation (see Chapter 4).

spots nicely arranged in perpendicular rows (Figure 1.12b). This is true for all planes and your crystal produces thousands of diffraction spots in a well-ordered lattice.

From their intensities, the structure of the molecules can be derived, and from the position of the spots, the repeating distances  $d$  in the crystal can be derived. The well-known Bragg<sup>5</sup> law relates  $d$  to the angle of reflection ( $\theta$ ) and the X-ray wavelength  $\lambda$  (Figure 1.14):

$$2d \sin \theta = \lambda$$

<sup>5</sup> W.L. Bragg was a 22-year-old student at Cambridge (UK) when he introduced his law by recognizing that the diffraction pattern of a crystal could be interpreted as reflection from planes in the crystal. He wrote later that it was an easily earned honor to have it named after him because, after all, it was “merely the familiar relation giving the colors reflected by thin films.” This discovery, published in 1913, was soon followed by structure determinations of crystalline sodium chloride and many mineral crystals. This was performed in close cooperation with his father W.H. Bragg. After his appointment as Cavendish Professor of Experimental Physics, in Cambridge, in 1938, he strongly promoted the first struggles toward the determination of a protein structure at atomic resolution. When W.L. Bragg died in 1971 he had seen the enormous progress by X-ray crystallography on structure determinations from small inorganic compounds to highly complicated biological structures.

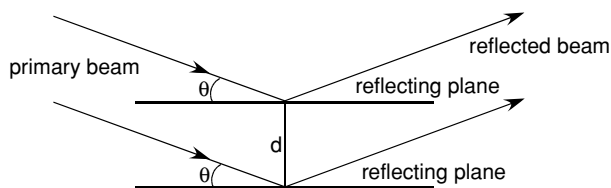


Figure 1.14. Reflection of the primary beam from lattice planes in the crystal according to Bragg's law.

The mercury derivative crystals will produce the same pattern as crystals of the native enzyme. However, close inspection will show that although the position of the spots is the same, the intensity of the diffracted beams is slightly different.

## 1.7. Cryocooling

Complete datasets are often collected with the protein crystal in a stream of cold nitrogen gas at a temperature in the range of 100–120 K with a stability of 1 K. The main reason for cooling protein crystals is that they are liable to radiation damage if exposed to X-rays, and this damage can be so serious that the X-ray pattern dies away after a few hours of exposure at room temperature. Cooling the crystals slows the destructive process appreciably (Section 3.8 of Chapter 3). The method and its development are extensively discussed by Garman and Schneider (1997), Garman (1999), Garman (2003) and Garman and Owen (2006). Cooling the crystals from room temperature to cryogenic temperature must occur suddenly, because the water in the mother liquor and in the crystal must freeze to a vitreous structure. The water should not crystallize because ice formation would damage the protein crystal structure by expanding the water structure in its transition to crystalline ice. Therefore, the method is called flash freezing or shock cooling. To prevent ice formation in and around the crystal, it is carefully transferred to a solvent containing an antifreeze that acts as a cryoprotectant. Glycerol, MPD, ethyleneglycol, and low-molecular-weight PEG are popular cryoprotectants. It is an advantage if the crystal was already grown in the presence of a cryoprotectant (e.g., an alcohol). A high salt concentration in the original mother liquor can cause problems because of precipitation of the salt in the cryoprotectant-containing solution and cracking the crystals. The salt must then be replaced by a more soluble salt or by additional cryoprotectant.

The effect of cooling is often small changes in cell dimensions and an increased divergence of the diffracted beams caused by strain developed in the crystal (increased mosaicity, Figure 4.29 of Chapter 4). This must be kept within acceptable limits.

Cooling is accomplished by nitrogen gas, boiled off from liquid nitrogen (boiling point 77 K at atmospheric pressure) or cooled in a heat exchanger. The accumulation of ice on the crystal and on the diffraction instrument is a problem.

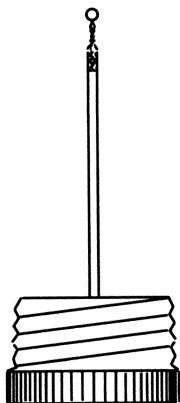


Figure 1.15. A cryoloop, approximately the size of the crystal, is mounted in a metal capillary that can be fixed to a base. This base has a magnetic plate at the bottom to attach it quickly to a goniometer head. The base can also be screwed to a cap for transport and storage.

To prevent its growth on the protein crystal, the cold gas stream is coaxially surrounded by a warm and dry stream of air or nitrogen. Turbulence between the two streams must be avoided by adjusting their flow speed. Ice formation can further be prevented by enclosing the entire diffraction apparatus in a box.

---

**Warning!** When working with liquid nitrogen, take the necessary precautions. For instance, always wear goggles and gloves when filling Dewars. Moreover, the room where liquid nitrogen evaporates should be well ventilated. Volatile organic cryogenes (e.g., propane) require additional precautions because there is danger of explosion and fire.

---

Because data collection with cryocooling is currently common practice, mounting a protein crystal in a glass capillary is no longer an advisable procedure. Instead, the crystal is mounted in a small loop made from a thin fiber (Teng, 1990) or, even better, in a lithographically produced hole in Mylar film.<sup>6</sup> Surface tension in the liquid keeps the crystal in the thin liquid layer spanning the loop. The size of the loop should approximate the size of the crystal or a little larger (“lasso technique”). If the liquid has a low surface tension, it might not hold the crystal in the loop. Under these conditions, a loop slightly smaller than the crystal should be chosen (“spatula technique”). Rayon or nylon fibers are preferred, but glass fibers—although somewhat brittle—are also suitable. Both ends of the loop are cemented in a capillary (Figure 1.15).

The thin capillary is fixed into a base that can accurately and quickly be positioned on the top of a goniometer head. It can also be screwed into a cap for transport and storage. Data collection with flash freezing always starts by determining the optimal conditions as to the kind and concentration of cryoprotectant. Salts must be replaced if required. A crystal is picked up from the solution with

---

<sup>6</sup>Litholoops are supplied by Molecular Dimensions, [www.moleculardimensions.com](http://www.moleculardimensions.com).

the loop and—to prevent loss of solvent by evaporation—as quickly as possible transferred to the cold nitrogen stream close to the cryonozzle. Alternatively, the crystal is dropped into liquid propane or immersed into liquid nitrogen for fast cooling and from there transferred to the cold nitrogen stream. The crystal is now ready for data collection. The diffraction pattern must be checked for strain in the crystal causing increased mosaicity. If the flash-cooled crystal shows unacceptably high mosaicity, it is sometimes helpful to “anneal” it: The crystal is quickly transferred from cryogenic conditions to the original cryosolvent at the temperature the crystal was grown, and it is incubated for at least 3 min before reflash cooling (Harp et al., 1998).

Additional advantages of cryocrystallography are as follows:

- The crystals can be stored and transported at liquid-nitrogen temperature for data collection at a later stage.
- There is less absorption by surrounding nonprotein material than in the capillary technique.

## 1.8. Notes

1. **Crystallization.** The first essential step in determining the X-ray structure of a protein is to grow crystals of sufficient size and quality. It is always amazing to see that these large molecules can arrange themselves so neatly that crystals with flat faces and sharp edges grow. There is great excitement in the laboratory when the first crystals of a protein appear and the excitement is even greater if those crystals produce a high-quality X-ray diffraction pattern. Although more steps are required to complete a structure determination, the growth of good quality crystals indicates a reasonable chance of success and suggests that the protein structure can indeed be determined.

What are the best conditions for crystal growth? Can they be predicted? These questions are difficult to answer for proteins because so many parameters play a role. In general, the chances of growing good quality crystals are higher if the protein solution is monodisperse (all molecules of the same size) (Ferré-d’Amaré and Burley, 1994). George and Wilson (1994) proposed to use the second virial coefficient as a predictor. They found that this coefficient is, for a protein solution, within a restricted value range for conditions under which good quality crystals can be grown. If it is outside that range, the chance of growing good crystals is low. The second virial coefficient is a measure of the interaction between the protein molecules in the solution and can be derived, for instance, from static light-scattering experiments.

However, choosing a crystallization technique and crystallization conditions is largely a matter of taste. The hanging or sitting drop methods are the most popular. Liquid–liquid diffusion in a small-bore capillary has the advantage of being somewhat slower in reaching equilibrium and this is sometimes an advantage. Dialysis is not frequently used, but it must be applied for salting-in precipitation.

After preparing the crystallization experiments, leave them in a quiet place with a minimum of vibration and keep the temperature fairly constant.

Protein crystallization is in essence a trial-and-error method, and the results are usually unpredictable. Serendipity also plays a role. In the author's laboratory a failure in the air-conditioning system, causing an unexpected rise in temperature, led to the growth of perfect crystals of an enzyme, which could not be obtained under more normal circumstances.

Commercially available robots make it possible to perform more experiments in the same time and to determine the optimum crystallization conditions more quickly. However, human intelligence is still required to tell the robot what to do. Useful hints for crystallization are presented in Chapter 16.

If crystallization does not occur, even after many experiments, the following can be tried:

- a. Crystallization of a homologous protein from another source.
- b. Crystallization of one or more proteolytic fragments of the protein. The polypeptide chain of the native protein is split by a proteolytic enzyme at a limited number of positions, or, alternatively, the required fragment is expressed and purified from a bacterial or eucariotic expression system.
- c. Engineering the protein, for instance by mutating surface residues or by removing flexible parts. The latter are particularly notorious in inhibiting crystallization. Pantazatos et al. (2004) have developed a rapid and efficient method to detect flexible parts in a protein structure. It is based on the much more rapid hydrogen exchange in disordered regions than in more static parts of the structure.

**2. Mounting the crystals.** X-ray capillaries are very fragile because of their thin glass wall. Why not mount them in a stronger glass tube? Although you can see the crystal just as well through a much thicker glass wall, X-rays cannot. A glass plate of 0.01 mm thickness has 93% transmission for the common X-ray wavelength of 1.54 Å, but this diminishes exponentially with increasing thickness of the glass (Table 1.1). The data show that transmission is highly dependent on the X-ray wavelength and is much higher for a shorter wavelength. This is one of the reasons that X-ray data collection at a synchrotron is preferably done around 1 Å instead of 1.5 Å, the usual wavelength in the home laboratory. The disadvantage of a lower diffraction intensity at shorter wavelength is compensated by the strong intensity of the synchrotron X-ray beam. Other advantages of a shorter wavelength

Table 1.1. Transmission Through Pyrex Glass

	Glass thickness (mm)	Transmission (%)
$\lambda = 1.54 \text{ \AA}$ (X-ray tube with Cu anode)	0.01	93
	0.1	50
	1.0	0.01
$\lambda = 0.71 \text{ \AA}$ (X-ray tube with Mo anode)	0.1	93
	1.0	40

are the more favorable crystal lifetime and better laser response for a detector with a fluorescent screen.

X-ray wavelength and atomic distances are usually expressed in Ångström units:  $1 \text{ \AA} = 10^{-10} \text{ m} = 10^{-1} \text{ nm}$ . Although the Ångström unit is not an SI unit, it has the advantage of giving simpler numbers. For example, the C–C distance in ethane is  $1.54 \text{ \AA}$ , and a frequently used wavelength in the X-ray diffraction of proteins is  $1.5418 \text{ \AA}$ . Sometimes the photon energy ( $E$ ) is given instead of the wavelength  $\lambda$ . The relationship is  $\lambda$  (in  $\text{\AA}$ ) =  $12.398/E$  (in keV).

3. **The X-ray pattern.** You have observed X-ray diffraction spots nicely arranged in rows. You should compare this with the laser + electron microscope grid experiment. There you saw a two-dimensional diffraction pattern with rows of spots produced by a two-dimensional grid and the diffraction pattern was reciprocal to the actual electron microscope grid. A crystal can be regarded as a three-dimensional grid and you can imagine that this will produce a three-dimensional X-ray diffraction pattern. As with the electron microscope grid, the pattern is reciprocal to the crystal lattice.

Although Bragg's law for diffraction by a crystal can easily be explained as a reflection from planes in the crystal, two questions remain: What is the nature of the lattice planes, and why do they reflect the X-ray beam as if they were mirrors? These questions will be answered in Chapter 4.

Diffraction can also be explained from a different point of view. The planes that intersect the sphere in Figure 1.13 are layers in a three-dimensional lattice that is not the crystal lattice, but its reciprocal lattice. The unit cell distances in this lattice are reciprocally related to the unit cell distances in the crystal and that is why the lattice is called a reciprocal lattice.

The reciprocal lattice is an imaginary but extremely convenient concept for determining the direction of the diffracted beams. If the crystal rotates, the reciprocal lattice rotates with it. In an X-ray diffraction experiment, the direction of the diffracted beams depends on two factors: the unit cell distances in the crystal from which the unit cell distances in the reciprocal lattice are derived and the X-ray wavelength.

As indicated in Figure 1.13, diffraction conditions are determined not only by the reciprocal lattice but also by the radius of the sphere, which is called the sphere of reflection or "Ewald sphere."<sup>7</sup> Its radius is reciprocal to the wavelength  $\lambda$ ; it is equal to  $1/\lambda$ . From the diffraction experiment with lysozyme, you can determine that not all diffracted beams occur at the same time. Only the ones corresponding to reciprocal lattice points on the Ewald sphere in Figure 1.13 are actually observed. Other points can be brought to diffraction by rotating the crystal and with it the reciprocal lattice, to bring these new lattice points on the sphere.

Diffracted beams are often called "reflections." This is due to the fact that each of them can be regarded as a reflection of the primary beam against planes in

---

<sup>7</sup> Paul P. Ewald, 1888–1985, professor of physics at several universities in Europe and the United States, was the first to apply the reciprocal lattice and the sphere named after him to the interpretation of an X-ray diffraction pattern.



the crystal. The relation between this Bragg reflection and the reciprocal lattice description is explained in Chapter 4.

## Summary

Protein crystal growth is mainly a trial-and-error process, but the primary rule is that the protein should be as pure as possible. The higher the purity, the better the chance of growing crystals by batch crystallization, by liquid–liquid or vapor diffusion, or by dialysis. The experiment with the hen egg white lysozyme, the growth of nicely shaped crystals, and the huge number of reflections in the X-ray diffraction pattern have provided an introduction to protein X-ray crystallography. From the X-ray diffraction experiment, it became clear that the X-ray pattern can be regarded as derived from the intersection of a lattice and a sphere. This lattice is not the crystal lattice but the reciprocal lattice, which is an imaginary lattice related to the crystal lattice in a reciprocal way. The sphere is called the Ewald sphere and has a radius of  $1/\lambda$ . An alternative and much more illuminating way is to regard X-ray diffraction as reflection from planes in the crystal. Bragg suggested this and his famous law is:

$$2d \sin \theta = \lambda.$$

Full X-ray datasets are usually collected in cryo conditions, preferably at a synchrotron with the crystal mounted in a loop together with a thin liquid layer. For room-temperature data collection, the crystal must be mounted in a thin-walled glass, quartz, or polyester capillary.

# Chapter 2

## X-ray Sources and Detectors

### 2.1. Introduction

In Chapter 1 you learned how crystals of a protein can be grown and you observed a diffraction pattern. The crystalline form of a protein is required to determine the protein's structure by X-ray diffraction, but equally necessary are the tools for recording the diffraction pattern. These will be described in this chapter on hardware. The various X-ray sources and their special properties are discussed, followed by a description of cameras and detectors for quantitative and qualitative X-ray data collection.

### 2.2. X-ray Sources

The main pieces of hardware needed for the collection of X-ray diffraction data are an X-ray source and an X-ray detector. X-rays are electromagnetic radiation with wavelengths of  $10^{-7}$ – $10^{-11}$  m (1000–0.1 Å). Such radiation was discovered by Roentgen<sup>1</sup> in 1895, but as the nature of the radiation was not yet understood, Roentgen called them X-rays. Von Laue's<sup>2</sup> diffraction theory, which he developed around 1910, inspired his assistants, Friedrich and Knipping, to use a crystal as a diffraction grating. Their results, published in 1912, were direct proof for the existence of lattices in crystals and for the wave nature of X-rays.

For the X-ray diffraction experiment with lysozyme crystals in Chapter 1, an X-ray generator in the home laboratory was used. These are typically either a

---

<sup>1</sup> Wilhelm Conrad Roentgen, 1845–1925, discovered X-rays on November 8, 1895 in Würzburg, Germany.

<sup>2</sup> Max von Laue, 1879–1960, German physicist, developed the theory of X-ray diffraction by a three-dimensional lattice.

generator with a sealed tube and fixed target or a more powerful system with a rotating anode. Both instruments are push-button operated but require some maintenance:

1. A sealed tube must be replaced if the filament burns out.
2. A rotating anode tube occasionally needs a new filament (cathode) and new seals.

Particle accelerators as synchrotrons and storage rings are the most powerful X-ray sources, but they are so complicated technically that the X-ray crystallographer is just a user at the front end. Because protein molecules are very large, their crystals diffract X-ray beams much less than do crystals of small molecules. The reason is that diffraction is a cooperative effect between the molecules in the crystal; for larger molecules, there are fewer in a crystal of same size and therefore the diffracted intensity is lower. Moreover, proteins consist mainly of C, N, and O. These are light elements with only a few electrons (6–8) per atom. Because the electrons are responsible for the diffraction, atoms of these light elements scatter X-rays much more weakly than do heavier elements. Because of this phenomenon of relatively low scattering power, protein crystallographers prefer a high-intensity source: a rotating anode tube or a much stronger synchrotron X-ray source rather than a sealed tube.

### 2.2.1. Sealed X-ray Tubes

In a sealed X-ray tube a cathode emits electrons (Figure 2.1). Because the tube is under vacuum and the cathode is at a high negative potential with respect to the metal anode, the electrons are accelerated and reach the anode at high speed. For protein X-ray diffraction, the anode is usually a copper plate onto which the electron beam is focused, to a focal spot, normally  $0.4 \times 8$  mm. Most of the electron energy is converted to heat, which is removed by cooling the anode, usually with water. However, a small part of the energy is emitted as X-rays in two different ways: as a smooth function of the wavelength and as sharp peaks at specific wavelengths (Figure 2.2). The continuous region is due to the physical phenomenon that decelerated (or accelerated) charged particles emit electromagnetic radiation called “Bremsstrahlung.” This region has a sharp cutoff at the short-wavelength side. At this edge, the X-ray photons obtain their full energy from the electrons when they reach the anode. The electron energy is  $e \times$  (accelerating voltage  $V$ ), where  $e$  is the electron charge. The photon energy is  $h\nu = hc/\lambda$ , where  $h$  is Planck’s constant,  $\nu$  is the frequency of the radiation,  $c$  is the speed of light, and  $\lambda$  is the wavelength. Therefore,

$$\lambda_{\min} = \frac{hc}{eV} = \frac{12.4}{V},$$

where  $V$  is in kilovolts. At  $V = 40$  kV the cutoff edge is at  $0.31 \text{ \AA}$ .

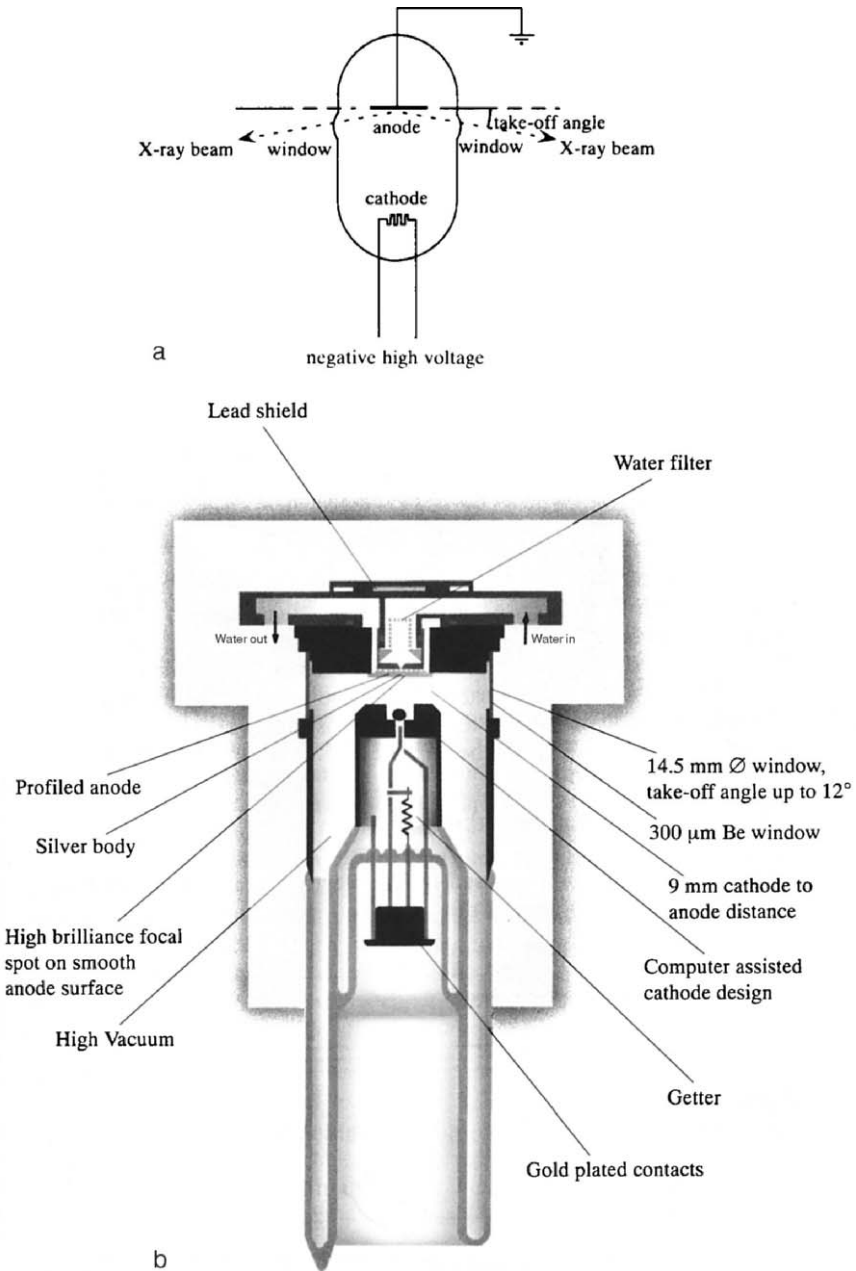


Figure 2.1. (a) A schematic drawing of a sealed X-ray tube. The windows are made of thin beryllium foil that has a low X-ray absorption. (b) Cross section of an X-ray tube: (Courtesy of Philips, Eindhoven, The Netherlands.)

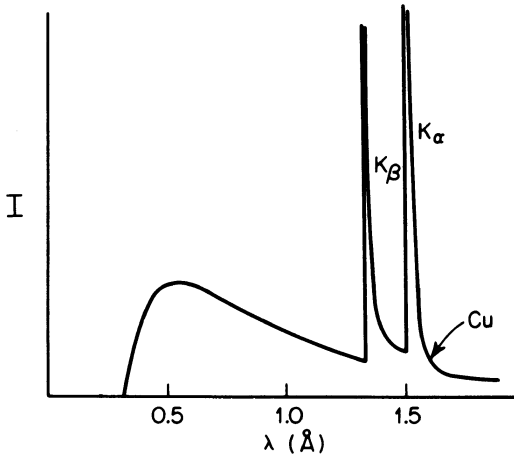


Figure 2.2. The spectrum from an X-ray tube with a copper anode. It shows a continuous spectrum and two sharp peaks due to quantized electrons in the copper.  $I$  is the energy of the emitted radiation on an arbitrary scale.

The sharp peaks in the spectrum are due to electron transitions between inner orbitals in the atoms of the anode material. The high-energy electrons reaching the anode shoot electrons out of low-lying orbitals in the anode atoms. Electrons from higher orbitals occupy the empty positions and the energy released in this process is emitted as X-ray radiation of specific wavelength:  $K_{\alpha}$  radiation if it comes from a transition from the L-shell to the K-shell and  $K_{\beta}$  for a transition from the M-shell to the K-shell. Because of the fine structure in the L-shell,  $K_{\alpha}$  is split into  $K_{\alpha}(1)$  and  $K_{\alpha}(2)$ . The energy levels in the M-shell are so close that for  $K_{\beta}$ , one wavelength value is given (Figure 2.3).

When copper is the anode material the following values for  $\lambda$  are given:

	$\lambda$ (Å)	
$K_{\alpha}(1)$	1.54051	The weight average value for $K_{\alpha}(1)$ and $K_{\alpha}(2)$ is taken as 1.54178 Å because the intensity of $K_{\alpha}(1)$ is twice that of $K_{\alpha}(2)$
$K_{\alpha}(2)$	1.54433	
$K_{\beta}$	1.39217	

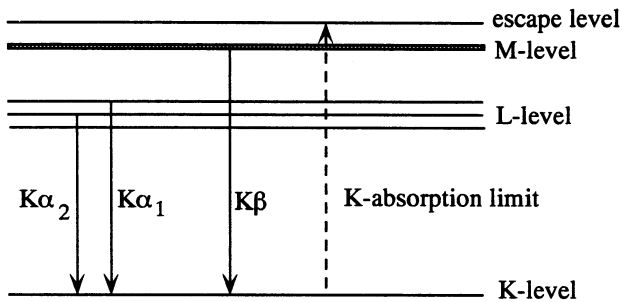


Figure 2.3. Schematic representation of the atomic energy levels and transitions causing characteristic X-ray wavelengths.

For emission of the characteristic lines in the spectrum, a minimum excitation voltage is required. For example, for the emission of the  $\text{CuK}_\alpha$  line,  $V$  should be at least 8 kV. If a higher voltage is applied, the intensity of the line is stronger with respect to the continuous radiation, up to about  $V/V_{\min} = 4$ . The intensity of the line is also proportional to the tube current, at least as long as the anode is not overloaded. A normal setting is  $V = 40$  kV with a tube current of 37 mA for a 1.5-kW tube.

### 2.2.2. Rotating Anode Tubes

The heating of the anode caused by the electron beam at the focal spot limits the maximum power of the tube. Too much power would ruin the anode. This limit can be moved to a higher power loading if the anode is a rotating cylinder instead of a fixed piece of metal. With a rotating anode tube, small source widths (0.1–0.2 mm) with a high brilliance<sup>3</sup> are possible. The advantage over the sealed tube is the higher radiation intensity and a disadvantage is that it requires continuous pumping to keep the vacuum at the required level.

The take-off angle (Figure 2.1a) is usually chosen near  $4^\circ$ . Then the observer “sees” the focal spot with dimensions of  $0.4 \times 0.5$  mm for a sealed tube or smaller for a rotating anode tube. Higher brilliance could be obtained with a smaller take-off angle, but a smaller angle results in a longer X-ray path in the anode material and, therefore, higher absorption and lower beam intensity.

### 2.2.3. Synchrotron Radiation

Synchrotrons are devices for circulating electrically charged particles (negatively charged electrons or positively charged positrons) at nearly the speed of light [a detailed discussion is given in Helliwell (1992)]. The particles are injected into the storage ring directly from a linear accelerator or through a booster synchrotron (Figure 2.4a). Originally these machines were designed for use in high-energy physics as particle colliders. When the particle beam changes direction, the electrons or positrons are accelerated toward the center of the ring and therefore emit electromagnetic radiation and, consequently, lose energy. This energy loss is compensated for by a radio-frequency input at each cycle. The physicists’ main aim was to study colliding particles; they were not interested in the radiation, which they regarded as an annoying byproduct and wasted energy. However, chemists and molecular biologists discovered (Rosenbaum et al., 1971) that the radiation was a useful and extremely powerful tool for their studies to the extent that radiation-dedicated synchrotrons have been constructed.

Since those early days, the use of synchrotron X-ray sources for macromolecular crystallography has increased enormously. Due to improvement of the

---

<sup>3</sup> Brilliance is defined as number of photons/sec/mrad<sup>2</sup>/mm<sup>2</sup>/0.1% relative bandwidth.

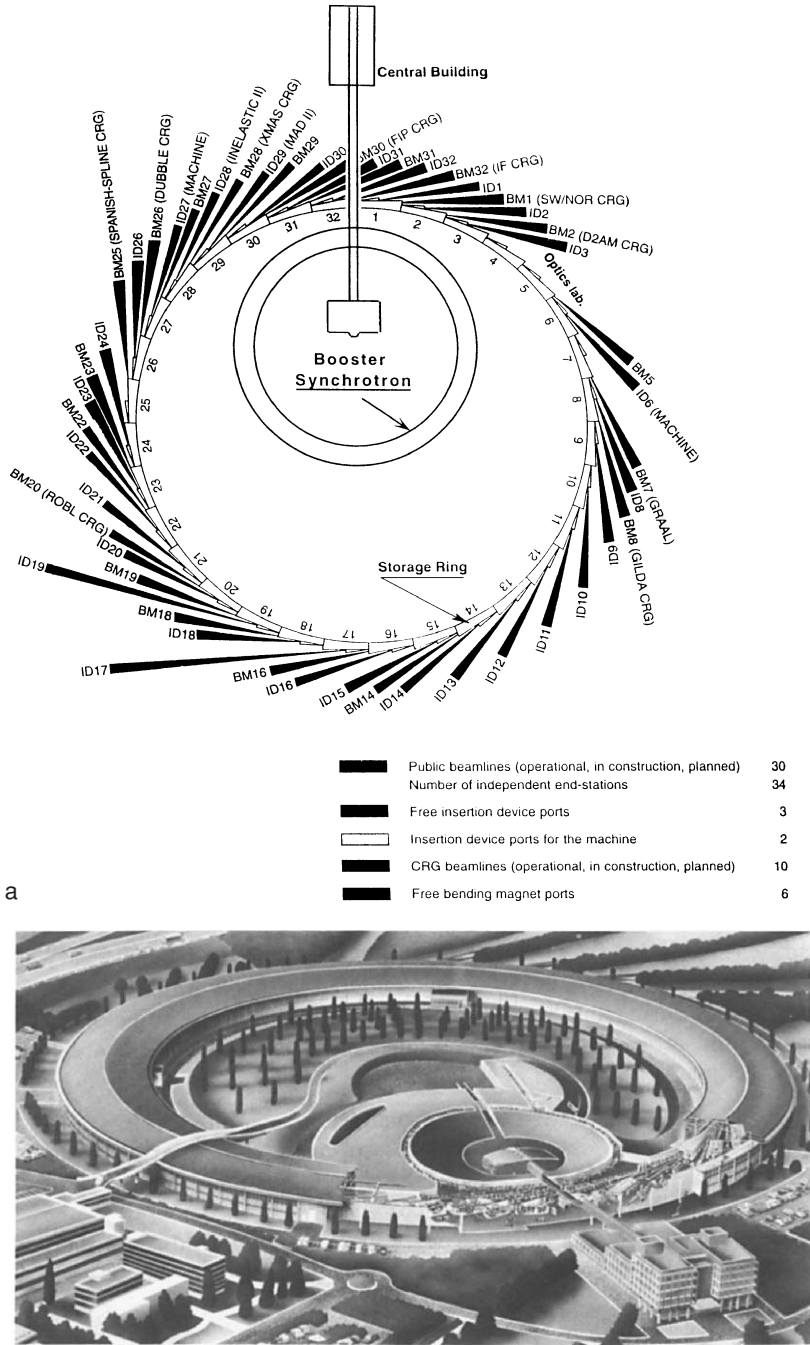


Figure 2.4. The European Synchrotron Radiation Facility (ESRF) in Grenoble, France. (a) The booster synchrotron and the storage ring are drawn with the large number of beamlines. (b) An artist's rendition of the Facility. (Reproduced with permission from ESRF.)

synchrotrons and technical developments in X-ray detectors as well as application of cryocrystallography, complete X-ray datasets can now be collected within a few hours. In addition, the highly increased need for a multiple-wavelength source (for MAD (multiple wavelength anomalous diffraction), see Chapter 9) has made a synchrotron trip standard procedure for the macromolecular X-ray crystallographer. Useful hints are given by Mitchell et al. (1999). Hendrickson (2000) presented the development of synchrotrons and their application to biological macromolecules.

Synchrotrons are extremely large and expensive facilities: the ring has a diameter of 10 to a few hundred meters. The trajectory of the particles is determined by their energy and by the magnetic field, which causes the charged particles to change their direction. There are four types of magnetic devices in storage rings:

1. *Bending magnets* needed to guide the electrons in their orbit. The other three devices extend the spectrum to shorter wavelength. These devices can be inserted into straight sections and give no net displacement of the particle trajectory.
2. A *wavelength shifter*, with a stronger local magnetic field and a sharper curvature than the bending magnets.
3. A *wiggler*, producing a number of sharp extra bends in the electron trajectory.
4. An *undulator*, similar to a wiggler but with the difference that interference effects cause the emission of radiation at more specific wavelengths.

Because freely traveling electrons (and positrons) are not quantized, the radiation ranges over a wide wavelength region depending on the energy of the charged particles and on the strength of the magnetic field. A useful quantity is the median of the distribution of power over the spectral region, called the critical photon energy  $E_c$ ; it divides the power spectrum into two equal energy parts:

$$E_c = 0.665E^2B \quad \text{or} \quad \lambda_c = \frac{18.64}{E^2B}. \quad (2.1)$$

$E_c$  is in keV and  $E$  is the circulating power in GeV:

$$E = \frac{\text{particle energy} \times \text{current}}{\text{revolution frequency}}, \quad (2.2)$$

$B$  is the magnetic field strength in T, and  $\lambda_c$  is in Å. The main photon flux is close to  $E_c$ , but above  $E_c$ , it drops exponentially as a function of the photon energy (Figure 2.5). The European Synchrotron Radiation Facility (ESRF) in Grenoble (Figure 2.4b) has a circumference of 844.39 m, is operated with an energy of 6 GeV, and has bending magnets with a 0.86-T field strength. Therefore,  $\lambda_c$  is 0.6 Å. The features of the ESRF synchrotron are presented in detail by Lindley (1999).

The radius of a storage ring depends on  $E$  and  $B$ : It is proportional to  $E$  and inversely proportional to  $B$ . If one wants to design a synchrotron for the home laboratory, relatively small dimensions of the instrument are required and therefore  $E$  should be low and  $B$  high. The most powerful superconducting magnets for laboratory use are found in nuclear magnetic resonance (NMR) instruments; they have a field strength of  $B = 15$  T. If  $\lambda_c$  has to be 0.6 Å for the home instrument, as it is for the Grenoble facility, and assume that suitable magnets of 15 T can be



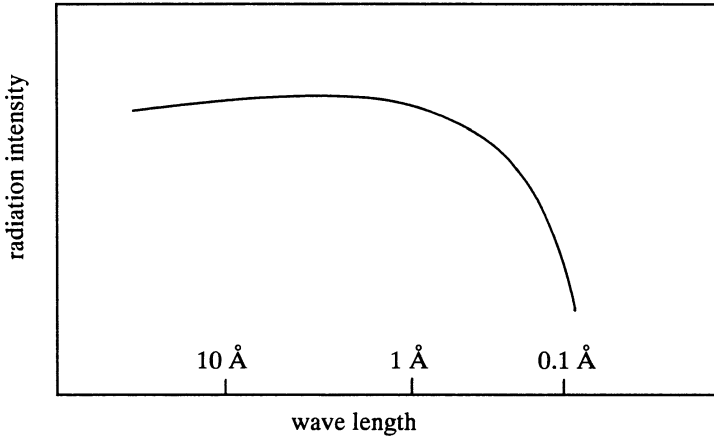


Figure 2.5. A typical curve of radiation intensity as a function of wavelength for a synchrotron radiation source.

constructed, we calculate the following for  $E$ :

$$E = \sqrt{E^2} = \sqrt{\frac{18.64}{\lambda_c B}} = 1.44 \text{ GeV}$$

The diameter of the instrument would then be  $\sim 4$  m. However, the feasibility of such a project also depends on other factors, such as the injection system, which must be at least 50 m in length. Other problems are the spreading of the beam and the slow rate at which the magnetic field can be increased after beam injection.

### 2.2.3.1. Insertion Devices

1. The wavelength shifter. According to Equation (2.1), the critical photon energy  $E_c$  is determined by  $E$  and  $B$ .  $E$  is everywhere constant in the ring, but the magnetic field strength  $B$  can be increased locally, resulting in an increase of  $E_c$  and the production of higher-intensity X-rays at a shorter wavelength. A schematic of a wavelength shifter is shown in Figure 2.6.

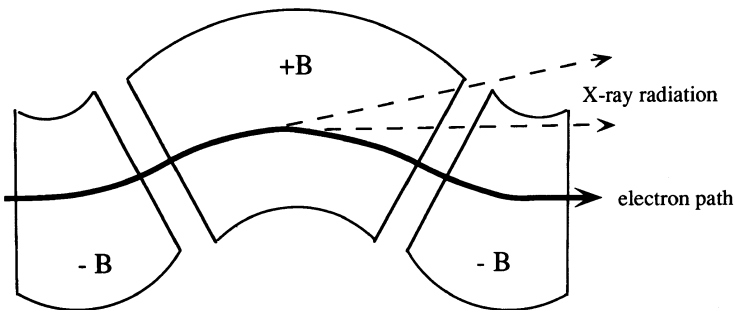


Figure 2.6. A wavelength shifter.  $B$  is the magnetic field strength. The emission of radiation comes essentially from the top of the bump in the electron path.

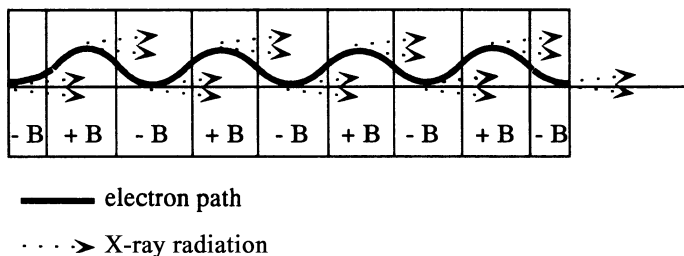


Figure 2.7. A multipole wiggler.  $B$  is the magnetic field strength.

2. The multipole wiggler. A series of wavelength shifters constitutes a multipole wiggler (Figure 2.7). The radiation from consecutive magnets is independent and adds up incoherently in the general direction of propagation of the electron beam. The total flux is simply  $2N$  times the flux generated by a single period, where  $N$  is the number of periods. It is easily tunable to the desired wavelength.
3. The undulator. Undulators are multipole wigglers but with moderate magnetic fields and a large number of poles close together. The effect of this difference is that in the undulator, strong interference occurs between the radiation from the consecutive magnets, which results in a spectral profile with a peak at a specific wavelength and a few harmonics. The radiation is tunable by adjustment of the magnetic pole piece distance. Its emitted intensity can be  $N^2$  times that of a single period, with  $N$  the number of poles. Moreover, the beam divergence of the radiation from an undulator is extremely small.

### 2.2.3.2. Properties of Synchrotron Radiation

#### Intensity

The main advantage of synchrotron radiation for X-ray diffraction is its high intensity, which is two orders of magnitude stronger than for a conventional X-ray tube, at least for radiation from a bending magnet. For radiation from a multipole wiggler or an undulator, it is again a few orders of magnitude stronger. This high intensity is profitably used by protein X-ray crystallographers for data collection. Another advantage is the low divergence of the beam resulting in sharper diffraction spots.

#### Tunability

Synchrotron radiation also differs from tube radiation in its tunability. Any suitable wavelength in the spectral range can be selected with a monochromator. This property is used in multiple-wavelength anomalous dispersion (Section 9.5 of Chapter 9) and for Laue diffraction studies (Chapter 12). In the latter method, a wide spectral range is used. Several types of modern detector for X-ray radiation have fluorescent material as their X-ray-sensitive component. This is more sensitive for radiation with a shorter wavelength (e.g.,  $1 \text{ \AA}$  instead of the conventional  $1.5 \text{ \AA}$  from a copper target). Therefore, in protein X-ray diffraction experiments, a

synchrotron is tuned to  $1 \text{ \AA}$  or even a shorter wavelength. The additional advantage of this shorter wavelength is lower absorption along its path and in the crystal. Moreover, radiation damage to the protein crystal is appreciably reduced and, often, all required diffraction data can be collected from just one crystal, especially if the crystal is flash frozen and held at 100 K.

### Lifetime

The lifetime of a storage ring filling is limited. Typical lifetimes are between a few and several hours. When the intensity of the radiation has fallen to a certain minimum value, a new injection is required. The factors determining the lifetime are many and of a complicated nature (e.g., collision with residual gas atoms). The positively charged ions that form accumulate in the electron beam, leading to instabilities in the beam due to the continuous loss of particles. A beam composed of positrons has a longer lifetime than an electron beam, because positrons repel positive ions created in the residual gas, thus avoiding ion trapping in the beam. The beam lifetime in the ESRF is between 50 and 80 h, depending on the current.

### Time Structure

Synchrotron radiation, in contrast to X-ray tube radiation, is produced in flashes by the circulating bunches of charged particles. The ESRF operates in a single-bunch or multibunch mode with a bunch length in the picosecond range. This allows structural changes in the nanosecond timescale to be observed.

### Polarization

The X-ray beam from an X-ray tube is not polarized; synchrotron radiation is highly polarized. If the radiation from a bending magnet is observed in the plane of the orbit, it is fully polarized with the electric vector in the orbit plane (parallel polarization). If the observer moves away from the plane, a small perpendicular component is added. The polarization of the X-ray beam from a synchrotron has not yet found extensive application in X-ray diffraction. However, it must be considered when applying the correct polarization factor (Section 4.14.1 of Chapter 4). Moreover, the polarization of the beam has an effect on the so-called anomalous X-ray scattering of atoms, which occurs when the X-ray wavelength approaches an absorption-edge wavelength (Section 7.8 of Chapter 7).

## 2.3. Monochromators

Except for Laue diffraction, where the crystal is exposed to a spectrum of wavelengths (Chapter 12), monochromatic X-rays are used in all other diffraction methods. Therefore, a narrow wavelength band must be selected from the spectrum supplied by the source. If a sealed X-ray tube with copper anode is the radiation source, the wavelength selected for protein X-ray diffraction is the high-intensity  $K_{\alpha}$  doublet ( $\lambda = 1.5418 \text{ \AA}$ ). The  $K_{\beta}$  radiation can be removed with a nickel filter. A nickel foil of 0.013 mm thickness reduces the  $K_{\beta}$  radiation to 2% and  $K_{\alpha}$  to 66%

of the original intensity. The continuous spectrum is also reduced but certainly not eliminated.

Much cleaner radiation can be obtained with a monochromator. For X-ray radiation from a tube, the monochromator is a piece of graphite that reflects X-rays of 1.5418 Å against its layer structure. The layer distance is the Van der Waals distance of 3.4 Å. By application of Bragg's law,  $2d \sin \theta = \lambda$ , the scanning angle  $\theta$  is easily calculated as 13.1°. Artificially made Bragg reflectors also consist of a multilayer system. They provide a higher energy and can act as collimating mirrors or as focusing mirrors by curving the mirror surface. Because the incident beam is somewhat divergent, scanning angles are not equal at every point of the mirror surface. In confocal max-flux optics, this is compensated for by varying the  $d$ -spacing along the mirror surface.<sup>4</sup> For synchrotron radiation, the preferable monochromators are made of germanium, silicon, or diamond because they select a very narrow wavelength band. Monochromators for synchrotron radiation are of the single or double type. Single monochromators are either flat or bent. The advantage of the bent monochromators is that they focus the divergent beam from the synchrotron, preferably onto the specimen. The focusing is in one direction only, producing a line focus. Focusing in the other direction is obtained with toroidal mirrors made from highly polished quartz or glass. The mirrors are often coated with a thin layer of gold or platinum. The X-ray beam is focused by total reflection. Short wavelengths are absorbed by the mirror instead of reflected. By adjusting the reflection angle, mirrors can be effective as filters to remove harmonics or  $K_{\beta}$ . Thin diamond plates form excellent mirrors because they can withstand an extremely high heat flux without deformation. Because of their high-energy resolution, they are often applied for splitting a synchrotron X-ray beam into a number of beams for different purposes: A first diamond crystal selects and reflects a very narrow wavelength region from the primary beam. The rest of the beam passes through the diamond, still with high intensity, and at least two other reflected beams can be generated with other diamond crystals, selecting slightly different wavelengths. A disadvantage of diamond crystals is their limited size, which restricts their use to the rather narrow undulator beams (Freund, 1996).

The single-type monochromators have a disadvantage: If they are tuned to another wavelength, the scanning angle of the monochromator changes and the entire X-ray diffraction equipment must be moved. This is not necessary for a double monochromator, for which the direction of the beam is independent of the wavelength (Figure 2.8).

## 2.4. Introduction to Cameras and Detectors

In the X-ray diffraction experiment with lysozyme in Chapter 1, a diffraction pattern was observed that could be regarded as corresponding to a three-dimensional lattice, reciprocal to the actual crystal lattice. For a crystal structure determination, the intensities of all (or a great many) diffracted beams must be measured. To do so,

---

<sup>4</sup> [www.osmic.com](http://www.osmic.com).

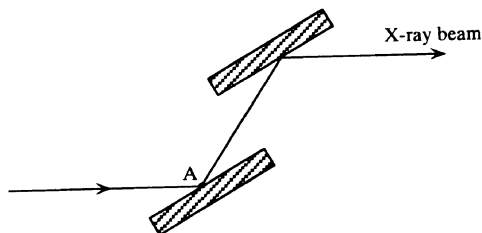


Figure 2.8. A double monochromator. The rotation axis for changing the wavelength is at A, perpendicular to the plane of the page. This gives a small vertical shift to the exit beam after rotation, but the incoming and exit beams are parallel.

all corresponding reciprocal lattice points must be brought to diffracting condition by rotating the lattice (i.e., by rotating the crystal) until the required reciprocal lattice points are on the sphere with radius  $1/\lambda$ . It follows that an X-ray diffraction instrument consists of two main parts:

1. A mechanical part for rotating the crystal.
2. A detecting device to measure the position and the intensity of the diffracted beams; it should be noted that this intensity is always the result of two measurements: the total intensity in the direction of the diffracted beam and, subtracted from it, the background scattering in that same direction.<sup>5</sup>

In the last decades, data collection in protein crystallography has changed tremendously. Formerly, a well-equipped protein crystallography laboratory had some precession cameras, a rotation camera, and a diffractometer. In both types of camera, X-ray film was the detector. The precession camera has the advantage of giving an undistorted image of the reciprocal lattice. Unit cell dimensions and symmetry in the crystal can easily be derived from such an undistorted image as can the quality of the crystal. For full three-dimensional X-ray data collection, the precession camera is not suitable, because it registers one reciprocal layer per exposure.

A rotation camera registers the data more efficiently, but the recognition of the diffraction spots is more complicated. Moreover, for each exposure, the crystal is oscillated over a small angle (e.g.,  $1^\circ$ – $2^\circ$ ) to avoid overlap of spots. Depending on the symmetry in the crystal, the total oscillating range for a complete data collection could be  $60^\circ$ ,  $90^\circ$ , or  $180^\circ$ .

The third classical detector is a computer-controlled diffractometer, which has a single counter—normally a scintillation counter. It measures the diffracted beams with high accuracy but only one at a time. Although it is computer controlled and automatically finds the diffracted beams, it is extremely slow.

The classical picture has been changed completely by the introduction of much faster image plates and electronic area detectors. Rotation “cameras” are now equipped with such a detector, either image plate or electronic area detector, although the principle of the “camera” has not changed. With an image plate, which

<sup>5</sup> Background scattering is mainly caused by the air through which the X-ray beam passes from the collimator to the beamstop. If the air path is long and absorption serious, it can appreciably be reduced if a cone filled with helium is put between the crystal and the plate.

must be read after each exposure, the data collection is still in the “film mode” [i.e., contiguous oscillations over a small angle and reading (analogous to film processing) after each exposure]. If the instrument has an electronic area detector, the oscillations are much smaller (e.g.,  $0.1^\circ$ ) and the data are immediately processed by an online data acquisition system.

Before describing these instruments in some detail, we will discuss the various types of X-ray-detecting system, including their advantages and disadvantages (Gruner, 1994; Helliwell, 1992).

## 2.5. Detectors

### 2.5.1. Single-Photon Counters

Single-photon counters have been used since the early days of X-ray diffraction and are now usually of the scintillation type. They give very accurate results, but because they measure X-ray reflections sequentially, it takes several weeks to collect a complete dataset from a protein crystal (of the order of 10,000 to 100,000 reflections).

Although the instrument with a single-photon counter is no longer used for data collection in protein X-ray crystallography, we will present its mechanical construction, because the angle nomenclature is standard in X-ray crystallography (Figure 2.9a). In this diffractometer, the X-ray beam, the counter, and the crystal

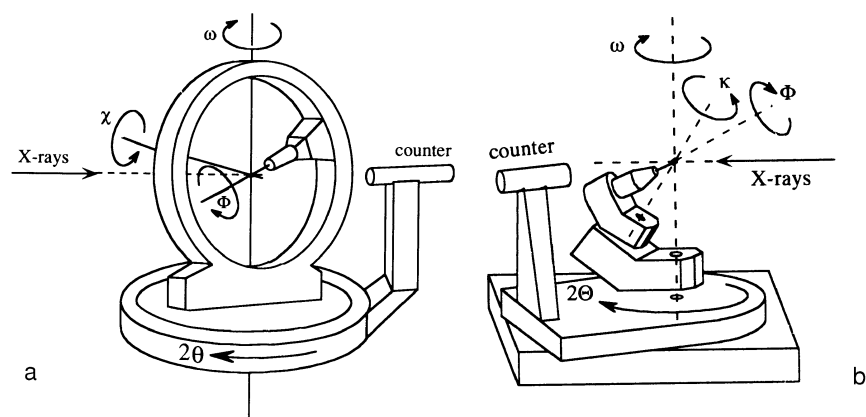


Figure 2.9. (a) In this four-circle diffractometer of classical design, the crystal is located in the center of the large circle. It can be rotated around three axes: by  $\phi$  around the axis of the goniometer head, by  $\omega$  around the vertical axis, and by  $\chi$  through sliding of the block that holds the goniometer head, along the large circle. The counter can be rotated around a fourth axis by the angle  $2\theta$ ; this axis is coincident with the  $\omega$ -axis. (b) A four-circle diffractometer with the  $\kappa$  construction. The  $\kappa$ -axis is at  $50^\circ$  with respect to the  $\omega$ -axis. The  $\phi$  rotation is again around the goniometer head axis. The  $\omega$ -axis and the  $2\theta$ -axis are as in the classical design. The crystal is at the intersection of all of the axes.

are in a horizontal plane. To measure the intensity of a diffracted beam, the crystal must be oriented such that this beam will also be in the horizontal plane. This orientation is achieved by the rotation of the crystal around three axes: the  $\phi$ -axis, the  $\omega$ -axis, and the  $\chi$ -axis (see Figure 2.9a). The counter can be rotated in the horizontal plane around the  $2\theta$ -axis, which is coincident with, but independent of, the  $\omega$ -axis. Data collection is done either with the  $\omega$ -axis and the  $2\theta$ -axis coupled or with the  $2\theta$ -axis fixed and the crystal scanned by rotation around the  $\omega$ -axis.

In an alternative construction, the rather bulky  $\chi$  circle is absent; instead, the instrument has another axis, the oblique  $\kappa$ -axis (Figure 2.9b). The  $\chi$  rotation is mimicked by a combined rotation around the  $\kappa$ -axis,  $\phi$ -axis, and  $\omega$ -axis. The other advantage is that rotation around an axis is mechanically more accurate than sliding along an arc.

### 2.5.2. Photographic Film

Photographic film is a classical detector for X-ray radiation, but it is not used much because of the availability of far more sensitive image plates and area detectors. The single advantage of film over other present-day area detectors is its superior resolution resulting from its fine grain. For historical reasons, we will devote one paragraph to this classical detector.

X-ray film is double-coated photographic film. The double coating of the film base prevents curling and provides a thick layer of sensitive silver-base material, which absorbs approximately two-thirds of the incoming photons. Processing of X-ray film is—although not difficult—somewhat cumbersome and time-consuming because of the developing process, the labeling of the films, as well as the handling of chemicals. Furthermore, for quantitative work, the density of the spots on the film must be measured with a densitometer. The density is defined as  $\log(I_0/I)$ , where  $I_0$  is the intensity of the light beam in the densitometer before it has passed through the film and  $I$  is the intensity after it has passed the film. The density of the spots is (up to a certain level) proportional to the number of X-ray photons that is absorbed by the film. Density, plotted as a function of the exposure time, is a straight line over a long exposure range, but it levels off at very high density values. These higher density values should be used only with careful calibration. This limited dynamic range (1:200) requires that for quantitative measurements, in which the full range of X-ray intensities must be measured, a pack of three consecutive films be used. The weakest spots are measured on the first film and the stronger ones are measured on the last film. Altogether, photographic film is a simple but rather slow and, in the long run, even expensive detector.

### 2.5.3. Image Plates

Image plates are used in the same manner as X-ray film but have several advantages. Image plates are made by depositing a thin layer of an inorganic storage phosphor on a flat base. X-ray photons excite electrons in the material to higher energy

levels. Part of this energy is emitted very soon as normal fluorescent light in the visible-wavelength region. However, an appreciable amount of energy is retained in the material by electrons trapped in color centers; it is dissipated only slowly over a period of several days. This stored energy is released on illumination with light. In practical applications, a red laser is used for scanning the plate and blue light is emitted. The red light is filtered away and the blue light is measured with a photomultiplier (Figure 2.10a). With certain precautions, the light emitted is proportional to the number of photons to which that particular position of the plate was exposed. The pixel size depends mainly on the reading system and is between  $100 \times 100$  and  $200 \times 200 \mu\text{m}^2$  (Amemiya, 1997).

Image plates are at least 10 times more sensitive than X-ray film and their dynamic range is much wider ( $1:10^4$  to  $1:10^5$ ). Therefore, the entire range from strong to weak reflections can be collected with one exposure on a single plate. The plates can be erased by exposure to intense white light and used repeatedly. Another advantage for application with synchrotron radiation is their high sensitivity at shorter wavelengths (e.g.,  $0.65 \text{ \AA}$ ). A further advantage of short wavelengths is that the absorption of the X-ray beam in the protein crystal becomes negligible and no absorption corrections are required. However, image plates are similar to photographic film in the sense that they require a multistep process: exposure as the first step and processing (in this case reading) as the second step. Reading takes only a few minutes.

The first commercially available instruments had a rather small size plate, but in new models, this has been increased [e.g., in the Mar Research instrument (Figure 2.10b) from 18 to 30 cm]. If synchrotron radiation is used, the smaller size is not a problem because with the shorter wavelength, the diffraction pattern is more compressed. A disadvantage of image plates is that the stored image fades away gradually. This decay is rather rapid in the first few minutes but then slows down; it takes a few hundred hours for a 50% decrease in the stored energy.

#### 2.5.4. Area Detectors

Although photographic film and image plates are area detectors, the use of this term is restricted to electronic devices that detect X-ray photons on a two-dimensional surface and process the signal immediately after photon detection. They are also called position-sensitive detectors, because both the intensity of a diffracted beam and the position where it hits the detector are determined. A basic difference with image plates is that area detectors scan through a diffraction spot every  $0.1^\circ$  or so, giving a three-dimensional picture of the spot. In contrast, for film and image plates, a much larger oscillation angle (e.g.,  $2^\circ$ ) is used for each exposure and, therefore, no profile is obtained of the diffraction spot in the oscillation direction.

The development of area detectors is a continuous process. New developments are presented in a special issue of the *Journal of Synchrotron Radiation* (Vol. 13, Part 2). The interest is now focused on CCD (charge-coupled device)-based detectors. Their advantages are a fast response, low noise, a reasonable dynamic range,



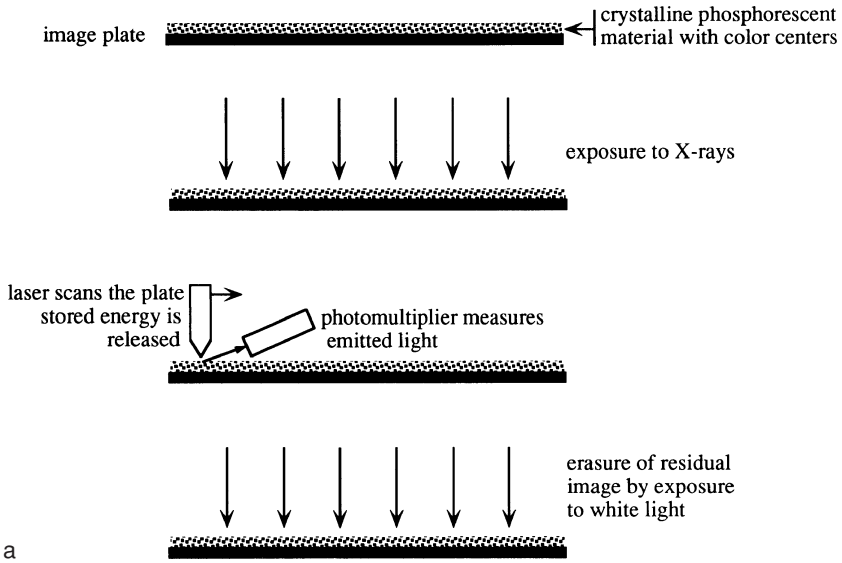


Figure 2.10. (a) The principle of the image plate as an X-ray detector. (b) The image plate instrument produced by Mar Research. It has a circular plate behind the black area where the plate is protected from daylight. For scanning, the plate rotates and the laser scans it along a radial line. In front is the cryogenic sample changer. (Courtesy of Mar Research, [info@marresearch.com](mailto:info@marresearch.com))

and a good linearity (Walter et al., 1995). A CCD-based system is an integrating device, just as an image plate. It collects all photons before readout. The quality of the data collected with a CCD is comparable with the quality of data collected with an image plate, but with a CCD, data collection is much faster.

A CCD detector uses the semiconducting properties of silicon. This material has a valence band and a conducting band available for the electrons. Normally, the conducting band is empty because the valence electrons cannot reach it. When subjected to photons with sufficient energy, electrons move from the valence band to the conducting band, leaving a hole behind. The CCD plate is divided into a large number of pixels. Each pixel is formed by a local voltage. On exposing the plate, electron—hole pairs are formed in a pixel and prevented from leaving it by the local voltage. For readout, the content of the pixels is moved along two perpendicular directions by sequential application of local voltages. They end up, one after the other, at a corner of the plate where their charge is converted to a voltage and digitized (Figure 2.11).

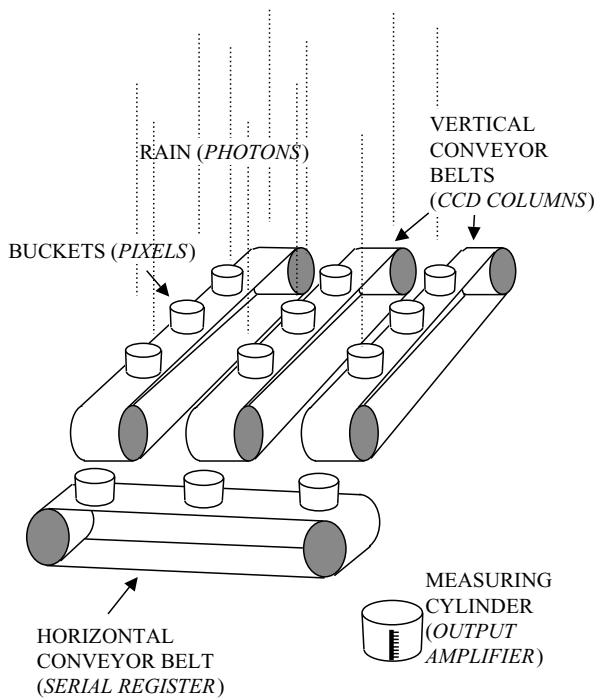


Figure 2.11. The principle of the charge flow in a CCD detector. After the pixels have absorbed the photons, their charge is moved in one direction (vertical conveyor belt). Successive rows of charges are then moved to a corner of the CCD (horizontal conveyor belt) where one after the other is converted to a voltage, amplified, and recorded. [Courtesy of Simon Tulloch of the Isaac Newton Group of Telescopes, La Palma, Canary Islands (<http://www.ing.iac.es/>).]

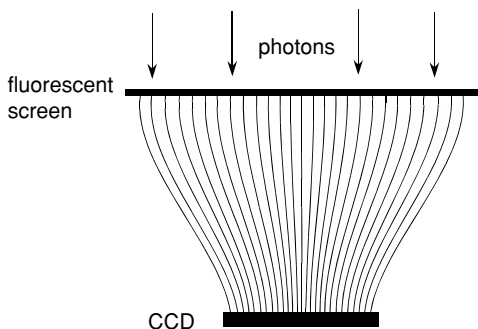


Figure 2.12. A tapered fiber-optics connection for demagnifying the image on a large screen to the smaller CCD.

There are several practical advantages to avoiding direct illumination of the CCD by X-ray photons. The photons are converted to visible light by means of a fast-response fluorescent screen. For high-resolution data collection, a screen with a large area is required. CCDs with a large front window are very expensive but are now the preferred detectors at synchrotron sources. The solution for a small-window CCD is to use a large screen but demagnify the image to the smaller CCD size by means of a tapered fiber-optics connection (Figure 2.12).

The CCD detectors can collect X-ray data at a high speed and exposure times of seconds are not unusual.

Several companies currently market CCD-equipped X-ray instruments (e.g., Bruker<sup>6</sup> and Mar Research<sup>7</sup>).

## 2.6. The Rotation (Oscillation) Instrument

In protein X-ray crystallography, efficient data collection is always screenless, whether photographic film, an image plate, or an electronic area detector is used. The crystal (and the reciprocal lattice) is rotated in small oscillation steps through the Ewald sphere (Chapter 1). Rotation around any arbitrary axis is not the correct procedure. An efficient strategy for data collection requires careful consideration of the crystal properties and the available hardware, such as X-ray source and detector. It is important to minimize systematic errors and maximize completeness; high redundancy is also an advantage. In Section 2.6.1, a few of the problems will be discussed. For a complete discussion of data collection strategy, one should consult Dauter (1999). The mechanical part of the first rotation instruments was very simple: just one rotation axis perpendicular to the direction of the X-ray beam. The detector (e.g., a fluorescent plate) is flat. The consequence of this simple design is that reciprocal lattice points near the rotation axis never pass through the Ewald sphere (Figure 2.13a). Therefore, it requires—in principle—mounting of another crystal in a different orientation to measure the diffracted beams in the

<sup>6</sup> <http://www.bruker.axs.nl>

<sup>7</sup> <http://www.marresearch.com>

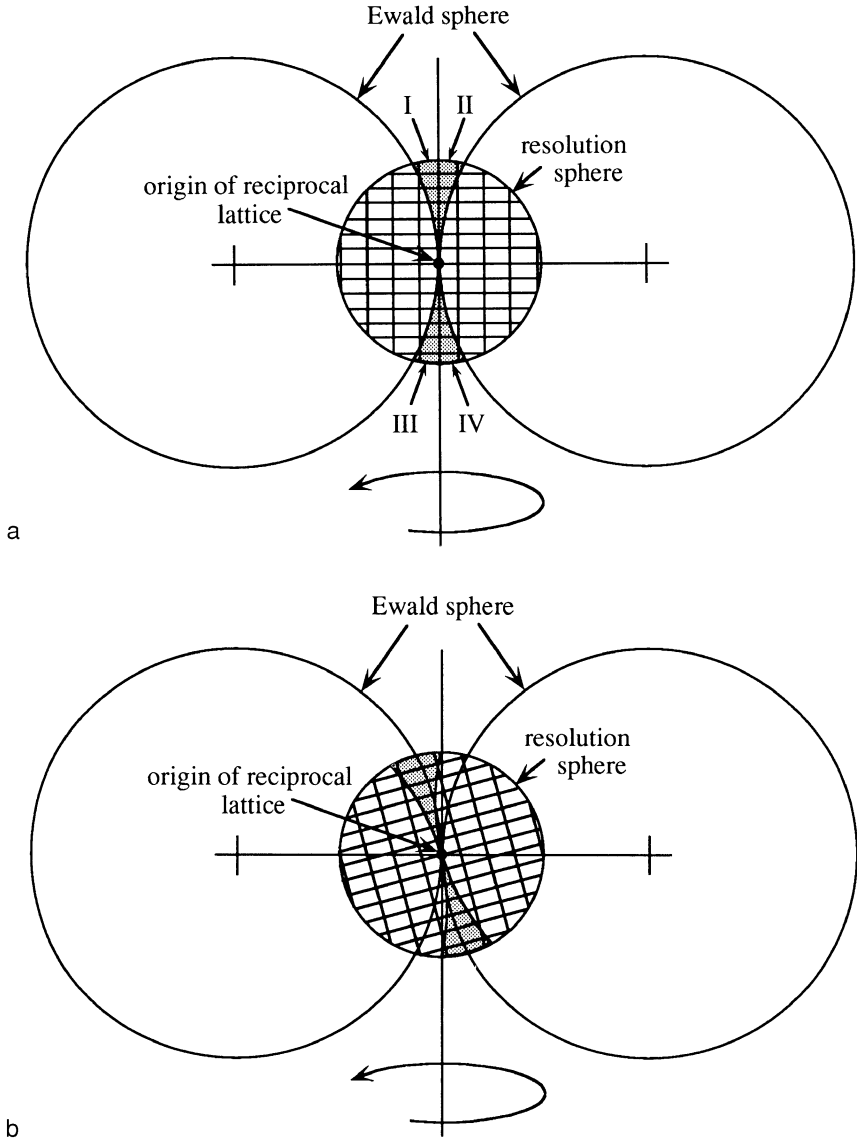


Figure 2.13. (a) For simplicity, the Ewald sphere is rotated instead of the reciprocal lattice. The vertical line in the center is the rotation axis. In its rotation around the axis, the Ewald sphere never passes through the reciprocal lattice regions I-IV. This is the “blind region.” (b) Here the reciprocal lattice is in a skew position. In this example, the reciprocal lattice has three perpendicular axes and, contrary to the situation in (a), all reflections within one octant formed by the three reciprocal lattice axes can be measured.

blind region. However, this is not always necessary. Suppose that the crystal has three perpendicular axes and that it is oriented with one of the crystal axes along the rotation axis; then the blind region is indeed a problem: Assuming sufficient symmetry in the crystal, the four shaded areas in Figure 2.13a contain reciprocal lattice points belonging to reflections with the same intensity in each region and none of the four regions is recorded. However, if the crystal is slightly misset, the problem is solved because now all reflections in at least one of the four regions can be recorded (Figure 2.13b).

Modern oscillation cameras allow the rotation of the crystal around one or more axes. The reflections appear in a seemingly disordered arrangement on the detector. Their position is determined by the following:

1. The crystal orientation.
2. The unit cell parameters in the crystal.
3. The crystal-to-film distance and the wavelength.
4. The film center.

However, this problem can be solved with intelligent software, which can recognize the spots, apply correction factors, and supply the crystallographer with a final dataset.

Because of basic differences between instruments equipped with an image plate and ones equipped with an electronic area detector, we will treat them separately.

### 2.6.1. Rotation Instruments with an Image Plate

With an image plate, data are collected in contiguous oscillation ranges, each of approximately  $2^\circ$ . The exact value is determined by the distance between the reciprocal lattice points, the maximum angle of reflection (resolution), and the width of the spots. In performing the oscillation, the maximum displacement is found for reciprocal lattice points in the plane through the origin perpendicular to the rotation axis at the edge of maximum diffraction angle (the resolution limit) (Figure 2.14). If the distance between adjacent points at this edge is  $d^*$  and their distance from the origin is  $d_{\text{lim}}$ , the angle  $\Delta_1$  has  $\tan \Delta_1 = d^*/d_{\text{lim}}$ . Because  $d^* \ll d_{\text{lim}}$ , the angle  $\Delta_1$  is approximately equal to  $d^*/d_{\text{lim}}$  (in radians<sup>8</sup>). However, the reflections have a certain angular width  $\Delta_2$ , determined by the crystal size, its mosaicity, and the divergence of the X-ray beam. Therefore, the maximum oscillation angle is  $\Delta_1 - \Delta_2$ .

To minimize the number of exposures, the oscillation range should be as large as possible and, therefore, the crystal should be oriented with its shortest reciprocal distance along the rotation axis. (This is not required for area detectors.) Because of the reciprocity between the crystal lattice and the reciprocal lattice, this orientation corresponds to the longest unit distance in the crystal lattice along the rotation axis. Another feature to consider for minimizing the number of exposures is the

---

<sup>8</sup> A full circle is  $2\pi$  radians.

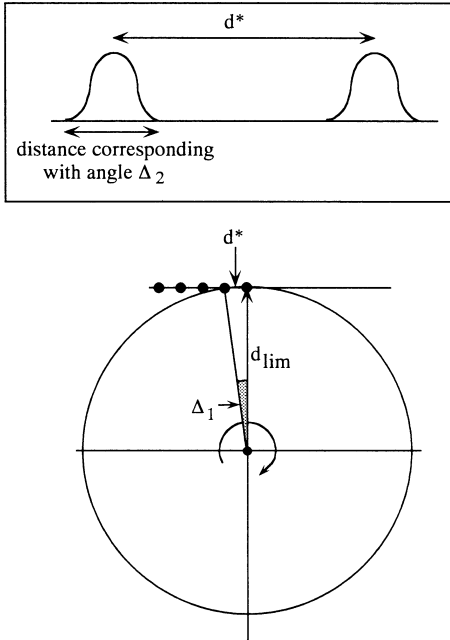


Figure 2.14. In the lower picture, the rotation axis is perpendicular to the plane of the paper. The black dots are reciprocal lattice points at the edge of the limiting resolution sphere, which has a radius  $d_{\text{lim}}$ . The angular distance between adjacent reflections is  $\Delta_1$  with  $\tan \Delta_1 = d^*/d_{\text{lim}}$ . In the box, two adjacent reflections are drawn. Suppose that the right reflection has just passed through the Ewald sphere and has caused a spot on the image plate. In the ongoing oscillation, the left reflection should not be allowed to reach the Ewald sphere before the right reflection has passed. If it does, then it would overlap the image of the right reflection. Therefore, the maximum oscillation angle permitted is  $\Delta_1 - \Delta_2$ .

symmetry in the crystal. This symmetry is also present in the reciprocal lattice. Lattice points related by this symmetry belong to diffracted beams with the same intensity and, therefore, fewer diffracted beams need to be measured.

Two disadvantages of the rotation method with image plates are immediately apparent: (1) The background is relatively high and (2) some spots appear partly on one and partly on the next or previous exposure. This second problem is especially severe for large unit cells in the crystal because of the close spacing of reciprocal lattice points and a very small oscillation range. For the solution to this problem, the two “partials” are treated as individual reflections and their intensities are added at a later stage. This requires extreme precision in the mechanical part of the instrument. Nevertheless, the accuracy in the intensity of reflections composed of partials is somewhat lower than for fully recorded reflections, and for this reason, they are sometimes completely neglected. The first problem is a signal-to-noise ratio problem. The background noise is proportional to the exposure time and, thus, to the oscillation angle. The intensity of a fully recorded reflection is independent of the oscillation angle. The signal-to-noise ratio is more favorable if the X-ray beam has a smaller divergence and the mosaic spread of the crystal is low. A smaller oscillation angle also improves the ratio but causes many more reflections to be recorded as partials.

After exposing the crystal in a few oscillation ranges, the software is able to find an approximate orientation of the crystal with rough unit cell dimensions (if these are not already known). It is assumed that the crystal-to-plate distance and the

position of the center of the plate are fixed instrument parameters. The approximate orientation and cell parameters can then be refined during the processing of all of the data. In this process, a rectangular box is defined around each spot. The integrated intensity in this box is the spot intensity; the background is estimated in the surrounding region. The measurement of weak reflections can be appreciably improved by profile fitting. A reliable two-dimensional spot profile is derived from the strong spots and then applied to the weak ones, of course assuming that the profiles are equal for strong and weak spots.

Image plates are also the detectors in Weissenberg cameras for protein X-ray crystallography. This very classical instrument, in which the rotation of the crystal is coupled to a translation of the plate, has been adapted to protein work by Sakabe (1983, 1991) at the Photon Factory (Tskuba, Japan). See also Stuart and Jones (1993).

### 2.6.2. Electronic Area Detectors

It was pointed out earlier that basic differences exist between rotation instruments equipped with an image plate and electronic area detectors. The main difference is that the oscillation angle for the electronic area detectors is much smaller; frames with an oscillation angle of  $0.1^\circ$  are contiguously measured. This is possible due to the immediate processing of the data from each frame. The advantages are that the background is low and that a three-dimensional profile of the reflection spots can be constructed, which is even more favorable for measuring the weak intensities than the two-dimensional profile.

With the more sophisticated mechanical part of the instrument, a crystal can be easily adjusted to nearly every orientation. The search for the initial orientation is also easier with these instruments than with a rotation instrument because the smaller oscillation angle defines more precisely the position of a spot.

---

#### **Radiation Protection**

The high-energy photons of X-rays have a harmful effect on living tissue. Therefore, they must be used with great care, taking all necessary precautions. Local regulations for the protection of personnel should be obeyed and unauthorized use of X-ray equipment must be forbidden. A somewhat confusing number of radiation units are in use and, therefore, a definition of them will be given.

The Curie (Ci) is the old unit for radioactivity:

$$1 \text{ Ci} = 37 \times 10^9 \text{ disintegrations /s}$$

One Curie is approximately equal to the activity of 1 g of radium. The Curie is not an SI unit and has, therefore, been replaced by the Becquerel (Bq), which stands for 1 disintegration/s:

$$1 \text{ Ci} = 37 \times 10^9 \text{ Bq.}$$

The radiation absorbed dose (rad) is a measure for the amount of radiation that corresponds to the energy absorption in a certain medium, such as a tissue. One rad is the dose of radiation corresponding to an energy absorption of 0.01 J/kg medium. The rad has been replaced by an SI unit: the Gray (Gy), corresponding to 1 J/kg or 1 m<sup>2</sup>/s<sup>2</sup>:

$$1 \text{ Gy} = 100 \text{ rad.}$$

The relative biological effect (RBE) was introduced because it has been found that the same absorbed dose from different types of radiation does not always have the same harmful effect in biological systems. Therefore, a quality factor  $Q$  has been introduced. In the rem (X-ray equivalent man), this quality factor has been taken into account:

$$1 \text{ rem} = 1 \text{ rad} \times Q.$$

The rem has now been replaced by the Sievert (Sv):

$$1 \text{ Sv} = 100 \text{ rem.}$$

A summary of the names and symbols is given in Table 2.1

Table 2.1. Radiation Units and Symbols

Physical or biological property	SI unit			
	Symbol	Value	Symbol	Value
Radioactivity	$A$	Becquerel	Bq	1 disintegration/s
		Old: Curie	Ci	1 Ci = $37 \times 10^9$ Bq
Absorbed dose	$D$	Gray	Gy	1 J/kg = 1 m <sup>2</sup> /s <sup>2</sup>
		Old: rad	rad	1 rad = 10 <sup>-2</sup> Gy
Dose equivalent	$H$	Sievert	Sv	1 J/kg = 1 m <sup>2</sup> /s <sup>2</sup>
		Old: rem	rem	1 rem = 10 <sup>-2</sup> Sv

## Summary

In this chapter, X-ray sources were discussed as well as instruments for the registration and measurement of the diffracted beams. Conventional X-ray sources in the laboratory are sealed tubes and tubes with a rotating anode, the latter being preferred for protein X-ray crystallography because of their higher intensity. The most commonly used radiation from a tube has a wavelength of 1.5418 Å. This is the characteristic  $K_{\alpha}$  wavelength emitted by a copper anode and is selected from the spectral distribution by a filter or, preferably, with a monochromator. The extremely high-intensity X-ray radiation from a synchrotron is of great value for collecting data. The beam is not only strong, but it is also highly parallel, causing smaller but more brilliant spots on the detector. Therefore, with synchrotron



radiation, the resolution is somewhat better than in the home laboratory (more diffracted beams at a high diffraction angle with greater details in the resulting protein structure).

Another advantage of synchrotron radiation is its tunability, which allows the selection of radiation with a wavelength at or below 1 Å. Although the specimen diffracts this radiation more weakly than the 1.5418-Å copper radiation, the fluorescent-type detectors are more sensitive at this shorter wavelength. Another important advantage is the lower absorption of radiation with a shorter wavelength and, consequently, less radiation damage to the crystals. For a protein structure determination, the number of diffracted beams to be recorded is extremely high, of the order of  $10^4$ – $10^5$ . To achieve this within a reasonable time requires highly efficient hardware. The optimal situation is using synchrotron radiation combined with a CCD-based detector. The advantages and limitations of the different instruments are indicated.

An important issue in X-ray crystallography is the protection of personnel against the harmful effect of X-rays on the human body. Different radiation units are defined.

# Chapter 3

## Crystals

### 3.1. Introduction

The beauty and regularity of crystals impressed people to such an extent that, in the past, crystals were regarded as products of nature with mysterious properties. Scientific investigation of crystals started in 1669, when Nicolaus Steno, a Dane working as a court physician in Tuscan, proposed that during crystal growth, *the angles between the faces remained constant*. For a given crystal form, individual crystals might differ in shape (i.e, in the development of their faces), but they always have identical angles between the same faces (Figure 3.1). The specific morphology might depend on factors such as the supply of material during growth, on the presence of certain substances in the mother liquor, or on the mother liquor itself. For a single crystal form, the angles between the faces are constant, but this is not true if the crystals belong to different crystal forms. Figure 3.2 shows four different crystal forms of deoxyhemoglobin from the sea lamprey *Petromyzon marinus*. Their appearance depends on the buffer and on the precipitating agent, although, occasionally, two different forms appear under the same conditions.

Before the famous first X-ray crystallographic diffraction experiment by von Laue, Friedrich, and Knipping in 1912, the internal regularity of a crystal was suggested but never proven. X-ray crystallography has dramatically changed this situation.

Determining the atomic structure of a molecule, particularly one as complex as a protein molecule, is greatly facilitated if a large number of identical molecules can be packed in a regular arrangement. The highest order is present in crystals of the material, although structural information can also be obtained from fibers. Not much can be done with an amorphous solid or a solution, which give weak and diffuse X-ray diffraction patterns and from which little structural information can be derived. In this volume, we restrict ourselves to crystals.

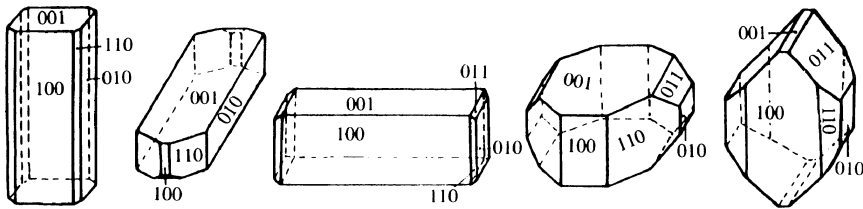


Figure 3.1. Crystals of trimethylammonium bromide belonging to the same crystal form but exhibiting a range of morphologies.

A crystal of organic material is a three-dimensional periodic arrangement of molecules. When the material precipitates from a solution, its molecules attempt to reach the lowest free-energy state. This is often accomplished by packing them in a regular way; in other words, a crystal grows. It is surprising to observe that even large protein molecules follow this principle, although, occasionally, they unfortunately do not crystallize. Flat planes at the surface of a well-developed crystal reflect the regular packing of the molecules in the crystal. In this regular packing, three repeating vectors  $\mathbf{a}$ ,<sup>1</sup>  $\mathbf{b}$ , and  $\mathbf{c}$  can be recognized with the angles  $\alpha$ ,  $\beta$ , and  $\gamma$ , respectively, between them. These three vectors define a unit cell in the crystal lattice (Figure 3.3).

If the content of the unit cells is neglected for the moment, the crystal can be regarded as a three-dimensional stack of unit cells with their edges forming a grid or lattice (Figure 3.4). The line in the  $\mathbf{a}$  direction is called the  $x$ -axis of the lattice; the  $y$ -axis is in the  $\mathbf{b}$  direction and the  $z$ -axis is in the  $\mathbf{c}$  direction. The  $x$ -,  $y$ - and  $z$ -axes together form a coordinate system that by convention is right-handed. We will later see (Section 4.7.2 of Chapter 4) that diffraction of X-rays by a crystal can be regarded as reflection against planes in the lattice. These planes are constructed through the lattice points and a great many sets of these planes can be drawn (Figure 3.5).

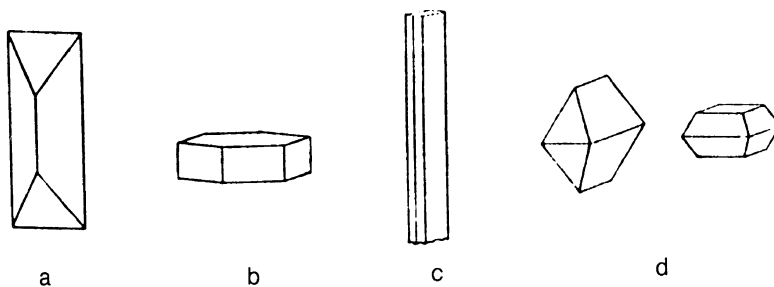


Figure 3.2. The crystals a–d belong to four different crystal forms of deoxyhemoglobin from the sea lamprey *Petromyzon marinus*. [Reproduced with permission from Hendrickson et al. (1968).]

<sup>1</sup> Vectors are in boldface type.

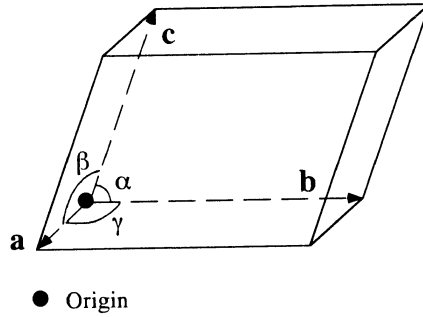


Figure 3.3. One unit cell in the crystal lattice.

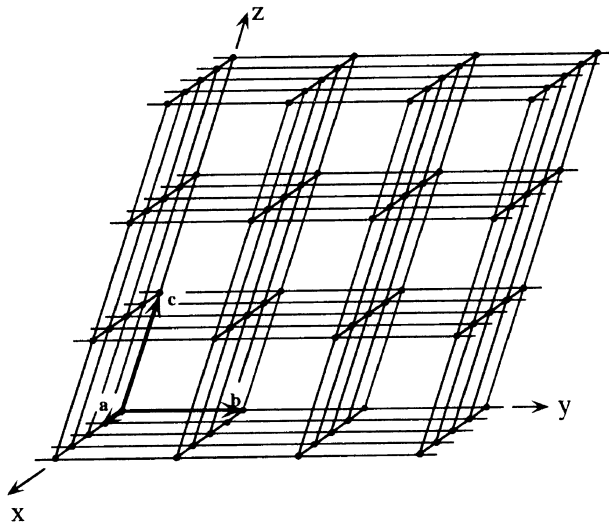


Figure 3.4. A crystal lattice is a three-dimensional stack of unit cells.

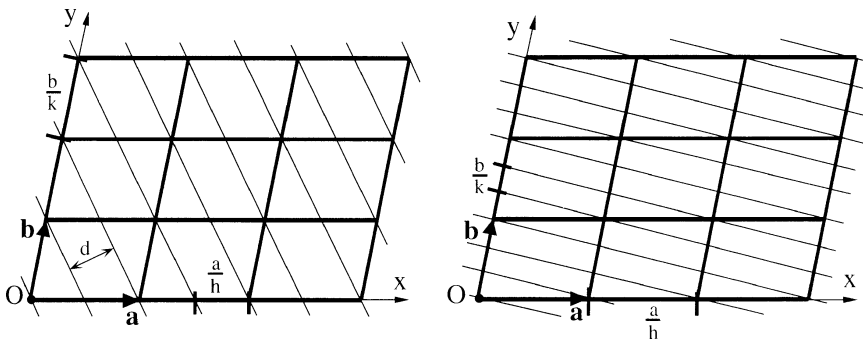


Figure 3.5. Lattice planes in a two-dimensional lattice. On the left,  $h = 2$  and  $k = 1$ ; on the right,  $h = 1$  and  $k = 3$ .

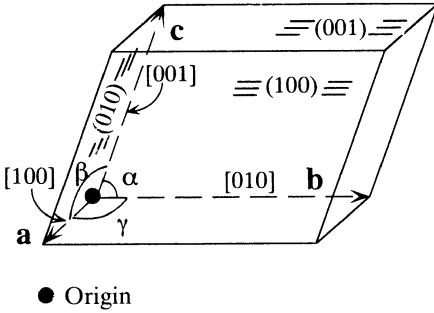


Figure 3.6. One unit cell bounded by the planes (100), (010), and (001). The directions along  $a$ ,  $b$ , and  $c$  are indicated by  $[100]$ ,  $[010]$ , and  $[001]$ , respectively.

Within a set, the planes are parallel and equidistant with perpendicular distance  $d$ . As can be derived from Figure 3.5, the lattice planes cut an axis (e.g., the  $x$ -axis) into equal parts that have a length  $a/1$ ,  $a/2$ ,  $a/3$ ,  $a/4$ , and so forth. The whole numbers 1, 2, 3, 4, ... are called indices. A set of lattice planes is determined by three indices  $h$ ,  $k$ , and  $l$ , if the planes cut the  $x$ -axis in  $a/h$  pieces, the  $y$ -axis in  $b/k$  pieces, and the  $z$ -axis in  $c/l$  pieces. If a set of planes is parallel to an axis, that particular index is 0 (the plane intercepts the axis at infinity). Therefore, the unit cell is bounded by the planes (100), (010), and (001) (Figure 3.6). The flat faces of a crystal are always parallel to lattice planes (Figures 3.1 and 3.7). The parentheses in  $(hkl)$  are used to distinguish a lattice plane from a line segment in the unit cell, which is given in brackets; for example,  $[100]$  is the line segment from the origin of the unit cell to the end of the  $a$ -axis and  $[111]$  is the body diagonal from the origin to the opposite corner.

From Figure 3.5 it is clear that the projection of  $a/h$ ,  $b/k$ , and  $c/l$  on the line perpendicular to the corresponding lattice plane  $(hkl)$  is equal to the lattice plane distance  $d$ . We have not yet discussed the choice of unit cell in the crystal. For

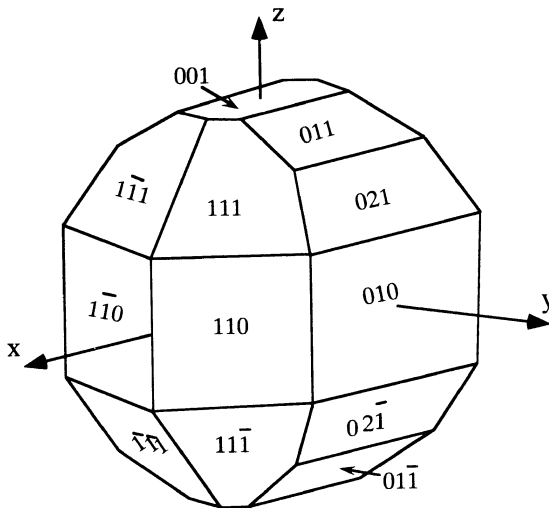
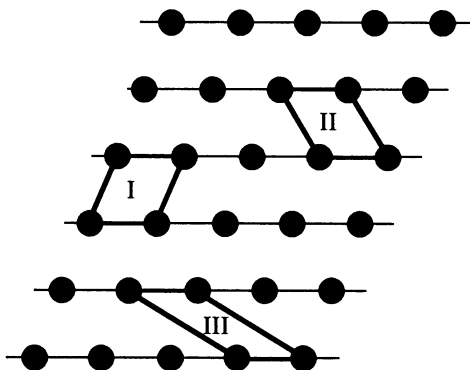


Figure 3.7. A crystal showing several faces.

Figure 3.8. In this two-dimensional lattice, the unit cell can be chosen in different ways: as I, as II, or as III.



example, in Figure 3.8, the choice could be either unit cell I, II, or III. Often the problem does not exist because of symmetry considerations in the crystal (Section 3.2). If the choice does exist, then certain rules should be followed, given in *International Tables for Crystallography*, Vol. A, Chapter 9 (Hahn, 2002).

The main conditions are as follows:

1. The axis system should be right-handed.
2. The basis vectors should coincide as much as possible with directions of highest symmetry (Section 3.2).
3. The cell taken should be the smallest one that satisfies condition 2. This condition sometimes leads to the preference of a face-centered (A, B, C, or F) or a body-centered (I) cell over a primitive (P) smallest cell (Figure 3.9). Primitive cells have only one lattice point per unit cell, whereas nonprimitive cells contain two or more lattice points per unit cell. These cells are designated A, B, or C if one of the faces of the cell is centered: It has extra lattice points on opposite faces of the unit cell, respectively, on the  $bc$  (A),  $ac$  (B), or  $ab$  (C) faces. If all faces are centered, the designation is F (Figure 3.9).
4. Of all lattice vectors, none is shorter than  $a$ .
5. Of those not directed along  $a$ , none is shorter than  $b$ .
6. Of those not lying in the  $a, b$  plane none is shorter than  $c$ .
7. The three angles between the basis vectors  $\mathbf{a}$ ,  $\mathbf{b}$ , and  $\mathbf{c}$  are either all acute ( $<90^\circ$ ) or all obtuse ( $\geq 90^\circ$ ).

## 3.2. Symmetry

The search for a minimum free energy and, as a consequence, the regular packing of molecules in a crystal lattice often leads to a symmetric relationship between the molecules. As we have seen in the previous section, a characteristic of a crystal is that it has unit translations in three dimensions, also called three-dimensional translational symmetry, corresponding to the repetition of the unit cells. Often, additional symmetry is encountered.

Examples are given in Figures 3.10 and 3.11, which show operations having twofold and threefold (screw) rotation axes as symmetry elements, respectively.

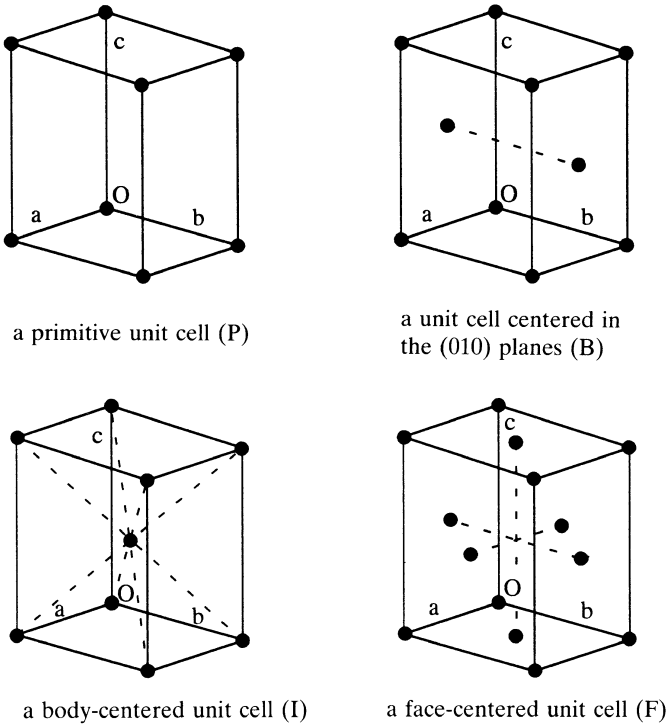


Figure 3.9. Noncentered and centered unit cells.

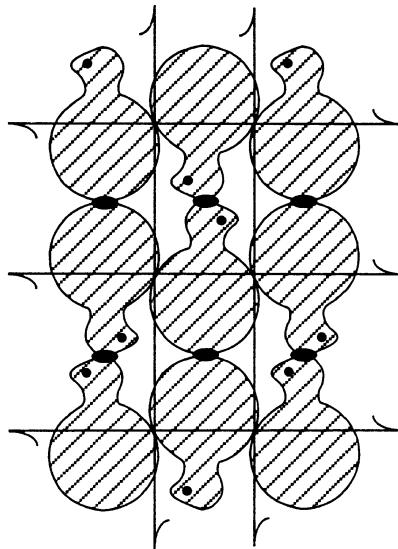


Figure 3.10. A two-dimensional lattice with 2-fold symmetry axes perpendicular to the plane of the figure and 2-fold screw axes in the plane.

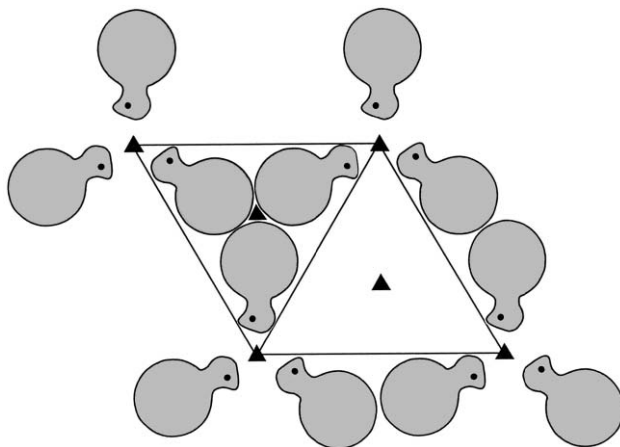


Figure 3.11. A two-dimensional lattice with 3-fold symmetry axes perpendicular to the plane of the figure.

Figures 3.12 and 3.13 give further examples of 2-fold and 3-fold symmetry operations, respectively;  $n$ -fold axes with  $n = 5$  or  $n > 6$  do not occur. The reason is that space cannot be filled completely with, for example, a 5-fold or a 7-fold axis. In addition to axes of symmetry, crystals can have mirror planes, inversion centers (centers of symmetry) (Figure 3.14), and rotation inversion axes, which combine an inversion and a rotation. Table 3.1 lists all possible symmetry operations together with their symbols and the translation operation.

Another way of looking at symmetry is the following. Application of the symmetry operators, such as rotations with or without translations, leaves the entire crystal unchanged; it looks exactly as it was. Therefore, the properties of the crystal, such as those of an electrical or mechanical nature, obey at least the same symmetry. There are 230 different ways to combine the allowed symmetry operations in a

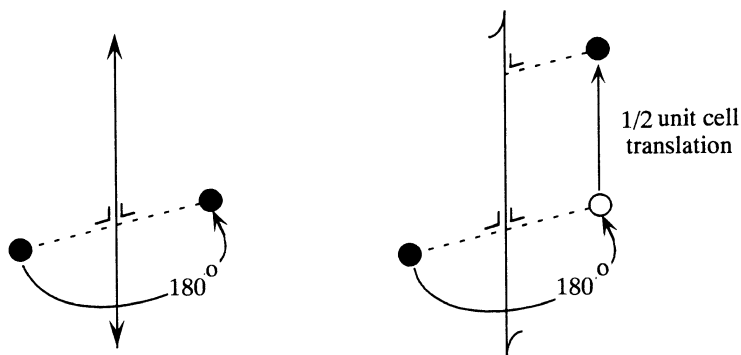


Figure 3.12. A 2-fold axis (left) and a 2-fold screw axis (right); the latter relates one molecule to another by a  $180^\circ$  rotation plus a translation over half of the unit cell.



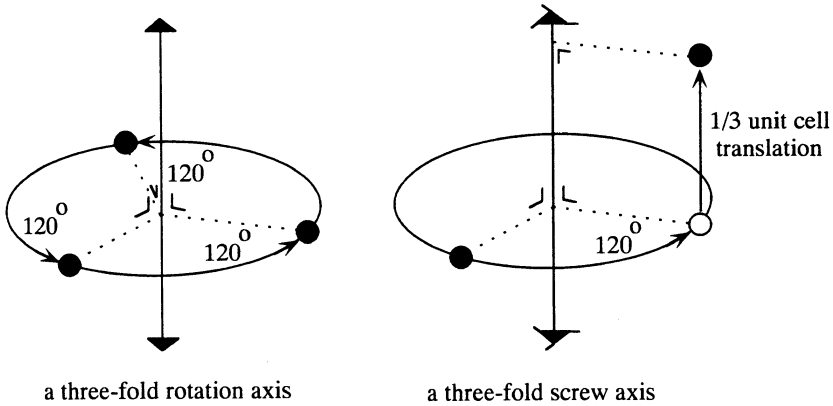


Figure 3.13. A 3-fold axis (left) and a 3-fold screw axis (right); the latter relates one molecule to another by a  $120^\circ$  rotation and a translation over one-third of the unit cell.

crystal, leading to 230 space groups. They can be found in the *International Tables for Crystallography*, Volume A (Hahn, 2002). Before using Volume A of the *International Tables*, one should take note of the meaning of the different symbols, beginning with the inside front cover and back cover pages “Explanation of the space group data,” or consult the Brief Teaching Edition of Volume A (Hahn, 2002).

The restrictions given above for the symmetry axes of “ordinary” crystals are the consequence of their three-dimensional translation symmetry because this requires space to be filled entirely by identical repeating units. This symmetry is not present

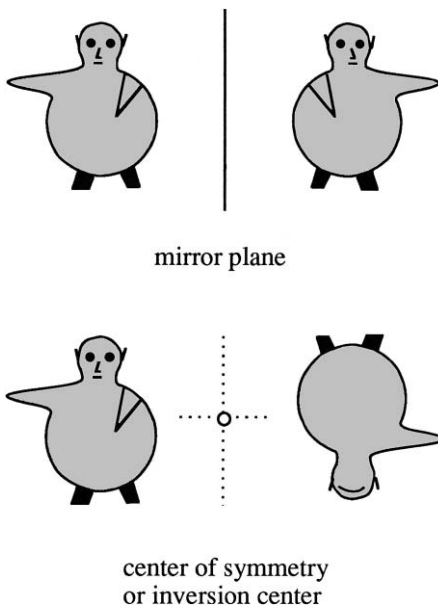
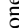


















Figure 3.14. The effect of a mirror and of an inversion center.

Table 3.1. Graphic Symbols for Symmetry Elements

Symmetry axis or symmetry point	Graphic symbol	Screw vector of a right-handed screw rotation in units of the shortest lattice translation vector parallel to the axis	Printed symbol
Symmetry axes normal to the plane of projection (three dimensions) and symmetry points in the plane of the figure (two dimensions)			
Identity	None	None	1
Twofold rotation axis		None	2
Twofold rotation point (two dimensions)			
Twofold screw axis: "2 sub 1"		$\frac{1}{2}$	2 <sub>1</sub>
Threefold rotation axis		None	3
Threefold rotation point (two dimensions)		$\frac{1}{3}$	3 <sub>1</sub>
Threefold screw axis: "3 sub 1"		$\frac{2}{3}$	3 <sub>2</sub>
Threefold screw axis: "3 sub 2"		None	4
Fourfold rotation axis			
Fourfold rotation point (two dimensions)		$\frac{1}{4}$	4 <sub>1</sub>
Fourfold screw axis: "4 sub 1"		$\frac{1}{2}$	4 <sub>2</sub>
Fourfold screw axis: "4 sub 2"		$\frac{3}{4}$	4 <sub>3</sub>
Fourfold screw axis: "4 sub 3"		None	6
Sixfold rotation axis			
Sixfold rotation point (two dimensions)		$\frac{1}{6}$	6 <sub>1</sub>
Sixfold screw axis: "6 sub 1"		$\frac{1}{3}$	6 <sub>2</sub>
Sixfold screw axis: "6 sub 2"		$\frac{1}{2}$	6 <sub>3</sub>
Sixfold screw axis: "6 sub 3"			

(cont.)

Table 3.1. (Continued)

Symmetry axis or symmetry point	Graphic symbol	Screw vector of a right-handed screw rotation in units of the shortest lattice translation vector parallel to the axis	Printed symbol
Sixfold screw axis: "6 sub 4"		$\frac{2}{3}$	$6_4$
Sixfold screw axis: "6 sub 5"		$\frac{5}{6}$	$6_5$
Center of symmetry, inversion center: "1 bar" } Reflection point, mirror point (one dimension) }		None	$\bar{1}$
Twofold rotation axis with center of symmetry		None	$2/m$
Twofold screw axis with center of symmetry		$\frac{1}{2}$	$2_1/m$
Inversion axis: "3 bar"		None	$\bar{3}$
Inversion axis: "4 bar"		None	$\bar{4}$
Fourfold rotation axis with center of symmetry		None	$4/m$
"4 sub 2" screw axis with center of symmetry		$\frac{1}{2}$	$4_2/m$
Inversion axis: "6 bar"		None	$\bar{6}$
Sixfold rotation axis with center of symmetry		None	$6/m$
"6 sub 3" screw axis with center of symmetry		$\frac{1}{3}$	$6_3/m$

	Symmetry axes parallel to the plane of projection			
Twofold rotation axis		None	2	
Twofold screw axis: "2 sub 1"		$\frac{1}{2}$	2 <sub>1</sub>	
Fourfold rotation axis		None	4	
Fourfold screw axis: "4 sub 1"		$\frac{1}{4}$	4 <sub>1</sub>	
Fourfold screw axis: "4 sub 2"		$\frac{1}{2}$	4 <sub>2</sub>	
Fourfold screw axis: "4 sub 3"		$\frac{3}{4}$	4 <sub>3</sub>	
Inversion axis: "4 bar"		None	$\bar{4}$	
Symmetry axes inclined to the plane of projection (in cubic space groups only)				
Twofold rotation axis		None	2	
Twofold screw axis: "2 sub 1"		$\frac{1}{2}$	2 <sub>1</sub>	
Threefold rotation axis		None	3	
Threefold screw axis: "3 sub 1"		$\frac{1}{3}$	3 <sub>1</sub>	
Threefold screw axis: "3 sub 2"		$\frac{2}{3}$	3 <sub>2</sub>	
Inversion axis: "3 bar"		None	$\bar{3}$	

Source: Reprinted from the *International Tables of Crystallography*, Volume A (Hahn, 1983), with permission of The International Union for Crystallography.

in so-called quasicrystals, which consist of two or more (but a finite number) different units. The position of the units in the lattice of a quasicrystal is determined according to a predictable sequence that never quite repeats: They are quasiperiodic and can have any rotational symmetry, including 5-fold and 7-fold, which are forbidden in “ordinary” crystals. So far, no quasicrystalline protein crystals have been found and they will not be considered further.

### 3.3. Possible Symmetry for Protein Crystals

Not all 230 space groups are allowed for protein crystals. The reason is that in protein crystals, the application of mirror planes and inversion centers (centers of symmetry) would change the asymmetry of the amino acids: An *l*-amino acid would become a *d*-amino acid, but these are never found in proteins. This limitation restricts the number of space groups for proteins appreciably: Only those without any symmetry (triclinic) or with exclusively rotation or screw axes are allowed. However, mirror lines and inversion centers do occur in projections of protein structures along an axis. For example, a projection along a 2-fold axis has an inversion center, and mirror lines do occur in a projection of the structure on a plane parallel to a 2-fold axis.

### 3.4. Coordinate Triplets: General and Special Positions

The position of a point  $P$  in the unit cell is given by its position vector  $\mathbf{r}$  (Figure 3.15). In terms of its fractional coordinates  $x$ ,  $y$ , and  $z$  with respect to the crystal axes  $\mathbf{a}$ ,  $\mathbf{b}$ , and  $\mathbf{c}$ ,  $\mathbf{r}$  is given by

$$\mathbf{r} = x\mathbf{a} + y\mathbf{b} + z\mathbf{c}. \quad (3.1)$$

The position of  $P$  can thus be described by its fractional coordinates (i.e., by its coordinate triplet  $x, y, z$ ). The coordinate triplets of the points  $P$  and  $P'$ , related

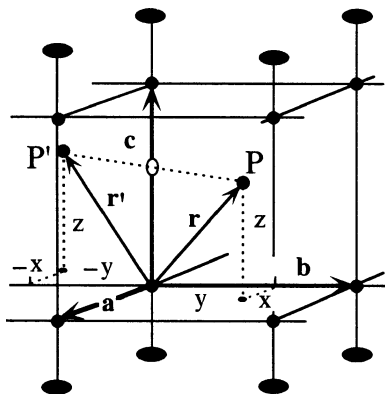


Figure 3.15. This crystal has a 2-fold axis along  $c$ . The point  $P$  with coordinate triplet  $x, y, z$  is related by the symmetry operation to point  $P'$  with coordinate triplet  $-x, -y, z$ .

by the 2-fold axis along  $c$  in Figure 3.15, are  $x, y, z$  and  $-x, -y, z$ . If a molecule occupies position  $x, y, z$ , then an identical molecule occupies position  $-x, -y, z$ . These molecules are said to occupy general positions.

If, however, the molecule itself has a 2-fold axis that coincides with the crystallographic 2-fold axis, half of the molecule is mapped onto the other half by the symmetry operation. This molecule occupies a “special” position. Each special position has a certain point symmetry. In the present example, the point symmetry would be given by the symbol 2.

### 3.5. Asymmetric Unit

If the lattice has a level of symmetry higher than triclinic, then each particle in the cell will be repeated a number of times as a consequence of the symmetry operations. For example, in space group  $P2_12_12_1$  (space group number 19 in the *International Tables*), one can always expect at least four equal particles in the unit cell related by the symmetry operations (Figure 3.16). This unit cell has four asymmetric units. The number of molecules in a unit cell is not necessarily equal to the number of asymmetric units. There might be two or more independent molecules in each asymmetric unit. On the other hand, if a molecule occupies a special position (e.g., if a symmetry axis passes through a molecule, relating one part of the molecule to one or more other parts in that molecule), the unit cell contains fewer molecules than anticipated from the number of asymmetric units.

It is important to note that molecules related by crystallographic symmetry are identical and have identical crystallographic environments. However, if two

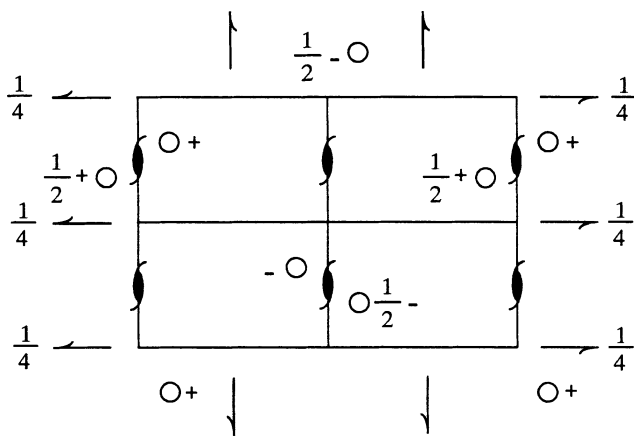


Figure 3.16. The projection of a  $P2_12_12_1$  unit cell; it contains four asymmetric units. The circles represent identical particles related by the symmetry of the space group. The symbol + means that the particle is at a certain distance (for instance,  $z$ ) above the bottom plane of the unit cell and  $1/2+$  at distance  $z$  above the middle plane. The  $-$  sign indicates that the particle is at distance  $z$  below the bottom plane. With  $1/2-$ , it is  $z$  below the middle plane. The screw axes  $1/4$  are located at height  $1/4$  (and  $3/4$ ) of the unit cell.

or more molecules occur in the asymmetric unit, they do not have an identical environment and, moreover, they might differ in conformation.

### 3.6. Point Groups

A characteristic feature of crystals is the presence of flat boundary faces with sharp edges between them. Internal symmetry in the crystal is reflected in the arrangement of these boundary faces. However, the translation components of the symmetry operations cannot be observed on the macroscopic level, and for the outer shape of the crystals, we are left with symmetry without translation (e.g., a 2-fold screw axis becomes a 2-fold axis). This limited group of symmetry elements forms a collection of point groups, because the symmetry elements always pass through one point. The absence of 5-fold, 7-fold, and so forth axes in crystals (because of the requirement of unit translation symmetry) limits the number of point groups to 32. The absence of a 5-fold crystallographic axis does not mean that a 5-fold axis never occurs. For instance, in virus particles, no unit translation symmetry exists and 5-fold axes do occur.

### 3.7. Crystal Systems

With the choice of the unit cell according to the rules in Section 3.1, the 32 point groups can be assigned to 7 and not more than 7 crystallographic systems (shown in Table 3.2). This limitation to seven systems is due to the combination of symmetry elements. We will show this with an example.

If the unit cell has one 2-fold axis, the system is clearly monoclinic. If a second 2-fold axis is added, the two axes must be perpendicular or make an angle of  $30^\circ$  or  $60^\circ$  with each other, because, otherwise, an unlimited number of 2-fold axes would be generated in the same plane (Figure 3.17). From Figure 3.17 it is evident that

Table 3.2. The Seven Crystal Systems

Crystal system	Conditions imposed on cell geometry	Minimum point group symmetry
Triclinic	None	1
Monoclinic	$\alpha = \gamma = 90^\circ$ (b is the unique axis; for proteins this is a 2-fold axis or screw axis) or: $\alpha = \beta = 90^\circ$ (c is unique axis; for proteins this is a 2-fold axis or screw axis)	2
Orthorhombic	$\alpha = \beta = \gamma = 90^\circ$	222
Tetragonal	$a = b$ ; $\alpha = \beta = \gamma = 90^\circ$	4
Trigonal	$a = b$ ; $\alpha = \beta = 90^\circ$ ; $\gamma = 120^\circ$ (hexagonal axes) or: $a = b = c$ ; $\alpha = \beta = \gamma$ (rhombohedral axes)	3
Hexagonal	$a = b$ ; $\alpha = \beta = 90^\circ$ ; $\gamma = 120^\circ$	6
Cubic	$a = b = c$ ; $\alpha = \beta = \gamma = 90^\circ$	23

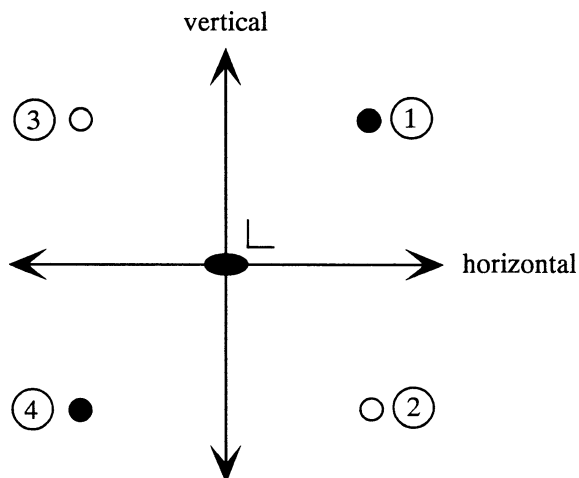


Figure 3.17. The two 2-fold axes in the plane of the page relate the four circles to each other. The open circles are above the plane, the filled circles are below it. If a molecule is placed at position 1, the horizontal 2-fold axis generates a molecule in position 2 and the vertical axis in position 3. However, then the horizontal axis also generates a molecule in position 4. It is evident that a third 2-fold axis is generated perpendicular to the first two.

two perpendicular 2-fold axes generate a third one perpendicular to the plane of the first two axes. Therefore, crystal symmetry excludes the existence of a crystal system with one angle equal to  $90^\circ$  and two angles different from  $90^\circ$ .

The trigonal system can be treated either with hexagonal axes or with rhombohedral axes (Figure 3.18). In the hexagonal unit cell,  $a$  and  $b$  are equal in length

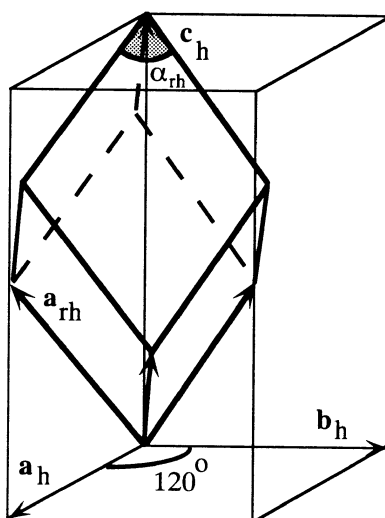


Figure 3.18. A rhombohedral unit cell and its corresponding hexagonal cell.



and have an angle of  $120^\circ$  to each other.  $c$  is perpendicular to the  $ab$ -plane and differs in length from  $a$  and  $b$ . The rhombohedral cell has three equal axes at angles not necessarily  $90^\circ$  with each other. It can be regarded as a cube either compressed or elongated along a body diagonal. The rhombohedral cell corresponds to a hexagonal cell centered at  $2/3, 1/3, 1/3$  and  $1/3, 2/3, 2/3$ . The relation between the cell parameters  $a$  and  $c$  of the hexagonal cell and the parameters  $a'$  and  $\alpha'$  of the rhombohedral cell are as follows:

$$a = a' \sqrt{2} \sqrt{1 - \cos \alpha'} = 2a' \sin \frac{\alpha'}{2},$$

$$c = a' \sqrt{3} \sqrt{1 + 2 \cos \alpha'},$$

$$\frac{c}{a} = \sqrt{\frac{3}{2}} \sqrt{\frac{1 + 2 \cos \alpha'}{1 - \cos \alpha'}} = \sqrt{\frac{9}{4 \sin^2(\alpha'/2)} - 3},$$

$$a' = \frac{1}{3} \sqrt{3a^2 + c^2},$$

$$\sin \frac{\alpha'}{2} = \frac{3}{2\sqrt{3 + (c^2/a^2)}} \text{ or } \cos \alpha' = \frac{(c^2/a^2) - 3/2}{(c^2/a^2) + 3}.$$

It is important to realize that the conditions imposed on cell geometry are not sufficient to distinguish between the crystal systems. For instance, if a unit cell is found to have three angles of  $90^\circ$ , it does not necessarily mean that the crystal belongs to the orthorhombic system. It could also be triclinic with three angles of  $90^\circ$  in the unit cell by coincidence. By being orthorhombic it is, in addition, required to have a minimum point group symmetry of 222 in the crystal, which expresses itself as mmm symmetry in the diffraction pattern (“mmm” means three perpendicular mirror planes).

### 3.8. Radiation Damage

In Chapter 2, it was mentioned that the high-energy photons of X-rays have a harmful effect on living tissue. This also applies to crystals of biological macromolecules that undergo radiation damage if exposed to X-rays. Some systems are far more sensitive to it than others. Radiation damage is sometimes so serious that after only a few hours of exposure at room temperature, the X-ray pattern dies away. The photons cause the formation of radicals, which leads to subsequent chemical reactions that gradually destroy the crystalline order.

The radicals are produced in the biological macromolecules and the solvent. Some of these radicals (e.g., oxygen or hydroxy radicals) diffuse away and exercise their damaging effect at other sites in the crystal. Although the problem of radiation damage has been reduced with modern, sensitive X-ray detectors that allow relatively short exposure times, it is strongly reduced by cooling the crystals to cryogenic temperatures (the region between 100 and 120 K) (Section 1.7 of Chapter 1). At these temperatures, radicals are still created by the X-ray photons,

but their diffusion through the crystal is eliminated. This allows for most biological macromolecules to collect a complete dataset on one crystal. Problems arise with extremely strong undulator radiation. Even at cryotemperature, specific groups in the protein are damaged. Disulfide bonds are especially prone to be damaged, leading to bond cleavage. Carboxylic acids can be decarboxylated; cysteine, methionine and tyrosine can also suffer. Moreover, an increase in atomic B-factors and in unit cell parameters has been observed (Burmeister, 2000; Schröder Leiros, 2001; Welk et al., 2001; Diederichs 2001. Diederichs (2006) and Diederichs et al. (2003) measured a decay function that is fitted to the intensities of all observations of a unique reflection as a function of radiation dose. Extrapolation to zero dose gives an improved value of the intensity of that unique reflection.

### 3.9. Characterization of the Crystals

If crystals of sufficient size ( $\geq 0.1$  mm) have been grown, they must first be characterized:

- What is their quality?
- What are the unit cell dimensions?
- To what space group do they belong?
- How many protein molecules are in the unit cell and in one asymmetric unit?

The quality of the crystals depends on the ordering of the molecules in the unit cell. Because of thermal vibrations and static disorder, the positions of the atoms are not strictly fixed. As a consequence, the intensities of the X-ray reflections drop at higher diffraction angles. In Section 4.7.2 of Chapter 4 it will be shown that the diffracted X-ray beams can be considered as being reflected against lattice planes and that the relation between the lattice plane distance  $d$  and the diffraction angle  $\theta$  is given by  $2d \sin \theta = \lambda$  (Bragg's law). Diffraction patterns with maximal observed resolution corresponding to a lattice spacing of  $5 \text{ \AA}$  can be regarded as poor, of  $2.0\text{--}2.5 \text{ \AA}$  as normal, and of  $1.0\text{--}1.5 \text{ \AA}$  as high quality.

Most crystals cannot be considered as ideal single crystals because the regular repetition of the unit cells is interrupted by lattice defects. The diffraction pattern of such crystals can be regarded as the sum of the diffraction patterns originating from mosaic blocks with slightly different orientations. The mosaicity in good quality protein crystals is moderate, between  $0.2^\circ$  and  $0.5^\circ$ .<sup>2</sup> The cell dimensions can easily be derived from the diffraction pattern collected with an image plate or area detector.

From the symmetry in the diffraction pattern and the systematic absence of specific reflections in that pattern, one can deduce the space group to which the crystal belongs. As discussed in Section 3.3, space groups with mirror planes or

---

<sup>2</sup> The Program DENZO defines mosaicity as “the rocking angle in degrees, in both the vertical and the horizontal directions which would generate all the spots seen on a still diffraction photograph. It includes contributions due to X-ray bandwidth, beam crossfire, etc.” (Gewirth, 1997).

inversion centers do not apply to protein crystals. An inversion center does occur, however, *in the X-ray diffraction pattern* if anomalous scattering (Section 7.8 of Chapter 7) is absent.

An estimation of the number of molecules per unit cell ( $Z$ ) can be made by a method proposed by Matthews. He found that for many protein crystals the ratio of the unit cell volume and the molecular weight is between 1.7 and 3.5 Å<sup>3</sup>/Dalton, with most values around 2.15 Å<sup>3</sup>/Dalton. This number is called  $V_M$  (Matthews, 1968).

**Example:** Suppose a crystal belongs to space group  $C2$  and has a unit cell volume of 319,000 Å<sup>3</sup>. The molecular weight  $M_r$  of the protein is known to be 32,100. Then, for  $Z = 2, 4, \text{ or } 8$ ,  $V_M$  is respectively 5, 2.5, or 1.25 Å<sup>3</sup>/Dalton. This crystal most likely has four molecules in the unit cell. Space group  $C2$  (No. 5 in the *International Tables*) has four asymmetric units and, therefore, there is one protein molecule per asymmetric unit.

For a more accurate determination of the number of protein molecules per unit cell, the density of the crystal and its solvent content should be determined. The density can best be measured in a density gradient column, made up from organic solvents, or from a water solution of the polymer compound Ficoll at a concentration of 30–60%. Because of the high viscosity of the Ficoll solutions, these measurements must be done in a centrifuge (Leung et al., 1999; Westbrook, 1985).

The solvent content of the crystals could—in principle—be determined by weighing a number of crystals before and after drying. However, a problem arises because in the wet state, solvent around the crystals must be removed, but not the internal solvent that fills the pores inside the crystals and that is part of the crystal structure. This separation is difficult to achieve. With the unit cell volume ( $V_{\text{cell}}$ ), the density  $\rho$ , and the solvent content (weight fraction  $x$ ) known,  $Z$  can be calculated<sup>3</sup>:

$$\frac{ZM_r}{N} = (1 - x)\rho V_{\text{cell}}, \quad (3.2)$$

where  $N$  is Avogadro's number. From  $V_M$ , the volume fraction of the solvent in the crystal can be calculated in the following way:

$$\begin{aligned} V_{\text{protein}} &= \frac{\text{Volume of protein in the unit cell}}{V_{\text{cell}}} \\ &= \frac{Z \times M_r \times (\text{specific volume of the protein})/N}{V_M \times Z \times M_r} \\ &= \frac{\text{specific volume in cm}^3/\text{g}}{V_M \text{ in } \text{Å}^3/\text{Dalton} \times N} \end{aligned}$$

<sup>3</sup>For unit cells with nonorthogonal axes., the equation for calculating  $V_{\text{cell}}$  is rather complicated:

$$V_{\text{cell}} = abc [1 - \cos^2 \alpha - \cos^2 \beta - \cos^2 \gamma + 2 \cos \alpha \cos \beta \cos \gamma]^{1/2}$$

(Wilson and Prince, 1999, p. 2). See also Table 4.1 of Chapter 4.

The specific volume of a protein molecule is always  $\sim 0.74 \text{ cm}^3/\text{g}$ , and this gives

$$V_{\text{protein}} = 1.23/V_M \quad \text{and} \quad V_{\text{solvent}} = 1 - 1.23/V_M.$$

For the example given earlier, where  $V_M = 2.5$ ,  $V_{\text{solvent}} = 0.51$ .

## Summary

People have been fascinated by crystals since prehistoric times. However, before the introduction of X-ray diffraction in 1912, only their external properties could be studied, such as the angles between their faces or physical properties like hardness. X-ray diffraction not only showed the wave nature of X-rays but also allowed the investigation of the internal structure of crystals and of their constituent molecules or ions, in atomic detail. Therefore, for a protein crystallographer, the beauty of protein crystals is not in their external faceted shape, but in the periodic arrangement of the molecules in the crystal. Without crystals there is no structure determination (at least not by X-ray crystallography), and the better the quality of the crystals, the more accurately the structure can be determined. Because crystals are the main tool for a crystallographer, familiarity with their properties, with lattice planes, symmetry, space groups, and asymmetric units, is a requirement.

# Chapter 4

## Theory of X-ray Diffraction by a Crystal

### 4.1. Introduction

The best way to learn protein X-ray diffraction is by practical work in the laboratory. However, it would be very unsatisfying to perform the experiments without understanding why they have to be done in such and such a way. Moreover, at several stages in the determination of protein structures, it is necessary to decide what the next step should be. For instance, after growing suitable crystals and soaking these crystals in solutions of heavy atom reagents, applying the isomorphous replacement method, how do you obtain the positions of the heavy atoms in the unit cell and, if you do have them, how do you proceed? Questions such as these can be answered only if you have some knowledge of the theoretical background of protein X-ray crystallography. This is presented in this chapter. A slow path will be followed, and a student with a minimal background in mathematics but the desire to understand protein X-ray crystallography should be able to work through the chapter. A working knowledge of differentiation and integration is required. If you further accept that an X-ray beam can be regarded as a wave that travels as a cosine function and if you know what a vector is, you have a good start. Derivations and explanations that are not absolutely necessary to follow the text are set off within rules; these can be skipped, if you want.

In Chapter 1 the diffraction of X-rays by a crystal was introduced. In analogy with the scattering of visible light by a two-dimensional grid, a crystal diffracts an X-ray beam in a great many directions. From the diffraction experiment with lysozyme, it was concluded that diffraction by an X-ray beam can be understood as being derived from the intersection of an imaginary lattice, the reciprocal lattice, and a sphere, called the Ewald sphere. From the direction of the diffracted beams, the dimensions of the unit cell can be derived. However, we

are, of course, more interested in the content of the unit cell (i.e., in the structure of the protein molecules). The molecular structure and the arrangement of the molecules in the unit cell determine the intensities of the diffracted beams. Therefore, a relationship must be found between the intensities of the diffracted beams and the crystal structure. In fact, this relation is between the diffraction data and the electron density distribution in the crystal structure, because X-rays are scattered almost exclusively by the electrons in the atoms and not by the nuclei.

The scattering is an interaction between X-rays as electromagnetic waves and the electrons. If an electromagnetic wave is incident on a system of electrons, the electric and magnetic components of the wave exert a force on the electrons. This causes the electrons to oscillate with the same frequency as the incident wave. The oscillating electrons act as radiation scatterers and they emit radiation of the same frequency as the incident radiation. Energy from the incident wave is absorbed by the electrons and then emitted. Because of the attraction between the electrons and the atomic nucleus, an electrical restoring force exists for the electrons of an atom. However, in X-ray diffraction, the electrons in an atom can be regarded, to a good approximation, as free electrons.

The wave scattered by the crystal might be described as a summation of the enormous number of waves, each scattered by one electron in the crystal. This might sound somewhat intimidating because a single unit cell in a protein crystal contains  $\sim 10,000$  or more electrons and there are a great many unit cells in a crystal. All of these waves must be added! It is clear that we need a convenient way to add waves. This method will be presented first; familiarity with the technique will reveal how it simplifies the whole process. It is then fairly easy to derive an expression that relates each wave scattered by the crystal to the electron density distribution in the crystal and in its unit cells. The next step is to reverse this expression and derive the electron density distribution as a function of the scattering information.

## 4.2. Waves and Their Addition

An electromagnetic wave travels as a cosine function (Figure 4.1a).  $E$  is the electromagnetic field strength,  $\lambda$  is the wavelength of the radiation, and  $\nu = c/\lambda$  is the frequency, with  $c$  the speed of light (and of any other electromagnetic radiation).  $A$  is the amplitude of the wave.

Let Figure 4.1a show the wave at time  $t = 0$ . The electric field strength at time  $t = 0$  and position  $z$  is

$$E(t = 0; z) = A \cos 2\pi \frac{z}{\lambda}.$$

During a time period  $t$ , the wave travels over a distance  $t \times c = t \times \lambda \times \nu$ . Therefore, at time  $t$ , the field strength at position  $z$  is equal to what it was at time  $t = 0$

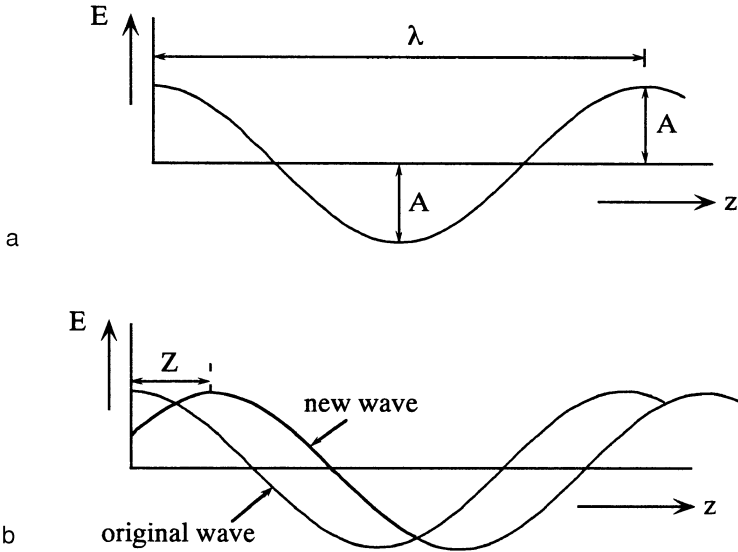


Figure 4.1. (a) The electric component of an electromagnetic wave.  $A$  is the amplitude and  $\lambda$  is the wavelength. The accompanying magnetic component is perpendicular to the electric one, but we do not need to consider it here. (b) A new wave, displaced over a distance  $Z$ , is added.

and position  $z - t \times \lambda \times \nu$ .

$$\begin{aligned}
 E(t; z) &= A \cos 2\pi \frac{1}{\lambda} (z - t \times \lambda \times \nu) \\
 &= A \cos 2\pi \left( \frac{z}{\lambda} - \nu t \right) = A \cos 2\pi \nu \left( t - \frac{z}{c} \right).
 \end{aligned}$$

At  $z = 0$ , the field strength is  $E(t; z = 0) = A \cos 2\pi \nu t$ , and substituting, for convenience,  $\omega$  for  $2\pi \nu$ , we have

$$E(t; z = 0) = A \cos \omega t.$$

Let us now consider a new wave with the same  $\lambda$  and the same amplitude  $A$ , but displaced over a distance  $Z$  with respect to the original wave (Figure 4.1b).  $Z$  corresponds with a phase shift  $(Z/\lambda) \times 2\pi = \alpha$ .

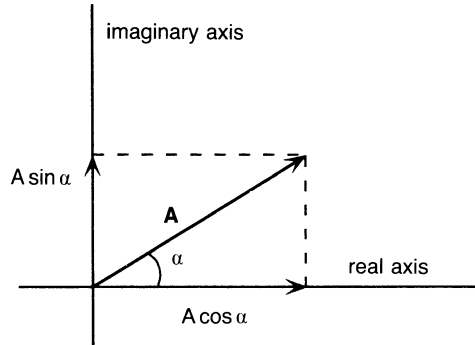
$$\text{Original wave at } z = 0 \text{ and time } t : E_{\text{orig}}(t; z = 0) = A \cos \omega t$$

$$\text{New wave at } z = 0 \text{ and time } t : E_{\text{new}}(t; z = 0) = A \cos(\omega t + \alpha)$$

Let us now consider only the new wave as representing any wave with a phase angle difference with respect to a reference wave:

$$\begin{aligned}
 A \cos(\omega t + \alpha) &= A \cos \alpha \cos \omega t + A \sin \alpha \sin \omega t \\
 &= A \cos \alpha \cos \omega t + A \sin \alpha \cos(\omega t + 90^\circ)
 \end{aligned}$$

Figure 4.2. The real component  $A \cos \alpha$  and the imaginary component  $A \sin \alpha$  of vector  $\mathbf{A}$  in an Argand diagram.



Therefore, the wave  $A \cos(\omega t + \alpha)$  can be regarded as being composed of two waves: wave 1 of amplitude  $A \cos \alpha$  and phase angle  $0^\circ$  and wave 2 of amplitude  $A \sin \alpha$  and phase angle  $90^\circ$ . Wave 1 is called the real part and wave 2 is called the imaginary part of the total wave. To add several waves with different phase angles, their real parts can be added together because they all have phase angle 0. Similarly, their imaginary parts, with phase angle  $90^\circ$ , can be added together. This can be represented conveniently in an axial system called an Argand diagram, in which the real axis is horizontal and the imaginary axis is vertical (Figure 4.2). The wave itself is represented by vector  $\mathbf{A}$ , with projections  $A \cos \alpha$  on the real axis and  $A \sin \alpha$  on the imaginary axis.<sup>1</sup> Addition of all of the real parts and of all of the imaginary parts of several waves is the same as adding several wave vectors (like  $\mathbf{A}$ ) together. The plane with the real axis and the imaginary axis is called the complex plane.

*Conclusion:* We have simplified the problem of adding waves with the same frequency (or wavelength) by applying the following procedure:

- Represent each wave as a vector in a two-dimensional axial system. The length of each vector is equal to the amplitude of the wave. The vector makes an angle with the horizontal, or real, axis equal to its phase with respect to a reference wave (angle  $\alpha$  in Figure 4.2).
- The vector representing the total wave of a system is obtained by adding the vectors of the separate waves together.

Although the representation of waves as vectors in the Argand diagram is extremely convenient, it would still require an enormous amount of work to add thousands of these vectors together manually. This problem is solved by writing the vectors in mathematical form. Consider the wave of Figure 4.2 with the two components  $A \cos \alpha$  (horizontal) and  $A \sin \alpha$  (vertical). The entire wave is written in mathematical form as  $A \cos \alpha + iA \sin \alpha$ .  $i$  simply means that the  $A \sin \alpha$  component points vertical, or  $i$  means that this component has been rotated  $90^\circ$

<sup>1</sup> A vector will be indicated by boldface type ( $\mathbf{A}$ ). The length of this vector is given by  $|\mathbf{A}|$ .



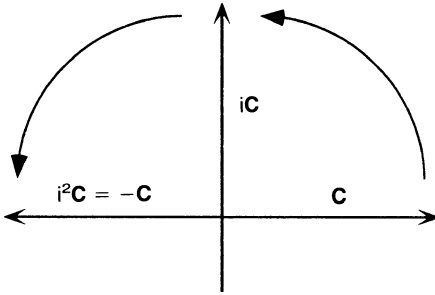


Figure 4.3. Multiplication of a vector  $\mathbf{C}$  in the Argand diagram by  $i$  simply means rotating  $\mathbf{C}$   $90^\circ$  counterclockwise. Therefore,  $i^2 \mathbf{C} = -\mathbf{C}$ .

counterclockwise with respect to the positive direction of the horizontal axis. It is then clear that  $i = \sqrt{-1}$  (Figure 4.3). A further simplification is to write  $A \cos \alpha + iA \sin \alpha$  as  $A \exp[i\alpha]$ .

---

### Properties of Exponential Terms

We will not prove that  $A \cos \alpha + iA \sin \alpha = A \exp[i\alpha]$ . You must know, however, the properties of exponential terms:

$$\begin{aligned} \exp[a] \exp[b] &= \exp[a + b]; & \frac{\exp[a]}{\exp[b]} &= \exp[a - b]; \\ \exp[k \cdot a] &= \{\exp[a]\}^k; & \exp[0] &= 1; \\ \exp[a] &\rightarrow +\infty \text{ for } a \rightarrow +\infty; \\ \exp[a] &\rightarrow 0 \text{ for } a \rightarrow -\infty. \end{aligned}$$


---

Now we are ready to work with waves and electrons. We will start with a simple system of only two electrons.

### 4.3. A System of Two Electrons

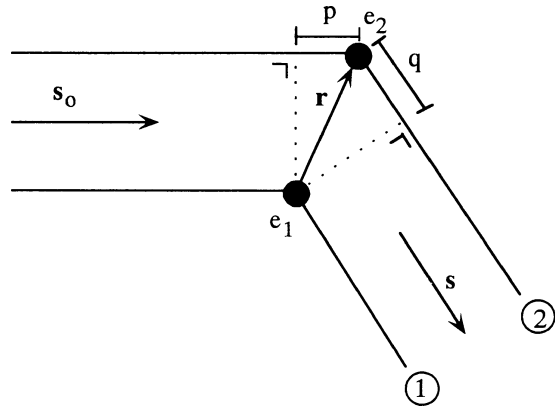
The system in Figure 4.4 has only two electrons:  $e_1$  and another electron  $e_2$  at position  $\mathbf{r}$  with respect to  $e_1$ . An X-ray beam, indicated by the wave vector  $\mathbf{s}_0$  with length  $1/\lambda$  hits the system and is diffracted in the direction of wave vector  $\mathbf{s}$ , which also has length  $1/\lambda$ . The beam that passes along electron  $e_2$  follows a longer path than the beam along electron  $e_1$ .

The path difference between the two beams ( $p + q$ ) depends on (1) the position of electron  $e_2$  with respect to  $e_1$  and (2) the direction of diffraction. Because  $\mathbf{s}_0$  and  $\mathbf{s}$  are wave vectors of magnitude  $1/\lambda$  each,  $p = \lambda \cdot \mathbf{r} \cdot \mathbf{s}_0$  and  $q = -\lambda \cdot \mathbf{r} \cdot \mathbf{s}$  (the minus sign is due to the fact that the projection of  $\mathbf{r}$  on  $\mathbf{s}$  has a direction opposite to  $\mathbf{s}$ ).<sup>2</sup> The path difference is, therefore,  $p + q = \lambda \cdot \mathbf{r} \cdot (\mathbf{s}_0 - \mathbf{s})$ .

---

<sup>2</sup>  $\mathbf{r} \cdot \mathbf{s}$  is the scalar product of the vectors  $\mathbf{r}$  and  $\mathbf{s}$ .

Figure 4.4. A system of two electrons:  $e_1$  and  $e_2$ . The path difference between the scattered waves 1 and 2 is  $p + q$ .



The wave along electron  $e_2$  is lagging behind in phase compared with the wave along  $e_1$ . With respect to wave 1, the phase of wave 2 is

$$-\frac{2\pi\mathbf{r} \cdot (\mathbf{s}_0 - \mathbf{s}) \cdot \lambda}{\lambda} = 2\pi\mathbf{r} \cdot \mathbf{S},$$

where

$$\mathbf{S} = \mathbf{s} - \mathbf{s}_0 \tag{4.1}$$

It is interesting to note that the wave can be regarded as being reflected against a plane with  $\theta$  as the reflecting angle and  $|\mathbf{S}| = 2(\sin \theta)/\lambda$  (Figure 4.5). The physical meaning of vector  $\mathbf{S}$  is the following: Because  $\mathbf{S} = \mathbf{s} - \mathbf{s}_0$ , with  $|\mathbf{s}| = |\mathbf{s}_0| = 1/\lambda$ ,  $\mathbf{S}$  is perpendicular to the imaginary “reflecting plane,” which makes equal angles with the incident and reflected beam.

### The Product of Two Vectors $\mathbf{a}$ and $\mathbf{b}$

Let vectors  $\mathbf{a}$  and  $\mathbf{b}$ , with lengths  $|\mathbf{a}|$  and  $|\mathbf{b}|$ , be inclined at an angle  $\theta$ .

*Scalar product:* Their scalar product is the number  $\mathbf{a} \cdot \mathbf{b} = ab \cos \theta$  and  $\mathbf{a} \cdot \mathbf{b} = \mathbf{b} \cdot \mathbf{a}$ .

*Vector product:* Let  $\mathbf{a}$  and  $\mathbf{b}$  again be inclined at an angle  $\theta$ , with  $0 \leq \theta \leq \pi$ . Their vector product is a vector  $\mathbf{c}$ , which has a length  $|\mathbf{c}| = ab \sin \theta$  and points in

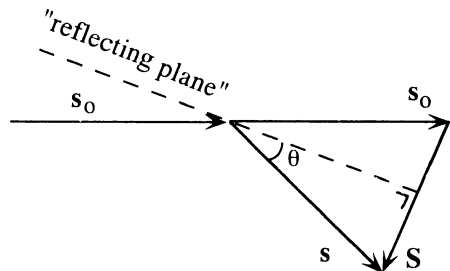
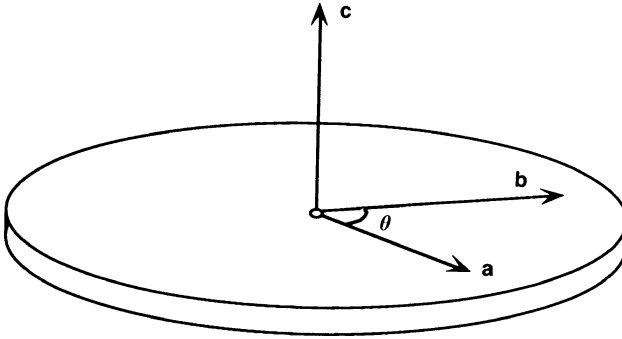


Figure 4.5. The primary wave, represented by  $\mathbf{s}_0$ , can be regarded as being reflected against a plane.  $\theta$  is the reflecting angle. Vector  $\mathbf{S}$  is perpendicular to this plane.

a direction perpendicular to both  $\mathbf{a}$  and  $\mathbf{b}$ , such that the vector system  $\mathbf{a}$ ,  $\mathbf{b}$ ,  $\mathbf{c}$  is a right-handed triad;  $\mathbf{c} = \mathbf{a} \times \mathbf{b} = -\mathbf{b} \times \mathbf{a}$ .



If we add the waves 1 and 2 in Figure 4.4, the Argand diagram shows two vectors,  $\mathbf{1}$  and  $\mathbf{2}$ , with equal length (amplitude) and a phase of  $2\pi\mathbf{r} \cdot \mathbf{S}$  for wave  $\mathbf{2}$  with respect to wave  $\mathbf{1}$  (Figure 4.6). Vector  $\mathbf{T}$  represents the sum of the two waves. In mathematical form:  $\mathbf{T} = \mathbf{1} + \mathbf{2} = \mathbf{1} + \mathbf{1} \exp[2\pi i\mathbf{r} \cdot \mathbf{S}]$  if the length of the vectors equals 1. So far we had the origin of this two-electron system in  $e_1$ . Suppose we move the origin over  $-\mathbf{R}$  from  $e_1$  to point  $O$  (Figure 4.7). Then we obtain the following: With respect to a wave  $\mathbf{0}$ , wave  $\mathbf{1}$  has a phase of  $2\pi\mathbf{R} \cdot \mathbf{S}$ , and wave  $\mathbf{2}$  has a phase of  $2\pi(\mathbf{r} + \mathbf{R}) \cdot \mathbf{S}$  (Figure 4.8)

$$\begin{aligned} \mathbf{T} &= \mathbf{1} + \mathbf{2} = \exp[2\pi i\mathbf{R} \cdot \mathbf{S}] + \exp[2\pi i(\mathbf{r} + \mathbf{R}) \cdot \mathbf{S}] \\ &= \exp[2\pi i\mathbf{R} \cdot \mathbf{S}]\{1 + \exp[2\pi i\mathbf{r} \cdot \mathbf{S}]\} \end{aligned}$$

*Conclusion:* A shift of the origin by  $-\mathbf{R}$  causes an increase of all phase angles by  $2\pi\mathbf{R} \cdot \mathbf{S}$ . The amplitude and intensity (which is proportional to the square of the amplitude) of wave  $\mathbf{T}$  do not change.

From the two-electron system we shall now move to more complicated systems: first an atom, then a combination of atoms in a unit cell, and finally a crystal.

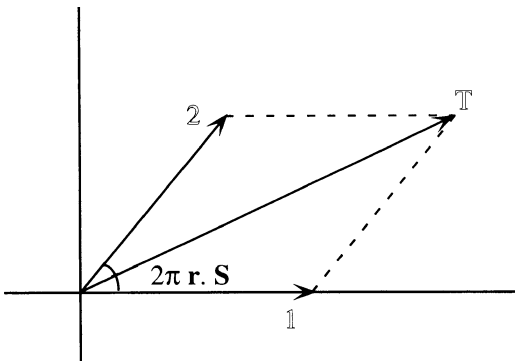


Figure 4.6. The summation of the two scattered waves in Figure 4.4 with the origin in electron  $e_1$ .

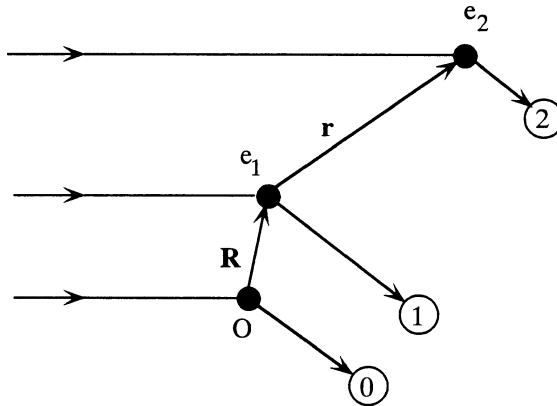


Figure 4.7. The origin, or reference point, for the scattered waves of the two-electron system is now located at  $O$ .

### 4.4. Scattering by an Atom

The electron cloud of an atom scatters an X-ray beam; the scattering is dependent on the number of electrons and their positions in the cloud. We wish to understand the scattering of an atom with the origin of the system in the nucleus (Figure 4.9) because the scattering by an atom located elsewhere will be the same, except for a phase shift, as was shown in the previous section. The electron density at position  $\mathbf{r}$  is denoted by  $\rho(\mathbf{r})$ . The cloud is centrosymmetric around the origin, which means that  $\rho(\mathbf{r}) = \rho(-\mathbf{r})$ . From Figure 4.10 we can easily derive that the scattering by an atom is always real; the vector of the scattered wave is directed along the real axis in the Argand diagram.

The atomic scattering factor  $f$  is

$$f = \int_{\mathbf{r}} \rho(\mathbf{r}) \exp[2\pi i \mathbf{r} \cdot \mathbf{S}] d\mathbf{r}, \tag{4.2}$$

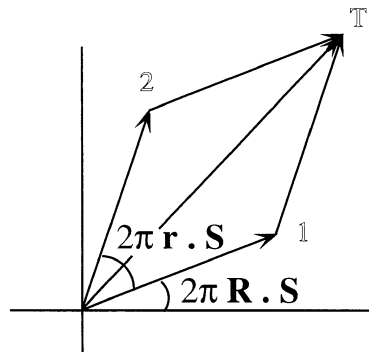


Figure 4.8. The summation of waves 1 and 2 with the origin of the two-electron system in position  $O$ .

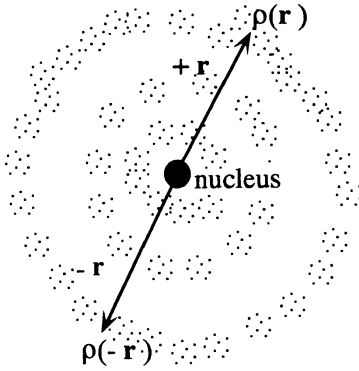


Figure 4.9. The electron cloud of an atom.  $\rho(\mathbf{r})$  is the electron density. Because of the centrosymmetry,  $\rho(\mathbf{r}) = \rho(-\mathbf{r})$ .

where the integration is over the entire space  $\mathbf{r}$ . From Figure 4.10,

$$\begin{aligned} f &= \int_{\mathbf{r}} \rho(\mathbf{r}) \{ \exp[2\pi i \mathbf{r} \cdot \mathbf{S}] + \exp[-2\pi i \mathbf{r} \cdot \mathbf{S}] \} d\mathbf{r} \\ &= 2 \int_{\mathbf{r}} \rho(\mathbf{r}) \cos[2\pi \mathbf{r} \cdot \mathbf{S}] d\mathbf{r}. \end{aligned}$$

Now the integration is over half of the entire space. Generally in X-ray crystallography, it is assumed that the electron cloud of an atom is not only centrosymmetric but spherically symmetric. Therefore, it does not make any difference if the orientation of the atom changes with respect to the direction of  $\mathbf{S}$ . The atomic scattering factor is independent of the direction of  $\mathbf{S}$ , but it does depend on the length of  $\mathbf{S}$ :

$$|S| = \frac{2 \sin \theta}{\lambda}.$$

Values for the atomic scattering factor  $f$  can be looked up in tables, in which  $f$  is expressed as a function of  $2(\sin \theta)/\lambda$  (see Figure 4.11).

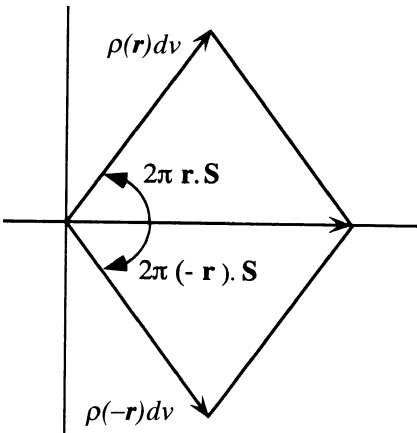


Figure 4.10. The scattering factor  $f$  of an atom is always real if we assume centrosymmetry of the electron cloud. The imaginary part of every scattering vector is compensated by the imaginary part of a vector with equal length but a phase angle of opposite sign.

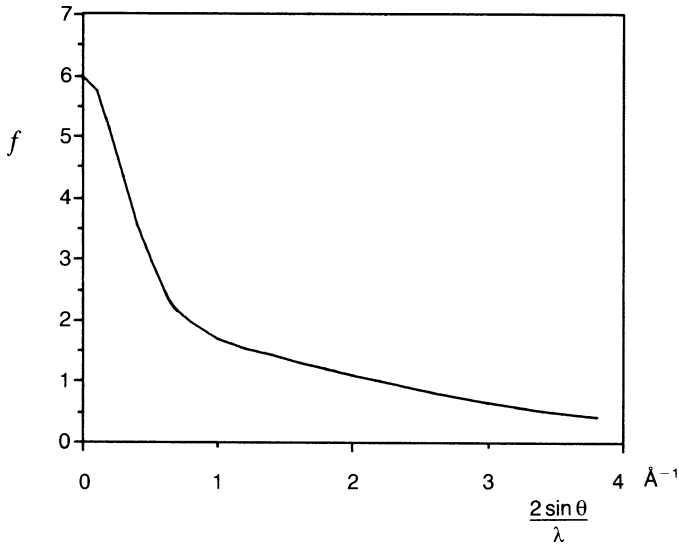


Figure 4.11. The scattering factor  $f$  for a carbon atom as a function of  $2(\sin \theta)/\lambda$ .  $f$  is expressed as electron number, and for the beam with  $\theta = 0$ ,  $f = 6$ .

### 4.5. Scattering by a Unit Cell

Suppose a unit cell has  $n$  atoms at positions  $\mathbf{r}_j$  ( $j = 1, 2, 3, \dots, n$ ) with respect to the origin of the unit cell (Figure 4.12). With their own nuclei as origins, the atoms diffract according to their atomic scattering factor  $f$ . If the origin is now transferred to the origin of the unit cell, the phase angles change by  $2\pi \mathbf{r}_j \cdot \mathbf{S}$ . With respect to the new origin, the scattering is given by

$$\mathbf{f}_j = f_j \exp[2\pi i \mathbf{r}_j \cdot \mathbf{S}],$$

where the  $\mathbf{f}_j$ 's are the vectors in the Argand diagram. The total scattering from the

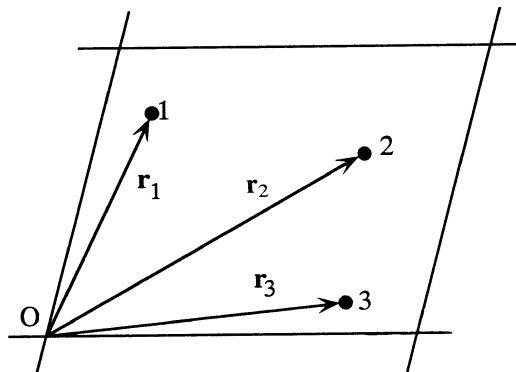


Figure 4.12. A unit cell with three atoms (1, 2, and 3) at positions  $\mathbf{r}_1$ ,  $\mathbf{r}_2$ , and  $\mathbf{r}_3$ .

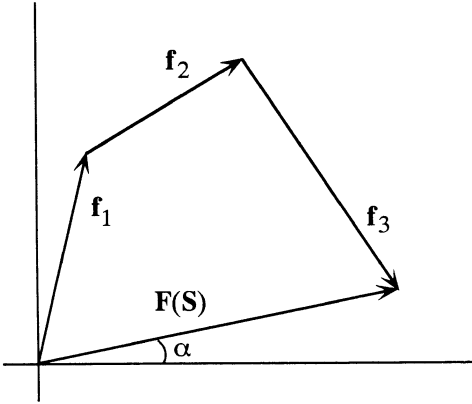


Figure 4.13. The structure factor  $\mathbf{F}(\mathbf{S})$  is the sum of the scattering by the separate atoms in the unit cell.

unit cell is

$$\mathbf{F}(\mathbf{S}) = \sum_{j=1}^n f_j \exp[2\pi i \mathbf{r}_j \cdot \mathbf{S}]. \quad (4.3)$$

$\mathbf{F}(\mathbf{S})$  is called the *structure factor* because it depends on the arrangement (structure) of the atoms in the unit cell (Figure 4.13).

## 4.6. Scattering by a Crystal

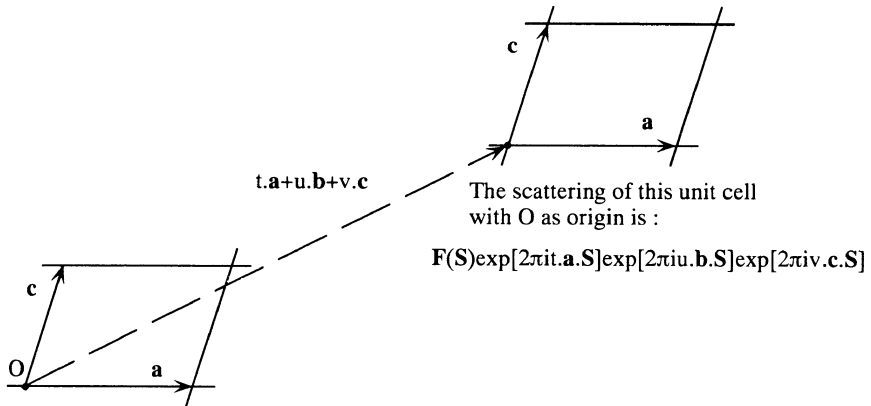
Suppose that the crystal has translation vectors  $\mathbf{a}$ ,  $\mathbf{b}$ , and  $\mathbf{c}$  and contains a large number of unit cells:  $n_1$  in the  $\mathbf{a}$  direction,  $n_2$  in the  $\mathbf{b}$  direction, and  $n_3$  in the  $\mathbf{c}$  direction (Figure 4.14). To obtain the scattering by the crystal, we must add the scattering by all unit cells with respect to a single origin. We choose the origin  $O$  in Figure 4.14. For a unit cell with its own origin at position  $t \cdot \mathbf{a} + u \cdot \mathbf{b} + v \cdot \mathbf{c}$ , in which  $t$ ,  $u$ , and  $v$  are whole numbers, the scattering is

$$\mathbf{F}(\mathbf{S}) \times \exp[2\pi i t \mathbf{a} \cdot \mathbf{S}] \times \exp[2\pi i u \mathbf{b} \cdot \mathbf{S}] \times \exp[2\pi i v \mathbf{c} \cdot \mathbf{S}].$$

The total wave  $\mathbf{K}(\mathbf{S})$  scattered by the crystal is obtained by a summation over all unit cells:

$$\mathbf{K}(\mathbf{S}) = \mathbf{F}(\mathbf{S}) \times \sum_{t=0}^{n_1} \exp[2\pi i t \mathbf{a} \cdot \mathbf{S}] \times \sum_{u=0}^{n_2} \exp[2\pi i u \mathbf{b} \cdot \mathbf{S}] \times \sum_{v=0}^{n_3} \exp[2\pi i v \mathbf{c} \cdot \mathbf{S}].$$

Because  $n_1$ ,  $n_2$ , and  $n_3$  are very large, the summation  $\sum_{t=0}^{n_1} \exp[2\pi i t \mathbf{a} \cdot \mathbf{S}]$  and the other two over  $u$  and  $v$  are almost always equal to zero unless  $\mathbf{a} \cdot \mathbf{S}$  is an integer  $h$ ,  $\mathbf{b} \cdot \mathbf{S}$  is an integer  $k$ , and  $\mathbf{c} \cdot \mathbf{S}$  is an integer  $l$ . This is easy to understand if we regard  $\exp[2\pi i t \mathbf{a} \cdot \mathbf{S}]$  as a vector in the Argand diagram with a length of 1 and a phase angle  $2\pi t \mathbf{a} \cdot \mathbf{S}$  (see Figure 4.15).



The scattering of this unit cell with O as origin is  $F(\mathbf{S})$

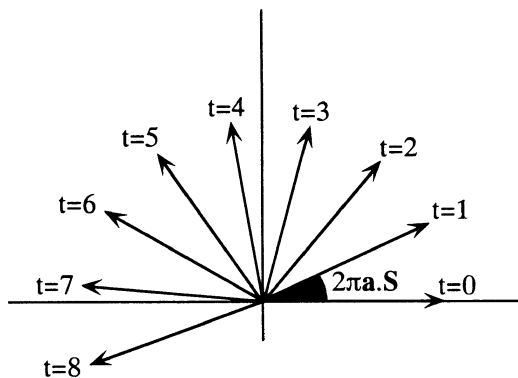
Figure 4.14. A crystal contains a large number of identical unit cells. Only two of them are drawn in this figure.

*Conclusion:* A crystal does not scatter X-rays, unless

$$\begin{aligned} \mathbf{a} \cdot \mathbf{S} &= h, \\ \mathbf{b} \cdot \mathbf{S} &= k, \\ \mathbf{c} \cdot \mathbf{S} &= l. \end{aligned} \tag{4.4}$$

These are known as the Laue conditions.  $h, k,$  and  $l$  are whole numbers, either positive, negative, or zero. The amplitude of the total scattered wave is proportional to the amplitude of the structure factor  $F(\mathbf{S})$  and the number of unit cells in the crystal.

Figure 4.15. Each arrow represents the scattering by one unit cell in the crystal. Because of the huge number of unit cells and because their scattering vectors are pointing in different directions, the scattering by a crystal is, in general, zero. However, in the special case that  $\mathbf{a} \cdot \mathbf{S}$  is an integer  $h$ , all vectors point to the right and the scattering by the crystal can be of appreciable intensity.





## 4.7. Diffraction Conditions

### 4.7.1. Laue Conditions

For the formulation of the diffraction conditions, we consider an infinitely large crystal. As we have just seen, the scattered wave has zero amplitude [ $\mathbf{K}(\mathbf{S}) = 0$ ] unless the Laue conditions are fulfilled ( $\mathbf{a} \cdot \mathbf{S} = h$ , etc.), in which case, all unit cells scatter in phase and  $\mathbf{K}(\mathbf{S})$  is proportional to  $\mathbf{F}(\mathbf{S})$ .

### 4.7.2. Bragg's Law

In Section 4.3, we noted that vector  $\mathbf{S}$  is perpendicular to a “reflecting” plane. With a chosen origin for the system,  $\mathbf{r} \cdot \mathbf{S}$  is the same for all points in the reflecting plane. This is true because the projection of each  $\mathbf{r}$  on  $\mathbf{S}$  has the same length. Because  $\mathbf{r} \cdot \mathbf{S}$  determines the phase angle, the waves from all points in a reflecting plane reflect in phase. Choose the origin of the system in the origin  $O$  of the unit cell. The waves from a reflecting plane through the origin have phase angle 0 ( $\mathbf{r} \cdot \mathbf{S} = 0$ ). For a parallel plane with  $\mathbf{r} \cdot \mathbf{S} = 1$ , they are shifted by  $1 \times 2\pi$ , and so forth. All parallel planes with  $\mathbf{r} \cdot \mathbf{S}$  equal to an integer are reflecting in phase and form a series of Bragg planes. The plane with  $\mathbf{r} \cdot \mathbf{S} = 1$  cuts the  $\mathbf{a}$ -axis at position  $\mathbf{r} = \frac{\mathbf{a}}{\xi}$ . Thus  $\frac{\mathbf{a}}{\xi} \cdot \mathbf{S} = 1$ . But from the Laue conditions we know that  $\frac{\mathbf{a}}{h} \cdot \mathbf{S} = 1$ . Therefore,  $\xi = h$  and in the same way the reflecting plane cuts the  $\mathbf{b}$ -axis at  $\mathbf{b}/k$  and the  $\mathbf{c}$ -axis at  $\mathbf{c}/l$ . The result is that the reflecting planes are the lattice planes. The projection of  $\mathbf{a}/h$  on  $\mathbf{S}$  has a length  $1/|\mathbf{S}|$ , but this projection is also equal to the distance  $d$  between the lattice planes (Figure 4.16). From  $1/|\mathbf{S}| = d$  and  $|\mathbf{S}| = 2(\sin \theta)/\lambda$

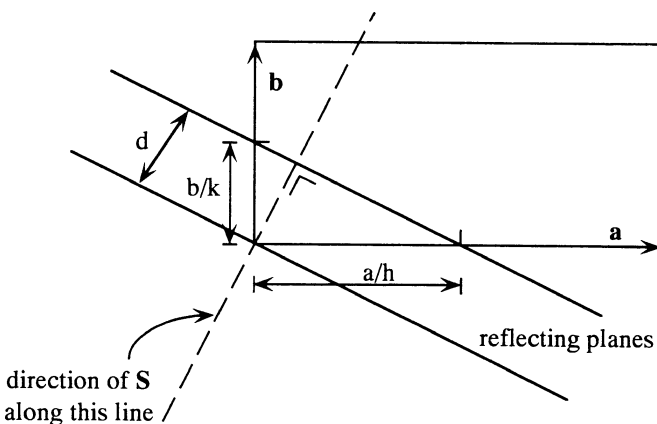


Figure 4.16. For simplicity, a two-dimensional unit cell is drawn. The end points of the vectors  $\mathbf{a}/h$ ,  $\mathbf{b}/k$ , and  $\mathbf{c}/l$  form a lattice plane perpendicular to vector  $\mathbf{S}$  (see the text).  $d$  is the distance between these lattice planes.

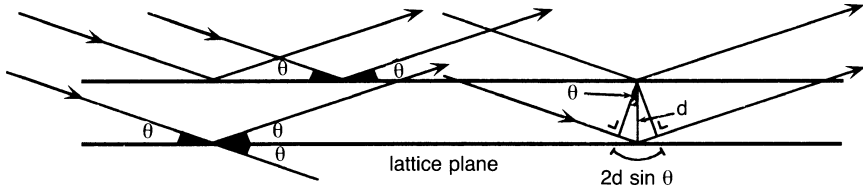


Figure 4.17. Two lattice planes are drawn separated by a distance  $d$ . The incident and the reflected beams make an angle  $\theta$  with the lattice planes. Note that the beam is thus deflected through an angle of  $2\theta$  relative to its incident direction.

(Section 4.3), the well-known Bragg law emerges:

$$\frac{2d \sin \theta}{\lambda} = 1. \tag{4.5}$$

The incident and reflected beam make an equal angle with the plane (Figure 4.17). In a series of parallel reflecting planes (Bragg planes), the phase difference between the radiation from successive planes is  $2\pi$ . The diffraction of X-rays by lattice planes can easily form the impression that only atoms on lattice planes contribute to the reflection. This is completely wrong! All atoms in the unit cell contribute to each reflection, atoms on lattice planes and in between. The advantage of lattice plane reflection and Bragg's law is that it offers a visual picture of the scattering process.

## 4.8. Reciprocal Lattice and Ewald Construction

In Chapter 1 we noted the reciprocity between the crystal lattice and the diffraction pattern. The Ewald sphere was also introduced, as a convenient tool to construct the diffraction pattern. This will now be formulated in a more quantitative way. There is a crystal lattice and a reciprocal lattice. The crystal lattice is real, but the reciprocal lattice is an imaginary lattice.

Question: What is the advantage of the reciprocal lattice?

Answer: With the reciprocal lattice, the directions of scattering can easily be constructed.

### 4.8.1. Construction of the Reciprocal Lattice

In Section 4.3 we noted that vector  $\mathbf{S}$  is related to the direction and angle of the reflected beam. Properties of  $\mathbf{S}$  are as follows:

$\mathbf{S} \perp$  reflecting plane;

$$|\mathbf{S}| = \frac{2 \sin \theta}{\lambda} \text{ because } \mathbf{S} = \mathbf{s} - \mathbf{s}_0; \text{ and } |\mathbf{s}_0| = |\mathbf{s}| = \frac{1}{\lambda}.$$

We also noted (Section 4.7) that the reflecting planes are in fact the lattice planes and that these lattice planes divide the  $\mathbf{a}$ -,  $\mathbf{b}$ -, and  $\mathbf{c}$ -axes into an integral number

( $h, k,$  and  $l$ ) of equal pieces. Moreover, we found that  $|S| = 1/d$ , where  $d$  is the distance between the lattice planes in one set of planes.

We now pay attention to the special planes (100), (010), and (001). For (100), the indices are  $h = 1, k = 0,$  and  $l = 0$ .  $S(100)$  is perpendicular to this plane and has a length of  $1/d(100)$ ; we call this vector  $\mathbf{a}^*$ . In the same way,  $S(010) \perp$  plane (010) with length  $1/d(010)$ ; we call this vector  $\mathbf{b}^*$ . Additionally,  $S(001) \perp$  plane (001) with length  $1/d(001)$ ; we call this vector  $\mathbf{c}^*$ . Because  $\mathbf{a}^* \perp$  plane (100), it is perpendicular to the  $\mathbf{b}$ -axis and the  $\mathbf{c}$ -axis, and, therefore,  $\mathbf{a}^* \cdot \mathbf{b} = \mathbf{a}^* \cdot \mathbf{c} = 0$ , but  $\mathbf{a} \cdot \mathbf{a}^* = \mathbf{a} \cdot S(100) = h = 1$ . In the same way, it can be shown that  $\mathbf{b} \cdot \mathbf{b}^* = \mathbf{b} \cdot S(010) = k = 1$  and  $\mathbf{c} \cdot \mathbf{c}^* = \mathbf{c} \cdot S(001) = l = 1$ .

Why did we introduce the vectors  $\mathbf{a}^*, \mathbf{b}^*,$  and  $\mathbf{c}^*$ ? The answer is that the end points of the vectors  $S(hkl)$  are located in the lattice points of a lattice constructed with the unit vectors  $\mathbf{a}^*, \mathbf{b}^*,$  and  $\mathbf{c}^*$ .

*Proof:*  $S$  can always be written as  $S = X \cdot \mathbf{a}^* + Y \cdot \mathbf{b}^* + Z \cdot \mathbf{c}^*$ . Multiply by  $\mathbf{a}$ :

$$\begin{aligned} \mathbf{a} \cdot \mathbf{S} &= X \times \mathbf{a} \cdot \mathbf{a}^* + Y \times \mathbf{a} \cdot \mathbf{b}^* + Z \times \mathbf{a} \cdot \mathbf{c}^* \\ \dots &\dots\dots\dots \\ &= h \qquad = X \times 1 \qquad = 0 \qquad = 0 \end{aligned}$$

It follows that  $X = h$ , and by the same token  $Y = k$  and  $Z = l$ . Therefore,  $S = h \cdot \mathbf{a}^* + k \cdot \mathbf{b}^* + l \cdot \mathbf{c}^*$ . The crystal lattice based on  $\mathbf{a}, \mathbf{b},$  and  $\mathbf{c}$  is called the *direct* lattice and that based on  $\mathbf{a}^*, \mathbf{b}^*,$  and  $\mathbf{c}^*$  is called the *reciprocal* lattice. Each reflection ( $hkl$ ) is denoted by a point ( $hkl$ ) in the reciprocal lattice. The relation between direct and reciprocal unit cells is drawn schematically in Figure 4.18.

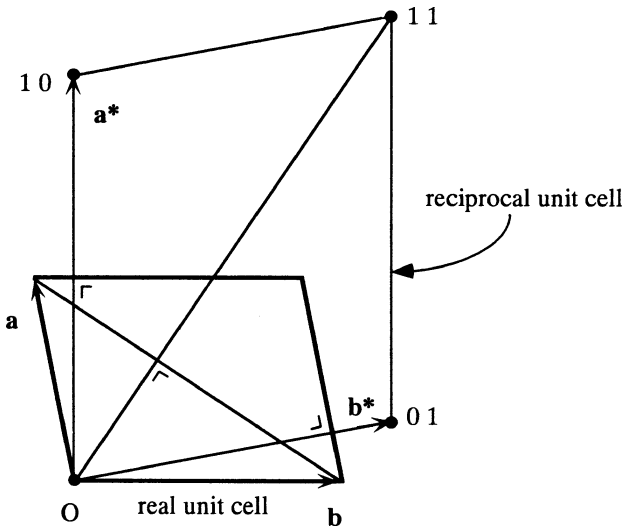


Figure 4.18. The relation between a real unit cell and the corresponding reciprocal unit cell. For simplicity, a two-dimensional cell is chosen.

Table 4.1. Relationship Between the Axes and Angles in the Direct and the Reciprocal Lattices in a Triclinic Space Group

$a^* = \frac{bc \sin \alpha}{V}$	$a = \frac{b^*c^* \sin \alpha^*}{V^*}$
$b^* = \frac{ac \sin \beta}{V}$	$b = \frac{a^*c^* \sin \beta^*}{V^*}$
$c^* = \frac{ab \sin \gamma}{V}$	$c = \frac{a^*b^* \sin \gamma^*}{V^*}$
$V = \frac{1}{V^*} = abc\sqrt{1 - \cos^2 \alpha - \cos^2 \beta - \cos^2 \gamma + 2 \cos \alpha \cos \beta \cos \gamma}$	
$V^* = \frac{1}{V} = a^*b^*c^*\sqrt{1 - \cos^2 \alpha^* - \cos^2 \beta^* - \cos^2 \gamma^* + 2 \cos \alpha^* \cos \beta^* \cos \gamma^*}$	
$\cos \alpha^* = \frac{\cos \beta \cos \gamma - \cos \alpha}{\sin \beta \sin \gamma}$	$\cos \alpha = \frac{\cos \beta^* \cos \gamma^* - \cos \alpha^*}{\sin \beta^* \sin \gamma^*}$
$\cos \beta^* = \frac{\cos \alpha \cos \gamma - \cos \beta}{\sin \alpha \sin \gamma}$	$\cos \beta = \frac{\cos \alpha^* \cos \gamma^* - \cos \beta^*}{\sin \alpha^* \sin \gamma^*}$
$\cos \gamma^* = \frac{\cos \alpha \cos \beta - \cos \gamma}{\sin \alpha \sin \beta}$	$\cos \gamma = \frac{\cos \alpha^* \cos \beta^* - \cos \gamma^*}{\sin \alpha^* \sin \beta^*}$

The relationship between the axes and the angles of the unit cell in both lattices is given in Table 4.1 for a triclinic lattice. Note that the volume  $V$  of the unit cell in the direct lattice is the reciprocal of the unit cell volume  $V^*$  in the reciprocal lattice:  $V = 1/V^*$ .

If the magnitude of scattering  $\mathbf{G}(\mathbf{S})$ , corresponding to each vector  $\mathbf{S}$ , is plotted at the tip of  $\mathbf{S}$  in reciprocal space, a so-called *weighted reciprocal lattice* is obtained. For crystals,  $\mathbf{G}(\mathbf{S})$  has nonzero values only at the lattice points and then  $\mathbf{G}(\mathbf{S}) = \mathbf{F}(\mathbf{S})$ . However, for nonperiodic objects,  $\mathbf{G}(\mathbf{S})$  can have a nonzero value anywhere in reciprocal space.

With the reciprocal lattice, the diffraction directions can easily be constructed. The following procedure is applied:

- Step 1: Direct the incoming (primary) X-ray beam ( $\mathbf{s}_0$ ) toward the origin  $O$  of reciprocal space. Take the length of  $\mathbf{s}_0$  equal to  $1/\lambda$ . (Figure 4.19).
- Step 2: Construct a sphere with the origin  $O$  of reciprocal space on its surface, with center  $M$  on the line  $\mathbf{s}_0$ , and radius  $MO = 1/\lambda$ . This sphere is called the Ewald sphere.
- Step 3: If a wave vector  $\mathbf{S}$  has its end point on the Ewald sphere (e.g., at point  $P$ ), then  $MP$  is the scattered beam  $\mathbf{s}$ . This is true because, as shown in Figure 4.3,  $\mathbf{s}_0 + \mathbf{S} = \mathbf{s}$ , or  $\mathbf{S} = \mathbf{s} - \mathbf{s}_0$ .

#### 4.8.2. Conclusions Concerning the Reciprocal Lattice

The reciprocal lattice is a convenient concept useful for constructing the directions of diffraction by a crystal. However, remember that it exists only theoretically, not in reality.

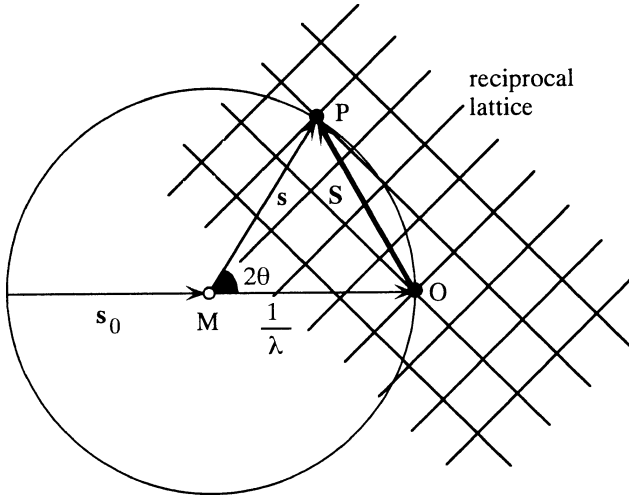


Figure 4.19. The Ewald sphere as a tool to construct the direction of the scattered beam. The sphere has radius  $1/\lambda$ . The origin of the reciprocal lattice is at  $O$ .  $s_0$  indicates the direction of the incident beam;  $s$  indicates the direction of the scattered beam.

Scattering occurs for all scattering vectors  $\mathbf{S}$  having their end point  $P$  on the sphere and  $\mathbf{G}(\mathbf{S}) \neq 0$ . For crystals,  $\mathbf{G}(\mathbf{S}) \neq 0$  implies that  $P$  must be a reciprocal lattice point. Crystal lattice planes for which the reciprocal lattice points  $(hkl)$  do not lie on the sphere and thus are not in reflecting position can be brought to reflection by rotating the reciprocal lattice around  $O$ . From this construction with the imaginary reciprocal lattice, we now return to the reality of the crystal lattice and note the following:

- The reciprocal lattice rotates exactly as the crystal does.
- The direction of the beam diffracted from the crystal is parallel to  $MP$  for the orientation of the crystal, which corresponds to the orientation of the reciprocal lattice.

From Figure 4.19, two properties of  $\mathbf{S}(hkl)$  can easily be derived:

1. The reciprocal space vector  $\mathbf{S}(hkl) = \mathbf{OP}(hkl)$  is perpendicular to the reflecting plane  $hkl$ , which is in agreement with the definition of  $\mathbf{S}$  in Section 4.3.
2.  $|\mathbf{S}(hkl)| = 2(\sin \theta)/\lambda = 1/d$  and Bragg's law is fulfilled.

One more comment on lattice planes: If the beam  $hkl$  corresponds to reflection against one face (let us say the front) of a lattice plane, then  $(\bar{h}\bar{k}\bar{l})$  [or  $(-h, -k, -l)$ ] corresponds to the reflection against the opposite face (the back) of the plane (Figure 4.20).

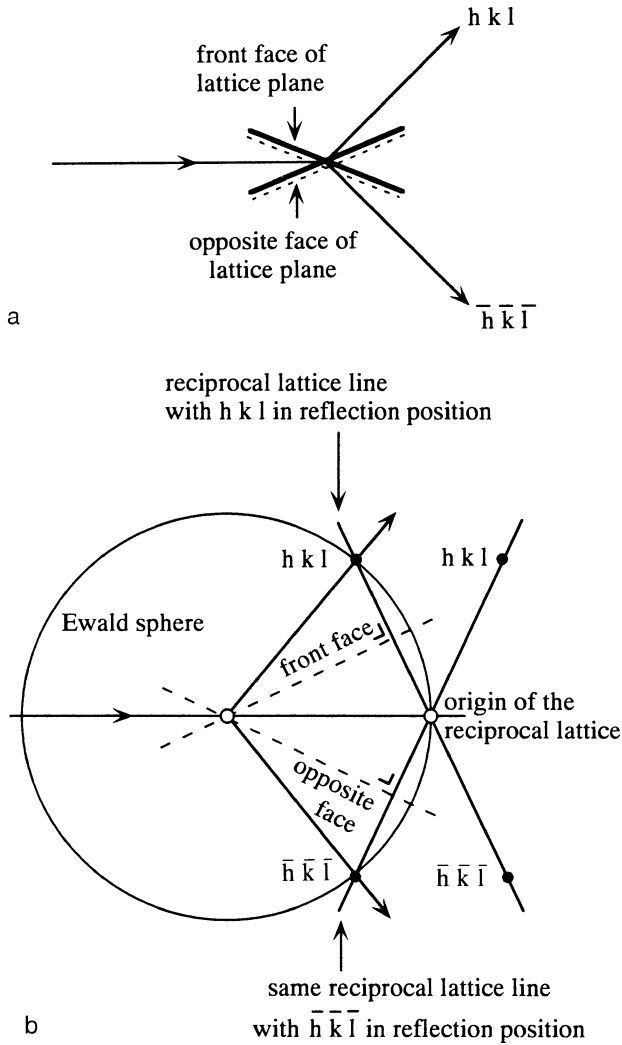


Figure 4.20. If the reflection  $(h k l)$  corresponds to a reflection against the front face of a lattice plane, then  $(\bar{h} \bar{k} \bar{l})$  corresponds to reflection against the opposite face of the plane. (a) Simple presentation of the reflections; (b) an explanation by means of the reciprocal lattice.

## 4.9. The Temperature Factor

The size of the electron density cloud around an atomic nucleus is independent of the temperature, at least under normal conditions. This would suggest that X-ray scattering by a crystal would also be independent of the temperature. However, this is not true because the atoms vibrate around an equilibrium position. The X-rays do not meet identical atoms on exactly the same position in successive unit cells. This

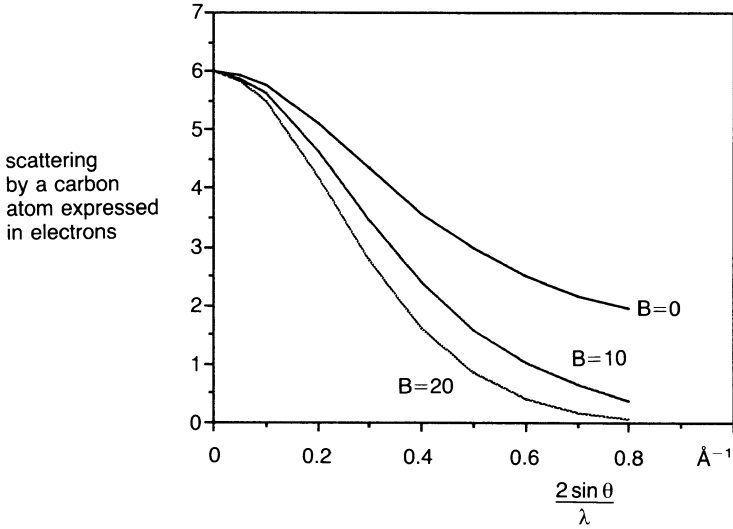


Figure 4.21. The atomic scattering factor of a carbon atom multiplied by the appropriate temperature factor.

is similar to an X-ray beam meeting a smeared atom on a fixed position, the size of the atom being larger if the thermal vibration is stronger. This diminishes the scattered X-ray intensity, especially at high scattering angles. Therefore, the atomic scattering factor of the atoms must be multiplied by a temperature-dependent factor (Figure 4.21).

The vibration of an atom in a reflecting plane  $hkl$  has no effect on the intensity of the reflection ( $hkl$ ). Atoms in a plane diffract in phase and, therefore, a displacement in that plane has no effect on the scattered intensity. The component of the vibration perpendicular to the reflecting plane does have an effect. In the simple case in which the components of vibration are the same in all directions, the vibration is called *isotropic*.

Then the component perpendicular to the reflecting plane and thus along  $\mathbf{S}$  is equal for each ( $hkl$ ), and the correction factor for the atomic scattering factor is

$$\begin{aligned}
 T(\text{iso}) &= \exp \left[ -B \frac{\sin^2 \theta}{\lambda^2} \right] = \exp \left[ -\frac{B}{4} \left( \frac{2 \sin \theta}{\lambda} \right)^2 \right] \\
 &= \exp \left[ -\frac{B}{4} \left( \frac{1}{d} \right)^2 \right].
 \end{aligned} \tag{4.6}$$

Assuming isotropic and harmonic vibration, it can be shown that the thermal parameter  $B$  is related to the mean square displacement  $\bar{u}^2$  of the atomic vibration:

$$B = 8\pi^2 \times \bar{u}^2 \tag{4.7}$$

If the atomic vibration is split into three perpendicular components—one perpendicular to the reflecting plane [ $\text{vibr}(\perp)$ ] and two in the plane,  $\text{vibr}(\parallel_1)$  and  $\text{vibr}(\parallel_2)$ —then  $\text{vibr}(\perp)$  is the only one giving rise to the temperature factor with parameter  $B = 3 \times 8\pi^2 \times \bar{u}^2(\perp)$  (Garcia et al., 1997). We do not observe the other two, but in the isotropic vibration, they are just as large as the observed one and  $\bar{u}^2 = 3 \times \bar{u}^2(\perp)$ .

For anisotropic vibration, the temperature factor is much more complicated. In this case,  $\bar{u}^2$  depends on the direction of  $\mathbf{S}$ . It can be shown that the temperature factor is given by

$$T(\text{aniso}; hkl) = \exp 2 \left[ -2\pi^2 \left( U_{11}h^2a^{*2} + U_{22}k^2b^{*2} + U_{33}l^2c^{*2} + 2U_{12}hka^*b^* + 2U_{13}hla^*c^* + 2U_{23}klb^*c^* \right) \right]$$

with  $U_{11}$  the  $\bar{u}^2$  value along  $\mathbf{a}^*$ ,  $U_{22}$  along  $\mathbf{b}^*$ , and  $U_{33}$  along  $\mathbf{c}^*$ . In general,  $\bar{u}^2(\mathbf{e})$  along a unit vector  $\mathbf{e}$  is given by

$$\bar{u}^2(\mathbf{e}) = U_{11} \cdot e_1^2 + U_{22} \cdot e_2^2 + U_{33} \cdot e_3^2 + 2U_{12} \cdot e_1e_2 + 2U_{13} \cdot e_1e_3 + 2U_{23} \cdot e_2e_3$$

with  $e_1$ ,  $e_2$ , and  $e_3$  the components of  $\mathbf{e}$  along unit axes  $\mathbf{a}^*$ ,  $\mathbf{b}^*$ , and  $\mathbf{c}^*$ . The points for which  $\bar{u}^2(\mathbf{e})$  is constant form an ellipsoid: *the ellipsoid of vibration*. For display purposes, the constant can be chosen such that the vibrating atom has a chance (e.g., 50%) of being within the ellipsoid (Figure 4.22).

In protein structure determinations, it is common to work with isotropic temperature factors for the individual atoms. This is because of the restricted resolution

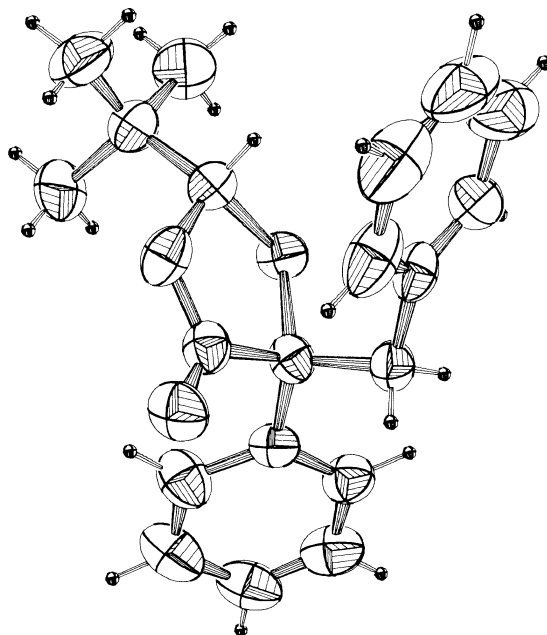


Figure 4.22. The plot of an organic molecule with 50% probability of thermal ellipsoids. (Reproduced with permission from Strijtveen and Kellogg © 1987 Pergamon Press PLC.)



and, consequently, the limited number of data. However, because of improvements in hardware, an increasing number of structures is determined at a sufficiently high resolution to use anisotropic temperature factors. However, in the normal situation one is restricted to isotropic temperature factors. Then there are four unknown parameters per atom:  $x$ ,  $y$ ,  $z$ , and  $B$ . For a protein with 2000 atoms in the asymmetric unit, 8000 unknown parameters must be determined. To obtain a reliable structure, the number of measured data (reflection intensities) should well exceed the number of parameters. In general, because of the restricted number of data, this condition is fulfilled for the determination of isotropic, but not anisotropic, temperature factors. Average values for  $B$  in protein structures range from as low as a few square Ångstroms to  $30 \text{ Å}^2$  in well-ordered structures. The highest values are found in more or less flexible surface loops.

The temperature factor is a consequence of the dynamic disorder in the crystal caused by the temperature-dependent vibration of the atoms in the structure. In addition to this *dynamic disorder*, protein crystals have *static disorder*: Molecules, or parts of molecules, in different unit cells do not occupy exactly the same position and do not have exactly the same orientation. The effect of this static disorder on the X-ray diffraction pattern is the same as for the dynamic disorder and they cannot be distinguished, unless intensity data at different temperatures are collected. For  $B = 30 \text{ Å}^2$ , the root mean square displacement  $\sqrt{\bar{u}^2}$  of the atoms from their equilibrium position is  $\sqrt{30}/8\pi^2 = 0.62 \text{ Å}$ . This gives an impression of the flexibility or disorder in protein structures, which are by no means completely rigid. Because of the disorder in the crystal, the diffraction pattern fades away at some diffraction angle  $\theta_{\max}$ . The corresponding lattice distance  $d_{\min}$  is determined by Bragg's law:

$$d_{\min} = \frac{\lambda}{2 \sin \theta_{\max}}.$$

$d_{\min}$  is taken as the resolution of the diffraction pattern and it is said that a structure has been determined to a resolution of, for instance,  $2 \text{ Å}$ . It is clear that the accuracy with which a structure can be determined depends strongly on the resolution of the diffraction pattern.

#### 4.10. Calculation of the Electron Density $\rho(x, y, z)$

The intensity of the diffracted beam ( $hkl$ ) is proportional to the square of the amplitude of the structure factor  $\mathbf{F}(hkl)$ . The structure factor is a function of the electron density distribution in the unit cell:

$$\mathbf{F}(\mathbf{S}) = \sum_j f_j \exp[2\pi i \mathbf{r}_j \cdot \mathbf{S}]. \quad (4.3)$$

The summation is over all atoms  $j$  in the unit cell. Instead of summing over all

separate atoms, we can integrate over all electrons in the unit cell:

$$\mathbf{F}(\mathbf{S}) = \int_{\text{cell}} \rho(\mathbf{r}) \exp[2\pi i \mathbf{r}_j \cdot \mathbf{S}] dv. \quad (4.8)$$

where  $\rho(\mathbf{r})$  is the electron density at position  $\mathbf{r}$  in the unit cell. If  $x$ ,  $y$ , and  $z$  are fractional coordinates in the unit cell ( $0 \leq x < 1$ ; the same for  $y$  and  $z$ ) and  $V$  is the volume of the unit cell, we have

$$dv = V \cdot dx dy dz$$

and

$$\begin{aligned} \mathbf{r} \cdot \mathbf{S} &= (\mathbf{a} \cdot x + \mathbf{b} \cdot y + \mathbf{c} \cdot z) \cdot \mathbf{S} = \mathbf{a} \cdot \mathbf{S} \cdot x + \mathbf{b} \cdot \mathbf{S} \cdot y + \mathbf{c} \cdot \mathbf{S} \cdot z \\ &= hx + ky + lz. \end{aligned}$$

Therefore,  $\mathbf{F}(\mathbf{S})$  can also be written as  $\mathbf{F}(hkl)$ :

$$F(hkl) = V \int_{x=0}^1 \int_{y=0}^1 \int_{z=0}^1 \rho(x, y, z) \exp[2\pi i(hx + ky + lz)] dx dy dz. \quad (4.9)$$

However, the goal of protein X-ray crystallography is not to calculate the diffraction pattern but to calculate the electron density  $\rho$  at every position  $x$ ,  $y$ ,  $z$  in the unit cell. How can this be done? The answer is by Fourier transformation.

$\mathbf{F}(hkl)$  is the Fourier transform of  $\rho(x, y, z)$ , but the reverse is also true:  $\rho(x, y, z)$  is the Fourier transform of  $\mathbf{F}(hkl)$  and, therefore,  $\rho(x, y, z)$  can be written as a function of all  $\mathbf{F}(hkl)$ :

$$\rho(x, y, z) = \frac{1}{V} \sum_h \sum_k \sum_l \mathbf{F}(hkl) \exp[-2\pi i(hx + ky + lz)]. \quad (4.10)$$

The Laue conditions tell us that diffraction occurs only in discrete directions and, therefore, in Equation (4.10), the integration has been replaced by a summation. Because  $\mathbf{F} = |F| \exp[ia]$ , we can also write

$$\rho(x, y, z) = \frac{1}{V} \sum_h \sum_k \sum_l |F(hkl)| \exp[-2\pi i(hx + ky + lz) + i\alpha(hkl)] \quad (4.11)$$

It now seems easy to calculate the electron density  $\rho(x, y, z)$  at every position  $(x, y, z)$  in the unit cell. However, there is a problem. Although the  $|F(hkl)|$ 's can be derived from the intensities  $I(hkl)$ , the phase angles  $\alpha(hkl)$  cannot be derived straightforwardly from the diffraction pattern. Fortunately, several methods have been developed to solve this problem; they will be discussed later.

Notes

1.  $\mathbf{F}(hkl)$  is the Fourier transform of the electron density  $\rho(x, y, z)$  in the entire unit cell. Often the unit cell contains more than one molecule. Then  $\mathbf{F}(hkl)$  is

- composed of the sum of the transforms of the separate molecules at position  $(h k l)$  in reciprocal space.
- Because of the crystallographic repeat of the unit cells, the value of the transform  $F(h k l)$  is zero in between the reciprocal space positions  $(h k l)$ . If there were no crystallographic repeat, the transform would be spread over the entire reciprocal space and its value is not restricted to reciprocal space positions  $(h, k \ell)$ .
  - A special term in the Fourier summation of Equation (4.11) is  $F(000) \exp[0] = F(000)$ ; the phase angle  $\alpha(000)$  is zero because there is no phase difference in the scattering by the electrons in the forward direction. The “reflection”  $(000)$  is not observable because it is in the line of the direct beam. Nevertheless,  $F(000)$  adds a constant term to the Fourier summation, which is equal to the total number of electrons in the cell. This requires that  $F(000)$  and all other  $F$ 's be expressed in electrons. They are then on an *absolute scale*. Normally, the measured intensities and the structure factor amplitudes derived from them are on an arbitrary scale. The resulting electron density map is then also on an arbitrary scale, but this does not prevent its interpretation. In Section 5.2 of Chapter 5 it is described how intensities can be put on the absolute scale.
  - The contribution to the electron density map by all other terms than  $F(000)$  has an average value of zero over one full cycle. Therefore, the average electron density in the unit cell is zero if  $F(000)$  is not incorporated in the Fourier summation. However, a constant term can be added to remove negative electron density and the absence of  $F(000)$  does not inhibit the interpretation of an electron density map. The limited resolution of a protein X-ray diffraction pattern prevents the calculation of the electron density map at atomic resolution: Although amino acid residues can be distinguished, atoms are not separated

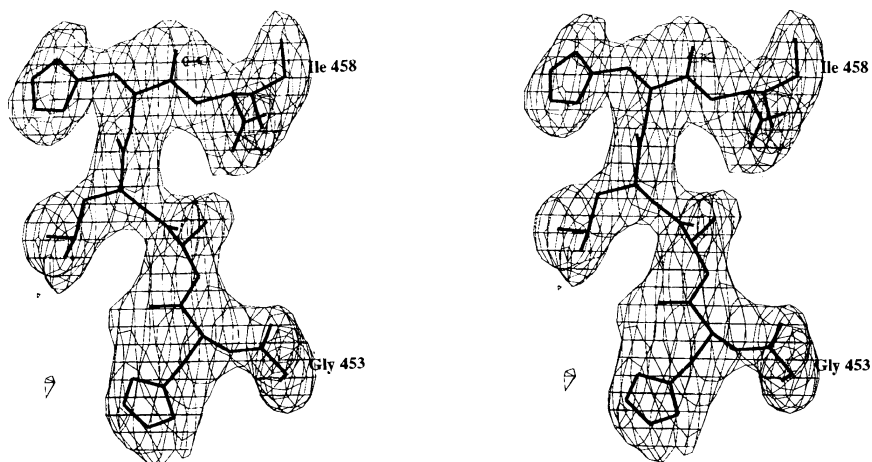


Figure 4.23. Stereo picture for the C-terminal residues 453–458 of the enzyme lipamide dehydrogenase of *Pseudomonas putida* at 2.45 Å resolution. (Reproduced with permission from the thesis by Andrea Mattevi, University of Groningen, 1992.)

(Figure 4.23), except if the electron density map is calculated with very high-resolution data (near 1 Å). Therefore, it seems surprising that the error in the atomic positions is not more than  $\sim 0.2$  Å for a structure derived from a high-resolution electron density map. The reason is that the structure of the building blocks—amino acids and small peptides—is known with high accuracy and one can safely assume that the atomic distances and bond angles are the same in the proteins as they are in the small compounds.

5. The two-dimensional electron density projection along an axis can easily be calculated with a limited number of reflections. For protein structures, this is usually not very useful because of the overlap of density and the inability to detect any interesting features in the projected density. Moreover, considering the speed and cost of modern computers and the speed of modern data collection methods, three-dimensional electron density information can easily be obtained. However, one should at least know the existence of the method. We will discuss the projection of the electron density  $\rho$  along the  $c$ -axis onto the  $ab$ -plane. Expression (4.9) for the structure factor gives the following for the reflections  $(h k 0)$ :

$$\mathbf{F}(h k 0) = V \int_{xyz} \rho(x y z) dz \exp[2\pi i(hx + ky)] dx dy. \quad (4.12)$$

In Equation (4.12), the integration over  $z$  is first performed. Let us assume that the unit cell has an angle of  $90^\circ$  between the  $c$ -axis and the  $ab$ -plane. The volume of the unit cell  $V$  is then equal to  $A \times c$ , in which  $A$  is the surface of the  $ab$ -plane. In Equation (4.12),  $z$  and  $dz$  are fractional coordinates. Therefore,  $V dz$  can be written as  $Ac dz$  and  $\mathbf{F}(h k 0)$  can be written as

$$\mathbf{F}(h k 0) = A \int_{xyz} \rho(x y z) c dz \exp[2\pi i(hx + ky)] dx dy. \quad (4.13)$$

With  $\int_z \rho(x y z)$ , the electron density in the projected structure in  $e/\text{Å}^2$ , we obtain

$$\mathbf{F}(h k 0) = A \int_{xy} \rho(x y) \exp[2\pi i(hx + ky)] dx dy. \quad (4.14)$$

The projected electron density  $\rho$  is obtained by Fourier inversion:

$$\rho(x y) = \frac{1}{A} \sum_h \sum_k \mathbf{F}(h k 0) \exp[-2\pi i(hx + ky)]. \quad (4.15)$$

If the projection is along a 2-fold axis or screw axis along  $z$ , the expressions for  $\mathbf{F}(h k 0)$  and  $\rho(x y)$  are further simplified, because in that case  $\rho(x y) = \rho(\bar{x} \bar{y})$ :

$$\begin{aligned} \mathbf{F}(h k 0) &= \frac{1}{2} A \int_{xy} \rho(x y) \{ \exp[2\pi i(hx + ky)] + \exp[-2\pi i(hx + ky)] \} dx dy \\ &= A \int_{xy} \rho(x y) \cos[2\pi(hx + ky)] dx dy. \end{aligned} \quad (4.16)$$

and

$$\begin{aligned} \rho(x y) &= \frac{1}{2} \frac{1}{A} \sum_h \sum_k \mathbf{F}(h k 0) \{ \exp[-2\pi i(hx + ky)] + \exp[2\pi i(hx + ky)] \} \\ &= \frac{1}{A} \sum_h \sum_k \mathbf{F}(h k 0) \cos[2\pi(hx + ky)]. \end{aligned} \quad (4.17)$$

For such a centrosymmetric case,  $\mathbf{F}(h k 0)$  always points along the real axis in the Argand diagram. It has a positive sign for a phase angle of  $0^\circ$  and a negative sign for a phase angle of  $180^\circ$ .

### Fourier Transforms and the Delta Function

We want to know why Equation (4.10) is true, or why  $\rho(xyz)$  is the Fourier transform of  $\mathbf{F}(h k l)$ . Take  $\mathbf{F}(h k l)$  in the form of Equation (4.8):

$$\mathbf{F}(\mathbf{S}) = \int_{\substack{r \\ \text{over} \\ \text{the cell}}} \rho(\mathbf{r}) \exp[2\pi i \mathbf{r} \cdot \mathbf{S}] dv_r.$$

Multiply by  $\exp[-2\pi i \mathbf{r}' \cdot \mathbf{S}]$  and integrate over  $\mathbf{S}$ .  $dv_r$  is a small volume in real space ( $\mathbf{r}$  space) and  $dv_s$  in reciprocal space ( $\mathbf{S}$  space):

$$\int_{\mathbf{S}=-\infty}^{+\infty} \mathbf{F}(\mathbf{S}) \exp[-2\pi i \mathbf{r}' \cdot \mathbf{S}] dv_s = \int_{\mathbf{S}=-\infty}^{+\infty} dv_s \int_{\mathbf{r}} \rho(\mathbf{r}) \exp[2\pi i (\mathbf{r} - \mathbf{r}') \cdot \mathbf{S}] dv_r. \quad (4.18)$$

Because  $\rho(\mathbf{r})$  is independent of  $\mathbf{S}$ , Equation (4.18) is equal to

$$\int_{\mathbf{r}} dv_r \rho(\mathbf{r}) \int_{\mathbf{S}=-\infty}^{+\infty} \exp[2\pi i (\mathbf{r} - \mathbf{r}') \cdot \mathbf{S}] dv_s. \quad (4.19)$$

The integral  $\int_{\mathbf{S}=-\infty}^{+\infty} \exp[2\pi i (\mathbf{r} - \mathbf{r}') \cdot \mathbf{S}] dv_s$  can be regarded as a summation of vectors in the Argand diagram. These vectors have a length equal to 1 but point in many different directions, because  $\mathbf{S}$  has an infinite number of values in reciprocal space and, hence, the result of the integration is, in general, zero, except if  $\mathbf{r} - \mathbf{r}' = 0$  or  $\mathbf{r} = \mathbf{r}'$ . In that case, all vectors in the Argand diagram point to the right along the horizontal axis. Therefore,  $\int_{\mathbf{S}=-\infty}^{+\infty} \exp[2\pi i (\mathbf{r} - \mathbf{r}') \cdot \mathbf{S}] dv_s$  is a strange function:

It is zero for  $\mathbf{r} \neq \mathbf{r}'$  and infinite for  $\mathbf{r} = \mathbf{r}'$ . Such a function is called a delta function; the following is a three-dimensional delta function:

$$\int_{\mathbf{S}=-\infty}^{+\infty} \exp[2\pi i(\mathbf{r} - \mathbf{r}') \cdot \mathbf{S}] d\nu_{\mathbf{S}} = \delta(\mathbf{r} - \mathbf{r}').$$

A (one-dimensional) delta function has the property

$$\int_{\mathbf{S}=-\infty}^{+\infty} f(x) \delta(x - a) dx = f(a) \tag{4.20}$$

and in our three-dimensional case, Equation (4.19) becomes

$$\int_{\mathbf{r}} \rho(\mathbf{r}) \cdot \delta(\mathbf{r} - \mathbf{r}') d\nu_r = \rho(\mathbf{r}').$$

This property will be proven later. Equation (4.18) can now be written as

$$\rho(\mathbf{r}') = \int_{\mathbf{S}=-\infty}^{+\infty} \mathbf{F}(\mathbf{S}) \exp[-2\pi i \mathbf{r}' \cdot \mathbf{S}] d\nu_{\mathbf{S}},$$

or with  $\mathbf{r}'$  replaced by  $\mathbf{r}$ ,

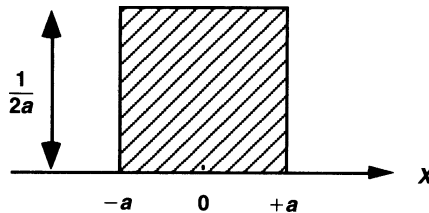
$$\rho(\mathbf{r}) = \int_{\mathbf{S}=-\infty}^{+\infty} \mathbf{F}(\mathbf{S}) \exp[-2\pi i \mathbf{r} \cdot \mathbf{S}] d\nu_{\mathbf{S}}. \tag{4.21}$$

This proves the Fourier transformation.

Because of the Laue conditions, the integration in Equation (4.21) can be replaced by summations over  $h, k$ , and  $l$ , giving a weight  $V^*$  to each term.  $V^*$  is the volume of the unit cell in reciprocal space and is equal to  $1/V$ , where  $V$  is the volume of the crystallographic unit cell (Section 4.8). With  $\mathbf{r} \cdot \mathbf{S} = hx + ky + lz$ , Equation (4.21) is transformed into Equation (4.10).

### The One-Dimensional Delta Function

Consider the function  $\delta_a(x)$ , which has a constant value  $1/2a$  between  $-a$  and  $+a$ , and is zero outside this region.



The surface of the hatched area is  $\int_{x=-\infty}^{+\infty} \delta_a(x) dx = 1$  and is independent of  $a$ .

Now let  $a$  tend to zero. Then  $\lim_{a \rightarrow 0} \delta_a(x)$  is defined as  $\delta(x)$  with  $\delta(x) = 0$  for  $x \neq 0$  and  $\delta(x) = \infty$  for  $x = 0$ , but  $\int_{x=-\infty}^{+\infty} \delta(x) dx = 1$ . Although at  $x = 0$  the function  $\delta(x)$  is  $\infty$ , it is also infinitely thin and the surface area under the function is independent of  $a$  and remains 1. Of special importance for us is the following property of a delta function:

$$\int_{x=-\infty}^{+\infty} f(x) \delta(x) dx = f(0), \quad (4.22)$$

where  $f(x)$  is any normal function. This property can be proven by starting with  $\delta_a(x)$ :

$$\int_{s=-\infty}^{+\infty} f(x) \delta_a(x) dx = \frac{1}{2a} \int_{-a}^{+a} f(x) dx. \quad (4.23)$$

If  $a$  tends to zero, the left part of Equation (4.17) becomes  $\int_{x=-\infty}^{+\infty} f(x) \delta(x)$ , and the right part becomes

$$\lim_{a \rightarrow 0} \frac{1}{2a} \int_{-a}^{+a} f(x) dx = f(0). \quad (4.24)$$

That Equation (4.24) is true can be understood in the following way: In a very narrow region around  $x = 0$ , we can assume for  $f(x)$  the constant value  $f(0)$ . The surface area under the function between  $-a$  and  $+a$  [ $\int_{-a}^{+a} f(x) dx$ ] is then  $f(0) \times 2a$  and, therefore, Equation (4.18) is true. With a change of variables Equation (4.16) can be written as

$$\int_{x=-\infty}^{+\infty} f(x) \delta(x - a) dx = f(a).$$

This proves Equation (4.20).

We have already met the delta function in deriving the scattering by a crystal (Section 4.6) without mentioning it explicitly. There we had  $\sum_{t=0}^{n_1} \exp[2\pi i \mathbf{t} \cdot \mathbf{S}]$  and two similar functions. In fact, the presence of diffraction spots on an otherwise blank detector can be regarded as the physical appearance of delta functions.

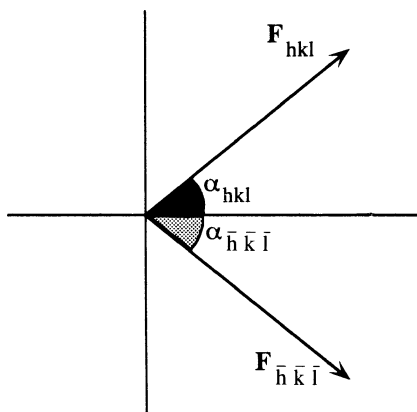
## 4.11. Comparison of $\mathbf{F}(h k l)$ and $\mathbf{F}(\bar{h} \bar{k} \bar{l})$

$$\mathbf{F}(h k l) = V \int_{\text{cell}} \rho(x y z) \exp[2\pi i(hx + ky + lz)] dx dy dz$$

[see Equation (4.9)]. In the same way, we can write the following for the reflection  $(\bar{h} \bar{k} \bar{l})$ :

$$\mathbf{F}(\bar{h} \bar{k} \bar{l}) = V \int_{\text{cell}} \rho(x y z) \exp[2\pi i(-hx - ky - lz)] dx dy dz. \quad (4.25)$$

Figure 4.24. Argand diagram for the structure factors of the reflections  $\mathbf{F}(hkl)$  and  $\mathbf{F}(\bar{h}\bar{k}\bar{l})$ .



$\mathbf{F}(hkl)$  is obtained as the result of a vector summation in which the amplitudes of the constituent vectors are  $\rho(xyz)dx dy dz$  and the phase angles are  $2\pi(hx + ky + lz)$ . For  $\mathbf{F}(\bar{h}\bar{k}\bar{l})$ , the amplitudes are the same, but the phase angles have just the opposite value:  $-2\pi(hx + ky + lz)$ . Therefore, the resulting vectors  $\mathbf{F}(hkl)$  and  $\mathbf{F}(\bar{h}\bar{k}\bar{l})$  have the same length, but opposite phase angles:  $\alpha$  and  $-\alpha$  in Figure 4.24. The consequence is that Equation (4.11) reduces to

$$\rho(xyz) = \frac{2}{V} \sum_{hkl=0}^{+\infty} |F(hkl)| \cos[2\pi(hx + ky + lz) - \alpha(hkl)].$$

This expression does not contain an imaginary term but is real.

Because the intensity of a diffracted beam is proportional to the square of its amplitude [ $I(hkl)$  proportional to  $|F(hkl)|^2$ ], the intensities  $I(hkl)$  and  $I(\bar{h}\bar{k}\bar{l})$  are also equal. The reflections  $(hkl)$  and  $(\bar{h}\bar{k}\bar{l})$  are called *Friedel* or *Bijvoet*<sup>3</sup> *pairs*. Their equal intensities give rise to a center of symmetry in the diffraction pattern, even if such a center is not present in the crystal structure. The  $I(hkl) = I(\bar{h}\bar{k}\bar{l})$  equality is usually assumed to be true in crystal structure determinations. It depends, however, on the condition that anomalous scattering is absent (Section 7.8 of Chapter 7).

## 4.12. Symmetry in the Diffraction Pattern

In the previous section we noted that the diffraction pattern from a crystal has a center of symmetry. In addition, more symmetry in the pattern can be present, depending on the symmetry elements in the crystal. After the application of a symmetry operation, the crystal structure looks exactly as it was. For this reason and because the diffraction pattern rotates with the crystal, the symmetry of the

<sup>3</sup> J. M. Bijvoet, 1892–1980, the famous Dutch crystallographer, was the first to determine the absolute configuration of an organic compound.



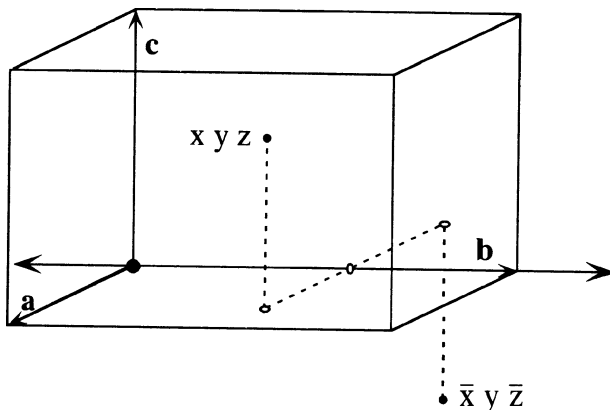


Figure 4.25. A unit cell with a 2-fold axis through the origin and along  $y$ . The electron density is equal at positions  $x y z$  and  $\bar{x} y \bar{z}$ .

diffraction pattern must be at least the same as for the crystal. Reflections in the diffraction pattern related by symmetry will have the same intensity and only a portion of all data is unique in terms of intensity.

As we saw in Section 3.3 of Chapter 3, the only symmetry elements allowed in protein crystals are symmetry axes. In the next section we will show the effect on the diffraction pattern of a 2 fold axis along the  $y$ -axis and a 2 fold screw axis along the  $y$ -axis.

#### 4.12.1. A 2-Fold Axis Along $y$

If a 2-fold axis through the origin and along  $y$  is present, then the electron density  $\rho(x y z) = \rho(\bar{x} y \bar{z})$  (Figure 4.25). Therefore,

$$\mathbf{F}(h k l) = V \int_{\text{asymm unit}} \rho(x y z) \{ \exp[2\pi i(hx + ky + lz)] + \exp[2\pi i(-hx + ky - lz)] \} dx dy dz \quad (4.26)$$

The integration in Eq. (4.26) is over one asymmetric unit (half of the cell), because the presence of the second term under the integral takes care of the other half of the cell.

$$\mathbf{F}(\bar{h} k \bar{l}) = V \int_{\text{asymm unit}} \rho(x y z) \{ \exp[2\pi i(-hx + ky - lz)] + \exp[2\pi i(hx + ky + lz)] \} dx dy dz \quad (4.27)$$

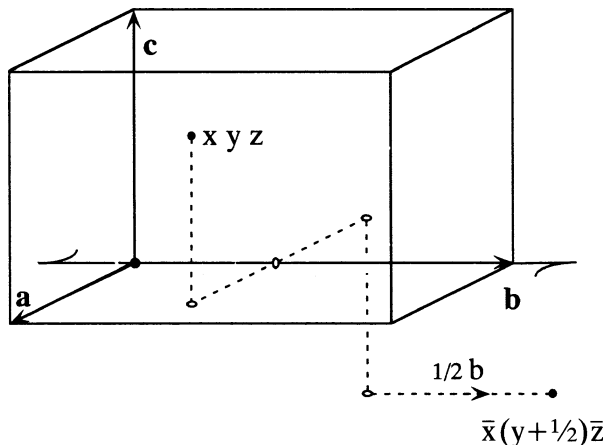


Figure 4.26. A unit cell with a 2-fold screw axis through the origin and along  $y$ . The electron density is equal at positions  $x y z$  and  $\bar{x}(y + 1/2)\bar{z}$ .

It follows that  $\mathbf{F}(h k l) = \mathbf{F}(\bar{h} \bar{k} \bar{l})$  and also  $I(h k l) = I(\bar{h} \bar{k} \bar{l})$ , because the intensities  $I$  are proportional to  $|\mathbf{F}|^2$ . Therefore, the diffraction pattern has the same 2-fold axis as the crystal.

#### 4.12.2. A 2-Fold Screw Axis Along $y$

For a 2-fold screw axis along  $y$  (Figure 4.26),

$$\begin{aligned} \rho(x y z) &= \rho\{\bar{x}(y + 1/2)\bar{z}\} \\ &\quad \text{term I } \downarrow \\ \mathbf{F}(h k l) &= V \int_{\text{asymm unit}} \rho(x y z) \{ \exp[2\pi i(hx + ky + lz)] \\ &\quad + \exp[2\pi i(-hx + k(y + 1/2) - lz)] \} dx dy dz \quad (4.28) \\ &\quad \text{term II } \uparrow \end{aligned}$$

$$\begin{aligned} \mathbf{F}(\bar{h} \bar{k} \bar{l}) &= V \int_{\text{asymm unit}} \rho(x y z) \{ \exp[2\pi i(-hx + ky - lz)] \\ &\quad + \exp[2\pi i(hx + k(y + 1/2) + lz)] \} dx dy dz. \quad (4.29) \\ &\quad \text{term IV } \uparrow \end{aligned}$$

In Equation (4.28), term II is

$$\exp\{2\pi i[-hx + k(y + 1/2) - lz]\} = \exp\{2\pi i(-hx + ky - lz + 1/2k)\}.$$

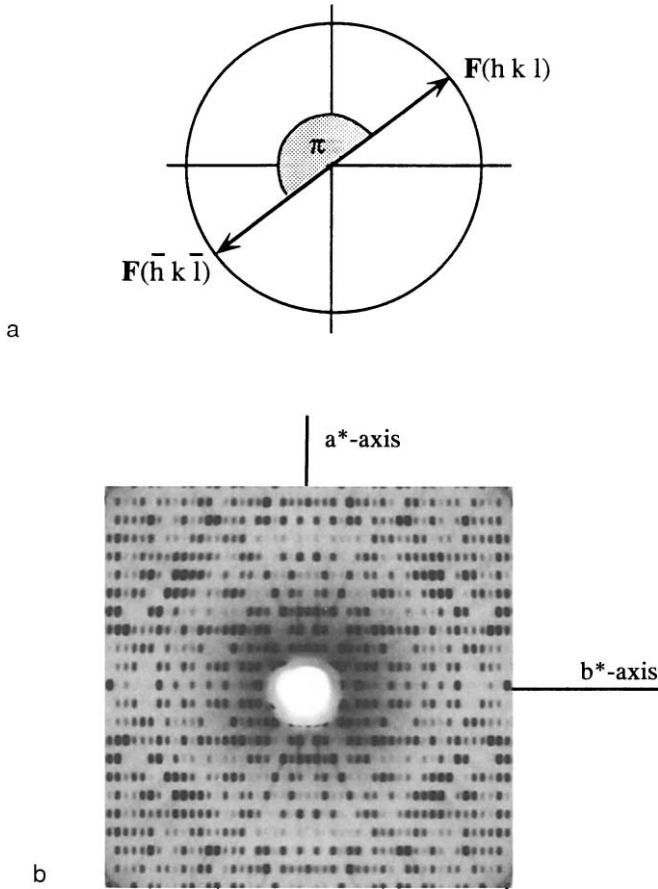


Figure 4.27. (a) The Argand diagram with the structure factors  $\mathbf{F}(h k l)$  and  $\mathbf{F}(\bar{h} k \bar{l})$  for a structure with a 2-fold screw axis along  $y$  with  $k$  odd. (b) A diffraction picture of a crystal of the enzyme papain. The crystal belongs to space group  $P2_12_12_1$ . Note the absence of reflections  $(h 0 0)$  for  $h$  odd and of reflections  $(0 k 0)$  for  $k$  odd.

For  $k$  even, this is equal to term III in Equation (4.29). The same is true for term IV in Equation (4.29) and term I in Equation (4.28). Therefore, when  $k$  is even,  $\mathbf{F}(h k l) = \mathbf{F}(\bar{h} k \bar{l})$  and  $I(h k l) = I(\bar{h} k \bar{l})$ . When  $k$  is odd, terms I and IV have a difference of  $\pi$  in their phase angles:  $2\pi(hx + ky + lz)$  and  $2\pi(hx + ky + lz + 1/2k)$ . The same is true for terms II and III. If we again regard these exponential terms as vectors in the Argand diagram with a length of 1 and appropriate phase angles, we easily see that when  $k$  is odd,  $\mathbf{F}(h k l)$  and  $\mathbf{F}(\bar{h} k \bar{l})$  have equal length but a phase difference of  $\pi$  (Figure 4.27a). However, again,  $I(h k l) = I(\bar{h} k \bar{l})$  because  $I(h k l) = |F(h k l)|^2$ .

The result is that a 2-fold screw axis in the crystal is found as a 2-fold axis in the X-ray diffraction pattern. The phase angles of symmetry-related reflections are the same or differ by  $\pi$ , but this cannot be observed in the diffraction pattern. The other possible screw axes also express themselves in the X-ray diffraction pattern as normal nonscrew rotation axes. Although the screw character of a 2-fold screw axis is not detected in the symmetry of the X-ray diffraction pattern, it has an effect on the reflections along the corresponding 2-fold axis in the diffraction pattern. Again, take a 2-fold screw axis along  $y$ :

$$\mathbf{F}(0k0) = V \int_{\text{asymm unit}} \rho(x y z) \{ \exp[2\pi i k y] + \exp[2\pi i k (y + 1/2)] \} dx dy dz. \quad (4.30)$$

When  $k$  is even, this is  $2 \times V \int \rho(x y z) \exp[2\pi i k y] dx dy dz$ . However, when  $k$  is odd, the two terms in Equation (4.30) cancel and  $\mathbf{F}(0k0) = 0$  (Figure 4.27b).

The conditions for these reflections are called *serial reflection conditions* because they apply to a set of reflections lying on a line through the origin in the reciprocal lattice. *Integral reflection conditions* involve all reflections; they are observed for centered lattices as discussed in the next section.

### 4.13. Integral Reflection Conditions for Centered Lattices

Consider, for example, a lattice centered in the  $ab$ -plane, also called the  $C$ -plane (Figure 4.28). The following electron density relationship exists:

$$\rho(x y z) = \rho(x + 1/2, y + 1/2, z).$$

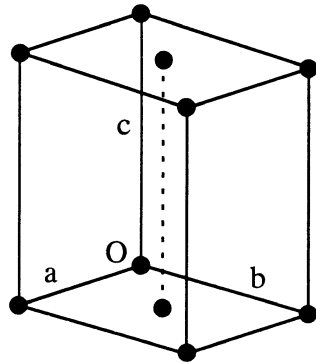


Figure 4.28. A unit cell centered in the  $ab$ -plane.

The structure factor  $\mathbf{F}$  can now be written as

$$\mathbf{F}(hkl) = V \int \rho(xyz) \{ \exp[2\pi i(hx + ky + lz)] + \exp[2\pi i(h(x + 1/2) + k(y + 1/2) + lz)] \} dx dy dz. \quad (4.31)$$

$$0 \leq x < 1$$

$$0 \leq y < 1/2$$

$$0 \leq z < 1$$

The second exponential term on the right-hand side of Equation (4.31) is equal to

$$\exp\{2\pi i[hx + ky + lz + 1/2(h + k)]\}.$$

If  $h + k$  is odd, the two contributions to  $\mathbf{F}$  cancel each other because of opposite phase angles.

The conclusion is that in the diffraction pattern of a crystal that has its  $C$ -face centered, all reflections for which  $h + k$  is odd have a zero value for their intensities. The *International Tables* give complete information about the extinction of reflections for all space groups.

## 4.14. Intensity Diffracted by a Crystal

Starting from the wave  $\mathbf{F}(\mathbf{S})$  diffracted by a unit cell, an expression can be derived for the integrated intensity  $I(\text{int.}, hkl)$  of the reflection  $(hkl)$ .

The crystal is not perfect; rather, it is imperfect and of finite size. These imperfect crystals can be regarded as being composed of small mosaic blocks, which can be considered as optically independent fragments (Figure 4.29). For such an imperfect crystal, the intensity profile of a reflection has a certain width because of the angular spread of the mosaic blocks; for a protein crystal, it is generally  $0.25^\circ$ – $0.5^\circ$ . Moreover, each tiny mosaic block has a small intrinsic reflection width (less than  $0.01^\circ$ ) because it does not strictly obey the reflection condition of an infinite number of unit cells. This implies that diffraction occurs not only for a sharp point  $(hkl)$  in the reciprocal lattice but also for a small region in reciprocal space around the sharp point.

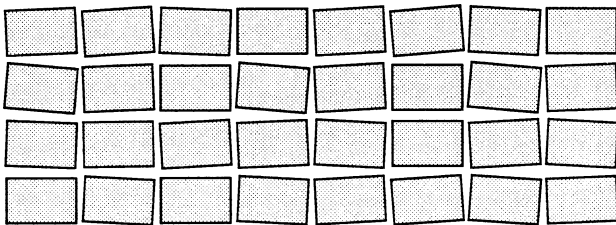


Figure 4.29. Most crystals are imperfect and can be regarded as being composed of small mosaic blocks.

We have the following assumptions:

1. Apart from ordinary absorption, the intensity  $I_0$  of the incident beam is the same throughout the crystal.
2. The mosaic blocks are so small that a scattered wave is not scattered again (i.e., multiple scattering does not occur).
3. The mosaic blocks scatter independently of each other.

With these assumptions, the expression for  $I$  (int.,  $hkl$ ), if the crystal is rotated with an angular velocity  $\omega$  through the reflection position, is

$$I(\text{int.}, hkl) = \frac{\lambda^3}{\omega \cdot V^2} \times \left( \frac{e^2}{mc^2} \right)^2 \times V_{\text{cr}} \times I_0 \times L \times P \times T_r \times |F(hkl)|^2. \quad (4.32)$$

The complete scattering equation (4.32) not only contains  $|F(hkl)|^2$  but has also terms related to the scattering by the electrons themselves, to the wavelength  $\lambda$ , to the volume  $V_{\text{cr}}$  of the crystal, and to the volume  $V$  of the unit cell. We will explain the various terms of Equation (4.32) instead of deriving them from first principles.  $I_0$  is the intensity of the incident beam and  $I$  is the integrated intensity of the reflected beam.  $e$  is the charge and  $m$  the mass of an electron and  $c$  is the velocity of light. Thomson showed that if the electron is a completely free electron and scatters the X-ray photons elastically (i.e., with the same frequency as the incident beam), the following are true:

- The phase difference between the incident and the scattered beam is  $\pi$ . This is because the scattered radiation is proportional to the displacement of the electron, which differs  $\pi$  in phase with its acceleration imposed by the electric vector. This can easily be understood when comparing the directions of displacement and acceleration for a harmonic pendulum. When it moves from its central position, its displacement is increasing (positive direction). However, it experiences a force and, therefore, acceleration in the opposite direction, toward the center.
- The amplitude of the electric component of the scattered wave at a distance  $r$ , large in comparison with the wavelength of the radiation, is

$$E_{\text{el.}} = E_0 \frac{1}{r} \frac{e^2}{mc^2} \sin \alpha, \quad (4.33)$$

where  $E_0$  is the amplitude of the electric vector of the incident beam and  $\alpha$  is the angle between the oscillation direction of the electron and the scattering direction (Figure 4.31a). Note that the component of  $E_0$  perpendicular to the scattering direction is  $E_0 \sin \alpha$ .

In terms of energy,

$$I_{\text{el.}} = I_0 \frac{1}{r^2} \left( \frac{e^2}{mc^2} \right)^2 \sin^2 \alpha. \quad (4.34)$$

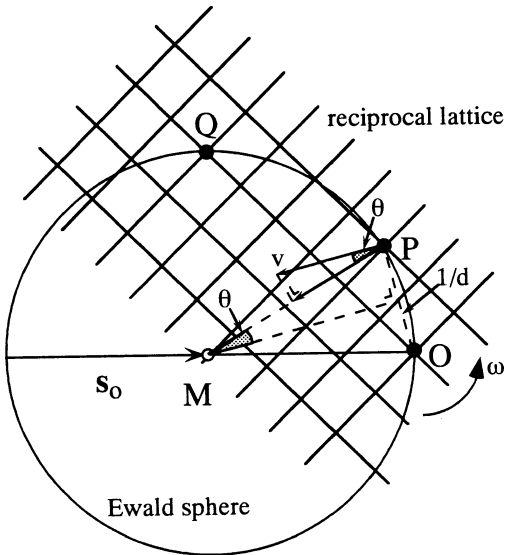


Figure 4.30. If the rotation of the reciprocal lattice is around an axis through the origin  $O$  and perpendicular to the plane of the drawing, point  $P$  will be in reflection condition much longer than point  $Q$ . Note that  $OP = 1/d(P)$ ,  $OQ = 1/d(Q)$ ,  $MP = s(P)$  and  $MQ = s(Q)$ .

Per unit solid angle the scattered energy is

$$I_{\text{el.}}(\Omega = 1) = I_{\text{el.}} \times r^2. \quad (4.35)$$

It has been derived by Klein and Nishina (1929) [see also Heitler (1966)] that the scattering by an electron can be discussed in terms of the classical Thomson scattering if the quantum energy  $h\nu \ll mc^2$ . This is not true for very short X-ray wavelengths. For  $\lambda = 0.0243 \text{ \AA}$ ,  $h\nu$  and  $mc^2$  are exactly equal, but for  $\lambda = 0.1 \text{ \AA}$ ,  $h\nu$  is 0.0243 times  $mc^2$ . Because in macromolecular crystallography wavelengths are usually in the range 0.8–2.5  $\text{\AA}$ , the classical approximation is allowed. The following should be noted:

- The intensity scattered by a free electron is independent of the wavelength.
- Thomson's equation can also be applied to other charged particles (e.g., a proton). Because the mass of a proton is 1800 times the electron mass, scattering by a proton and by atomic nuclei can be neglected.
- For an unpolarized beam,  $\sin^2\alpha$  in Equation (4.34) is replaced by a suitable polarization factor  $P$ . The polarization factor will be discussed in Section 4.14.1 and the transmission factor  $\text{Tr}$  in Section 4.14.2. The Lorentz factor  $L$  depends on the data acquisition system. If the electron is replaced by a unit cell of the crystal, the scattered amplitude is enhanced by a factor  $|F(hkl)|$  and the intensity by  $|F(hkl)|^2$ .

The factor  $V_{\text{cr}}/V^2$  in Equation (4.32) requires some discussion. It depends on the existence of the independently scattering mosaic blocks. The larger the crystal, the more mosaic blocks and, therefore, the greater the proportionality of the integrated intensity with  $V_{\text{cr}}$ . However, why is it proportional to  $1/V^2$ ? In the

reflection position, all unit cells in a mosaic block scatter in phase. For a unit cell of volume  $V$ , the number of unit cells for a given volume of the mosaic blocks is proportional to  $1/V$ , as is the scattered amplitude. Therefore, the intensity is proportional to  $1/V^2$ .

$I$  (int.,  $h k l$ ) is proportional to  $\lambda^3$ . This can be understood as follows:

- Consider the diffracting region around the reciprocal lattice point  $P$ . For a fixed position of the crystal, scattering occurs for the intersection of the diffracting region with the Ewald sphere.
- The intensity scattered by an electron into all directions or, in other words, toward the complete surface  $4\pi(1/\lambda^2)$  of the Ewald sphere (radius  $1/\lambda$ ) has a fixed value and is independent of  $\lambda$ . Therefore, the scattering per unit surface (also the scattering by the intersection considered) is proportional to  $\lambda^2$ .

This  $\lambda^2$  dependence must be multiplied by a  $\lambda$ -dependent term, which is related to the time  $t$  it takes for the complete diffracting region to pass through the Ewald sphere. For the simple case in which the incident and the diffracted beams are perpendicular to the rotation axis,  $t$  is found as follows (Figure 4.30).

If the angular speed of rotation is  $\omega$ , then for the reciprocal lattice point  $P$  at a distance  $1/d$  from the origin  $O$ , the linear speed perpendicular to  $OP$  is  $v = (1/d)\omega$ . Its component  $v_{\perp}$  along  $PM$ , and thus perpendicular to the surface of the sphere, should be regarded:

$$v_{\perp} = \frac{1}{d}\omega \cos \theta.$$

Because according to Bragg's law  $d = \lambda/(2 \sin \theta)$ , we find

$$v_{\perp} = \frac{2 \sin \theta \cos \theta}{\lambda} \omega = \frac{\sin 2\theta}{\lambda} \omega.$$

The time  $t$  required to pass the sphere is proportional to

$$\frac{1}{v_{\perp}} = \frac{1}{\omega} \times \frac{\lambda}{\sin 2\theta}.$$

Multiplying by the  $\lambda^2$  dependence, found earlier, gives  $\lambda^3$ . The  $\theta$ -dependent factor  $1/\sin 2\theta$  represents the Lorentz factor  $L$  for the present case. For other acquisition techniques,  $L$  might be a more complicated function of  $(h k l)$ . Note that for small  $\theta$  values,  $\lambda/\sin 2\theta$  is approximately equal to  $\lambda/(2 \sin \theta) = d$  (error less than 10% for  $\theta < 25^\circ$ ) and  $\lambda$  drops out. This implies that the intensity of reflections from protein crystals, with their small  $\theta$  values, is not proportional to  $\lambda^3$ , but rather to  $\lambda^2$ .

#### 4.14.1. The Polarization Factor

The polarization factor  $P$  in Equation (4.32) originates from the fact that an electron does not scatter along its direction of vibration. In other directions, electrons radiate with an intensity proportional to  $(\sin \alpha)^2$  (Figure 4.31a). The effect is that if the incident X-ray beam is unpolarized and then reflected against a plane, the



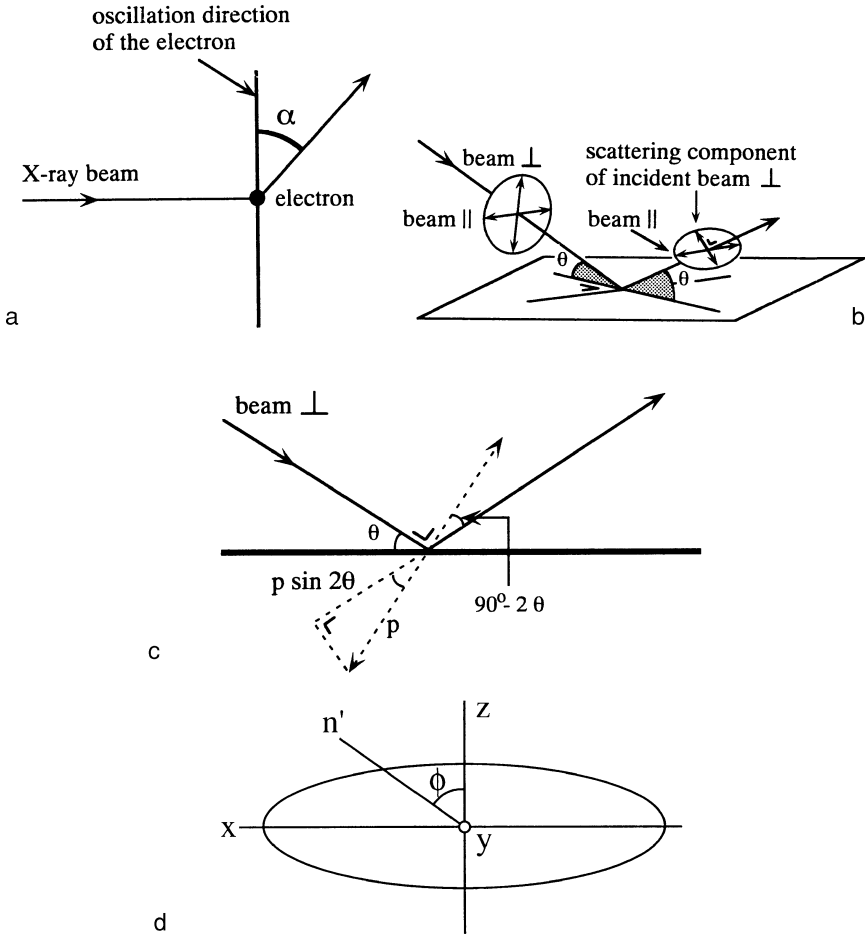


Figure 4.31. An explanation of the polarization factor. (a) The intensity of the radiation scattered by an oscillating electron is proportional to  $(\sin \alpha)^2$ . (b) An unpolarized incident beam can be split into two others with the same intensity: one polarized in a direction parallel to the reflecting plane (beam  $\parallel$ ) and the other one in a direction perpendicular to the first one (beam  $\perp$ ); both polarization directions lie in a plane perpendicular to the direction of the incident beam. (c) The dotted line ( $p$ ) indicates the polarization direction of incident beam  $\perp$ . Electrons induced by component  $p \sin 2\theta$  do not contribute to the scattering. (d) Cross section through a polarized beam with an intensity  $I_h$  in the horizontal direction and  $I_v$  in the vertical direction. The polarized beam is directed toward the reflecting plane along  $y$ , with  $y$  perpendicular to the plane of the drawing. The ellipse indicates the polarization. The normal  $n$  to the reflecting plane (not drawn) makes certain angles with  $x$ ,  $y$ , and  $z$ .  $n'$  is the projection of  $n$  on the  $xz$ -plane.  $\phi$  is the angle between  $n'$  and the  $z$ -axis.

reflected beam is more or less polarized. This affects the intensity. This is illustrated in Figure 4.31b. The unpolarized beam is split into two other beams with equal intensity: one polarized in a direction parallel to the reflecting plane (beam  $\parallel$ ) and the other one in a direction perpendicular to the first one (beam  $\perp$ ). The polarization direction of incident beam  $\perp$  has, on a relative scale, a component  $\sin 2\theta$  along the scattering direction (Figure 4.31c). The oscillation of electrons induced by this component does not contribute to the scattered intensity ( $\alpha$  in Figure 4.31a is 0). Only the other component ( $\cos 2\theta$ ) does. Therefore, the scattered intensity is reduced by a factor  $(1 - \sin^2 2\theta) = \cos^2 2\theta$ . For incident beam  $\parallel$ , which is polarized perpendicular to the scattering direction, no reduction of intensity occurs. Combining the intensities of the two reflected beams results in the  $\theta$ -dependent polarization factor  $(1 + \cos^2 2\theta)/2$ . It should be emphasized that the polarization factor as given here is valid only if the crystal is radiated with an unpolarized beam. With a monochromator in the incident beam path, this is not true and it is certainly not true for synchrotron radiation, which is strongly polarized. For a polarized beam, the polarization factor is (Azaroff, 1955; Kahn et al., 1982)

$$P = \frac{1}{2}(1 + \cos^2 2\theta - \tau \cos 2\phi \sin^2 2\theta).$$

For  $\phi$  see Figure 4.31d;

$$\tau = \frac{I_h - I_v}{I_h + I_v},$$

where  $I_h$  and  $I_v$  are the intensities of respectively the horizontal and vertical component of the polarized beam.

#### 4.14.2. Absorption and Extinction

The transmission factor  $Tr$  is related to the absorption factor  $A$  :  $Tr = 1 - A$ . If an X-ray beam passes through matter, its intensity  $I$  diminishes as a consequence of absorption:  $I = I_0 \exp[-\mu \cdot t]$ .  $t$ (cm) is the path length in the matter and  $\mu$ ( $\text{cm}^{-1}$ ) is the total linear absorption coefficient.  $\mu$  can be obtained as the sum of the atomic mass absorption coefficients  $\mu_a$  because these are, to a good approximation, additive with respect to the elements composing the material (for a definition of  $\mu_a$ , see the legend to Figure 4.32):

$$\mu = \frac{1}{V} \sum_i n_i (\mu_a)_i,$$

where  $n_i$  is the number of atoms of elements  $i$  in volume  $V$ . The value of  $\mu_a$  is more or less independent of the physical state of the material. In general,  $\mu_a$  is larger for a longer wavelength and for atoms with a higher atomic number (Figure 4.32). A protein crystal of 0.5 mm has, for Cu radiation, a transmission of  $\sim 60\%$ . For paper of 0.1 mm thickness and for glass of 0.01 mm thickness, transmission is 93%. Air also absorbs X-ray radiation.

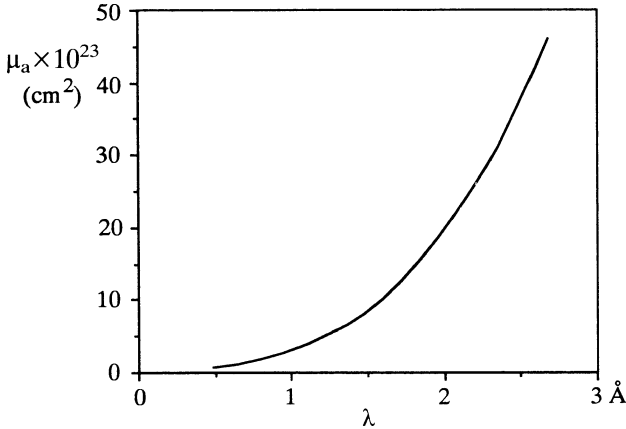


Figure 4.32. The atomic mass absorption coefficient  $\mu_a$  of the element carbon as a function of the wavelength. The atomic mass absorption coefficient ( $\text{cm}^2$ ) for element  $i$  is defined as  $(\mu_a)_i = \mu_i/\rho_i \times A_i/N$ , where  $\mu_i$  is the linear absorption coefficient,  $\rho_i$  is the density, and  $A_i$  is the atomic weight;  $N$  is Avogadro's number.

Absorption of X-rays is mainly caused by two effects:

1. Photoelectric absorption: The X-ray photon disappears completely. If the photon energy is sufficient to remove an electron from the atom, the absorption becomes particularly strong.
2. Scattering is the result of a collision between the X-ray photons and the electrons. One can distinguish two kinds of scattering: Compton scattering and Rayleigh scattering. In Compton scattering, the photons lose part of their energy in the collision process (inelastic scattering), resulting in scattered photons with a lower energy and a longer wavelength. Compton scattering contributes to the background in an X-ray diffraction experiment. In Rayleigh scattering, the photons are elastically scattered, do not lose energy, and leave the material with an unchanged wavelength. In a crystal, they interfere with each other and give rise to Bragg reflections. Between the Bragg reflections there is no loss of energy because of elastic scattering and the incident beam is hardly reduced. The crystal is considered as an ideal mosaic if, in the Bragg position, the reduction in intensity of the incident beam, as a result of elastic scattering, can still be neglected. For nonideal mosaic crystals (or nearly perfect crystals) the beam is reduced by *extinction*
  - The blocks are too large and multiple reflection occurs within a block. At each reflection process, the phase angle shifts  $\pi/2$  (Section 4.15). After two reflections, the beam travels in the same direction as the incident beam but with a phase difference of  $\pi$  and this reduces the intensity. This is called "primary extinction" (Figure 4.33).
  - The angular spread of the mosaic blocks is too small. Part of the incident beam is reflected by blocks close to the surface before it reaches lower-lying

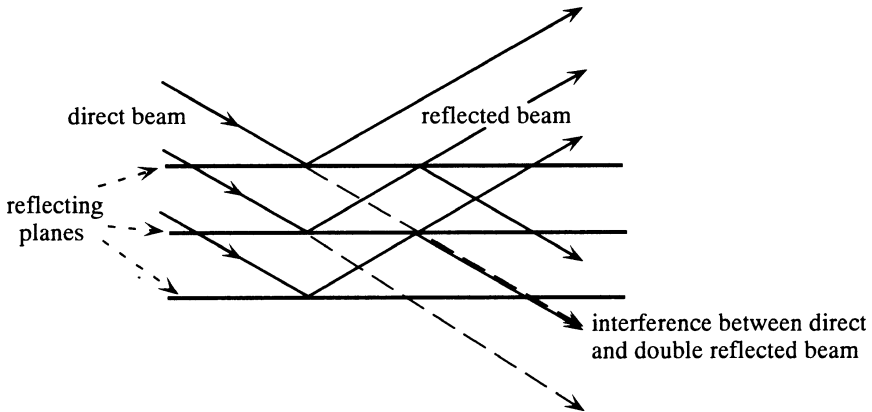


Figure 4.33. In primary extinction, interference occurs between the incident and scattered waves. Because at each reflection there is a phase shift of  $\pi/2$ , the double-reflected beam has a phase difference of  $\pi$  with the incident beam and reduces its intensity (Section 4.15).

blocks that are also in the reflecting position. This reduces the intensity of the incident beam for the lower-lying blocks and, consequently, also their diffracted intensity; it is called “secondary extinction.” For the relatively weak reflections of protein crystals, extinction does not play a significant role. Polikarpov and Sawyer (1995) noted that some protein crystals are rather perfect crystals, which is equivalent to large mosaic blocks, and that primary extinction does play a role, especially for larger crystals and longer wavelength (1.5 Å instead of 1.0 Å). The correction can be as much as 13–15% for the strongest reflections.

## 4.15. Scattering by a Plane of Atoms

A plane of atoms reflects an X-ray beam with a phase retardation of  $\pi/2$  with respect to the scattering by a single atom. The difference is caused by the difference in path length: Source—atom—Detector, for the different atoms in the plane. Suppose that the plane is infinitely large. The source is at S and the detector at D (Figure 4.34). The shortest connection between S and D via the plane is S–M–D. The plane containing S, M, and D is  $\perp$  the reflecting plane and the lines S–M and M–D make equal angles with the reflecting plane. Moving outward from atom M in the reflecting plane, for instance to P, the path length S–P–D is longer. At the edge of the first Fresnel zone, the path is  $\pi/2$  longer (Figure 4.34). This edge is an ellipse with its center at M and its major axis is on the line of intersection between plane S–M–D and the reflecting plane. Continuing outward, many more elliptic Fresnel zones are formed. Clearly, the beams radiated by the many atoms in the plane interfere with each other. The situation is represented in the Argand diagram of Figure 4.35. Successive Fresnel zones can be subdivided into an equal

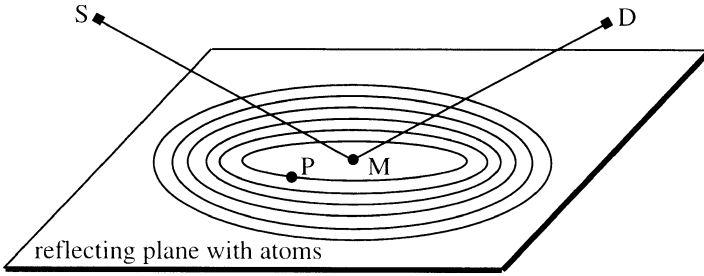


Figure 4.34. S is the X-ray source and D is the detector. Scattering is by the atoms in a plane. The shortest distance between S and D via a point in the plane is through M. Path lengths via points in the plane outward from M are longer, and when the beams reach the detector, they lag behind in phase with respect to the MD beam. The plane is divided in zones, such that from one zone to the next, the path difference is  $\lambda/2$ .

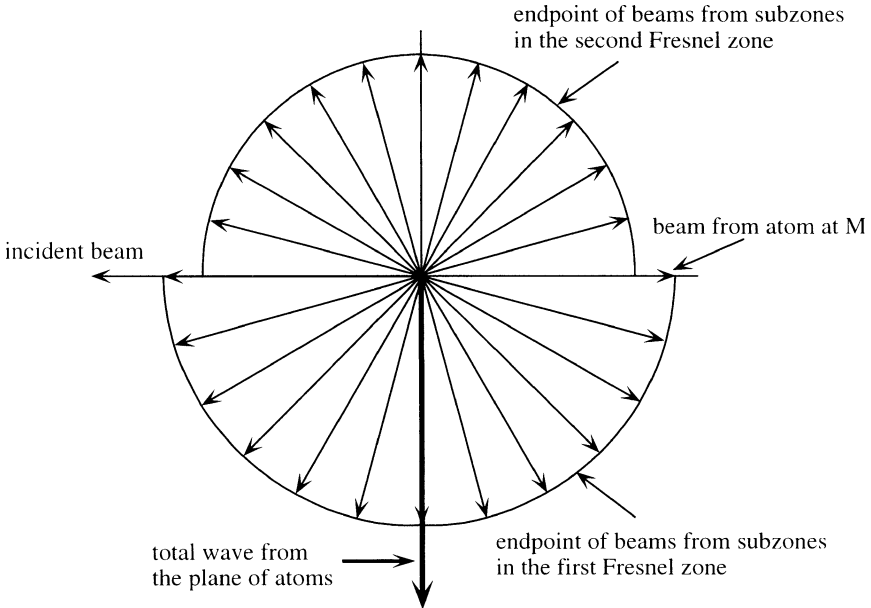


Figure 4.35. Schematic of the Argand diagram for the scattering by atoms in a plane. All electrons are considered as free electrons. The vector of the incident beam is pointing to the left. The electrons of atom M, regarded as free electrons, have a phase difference of  $\pi$  with respect to the incident beam. Subzones in the first Fresnel zone have the end point of their vectors on the lower half-circle. For the next Fresnel zone, they are on the upper half-circle, which has a smaller radius because the amplitude decreases gradually for subsequent Fresnel zones (Kauzmann, 1957). The sum of all vectors is pointing down, meaning a phase lag of  $\pi/2$  with respect to the beam scattered by the atom at M.

number of subzones. If the distribution of electrons is sufficiently homogeneous, it can be assumed that the subzones in one Fresnel zone give the same amplitude at D. Their phases are spaced at regular intervals and their vectors in the Argand diagram lie in a half-circle. In the lower part of Figure 4.35, this is illustrated for the first Fresnel zone. For the second Fresnel zone (upper part), the radius is slightly smaller because the intensity radiated by more distant zones decreases (Kauzmann, 1957). Therefore, the sum of vectors pointing upward is shorter than for those pointing downward, and the resulting scattered wave lags  $\pi/2$  in phase behind the scattering by the atom at M. In Section 4.14 it was mentioned that the phase difference between the incident beam and the beam scattered by the free electrons in an atom is  $\pi$ . Therefore, the scattering by a plane of atoms has a phase difference of  $\pi/2$  with the incident beam.

## 4.16. Choice of Wavelength, Size of Unit Cell, and Correction of the Diffracted Intensity

### 4.16.1. Choice of Wavelength

The wavelength  $\lambda$  has an appreciable influence on the intensity of the X-rays diffracted by a crystal [Equation (4.32)]. Using a longer wavelength has the advantage of a stronger diffracted intensity, but the disadvantage of higher absorption (Weiss et al., 2001, 2004). An optimal choice for protein crystallography is the Cu  $K_\alpha$  wavelength of 1.5418 Å. However, if high-intensity synchrotron radiation is available, a shorter wavelength (e.g., close to 1 Å) has the advantage of lower absorption (Gonzalez et al., 1994; Helliwell et al., 1993). For an X-ray detector with a fluorescent screen, the optimum wavelength might also be below 1.5 Å because more visible light is created per X-ray photon. However, part of the shorter-wavelength X-ray beam might not be absorbed in the fluorescent layer. There is also more chance that the diffracted beams overlap. A further advantage of a short wavelength is that the “blind region” is smaller because of a larger Ewald sphere (Section 2.7 of Chapter 2).

Polikarpov et al. (1997) discussed the ultimate wavelength for protein crystallography from a theoretical point of view. Their conclusion was that it has no advantage to go below 0.9 Å. For very small crystals, where absorption is not a serious problem, a longer wavelength has the advantage of stronger reflection intensities. A special choice of wavelength is required if anomalous scattering is optimally used in protein phase angle determination (Chapter 9).

### 4.16.2. Effect of the Size of the Unit Cell on the Diffraction Intensity

If a crystal is larger, its diffraction (and also its absorption) is stronger. In protein crystallography, a crystal size of 0.2–0.4 mm is regarded as optimal. Protein crystals

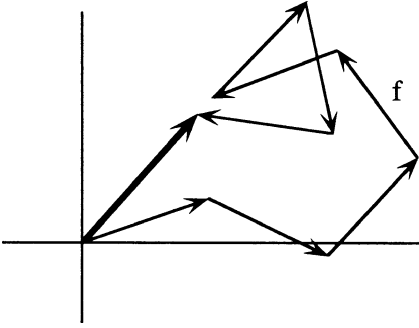


Figure 4.36. The displacement of a particle under the influence of Brownian motion. For  $n$  steps, where  $n$  is very large and each step has a length  $f$ , the final distance to the origin is  $f\sqrt{n}$ .

are relatively weak scatterers for two reasons. The first is because they consist only or mainly of light atoms: C, N, and O. The second and more important reason is the large size of their unit cells. This we can understand as follows. A crystal with a larger unit cell volume diffracts more weakly but has larger values of  $|F(hkl)|^2$ . We can combine these two effects by first calculating the mean square value  $\overline{|F(hkl)|^2}$ . Suppose that we have the simple situation of a crystal with one kind of atom, each atom with a scattering factor  $f$  and  $n$  atoms in the unit cell.  $\overline{|F(hkl)|^2}$  can be calculated by assigning random phases to the contributions  $f$  of the individual atoms in the Argand diagram. This problem is analogous to that of the displacement caused by Brownian motion (Figure 4.36): A number of  $n$  equal steps of length  $f$  gives a root mean square displacement from the origin of  $f \times \sqrt{n}$ . The root mean square value of  $|F(hkl)|$  is then

$$\sqrt{\overline{|F(hkl)|^2}} = f \times \sqrt{n} \quad \text{and} \quad \overline{|F(hkl)|^2} = f^2 \times n.$$

Combining the effect of the unit cell volume  $V$  and  $|F(hkl)|$  in the scattering equation (4.32) leads to

$$\overline{I(int., hkl)} \text{ is proportional to } \frac{\overline{|F(hkl)|^2}}{V^2} = \frac{f^2}{V^2} \times n. \quad (4.36)$$

If, through a reorganization of the molecular packing, a unit cell becomes two times as large and the number of molecules per unit cell doubles,  $V$  would become  $2V$  and  $n \rightarrow 2n$ . Applying Equation (4.36) results in an average intensity for the reflected beams that is half the original one. Note, however, that the total scattered intensity remains the same because the number of reflections doubles.

#### 4.16.3. Correction of the Measured Intensity

In Equation (4.32),  $(\lambda^3/\omega V^2) \times (e^2/mc^2)^2 \times V_{cr} \times I_0$  is a constant for a given experiment. The intensity  $|F(hkl)|^2$  is obtained on a relative scale by calculating  $I(int., hkl)/(L \times P \times Tr)$ . This is called “correction” of the measured intensity for  $L$ ,  $P$ , and  $Tr$  with  $Tr = 1 - A$ . In the following, the resulting intensity will be

called

$$I(hkl) = |F(hkl)|^2 \text{ on relative scale.} \quad (4.37)$$

The correction factors  $L$  and  $P$  are usually incorporated into the software package for the processing of the intensity data.<sup>4</sup> Whether correction for absorption is required depends on the shape of the crystal, the wavelength, and the diffraction technique. For oscillation pictures, the path lengths of the primary and secondary beam in the crystal are not very different for all of the reflections on a particular image plate. As a result, the absorption is approximately the same for all of those reflections. The absorption correction is then incorporated into the scaling factor for the exposures. It should be noted that inhomogeneously distributed mother liquor around the crystal mounted in an X-ray capillary can also have an appreciable absorption effect. If an absorption correction is applied, it is done in an empirical way in which absorption and extinction are considered simultaneously. For an area detector, one can, for example, measure the intensity of symmetry-related reflections that follow different paths in the crystal. The solvent around the crystal not only has an effect on the absorption but also causes a relatively strong but very diffuse ring in the diffraction pattern, to which the disordered solvent inside the crystal also contributes. The ring is in the region corresponding to 3–4 Å resolution, which is somewhat longer than has been found for pure water, which has its maximum near 3 Å (Narten and Levy, 1972).

As was pointed out by Blessing et al. (1996), the strong intensity at 3–4 Å resolution is also the result of ubiquitous atomic distances in proteins.

## Summary

It requires some simple mathematics to understand the diffraction of X-rays by a crystal. In this chapter, it is presented via the addition of waves, the scattering by a simple two-electron system, by an atom, by one unit cell, and by the arrangement of unit cells in a crystal. The crystal periodicity leads to the Laue diffraction conditions

$$\begin{aligned} \mathbf{a} \cdot \mathbf{S} &= h, \\ \mathbf{b} \cdot \mathbf{S} &= k, \\ \mathbf{c} \cdot \mathbf{S} &= l, \end{aligned}$$

and to Bragg's law:

$$2d \sin \theta = \lambda.$$

They tell us that for suitable orientations, a crystal diffracts an X-ray beam only in certain specific directions. With the reciprocal lattice formalism, the required orientations and diffraction directions can be easily constructed.

---

<sup>4</sup> Several programs are available for data processing, for instance HKL-3000 (Minor et al., 2006).



A crystal structure is not static: The atoms vibrate around an equilibrium position, some more and others less. As a consequence, the intensity of the diffracted beams is weakened. This is expressed in the temperature factor.

The result of an X-ray structure determination is the electron density in the crystal, and the fundamental equation for its calculation is

$$\rho(x y z) = \frac{1}{V} \sum_h \sum_k \sum_l \left| F(hkl) \right| \exp[-2\pi i(hx + ky + lz) + i\alpha(h k l)].$$

In this equation,  $\rho(x y z)$  is expressed as a Fourier transformation of the structure factors  $F(h k l)$ . The amplitude of these structure factors is obtained from the intensity of the diffracted beam after application of certain correction factors:  $I(h k l) = |F(h k l)|^2$ . The phase angles  $\alpha(h k l)$  cannot be derived in a straightforward manner, but they can be found in an indirect way, which will be discussed in later chapters.

Further processing of the intensity of the diffracted beams requires that they be corrected by a number of factors: absorption of the X-ray beam, the polarization factor, and the Lorentz factor; the latter being an instrumental factor.

It might be surprising that the beam reflected by a plane of atoms differs  $\pi/2$  in phase with the beam scattered by a single atom. This can be explained considering the differences in path length for the reflections from the distribution of the many atoms in the plane.

# Chapter 5

## Average Reflection Intensity and Distribution of Structure Factor Data

### 5.1. Introduction

A quick glance through this chapter indicates that it is short but that it is mainly of a mathematical nature. However, it is not as difficult as it seems.

In Section 4.16.2 of Chapter 4 we calculated the average reflection intensity for a structure consisting of identical atoms. In this chapter we will extend this calculation to structures composed of different atoms and use the result to place the experimentally determined intensities on an absolute scale<sup>1</sup> and obtain a rough estimate of the temperature factor. In later chapters, we will need to know not only the average intensity but also the probability distribution of the structure factors and their amplitudes. In the derivation of these distribution functions, the Gaussian distribution function, also called the Gauss error function, plays an important role. This function is now presented.

Two Gauss error curves are drawn in Figure 5.1. They obey the equation

$$f(x) = \frac{1}{\sigma\sqrt{2\pi}} \exp\left[-\frac{(x-m)^2}{2\sigma^2}\right]. \quad (5.1)$$

We note the following:

1. The probability of finding a value between  $x$  and  $x + dx$  is equal to  $f(x) dx$ .
2. Because it is certain that  $x$  lies somewhere between  $+\infty$  and  $-\infty$ , the probability of finding  $x$  between  $+\infty$  and  $-\infty$  is 1 and, therefore,

$$\int_{-\infty}^{+\infty} f(x) dx = 1.$$

---

<sup>1</sup> Intensities are on absolute scale if the amplitudes of the structure factors  $|F| = \sqrt{I}$  are expressed in electrons.

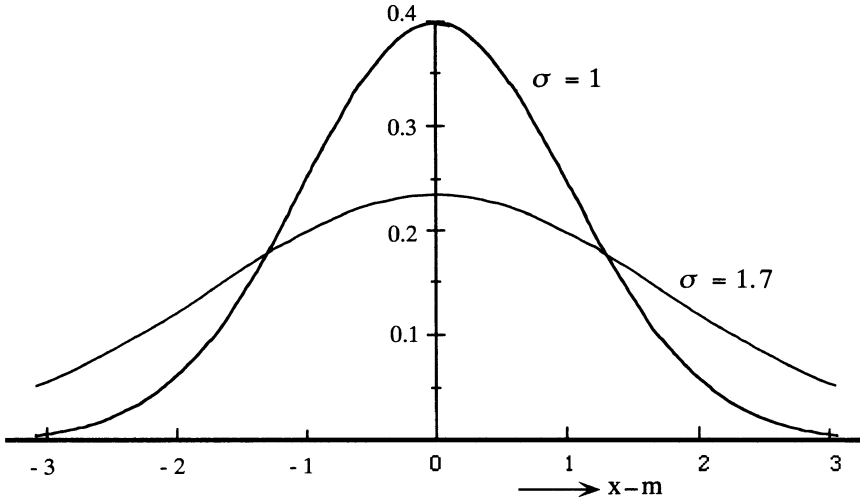


Figure 5.1. Gauss error functions:  $(1/\sigma\sqrt{2\pi}) \exp[-(x-m)^2/2\sigma^2]$  plotted as a function of  $x-m$  for  $\sigma = 1$  and  $\sigma = 1.7$ .

This is called normalization of the function  $f(x)$ .

3. The mean value of  $x$  is  $m$ :  $\bar{x} = m$ . This follows directly from the symmetry of the function  $f(x)$  around  $m$ .
4. For  $x = m$ , the value of the function is given by  $f(m) = 1/\sigma\sqrt{2\pi}$ .
5. The spread of the curve is expressed in the variance  $\sigma^2$  of  $x$ , which is defined as the average value of  $(x-m)^2$ :

$$\overline{(x-m)^2} = \sigma^2 = \int_{x=-\infty}^{+\infty} (x-m)^2 f(x) dx;$$

$\sigma$  is called the standard deviation. Figure 5.1 shows that the width of the curve increases with  $\sigma$ , as expected. The variance  $\sigma^2$ , is calculated for data  $x$  with a frequency distribution  $f(x)$  and assuming random errors in the data.

6. In a large set of data with random errors, only a few measurements occur far away from the center because the curve falls off on either side of the maximum. For a distance  $\geq 3\sigma$  from  $m$ , the chance of finding a measurement is only 2.7%. Therefore, it is assumed that a measurement greater than  $3\sigma$  from  $m$  is significantly different from  $m$ .
7. If the frequency distribution is not known, we might still have a number of measurements. In such a case, the average  $\bar{x}$  of the observations is determined, rather than the mean value  $m$ . The variance is then defined as

$$\sigma^2 = \frac{\sum_i (x_i - \bar{x})^2}{N-1}.$$

where  $N$  is the number of measurements. The denominator is  $N-1$  and not  $N$ , because one degree of freedom is lost in calculating  $\bar{x}$  from the measurements.

As an example in which the Gaussian distribution is used, we consider the measurement of an X-ray reflection intensity. Suppose that its actual value is  $I_{\text{true}}$ , but that values  $I_i$  are obtained by measuring the intensity a number of times or by considering the intensity of symmetry-related reflections. Because of experimental errors, the values  $I_i$  show deviations  $I_i - I_{\text{true}}$  from the actual value. If only random errors occur, the intensities observed for the particular reflection obey the Gauss error function, which for the present example is

$$f(I) = \frac{1}{\sigma[I]\sqrt{2\pi}} \exp \left[ -\frac{(I - I_{\text{true}})^2}{2(\sigma[I])^2} \right],$$

in which  $(\sigma[I])^2$  is the average of  $(I - I_{\text{true}})^2$ . Because in practice the number of measurements is too small to obtain the complete distribution function, we have to be satisfied with best estimates of  $I_{\text{true}}$  and  $\sigma[I]$ . For  $I_{\text{true}}$ , the best estimate is the average value  $\bar{I}$  of the measured intensities, and for  $\sigma[I]$ , it is given by

$$\sigma_e[I] = \left[ \frac{\sum_i (I_i - \bar{I})^2}{N - 1} \right]^{1/2}.$$

In practice, the estimated standard deviation  $\sigma_e$  (ESD) is usually called  $\sigma$ . Outliers that differ more than  $3\sigma[I]$  from the mean value are usually rejected.

For a small number of intensity measurements,  $\sigma_e$  is not a good estimate for  $\sigma$ . However, even if there is only one measurement of the intensity, a standard deviation for the intensity  $I$  can still be given. This is based on counting statistics and the estimated standard deviation is given as  $\sigma_e[I] = \sqrt{I}$  this is explained in Appendix 3.

The precision of the mean  $\bar{I}$  is given by the standard error  $\sigma[I]/\sqrt{N}$ . The standard deviation is also frequently used in electron density plots. In such a plot, peak heights are often given as a multiple of the standard deviation. For instance, the electron density  $\rho$  of a significant peak should be at least  $3 \times \sigma[\rho]$ . Here,  $\sigma[\rho]$  is obtained as

$$\sigma[\rho] = \left[ \frac{\sum_{i=1}^N \{\rho(x_i, y_i, z_i) - \bar{\rho}\}^2}{N} \right]^{1/2}.$$

## 5.2. Average Intensity; Wilson Plots

Early in the process of determining a crystal structure, it is possible to obtain a rough estimate of the value of the temperature factor and of the factor required for putting the intensities  $I(S)$  on an absolute scale. To this end we calculate the

average intensity for a series of reflections  $\mathbf{S}$ , starting from the expression for the structure factor [Equation (4.3) of Chapter 4]:

$$\mathbf{F}(\mathbf{S}) = \sum_{i=1}^n f_i \exp[2\pi i \mathbf{r}_i \cdot \mathbf{S}],$$

where the scattering factor  $f_i$  of atom  $i$  includes the effect of thermal motion, and  $n$  is the number of atoms in the unit cell. On an absolute scale, the intensity is given by

$$I(\text{abs}, \mathbf{S}) = \mathbf{F}(\mathbf{S}) \cdot \mathbf{F}^*(\mathbf{S}) = |\mathbf{F}(\mathbf{S})|^2 = \sum_i \sum_j f_i f_j \exp[2\pi i (\mathbf{r}_i - \mathbf{r}_j) \cdot \mathbf{S}]^2.$$

Suppose that we consider a series of reflections for which  $\mathbf{S}$  varies so strongly that the values for the angles  $[2\pi(\mathbf{r}_i - \mathbf{r}_j) \cdot \mathbf{S}]$  are distributed evenly over the range 0 to  $2\pi$  for  $i \neq j$ . Then, the average value for all terms with  $i \neq j$  will be zero. Only the terms with  $i = j$  remain, and we obtain<sup>2</sup>

$$\overline{|\mathbf{F}(\mathbf{S})|^2} = \overline{I(\text{abs}, \mathbf{S})} = \sum_i f_i^2. \quad (5.2)$$

This result is true for noncentric reflections (any phase angle) as well as for centric reflections (phase angles  $0^\circ$  or  $180^\circ$ ). We presented this result previously (Section 4.16.2 of Chapter 4) for a structure with identical atoms. There the equation was not rigorously derived, but it was obtained by comparison with Brownian motion. To obtain a rough estimate of the temperature factor and of the scale factor, it is assumed that all atoms in the cell have the same isotropic thermal motion, or

$$f_i^2 = \exp\left[-2B \frac{\sin^2 \theta}{\lambda^2}\right] \times (f_i^0)^2,$$

where  $f_i^0$  is the scattering factor of atom  $i$  at rest. Comparison of the calculated values  $\overline{I(\text{abs}, \mathbf{S})}$  with the experimental data  $\overline{I(\mathbf{S})}$  requires a scale factor  $C$ :

$$\overline{I(\mathbf{S})} = C \times \overline{I(\text{abs}, \mathbf{S})} = C \exp\left[-2B \frac{\sin^2 \theta}{\lambda^2}\right] \sum_i (f_i^0)^2.$$

Both  $f_i^0$  and the temperature factor depend on  $(\sin \theta)/\lambda$ . Therefore, average intensities are calculated for reflections in shells of (almost) constant  $(\sin \theta)/\lambda$ . To determine  $B$  and  $C$ , the equation is written in the form

$$\ln \frac{\overline{I(\mathbf{S})}}{\sum_i (f_i^0)^2} = \ln C - 2B \frac{\sin^2 \theta}{\lambda^2} \quad (5.3)$$

and  $\ln \overline{I(\mathbf{S})} / \sum_i (f_i^0)^2$  is plotted against  $(\sin^2 \theta)/\lambda^2$ . The result should be a straight line—the so-called Wilson plot (Wilson, 1942)—from which both the temperature factor and the absolute scale of the intensities can be derived (Figure 5.2). For proteins, the Wilson plot does not give a fully accurate result because the condition

<sup>2</sup>  $\mathbf{F}^*(\mathbf{S}) = \mathbf{F}(-\mathbf{S})$  is the conjugate complex of  $\mathbf{F}(\mathbf{S})$ .

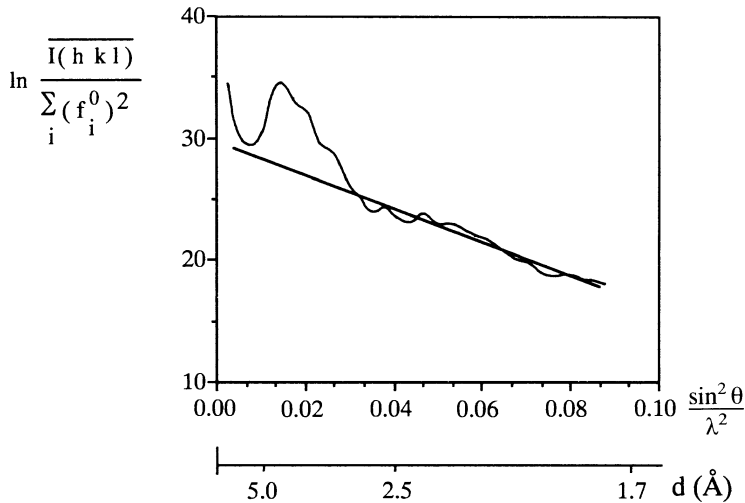


Figure 5.2. The Wilson plot for phospholipase A2 with data to 1.7 Å resolution. Only beyond 3 Å resolution is it possible to fit the curve to a straight line.

that the angles  $[2\pi(\mathbf{r}_i - \mathbf{r}_j) \cdot \mathbf{S}]$  are distributed evenly over the 0 to  $2\pi$  range is not fulfilled for shells of reflections with (almost) constant  $(\sin \theta)/\lambda$  (see below).

---

### The Wilson Plot for a Protein Structure

For practical purposes, the condition that the angles  $2\pi(\mathbf{r}_i - \mathbf{r}_j) \cdot \mathbf{S}$  are distributed evenly over the 0 to  $2\pi$  range is replaced by the more relaxed condition that the range in the angular values should at least be  $2\pi$ . In proteins, the shortest distance encountered between bonded atoms is approximately 1.5 Å. For this distance and given  $\mathbf{S}$ , the scalar product varies from  $-3\pi|\mathbf{S}|$  ( $\mathbf{S}$  and  $\mathbf{r}_i - \mathbf{r}_j$  antiparallel) to  $+3\pi|\mathbf{S}|$  ( $\mathbf{S}$  and  $\mathbf{r}_i - \mathbf{r}_j$  parallel). The condition that the range  $6\pi|\mathbf{S}|$  should be at least  $2\pi$  requires that  $|\mathbf{S}| = 1/d$  is not smaller than  $\frac{1}{3} \text{Å}^{-1}$  or  $d < 3 \text{Å}$  (Figure 5.3).

Therefore, we conclude that the Wilson plot gives reliable information only if reflections are used corresponding to Bragg spacings less than 3 Å. For longer distances, Figure 5.2 shows deviations from the straight line. For instance, around

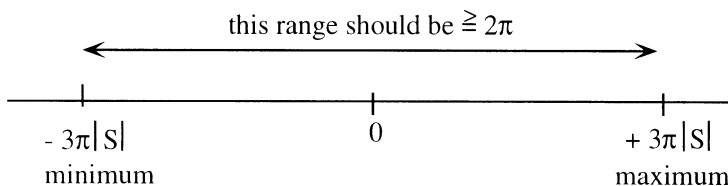


Figure 5.3. The range for  $2\pi(\mathbf{r}_i - \mathbf{r}_j) \cdot \mathbf{S}$  in protein structures. The shortest value for  $(\mathbf{r}_i - \mathbf{r}_j)$  is 1.5 Å. Therefore, the minimum value for  $2\pi(\mathbf{r}_i - \mathbf{r}_j) \cdot \mathbf{S}$  is  $-3\pi|\mathbf{S}|$  and the maximum value is  $+3\pi|\mathbf{S}|$ .

$d = 4\text{\AA}$  or  $|S| = 0.25\text{\AA}^{-1}$ , there is a maximum that can be ascribed to the presence of many nonbonded distances around  $4\text{\AA}$  in the protein structure. Therefore, the angles  $2\pi(\mathbf{r}_i - \mathbf{r}_j) \cdot \mathbf{S}$ , with  $i \neq j$ , tend to cluster around  $2\pi$  for  $|S| = 0.25\text{\AA}^{-1}$  and terms  $\exp[2\pi i(\mathbf{r}_i - \mathbf{r}_j) \cdot \mathbf{S}]$ ,  $i \neq j$ , do not average to zero.

### 5.3. The Distribution of Structure Factors $\mathbf{F}$ and Structure Factor Amplitudes $|F|$

With the information that  $|F(\mathbf{S})|^2 = \sum_i f_i^2$  [Equation (5.2)], it is now easy to derive distribution functions for the structure factors and their amplitudes. However, we will not need this information before Chapter 8 and, therefore, as an alternative, you can skip it now and read it later.

First, we consider for general reflections the probability  $p(\mathbf{F})d(\mathbf{F})$  of finding a structure factor between  $\mathbf{F}$  and  $\mathbf{F} + d\mathbf{F}$ . In the two-dimensional Argand diagram,  $\mathbf{F}$  is expressed as a vector with real component  $A$  and imaginary component  $B$ :  $|F|^2 = A^2 + B^2$ . Let  $A$  have the probability  $p(A)d(A)$  of lying between  $A$  and  $A + dA$  and similarly for  $B$ . Because the components  $A$  and  $B$  are independent of each other, the probability for  $\mathbf{F}$  to point to the volume element  $d\mathbf{F} = dA \times dB$  is given by

$$p(\mathbf{F})d(\mathbf{F}) = p(A)d(A) \times p(B)d(B).$$

A protein structure consists of a great many light atoms with an occasional heavy atom. For such a structure, a Gaussian distribution can be assumed for the components  $A$  and  $B$  if the reflections considered show a sufficiently large variation in their diffraction vectors  $\mathbf{S}$ . Therefore, the distribution functions of  $A$  and  $B$  are determined by the average values  $\bar{A}$  and  $\bar{B}$  and by the variances  $\sigma^2[A]$  and  $\sigma^2[B]$ . Because within the series of reflections all directions for the atomic scattering factors  $\mathbf{f}_i$  are equally possible, we obtain

$$\begin{aligned} \bar{A} &= \bar{B} = 0, \\ \sigma^2[A] &= \overline{(A - \bar{A})^2} = \bar{A}^2 \text{ and } \sigma^2[B] = \overline{(B - \bar{B})^2} = \bar{B}^2, \\ \bar{A}^2 &= \bar{B}^2 = \frac{1}{2} |\bar{F}|^2 = \frac{1}{2} \sum_i f_i^2 \text{ (Eq. 5.2),} \\ \sigma^2[A] &= \sigma^2[B] = \frac{1}{2} [|\bar{F}|]^2 = \frac{1}{2} \sum_i f_i^2, \\ p(\mathbf{F})d(\mathbf{F}) &= \frac{1}{2\pi \times \sigma(A) \times \sigma(B)} \exp\left[-\frac{A^2 + B^2}{2\sigma^2(A)}\right] d(A)d(B), \\ &= \frac{1}{\pi \times \sum_{i=1}^n f_i^2} \exp\left[-\frac{|F|^2}{\sum_{i=1}^n f_i^2}\right] d(\mathbf{F}). \end{aligned} \quad (5.4)$$

It is now easy to derive  $p(|F|)d|F|$ . This is the probability that the magnitude of a structure factor lies between  $|F|$  and  $|F| + d|F|$  or that the end of vector  $\mathbf{F}$  in the Argand diagram is in an annulus between  $|F|$  and  $|F| + d|F|$ :

$$p(|F|)d|F| = p(\mathbf{F}) \times 2\pi|F|d|F| = \frac{2|F|}{\sum_{i=1}^n f_i^2} \exp \left[ -\frac{|F|^2}{\sum_{i=1}^n f_i^2} \right] d|F|. \quad (5.5)$$

The probability for  $I = |F|^2$  is the same as for  $|F|$ . Moreover,  $dI = d|F|^2 = 2|F|d|F|$  and  $\sum_{i=1}^n f_i^2 = \bar{I}$ . Therefore,

$$p(I)dI = \frac{1}{\bar{I}} \exp \left[ -\frac{I}{\bar{I}} \right] dI. \quad (5.6)$$

We will also derive the expression for the probability distribution of centric structures. Compared with the noncentric reflections, we now have  $B = 0$  and  $A = F$ . The average value of  $F = 0$  and, therefore,

$$\sigma^2 [F] = \bar{F}^2 = \sum_i f_i^2,$$

$$p(|F|)d|F| = \frac{1}{\sqrt{2\pi \sum_i f_i^2}} \exp \left[ -\frac{|F|^2}{2 \sum_i f_i^2} \right] d|F|. \quad (5.7)$$

Notes

1. Because of the decrease of  $f_i$  with  $(\sin \theta)/\lambda$ , the variance  $\frac{1}{2} \sum_{i=1}^n f_i^2$  for noncentric structures depends on  $(\sin \theta)/\lambda$  and must be taken in shells of  $(\sin \theta)/\lambda$ . This problem does not exist if, instead of the structure factors  $\mathbf{F}(\mathbf{S})$ , normalized structure factors  $\mathbf{E}(\mathbf{S})$  are used (Chapter 6):

$$\mathbf{E}(\mathbf{S}) = \frac{\mathbf{F}(\mathbf{S})}{\left( \sum_i f_i^2 \right)^{1/2}}.$$

- In the calculation of normalized structure factors, the atoms are regarded as points and their scattering is independent of  $(\sin \theta)/\lambda$ .
2. The probability distribution of structure factor amplitudes is different for centric and noncentric crystal structures. If it is not immediately apparent whether a structure is centric, this difference is an easy check to solve the problem. This does not apply to proteins because they have a noncentric structure by nature. However, probability distributions of structure factor amplitudes or of the related intensities do play a role in protein X-ray crystallography as a diagnostic for detecting twinning in a crystal.



## 5.4. Crystal Twinning

Twinned crystals consist of intergrown lattices (Parsons, 2003; Yeates and Fam, 1999). If the lattices match in one or two dimensions, but not in all three dimensions, the diffraction spots occupy, in general, different positions and this can easily be detected. If the lattices have all three dimensions identical, the diffraction spots overlap and their intensity is the sum of the intensities contributed by the related lattices (merohedral twinning). In this case, the diffraction pattern looks quite the same as from an untwinned crystal, but the content of the asymmetric unit is different for the twin components. Moreover, the symmetry can be higher than that of the individual components (Figure 5.4). A structure determination based

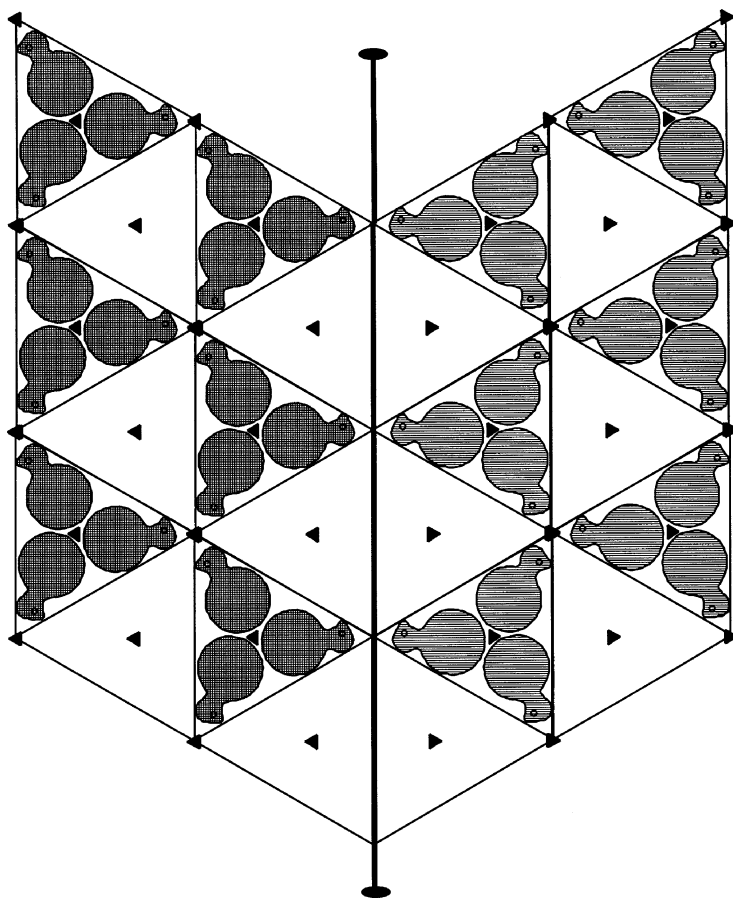


Figure 5.4. An example of merohedral twinning. A two-dimensional presentation of a structure with a 3-fold rotation axis. The light and dark gray molecules belong to two different structures, related by a twin axis, which is, here, a vertical 2-fold rotation axis. The consequence is that the diffraction pattern shows a pseudo-2-fold axis.

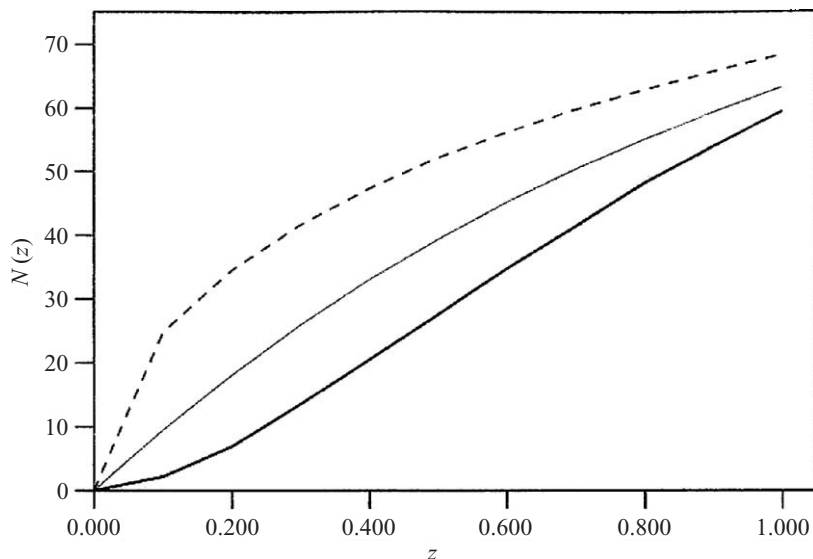


Figure 5.5.  $N(z)$  is plotted as a function of  $z$  in which  $z = I/\bar{I}$  and  $N(z)$  is the fraction of the reflections with intensities less than or equal to  $z$ . The dashed line shows the theoretical distribution for centric structures, the thin line shows that for noncentric structures. The black line gives the distribution as observed for the noncentric reflections of a twinned protein crystal. [Reproduced from *Acta Crystallographica* (2001) **D57**, 1776, with permission of the International Union of Crystallography.]

on the dataset from a merohedrally twinned crystal will fail at some stage in the process or result in a poor structure if the data are not detwinned. Because two or more twin components contribute to the intensity of the diffraction spots, the number of low-intensity spots will be less than for a nontwinned crystal. This is the basis for application of the probability distribution as a check for twinning. The probabilities are usually presented as cumulative intensity distribution curves. An example is given in Figure 5.5. This check for twinning should be standard procedure in every protein structure determination.

Several methods have been developed to untwin the data from a twinned crystal (Terwisscha van Scheltinga et al., 2001, 2003). A rough indication can be derived from the distance between the observed cumulative intensity distribution curve and the theoretical curve. It is normally assumed that only two components are present in the crystal (hemihedral twinning) and that these components are related by a 2-fold rotation axis (Figure 5.4). The consequence is that the X-ray diffraction pattern has an additional pseudo-2-fold axis and, therefore, shows a higher symmetry than it should have. However, this is only exactly true if the two components have equal volumes: the twinning fraction  $\alpha = 1/2$  (perfect twinning).  $\alpha$  is the twinning fraction for the smaller component and is usually  $<1/2$  and can even vary between crystals from the same batch. Each of the two components (1 and 2) contributes to a certain reflection. For a crystal exclusively composed of lattice 1,

this would be  $I_1$ , and for component 2, this would be  $I_2$ . The observed intensity for this reflection is  $I(\text{obs},1)$  and for its pseudo-symmetry-related mate  $I(\text{obs},2)$ :

$$I(\text{obs}, 1) = (1 - \alpha) I_1 + \alpha I_2,$$

$$I(\text{obs}, 2) = \alpha I_1 + (1 - \alpha) I_2.$$

From these equations, the intensity of the reflections for the pure components can be derived:

$$I_1 = \frac{I(\text{obs}, 1) - \alpha[I(\text{obs}, 1) + I(\text{obs}, 2)]}{(1 - 2\alpha)},$$

$$I_2 = \frac{I(\text{obs}, 2) - \alpha[I(\text{obs}, 1) + I(\text{obs}, 2)]}{(1 - 2\alpha)}.$$

The error in  $(1 - 2\alpha) \times I_{1 \text{ or } 2}$  is of the same order as for the observed intensities. Because  $0 < (1 - 2\alpha) < 1$ , the error in  $I_{1 \text{ or } 2}$  will be larger than the error in the observed intensities and will increase with increasing value of  $\alpha$ . For perfect twins ( $\alpha = 1/2$ ), the errors are infinite and detwinning is not possible in this way. A different method can then be chosen if a preliminary, not well-refined structure is available. For  $\alpha$  close to  $1/2$ , the intensities of reflections related by the twin axis are equal or nearly equal. They are “idealized to  $\alpha = 1/2$ ” by averaging. These intensities are composed of unequal contributions by each of the twin members. Their relative contributions can be easily obtained from the preliminary model. This allows detwinning and a more accurate structure can then be calculated (Yeates, 1997).

## Summary

In this chapter we have derived an important equation for the average intensity:

$$\overline{I(\text{abs}, \mathbf{S})} = \sum_i f_i^2.$$

We will need this result frequently. It has already been applied in this chapter in the derivation of distribution functions for the structure factors  $\mathbf{F}(\mathbf{S})$ , for their amplitudes  $|F(\mathbf{S})|$ , and for the intensities  $I(\mathbf{S})$ . The Gauss error function played a central role in the derivation of these distribution functions. In protein X-ray crystallography, the  $I(\mathbf{S})$  distribution is a useful tool for detecting twinning in crystals. Twinning appreciably hampers a crystal structure determination and it is essential to be aware of it. Several more or less accurate methods exist for determining the twin fraction  $\alpha$ . Once this is known, the observed intensities can be detwinned. This opens the door to a reliable structure determination.

# Chapter 6

## Special Forms of the Structure Factor

### 6.1. Introduction

In this chapter some special forms of the structure factor will be presented. It is not essential reading to understand the following chapters, but it does provide an introduction to and definitions of *unitary structure factors* and *normalized structure factors*. The chapter is put in this position in the book because the material can be easily understood using the results presented in the section on the Wilson plot (Section 5.2 of Chapter 5). However, if this is your first introduction to protein X-ray crystallography, you can skip this chapter for the time being.

### 6.2. The Unitary Structure Factor

For statistical studies of structure factor amplitude distributions, the normal form of the structure factor

$$\mathbf{F}(\mathbf{S}) = \sum_i f_j \exp[2\pi i(\mathbf{r}_j \cdot \mathbf{S})]$$

is not quite suitable.  $\mathbf{F}(\mathbf{S})$  decreases with  $|\mathbf{S}|$  because of the  $|\mathbf{S}|$  dependence of  $f_j$  and because of the temperature factor, and these effects are disturbing and must be eliminated. Therefore, the following modified structure factors have been introduced: the unitary structure factor  $\mathbf{U}(\mathbf{S})$  and the normalized structure factor  $\mathbf{E}(\mathbf{S})$ .

The unitary structure factor is defined as

$$\mathbf{U}(\mathbf{S}) = \frac{\mathbf{F}(\mathbf{S})_{pt}}{\sum_j Z_j} \quad (6.1)$$

where  $Z_j$  is the atomic number of atom  $j$  and  $\sum_j Z_j = F(0\ 0\ 0)$ .  $\mathbf{F}(\mathbf{S})_{\text{pt}}$  is the structure factor on an absolute scale with the assumption that the individual scatterers are point atoms. Their scattering is independent of  $|S|$  and is equal to the atomic number  $Z$  over the entire  $|S|$  region. This also excludes any thermal motion. When there is only one type of atom in the unit cell but equal thermal motion for all atoms,

$$\mathbf{F}(\mathbf{S})_{\text{pt}} = \frac{Z \times \exp[B(\sin^2 \theta / \lambda^2)]}{f} \times \mathbf{F}_{\text{obs}}, \quad (6.2)$$

where  $\mathbf{F}_{\text{obs}}$  is the normal structure factor on the absolute scale. For more than one type of atom but the same thermal parameter for all atoms,  $\mathbf{F}(\mathbf{S})_{\text{pt}}$  is taken as

$$\mathbf{F}(\mathbf{S})_{\text{pt}} = \frac{\sum_j Z_j \times \exp[B(\sin^2 \theta / \lambda^2)]}{\sum_j f_j} \times \mathbf{F}_{\text{obs}}; \quad (6.3)$$

combining Equations (6.1) and (6.3):

$$\mathbf{U}(\mathbf{S}) = \frac{\exp[B(\sin^2 \theta / \lambda^2)] \times \mathbf{F}_{\text{obs}}}{\sum_j f_j}. \quad (6.4)$$

The exponential term eliminates the effect of the temperature factor and the division by  $\sum_j f_j$  converts the atoms to point atoms.

Clearly,  $|U(\mathbf{S})| \leq 1$ . For proteins with a great many atoms scattered over the unit cell, the  $\mathbf{U}(\mathbf{S})$  values are rather small, and if probability distributions of structure factors are discussed, it is more convenient to use normalized structure factors. They have the advantage of being independent of scaling factors between sets of reflections.

### 6.3. The Normalized Structure Factor

The normalized structure factor is

$$\mathbf{E}(\mathbf{S}) = \frac{\mathbf{F}(\mathbf{S})}{\left(\sum_j f_j^2\right)^{1/2}}. \quad (6.5)$$

Neither  $f_j$  nor  $\mathbf{F}(\mathbf{S})$  includes the temperature factor.

$$\mathbf{F}(\mathbf{S}) = \mathbf{F}_{\text{obs}}(\mathbf{S}) \times \exp\left[B \frac{\sin^2 \theta}{\lambda^2}\right]$$

with  $\mathbf{F}_{\text{obs}}(\mathbf{S})$  including the temperature factor. Both  $\mathbf{F}(\mathbf{S})$  and  $\mathbf{F}_{\text{obs}}(\mathbf{S})$  are on an absolute scale here. According to Equation (5.2) of Chapter 5,

$$\overline{|F(\mathbf{S})|^2} = \sum_j f_j^2$$

and, therefore,

$$\overline{|E(\mathbf{S})|^2} = \frac{\overline{|F(\mathbf{S})|^2}}{\left(\sum_j f_j^2\right)} = \frac{\overline{|F(\mathbf{S})|^2}}{\overline{|F(\mathbf{S})|^2}} = 1.$$

Moreover, if  $\mathbf{E}(\mathbf{S})$  is written as

$$\mathbf{E}(\mathbf{S}) = \frac{\mathbf{F}(\mathbf{S})}{(|F(\mathbf{S})|^2)^{1/2}},$$

we see that the scale factor is not important because the numerator and the denominator are on the same scale.  $\mathbf{E}(\mathbf{S})$  can be obtained from the experimental data in the following way:

$$\mathbf{E}(\mathbf{S}) = \frac{\mathbf{F}(\mathbf{S})_{\text{exp}} \times \exp [B(\sin^2 \theta / \lambda^2)]}{(|F(\mathbf{S})_{\text{exp}}|^2)^{1/2}}. \quad (6.6)$$

Sometimes a complication exists with the use of  $\mathbf{E}(\mathbf{S})$  values in probability distributions of X-ray intensities. This is caused by the fact that for some groups of reflections, the  $E$ -values are higher than expected. An example will show this: Suppose that the cell has an  $n$ -fold symmetry axis along  $z$ . For the  $(0\ 0\ l)$  reflections, only the  $z$  coordinate counts and  $2\pi(hx + ky + lz) \rightarrow 2\pi lz$ . The cell has  $N$  atoms, but because of the symmetry, there are  $N/n$  groups, each of  $n$  symmetry-related atoms. The contribution by one group of symmetry related atoms to  $\mathbf{F}(00l)$  is  $n \times f_j \exp[2\pi i lz_j]$  instead of  $f_1 \exp[2\pi i lz_1] + f_2 \exp[2\pi i lz_2] + \dots + f_n \exp[2\pi i lz_n]$ . This contribution to the structure factor  $\mathbf{F}(00l)$  is equal to the contribution by a superatom with scattering factor  $nf_j$ . If we take the sum over all superatoms  $N/n$  and calculate the average  $\overline{|F(00l)|^2}$  over all reflections, we obtain

$$\overline{|F(00l)|^2} = \sum_{j=1}^{N/n} (nf_j)^2 = n \sum_{j=1}^N f_j^2$$

instead of  $f_1^2 + f_2^2 + \dots + f_N^2 = \sum_{j=1}^N f_j^2$ .  $\overline{|E|^2}$ , where the average is over all reflections, always remains 1. To allow statistical comparison of all reflections, the  $E$ -values for reflections belonging to the special groups with too high values of  $E$  are reduced by a factor  $\sqrt{\varepsilon}$ .  $\varepsilon$  is easily found by a procedure proposed by Stewart and Karle (1976). The more general form of  $\mathbf{E}(\mathbf{S})$  is

$$\mathbf{E}(\mathbf{S}) = \frac{\mathbf{F}(\mathbf{S})_{\text{exp}} \times \exp [B(\sin^2 \theta / \lambda^2)]}{(\varepsilon \times |F(\mathbf{S})_{\text{exp}}|^2)^{1/2}}. \quad (6.7)$$

## Summary

In this chapter two alternative expressions for the structure factor have been introduced:

- The unitary structure factor:

$$\mathbf{U}(\mathbf{S}) = \frac{\mathbf{F}(\mathbf{S})_{\text{exp}} \times \exp[B \sin^2 \theta / \lambda^2]}{\sum_j f_j}.$$

- The normalized structure factor:

$$\mathbf{E}(\mathbf{S}) = \frac{\mathbf{F}(\mathbf{S})_{\text{exp}} \times \exp[B \sin^2 \theta / \lambda^2]}{\left(\varepsilon \times |F(\mathbf{S})_{\text{exp}}|^2\right)^{1/2}}$$

They are more convenient in statistical studies of structure factor amplitude distributions than the common form  $\mathbf{F}(\mathbf{S})$  of the structure factor.

# Chapter 7

## The Solution of the Phase Problem by the Isomorphous Replacement Method

### 7.1. Introduction

As we have seen in Chapter 4, the electron density in a crystal can be obtained by calculating the Fourier summation:

$$\rho(x\ y\ z) = \frac{1}{V} \sum_{hkl} |F(h\ k\ l)| \exp[-2\pi i(hx + ky + lz) + ia(h\ k\ l)] \quad (7.1)$$

in which  $|F(h\ k\ l)|$  is the structure factor amplitude of reflection  $(h\ k\ l)$ , including the temperature factor, and  $\alpha(h\ k\ l)$  is the phase angle.  $x, y$ , and  $z$  are coordinates in the unit cell. From the diffraction pattern, the values of  $I(h\ k\ l)$  are obtained after applying the correction factors  $L, P$ , and  $A$ . Because  $I(h\ k\ l) = |F(h\ k\ l)|^2$ , the amplitudes  $|F(h\ k\ l)|$  can be found. Unfortunately, no information is available on the phase angles. In principle, five techniques exist for solving the phase problem in protein X-ray crystallography:

1. The isomorphous replacement method, which requires the attachment of heavy atoms (atoms with high atomic number) to the protein molecules in the crystal.
2. The multiple wavelength anomalous diffraction method. It depends on the presence of sufficiently strong anomalously scattering atoms in the protein structure itself. Anomalous scattering occurs if the electrons in an atom cannot be regarded as free electrons.
3. The single-wavelength anomalous diffraction method
4. The molecular replacement method, for which the similarity of the unknown structure to an already known structure is a prerequisite.
5. Direct methods, the methods of the future, still in a stage of development toward practical application for proteins.



Molecular replacement, which will be discussed in Chapter 10, is the most rapid method for determining a protein structure. However, it requires the availability of a known model structure (e.g., of a homologous protein). If this does not exist, isomorphous replacement or multiple- or single-wavelength anomalous diffraction must be applied. They are the most general methods for determining protein phase angles and are used if nothing is, as yet, known about the three-dimensional structure of the protein.

The multiple- and single-wavelength diffraction methods do not necessarily depend on the attachment of a heavy-atom-containing reagent to the protein, but they do require the presence of an anomalously scattering atom and this can be a heavy atom inherent to the protein. Data collection is—in general—with synchrotron radiation. These methods for phase determination will be discussed in Chapter 9.

We will first discuss the isomorphous replacement method. The initial step in this method requires the attachment of heavy atoms and, subsequently, the determination of the coordinates of these heavy atoms in the unit cell. A useful role in this process is played by the Patterson function. Therefore, we will begin by discussing this function and its physical interpretation.

## 7.2. The Patterson Function

The Patterson function  $P(\mathbf{u})$  or  $P(uvw)$  is a Fourier summation with intensities as coefficients and without phase angles, or, rather, with all phase angles equal to zero

$$P(uvw) = \frac{1}{V} \sum_{hkl} |F(hkl)|^2 \cos[2\pi(hu + kv + lw)]; \quad (7.2)$$

or, shorter,

$$P(\mathbf{u}) = \frac{1}{V} \sum_{\mathbf{S}} |F(\mathbf{S})|^2 \cos[2\pi\mathbf{u} \cdot \mathbf{S}] \quad (7.3)$$

$u$ ,  $v$ , and  $w$  are relative coordinates in the unit cell. To avoid confusion with the coordinates  $x$ ,  $y$ , and  $z$  in the real cell, we use  $u$ ,  $v$ , and  $w$  in the Patterson cell, which, however, has dimensions identical to the real cell. Note that the coefficients in the summations (7.2) and (7.3) are  $|F(hkl)|^2$ , not  $|F(hkl)|$  as in Equation (7.1). Because all phase angles are zero in the Patterson function, it can be calculated without any previous knowledge of the structure.

Further, it can be shown that the Patterson function  $P(\mathbf{u})$  can alternatively be written as

$$P(\mathbf{u}) = \int_{\mathbf{r}_1} \rho(\mathbf{r}_1) \times \rho(\mathbf{r}_1 + \mathbf{u}) d\mathbf{v}. \quad (7.4)$$

The integration is for  $\mathbf{r}_1$  over all positions in the real unit cell. Assuming for the moment that this is true, we can use this form of  $P(\mathbf{u})$  to understand its physical

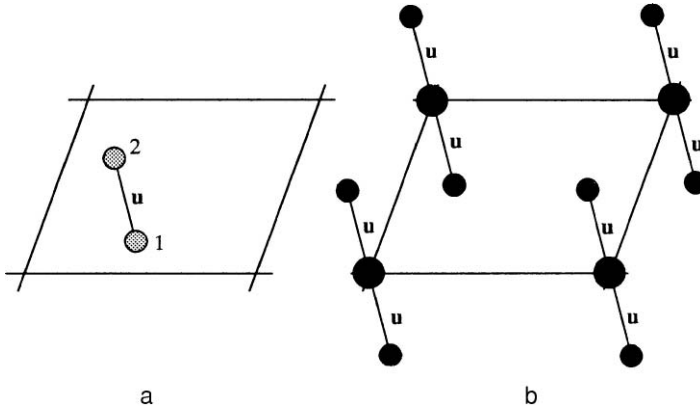


Figure 7.1. (a) A two-dimensional unit cell with only two atoms. (b) The corresponding Patterson cell.

interpretation: Move through the *real unit cell* with a vector  $\mathbf{u}$ , multiply in every position of  $\mathbf{u}$  the electron density  $\rho$  at the beginning of  $\mathbf{u}$  (in position  $\mathbf{r}_1$ ) with the electron density at the end of vector  $\mathbf{u}$  (in position  $\mathbf{r}_1 + \mathbf{u}$ ), and take the integral of these values. Only if nonzero electron density is present at both the beginning and the end of  $\mathbf{u}$  will the result of the multiplication be nonzero. What this leads to can best be understood from Figure 7.1, in which the real cell contains only two atoms.

$\rho(\mathbf{r}_1) \times \rho(\mathbf{r}_1 + \mathbf{u})$  has a significant value only if  $\mathbf{u}$  starts in atom 1 and ends in atom 2, or the other way around. In the corresponding Patterson cell, the vector  $\mathbf{u}$  starts in the origin of the cell and points either in one direction (atom 1 to atom 2) or in the opposite direction (atom 2 to atom 1). A peak in a Patterson map at position  $\mathbf{u}$  (or  $uvw$ ), therefore, means that in the real cell atoms occur at a certain position  $x, y$ , and  $z$ , and at the position  $x + u, y + v$ , and  $z + w$ , or  $x - u, y - v$ , and  $z - w$ . So far, the real atomic positions are not known, but the vectorial distance between them is clear from the Patterson map.

In simple structures with a limited number of atoms, the atomic positions can be derived fairly straightforwardly from the Patterson map. However, this is impossible for complicated structures, like proteins. If a real unit cell contains  $N$  atoms, the corresponding Patterson map will show  $N^2$  peaks, because one can draw  $N$  vectors from each atom. However,  $N$  vectors of the total number of  $N^2$  vectors will have a length 0, because they go from an atom to the same atom. Therefore, the highest peak in a Patterson map is situated in the origin of the cell (Figure 7.2). The number of nonorigin peaks is  $N^2 - N = N(N - 1)$ . If the unit cell of a protein crystal contains 5000 nonhydrogen atoms, then the number of Patterson peaks would be  $25 \times 10^6$ . It is clear that such a Patterson map is uninterpretable. If, however, a limited number of heavy atoms in the large unit cell must be located, the Patterson function is extremely useful, as can be seen in Figure 7.4c.

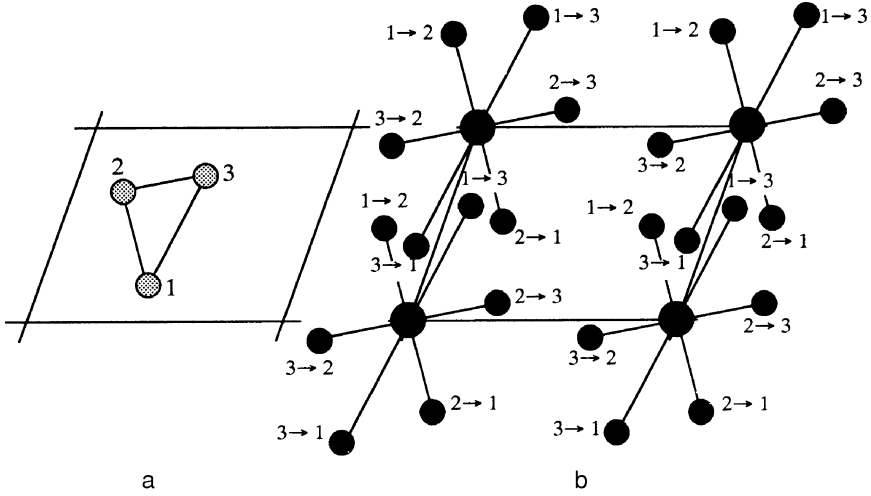


Figure 7.2. (a) A two-dimensional unit cell with three atoms. (b) The corresponding Patterson map. Note the large increase in the number of Patterson peaks compared with Figure 7.1. The total number of peaks is  $N^2$ , but the  $N$  self-peaks overlap at the origin and, therefore,  $N(N - 1)$  nonorigin peaks are found in a Patterson map. Because of the centrosymmetry in the map, the number of unique peaks is  $[N(N - 1)]/2$ ; in this figure,  $1 \rightarrow 2$ ,  $1 \rightarrow 3$ , and  $2 \rightarrow 3$  are unique peaks.

We have presented two different expressions for the Patterson function: Equation (7.2) or (7.3), which tells us how to calculate it, and Equation (7.4), which facilitates understanding of the physical meaning of the Patterson function.

We will now prove that

$$P(\mathbf{u}) = \int_{\mathbf{r}_1} \rho(\mathbf{r}_1) \times \rho(\mathbf{r}_1 + \mathbf{u}) dv = \frac{1}{V} \sum_S |F(\mathbf{S})|^2 \cos[2\pi \mathbf{u} \cdot \mathbf{S}]; \quad (7.5)$$

and start with

$$\rho(\mathbf{r}_1) = \frac{1}{V} \sum_S |F(\mathbf{S})| \exp[-2\pi i \mathbf{r}_1 \cdot \mathbf{S} + i\alpha(\mathbf{S})], \quad (7.6)$$

$$\rho(\mathbf{r}_2) = \rho(\mathbf{r}_1 + \mathbf{u}) = \frac{1}{V} \sum_{S'} |F(\mathbf{S}')| \exp[-2\pi i (\mathbf{r}_1 + \mathbf{u}) \cdot \mathbf{S}' + i\alpha(\mathbf{S}')]. \quad (7.7)$$

In Equation (7.7), for  $\rho(\mathbf{r}_2)$  we use  $\mathbf{S}'$ , just to distinguish it from  $\mathbf{S}$  in the equation for  $\rho(\mathbf{r}_1)$ .

$$\begin{aligned} \rho(\mathbf{r}_1) \times \rho(\mathbf{r}_1 + \mathbf{u}) &= \frac{1}{V^2} \sum_S \sum_{S'} |F(\mathbf{S})| |F(\mathbf{S}')| \exp[-2\pi i \{\mathbf{r}_1 \cdot (\mathbf{S} + \mathbf{S}') \\ &\quad + \mathbf{u} \cdot \mathbf{S}'\} + i\alpha(\mathbf{S}) + i\alpha(\mathbf{S}')]. \end{aligned} \quad (7.8)$$

In Section 4.11 of Chapter 4 we have seen that  $|F(hkl)| = |F(\bar{h}\bar{k}\bar{l})|$  or  $|F(\mathbf{S})| = |F(-\mathbf{S})|$  and also that  $\alpha(hkl) = -\alpha(\bar{h}\bar{k}\bar{l})$  or  $\alpha(\mathbf{S}) = -\alpha(-\mathbf{S})$ . Therefore, in

Equation (7.8), the coefficients  $|F(\mathbf{S})||F(\mathbf{S}')|$  are equal for  $\mathbf{S}$  and  $-\mathbf{S}$ , as well as for  $\mathbf{S}'$  and  $-\mathbf{S}'$ , whereas the exponential terms have just the opposite sign. This simplifies Equation (7.8) to a summation of cos terms:

$$\sigma(\mathbf{r}_1) \times \sigma(\mathbf{r}_1 + \mathbf{u}) = \frac{1}{V^2} \sum_{\mathbf{S}} \sum_{\mathbf{S}'} |F(\mathbf{S})||F(\mathbf{S}')| \cos[2\pi\{\mathbf{r}_1 \cdot (\mathbf{S} + \mathbf{S}') + \mathbf{u} \cdot \mathbf{S}'\} - \alpha(\mathbf{S}) - \alpha(\mathbf{S}')]. \quad (7.9)$$

The next step is an integration with  $\mathbf{r}_1$  over the entire unit cell. In other words,  $\mathbf{r}_1$  assumes different lengths and different directions:

$$\begin{aligned} \rho(\mathbf{u}) &= \int_{\mathbf{r}_1} \rho(\mathbf{r}_1) \times \rho(\mathbf{r}_1 + \mathbf{u}) d\mathbf{v} \\ &= \frac{1}{V^2} \sum_{\mathbf{S}} \sum_{\mathbf{S}'} |F(\mathbf{S})||F(\mathbf{S}')| \int_{\mathbf{r}_1} \cos[2\pi\{\mathbf{r}_1 \cdot (\mathbf{S} + \mathbf{S}') + \mathbf{u} \cdot \mathbf{S}'\} - \alpha(\mathbf{S}) - \alpha(\mathbf{S}')] d\mathbf{v}. \end{aligned} \quad (7.10)$$

The integration with  $\mathbf{r}_1$  over the entire unit cell means that the constant vector  $\mathbf{u}$  must move through the unit cell and has its beginning in every position  $\mathbf{r}_1$  of the unit cell. Because  $\mathbf{r}_1$  can have different lengths and many different directions, the angles

$$2\pi\{\mathbf{r}_1 \cdot (\mathbf{S} + \mathbf{S}') + \mathbf{u} \cdot \mathbf{S}'\} - \alpha(\mathbf{S}) - \alpha(\mathbf{S}')$$

can assume all values between 0 and  $2\pi$  for  $\mathbf{S} + \mathbf{S}' \neq 0$ . Therefore, the integration

$$\int_{\mathbf{r}_1} \cos[2\pi\{\mathbf{r}_1 \cdot (\mathbf{S} + \mathbf{S}') + \mathbf{u} \cdot \mathbf{S}'\} - \alpha(\mathbf{S}) - \alpha(\mathbf{S}')] d\mathbf{v}$$

will, in general, lead to zero. However, in the special case when  $\mathbf{S} + \mathbf{S}' = 0$  or  $\mathbf{S}' = -\mathbf{S}$  and  $\alpha(\mathbf{S}') = -\alpha(-\mathbf{S}') = -\alpha(\mathbf{S})$ , a nonzero value will result:

$$P(\mathbf{u}) = \frac{1}{V^2} \sum_{\mathbf{S}} |F(\mathbf{S})|^2 \cos[2\pi\mathbf{u} \cdot \mathbf{S}] \int_{\mathbf{r}_1} d\mathbf{v} = \frac{1}{V} \sum_{\mathbf{S}} |F(\mathbf{S})|^2 \cos[2\pi\mathbf{u} \cdot \mathbf{S}] \quad (7.11)$$

because  $\int_{\mathbf{r}_1} d\mathbf{v} = V$ .

The Patterson function has the following properties:

1. The Patterson map has peaks at end points of vectors  $\mathbf{u}$  equal to vectors *between* atoms in the real cell.
2. For every pair of atoms in the real cell, there exists a unique peak in the Patterson map.
3. A Patterson map is always centrosymmetric. Therefore,  $P(\mathbf{u})$  [Equation (7.11)] can also be written in exponential form:

$$P(\mathbf{u}) = \frac{1}{V} \sum_{\mathbf{S}} |F(\mathbf{S})|^2 \exp[2\pi\mathbf{u} \cdot \mathbf{S}],$$

or as

$$P(\mathbf{u}) = \frac{1}{V} \sum_{\mathbf{S}} |F(\mathbf{S})|^2 \exp[-2\pi\mathbf{u} \cdot \mathbf{S}].$$

This is allowed because

$$\exp[2\pi i \mathbf{u} \cdot \mathbf{S}] = \cos[2\pi\mathbf{u} \cdot \mathbf{S}] + i \sin[2\pi\mathbf{u} \cdot \mathbf{S}]$$

and

$$\exp[-2\pi i \mathbf{u} \cdot \mathbf{S}] = \cos[2\pi\mathbf{u} \cdot \mathbf{S}] - i \sin[2\pi\mathbf{u} \cdot \mathbf{S}].$$

and the sin term disappears because of the centrosymmetry.

4. Screw axes in a real cell become normal axes in a Patterson cell. We will prove this for a 2-fold screw axis along  $y$ .

In Section 4.12.2 of Chapter 4, we showed that for a 2-fold screw axis along  $y$ , the diffraction pattern has a 2-fold axis along  $y$ :

$$I(hkl) = I(\bar{h}k\bar{l}).$$

We must now prove that  $P(uvw) = P(\bar{u}v\bar{w})$ .

$$P(uvw) = \frac{1}{V} \sum_{hkl} |F(hkl)|^2 \cos[2\pi(hu + kv + lw)].$$

This is exactly equal to

$$P(uvw) = \frac{1}{V} \sum_{hkl} |F(\bar{h}k\bar{l})|^2 \cos[2\pi(\bar{h}u + kv + \bar{l}w)]$$

because the summation is still over all reflections  $hkl$ . We know already that  $I(\bar{h}k\bar{l}) = I(hkl)$  or  $|F(\bar{h}k\bar{l})|^2 = |F(hkl)|^2$ . Therefore, we can write  $P(uvw)$  as

$$P(uvw) = \frac{1}{V} \sum_{hkl} |F(hkl)|^2 \cos[2\pi(h\bar{u} + kv + l\bar{w})]$$

and this is precisely  $P(\bar{u}v\bar{w})$ . This proves that

$$P(uvw) = P(\bar{u}v\bar{w}).$$

5. Symmetry elements can cause a concentration of peaks in certain lines or planes: "Harker lines" or "Harker planes." Examples are given in Figures 7.3 and 7.4.
6. The Patterson function

$$P(\mathbf{u}) = \int_{\mathbf{r}_1} \rho(\mathbf{r}_1) \times \rho(\mathbf{r}_1 + \mathbf{u}) dv \quad (7.12)$$

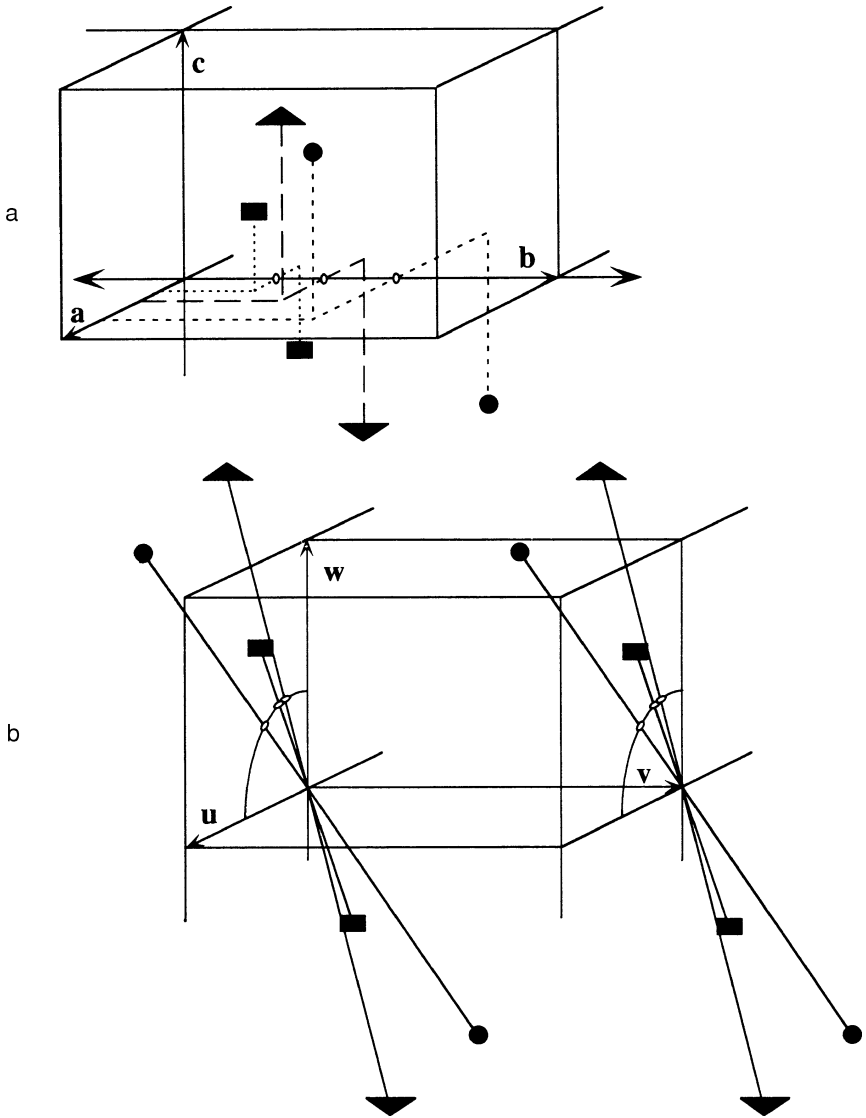
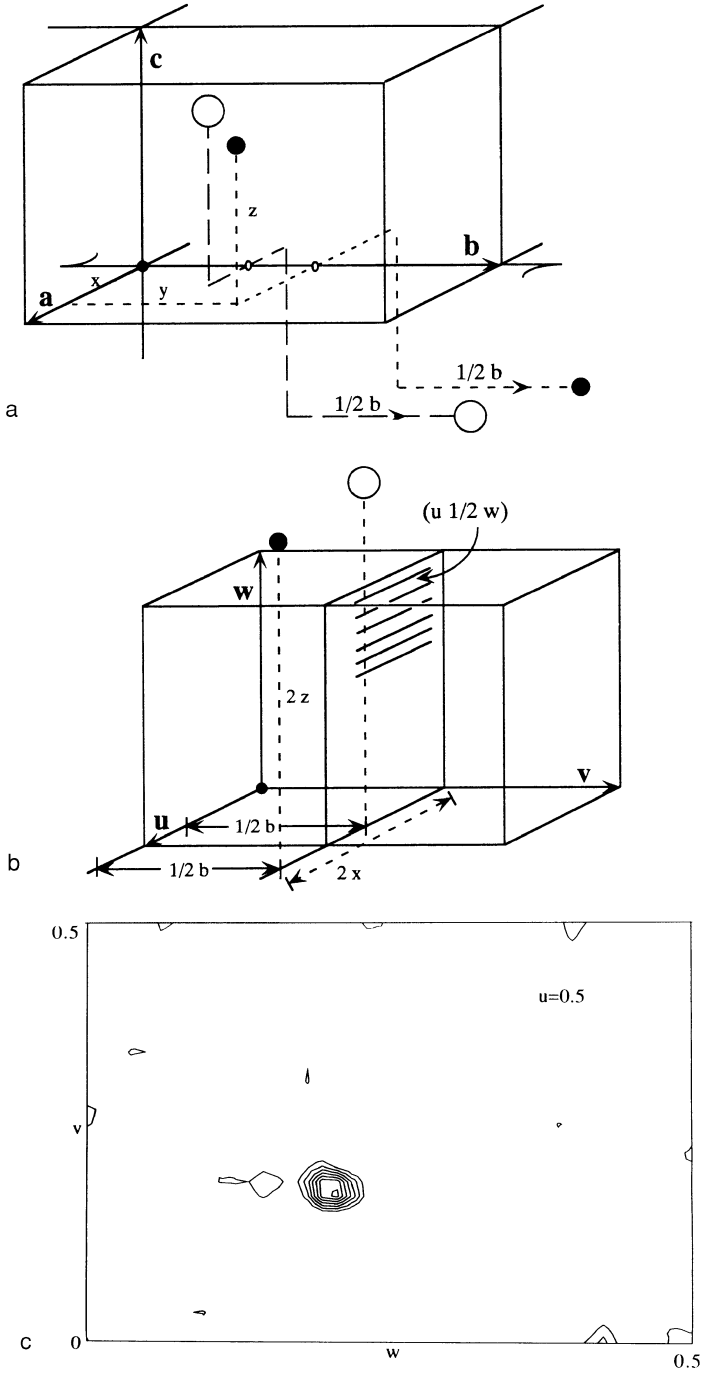


Figure 7.3. (a) A unit cell with a 2-fold axis along  $y$ ; (b) the corresponding Patterson cell with Harker peaks in the  $(u\ 0\ w)$  plane.

is the convolution of the structure and its inverse. The mathematical definition of the convolution  $C(x)$  of two real, periodic functions  $f(h)$  and  $g(h)$  is

$$C(x) = \int_{\eta=0}^1 f(\eta) g(x - \eta) d\eta. \quad (7.13)$$



The Patterson function can be put into this form as follows: Replacing  $\mathbf{r}_1 + \mathbf{u}$  by  $\mathbf{r}''$  in Equation (7.12) gives

$$P(\mathbf{u}) = \int_{\mathbf{r}''} \rho(\mathbf{r}'' - \mathbf{u}) \rho(\mathbf{r}'') d\mathbf{v}. \quad (7.14)$$

With  $\rho(\mathbf{r}'' - \mathbf{u}) = \rho_{\text{inv}}(\mathbf{u} - \mathbf{r}'')$ , where  $\rho_{\text{inv}}(\mathbf{u} - \mathbf{r}'')$  is the electron density distribution of the inverse structure, Equation (7.14) transforms into<sup>1</sup>

$$P(\mathbf{u}) = \int_{\mathbf{r}''} \rho(\mathbf{r}'') \rho_{\text{inv}}(\mathbf{u} - \mathbf{r}'') d\mathbf{v}, \quad (7.15)$$

which is of the same form as Equation (7.13) and this proves property 6. A general property of the Fourier transform of a convolution is the following: If  $F(h)$  is the transform of  $f(\eta)$  in Equation (7.13) and  $G(h)$  is the transform of  $g(\eta)$ , then the product  $F(h)G(h)$  is the Fourier transform of  $C(x)$ . Application to Equation (7.15) gives the following: The product of the transform of  $\rho(\mathbf{r}'')$  [which is  $\mathbf{F}(\mathbf{S})$ ] and the transform of  $\rho_{\text{inv}}(\mathbf{r}'')$  [which is  $\mathbf{F}^*(\mathbf{S})$ ] is equal to the transform of  $P(\mathbf{u})$  and, therefore, the transform of  $P(\mathbf{u})$  is equal to  $\mathbf{F}(\mathbf{S})\mathbf{F}^*(\mathbf{S}) = |\mathbf{F}(\mathbf{S})|^2$ ;  $\mathbf{F}^*(\mathbf{S})$  is the conjugate complex of  $\mathbf{F}(\mathbf{S})$ ; if  $\mathbf{F} = |F| \exp[i\alpha]$ , then its conjugate complex is  $\mathbf{F}^* = |F| \exp[-i\alpha]$ .

7. In locating Patterson peaks of heavy atoms in the isomorphous replacement method, it is useful to realize that the height of a peak is proportional to the product of the atomic numbers of the atoms that are responsible for the peak.

---

### Convolution Explained

The mathematical definition of a convolution is

$$C(x) = \int_{\eta=0}^1 f(\eta) g(x - \eta) d\eta;$$

---

<sup>1</sup>The electron density of an inverse structure at  $\mathbf{r}$  is equal to the electron density in the original structure at  $-\mathbf{r}$ :  $\rho_{\text{inv}}(\mathbf{r}) = \rho_{\text{orig}}(-\mathbf{r})$  and  $\mathbf{F}_{\text{inv}}(\mathbf{S}) = \mathbf{F}_{\text{orig}}^*(\mathbf{S})$ , where  $\mathbf{F}_{\text{orig}}^*(\mathbf{S})$  is the conjugate complex of  $\mathbf{F}_{\text{orig}}(\mathbf{S})$ .

---

←

Figure 7.4. (a) A unit cell with a 2-fold screw axis along  $y$ ; (b) In the  $(u^{1/2}w)$  plane of the corresponding Patterson cell, a concentration of peaks is found; only two Harker peaks are indicated; (c) A realistic example showing the Harker section at  $u = 0.5$  with  $0 < v < 0.5$  and  $0 < w < 0.5$ . The high-density peak indicates the end of the vector between the mercury atoms from a mercury-containing reagent attached to the protein hevamine. The crystals belong to space group  $P2_12_12_1$ . (Courtesy of Anke Terwisscha van Scheltinga.)



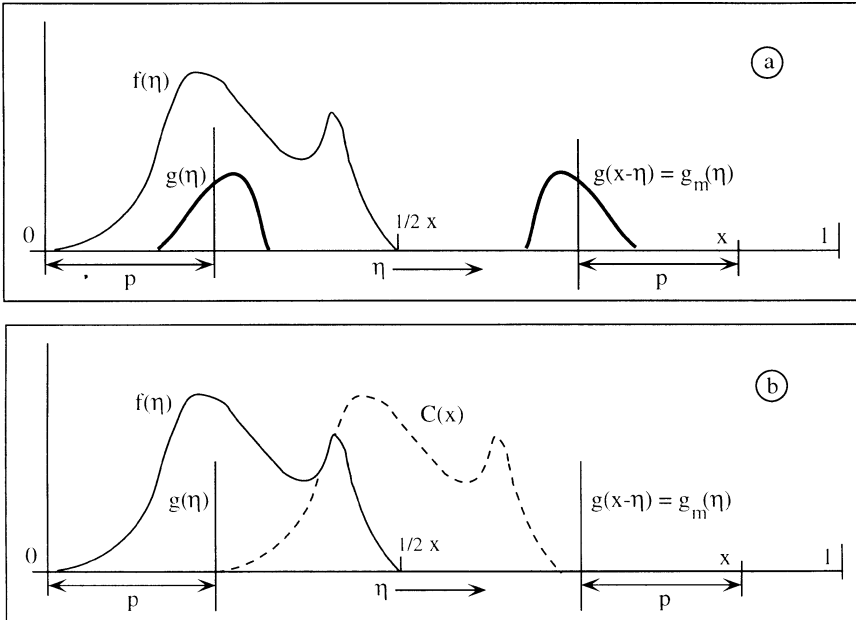


Figure 7.5. The convolution  $C(x) = \int_{\eta=0}^1 f(\eta)g(x-\eta)d\eta$  of two functions  $f(\eta)$  and  $g(x - \eta)$ . The moving variable for a fixed value of  $x$  is  $\eta$ . In (a), in addition to the functions  $f(\eta)$  and  $g(\eta)$ , also  $g(x - \eta)$  is drawn for an arbitrarily chosen value of  $x$ .  $g(x - \eta)$  is obtained from  $g(\eta)$  by taking its mirror image with respect to the position  $1/2 \times x$ ; it is called  $g_m(\eta)$ . In (a),  $C(x)$  is not drawn, but it is in (b). In (b),  $g(\eta)$  is a delta function. The convolution  $C(x)$  of this delta function with  $f(\eta)$  is the dashed line.  $C(x)$  is here a true representation of  $f(\eta)$  because  $g(\eta)$  is a delta function. The less sharp  $g(\eta)$  is, the more blurred  $C(x)$  will be.

$f$  and  $g$  are both functions of  $x$ . The mathematical process can be illustrated with Figure 7.5. A fixed value of  $x$  is chosen and the variable is  $\eta$ , which moves from  $\eta = 0$  to  $\eta = 1$ . In Figure 7.5, arbitrary functions  $f(\eta)$  and  $g(\eta)$  are drawn. The convolution does not require  $g(\eta)$ , but it does require  $g(x - \eta)$ . For the arbitrarily chosen value of  $x$ , the function  $g(x - \eta)$  is found on the right in Figure 7.5a as the mirror image of  $g(\eta)$  with respect to the position  $1/2 \times x$ . This new function differs from  $g$ , and, therefore, it will be called  $g_m(\eta)$ . In the convolution process,  $f(\eta)$  and  $g_m(\eta)$  must be multiplied for every value of  $\eta$  between 0 and 1. Summation of the products gives the value of  $C(x)$  for the chosen value of  $x$ . It is clear for the chosen value of  $x$  in Figure 7.5a that the result will be zero because  $f(\eta)$  and  $g_m(\eta)$  do not overlap. However, if  $x$  moves to a sufficiently small value, the two functions do overlap and the resulting  $C(x)$  will be different from zero.

A special situation exists if  $g(\eta)$  is a needle-sharp function, a delta function (Section 4.10 of Chater 4) (Figure 7.5b). If  $x$  moves to smaller values, the  $g_m(\eta)$

needle starts to scan  $f(\eta)$  and the result will be an undistorted image of  $f(\eta)$  but displaced over  $p$  to the right of the original  $f(\eta)$ . If the needle is blunt instead of sharp, the image of  $f(\eta)$  will be blurred. This is comparable to the scanning in the atomic force microscope, in which an ideally sharp probe gives an undistorted image of the specimen. With a blunt probe, the image is the convolution of the probe shape and the object. Another example is the electron density of atoms with thermal motion. The density is the convolution of the fixed-atom structure and the function describing the thermal motion. Convolution is illustrated here with rather simple functions  $f$  and  $g$ , but the principle is the same for more complicated functions.

A convolution is often represented by the symbol “\*” which is on the line:  $C(x) = f(\eta)*g(\eta)$ . The convolution symbol should not be mistaken for the symbol indicating the conjugate complex “\*”; this is above the line.

---

### 7.3. The Isomorphous Replacement Method

In the isomorphous replacement method, the X-ray diffraction pattern of the native protein crystal is compared with that of a crystal of the same type but containing, in addition, at least one heavy atom. The method was originally used in the structure determination of small molecules and, for the first time, successfully applied to proteins by Perutz<sup>2</sup> in his structure determination of hemoglobin. For a perfect isomorphism, the conformation of the protein, the position and orientation of its molecules, as well as the unit cell parameters in the native and in the derivative crystals must be exactly the same. The intensity differences between the native and the other patterns are then exclusively due to the attached heavy atoms. For an example, see Figure 7.6. From these differences, the positions of the heavy atoms can be derived either manually or by an automatic Patterson search procedure—for instance, SIR 2002 (Burla et al., 2004) or a direct method—for instance, SHELXD (Schneider and Sheldrick, 2002), SnB (Weeks and Miller, 1999), and ACORN (Foadi et al., 2000); this is the starting point for the determination of the protein phase angles. A perfect isomorphism hardly ever occurs. Errors due to nonisomorphism are usually more serious than errors in the X-ray data. However, a modest change in the protein structure is not a great obstacle. Nonisomorphism often presents itself as a change in the cell dimensions. In a quick data collection, one can determine whether the heavy atom has attached itself to the protein, by comparing the intensities of the reflections with those of the native crystal as well as whether this has seriously affected the cell dimensions and the quality of the

---

<sup>2</sup> Max Ferdinand Perutz (1914–2002) was one of the first famous pioneers in structural biology. He was born in Austria, studied chemistry, and moved in 1936 to Cambridge (UK) where he started his work on proteins, especially the X-ray structure determination of horse hemoglobin. Despite interruptions due to World War II and the huge difficulties of the problem, he tenaciously held on. His application of the isomorphous replacement method meant a tremendous breakthrough in structural biology.

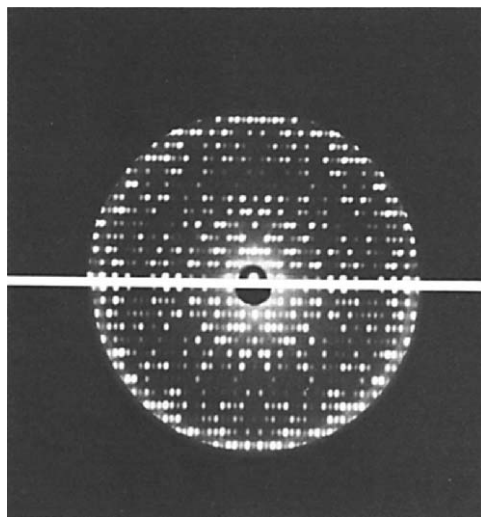


Figure 7.6. A comparison of the diffraction photographs of the same reciprocal lattice plane for a native papain crystal and a heavy atom derivative in which one mercury atom was attached to each protein molecule. Appreciable differences in intensity between corresponding diffraction spots can be seen.

diffraction pattern. A change in the cell dimensions of  $d_{\min}/4$ , where  $d_{\min}$  is the resolution limit, is tolerable. In principle, nonisomorphism can occur without expressing itself in the cell dimensions (for instance, if a slight rotation of the protein molecules has occurred as a consequence of the heavy atom binding). This will later result in a poor refinement of the heavy atom parameters.

The isomorphous replacement method requires the following steps:

1. Preparation of at least one, but preferably a few heavy-atom-containing derivatives of the protein in the crystalline state. A first check for isomorphism is measuring the cell dimensions.
2. X-ray intensity data must be collected for crystals of the native protein as well as for crystals of the derivatives.
3. Application of the Patterson function for the determination of the heavy atom coordinates.
4. Refinement of the heavy atom parameters and calculation of the protein phase angles.
5. Calculation of the electron density of the protein.

### 7.3.1. The Attachment of Heavy Atoms

The search for heavy atom derivatives is still basically an empirical method and very often dozens of reagents are tried before a few suitable ones are found. The preferred method is by soaking the protein crystal in a solution of the reagent. The

composition of this solution is identical to the mother liquor, except for the added reagent, often with a slight increase of precipitant concentration. Cocrystallization is not commonly used, because of the risk that crystals will not grow or grow nonisomorphously. However, for covalently attached reagents, cocrystallization is sometimes an advantage because of the better control over the stoichiometry and the ability to prevent excess binding.

The soaking procedure depends on the existence of relatively wide pores in the crystal, wide enough to allow the reagent to diffuse into the crystal and to reach the reactive sites on the surface of all protein molecules in the crystal. An extremely high excess of reagent is commonly used, as the following example shows.

Let the protein have a molecular weight of 40,000 and the crystal a size of  $0.5 \times 0.5 \times 0.5 \text{ mm}^3$ . This crystal contains  $\sim 2 \text{ nmol}$  of protein. If the crystal is soaked in 1 ml of solution with a reagent concentration of 10 mM, the amount of reagent in the solution is  $10^4 \text{ nmol}$ , an enormous excess in molarity of reagent with respect to protein. However, the position of the equilibrium is not determined by the total amount of the reagent and the protein, but by the concentrations of the reagent and the protein and the value of the equilibrium constant  $K$ . For the reaction, reagent + protein  $\rightarrow$  derivative,

$$K = \frac{[\text{derivative}]}{[\text{reagent}] \times [\text{protein}]}$$

The crystallographer is interested in the occupancy of the binding site:

$$\text{occupancy} = \frac{[\text{derivative}]}{[\text{derivative}] + [\text{protein}]} = \frac{K \times [\text{reagent}]}{\{K \times [\text{reagent}]\} + 1}$$

The occupancy depends only on  $K \times [\text{reagent}]$  and is close to 100% for  $K \times [\text{reagent}] > 10^2$ . If the binding is not very strong and the occupancy of the protein-binding site does not reach 100%, it is tempting to increase the reagent concentration. However, then the danger exists that the reagent will react with more sites and the chances of nonisomorphism or even crystal degradation are high.

The soaking time varies between hours and months. The minimum time required to reach the equilibrium of the reaction is determined by a number of factors. The diffusion of the reagent through the pores in the crystal is the first important step, and depends on the relative size of the pores and the reagent. Second, a slight conformational change in the protein might be required for a snug fitting of the reagent into its binding site. Finally, there is the chemical reaction itself. Sometimes it is an advantage to use a short soaking time e.g., if the protein molecule presents a great many binding sites to the reagent. If some of them are slow binding sites and others are fast, then if the crystal is soaked for a short time, only the fast binding sites will react and the chances of maintaining the quality of the crystal are higher. In some cases, it is better to soak the crystal for a long time (e.g., if the reagent or the protein changes while standing and a suitable reagent or a reactive site on the protein develops in the course of weeks or months). For instance, Pt compounds can gradually change their ligands. If  $\text{K}_2\text{PtCl}_4$  is kept in an ammonium sulfate solution,  $[\text{PtCl}_4]^{2-}$  can exchange  $\text{Cl}^-$  for  $\text{NH}_3$ , and  $[\text{Pt}(\text{NH}_3)\text{Cl}_3]^-$  or  $[\text{Pt}(\text{NH}_3)_2\text{Cl}_2]$  or even

$[\text{Pt}(\text{NH}_3)_4]^{2+}$ , which has an opposite charge, can be formed with a concomitant change in reactivity. Protein modification with time might be caused by a chemical reaction in the protein, such as deamidation of asparagine or glutamine residues or oxidation of sulfhydryl groups. This changes the overall charge of the protein and might influence its affinity for charged reagents. The solution can also change slowly (e.g., if an ammonium sulfate solution loses ammonia).

A more complete overview of the screening for phasing atoms is given by Boggon and Shapiro (2000) and Garman and Murray (2003).

### 7.3.2. Site of Attachment of Heavy Atoms

Although the search for a suitable heavy atom reagent is an empirical process, one should employ all available chemical and biochemical properties of the protein. If the protein contains a free sulfhydryl group, it is obvious that mercury-containing compounds should be tried. Even if sulfhydryl groups are absent, mercurials still have a chance. Histidine residues are frequently found as ligands to heavy atoms, but the pH should not be too low because it is the neutral histidine side chain that acts as the ligand. The sulfur atom in methionine is a preferred binding site for platinum compounds.

For proteins containing  $\text{Ca}^{2+}$  or  $\text{Mg}^{2+}$  ions, an attempt should always be made to replace the metal ion by a heavier one, notably rare earth ions. If  $\text{Ca}^{2+}$  is replaced by  $\text{Sm}^{3+}$ , for example, only the difference in electrons between the two elements is added: 41, not 59 electrons. However, anomalous scattering helps because it is strong for these heavy ions (see Section 7.8). The radius of the ions is also important, because the cavity containing the metal ion is least disturbed if the diameter of the introduced metal ions is close to the diameter of  $\text{Ca}^{2+}$  or  $\text{Mg}^{2+}$  ions. In Table 7.1 one can see that  $\text{Ba}^{2+}$  and  $\text{Pb}^{2+}$  are much larger than  $\text{Ca}^{2+}$  and are not good replacements for  $\text{Ca}^{2+}$ . However, this does not mean that they can never replace  $\text{Ca}^{2+}$  because the flexibility of the binding site also plays a role.  $\text{Ca}^{2+}$  can best be replaced by one of the first rare earth ions because their radius is close to that of  $\text{Ca}^{2+}$ . The radius becomes smaller for the higher elements. Sometimes heavy atom derivatives of a biological substrate or cofactor are used, but this is not frequently done.

The pH of the solution should not be neglected. It has already been mentioned that histidine is a better ligand at neutral or higher pH values. The pH is also

Table 7.1. Radii of Some Ions with 6-Coordination

	$\text{Ca}^{2+}$	$\text{Mg}^{2+}$	$\text{Ba}^{2+}$	$\text{Pb}^{2+}$					
Electrons	18	10	54	80					
Radius (pm)	114	86	149	133					
	$\text{La}^{3+}$	$\text{Pr}^{3+}$	$\text{Sm}^{3+}$	$\text{Eu}^{3+}$	$\text{Gd}^{3+}$	$\text{Dy}^{3+}$	$\text{Er}^{3+}$	$\text{Tm}^{3+}$	$\text{Yb}^{3+}$
Electrons	54	56	59	60	61	63	65	66	67
Radius (pm)	117	113	110	109	108	105	103	102	101

important in the binding of charged reagents such as  $\text{HgI}_4^{2-}$ ,  $\text{Au}(\text{CN})_2^-$ ,  $\text{PtCl}_6^{2-}$ , and so forth. At higher pH values, where the protein has a higher negative charge, these reagents react less readily with the protein. This is an advantage if the reaction is too strong at lower pH values when too many sites react and nonisomorphism occurs. On the other hand, if these negative ions do not bind at all or bind only poorly, the pH should be lowered slightly. This is, of course, possible only if the protein crystal permits this change. Heavy atom salts, which are easily hydrolyzed, such as  $\text{UO}_2^{2+}$  or  $\text{Sm}^{3+}$  salts cannot be used at an alkaline pH.

If the medium is a water–organic solvent mixture, electrostatic forces are stronger because of the lower dielectric constant and the binding of ionic compounds will be stronger. However, the organic solvent might be a chelating agent for the heavy ion; this is true for 2-methyl-2,4-pentandiol (MPD), a popular organic solvent in protein crystallization experiments.

In the structure determination of protein–oligonucleotide complexes, brominated or iodinated oligos are convenient heavy atom compounds. Xenon as a heavy atom is a different story. The atoms of this inert gas can occupy holes in a protein molecule, but the binding by purely Van der Waals interaction is rather weak, preventing a reasonable occupancy. To raise it close to 100%, pressurized xenon must be applied. The pressure is in the 0.5–5-Mpa<sup>3</sup> range and must be maintained during data collection. The requirement of pressurized equipment is an extra problem. Sauer et al. (1997) have circumvented this problem by performing data collection at cryotemperature, the most popular crystal mounting and data collection technique anyway (Section 1.7 of Chapter 1). The crystal in the cryoloop is inserted into a high-pressure cell and xenon pressure between 0.5 and 5 MPa is applied for 1–30 min. After fast release of the xenon pressure, the crystal is immediately shock-cooled and transferred to the X-ray diffraction instrument. At cryotemperature, the vapor pressure of xenon is sufficiently low to prevent evaporation (according to GMELIN,<sup>4</sup> 0.00026 atm = 0.26 hPa at 91 K). Another advantage of the cryotechnique is that the strong X-ray absorption by the xenon gas in a pressurized cell is avoided.

Halide ions can be rapidly attached to protein molecules by a short soak in the cryoprotectant solution containing these ions. They bind at the surface of the protein molecule in a nonspecific way by hydrogen-bonding and hydrophobic interaction. Formation of ion pairs with lysine or arginine side chains is also observed (Dauter et al., 2000).

### 7.3.3. Chemical Modification of the Native Protein

If straightforward soaking does not result in a useful complex, the situation is not completely hopeless. One can still try to modify the protein by covalently attaching a heavy-atom-containing reagent (see, e.g., Evans and Bricogne, 2003;

<sup>3</sup> 1 MPa  $\approx$  10 atm.

<sup>4</sup> *Handbook of Inorganic and Organometallic Chemistry*, GMELIN Reg. No. (GRN) 16318.

Ghosh et al., 1999; Spurlino et al., 1994) such as *p*-iodophenyliso-thiocyanate or *p*-iodophenylisocyanate. They react with the  $\epsilon$ -NH<sub>2</sub> of lysine side chains to form a thiourea or urea derivative, at least at sufficiently high pH. Another chemical reaction is the iodination of tyrosine side chains (Brzozowski et al., 1992; Derewenda, 1994; Sigler, 1970; Spurlino et al., 1994). They can take up a maximum of three iodine atoms. Iodine has a reasonable number of electrons (53), but despite its successful use in a number of cases, it is not a very popular method. The reason is probably its tendency to react with other groups in the protein.

#### 7.3.4. Genetic Modification of the Protein

Genetic engineering has opened up new areas for protein modification. For the preparation of heavy atom derivatives, it is sometimes useful to replace one of the amino acids by a cysteine (Nagai et al., 1990; Tucker et al., 1989). Of course, this replacement helps only if the cysteine residue is not oxidized readily, which is a potential danger. Therefore, mutants should be treated with an antioxidant, such as dithiothreitol, before reaction with the mercury-containing compound (Nagai et al., 1991). Of course, the new cysteine residue should not disturb the protein structure and should be accessible. This is difficult to predict beforehand. The best one can do is to replace a residue in a very polar region of the amino acid sequence, which, hopefully, is a loop at the surface of the molecule. On the other hand, cysteines can also prevent crystallization by forming a disulfide bond between molecules. If this is suspected, one should replace the cysteine by an alanine.

Another biological modification is to incorporate selenomethionine in place of methionine and solve the structure by the multiple-wavelength anomalous diffraction (MAD) technique (see Section 9.5 of Chapter 9).

#### 7.3.5. Problems Commonly Encountered in the Search for Heavy Atom Derivatives

##### 7.3.5.1. Increased Radiation Damage

X-ray radiation damage is caused by radical formation and subsequent chemical reactions. This process can be slowed down by lowering the temperature of the crystal in the X-ray beam (Section 1.7 of Chapter 1); even a few degrees lower will help (e.g., a temperature of 5°C instead of room temperature).

##### 7.3.5.2. Insolubility of Phosphates

Phosphate buffers are often used for protein crystallization and soaking. However, some heavy metal phosphates are insoluble, including those of the rare earths and of uranyl ions. In such cases, the phosphate buffer should be replaced by a suitable buffer, usually an organic one.

### 7.3.5.3. Ammonium Sulfate

Ammonium sulfate is a very popular precipitating agent. However, it can prevent the binding of heavy metals in two ways. First, it is in equilibrium with ammonia. At somewhat higher pH values, the ammonia concentration in the solution is appreciable and this can act as a ligand for the heavy ion, which might prevent binding to the protein. The solution of this problem is to replace the ammonium sulfate by another salt, such as Li-sulfate or Cs-sulfate or by polyethylene glycol (PEG). The other problem with ammonium sulfate is its high ionic strength. This weakens electrostatic interactions and in this way can prevent the binding of a heavy ion. The solution is to change from ammonium sulfate to PEG.

## 7.4. Effect of Heavy Atoms on X-ray Intensities

Can the attachment of one or a few heavy atoms to a large protein molecule sufficiently change the intensities of the reflections? Suppose that we have a protein with a molecular weight of 42,000. Each of its molecules contains about 3000 nonhydrogen atoms or  $3000 \times 7 = 21,000$  electrons. In this ocean of 21,000 electrons, a mercury atom adds only 80 electrons and yet its attachment changes the intensities of the X-rays diffracted by the crystal of the protein in a measurable way. This seems impossible, but it is nevertheless true, as we will see.

Crick and Magdoff (1956) estimated the expected intensity changes resulting from heavy atom attachment and arrived at the following result: For centric reflections that have their structure factor along the real axis in the Argand diagram, they found that the relative root-mean-square intensity change is

$$\frac{\sqrt{(\Delta I)^2}}{\overline{I_P}} = 2 \times \frac{\sqrt{\overline{I_H}}}{\overline{I_P}}, \quad (7.16)$$

and for noncentric reflections,

$$\frac{\sqrt{(\Delta I)^2}}{\overline{I_P}} = \sqrt{2} \times \frac{\sqrt{\overline{I_H}}}{\overline{I_P}}, \quad (7.17)$$

where  $\overline{I_H}$  is the average intensity of the reflections if the unit cell would contain the heavy atoms only and  $\overline{I_P}$  is the average intensity of the reflections for the native protein (see the derivation below).

---

### **Crick and Magdoff's Estimation of X-ray Reflection Intensity Changes If Heavy Atoms Are Attached to the Protein**

First, centric reflections will be considered. If the origin of the system is placed in the center of symmetry, they have their structure factors  $\mathbf{F}$  pointing along the horizontal axis in the Argand diagram, to the right for phase angle  $\alpha = 0^\circ$  and to the left for  $\alpha = 180^\circ$ . Therefore,  $\mathbf{F}$  can be expressed as a real number, equal to its



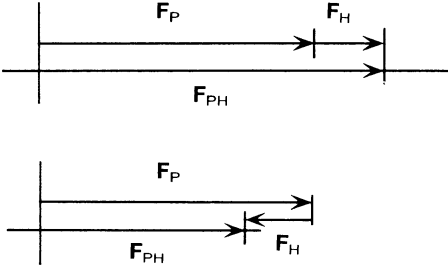


Figure 7.7. Structure factors in the isomorphous replacement method for centric reflections.  $F_P$  is for the protein,  $F_{PH}$  is for the derivative, and  $F_H$  is for the heavy atom contribution.

amplitude, with positive sign for  $\alpha = 0^\circ$  and negative sign for  $\alpha = 180^\circ$ , because for  $\alpha = 0^\circ$ ,

$$\mathbf{F} = |F| \exp[i\alpha] = |F| (\cos \alpha + i \sin \alpha) = +F$$

and for  $\alpha = 180^\circ$ ,

$$\mathbf{F} = |F| \exp[i\alpha] = |F| (\cos \alpha + i \sin \alpha) = -F$$

In the following discussion, P stands for the native protein, PH for the heavy atom derivative, and H for the heavy atoms. For centric reflections (Figure 7.7):

$$I_{PH} = (F_P + F_H)^2.$$

Note that  $F_P$  and  $F_H$  can be either positive or negative.

$$\begin{aligned} I_P &= F_P^2, \\ \Delta I &= 2F_P F_H + F_H^2, \\ (\Delta I)^2 &= 4F_P^2 F_H^2 + 4F_P F_H^3 + F_H^4 \end{aligned}$$

and the mean square change in intensity is

$$\overline{(\Delta I)^2} = 4\overline{F_P^2 F_H^2} + 4\overline{F_P F_H^3} + \overline{F_H^4}.$$

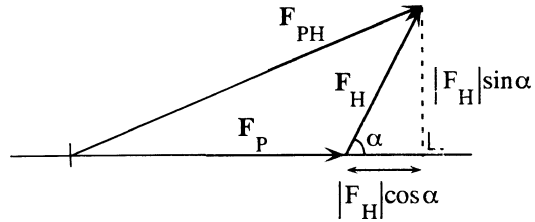
Because  $F_P$  and  $F_H$  are not correlated,  $\overline{F_P F_H^3} = 0$  and  $\overline{F_P^2 F_H^2} = \overline{F_P^2} \times \overline{F_H^2}$ .

$$\frac{\sqrt{\overline{(\Delta I)^2}}}{I_P} = \frac{\sqrt{4\overline{F_P^2} \times \overline{F_H^2} + \overline{F_H^4}}}{F_P^2} = 2 \sqrt{\frac{\overline{F_H^2}}{F_P^2}} \sqrt{1 + \frac{\overline{F_H^4}}{4 \times \overline{F_P^2} \times \overline{F_H^2}}} \cong 2 \sqrt{\frac{\overline{F_H^2}}{F_P^2}} = 2 \sqrt{\frac{I_H}{I_P}}$$

assuming that  $\overline{F_H^4} \ll 4\overline{F_P^2} \times \overline{F_H^2}$ . We will now do the same for noncentric reflections (Figure 7.8):

$$\begin{aligned} \mathbf{F}_{PH} &= \mathbf{F}_P + \mathbf{F}_H, \\ I_{PH} &= |\mathbf{F}_P + \mathbf{F}_H|^2 = |F_{PH}|^2 = |F_P|^2 + 2|F_P||F_H| \cos \alpha + |F_H|^2, \\ \Delta I &= 2|F_P||F_H| \cos \alpha + |F_H|^2, \\ (\Delta I)^2 &= 4|F_P|^2|F_H|^2 \cos^2 \alpha + 4|F_P||F_H|^3 \cos \alpha + |F_H|^4, \\ \overline{(\Delta I)^2} &= 2\overline{|F_P|^2|F_H|^2} + 4\overline{|F_P||F_H|^3 \cos \alpha} + \overline{|F_H|^4} \end{aligned}$$

Figure 7.8. Structure factors in the isomorphous replacement method for noncentric reflections; the horizontal direction of  $F_P$  is arbitrary.



because  $|F_P|$  and  $|F_H|$  are not correlated and  $\overline{\cos\alpha} = 0$ :

$$\begin{aligned} \overline{(\Delta I)^2} &= 2|F_P|^2 \times |F_H|^2 + 0 + |F_P|^4, \\ \frac{\sqrt{\overline{(\Delta I)^2}}}{\bar{I}_P} &= \sqrt{\frac{2|F_P|^2 \times |F_H|^2 + |F_P|^4}{(|F_P|^2)^2}} = \sqrt{2} \times \sqrt{\frac{|F_H|^2}{|F_P|^2} + \frac{|F_H|^4}{2(|F_P|^2)^2}} \\ &= \sqrt{2} \times \sqrt{\frac{|F_H|^2}{|F_P|^2}} \times \sqrt{1 + \frac{|F_H|^4}{2 \times |F_P|^2 \times |F_H|^2}} \\ &\qquad\qquad\qquad \text{small with respect to 1} \\ &\cong \sqrt{2} \times \sqrt{\frac{|F_H|^2}{|F_P|^2}} = \sqrt{2} \times \sqrt{\frac{\bar{I}_H}{\bar{I}_P}}. \end{aligned}$$

In Table 7.2 this result is used to calculate the size of the relative change in intensity that can be expected for the noncentric reflections of a protein crystal, if one mercury atom is attached per protein molecule.  $\bar{I}$  is obtained with the expression

$$\bar{I} = \sum_i f_i^2$$

(see Section 5.2 of Chapter 5), where  $f_i$  is 80 for a mercury atom and, on average, 7 for a typical protein atom. If we assume that the intensities can be determined

Table 7.2. Average Relative Change in Intensity for the Acentric Reflections of a Protein Crystal if One Mercury Atom is Attached per Protein Molecule<sup>a</sup>

Molecular Weight of the Protein	100% Occupancy	50% Occupancy
14,000	0.51	0.25
28,000	0.36	0.18
56,000	0.25	0.12
112,000	0.18	0.09
224,000	0.13	0.06
448,000	0.09	0.04

<sup>a</sup>The data are for  $(\sin\theta)/\lambda = 0$ . With increasing diffraction angle the relative contribution of Hg is somewhat higher because its atomic scattering falls off less rapidly than for the light elements.

with an accuracy of 10%, then the practical limit for  $\sqrt{(\Delta I)^2/I_P}$  is  $0.10 \times \sqrt{2} = 0.14$  (the factor  $\sqrt{2}$  stems from the fact that the intensity difference is the result of two measurements). From Table 7.2 we see that this corresponds to a maximum molecular weight of 200,000 for full occupancy by one mercury atom per protein molecule and 50,000 for half-occupancy. The changes are, of course, larger if more than one heavy atom is bound per protein molecule but lower if the binding sites are not fully occupied. The conclusion is that the isomorphous replacement method can be applied successfully for the determination of a protein crystal structure, even for large protein molecules and protein complexes.

---

## 7.5. Determination of the Heavy Atom Parameters from Centrosymmetric Projections

In Step 3 of the isomorphous replacement method, the coordinates of the heavy atoms must be found. This is an easy procedure if the crystal has centrosymmetric projections (e.g., in space group  $P2_12_12_1$ ), where the three projections along the axes of the unit cell are centrosymmetric because of the 2-fold screw axes. For centrosymmetric projections, the vectorial summation (Figure 7.7)

$$\mathbf{F}_{\text{PH}} = \mathbf{F}_P + \mathbf{F}_H$$

is simplified to

$$\begin{aligned} |F_{\text{PH}}| &= |F_P| \pm |F_H|, \\ |F_H| &= |F_{\text{PH}}| - |F_P| \end{aligned}$$

or

$$|F_H| = |F_P| - |F_{\text{PH}}|$$

and

$$|F_H|^2 = (|F_{\text{PH}}| - |F_P|)^2.$$

We have made the assumption that  $F_{\text{PH}}$  and  $F_P$  have the same sign, either both positive or both negative. With this assumption, the Patterson summation with the coefficients  $(|F_{\text{PH}}| - |F_P|)^2$  will give a Patterson map of the heavy atom arrangement in the unit cell. For the majority of the reflections, the assumption will be true, because, in general,  $F_H$  will be small compared with  $F_P$  and  $F_{\text{PH}}$ . If, however,  $F_P$  is small,  $F_{\text{PH}}$  could have the opposite sign and  $F_H$  would be  $F_P + F_{\text{PH}}$ . Fortunately, this does not occur often enough to distort the Patterson map seriously.

To calculate  $|F_H|$ , the structure factor amplitudes  $|F_{\text{PH}}|$  and  $|F_P|$  should, of course, be put on the same scale. This can be done in an approximate way by applying the Wilson plot and putting the  $|F_P|^2$  and  $|F_{\text{PH}}|^2$  values on an absolute

scale [Equation (5.3) of Chapter 5]. This gives the factors  $C_P$  and  $C_{PH}$  with  $B_P$  and  $B_{PH}$ . Alternatively, a relative Wilson plot is calculated:

$$\ln \frac{\overline{I_{PH}}}{\sum_i (f_i^0)^2 + (f_H)^2} - \ln \frac{\overline{I_P}}{\sum_i (f_i^0)^2} = \ln \frac{C_{PH}}{C_P} - 2(B_{PH} - B_P) \frac{\sin^2 \theta}{\lambda^2}.$$

With the relative value  $C_{PH}/C_P$  and the difference between  $B_P$  and  $B_{PH}$ ,  $|F_{PH}|^2$  and  $|F_P|^2$  can be put on the same scale. For the native protein,  $\sum_i (f_i^0)^2$  must be calculated for all protein atoms, but for the derivative, an estimated heavy atom contribution  $(f_H)^2$  should be added. In the subsequent process of refining the heavy atom parameters, the scale factor is refined together with the other parameters. Sometimes the  $(f_H)$  contribution to the structure factor  $\mathbf{F}_{PH}$  is neglected and the  $|F_P|$  and  $|F_{PH}|$  values are put on the same scale by minimizing a least squares function  $E$  with respect to the relative scale factor (for the method of least squares, see Section 7.11):

$$E = \sum_h \frac{1}{\sigma_F^2} (k |F_{PH}| - |F_P|)^2, \quad (7.18)$$

where  $k$  is a scale factor and  $\sigma_F^2$  is the variance to be chosen for either the  $|F_{PH}|$  or the  $|F_P|$  values and the summation is over all reflections  $h$ . The minimization of  $E$  with respect to  $k$  gives

$$k = \frac{\sum_h \frac{1}{\sigma_F^2} |F_{PH}| \times |F_P|}{\sum_h \frac{1}{\sigma_F^2} |F_{PH}|^2}. \quad (7.19)$$

If the morphology of the crystal(s) used for collecting the native dataset differs appreciably from the morphology of the derivative crystals, differences in absorption might affect the comparison of the two datasets. The isomorphous differences and  $R_{deriv.}$  (see Appendix 2) appear larger than they really are. Therefore, it is always advisable to correct for absorption, such as by comparing and equalizing symmetry-related reflections within one dataset or collect data at a shorter wavelength.

It is sometimes observed that after scaling, as just described, reflections that should have the same intensity tend to be stronger in one region of reciprocal space than in another. This can be due to problems of an instrumental nature or to poor absorption correction. In those cases, local scaling must be applied, in which reciprocal space is divided into blocks of  $hkl$  with an individual scaling factor for each block (Matthews and Czerwinski, 1975).

If the Patterson map of a centrosymmetric projection can be interpreted, it gives two coordinates of the heavy atoms, and with a second projection, it gives the third coordinate as well. With the positions of the heavy atoms known, the structure factors  $\mathbf{F}_H$  can be calculated, including their sign (for centrosymmetric projections) or their phase angle (for acentric reflections). In principle, one heavy

atom derivative is sufficient to determine the signs of centrosymmetric protein reflections. For example, if  $|F_{PH}| > |F_P|$  and the sign of  $F_H$  is +, then  $F_P$  will have a + sign. For a second heavy atom derivative, it is not absolutely necessary to calculate a Patterson map, because the sign of the centric protein reflections in combination with the difference between  $|F_P|$  and  $|F_{PH}|$  of the second heavy atom derivative gives the sign of  $F_H$  immediately. This allows the calculation of a Fourier summation, resulting in the projection of the heavy atom arrangement from which the coordinates can be obtained.

## 7.6. Parameters of Heavy Atoms Derived from Acentric Reflections

It is also not a problem to derive heavy-atom positions from three-dimensional data. The two sets of known data are the amplitudes of the structure factors  $\mathbf{F}_P$  and  $\mathbf{F}_{PH}$ . Their phase angles are not yet known. For each reflection, there is a difference in length (Figure 7.9):

$$\Delta |F|_{\text{iso}} = |F_{PH}| - |F_P|.$$

We will now see that the coordinates of the heavy atoms can generally be derived from a Patterson map calculated with  $(\Delta |F|_{\text{iso}})^2$ . The triangle ABC in Figure 7.9 expresses the vector sum:  $\mathbf{F}_{PH} = \mathbf{F}_P + \mathbf{F}_H$ . However, for the time being, only the lengths of  $\mathbf{F}_{PH}$  ( $|F_{PH}|$ ) and that of  $\mathbf{F}_P$  ( $|F_P|$ ) are known, but not their directions. For  $\mathbf{F}_H$ , both the length and direction are unknown.

In Figure 7.9,  $CE = |F_H| \cos(\alpha_{PH} - \alpha_H)$ . In general,  $\alpha_P - \alpha_{PH}$  is small, because for most reflections,  $|F_H| \ll |F_P|$  and  $|F_{PH}|$ . Therefore,  $CE \cong \Delta |F|_{\text{iso}}$  and the result is

$$\Delta |F|_{\text{iso}} = |F_H| \cos(\alpha_{PH} - \alpha_H). \quad (7.20)$$

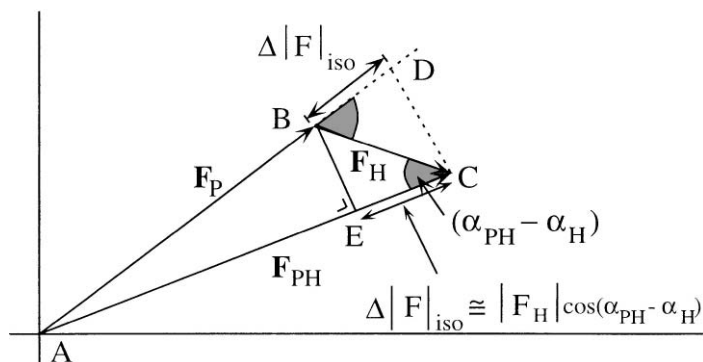


Figure 7.9. The structure factor triangle for isomorphous replacement:  $\Delta |F|_{\text{iso}} = |F_{PH}| - |F_P|$ .

The result is that a Patterson summation with  $(\Delta|F|_{\text{iso}})^2$  as the coefficients will in fact be a Patterson summation with coefficients  $|F_H|^2 \cos^2(\alpha_{\text{PH}} - \alpha_H)$ . Because

$$\cos^2(\alpha_{\text{PH}} - \alpha_H) = \frac{1}{2} + \frac{1}{2} \cos 2(\alpha_{\text{PH}} - \alpha_H),$$

we obtain

$$|F_H|^2 \cos^2(\alpha_{\text{PH}} - \alpha_H) = \frac{1}{2} |F_H|^2 + \frac{1}{2} |F_H|^2 \cos 2(\alpha_{\text{PH}} - \alpha_H).$$

Because the angles  $\alpha_{\text{PH}}$  and  $\alpha_H$  are not correlated, the second term on the right-hand side will contribute only noise to the Patterson map. However, the first term,  $1/2|F_H|^2$ , will give the Patterson function for the heavy atom structure on half of the scale.

Because a Patterson map is centrosymmetric, the choice is between two sets of heavy atom positions, which are centrosymmetrically related. It is not yet known what the correct one is, but for the moment, this does not matter and either of the two sets can be chosen. Later, in determining the absolute configuration of the protein (Section 9.4 of Chapter 9), this problem will be discussed again.

## Conclusion

$$P(u v w) = \frac{1}{V} \sum_h (\Delta|F|_{\text{iso}})^2 \cos[2\pi(hu + kv + lw)] \quad (7.21)$$

Calculation with the coefficients  $(\Delta|F|_{\text{iso}})^2$  results (apart from the extra noise and the reduction in height) in a Patterson map of the heavy atom arrangement.

If the difference Patterson map cannot be interpreted in terms of the heavy atom positions, one can try to apply one of the direct methods for phase determination, as they are developed for the X-ray structure determination of small molecules, because the problem is very similar: For only a relatively small number of sites in the unit cell, the parameters must be found. Several programs are available—for instance: SHELXD (Schneider and Sheldrick, 2002), SnB (Sheldrick et al., 2001; Weeks and Miller, 1999), SIR 2002 (Burla et al., 2004), ACORN (Foadi et al., 2000) and CRUNCH (Graaff et al., 2001).

We are now able to find the parameters of the attached heavy atoms in the crystal structure. We will discuss how a common origin for the coordinates of the heavy atoms from different derivatives can be found and how the heavy atom parameters can be refined. Subsequently, the protein phase angles will be calculated. However, before doing so, we will discuss another extremely useful Fourier summation: “the difference Fourier.” We will also introduce so-called “anomalous scattering,” because this can contribute to localization of the heavy atoms.

## 7.7. The Difference Fourier Summation

With this summation, we can find the position of reagents attached to protein molecules in the crystal, either heavy atoms or other reagents, such as enzyme inhibitors. However, it is necessary that we know protein phase angles  $\alpha_P(hkl)$ !

$$\begin{aligned}\Delta\rho(xyz) &= \frac{1}{V} \sum_{hkl} \Delta |F(hkl)|_{\text{iso}} \exp[-2\pi i(hx + ky + lz) + i\alpha_P(hkl)] \\ &= \frac{1}{V} \sum_{hkl} \Delta |F(hkl)|_{\text{iso}} \cos[2\pi(hx + ky + lz) - \alpha_P(hkl)].\end{aligned}$$

Written more compactly,

$$\Delta\rho(\mathbf{r}) = \frac{1}{V} \sum_{\mathbf{h}} \Delta |F(\mathbf{h})|_{\text{iso}} \exp[-2\pi i\mathbf{h} \cdot \mathbf{r} + i\alpha_P(\mathbf{h})]. \quad (7.22)$$

Thus, a difference Fourier summation is calculated with the coefficients  $\Delta |F|_{\text{iso}}$  and the phase angles  $\alpha_P$  of the protein. Now we will see where this leads. Suppose that the structure factors of the attached reagent are the still unknown vectors  $\mathbf{F}_H$ . In Section 7.6 we derived that

$$\Delta |F|_{\text{iso}} \approx |F_H| \cos(\alpha_{PH} - \alpha_H). \quad (7.20)$$

Because  $\exp[i\alpha] = \cos \alpha + i \sin \alpha$  and  $\exp[-i\alpha] = \cos \alpha - i \sin \alpha$ ,

$$\Delta |F|_{\text{iso}} \approx \frac{1}{2} |F_H| \{ \exp[i(\alpha_{PH} - \alpha_H)] + \exp[-i(\alpha_{PH} - \alpha_H)] \}$$

and

$$\begin{aligned}\Delta |F|_{\text{iso}} \exp[i\alpha_P] &\approx \frac{1}{2} |F_H| \{ \exp[i(\alpha_{PH} - \alpha_H)] \times \exp[i\alpha_P] \\ &\quad + \exp[-i(\alpha_{PH} - \alpha_H)] \times \exp[i\alpha_P] \}.\end{aligned}$$

For  $|F_H| \exp[i\alpha_H]$ , we can write  $\mathbf{F}_H$ , and for  $|F_H| \exp[-i\alpha_H]$ , we write  $\mathbf{F}_H^*$ .

$$\Delta |F|_{\text{iso}} \exp[i\alpha_P] = \frac{1}{2} \mathbf{F}_H \exp[-i\alpha_{PH}] \times \exp[i\alpha_P] + \frac{1}{2} \mathbf{F}_H^* \exp[i\alpha_{PH}] \times \exp[i\alpha_P].$$

The term  $\frac{1}{2} \mathbf{F}_H^* \exp[2i\alpha_P]$  will give noise in the Fourier map because the vectors  $\mathbf{F}_H^*$  and  $\exp[2i\alpha_P]$  are not correlated in their direction in the Argand diagram. Therefore, and because  $\alpha_P \cong \alpha_{PH}$ :

$$\Delta |F|_{\text{iso}} \exp[i\alpha_P] \approx \frac{1}{2} \mathbf{F}_H.$$

If this result is combined with Equation (7.22), then

$$\Delta\rho(\mathbf{r}) = \frac{1}{V} \sum_{\mathbf{h}} \frac{1}{2} \mathbf{F}_H \exp[-2\pi i\mathbf{h} \cdot \mathbf{r}]$$

$$= \frac{1}{2} \frac{1}{V} \sum_h |F_H(\mathbf{h})| \exp[-2\pi i \mathbf{h} \cdot \mathbf{r} + i\alpha_H]. \quad (7.23)$$

### Conclusion

A difference Fourier map shows positive electron density at the site of atoms that were not present in the native structure and it shows negative density at the positions of atoms present in the native, but not in the derivative structure. The height of the peaks is only half of what it would be in a normal Fourier map. With a difference Fourier map, even small changes in the electron density can be observed, such as the attachment or removal of a water molecule. It is a powerful method, even if only preliminary values for the protein phase angles are known. For example, after the main heavy atom sites have been found from a difference Patterson map, additional weakly occupied sites can be detected with a difference Fourier map.

An improved difference Fourier map can be calculated if anomalous scattering data are incorporated in the calculation of the protein phase angles, which will be discussed in Chapter 9. Another useful Fourier summation has as coefficients  $2|F_{PH}| - |F_P|$  and as phase angles the protein phase angles  $\alpha_P$ :

$$\rho(\mathbf{r}) = \frac{1}{V} \sum_h (2|F_{PH}| - |F_P|) \exp[-2\pi i \mathbf{r} \cdot \mathbf{h} + i\alpha_P]. \quad (7.24)$$

The coefficients can be written as

$$2|F_{PH}| - |F_P| = 2(|F_{PH}| - |F_P|) + |F_P| = 2\Delta |F|_{\text{iso}} + |F_P|.$$

Thus, this electron density map will give the native protein structure and, apart from noise, the electron density of the attached atoms but now at full height, not half-height. Sometimes  $\{3|F_{PH}| - 2|F_P|\}$  coefficients are preferred (Lamzin and Wilson, 1997).

Structural information in electron density maps is determined to a greater extent by the phase angles than by the Fourier coefficients. Therefore, the electron density maps calculated with native protein phase angles are biased toward the native protein. Read (1986) showed that the bias can be minimized if the electron density is calculated with protein phase angles  $\alpha_P$  and as coefficients  $2m|F_{PH}| - D|F_P|$ , where  $m$  is the figure of merit (Section 7.12) and  $D$  is a multiplier equal to the Fourier transform of the probability distribution of  $\overline{\Delta r}$ , the mean error in the atomic positions (see Section 15.6 of Chapter 15).

The difference Fourier should not be mistaken for the residual Fourier (Res. Fourier), which can be calculated after the structure determination is almost complete. Its coefficients are  $(|F_{PH}| - |\mathbf{F}_P + \mathbf{F}_H|)$ . The values of  $|F_{PH}|$  are the amplitudes measured for the derivative;  $\mathbf{F}_P$  and  $\mathbf{F}_H$  are the structure factors calculated for the present protein and heavy atom models.

$$\text{Res. Fourier} = \frac{1}{V} \sum_h (|F_{PH}| - |F_P + F_H|) \exp[-2\pi i \mathbf{h} \cdot \mathbf{r} + i\alpha_{PH}]. \quad (7.25)$$



The phase angles  $\alpha_{\text{PH}}$  are calculated for the present model of the derivative.  $|F_{\text{PH}}| \exp[i\alpha_{\text{PH}}]$  represents the actual structure as far as its amplitude is concerned, but its phase corresponds with the present model of the structure. If the difference between the actual structure and the model is not too large, the residual Fourier can be shown to give this difference on half of the scale. The map can be used in the search for undetected heavy atom sites.

Ideally, any Fourier summation, whether it is a Patterson map, an electron density map, or a difference Fourier, should be calculated with an infinite number of terms. In practice, this is never true and only a limited number of terms is used (truncation). This series termination causes ripples around maxima in the map.

## 7.8. Anomalous Scattering

If the absorption by an element, such as copper, is plotted as a function of the X-ray wavelength  $\lambda$ , a typical curve is obtained (Figure 7.10). The sharp change in the curve is called an absorption edge. It is caused by photon absorption: An electron is ejected from an atom by the photon energy of the X-ray beam. For copper, the K-absorption edge is at  $\lambda = 1.380 \text{ \AA}$ . At this wavelength, an electron is ejected from the K-shell to a state in the continuous-energy region. Copper emits at its characteristic wavelength of  $K_{\alpha} = 1.5418 \text{ \AA}$ , somewhat above the K-absorption edge, because now the electron falls back from the L-shell into the K-shell and

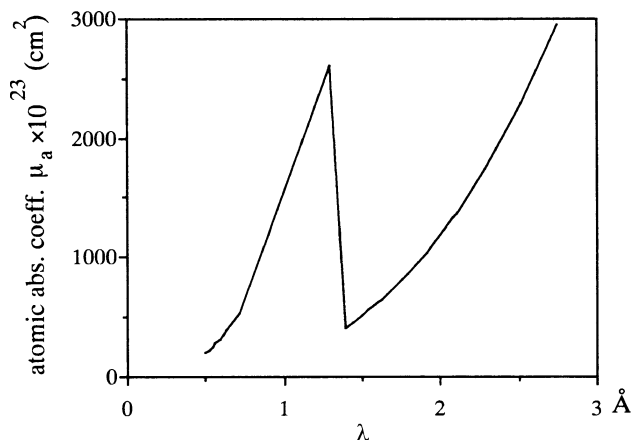
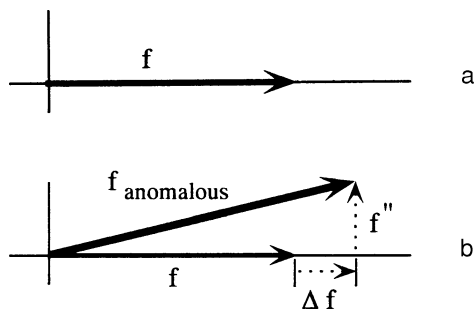


Figure 7.10. The atomic absorption coefficient for copper. The K-absorption edge is at  $1.380 \text{ \AA}$ . The atomic absorption coefficient or “atomic cross section” for absorption,  $\mu_a$  ( $\text{cm}^2$ ), is defined by  $\mu_a = (\mu/\rho) \times (A/N)$ , where  $\mu/\rho$  is the mass absorption coefficient ( $\text{cm}^2/\text{g}$ ),  $\rho$  is the density of the absorber,  $A$  is its atomic weight, and  $N$  is Avogadro’s number.  $\mu$  ( $\text{cm}^{-1}$ ) is the total linear absorption coefficient defined by  $I = I_0 \exp[-\mu t]$ , with  $t$  the thickness of the material (in cm),  $I_0$  the intensity of the incident, and  $I$  the intensity of the transmitted beam.

Figure 7.11. The atomic scattering factor for a completely free electron (a) and for a bound electron (b). The anomalous contribution consists of two parts: a real part  $\Delta f$  and an imaginary part  $if''$ . The direction of the primary beam is pointing to the left; it has a  $180^\circ$  phase difference with  $f$ .



this is a smaller energy difference. Remember that  $E = hc/\lambda$ . (See Figure 2.3 of Chapter 2 for the energy levels.)

So far, we have always regarded the electrons in an atom as free electrons. However, this is no longer true if the X-ray wavelength approaches an absorption-edge wavelength. Classical dispersion theory has derived the scattering power of an atom by supposing that it contains dipole oscillators. In units of the scattering of a free electron, the scattering of an oscillator with eigenfrequency  $\nu_n$  and moderate damping factor  $\kappa_n$  was found to be a complex quantity:

$$f_n = \frac{\nu^2}{\nu^2 - \nu_n^2 - i\kappa_n\nu}, \quad (7.26)$$

where  $\nu$  is the frequency of the incident radiation (James, 1965; Wilson and Prince, 1999, p. 244). For  $\nu \gg \nu_n$ , Equation (7.26) approaches  $f_n = 1$ , the scattering by a free electron, and for  $\nu \ll \nu_n$ , it approaches  $f_n = 0$ , the lack of scattering from a fixed electron. Only for  $\nu \cong \nu_n$  does the imaginary part have an appreciable value.

Fortunately, quantum mechanics arrives at the same result by adding a rational meaning to the damping factors and interpreting  $\nu_n$  as absorption frequencies of the atom (Hönl, 1933). For heavy atoms, the most important transitions are to a continuum of energy states with  $\nu_n \geq \nu_K$  or  $\nu_n \geq \nu_L$ , and so on, the frequencies of the K, L, and so on, absorption edges. Whereas free electrons have a phase difference of  $180^\circ$  with respect to the incident beam, the diffracted beam of the inner-shell electrons of the heavy atoms does not differ  $180^\circ$  in phase from the incident beam. The situation is drawn in Figure 7.11. The atomic scattering factor for a completely free electron is shown in Figure 7.11a, and for a bound electron, it is shown in Figure 7.11b; its scattering is anomalous and can be written as<sup>5</sup>

$$f_{\text{anom.}} = f + \Delta f + if'' = f' + if'';$$

$\Delta f$  is the change in the electron scattering factor along the horizontal axis in the Argand diagram and  $if''$  along the vertical axis (remember that  $i$  indicates a

<sup>5</sup>The nomenclature of  $f'$  can be confusing. What here is called  $\Delta f$  is in other publications often indicated by  $f'$ .

Table 7.3. The Anomalous Scattering in Electrons of Hg for Copper Radiation

	$(\sin \theta)/\lambda$		
	0 $(\infty)^a$	0.4 ( $\text{\AA}^{-1}$ ) $(1.25 \text{\AA})^a$	0.6 ( $\text{\AA}^{-1}$ ) $(0.83 \text{\AA})^a$
$f$	80	53	42
$\Delta f$	-5	-5	-5
$f''$	8	8	8

<sup>a</sup>Corresponding lattice spacing.

counterclockwise rotation of  $90^\circ$  (Section 4.2 of Chapter 4). For higher scattering angles, the anomalous scattering becomes relatively more important. The reason is that it is nearly constant as a function of  $(\sin \theta)/\lambda$ , because it stems mainly from the inner electrons (Table 7.3). The effect of anomalous scattering is that in the Argand diagram, the atomic scattering vector is rotated counterclockwise. As a consequence, the structure factors  $\mathbf{F}_{\text{PH}}(h k l)$  and  $\mathbf{F}_{\text{PH}}(\bar{h} \bar{k} \bar{l})$  for the heavy atom derivative of the protein are no longer equal in length and have a different phase angle (Figure 7.12). This difference can be used separately or in combination with the isomorphous replacement method in the search for the heavy atom positions.

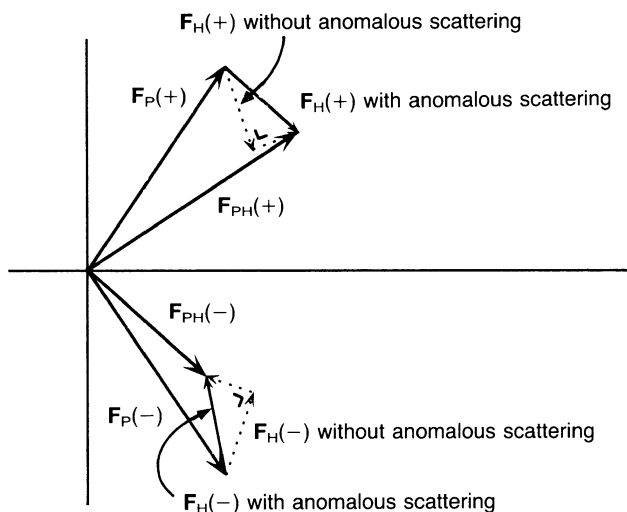


Figure 7.12.  $\mathbf{F}_P(+)$  and  $\mathbf{F}_P(-)$  are symmetric with respect to the horizontal axis in the Argand diagram, assuming the absence of anomalous scatterers in the protein. Without anomalous scattering,  $\mathbf{F}_H(+)$  and  $\mathbf{F}_H(-)$  are also symmetric. The imaginary part of the anomalous scattering contribution has been exaggerated. In this example,  $|\mathbf{F}_{\text{PH}}(+)| > |\mathbf{F}_{\text{PH}}(-)|$ .

Table 7.4. The Anomalous Scattering in Electrons for  $\text{CuK}\alpha$  Radiation by Mercury, Sulfur, and Selenium for  $(\sin \theta)/\lambda = 0^a$

	$f$	$\Delta f$	$f''$
Hg	80	-5.0	7.7
S	16	0.3	0.6
Se	34	-0.9	1.1

<sup>a</sup> It is assumed that the anomalous scattering is isotropic. This is not true if the wavelength is close to an absorption edge corresponding to an electron ejection to an upper state with nonspherical symmetry; for a detailed discussion see Templeton and Templeton (1991).

We define

$$\Delta|F|_{\text{ano}} = \{|F_{\text{PH}}(+)| - |F_{\text{PH}}(-)|\} \frac{f'}{2f''}. \quad (7.27)$$

$|F_{\text{PH}}(+)|$  represents the amplitude of the structure factor for a reflection  $(hkl)$ , and  $|F_{\text{PH}}(-)|$  is the amplitude for the reflection  $(\bar{h}\bar{k}\bar{l}) \equiv (-h, -k, -l)$ .  $\Delta|F|_{\text{ano}}$  is the difference between the amplitudes of the structure factor for the reflections  $hkl$  and  $\bar{h}\bar{k}\bar{l}$  (Bijvoet or Friedel pairs), scaled up with the factor  $f'/2f''$ .

From the anomalous Patterson map, calculated with  $(\Delta|F|_{\text{ano}})^2$ , the location of anomalous scatterers can be derived. These anomalous scatterers can be either extra heavy atoms attached to the protein or heavy atoms such as copper, iron, or even sulfur that are already present in the native protein structure. The anomalous scattering by sulfur atoms is relatively weak and it can be used only with rather small protein molecules. If the sulfur in the protein can be replaced by selenium, the situation is more favorable (see Table 7.4) and even more favorable if a wavelength close to the K-absorption edge of Se (0.98 Å) is chosen. This replacement of sulfur by selenium can be done biologically by incorporation of selenomethionine instead of methionine.

In Chapter 9 we will see how information from anomalous scattering can contribute to the determination of protein phase angles. In the next section, the following will be shown:

1.  $(\Delta|F|_{\text{ano}})^2$  as the coefficients in a Patterson summation will result in a Patterson map of the anomalous scatterers (the heavy atoms).
2.  $(\Delta|F|_{\text{iso}})^2 + (\Delta|F|_{\text{ano}})^2$  as coefficients will give the same Patterson map, but with less noise in the background than for separate Patterson maps.
3. Various methods exist to find the position of the heavy atoms in the different derivatives with respect to each other.

Moreover, as will be shown in Section 9.4 of Chapter 9, the absolute configuration of the protein can be determined with  $\Delta|F|_{\text{ano}}$ .

---

### Some special features concerning anomalous scattering

a. If the protein crystal contains anomalous scatterers, it is essential to differentiate between the reflections  $(+h, +k, +l)$  and  $(-h, -k, -l)$ . This can be done by applying the following rules:

1. Choose the unit cell angles  $\alpha$ ,  $\beta$ , and  $\gamma$  between the positive axes (**a**, **b**, and **c**)  $\geq 90^\circ$ .
2. Use a right-handed coordinate system (see, e.g., Figure 3.3 of Chapter 3).

As a result, the set of axes is always chosen in the same way with respect to the content of the unit cell for all crystals of the protein or protein derivative.

b. The imaginary part of the radiation from anomalous scatterers contributes to the electron density. In Section 4.11 of Chapter 4, the electron density was calculated using

$$\rho(xyz) = \frac{2}{V} \sum_{hkl=0}^{+\infty} |F(hkl)| \cos [2\pi(hx + ky + lz) - \alpha(hkl)].$$

The assumptions were that the amplitudes are the same for the reflections  $(hkl)$  and  $(\bar{h}\bar{k}\bar{l})$  but that their phase angles were just opposite. In the presence of anomalous scatterers, the summation of  $\mathbf{F}(hkl)$  and  $\mathbf{F}(\bar{h}\bar{k}\bar{l})$  results again in cosine terms along the real axis in the Argand diagram but has, in addition, a small component ( $\mathbf{F}''$ ) along the imaginary axis. This contributes to the electron density with  $\rho_{im}(xyz)$  that adds to the density at the positions  $x, y, z$  of the anomalous scatterers (see Note 8 in Section 9.5.3 of Chapter 9)

---

## 7.9. The Anomalous Patterson Summation

The heavy atom contribution to the structure factor consists of a normal part,  $\mathbf{F}_H$ , and an anomalous part,  $\mathbf{F}_{H''}$ . In Figure 7.13 this is drawn for a reflection  $(hkl)$  and for  $(\bar{h}\bar{k}\bar{l})$ . However, for convenience, the structure factors for  $(\bar{h}\bar{k}\bar{l})$  have been reflected with respect to the horizontal axis. It can be derived that a Patterson summation with the coefficients  $(\Delta|F|_{\text{ano}})^2$  can be approximated by a summation with the coefficients  $|F_H|^2 \sin^2(\alpha_{\text{PH}} - \alpha_H) = \frac{1}{2}|F_H|^2 - \frac{1}{2} \cos 2(\alpha_{\text{PH}} - \alpha_H)$ . This will give a Patterson map of the anomalous scatterers (the heavy atoms, see below).

---

### The Patterson Summation with the Coefficients $(\Delta|F_{\text{ano}})^2$

To simplify the derivation, the structure factors  $\mathbf{F}_P(-)$ ,  $\mathbf{F}_{\text{PH}}(-)$ ,  $\mathbf{F}_H(-)$ , and  $\mathbf{F}''_H(-)$  have been reflected with respect to the horizontal axis in the Argand diagram and combined with the structure factors for the reflection  $hkl$ . The structure factors  $\mathbf{F}_{\text{PH}}(+)$  and  $\mathbf{F}_{\text{PH}}(-)$  have the imaginary part of the anomalous scattering included

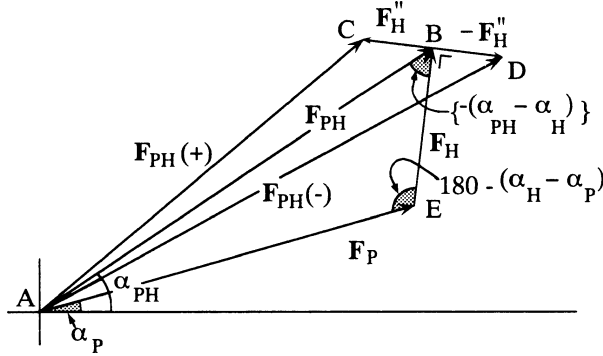


Figure 7.13. In this drawing, the structure factors  $F_P(-)$ ,  $F_{PH}(-)$ ,  $F_H(-)$ , and  $F_H''(-)$  have been reflected with respect to the horizontal axis and combined with the structure factors for the reflection  $(hkl)$ . Note that  $\alpha_H$  is the phase angle for the nonanomalous part of  $F_H$ .

and  $F_{PH}$  has it excluded. The application of the cos rule in triangle  $ABC$  gives

$$\begin{aligned} |F_{PH(+)}|^2 &= |F_{PH}|^2 + |F_H''|^2 - 2|F_H''| \times |F_{PH}| \cos\{90^\circ + (\alpha_{PH} - \alpha_H)\} \\ &= |F_{PH}|^2 + |F_H''|^2 + 2|F_H''| \times |F_{PH}| \sin(\alpha_{PH} - \alpha_H), \end{aligned}$$

and in triangle  $ABD$

$$\begin{aligned} |F_{PH(-)}|^2 &= |F_{PH}|^2 + |F_H''|^2 - 2|F_H''| \times |F_{PH}| \cos\{90^\circ - (\alpha_{PH} - \alpha_H)\} \\ &= |F_{PH}|^2 + |F_H''|^2 - 2|F_H''| \times |F_{PH}| \sin(\alpha_{PH} - \alpha_H) \end{aligned}$$

$$|F_{PH(+)}|^2 - |F_{PH(-)}|^2 = 4|F_H''| \times |F_{PH}| \sin(\alpha_{PH} - \alpha_H),$$

but

$$\begin{aligned} |F_{PH(+)}|^2 - |F_{PH(-)}|^2 &= (|F_{PH(+)}| + |F_{PH(-)}|) \times (|F_{PH(+)}| - |F_{PH(-)}|) \\ &\cong 2|F_{PH}| \times (|F_{PH(+)}| - |F_{PH(-)}|), \end{aligned}$$

and it follows that

$$|F_{PH(+)}| - |F_{PH(-)}| = 2|F_H''| \sin(\alpha_{PH} - \alpha_H). \quad (7.28)$$

The scattering factor of a heavy atom  $j$  is  $f_j = f'_j + if''_j$ . Assuming that the proportion  $f''_j/f'_j$  is the same for all heavy atoms in the structure,

$$\begin{aligned} |F_H''| &= \left| \sum_j f''_j \exp[2\pi i \mathbf{h} \cdot \mathbf{r}_j] \right| = \left| \sum_j \frac{f''_j}{f'_j} \times f'_j \exp[2\pi i \mathbf{h} \cdot \mathbf{r}_j] \right| \\ &= \frac{f''_j}{f'_j} \times \left| \sum_j f'_j \exp[2\pi i \mathbf{h} \cdot \mathbf{r}_j] \right| = \frac{f''}{f'} \times |F_H|, \end{aligned}$$

$$|F_{PH(+)}| - |F_{PH(-)}| = \frac{2f''}{f'} |F_H| \sin(\alpha_{PH} - \alpha_H) \quad (7.29)$$

or

$$\begin{aligned}\Delta|F|_{\text{ano}} &= |F_H| \sin(\alpha_{\text{PH}} - \alpha_H), \\ (\Delta|F|_{\text{ano}})^2 &= |F_H|^2 \sin^2(\alpha_{\text{PH}} - \alpha_H) \\ &= \frac{1}{2}|F_H|^2 - \frac{1}{2}|F_H|^2 \cos 2(\alpha_{\text{PH}} - \alpha_H).\end{aligned}\tag{7.30}$$

As in the derivation of the  $(\Delta|F|_{\text{iso}})^2$  Patterson, we obtain two terms. The second term leads to noise in the Patterson map and the first one leads to the Patterson peaks of the heavy atoms.

---

It is interesting to compare the coefficients for the isomorphous and the anomalous Patterson:

$$\begin{aligned}(\Delta|F|_{\text{iso}})^2 &= |F_H|^2 \cos^2(\alpha_{\text{PH}} - \alpha_H) \\ \frac{(\Delta|F|_{\text{ano}})^2}{(\Delta|F|_{\text{iso}})^2 + (\Delta|F|_{\text{ano}})^2} &= \frac{|F_H|^2 \sin^2(\alpha_{\text{PH}} - \alpha_H)}{|F_H|^2}\end{aligned}$$

It is clear that a Patterson summation calculated with the coefficients

$$(\Delta|F|_{\text{iso}})^2 + (\Delta|F|_{\text{ano}})^2$$

will give, within the framework of the approximations made, an exact Patterson map of the heavy atoms, or at least a map with lower noise than the isomorphous or anomalous Patterson summation themselves.

## 7.10. One Common Origin for All Derivatives

If a number of heavy atom derivatives have been used for the phase determination, the position of the heavy atoms in all derivatives should be determined with respect to the same origin. In some space groups, it is not a serious problem to find a common origin because crystal symmetry limits the choice of origin. An example is given in Figure 7.14. The origin can be chosen in the positions I, II, III, or IV at  $z = 1/4$  or  $3/4$ . The choice has an effect on the phase angles. For instance, for the  $(h k 0)$  reflections:

Origin in I:

$$\mathbf{F}_{hk0} = \sum_j f_j \exp[2\pi i(hx_j + ky_j)]$$

Origin in II:

$$\mathbf{F}_{hk0} = \sum_j f_j \exp\left[2\pi i\left(hx_j + k\left\{y_j - \frac{1}{2}\right\}\right)\right] \sum_j f_j \exp[2\pi i(hx_j + ky_j) - i\pi k]$$

The phase angles stay the same if  $k$  is even, but they change by  $\pi$  if  $k$  is odd. By comparing the sets of protein phase angles obtained from different heavy

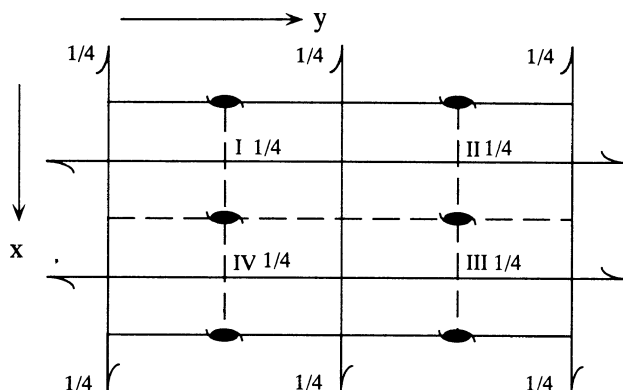


Figure 7.14. A unit cell (space group  $P2_12_12_1$ ) with origin at the midpoint of three nonintersecting pairs of parallel 2-fold screw axes: at position I, II, III, or IV at  $z = 1/4$  or  $3/4$ .

atom derivatives, one can easily determine a common origin. In another method, the protein phase angles are derived for a centrosymmetric projection from one derivative and then a difference Fourier is calculated for a second derivative. These preliminary heavy atom positions are now also fixed with respect to the same origin. For space groups with lower symmetry, the origin problem is different. For instance, in monoclinic space groups with the 2-fold axis along  $b$ , a common origin can easily be found in the  $xz$ -plane, but not along  $y$ . It is somewhere between  $y = 0$  and 1. A very straightforward method of finding a common origin is to calculate a difference Fourier summation with  $\{|F_{PH2}| - |F_P|\} \exp[\alpha_P]$ , where the phase angles  $\alpha_P$  are derived from derivative 1.  $|F_{PH2}|$  are the structure factor amplitudes for derivative 2. The “common origin” problem could also be solved, at least in principle, if a derivative could be prepared in which heavy atoms of type 1 and type 2 are jointly attached to the protein. A difference Patterson summation would then correspond to a structure containing both the heavy atoms 1 and 2. The coefficients for calculating this Patterson summation are

$$\begin{aligned} \mathbf{F}_{H_1+H_2} \mathbf{F}_{H_1+H_2}^* &= |\mathbf{F}_{H_1+H_2}|^2 = (\mathbf{F}_{H_1} + \mathbf{F}_{H_2})(\mathbf{F}_{H_1}^* + \mathbf{F}_{H_2}^*) \\ &= \mathbf{F}_{H_1} \mathbf{F}_{H_1}^* + \mathbf{F}_{H_2} \mathbf{F}_{H_2}^* + \mathbf{F}_{H_1} \mathbf{F}_{H_2}^* + \mathbf{F}_{H_1}^* \mathbf{F}_{H_2} \end{aligned} \quad (7.31)$$

I
II
III
IV.

The coefficients I give rise to the self-Patterson peaks of the heavy atoms 1, the coefficients II give rise to the self-Patterson peaks of the atoms 2, and the coefficients III give rise to cross-Patterson peaks between 1 and 2. Coefficient IIIa leads to cross-peaks on positions  $\mathbf{r}_{H_1} - \mathbf{r}_{H_2}$  and coefficient IIIb leads to the centrosymmetrically related cross-peaks  $\mathbf{r}_{H_2} - \mathbf{r}_{H_1}$ . For the derivation, see below.

---

**The Peaks in a Patterson Map If Two Kinds of Heavy Atoms Have Been Attached to the Protein Simultaneously**



To obtain the value of the Patterson at position  $\mathbf{u}$ , we scan, in principle, through the electron density in the real unit cell with a vector  $\mathbf{u}$  and calculate

$$P(\mathbf{u}) = \int_{\mathbf{r}} \rho(\mathbf{r}) \times \rho(\mathbf{r} + \mathbf{u}) dv.$$

$P(\mathbf{u})$  has a high value (a peak) if at both  $\mathbf{r}$  and  $\mathbf{r} + \mathbf{u}$  the electron density is high. For the cross-peaks,  $P(\mathbf{u})$  is high if the vector  $\mathbf{u}$  begins at a high density in the first heavy atom structure ( $\rho_1$ ) and ends at a high density in the second heavy atom structure ( $\rho_2$ );

$$P(\mathbf{u}) = \int_{\mathbf{r}_1} \rho_1(\mathbf{r}_1) \times \rho_2(\mathbf{r}_2) dv,$$

with

$$\mathbf{r}_2 = \mathbf{r}_1 + \mathbf{u} \text{ or } \mathbf{u} = \mathbf{r}_2 - \mathbf{r}_1,$$

$$\rho_1(\mathbf{r}_1) = \frac{1}{V} \sum_{\mathbf{S}} \mathbf{F}_1(\mathbf{S}) \exp[-2\pi i \mathbf{r} \cdot \mathbf{S}],$$

$$\rho_2(\mathbf{r}_1 + \mathbf{u}) = \frac{1}{V} \sum_{\mathbf{S}'} \mathbf{F}_2(\mathbf{S}') \exp[-2\pi i (\mathbf{r}_1 + \mathbf{u}) \cdot \mathbf{S}'].$$

Replace  $\mathbf{S}'$  by  $-\mathbf{S}'$  and  $\mathbf{F}_2(-\mathbf{S}')$  by  $\mathbf{F}_2^*(\mathbf{S}')$ :

$$\rho_2(\mathbf{r}_1 + \mathbf{u}) = \frac{1}{V} \sum_{\mathbf{S}'} \mathbf{F}_2^*(\mathbf{S}') \exp[2\pi i (\mathbf{r}_1 + \mathbf{u}) \cdot \mathbf{S}'],$$

$$\rho_1(\mathbf{r}_1) \times \rho_2(\mathbf{r}_1 + \mathbf{u}) = \frac{1}{V^2} \sum_{\mathbf{S}} \sum_{\mathbf{S}'} \mathbf{F}_1(\mathbf{S}) \mathbf{F}_2^*(\mathbf{S}') \exp[2\pi i \mathbf{r}_1(\mathbf{S}' - \mathbf{S}) + 2\pi i \mathbf{u} \cdot \mathbf{S}'],$$

$$\begin{aligned} \int_{\mathbf{r}_1} \rho_1(\mathbf{r}_1) \times \rho_2(\mathbf{r}_1 + \mathbf{u}) dv &= P(\mathbf{u}) \\ &= \frac{1}{V^2} \sum_{\mathbf{S}} \sum_{\mathbf{S}'} \mathbf{F}_1(\mathbf{S}) \mathbf{F}_2^*(\mathbf{S}') \exp[2\pi i \mathbf{u} \cdot \mathbf{S}'] \int_{\mathbf{r}_1} \exp[2\pi i \mathbf{r}_1(\mathbf{S}' - \mathbf{S})] dv. \end{aligned}$$

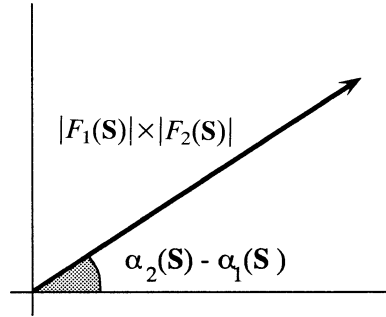
The integral on the right is zero unless

$$\mathbf{S}' - \mathbf{S} = 0 \text{ or } \mathbf{S}' = \mathbf{S}.$$

Therefore,

$$\begin{aligned} P(\mathbf{u}) &= \frac{1}{V^2} \sum_{\mathbf{S}} \mathbf{F}_1(\mathbf{S}) \mathbf{F}_2^*(\mathbf{S}) \exp[2\pi i \mathbf{u} \cdot \mathbf{S}] \int_{\mathbf{r}_1} 1 dv \\ &= \frac{1}{V} \sum_{\mathbf{S}} \mathbf{F}_1(\mathbf{S}) \mathbf{F}_2^*(\mathbf{S}) \exp[2\pi i \mathbf{u} \cdot \mathbf{S}] \\ &= \frac{1}{V} \sum_{\mathbf{S}} \mathbf{F}_1^*(\mathbf{S}) \mathbf{F}_2(\mathbf{S}) \exp[-2\pi i \mathbf{u} \cdot \mathbf{S}]. \end{aligned}$$

Figure 7.15. A cross-Patterson function between two heavy atom derivatives has Fourier terms with coefficients  $|F_1(\mathbf{S})| \times |F_2(\mathbf{S})| \exp[-i\{\alpha_2(\mathbf{S}) - \alpha_1(\mathbf{S})\}]$ .



$\mathbf{S}$  has been replaced by  $-\mathbf{S}$  because a Fourier summation is calculated with  $\exp[-2\pi i \mathbf{u} \cdot \mathbf{S}]$ . The coefficients in this Fourier summation are

$$\mathbf{F}_1^*(\mathbf{S})\mathbf{F}_2(\mathbf{S}) = |F_1(\mathbf{S})| \times |F_2(\mathbf{S})| \exp[i\{\alpha_2(\mathbf{S}) - \alpha_1(\mathbf{S})\}]$$

(see Figure 7.15). This result tells us that the Fourier summation will give a non-centrosymmetric structure of  $P(\mathbf{u})$  with peaks at the positions  $\mathbf{u} = \mathbf{r}_2 - \mathbf{r}_1$ .

If we use the coefficients

$$\mathbf{F}_1(\mathbf{S})\mathbf{F}_2^*(\mathbf{S}) = |F_1(\mathbf{S})| \times |F_2(\mathbf{S})| \exp[-i\{\alpha_2(\mathbf{S}) - \alpha_1(\mathbf{S})\}],$$

then  $P(\mathbf{u})$  has no peaks at the positions  $\mathbf{r}_2 - \mathbf{r}_1$  but, instead, at the centrosymmetrically related positions  $\mathbf{r}_1 - \mathbf{r}_2$ .

We summarize the four coefficients of the Patterson summation for the structure that would contain the heavy atoms of type 1 and type 2 as follows:

- I.  $\mathbf{F}_{H_1}\mathbf{F}_{H_1}^*$ : phase angle 0; Patterson of atoms 1  $\rightarrow$  1.
- II.  $\mathbf{F}_{H_2}\mathbf{F}_{H_2}^*$ : phase angle 0; Patterson of atoms 2  $\rightarrow$  2.
- IIIa.  $\mathbf{F}_{H_1}\mathbf{F}_{H_2}^*$ : phase angle  $\alpha_1 - \alpha_2$ ; Fourier with peaks at the end of the vectors  $\mathbf{u}$  that begin at a density on position  $\mathbf{r}_2$  in structure 2 and have their end on position  $\mathbf{r}_1$  in structure 1:  $\mathbf{u} = \mathbf{r}_1 - \mathbf{r}_2$ .
- IIIb.  $\mathbf{F}_{H_1}^*\mathbf{F}_{H_2}$ : phase angle  $\alpha_2 - \alpha_1$ ; Fourier with peaks at the end of the vectors  $\mathbf{u} = \mathbf{r}_2 - \mathbf{r}_1$ .

## 7.11. Refinement of the Heavy Atom Parameters Using Preliminary Protein Phase Angles

After the heavy atom structure has been derived from a Patterson map, the heavy atom parameters can be improved (refined) by modifying them in such a way that  $|F_{\text{PH}}(\text{obs})|$  and  $|F_{\text{PH}}(\text{calc})|$  approach each other as close as possible. The refinement

is carried out by means of the method of least squares or maximum likelihood. The least squares method will be discussed briefly in this section. For a more extensive discussion, see Section 13.2.1 of Chapter 13, and for the maximum likelihood method, see Section 13.2.2.

---

### The Method of Least Squares

In crystallography, the measured dataset has for each reflection  $(hkl)$  an intensity  $I(hkl)$  from which the amplitude of the structure factor  $|F_{\text{obs}}(hkl)|$  can be derived. From the preliminary model, values for the structure factors  $F_{\text{calc}}(hkl)$  can be calculated and in the refinement procedure the values of  $|F_{\text{calc}}(hkl)|$  should be brought as close as possible to  $|F_{\text{obs}}(hkl)|$  for all reflections  $(hkl)$ .  $|F_{\text{calc}}|$  can be varied by changing the parameters of the model. For some reflections,  $|F_{\text{calc}}|$  will be larger than  $|F_{\text{obs}}|$ , and for others, it is just the other way around. We assume that the  $|F_{\text{obs}}|$  values are free from systematic errors and distributed as in a Gaussian error curve (see Section 5.1 of Chapter 5) around their real values  $|F_{\text{real}}|$ , which means that the probability  $P$  of finding a value  $|F_{\text{obs}}(hkl)|$  for the reflection  $(hkl)$  between  $|F_{\text{obs}}(hkl)|$  and  $|F_{\text{obs}}(hkl)| + d|F_{\text{obs}}(hkl)|$  is

$$P(hkl) = \frac{1}{\sigma\sqrt{2\pi}} \exp\left[-\frac{\{|F_{\text{obs}}(hkl)| - |F_{\text{real}}(hkl)|\}^2}{2\sigma^2}\right] d|F_{\text{obs}}(hkl)|;$$

$\sigma^2$  is the variance caused by arbitrary errors in the measurements:

$$\sigma^2 = \int_{-\infty}^{+\infty} \{|F_{\text{obs}}(hkl)| - \overline{|F_{\text{obs}}(hkl)|}\}^2 P(hkl) d|F_{\text{obs}}(hkl)|.$$

Normalization requires

$$\int_{-\infty}^{+\infty} P(hkl) d\{|F_{\text{obs}}(hkl)|\} = 1.$$

With the assumption that the errors in the  $|F_{\text{obs}}(hkl)|$  values for different reflections are independent of each other, the total probability  $P$  for finding a certain set of  $|F_{\text{obs}}(hkl)|$  is

$$\begin{aligned} P &= \prod_{hkl} P(hkl) \\ &= \prod_{hkl} \frac{1}{\sigma(hkl)\sqrt{2\pi}} \exp\left[-\frac{\{|F_{\text{obs}}(hkl)| - |F_{\text{real}}(hkl)|\}^2}{2\sigma^2(hkl)}\right] d|F_{\text{obs}}(hkl)| \\ &= \exp\left[-\sum_{hkl} \frac{\{|F_{\text{obs}}(hkl)| - |F_{\text{real}}(hkl)|\}^2}{2\sigma^2(hkl)}\right] \times \prod_{hkl} \frac{1}{\sigma(hkl)\sqrt{2\pi}} d|F_{\text{obs}}(hkl)|. \end{aligned}$$

The problem is that the real values of the  $F(hkl)$ 's are unknown. However, it is assumed that these real values can be approximated by the calculated values. The goal is to bring the set of  $|F_{\text{calc}}|$ 's as close as possible to the  $|F_{\text{obs}}|$ 's. In the method

of least squares, this is defined as occurring at the maximum value of  $P$ . In other words, the optimal set of  $|F_{\text{calc}}|$ 's is the one that has the highest probability  $P$ . A maximum for  $P$  is obtained for a minimum of

$$\sum_{hkl} \frac{\{|F_{\text{obs}}(hkl)| - |F_{\text{calc}}(hkl)|\}^2}{2\sigma^2(hkl)}.$$

This is the principle of least squares.

The least squares minimum is found by varying the  $|F_{\text{calc}}(hkl)|$ 's. This is done by differentiating with respect to the parameters of the atoms and setting the derivatives equal to zero.

The parameters of the heavy atoms, as derived from the difference Pattersons, can be improved (refined) with the "lack of closure" method (Dickerson et al., 1968). This requires preliminary values for the protein phase angles  $\alpha_P$ . With the value of  $\alpha_P$  known, the vector triangle  $\mathbf{F}_P + \mathbf{F}_H = \mathbf{F}_{PH}$  (Figure 7.16a) can be drawn for each reflection. The length and direction of  $\mathbf{F}_P$  and  $\mathbf{F}_H$  are known and  $\mathbf{F}_{PH}$  is then pointed to the end of vector  $\mathbf{F}_H$ . In practice, the observed amplitude  $|F_{PH}|$  will be too short or too long to exactly reach the end point of  $\mathbf{F}_H$  (Figure 7.16b). The difference is called the "lack of closure error"  $\epsilon$ . It is due to measurement errors and nonisomorphism. The goal of the refinement is to make the errors  $\epsilon$  as small

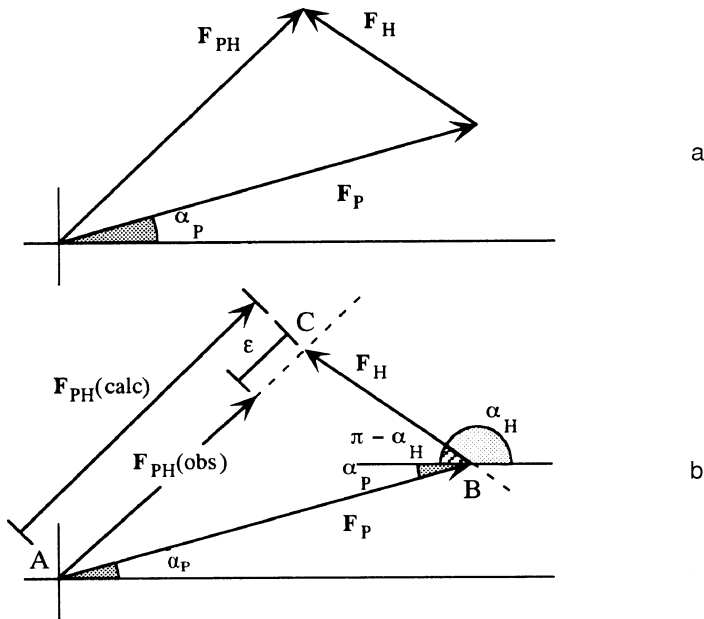


Figure 7.16. (a) The ideal isomorphous situation in which the vector triangle  $\mathbf{F}_P + \mathbf{F}_H = \mathbf{F}_{PH}$  closes exactly. Normally, this is not true and the observed and calculated values of  $|F_{PH}|$  differ by the lack of closure error  $\epsilon$  (b).

as possible. In other words, the criterion of the refinement is to bring  $|F_{\text{PH}}|_{\text{calc}}$  as close as possible to  $|F_{\text{PH}}|_{\text{obs}}$ . For each reflection,  $|F_{\text{PH}}|_{\text{calc}}$  is calculated with the cosine rule:

$$|F_{\text{PH}}|_{\text{calc}} = \{|F_P|^2 + |F_H|^2 + 2|F_P| \times |F_H| \cos(\alpha_H - \alpha_P)\}^{1/2}.$$

For the heavy atom derivative  $j$ ,  $\varepsilon_j$  is defined as

$$\varepsilon_j = \{k_j(|F_{\text{PH}}|_{\text{obs}})_j - (|F_{\text{PH}}|_{\text{calc}})_j\}, \quad (7.32)$$

where  $k_j$  is a scaling factor. Original refinement procedures were based on least squares, minimizing the function

$$E_j = \sum_{hkl} m_{hkl} \varepsilon_j(hkl)^2. \quad (7.33)$$

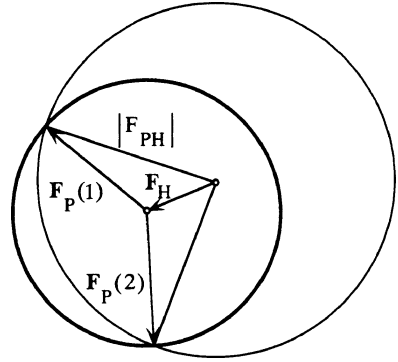
The variables are the parameters of the heavy atoms in derivative  $j$ : atomic coordinates, occupancy, and temperature factor. Their value determines the length and direction of  $\mathbf{F}_H$  and, therefore, its end point in the Argand diagram. Moreover, the scale factor  $k_j$  can be refined.  $m_{hkl}$  is a weighting factor that indicates the quality of the phase angle;  $m$  is the figure of merit, defined in the next section. After one or a few refinement cycles, new values for the protein phase angles  $\alpha_P$  are calculated, as will be described in the next section. It is advised to calculate the protein phase angles without using the isomorphous derivative  $j$  under consideration. Otherwise, the result depends to some extent on the input data. This is especially important if one derivative dominates the phase angle determination (Blow and Matthews, 1973).

Least squares refinement of diffraction data is not always the best procedure for finding optimal agreement between model data and experimental data. This will be pointed out in Section 13.2.2 of Chapter 13. In principle, a better technique employs a maximum likelihood algorithm in which data are replaced by their probabilities. For instance, in the program MLPHARE for the refinement of heavy atom positions, the single value of the protein phase angle is replaced by an integrated value of all phase angles, weighted by their likelihood (Otwinowski, 1991). This will be further discussed in Section 13.2.3 of Chapter 13 after an introduction to the principle of maximum likelihood (Section 13.2.2).

## 7.12. Protein Phase Angles

After the refinement of heavy atom positions, protein phase angles can be determined. The principle, due to Harker (1956), is as follows. Draw a circle with radius  $|F_P|$ . From the center of the circle vector  $-\mathbf{F}_H$  is drawn and then a second circle with radius  $|F_{\text{PH}}|$  and with its center at the end of vector  $-\mathbf{F}_H$  (Figure 7.17). The intersections of the two circles correspond to two equally probable protein phase angles, because for both points, the triangle  $\mathbf{F}_{\text{PH}} = \mathbf{F}_P + \mathbf{F}_H$  closes exactly. With a second heavy atom derivative, one can, in principle, distinguish between the two

Figure 7.17. Harker construction for protein phase determination. In the isomorphous replacement method, each heavy atom derivative gives two possibilities for the protein phase angle  $\alpha_P$ , corresponding to the two vectors  $\mathbf{F}_P(1)$  and  $\mathbf{F}_P(2)$ .



alternatives. However, because of errors, an exact intersection of the three circles with radii  $|F_P|$ ,  $|F_{PH(1)}|$ , and  $|F_{PH(2)}|$  will usually not be obtained, and some uncertainty as to the correct phase angle  $\alpha_P$  remains. The errors are introduced in X-ray intensity data collection or by poor isomorphism. In practice, more than two derivatives are used, if they are available, and, therefore, the method is called multiple isomorphous replacement (MIR).

For mathematical reasons, the best procedure to follow is the following: The vector triangle  $\mathbf{F}_{PH} = \mathbf{F}_P + \mathbf{F}_H$  closes exactly only at the two intersection points of the circles with radii  $|F_P|$  and  $|F_{PH}|$  (see Figure 7.17). These intersection points correspond to two values of  $\alpha_P$ . For all other values of  $\alpha_P$ , a closure error remains:

$$\varepsilon = AC - |F_{PH}|_{\text{obs}}$$

(see Figure 7.16b). It is assumed that all errors concern the length of  $\mathbf{F}_{PH}$  and that both  $\mathbf{F}_H$  and  $\mathbf{F}_P$  are error-free. For every value of the protein phase angle  $\alpha_P$ , the length of  $AC$  in Figure 7.16b can be calculated with the cosine rule in triangle  $ABC$ , because  $|F_P|$  and  $\mathbf{F}_H$  are known.  $\varepsilon(\alpha)$  is the difference between this calculated  $AC$  and the observed value for  $|F_{PH}|$  for a protein phase angle  $\alpha$ . If  $\varepsilon(\alpha)$  is smaller, chances for having the correct protein phase angle  $\alpha$  are higher.

A Gaussian probability distribution is assumed for  $\varepsilon$ , and for each reflection in the diffraction pattern of one derivative,

$$P(\alpha) = P(\varepsilon) = N \exp \left[ -\frac{\varepsilon^2(\alpha)}{2E^2} \right],$$

where  $N$  is a normalization factor. It is related to the fact that the phase angle  $\alpha$  is somewhere between 0 and  $2\pi$ :

$$\int_0^{2\pi} P(\alpha) d\alpha = 1;$$

$E^2$  is the “mean square” value of  $\varepsilon$ . If  $E$  is small, the probability curves will have sharp peaks and the protein phase angle is well determined, but for large  $E$ -values,

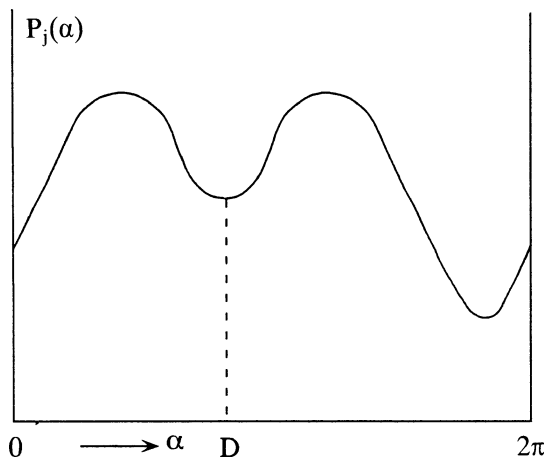


Figure 7.18. The probability  $P_j(\alpha)$  for a reflection having  $\alpha$  as the correct phase angle derived from derivative  $j$  is shown as a function of all angles between 0 and  $2\pi$ .

they are very poorly determined. For each reflection,  $P(\alpha)$  is obtained as a function of  $\alpha$  by calculating it for every few degrees around the phase circle. This function is symmetrical around a point  $D$  in Figure 7.18. The two equally high peaks to the left and right of  $D$  correspond to the intersection points of the circles with radii  $|F_P|$  and  $|F_{PH}|$ . These curves can be calculated for each reflection and each of the  $n$  heavy atom derivatives. The total probability for each reflection is obtained by multiplying the separate probabilities (see below):

$$P(\alpha) = \prod_{j=1}^n P_j(\alpha) = N' \exp \left[ - \sum_j \frac{\varepsilon_j^2(\alpha)}{2E_j^2} \right]. \quad (7.34)$$

The total  $P(\alpha)$  curve will normally not show the symmetry of Figure 7.18, but will look like Figure 7.19a or 7.19b.

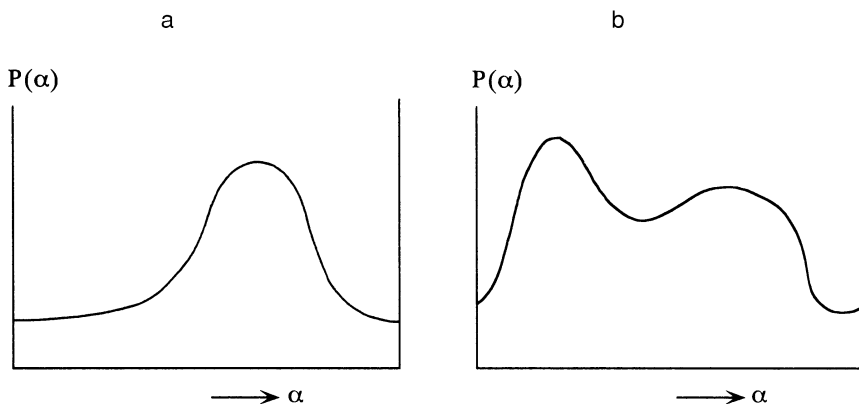


Figure 7.19. Two examples of the total probability  $P(\alpha)$  for the phase angle  $\alpha$  of a reflection as derived from more than one derivative.

---

The fundamental rule for combination of probabilities is as follows:

If events are independent of each other, the probability of their occurring at the same time is the *product* of the probabilities of their separate occurrence.

Probabilities should be *added* if the events exclude each other. For instance, the chance that a particular plane of a die is on top is  $1/6$ , but the chance that a 1 or a 5 is on top is  $1/6 + 1/6 = 1/3$ .

---

If an electron density map for a protein is calculated with a certain set of phase angles  $\alpha(hkl)$ , the probability that the particular map is correct is equal to  $\prod_{hkl} P_{hkl}(\alpha_{hkl})$ . However, how can we find the best Fourier map? At first thought, one would choose for each reflection that value  $\alpha(hkl)$  for which  $P_{hkl}(\alpha_{hkl})$  has a maximum and, therefore, their product  $\prod_{hkl} P_{hkl}(\alpha_{hkl})$  also has a maximum value. Accepting the maximum value of  $\prod_{hkl} P_{hkl}(\alpha_{hkl})$  would result in the most probable electron density map. However, this most probable map is not necessarily the best electron density map. This is defined as the map with the minimum mean square error in the electron density due to errors in the phase angles. The reason is that the function

$$P_{hkl}(\alpha) = \prod_{j=1}^n P_j(\alpha_{hkl})$$

does not always have a single maximum, but sometimes two, or is asymmetric around its maximum (Figure 7.19). In calculating the most probable electron density map, this is completely neglected. The best solution for this problem is as follows. For the structure factor  $\mathbf{F}_{hkl} = |F_{hkl}| \exp[i\alpha_{hkl}]$ , the amplitude is known, whereas from the experimental data of the derivatives, the probability distribution  $P_{hkl}(\alpha)$  for the phase angle  $\alpha$  can be derived. The probability for the structure factor  $\mathbf{F}_{hkl}$  to be  $|F_{hkl}| \exp[i\alpha]$  is thus  $P_{hkl}(\alpha)$ . The best estimate,  $\mathbf{F}_{hkl}(\text{best})$ , for the actual structure factor on the basis of the present experimental data is given by the least squares criterion:

$$Q = \int_{\alpha} \{P_{hkl}(\alpha) |F_{hkl}| \exp[i\alpha] - \mathbf{F}_{hkl}(\text{best})\}^2 d\alpha$$

should be a minimum. With

$$\frac{dQ}{d\{\mathbf{F}_{hkl}(\text{best})\}} = 0,$$

it is found that

$$\mathbf{F}_{hkl}(\text{best}) = \int_{\alpha} \{P_{hkl}(\alpha) |F_{hkl}| \exp[i\alpha]\} d\alpha = |F_{hkl}| \mathbf{m}, \quad (7.35)$$



with

$$\mathbf{m} = \int_{\alpha} \{P_{hkl}(\alpha) \exp[i\alpha]\} d\alpha; 0 \leq |m| \leq 1$$

As a result, the best value of  $\mathbf{F}_{hkl}$  is obtained by taking the weighted average over the range of possible  $\mathbf{F}_{hkl}$ 's.  $\mathbf{F}_{hkl}(\text{best})$  points to the center of gravity ("centroid") of the probability distribution of  $\mathbf{F}$  (Figure 7.20). In practice, the integration is replaced by a summation in steps of, say,  $5^\circ$  and

$$\mathbf{F}_{\text{best}} = \frac{\sum P(\alpha)\mathbf{F}(\alpha)}{\sum P(\alpha)}. \quad (7.36)$$

With  $\mathbf{m} = m \exp[i\alpha(\text{best})]$ , Equation (7.35) becomes

$$\mathbf{F}_{hkl}(\text{best}) = |F_{hkl}|m \exp[i\alpha(\text{best})] \quad (7.37)$$

and

$$m = \frac{|F_{hkl}(\text{best})|}{|F_{hkl}|}; \quad (7.38)$$

$m$  is called the "figure of merit."

If the  $\mathbf{F}_{hkl}(\text{best})$  values are used in the calculation of the electron density distribution, a map is obtained that minimizes the mean square error in the electron density due to errors in the phase angles. The interpretation of the isomorphous replacement map in terms of a polypeptide chain produces a first model of the protein molecular structure that is certainly not the final model. That final model is obtained after refinement, the aim of which is to adjust the model to find a closer agreement between the structure factors calculated on the basis of the model and the observed structure factors (Chapter 13). In the above-described procedure, which is due to Blow and Crick (1959), errors in the intensity measurements and in the heavy atom model are lumped together and treated as Gaussian errors in the measured  $|F_{\text{PH}}|$ .

This is, of course, an approximation and more detailed treatments of the propagation of the various errors into the protein phase angles have been given (Read, 1990a). The difference between these other procedures, which include errors, and the Blow and Crick procedure with sharp circles is schematically represented in Figure 7.21.

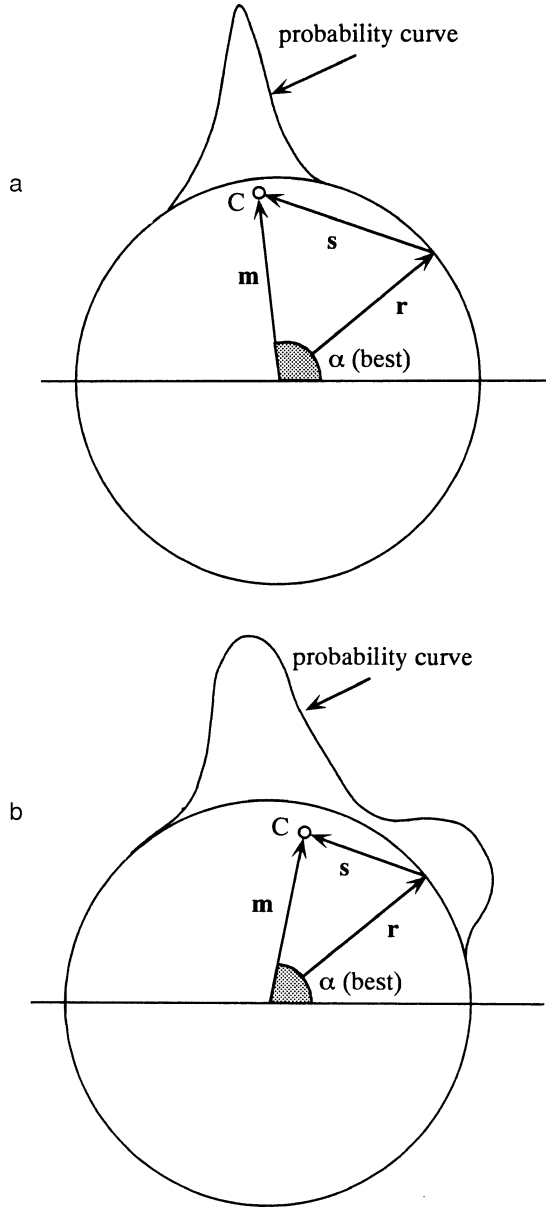


Figure 7.20. Three probability curves for the protein phase angle. The baseline for the curves is the circle with radius  $|r| = 1$ .  $C$  is the centroid of the probability distribution and  $\mathbf{m}$  is the vector that connects the center of the circle with  $C$ . In other words, the more spread out the probability curve is, the poorer is the determination of the phase angle and the shorter is  $\mathbf{m}$ . (a) The sharp peak of the probability curve positions point  $C$  close to the circle; (b) it is somewhat further away; (c) it is close to the center of the circle.

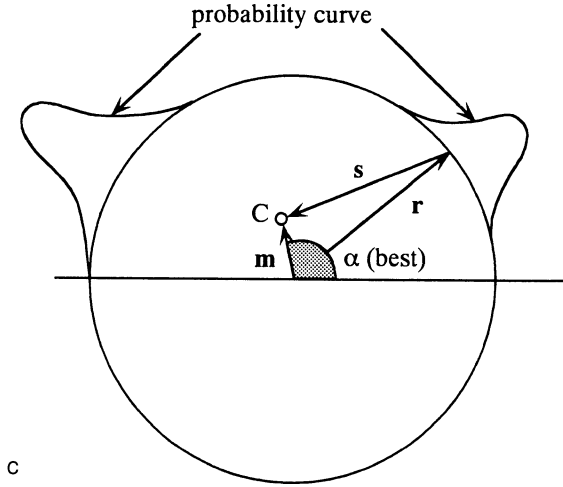


Figure 7.20. (Continued)

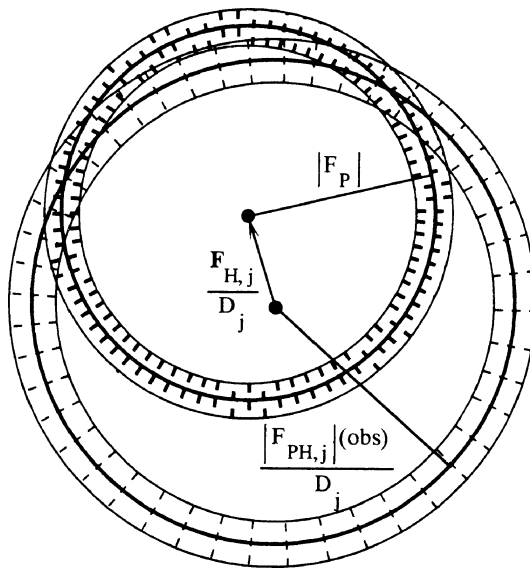


Figure 7.21. Schematic representation of the combination of information from native and derivative data. The shaded areas give an impression of the Gaussian distribution for errors in  $|F_P|$  and  $|F_{PH}|$ . Where the shaded areas cross, a high joint probability exists for the true structure factor conditional on the observed structure factor amplitude for the native protein (dark dashes) and conditional on the observed structure factor amplitude  $|F_{PH,j}|$  and the calculated structure factor  $F_{H,j}$  for the heavy atom derivative  $j$  (light dashes).  $D_j$  is a multiplication factor that is 1 for perfect isomorphism, but is usually less than 1;  $D_j$  will be discussed in Section 15.6 of Chapter 15.

### 7.13. The Remaining Error in the Best Fourier Map

The isomorphous replacement method provides us with a preliminary model of the protein structure; a final model is obtained only after refinement of the structure. Therefore, from a practical point of view, we are not particularly interested in the errors that are present in a best Fourier map as calculated in the previous section. From an instructional point of view, however, it is worthwhile to consider these errors.

In Figure 7.20, phase circles are drawn with radius  $|r| = 1$ . The curve that describes the probability that the phase angle is correct is drawn on the circle as a baseline. The centroid of the probability distribution is not on the circle, but at  $C$  somewhat closer to the center of the circle. If the probability distribution is sharp, as in Figure 7.20a, the centroid is nearly on the circle and the phase angle is well defined. If the distribution is as shown in Figure 7.20c, the centroid is near the center of the circle and the phase angle is extremely poorly defined.  $\mathbf{m}$  is the vector from the center of the circle to the centroid  $C$ ;  $\alpha(\text{best})$  is the best phase angle. If  $\alpha$  is an arbitrary phase angle,

$$\mathbf{F}(\text{best}) = \frac{\sum P(\alpha)\mathbf{F}(\alpha)}{\sum P(\alpha)},$$

dividing by  $|F|$  gives

$$m \cdot \exp[i\alpha(\text{best})] = \mathbf{m} = \frac{\sum P(\alpha)\mathbf{r}(\alpha)}{\sum P(\alpha)},$$

and because  $\mathbf{r}(\alpha) = 1 \cdot \exp[i\alpha]$ ,

$$\mathbf{m} = \frac{\sum P(\alpha)\exp(i\alpha)}{\sum P(\alpha)}. \quad (7.39)$$

The real part of vector  $\mathbf{m}$  is its projection on the horizontal axis in the Argand diagram,

$$m \cos \alpha(\text{best}) = \frac{\sum P(\alpha)\cos(\alpha)}{\sum P(\alpha)}$$

and its imaginary part is

$$m \sin \alpha(\text{best}) = \frac{\sum P(\alpha)\sin(\alpha)}{\sum P(\alpha)}.$$

If for every reflection the origin is moved from  $\alpha = 0$  to  $\alpha = \alpha(\text{best})$ , then  $\cos \alpha(\text{best}) \rightarrow 1$  and  $\sin \alpha(\text{best}) \rightarrow 0$ :

$$m = \frac{\sum P\{\alpha - \alpha(\text{best})\}\cos\{\alpha - \alpha(\text{best})\}}{\sum P(\alpha)} = \overline{\cos\{\alpha - \alpha(\text{best})\}}. \quad (7.40)$$

For reflections with a very well-defined phase angle both  $m$  and  $\overline{\cos\{\alpha - \alpha(\text{best})\}} \cong 1$ . In other words,  $\{\alpha - \alpha(\text{best})\}$  is very small for phase angles  $\alpha$ , which have a high value of  $P(\alpha)$ . If the curve for  $P(\alpha)$  shows a large spread, the value of  $\overline{\cos\{\alpha - \alpha(\text{best})\}}$  and of  $m$  is much smaller than 1. We can interpret  $m$  as the weighted mean of the cosine of the error in the phase angle.

Let us now estimate the error in the electron density map. Suppose that for reflection  $hkl$  the true structure factor is  $\mathbf{F}_{hkl}(\text{true})$ . However, because of errors in our dataset, it has been determined as  $\mathbf{F}_{hkl}(\text{best})$ . For  $\bar{h}\bar{k}\bar{l}$ , we have  $\mathbf{F}^*(\text{best})$  instead  $\mathbf{F}^*(\text{true})$ . The incorrect structure factors cause errors in the electron density map. The contribution to the error by reflections  $hkl$  and  $\bar{h}\bar{k}\bar{l}$  is, if we write  $\mathbf{F}_b$  for  $\mathbf{F}_{hkl}(\text{best})$  and  $\mathbf{F}_T$  for  $\mathbf{F}_{hkl}(\text{true})$ ,

$$\begin{aligned}\Delta\rho_{hkl} &= \frac{1}{V}\{(\mathbf{F}_b - \mathbf{F}_T)\exp[-2\pi i(hx + ky + lz)] \\ &\quad + (\mathbf{F}_b^* - \mathbf{F}_T^*)\exp[2\pi i(hx + ky + lz)]\}, \\ (\Delta\rho_{hkl})^2 &= \frac{1}{V^2}(\dots\dots\dots)^2\end{aligned}\quad (7.41)$$

Equation (7.41) contains the following terms on the right-hand side:

$$\begin{aligned}(\mathbf{F}_b - \mathbf{F}_T)^2 \exp[-4\pi i(hx + ky + lz)] &= (\mathbf{F}_b - \mathbf{F}_T)^2 \{\cos[\dots] - i \sin[\dots]\}, \\ (\mathbf{F}_b^* - \mathbf{F}_T^*)^2 \exp[4\pi i(hx + ky + lz)] &= (\mathbf{F}_b^* - \mathbf{F}_T^*)^2 \{\cos[\dots] + i \sin[\dots]\}, \\ 2(\mathbf{F}_b - \mathbf{F}_T)(\mathbf{F}_b^* - \mathbf{F}_T^*) &= 2|\mathbf{F}_b - \mathbf{F}_T|^2.\end{aligned}$$

If the average is taken over all positions  $x$ ,  $y$ , and  $z$  in the unit cell, the mean square value of  $\Delta\rho_{hkl}$  is obtained:  $\overline{(\Delta\rho_{hkl})^2}$ . Averaging over  $x$ ,  $y$ , and  $z$  makes all cosine and sine terms in Equation (7.41) equal to zero and the equation for  $\overline{(\Delta\rho_{hkl})^2}$  simplifies to

$$\overline{(\Delta\rho_{hkl})^2} = \frac{2}{V^2}|\mathbf{F}_b - \mathbf{F}_T|^2. \quad (7.42)$$

$\mathbf{F}_b = \mathbf{F}(\text{best})$  has a fixed length and phase angle, but  $\mathbf{F}_T$  is unknown and, therefore, also  $|\mathbf{F}_b - \mathbf{F}_T|^2$ . The best value is the weighted average over all possible phase angles for  $\mathbf{F}_T$ :

$$\overline{(\Delta\rho_{hkl})^2} = \frac{2}{V^2} \times \frac{\int_{\alpha=0}^{2\pi} P_{hkl}(\alpha)[|\mathbf{F}_{\text{best}} - \mathbf{F}(\alpha)|^2] d\alpha}{\int_{\alpha=0}^{2\pi} P_{hkl}(\alpha) d\alpha}. \quad (7.43)$$

Equation (7.43) tells us that the mean square error in the electron density is equal to  $(2/V^2) \times$  the variance in  $\mathbf{F}(\alpha)$  (see Section 5.1 of Chapter 5 on the Gauss error curve).

As earlier, the integration is replaced by a summation, and using

$$\begin{aligned}\mathbf{F}(\text{best}) &= |F| \times \mathbf{m}, \\ \mathbf{F}(\alpha) &= |F| \times \mathbf{r}, \\ |r| &= 1,\end{aligned}$$

$$\overline{(\Delta\rho_{hkl})^2} = \frac{2|F|^2}{V^2} \times \frac{\sum_{\alpha} P(\alpha)|\mathbf{m} - \mathbf{r}|^2}{\sum_{\alpha} P(\alpha)} = \frac{2|F|^2}{V^2} \times \frac{\sum_{\alpha} P(\alpha)|s|^2}{\sum_{\alpha} P(\alpha)}. \quad (7.44)$$

Applying the cosine rule gives

$$|s|^2 = |m|^2 + 1 - 2|m| \cos\{\alpha(\text{best}) - \alpha\}$$

for  $|s|^2$  (see Figure 7.20). Writing  $m$  for  $|m|$  and substituting  $|s|^2$  in Equation (7.44),

$$\begin{aligned} \overline{(\Delta\rho_{hkl})^2} &= \frac{2|F|^2}{V^2} \times \left\{ \frac{\sum_{\alpha} P(\alpha)}{\sum_{\alpha} P(\alpha)} (m^2 + 1) - \frac{2m \sum_{\alpha} P(\alpha) \cos\{\alpha(\text{best}) - \alpha\}}{\sum_{\alpha} P(\alpha)} \right\} \\ &= \frac{2|F|^2}{V^2} \times \{m^2 + 1 - 2m^2\} = \frac{2|F|^2}{V^2} \times (1 - m^2). \end{aligned} \quad (7.45)$$

This is the contribution to the mean square error in the electron density caused by errors in one reflection and its Bijvoet mate. Adding the contributions from all reflections,

$$\overline{(\Delta\rho)^2} = \frac{2}{V^2} \sum_h \sum_k \sum_l |F|_{hkl}^2 (1 - m_{hkl}^2), \quad (7.46)$$

where the summation is over the reflections in half of the reciprocal space. It can be derived that for difference Fourier maps a similar equation is valid:

$$\overline{\{\Delta(\Delta\rho)\}^2} = \frac{2}{V^2} \sum_h \sum_k \sum_l (\Delta|F|_{hkl})^2 (2 - m_{hkl}^2). \quad (7.47)$$

The extra  $(\Delta|F|_{hkl})^2$  is due to the intrinsic error in difference Fourier maps, which is due to the fact that the direction of  $\mathbf{F}_H$  is not known.

Suppose that the average  $m$  is 0.8 and  $m^2 = 0.64$ . For the normal Fourier map, we obtain

$$\overline{(\Delta\rho)^2} = 0.36 \times \left[ \frac{2}{V^2} \sum_h \sum_k \sum_l |F|_{hkl}^2 \right]$$

and

$$\overline{[(\Delta\rho)^2]}^{1/2} = 0.6 \times \left[ \frac{2}{V^2} \sum_h \sum_k \sum_l |F|_{hkl}^2 \right]^{1/2},$$

and for the difference Fourier map,

$$\overline{\{\Delta(\Delta\rho)\}^2} = 1.36 \times \left[ \frac{2}{V^2} \sum_h \sum_k \sum_l (\Delta|F|_{hkl})^2 \right].$$

If  $\Delta|F|$  is of the order of  $0.1 \times |F|$ , and, therefore,

$$(\Delta|F|)^2 = 0.01 \times |F|^2,$$

the error in the difference Fourier map is

$$\begin{aligned} \overline{\{\Delta(\Delta\rho)\}^2} &= 1.36 \times 0.01 \times \left[ \frac{2}{V^2} \sum_h \sum_k \sum_l (|F|_{hkl})^2 \right] \\ &= 0.0136 \times \left[ \frac{2}{V^2} \sum_h \sum_k \sum_l (|F|_{hkl})^2 \right], \\ \overline{\{\Delta(\Delta\rho)\}^2}^{1/2} &= 0.12 \times \left[ \frac{2}{V^2} \sum_h \sum_k \sum_l (|F|_{hkl})^2 \right]^{1/2}. \end{aligned}$$

This comparison between the errors in a Fourier and a difference Fourier map shows that the errors in a difference Fourier map are appreciably smaller than in a normal Fourier map. This is the reason that reasonably accurate data can be derived from a difference Fourier map.

## 7.14. The Single Isomorphous Replacement Method

A single heavy atom derivative gives two equally possible protein phase angles corresponding to the structure factors  $\mathbf{F}_P(1)$  and  $\mathbf{F}_P(2)$  (Figure 7.17). Only one of them is the correct phase angle. With a second heavy atom derivative, the choice can be made; but suppose that only one derivative is available. If the protein electron density map is then calculated with  $\mathbf{F}_P(1) + \mathbf{F}_P(2)$ , one can expect that the correct structure factors will lead to an acceptable map, whereas the incorrect ones will lead to noise in the map. The use of  $\mathbf{F}_P(1) + \mathbf{F}_P(2)$  in the single isomorphous replacement method is in fact the method of calculating the best electron density map.  $\mathbf{F}_P(1)$  and  $\mathbf{F}_P(2)$  each have a probability of 0.5 of being the correct structure factor. Therefore,

$$\mathbf{F}_P(\text{best}) = \frac{1}{2}[\mathbf{F}_P(1) + \mathbf{F}_P(2)].$$

This best structure factor,  $\mathbf{F}_P(\text{best})$ , points along  $\mathbf{F}_H$  (Figure 7.17) in the same or opposite direction of  $\mathbf{F}_H$ . It has either the phase angle  $\alpha_H$  of  $\mathbf{F}_H$  or  $\alpha_H + \pi$ , with  $\mathbf{F}_P(\text{best})$  within the smallest angle between  $\mathbf{F}_P(1)$  and  $\mathbf{F}_P(2)$ .

The single isomorphous replacement (SIR) method can work quite satisfactorily by producing sufficiently accurate protein phase angles for calculating an acceptable first electron density map. Its main problem is in a possible pseudocentrosymmetric relationship between the heavy atom positions. If the heavy atom arrangement has an exact center of symmetry, then for each reflection, the phase angles of  $\mathbf{F}_P(1)$  and  $\mathbf{F}_P(2)$  are symmetric to each other with respect to the real axis in the Argand diagram. A set of structure factors, all having a phase angle opposite to the correct one, will lead to an electron density map that is centrosymmetric to the correct map. Instead of having the correct map with noise superimposed, we have the correct map with the centrosymmetric map superimposed. As a result, the interpretation of the map is impossible. Although protein structures themselves

have no center of symmetry, the set of heavy atoms can have a pseudocenter of symmetry. This causes the appearance of the (undesirable) centrosymmetric protein structure in the electron density map. The result of the SIR method is appreciably improved if anomalous scattering by the heavy atoms is also taken into account in the phase determination of the protein (Section 9.2 of Chapter 9).

## Summary

1. The X-ray intensities of the native and the derivative structures should be measured as accurately as possible, because the method depends on relatively small differences between these intensities, especially if anomalous differences are used.
2. The scaling of the datasets is critical. If there are absorption differences due to the nonspherical shape of the crystals, or the solvent around the crystal, or the capillary, a correction for absorption must be applied.
3. It is an advantage but not an absolute necessity to have a low number of sites with a high occupancy, because it simplifies the interpretation of the difference Patterson map. Additional sites with low occupancy can be added later, after their locations are determined from difference Fourier maps.
4. After determining the position of the heavy atom sites, it should be checked whether the interatomic vectors correspond with peaks in the Patterson map. Calculation of an anomalous Patterson map and comparison with the isomorphous map give an indication of the significance of the anomalous signal.
5. If it is known that noncrystallographic symmetry is present (such as a 5-fold axis of symmetry within one molecule), this symmetry might also be present between the heavy atom sites. If it is, a vector search in the difference Patterson map should reveal it.



# Chapter 8

## Phase Improvement

### 8.1. Introduction

After a first set of protein phases is obtained using the isomorphous replacement method, the molecular replacement method, or the single- or multiple-wavelength anomalous diffraction method and an electron density map is calculated, the next step is the interpretation of the map in terms of the polypeptide chain. If this is successful and the major part of the chain can, indeed, be followed in the electron density map, refinement of the structure can begin. However, insufficient quality of the electron density map might hamper a complete and unambiguous tracing of the polypeptide chain, increasing the risk of introducing errors in the model, which cannot be easily removed during refinement. In such a case, refinement should be preceded by a process to improve the quality of the map through improvement of the protein phase angles (Podjarny et al., 1987). During phase improvement, all available information on the structure should be used (Brünger and Nilges, 1993). This information might be in one of the following forms:

1. The structure is partially known.
2. The protein molecules distinguish themselves as relatively high regions of electron density and their boundaries can be estimated. The electron density between them is then set to a constant value or adjusted otherwise.
3. Noncrystallographic symmetry within the asymmetric unit is present. As in method 2, molecular boundaries must then be determined and the solvent region modified. Moreover, the density of all molecules (or subunits of a molecule) related by noncrystallographic symmetry is averaged.
4. Correct protein electron density maps have a characteristic frequency distribution for the values of the electron density (histogram matching).

Methods 2 and 3 are examples of density modification methods. Usually, application of these methods improves the electron density map to such an extent that the interpretation is no longer a problem. The crystallographer is not necessarily restricted to the resolution limits set by the phase determination method. If the X-ray pattern of the native protein crystals allows, the data limit can be moved very gradually to higher resolution. We will now discuss these phase improvement methods in some detail.

## 8.2. The OMIT Map With and Without Sim Weighting

Frequently the interpretation of part of an electron density map is somewhat doubtful. For instance, a loop at the surface of the molecule cannot be traced satisfactorily. In such cases, it is useful to calculate an OMIT map—an electron density map with the observed structure factor amplitudes ( $|F|$ ) and with phase angles  $\alpha_K$ , calculated only for the part of the structure that is known correctly. This part should then show up in full height in the map, whereas the missing part is expected to show up at only about half of the actual height (Bhat, 1988; Bhat and Cohen, 1984). Because phase angles dominate electron density maps more than the amplitudes, such a map is biased toward the correctly known part of the structure (Read, 1997). The picture of the troublesome part can be improved by introducing a suitable weighting factor. A low weight should be given to the amplitudes of reflections for which the phase angles  $\alpha_K$  can be expected to differ appreciably from the correct phase angles, and more weight given to reflections for which this difference can be expected to be small. It is assumed that the best weights are those that minimize the mean square error in electron density due to the errors in the phase angles. It was shown by Sim (1959, 1960) that the best weights are

$$w = \frac{I_1(X)}{I_0(X)}$$

for noncentric reflections and

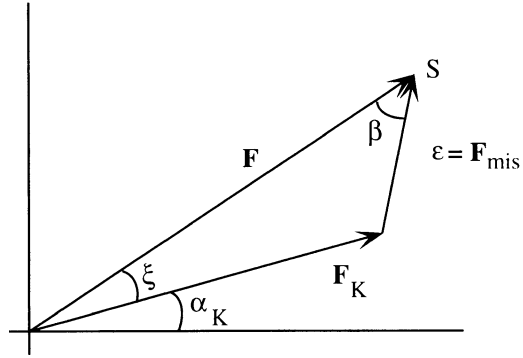
$$\tanh\left(\frac{X}{2}\right)$$

for centric reflections, where

$$X = \frac{2|F| \times |F_K|}{\sum_1^n f_i^2}, \quad (8.1)$$

$I_0(X)$  and  $I_1(X)$  are modified Bessel functions of order 0 and 1, respectively,  $|F|$  is the observed structure factor amplitude, and  $|F_K|$  is the amplitude for the known part of the structure (Figure 8.1). If  $f_i$ 's are atomic scattering factors for  $n$  missing atoms, then  $\sum_1^n f_i^2$  can be estimated from the structure factor amplitudes  $|F|$  and  $|F_K|$ . Bricogne (1976) suggested  $\frac{|F|^2 - |F_K|^2}{2|F|}$ , whereas Read (1986) proposed  $n(|F| - |F_K|)^2$ , with  $n = 1$  for centric and  $n = 2$  for noncentric reflections.

Figure 8.1. The structure factors involved in the calculation of an OMIT map.  $\mathbf{F}$  is the total structure factor for the reflection with an observed structure amplitude  $|F|$  and a phase angle  $\alpha_K + \xi$ .  $\mathbf{F}_K$  is the structure factor for the known part of the structure with phase angle  $\alpha_K$ . The structure factor for the missing part is  $\varepsilon = \mathbf{F}_{\text{mis}}$ .



Bricogne's suggestion can be understood by applying the cosine rule in the triangle in Figure 8.1.  $|F_{\text{mis}}|^2 = |F|^2 + |F_K|^2 - 2|F| \times |F_K| \cos \xi$ . With the assumption that  $|F| \cos \xi = |F_K|$ , we obtain  $\overline{|F_{\text{mis}}|^2} = \sum_1^n f_1^2 = \overline{|F|^2 - |F_K|^2}$ . Read's proposal can be easily understood for centric reflections, for which  $\|F| - |F_K|| = |F_{\text{mis}}|$ . For noncentric reflections, the assumption is made that  $|F_{\text{mis}}| \cos \beta = |F| - |F_K|$  (Figure 8.1). Then  $|F_{\text{mis}}|^2 = (|F| - |F_K|)^2 \times 1/\cos^2 \beta$ . In averaging over all reflections,  $\overline{\cos^2 \beta} = 1/2$  and therefore  $\overline{|F_{\text{mis}}|^2} = 2 \times \overline{(|F| - |F_K|)^2}$ .

The weighting factor  $w$  for the noncentric reflections can be derived in the following way. For one reflection, let the structure factor of the known part have an amplitude  $|F_K|$  and a phase angle  $\alpha_K$ . The correct structure factor for the entire structure has an amplitude  $|F|$  and a phase angle  $\alpha = \alpha_K + \xi$ .  $\varepsilon = \mathbf{F}_{\text{mis}}$  is the structure factor of the missing part. A single reflection  $(h k l)$  and its Friedel mate  $(\bar{h} \bar{k} \bar{l})$  contribute to the correct electron density  $\rho$  at position  $x, y, z$  with

$$\begin{aligned} \rho_{hkl}(xyz) &= \frac{2}{V} |F| \cos[2\pi(hx + ky + lz) - \alpha] \\ &= \frac{2|F|}{V} \cos \Psi. \end{aligned} \quad (8.2)$$

If the electron density is calculated with a correct  $|F|$  but an erroneous phase angle  $\alpha_K$ , then  $\alpha$  is replaced by  $\alpha_K = \alpha - \xi$  and  $\Psi$  is replaced by  $\Psi + \xi$  in Equation (8.2). In this case, if a weighting factor  $w$  is applied to the amplitude of reflection  $(h k l)$ , the error in the electron density is

$$\begin{aligned} \Delta\rho_{hkl}(xyz) &= \frac{2}{V} |F| [\cos \Psi - w \cos(\Psi + \xi)] \\ &= \frac{2}{V} |F| [\cos \Psi - w \cos \Psi \cos \xi + w \sin \Psi \sin \xi] \\ &= \frac{2}{V} |F| [\cos \Psi (1 - w \cos \xi) + w \sin \Psi \sin \xi], \end{aligned}$$

$$\{\Delta\rho_{hkl}(x\ y\ z)\}^2 = \frac{4|F|^2}{V^2}[\cos^2\Psi(1-w\cos\xi)^2 + w^2\sin^2\Psi\sin^2\xi + 2\cos\Psi\sin\Psi(1-w\cos\xi)w\sin\xi].$$

The mean value for  $\{\Delta\rho_{hkl}(xyz)\}^2$  over all  $x, y, z$  is obtained by averaging over  $\Psi$ :

$$\begin{aligned} \overline{\{\Delta\rho_{hkl}(xyz)\}^2} &= \frac{2}{V^2}|F|^2[(1-w\cos\xi)^2 + w^2\sin^2\xi] \\ &= \frac{2}{V^2}|F|^2(1-2w\cos\xi + w^2). \end{aligned}$$

The minimum of  $\overline{\{\Delta\rho_{hkl}(xyz)\}^2}$  with respect to  $w$  is found by differentiation:

$$\frac{d\{\Delta\rho_{hkl}(x\ y\ z)\}^2}{dw} = \frac{4}{V^2}|F|^2(w - \cos\xi) = 0. \tag{8.3}$$

It follows from Equation (8.3) that the best value of  $w$  is  $w = \cos\xi$ . However, the phase error  $\xi$  is unknown and the best that can be done is to use its average value, given by

$$w = \int_0^{2\pi} p(\xi) \cos\xi\ d\xi, \tag{8.4}$$

where  $p(\xi)$  is the probability of finding the phase angle error between  $\xi$  and  $\xi + d\xi$ . Note that  $w$  is equal to the figure of merit  $m$  as originally defined by Blow and Crick in their calculation of the “best” Fourier map. In Section 7.13 of Chapter 7, it was shown that  $m$  is the weighted mean of the cosine of the error in the phase angle, just as  $w$  is.

$p(\xi)$  can be derived from Figure 8.1 in the following way. In Section 5.3 [Equation 5.4] of Chapter 5, it was found that

$$p(\mathbf{F})d(\mathbf{F}) = \frac{1}{\pi \times \sum_{j=1}^n f_j^2} \exp\left[-\frac{|F|^2}{\sum_{j=1}^n f_j^2}\right] d(\mathbf{F}). \tag{8.5}$$

If the  $f_j$ 's are the atomic scattering factors for the  $n$  missing atoms,  $\sum_{j=1}^n f_j^2$  is the average value expected for  $|F_{\text{mis}}|^2$  of the missing atoms and the distribution function for the noncentrosymmetric reflections [Equation(8.5)] is

$$p(\varepsilon)d(\varepsilon) = \frac{1}{\pi \times \sum_{j=1}^n f_j^2} \exp\left[-\frac{|\varepsilon|^2}{\sum_{j=1}^n f_j^2}\right] d(\varepsilon). \tag{8.6}$$

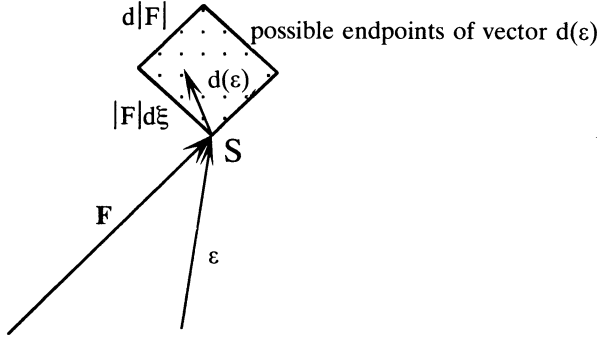


Figure 8.2. The possible end points of vector  $d(\epsilon)$  are found in a rectangle bounded by  $|F|d\xi$  and  $d|F|$ .

With  $d(\epsilon) = |F|d\xi d|F|$  (Figure 8.2):

$$p(\epsilon)d(\epsilon) = p(\epsilon)|F|d\xi d|F| = \frac{|F|}{\pi \times \sum_{j=1}^n f_j^2} \exp \left[ -\frac{|\epsilon|^2}{\sum_{j=1}^n f_j^2} \right] d|F|d\xi.$$

$p(\epsilon)$  is equal to the probability of finding the measured  $|F|$  with a certain  $\xi$ . Application of the cosine rule in Figure 8.1 gives the conditional probability:

$$p(\xi; |F|)d\xi = \frac{|F|}{\pi \times \sum_{j=1}^n f_j^2} \exp \left[ -\frac{(|F|^2 + |F_K|^2)}{\sum_{i=1}^n f_i^2} \right] \exp \left[ \frac{2|F| \times |F_K| \cos \xi}{\sum_{i=1}^n f_i^2} \right] d\xi. \tag{8.6a}$$

Normalization requires

$$\int_{\xi=0}^{2\pi} N \times p(\xi; |F|)d\xi = 1,$$

where  $N$  is a normalization constant.

$$2 \times N \times \frac{|F|}{\pi \times \sum_{j=1}^n f_j^2} \exp \left[ -\frac{(|F|^2 + |F_K|^2)}{\sum_{i=1}^n f_i^2} \right] \times \int_0^\pi \exp \left[ \frac{2|F| \times |F_K| \cos \xi}{\sum_{i=1}^n f_i^2} \right] d\xi = 1. \tag{8.7}$$

The integral is a modified Bessel function of order 0. The general form for a modified Bessel function of order  $n$  is

$$I_n(x) = \frac{1}{\pi} \int_{\xi=0}^{\pi} \exp[x \cos \xi] \cos n\xi \, d\xi,$$

$$I_0(x) = \frac{1}{\pi} \int_{\xi=0}^{\pi} \exp[x \cos \xi] \, d\xi.$$

Therefore,  $N$  can be written as

$$N = \left\{ 2 \times \frac{|F|}{\sum_{j=1}^n f_j^2} \exp \left[ -\frac{(|F|^2 + |F_K|^2)}{\sum_{i=1}^n f_i^2} \right] \times I_0 \left( \frac{2|F| \times |F_K|}{\sum_{i=1}^n f_i^2} \right) \right\}^{-1}$$

and the normalized distribution function becomes

$$p(\xi; |F|)d\xi = \left\{ \exp \left[ \frac{2|F| \times |F_K| \cos \xi}{\sum_{i=1}^n f_i^2} \right] d\xi \right\} / \left\{ 2\pi I_0 \left[ \frac{2|F| \times |F_K|}{\sum_{i=1}^n f_i^2} \right] \right\}$$

$$= \frac{\exp[X \cos \xi]d\xi}{2\pi I_0(X)}, \tag{8.8}$$

where

$$X = \frac{2|F| \times |F_K|}{\sum_1^n f_i^2};$$

or, because  $\alpha_K = \alpha - \xi$  and  $\alpha_K$  is a constant,

$$p_{\text{par}}(\alpha; |F|)d\alpha = \frac{1}{2\pi I_0(X)} \exp[X \cos(\alpha - \alpha_K)] d\alpha. \tag{8.9}$$

The weighting factor  $w$  [Equation (8.4)] becomes

$$w = \int_0^{2\pi} p(\xi) \cos \xi \, d\xi = \frac{\int_0^{2\pi} \exp[X \cos \xi] \cos \xi \, d\xi}{2\pi I_0(X)} = \frac{I_1(X)}{I_0(X)}.$$

For centric reflections, a different expression for  $w$  must be used:

$$w = \tanh \left( \frac{X}{2} \right).$$

This can be derived as follows.

For centric reflections the probability distribution of the structure factors is [Equation (5.7):

$$p(\varepsilon)d(\varepsilon) = \frac{1}{\sqrt{2\pi \sum_i f_i^2}} \exp \left[ -\frac{\varepsilon^2}{2 \sum_i f_i^2} \right] d(\varepsilon).$$

There are two possibilities:

1.  $F$  in the same direction as  $F_K$ , implying  $\xi_1 = 0$  and  $\cos \xi_1 = 1$ .

$$(\varepsilon)^2 = (|F| - |F_K|)^2 = |F|^2 + |F_K|^2 - 2|F||F_K|$$

and the probability for obtaining the required  $\varepsilon$  is

$$\begin{aligned} p_1(|\varepsilon|; |F|) &= \frac{1}{\sqrt{2\pi \sum_i f_i^2}} \exp \left[ -\frac{|F|^2 + |F_K|^2}{2 \sum_i f_i^2} \right] \exp \left[ \frac{2|F||F_K|}{2 \sum_i f_i^2} \right] \\ &= C \times \exp \left[ \frac{2|F||F_K|}{2 \sum_i f_i^2} \right]. \end{aligned}$$

2.  $F$  and  $F_K$  in opposite directions, implying  $\xi_2 = \pi$  and  $\cos \xi_2 = -1$ .

$$(\varepsilon)^2 = (|F| + |F_K|)^2 = |F|^2 + |F_K|^2 + 2|F||F_K|$$

and

$$p_2(|\varepsilon|; |F|) = C \times \exp \left[ -\frac{2|F||F_K|}{2 \sum_i f_i^2} \right].$$

According to Equation (8.4, the weight  $w$  of the reflection is given by the average value of  $\cos \xi$ . Thus,

$$w = \frac{p_1 \cos \xi_1 + p_2 \cos \xi_2}{p_1 + p_2} = \frac{p_1 - p_2}{p_1 + p_2}.$$

Writing  $X$  for

$$\frac{2|F||F_K|}{\sum_i f_i^2},$$

this becomes

$$w = \frac{\exp \left[ \frac{X}{2} \right] - \exp \left[ -\frac{X}{2} \right]}{\exp \left[ \frac{X}{2} \right] + \exp \left[ -\frac{X}{2} \right]} = \tanh \left( \frac{X}{2} \right).$$

As mentioned earlier,  $w$  is equal to the figure of merit  $m = \overline{\cos \xi}$ , where  $\xi$  is the deviation from the phase angle  $\alpha_K$ . In the calculation of  $w$ , it was assumed that the known part of the structure is exactly known and has no errors in the parameters of the atoms. In that case,

$$X = \frac{2|F| \times |F_K|}{\sum_1^n f_i^2}.$$

However, in practice, the known part of the structure does have errors.  $X$  must then be taken (Srinivasan, 1966) as

$$X = \frac{2\sigma_A|E| \times |E_K|}{1 - \sigma_A^2};$$

$|E|$  and  $|E_K|$  are normalized structure factors and  $\sigma_A$  will be defined in Section 15.6 of Chapter 15. The result of the OMIT map procedure can be improved further by previous refinement of the partial structure. It appears that this can best be done with simulated annealing, discussed in Section 13.4.5 of Chapter 13 (Hodel et al., 1992). It often occurs that phase information from different sources must be combined in a joint probability curve. In Chapter 14, a convenient method for doing this will be presented. The contribution from partial structure information is then  $p_{\text{par}}(\alpha)$  [Equation (8.9)].

$I_0(X)$  depends on known quantities only ( $|F|$ ,  $|F_K|$ , and  $\sum_1^n f_i^2$ ) and can be put into a normalizing constant ( $p(\xi) = N^* \times \exp[X \cos \xi]$ ), and

$$p_{\text{par}}(\alpha) = N^* \times \exp[X \cos(\alpha - \alpha_K)]. \quad (8.9a)$$

In Chapter 14, it will be shown how this probability curve is combined with probability curves from other sources.

### 8.3. Solvent Flattening

The principle of this method is fairly simple. From highly refined protein crystal structures it is known that the electron density map is rather flat in the solvent region between the protein molecules. This is due to the liquid character of the solvent molecules in those regions. This does not mean that no solvent molecules can be observed. However, the more static solvent molecules are found only internally in the protein molecules, or as a monolayer or double layer at their surface. The rest of the solvent has a dynamic nature and its time-averaged electron density has a low constant value. If the region occupied by the protein molecules can be identified, a nonoptimal electron density map shows noise peaks in the solvent region and they are removed simply by setting the electron density in this region to a low constant value.

The simplest method for defining a molecular envelope around the protein molecules is by visual inspection of the preliminary electron density map. However, this is rather subjective for a noisy map. An automated method proposed by Wang



(1985) and modified by Leslie (1987) is more objective and much easier to apply. In the Wang method, the noisy electron density map is smoothed in the following way:

A three-dimensional grid is superimposed on the unit cell. At each grid point  $j$ , the electron density is replaced by a new value that is proportional to the weighted sum of the densities within a sphere of radius  $R$  with the center in that grid point.  $R$  is typically on the order of 10 Å.

$$\rho'_j = K \sum_i^R w_i \rho_i,$$

with  $w_i = 0$  for  $\rho_i < 0$  and  $w_i = 1 - (r_{ij}/R)$  for  $\rho_i > 0$ . The summation is over the grid points  $i$  within the sphere,  $r_{ij}$  is the distance between the grid points  $i$  and  $j$ , and  $K$  is an arbitrary constant. A grid spacing of one-third of the resolution is adequate. The molecular boundary is revealed in the new map by tracing a threshold density level. In the beginning of the process, the threshold is usually chosen such that the volume of solvent in the map is a little smaller (e.g., 10–15%) than the known or estimated volume fraction of the solvent (estimated using the formula given in Section 3.9 of Chapter 3). Also, only low-resolution data should be used because the phase angles of the high-resolution data are still very poor. If necessary, the envelope can be polished (e.g., by removing internal voids). During the next cycles of solvent flattening, the solvent fraction can gradually be increased up to, for example, 5% below the estimated value. With the slightly smaller solvent region there are fewer chances that outer loops of the protein molecule are cut off. Moreover, the envelope should be updated in these cycles because the electron density map improves and this allows us to trace a better envelope. In the solvent region (outside the envelope), the average value of the solvent density is assigned to each grid point. Structure factor amplitudes and phases are calculated for this new map (a process known as map inversion) using the fast Fourier transform technique (Section 13.3 of Chapter 13).

In the next step, an electron density map is calculated with *observed* structure factor amplitudes and with phase angles either from the solvent flattening procedure alone or by combining them with phase angles from isomorphous or molecular replacement or any other phase information. The choice depends on the quality of the initial phases, the resolution limit, and the solvent content. If, at the present resolution, no further improvement is obtained, data at higher resolution can be added in small steps.

Abrahams (1997) noted that phase improvement converges prematurely because a large contribution to the calculated structure factors is from the original structure. This is not new information. In other words, the improved phase angles are, to a large extent, biased by the present electron density. This causes a problem in the recombination step of the density modification cycle, where independence between the recombined data is assumed. Abrahams proposed removing or diminishing this bias by inversion of the solvent features. They are not flattened to a low constant value, but their sign is reversed (solvent flipping). After this correction,

the modified structure factors can be treated as statistically independent, allowing a straightforward recombination. A similar treatment is valid for other types of density modification.

Terwilliger (2000) also recognized that the modified map contains, in addition to new information, information from the original map. To solve this problem, he chose a reciprocal space solution and used a maximum likelihood approach (Section 13.2.2 of Chapter 13). We will not go into details but just mention that probability functions play a major role in this process—for instance, the probability that the observed set of structure factors is correct and the probability that the calculated map is consistent with prior knowledge.

### Explanation of Solvent Flipping

The electron density map calculated without  $\mathbf{F}(0\ 0\ 0)$  has negative values at some grid points and positive values at others, with an average overall density at the zero level. However, it is convenient for the explanation if the mean density in the volume occupied by the solvent is zero. This can be achieved by adding a constant value to every grid point. This has no effect on the structure factors, except on  $\mathbf{F}(0\ 0\ 0)$ .

Proof of this statement, which we call here **Property 1**:

$$\mathbf{F}(\mathbf{h}) = V \int_{\text{cell}} \rho(\mathbf{x}) \exp[2\pi i \mathbf{h} \cdot \mathbf{x}] d\mathbf{v}_{\text{real}}. \quad (8.10)$$

If  $\rho(\mathbf{x})$  has a constant value  $c$ ,

$$\mathbf{F}(\mathbf{h}) = c \cdot V \int_{\text{cell}} \exp[2\pi i \mathbf{h} \cdot \mathbf{x}] d\mathbf{v}_{\text{real}}$$

The integral is a delta function (Section 4.10) and this is zero for  $\mathbf{h} \neq 0$  but is equal to one for  $\mathbf{h} = 0$ ; therefore  $\mathbf{F}(\mathbf{h} = 0) = c \cdot V$ . The reverse is also true (Property 2).

**Property 2:** If a function in reciprocal space is everywhere zero, except at the origin ( $\mathbf{h} = 0$ ), its transform in real space is a constant.

Let us call the uncorrected electron density  $\rho(\mathbf{x})$ :

$$\rho(\mathbf{x}) = \frac{1}{V} \int_{\mathbf{h}} \mathbf{F}(\mathbf{h}) \exp[-2\pi i \mathbf{h} \cdot \mathbf{x}] d\mathbf{v}_{\text{rec}}. \quad (8.11)$$

[for convenience, we use the integral over  $\mathbf{h}$  instead of the summation]

Now that the mean solvent density  $\rho(\mathbf{x})$  is zero, solvent flattening is equal to multiplying the electron density  $\rho(\mathbf{x})$  with a modifying function  $g(\mathbf{x})$ , which has the value 1 for grid points within the envelope and 0 outside of it. Its Fourier transform is  $\mathbf{G}(\mathbf{h})$ .

In real space:

$\rho(\mathbf{x})$  and  $g(\mathbf{x})$

In reciprocal space:

$\mathbf{F}(\mathbf{h})$  and  $\mathbf{G}(\mathbf{h})$

The solvent flattened map has density  $g(\mathbf{x}) \times \rho(\mathbf{x})$ . The reciprocal space equivalent of this multiplication is found by means of the convolution theorem (7.13) of Chapter 7 and the following property:

**Property 3:** The Fourier transform of a convolution of two functions is equal to the product of the individual Fourier transforms of each of the two functions (Section 7.2 of Chapter 7):

$$\text{Tr}[\mathbf{G}(\mathbf{h}) * \mathbf{F}(\mathbf{h})] = g(\mathbf{x}) \times \rho(\mathbf{x});$$

Tr means Fourier transform and  $*$  denotes convolution

$\mathbf{G}(\mathbf{h})$  can be split into two parts:  $\mathbf{G}(\mathbf{h} \neq 0) + \mathbf{G}(\mathbf{h} = 0)$ , and we redefine solvent flattening in reciprocal space accordingly:

$$\text{Tr}[\mathbf{G}(\mathbf{h}) * \mathbf{F}(\mathbf{h})] = \text{Tr}[\mathbf{G}(\mathbf{h} \neq 0) * \mathbf{F}(\mathbf{h})] + \text{Tr}[\mathbf{G}(\mathbf{h} = 0) * \mathbf{F}(\mathbf{h})].$$

Application of Property 3 results in

$$g(\mathbf{x}) \times \rho(\mathbf{x}) = g_1(\mathbf{x}) \times \rho(\mathbf{x}) + g_2(\mathbf{x}) \times \rho(\mathbf{x}). \quad (8.12)$$

where  $g_1(\mathbf{x})$  is the Fourier transform of  $\mathbf{G}(\mathbf{h} \neq 0)$  and  $g_2(\mathbf{x})$  is that of  $\mathbf{G}(\mathbf{h} = 0)$ .

From Property 2, it follows that  $g_2(\mathbf{x})$  is a constant, independent of  $\mathbf{x}$ . Abrahams (1997) called it  $\gamma$ . It is clear that the second term in the right-hand side of Equation (8.12) is the bias component. It is nothing more than a scaled-down version of what was already known. Its value is obtained as follows: Its transform  $\mathbf{G}(\mathbf{h} = 0)$  is equal to the number of grid points with a value 1 (the grid points inside the envelope), just as  $\mathbf{F}(\mathbf{h} = 0)$  is equal to the total number of electrons in the unit cell (Section 4.10 of Chapter 4). According to Property 1,  $\mathbf{G}(\mathbf{h} = 0) = g_2 \times V$  with  $V$  here equal to the total number of grid points in the cell:

$$\gamma = \frac{\text{sum of grid points in envelope}}{\text{total number of grid points in the cell}} = \frac{V_P}{V},$$

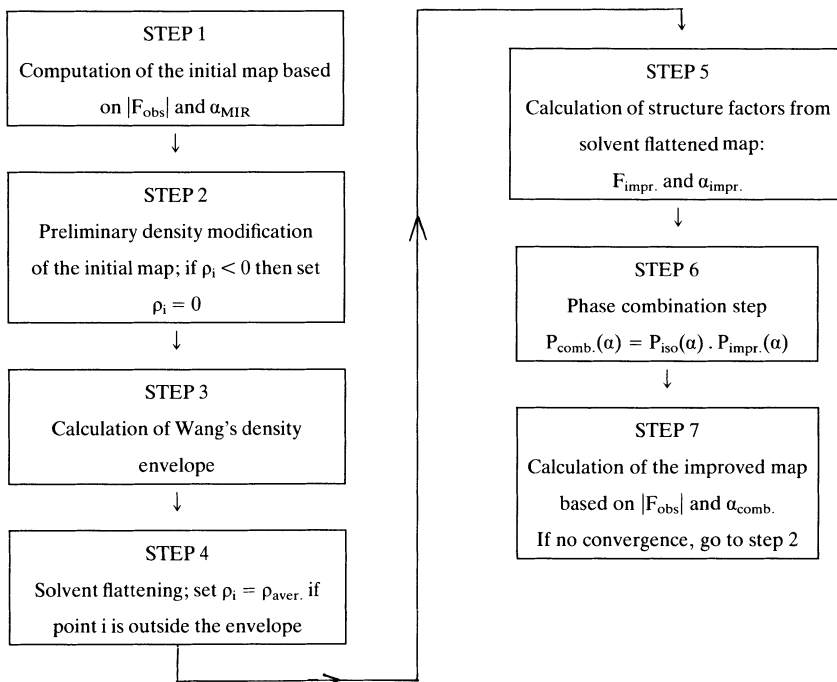
with  $V_P$  the volume of the envelope.

*Conclusion:* Solvent flattening corresponds to multiplication of  $\rho(\mathbf{x})$  with  $g(\mathbf{x})$ , but  $g(\mathbf{x})$  contains a term  $\gamma$  that leaves the original electron density unchanged. The seriousness of this bias depends on  $V_P/V$ . The larger the protein content, the more serious it is. The bias is removed by using  $g_1(\mathbf{x})$  not  $g(\mathbf{x})$  as the modifying function:

$$g_1(\mathbf{x}) = g(\mathbf{x}) - \gamma. \quad (8.13)$$

**Example:** Suppose  $V_P/V = 0.5$ . Application of Equation (8.13) results in values for  $g_1(\mathbf{x}) = 0.5$  within the envelope and  $-0.5$  in the solvent region. Rescaling gives 1 within the envelope and  $-1$  for the solvent region. In other words, the protein density is not affected, but the features in the solvent region change sign.

---



Scheme 8.1. Solvent flattening according to Wang (1985).

For the protein phase angles, a probability curve  $p_{\text{SF}}(\alpha)$  is chosen similar to  $p_{\text{par}}(\alpha)$  in the Sim weighting procedure [Equation (8.9a)]. The argument is that the solvent flattened structure can be regarded as the “known” part of the structure in the Sim conception:

$$p_{\text{SF}}(\alpha) = N \exp[X' \cos(\alpha_P - \alpha_{\text{calc}})], \quad (8.14)$$

where  $N$  is a normalizing constant,  $\alpha_P$  is the protein phase angle,  $\alpha_{\text{calc}}$  is the phase angle calculated for the map with the flattened solvent density, and  $X' = 2|F_{\text{obs}}| \times |F_{\text{calc}}| / |I_{\text{obs}} - I_{\text{calc}}|$ .

$|I_{\text{obs}} - I_{\text{calc}}|$  is the mean intensity contributed by the unknown part of the structure. It replaces  $\sum_{j=1}^n f_j^2$  in the Sim procedure. The closer the solvent flattened structure is to the true structure, the smaller  $|I_{\text{obs}} - I_{\text{calc}}|$  is and the stronger the phase indication. Appropriate scaling of the calculated to the observed structure factors is, of course, required.  $|I_{\text{obs}} - I_{\text{calc}}|$  is calculated in shells of increasing resolution.

From the phase probability curve—either the solvent flattened alone or a combined one—the “best” phases and figures of merit can be derived and used in the calculation of a “best” electron density map. The entire method can be repeated until no further improvement of the map is obtained. For a schematic representation of the method, see Scheme 8.1, and for an example, see Figure 8.3. Leslie (1987)

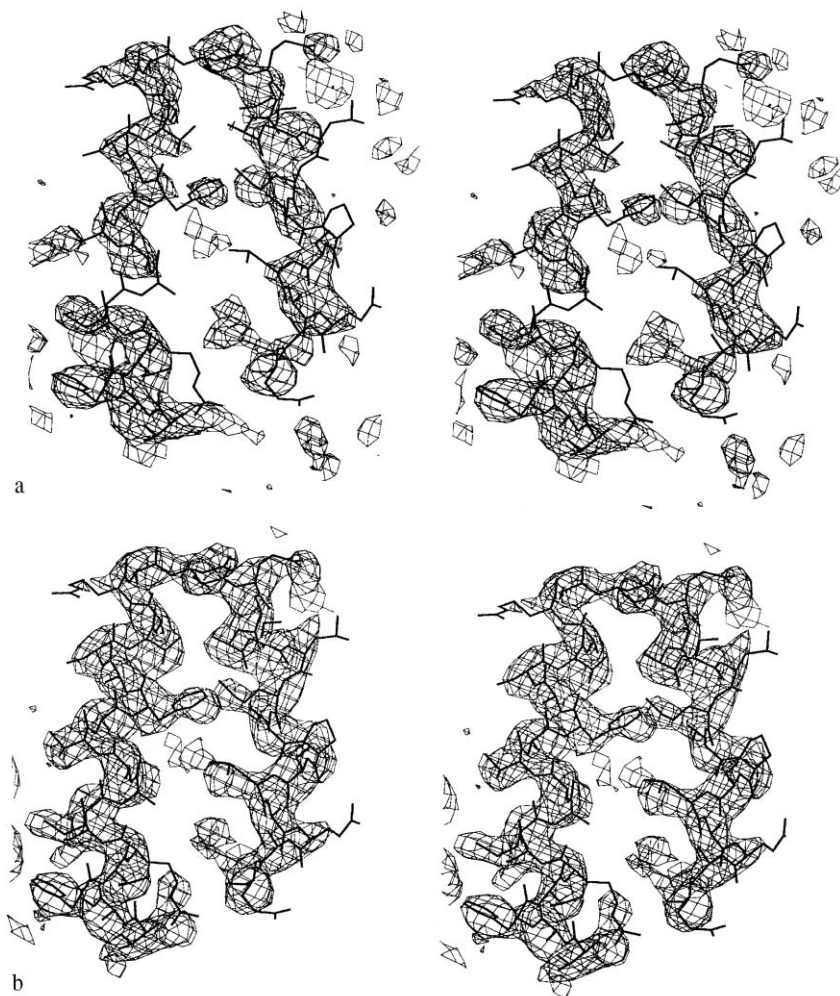


Figure 8.3. Stereo pairs of part of the electron density map of the *Escherichia coli* enzyme soluble lytic transglycosylase at 3.3 Å resolution. The crystal contained 60% solvent. **(a)** The map as obtained with the multiple isomorphous replacement method, using two derivatives and including anomalous scattering by the heavy atoms. **(b)** The solvent flattened map. Disconnected parts of density before solvent flattening are nicely connected in (b). (Courtesy of Dr. A.M.W.H. Thunnissen.)

has given a reciprocal space method for calculating the smoothed electron density map, which is computationally much faster than Wang's real space method. The density for the smoothed map is

$$\rho'(i) = \sum_{r=0}^R \rho(i+r) \times \left(1 - \frac{r}{R}\right) \quad (8.15)$$

with  $r \leq R$ . Equation (8.15) is a convolution of the function  $\rho$  with the function  $[1 - (r/R)]$  [see Equation (7.13) of Chapter 7]. Therefore, the transform of the function  $\rho(i)$  is equal to the product of the transform of  $\rho(i)$  and the transform of  $[1 - (r/R)]$ . The transform of  $\rho(i)$  is easily calculated with a fast Fourier program. The transform of  $[1 - (r/R)]$  is the transform of 1 minus the transform of  $r/R$ . The transform of a function that has a constant value of 1 in the region  $r \leq R$  and is 0 outside that region is the transform of a sphere with radius  $R$ . We will meet this transform (the  $G$ -function) again in discussing the rotation function (Section 10.2; Fig. 10.3 of Chapter 10). It has the form

$$G(x) = \frac{3(\sin x - x \cos x)}{x^3} \quad \text{with} \quad x = \frac{4\pi R \sin \theta}{\lambda}.$$

The transform of the function that is  $r/R$  in the region  $r \leq R$  and 0 for  $r > R$ , is

$$L(x) = \frac{3}{x^4} \{2x \sin x - (x^2 - 2) \cos x - 2\}.$$

The total transform of  $[1 - (r/R)]$  is then  $G(x) - L(x)$ .

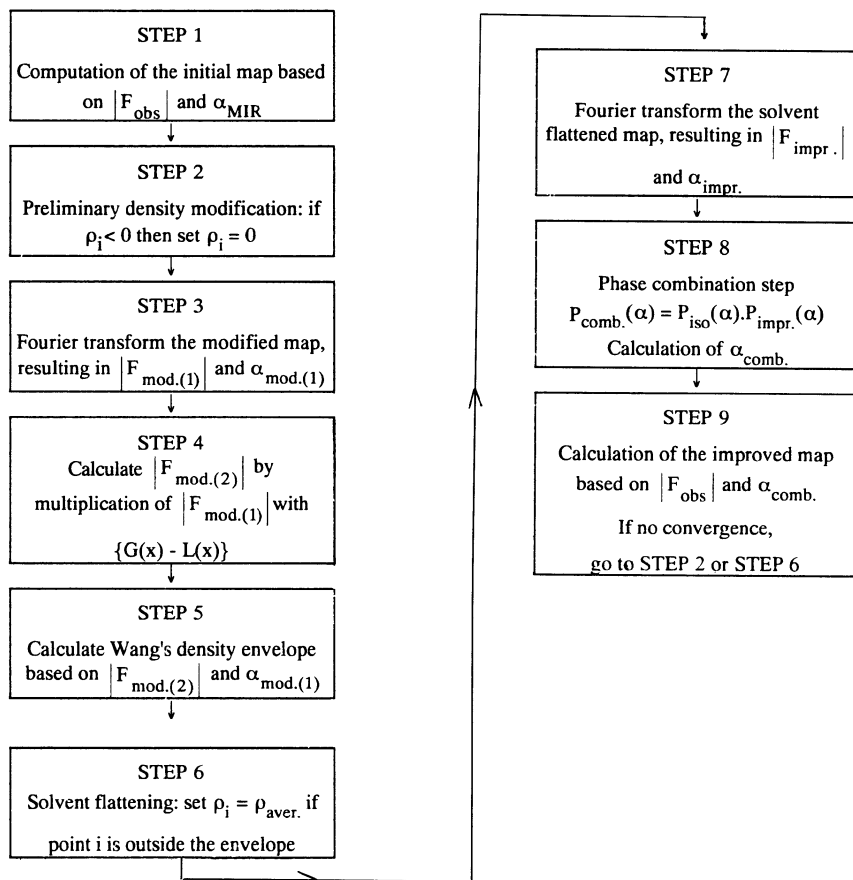
The following steps for calculating the smoothed map should be performed:

1. Calculate the structure factors for the original electron density  $\rho(r)$ , including all low-angle reflections, because they depend much more on the shape of the solvent region than the higher-resolution reflections.
2. Multiply them by  $G(x) - L(x)$ .
3. Use these modified structure factors for calculating the smoothed electron density map  $\rho'$ .

See Scheme 8.2 for a schematic representation. Solvent flattening is most powerful for crystals with a high solvent content. Terwilliger (2002) introduced “statistical density modification”. This is a sort of maximum likelihood approach (Section 13.2.2 of Chapter 13) to density modification. Instead of expected electron density values, he used probability functions for local regions in the electron density as well as uncertainties in these distributions. The method can be applied to solvent flattening and noncrystallographic symmetry (Section 8.4).

## 8.4. Noncrystallographic Symmetry and Molecular Averaging

From the first characterization of a protein crystal it usually becomes clear how many protein molecules or subunits are contained in the asymmetric unit. It is fairly common to find more than one molecule, related by one or more symmetry operators. This is noncrystallographic symmetry (NCS) and it is active only within each asymmetric unit, not through the entire crystal. The orientation and nature of a noncrystallographic axis follow from the self-rotation function (Chapter 10). A possible translation component along the axis (screw axis) is not detected in this way. The actual location of the axis can easily be found if a sufficient number of



Scheme 8.2. Solvent flattening according to Leslie (1987).

heavy atom positions is available from isomorphous replacement. If a sufficient number is not available, NCS axes can be located by maximizing the correlation coefficient (Appendix 2) between electron density regions in the asymmetric unit or by calculating the translation function (Chapter 10).

The electron density in the molecules (subunits), related by this NCS, is essentially equal, although the difference in the contact with neighbors might cause some deviation from exact equality. The equal density in the molecules related by the NCS imposes a constraint on the protein structure factors and, therefore, on the protein phase angles. Reciprocal space methods to derive these phase relationships were proposed by Rossmann and Blow (1963), Main (1967), and Crowther (1969). They were not very successful, but a real space approach, developed by Bricogne (1974), has found wide application. It consists of the following steps:

1. Determine the NCS operator(s).
2. The envelope of the molecules in the asymmetric unit must be defined in the electron density map, calculated with the available phase information. The envelope should contain as much protein density as possible, but it is sometimes chosen slightly smaller than the actually observed one, because of the possible difference between the molecules in the contact with their neighbors. One must be careful that no overlap with symmetrically related envelopes occurs. A special case occurs if a noncrystallographic axis is parallel to a crystallographic axis. Then the Patterson map can supply useful information (Section 10.3 and Figure 10.7 of Chapter 10).
3. The electron density of the molecules in the asymmetric unit is averaged, the solvent region flattened, and its density set equal to the average electron density in that region; then the asymmetric unit is reconstituted.
4. Phase angles for this new model are calculated by back-transforming the electron density map.
5. If necessary, this phase information is combined with previously known phase information and “best” phases and figures of merit are obtained.
6. A new and improved electron density map is calculated with observed structure factor amplitudes and phase information from Step 4.
7. The procedure is repeated starting in Step 1 with refinement of the NCS operator(s).

The phase information is derived from this averaging procedure in the same way as in the solvent flattening method and is based on Sim’s phase probability function. The average structure is regarded as the known part in Sim’s conception and  $p_{\text{average}}(\alpha_P)$  has the same form as  $p_{\text{SF}}(\alpha_P)$  [Eq. (8.14)]:

$$P_{\text{average}}(\alpha_P) = N \exp[X' \cos(\alpha_P - \alpha_{\text{calc}})]. \quad (8.16)$$

with  $X' = 2|F_{\text{obs}}| \times |F_{\text{calc}}| / \overline{|I_{\text{obs}} - I_{\text{calc}}|}$

The method of averaging is most powerful in cases of high NCS, such as in viruses, because averaging improves the signal-to-noise ratio of the order of  $\sqrt{N}$ , with  $N$  the number of independent copies. However, it can also give excellent improvement of a density map at lower NCS (Jacobson et al., 1994); an example is also shown in Figure 8.4. Moreover, the averaging method is not restricted to NCS within one crystal; it can be used equally well if proteins crystallize in more than one crystal form. A detailed discussion of NCS averaging in phase refinement and extension can be found in Vellieux and Read (1997) and in Kleywegt and Read (1997).

## 8.5. Histogram Matching

Like solvent flattening, the method of histogram matching rectifies a distorted image. Histogram matching is usually applied in combination with solvent flattening. It does not deal with the electron density map as such, like solvent flattening does,



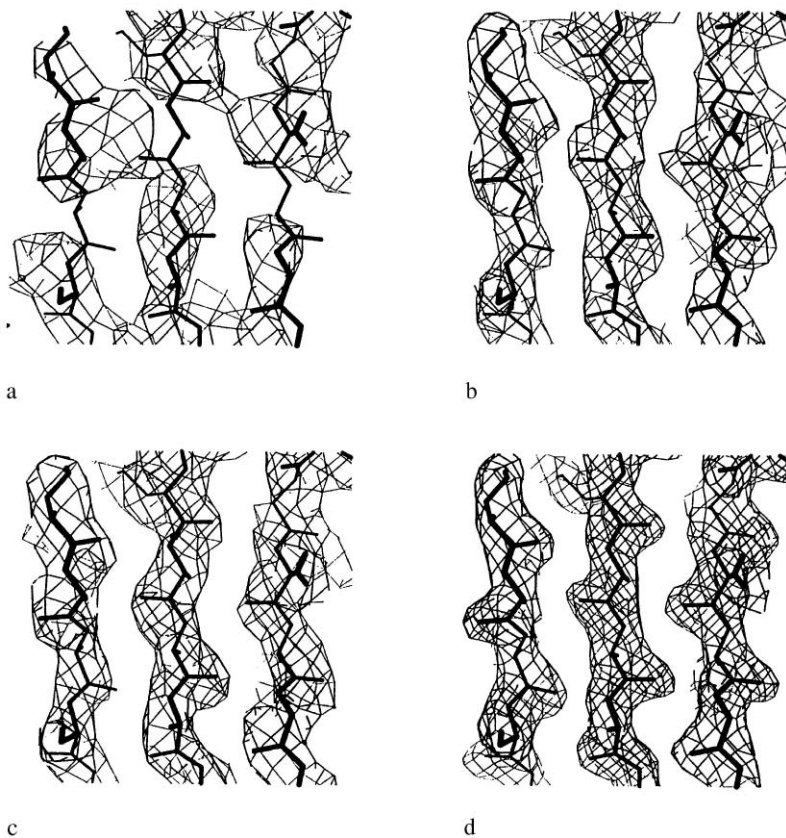


Figure 8.4. Example of the effect of density modification by NCS averaging and phase extension in the structure determination of the epoxide hydrolase from *Agrobacterium radiobacter* AD1; the asymmetric unit contains four molecules: **(a)** Electron density map from single isomorphous replacement supplemented by anomalous signal information (SIRAS) at 3.7 Å resolution; **(b)** electron density map after averaging at 3.7 Å resolution; **(c)** electron density map after averaging and phase extension from 3.7 Å to 2.6 Å resolution; **(d)** final  $\{2|F(\text{obs})| - |F(\text{calc})|\}$  map at 2.1 Å resolution. (Courtesy of Dr. Marco Nardini).

but it uses the frequency distribution of electron density values (Figure 8.5). It appears that these distributions as a function of  $\rho$  are fairly independent of the protein, at least at the same resolution. The temperature factor also has an effect, but this can be eliminated by using temperature-factor-corrected structure factors. Histogram matching is one of many techniques applied in the general field of image processing. It requires the availability of another image, preferably a high-quality image of the same kind. The assumption is that high-quality images of a particular kind of object have the same frequency distribution of gray levels, the standard distribution. A poor image has a different distribution and this is then scaled to the standard distribution and this process results in an improved image. It was pointed

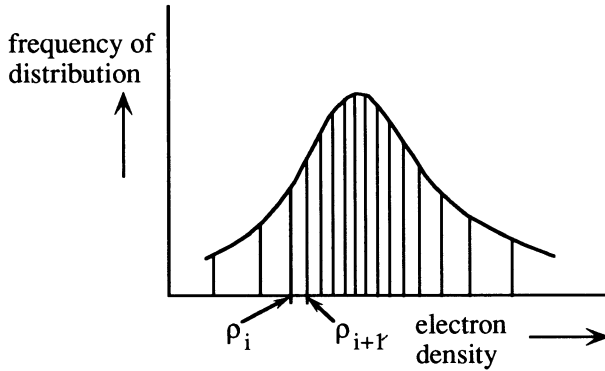


Figure 8.5. The frequency of electron density occurrence at grid points

out by Lunin in 1988 and in subsequent work (Lunin, 1988; Lunin & Skovoroda, 1991; Lunin et al., 1990; Lunin & Vernoslova, 1991) that histogram matching could be useful for improving electron density maps. Zhang and Main (1990a) presented it in a simplified form and incorporated it in the program SQUASH (Zhang and Main, 1990b); DM in the CCP4 library (CCP4, 1994; Cowtan and Main, 1996). The frequency distribution of electron density levels calculated at grid points is plotted as a function of  $\rho$  for the poor electron density map and compared with the standard plot. Next, the plots are divided into bins containing an equal number of grid points. The bin boundaries of the poor map are  $\rho_i, \rho_{i+1}$  with  $i \rightarrow n$  and  $n$  of the order 100, and for the standard map  $\rho'_i, \rho'_{i+1}$ . If the two maps are identical  $\rho_i = \rho'_i$  and  $\rho_{i+1} = \rho'_{i+1}$ , and so forth. In general, they are not. By scaling with a factor

$$a = \frac{\rho'_{i+1} - \rho'_i}{\rho_{i+1} - \rho_i},$$

the bin width from  $\rho_i$  to  $\rho_{i+1}$  is given the correct value. The bin is then moved over a distance  $b$  such that  $\rho_i$  moves to  $\rho'_i$  and  $\rho_{i+1}$  moves to  $\rho'_{i+1}$ . From  $\rho'_i = a \times \rho_i + b$ , it can easily be derived that

$$b = \frac{\rho_{i+1}\rho'_i - \rho_i\rho'_{i+1}}{\rho_{i+1} - \rho_i}.$$

The electron densities in each bin are corrected with the appropriate  $a$  and  $b$ . This results in an improved electron density map from which new phase angles can be calculated.

According to the experience of Zhang et al. (1997) with a particular protein, solvent flattening and averaging improve the phase angles of the low-resolution reflections, but not of the high-resolution reflections. Combined with histogram matching, the phasing of the higher-resolution reflections also improved considerably.

The histogram method can be further improved by combining electron density matching with electron density gradient matching (Nieh and Zhang, 1999). This increases one-dimensional (1D) to two-dimensional (2D) matching. The gradients

are derived from Equation (4.10) of Chapter 4 by differentiation of the electron density with respect to  $x$ ,  $y$ , and  $z$ :

$$\frac{\partial \rho(xyz)}{\partial x} = -\frac{2\pi i}{V} \sum_h \sum_k \sum_l h \mathbf{F}(hkl) \exp[-2\pi i(hx + ky + lz)] = g(x), \quad (8.17)$$

$$\frac{\partial \rho(xyz)}{\partial y} = -\frac{2\pi i}{V} \sum_h \sum_k \sum_l k \mathbf{F}(hkl) \exp[-2\pi i(hx + ky + lz)] = g(y), \quad (8.18)$$

$$\frac{\partial \rho(xyz)}{\partial z} = -\frac{2\pi i}{V} \sum_h \sum_k \sum_l l \mathbf{F}(hkl) \exp[-2\pi i(hx + ky + lz)] = g(z). \quad (8.19)$$

The gradients are calculated using these Fourier summations with coefficients  $h\mathbf{F}(hkl)$ ,  $k\mathbf{F}(hkl)$  and  $l\mathbf{F}(hkl)$ , respectively.

Two-dimensional histogram matching of the gradients follows the same procedure as for the 1D density matching. In the 2D procedure, 1D matching on density and on gradients is applied alternatively, starting with a set of structure factors  $\mathbf{F}_0(\text{obs})$ .

- Calculate a (poor) electron density map  $\rho_o$ .
- One-dimensional density matching gives an improved map  $\rho'$ .
- Fourier transform  $\rho'$  to  $\mathbf{F}_1$  and calculate  $h\mathbf{F}_1$ ,  $k\mathbf{F}_1$  and  $l\mathbf{F}_1$ .
- Calculate the gradients  $g(x)$ ,  $g(y)$  and  $g(z)$  with Equations (8.17), (8.18), and (8.19), respectively.
- One-dimensional gradient matching gives improved gradients  $g'(x)$ ,  $g'(y)$ , and  $g'(z)$ . Back-transform these gradients to  $h\mathbf{F}_2(hkl)$ ,  $k\mathbf{F}_2(hkl)$  and  $l\mathbf{F}_2(hkl)$ .
- Average the three values for the structure factor  $\mathbf{F}_2(hkl)$ .
- Calculate a new electron density map with amplitudes  $|\mathbf{F}_{(\text{obs})}|$  and the phase angles of  $\mathbf{F}_2(hkl)$ .

Repeat the procedure until convergence has been reached.

## 8.6. wARP: Weighted Averaging of Multiple-Refined Dummy Atomic Models

If an electron density map is still uninterpretable after solvent flattening, averaging, and histogram matching, but the resolution is at least  $2.5 \text{ \AA}$ , wARP can appreciably improve the protein phase angles (and the electron density map) by an automatic procedure (Lamzin and Wilson, 1993; Perrakis et al., 1997; van Asselt et al., 1998; <http://www.embl-hamburg.de/ARP/>). The condition is not only a reasonably high resolution but also that the protein region in the asymmetric unit can be identified.

A number of atoms, usually oxygen atoms, are placed in regions of significantly high electron density. This preliminary “seed model” of  $\sim 100$  atoms is expanded

fully automatically by adding more atoms at grid points with a density of at least  $2\sigma$  above the mean density and within 5 Å from atoms in the “seed model.” The grid should have small spacings, of  $\sim 0.25$  Å. The preliminary “seed model” is removed and the resulting “model” is further expanded by gradually adding atoms in significant electron density at distances of 1.1–1.8 Å from existing atoms. After this expansion in several cycles, the threshold density is lowered in steps of  $0.1\sigma$  from 2.0 to  $0.9\sigma$  and additional atoms are placed in these weaker electron density regions. The result is a “model” with many more atoms than the expected number of nonhydrogen protein atoms.

The efficacy of the method is greatly improved by producing more “models” and averaging them later. The extra “models” are built, for instance, by starting from intermediates that led to the first “model” or they are created by random positional shifts of 0.5 Å. Usually six “models” are produced. Before proceeding further, the number of free atoms in these “pseudoprotein models” is reduced to 110% of the number of nonhydrogen atoms in the asymmetric unit by removing atoms in weak density. In the next step, a refinement procedure starts. In this refinement (Section 13.1 of Chapter 13), the atoms are moved freely until the calculated structure factor amplitudes match the observed ones as close as possible. All six models are independently refined, preferably by a maximum likelihood procedure (Section 13.2.2 of Chapter 13). After a refinement cycle, electron density maps with calculated phase angles are subjected to an automatic correction procedure: It removes atoms from low-density regions in a  $(2m|F_o| - D|F_c|)$  map and adds them to high-density regions in a  $(m|F_o| - D|F_c|)$  difference map (Section 7.7 of Chapter 7), taking into account distance criteria (too close to or too far from existing atoms). The procedure of “model” refinement + correction is repeated in an iterative process until convergence is reached.

In the final step, the result from the six “models” is averaged to maximize the quality of the final phase set. In this averaging step, the calculated structure factor amplitudes are first scaled to the observed ones. Then the structure factors are averaged in the Argand diagram, assigning a weight to each vector depending on its distance from the average vector (Figure 8.6). The phase angles of the averaged

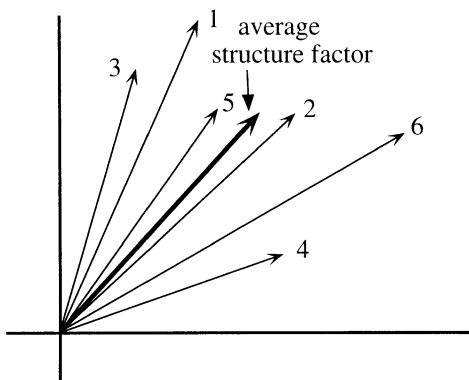


Figure 8.6. Argand diagram with the structure factors from the six “models” produced by wARP, and the average structure factor, for one reflection.

structure factors are combined with the observed amplitudes to calculate the final electron density map. The advantage of wARP is that it is a fast procedure to go from an uninterpretable to an interpretable map. Its main limitation is the restriction to electron density maps with a resolution better than 2.5 Å. The product of wARP is an electron density map that in favorable cases can be interpreted in terms of a protein atomic model.

In modern versions of wARP, automatic chain tracing coupled with refinement of macromolecular models is a new feature in the program (Morris et al., 2003). It starts by locating C $\alpha$  atoms and building fragments of the main chain. For each fragment, the most probable stretch is chosen from the amino acid sequence on the basis of connectivity features in the environment of each C $\alpha$  atom. Side chains are built in their electron density. In iterative cycles, alternating the addition of atoms with refinement, the chain grows gradually to its final shape.

## 8.7. Further Considerations Concerning Density Modification

Density modification procedures start with a poor electron density map that has been calculated with structure factors having the correct amplitude  $|F_{\text{obs}}|$ , but a wrong phase angle  $\alpha_{\text{wr}}$ . This structure factor can be thought of as composed of a contribution by the protein part of the crystal structure [ $\mathbf{F}_{\text{wr}}(\text{pr})$ ] and a contribution by the solvent part [ $\mathbf{F}_{\text{wr}}(\text{s})$ ]. The designation  $\mathbf{F}_{\text{wr}}$  means that the protein and also the solvent contribution are both incorrect in this stage. Flattening the solvent part in the structure means that  $\mathbf{F}_{\text{wr}}(\text{s})$  is replaced by an improved  $\mathbf{F}_{\text{impr}}(\text{s})$  (Figure 8.7).

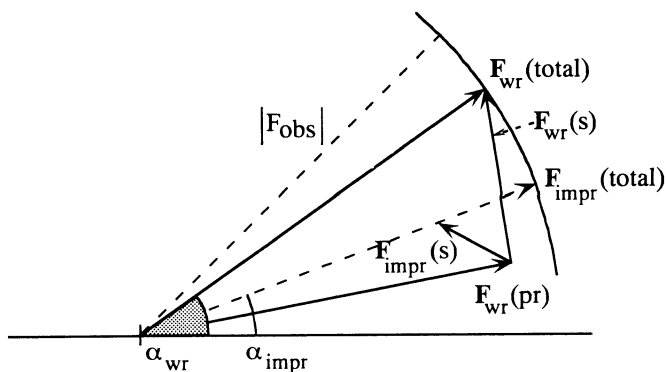


Figure 8.7. Structure factors in solvent flattening. The electron density maps are always calculated with observed structure factor amplitudes  $|F_{\text{obs}}|$ . For the starting map, the poor protein phase angles  $\alpha_{\text{wr}}$  are used for the structure factors  $\mathbf{F}_{\text{wr}}(\text{total})$ . This structure factor is composed of a protein contribution,  $\mathbf{F}_{\text{wr}}(\text{pr})$ , and a solvent contribution,  $\mathbf{F}_{\text{wr}}(\text{s})$ . The flattening does not change the protein contribution, but it does improve the solvent contribution, replacing  $\mathbf{F}_{\text{wr}}(\text{s})$  by  $\mathbf{F}_{\text{impr}}(\text{s})$ . The next electron density map is then calculated with structure factors having the same amplitudes as earlier,  $|F_{\text{obs}}|$ , but improved protein phase angles  $\alpha_{\text{impr}}$ .

A new and improved electron density map is then calculated with the structure factor  $\mathbf{F}_{\text{impr}}$  (total) having the amplitude  $|F_{\text{obs}}|$  and the improved phase angle  $\alpha_{\text{impr}}$ . From this new map an improved envelope can be derived and the process repeated. Usually, several cycles of density modification are required to shift the protein phase angles close enough to their correct value to allow an interpretation of the electron density map in terms of the polypeptide chain. If, in the process, the solvent area becomes flatter, the amplitudes of the  $\mathbf{F}(\text{s})$  contributions become smaller, except for the low-order reflections (see Section 13.1 of Chapter 13). The shape of the envelope is mainly determined by these reflections and they should be incorporated as much as possible in solvent flattening. If the solvent content of the crystal is high, the contribution of  $\mathbf{F}(\text{s})$  to the total structure factor is also relatively high and solvent flattening is more powerful.

In solvent flattening, the driving force is the gradual improvement of  $\mathbf{F}(\text{s})$ . In the averaging procedure, two density modifications are applied in each step: (1) averaging the electron densities of the noncrystallographically related molecules and (2) solvent flattening. Therefore, both  $\mathbf{F}_{\text{wr}}(\text{s})$  and  $\mathbf{F}_{\text{wr}}(\text{pr})$  are replaced by improved structure factor contributions:  $\mathbf{F}_{\text{impr}}(\text{s})$  and  $\mathbf{F}_{\text{impr}}(\text{pr})$ . This speeds up the process considerably compared with solvent flattening alone. As a result, it is much more powerful, particularly if the number of symmetry-related molecules is higher.

## Summary

The interpretation of an electron density map in terms of the polypeptide chain is based on the chemical structure of the protein. Additional information is the higher electron density in the protein compared with the rather flat electron density in the solvent region between the protein molecules and the noncrystallographic symmetry, if present. The application of this additional information (density modification) can make all the difference for the interpretation of an hitherto uninterpretable map. Moreover, the resolution can often be increased in small steps. Usually, several cycles of density modification and model building are required, using calculated model phases combined with previous phase information. For this procedure, the fast Fourier transform algorithm is indispensable. If only part of the electron density map (e.g., rather mobile loops) cannot satisfactorily be interpreted, OMIT maps, preferably with Sim weighting, should be calculated. If the protein region in the asymmetric unit can be identified and the resolution is at least 2.5 Å, the protein phase angles (and the electron density map) can be appreciably improved with the automatic wARP procedure.

## Chapter 9

# Anomalous Scattering in the Determination of the Protein Phase Angles and the Absolute Configuration

### 9.1. Introduction

Anomalous scattering is not a new subject. It was already introduced in Chapter 7. There, you learned that anomalous scattering by an atom is due to the fact that its electrons cannot be regarded as completely free electrons. This effect depends on the wavelength, but it is, in general stronger, for the heavier atoms than for the light atoms in the periodic system. If heavy atoms are present in a protein structure, the consequence of their anomalous scattering is that the intensities of a reflection  $h k l$  and its Bijvoet mate  $\bar{h} \bar{k} \bar{l}$  are no longer equal. In Chapter 7, this effect was used in combination with the isomorphous replacement differences in the search for the heavy atom positions and in the refinement of these positions. In this chapter it will be shown how anomalous scattering information can help to determine the phase angle of the protein reflections and the absolute configuration of the protein structure. Moreover, it will be discussed how anomalous scattering is exploited for protein phase angle determination by the multiple-wavelength anomalous diffraction (MAD) method and by single-wavelength anomalous diffraction (SAD).

### 9.2. Protein Phase Angle Determination with Anomalous Scattering

In principle, the anomalous scattering by heavy atoms contributes to the determination of the protein phase angles as much as the isomorphous replacement does. This can best be explained in Figure 9.1. Three circles are drawn in Figure 9.1, with radii  $F_P$ ,  $F_{PH(+)}$ , and  $F_{PH(-)}$ ; the (+) and the (-) indicate a Bijvoet pair of reflections. The  $F_P$  circle has its center at  $O$ . For the  $F_{PH(+)}$  circle, the

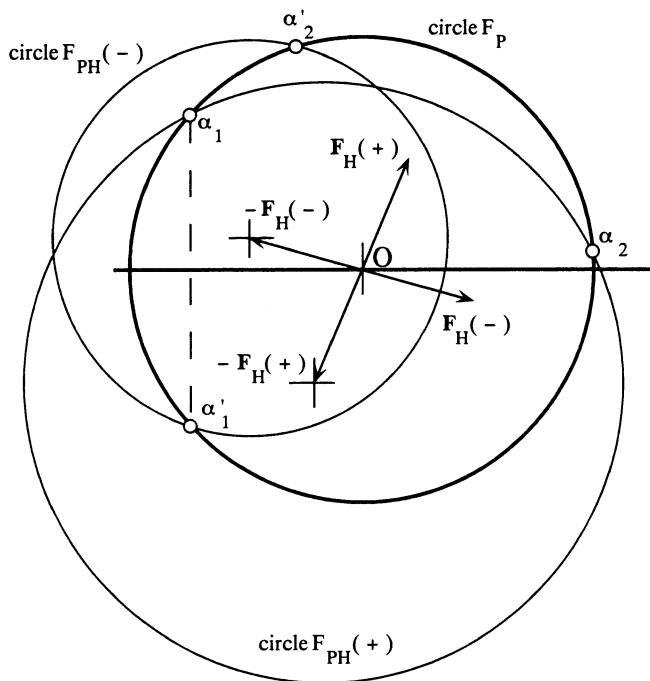


Figure 9.1. The Harker diagram for protein phase angle determination by anomalous scattering.  $|F_P|$  is the structure factor amplitude for the native protein and  $|F_{PH}(+)|$  and  $|F_{PH}(-)|$  are those for the Friedel mates of the heavy atom derivative. The contribution to the structure factor by the heavy atom is  $\mathbf{F}_H(+)$  for one member of the Friedel pair and  $\mathbf{F}_H(-)$  for the other member. These two structure factors are not symmetric with respect to the horizontal axis because of an anomalous component. The positions of the intersection points  $\alpha_1$  and  $\alpha'_1$  do have a position symmetric with respect to the horizontal axis because the structure factor of the native protein has no anomalous component.

center is at the end of the vector  $-\mathbf{F}_H(+)$ , and for the  $F_{PH}(-)$  circle, it is at the end of the vector  $-\mathbf{F}_H(-)$ . The two intersections of the  $F_P$  and  $F_{PH}(+)$  circles at  $\alpha_1$  and  $\alpha_2$  indicate two possible protein phase angles. Two other possibilities are found at the two intersections of the circles  $F_P$  and  $F_{PH}(-)$ :  $\alpha'_1$  and  $\alpha'_2$ . Because the reflections  $(h k l)$  and  $(\bar{h} \bar{k} \bar{l})$  of the native protein crystal have opposite phase angles (Section 4.11 of Chapter 4), the correct choice is for the phase angles  $\alpha_1$  for  $(h k l)$  and  $\alpha'_1$  for  $(\bar{h} \bar{k} \bar{l})$ . This is illustrated in a simpler way in Figure 9.2. Here, the vector  $-\mathbf{F}_H(-)$  is drawn with the opposite phase angle (mirror image with respect to the horizontal axis). Now the correct phase angle is found at the intersection of the three circles  $F_P$ ,  $F_{PH}(+)$ , and  $F_{PH}(-)$ , assuming that the data are error-free. The conclusion is that, in principle, the protein phase angle problem can be solved with one isomorphous heavy atom derivative if anomalous scattering is incorporated (SIRAS).



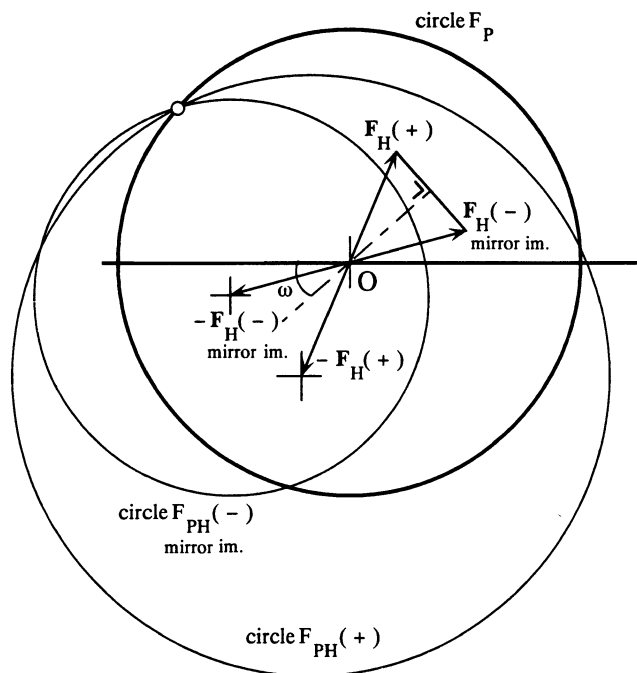


Figure 9.2. This figure gives the same information as Figure 9.1. The difference is that the vector  $-F_H(-)$  is now drawn with the opposite phase angle (mirror image with respect to the horizontal axis). The consequence is a different position for the  $F_{PH}(-)$  circle. The advantage of this drawing is that the three circles have one common point of intersection. The dashed line indicates the direction of the nonanomalous scattering part of the heavy atoms.

### 9.3. Improvement of Protein Phase Angles with Anomalous Scattering

From the isomorphous replacement method, a probability curve for the protein phase angle is obtained for each reflection:  $P_{iso}(\alpha)$ . The information from the anomalous scattering data could easily be combined with the  $P_{iso}(\alpha)$  curve if it could also be expressed in a probability curve:  $P_{ano}(\alpha)$ . The combined probability would then be

$$P(\alpha) = P_{iso}(\alpha) \times P_{ano}(\alpha).$$

This can be done in the following way:

$$|F_{PH}(+)| - |F_{PH}(-)| = \Delta P H_{obs}.$$

In Section 7.9 of Chapter 7 it was derived [Equation (7.28)] that

$$|F_{\text{PH}}(+)| - |F_{\text{PH}}(-)| = \frac{2f''}{f'} |F_{\text{H}}| \sin(\alpha_{\text{PH}} - \alpha_{\text{H}})$$

or

$$|F_{\text{PH}}(+)| - |F_{\text{PH}}(-)| = 2 \frac{|F_{\text{H}}|}{k} \sin(\alpha_{\text{PH}} - \alpha_{\text{H}}). \quad (9.1)$$

where

$$k = \frac{f'}{f''} = \frac{|F_{\text{H}}|}{|F_{\text{H}}''|}.$$

$\Delta PH_{\text{calc}}$  must be expressed as a function of the protein phase angle  $\alpha_{\text{P}}$ .

In triangle *ABE* in Figure 7.12 of Chapter 7, the sine rule gives

$$\frac{\sin -(\alpha_{\text{PH}} - \alpha_{\text{H}})}{|F_{\text{P}}|} = \frac{\sin(\alpha_{\text{H}} - \alpha_{\text{P}})}{|F_{\text{PH}}|}$$

or

$$\begin{aligned} \sin -(\alpha_{\text{PH}} - \alpha_{\text{H}}) &= \frac{|F_{\text{P}}|}{|F_{\text{PH}}|} \sin(\alpha_{\text{H}} - \alpha_{\text{P}}) \\ \Delta PH_{\text{calc}} &= \frac{2|F_{\text{H}}|}{k} \sin(\alpha_{\text{PH}} - \alpha_{\text{H}}) = -\frac{2|F_{\text{P}}| \times |F_{\text{H}}|}{k|F_{\text{PH}}|} \sin(\alpha_{\text{H}} - \alpha_{\text{P}}), \end{aligned}$$

In the ideal case,  $\Delta PH_{\text{calc}} = \Delta PH_{\text{obs}}$ . In practice, for each reflection a value  $\varepsilon_{\text{ano}}(\alpha) = \Delta PH_{\text{obs}} - \Delta PH_{\text{calc}}$  is found depending on the phase angle  $\alpha_{\text{P}}$  of the protein. This is comparable with the lack of closure error  $\varepsilon$  in the isomorphous replacement phase triangle of the protein. Here also a Gauss probability distribution is assumed:

$$P_{\text{ano}}(\alpha) = N' \exp \left[ -\frac{\varepsilon_{\text{ano}}^2(\alpha)}{2(E')^2} \right]; \quad (9.2)$$

$N'$  is a normalization constant and  $(E')^2$  is the mean square value of  $\varepsilon$ . Because anomalous scattering data are taken from the same crystal, lack of isomorphism does not cause errors in the values of  $|F_{\text{PH}}(+)| - |F_{\text{PH}}(-)|$ . Therefore, although these differences are small, the errors in  $|F_{\text{PH}}(+)| - |F_{\text{PH}}(-)|$  are inherently smaller than errors in  $|F_{\text{PH}}| - |F_{\text{P}}|$ , and  $E'$  is smaller than  $E$  and can be taken as (e.g.,  $\frac{1}{3}E$ ). Equation (9.2) can now be combined with  $P_{\text{iso}}(\alpha)$  [Equation (7.34) of Chapter 7]. One should be careful to combine the anomalous data with the correct set of isomorphous data [i.e., the set that gives the electron density of the protein in the absolute configuration (see next section)].

If the multiple isomorphous replacement method includes anomalous scattering information, it is called the MIRAS method. It should be stressed that in collecting anomalous scattering data, great care should be taken, because the difference in intensity between the Bijvoet pairs is very small. One generally prefers to collect Bijvoet pairs close in time to avoid experimental errors.

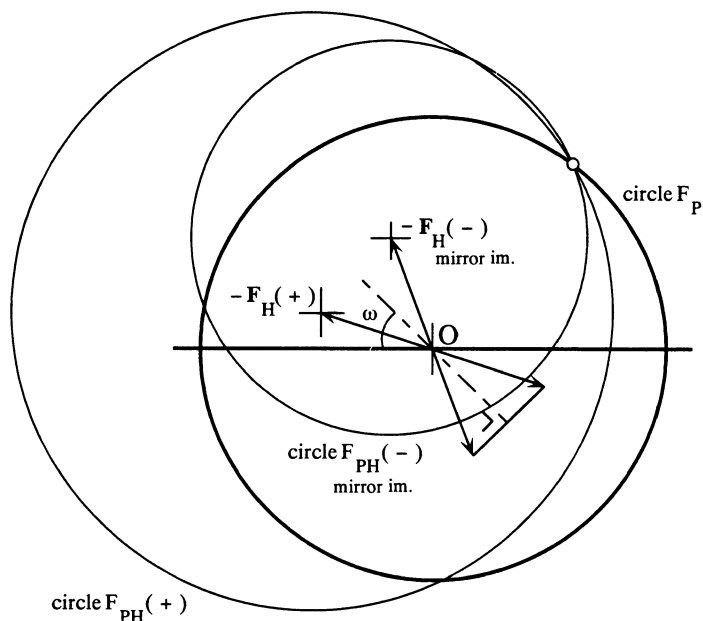


Figure 9.3. The crystallographic axes are chosen as in Figure 9.2, but the wrong (the centrosymmetric) set of heavy atom positions is chosen. The dashed line is the mirror image of the dashed line in Figure 9.2, and with respect to this dashed line, the vectors  $\mathbf{F}_H(+)$  and  $\mathbf{F}_H(-)$  (mirror image) are drawn.

## 9.4. The Determination of the Absolute Configuration

Without anomalous scattering, the isomorphous replacement method results in either the correct protein structure or its enantiomorph (mirror image). If the resolution in the electron density map is sufficiently high and the configuration at the  $C(\alpha)$  position in the amino acid residues can be observed, it can easily be checked whether the configuration is correct with the amino acid residues having the L-configuration. Also, if  $\alpha$ -helices appear in the map, they should be right-handed for the correct configuration of the protein. However, the absolute configuration of the protein can be derived more straightforwardly from the intensity differences between the two members of the Bijvoet pairs. This will be discussed below.

In Figures 9.1 and 9.2, the situation was presented with the correct set of heavy atom positions and  $|F_{PH}(+)| > |F_{PH}(-)|$ . In Figure 9.3, the situation is drawn with a correctly chosen set of axes,  $|F_{PH}(+)| > |F_{PH}(-)|$ , but the choice of the heavy atom positions was incorrect, because from the difference Patterson map, the wrong set of the two equally possible centrosymmetrically related sets of positions was chosen (see Section 7.6 of Chapter 7). The consequence is that the entire set of vectors  $\mathbf{F}_H(+)$ ,  $-\mathbf{F}_H(+)$ ,  $\mathbf{F}_H(-)$ , and  $-\mathbf{F}_H(-)$  is reflected with respect to the horizontal axis. This causes a rotation of the circles  $F_{PH}(+)$  and  $F_{PH}(-)$  by an angle

$2\omega$  around the center  $O$  of the  $F_P$  circle. As a result, an incorrect value for the phase angle of  $F_P$  will be found, which is different from the correct one by the value  $2\omega$ . If the anomalous information is combined with each of the two possibilities from the isomorphous data, the correct combination will give an electron density map of the protein that is superior to the map calculated with the incorrect combination.

An alternative method of finding the absolute configuration is the following. Use the single isomorphous replacement method with anomalous scattering (SIRAS), as just described, for the calculation of two sets of phase angles, corresponding to the two centrosymmetrically related sets of heavy atoms. With these two sets of protein phase angles, two difference Fourier maps are calculated for a second heavy atom derivative, PH(2):

1. Amplitudes  $|F_{PH(2)}| - |F_P|$  and one set of SIRAS phase angles
2. Amplitudes  $|F_{PH(2)}| - |F_P|$  and the alternative set of SIRAS phase angles

The difference Fourier map calculated with the correct set of phase angles (and the correct set of heavy atom positions) will show the highest peaks. This fixes the absolute configuration.

## 9.5. Multiple- and Single-Wavelength Anomalous Diffraction (MAD and SAD)

### 9.5.1. MAD

If the protein has anomalous scatterers in its molecule, the difference in intensity between the Bijvoet pairs,  $|F_H(+)|^2$  and  $|F_H(-)|^2$ , can profitably be exploited for the protein phase angle determination. In the multiple-wavelength method, the wavelength dependence of the anomalous scattering is used. The principle of this method is rather old, but it was the introduction of the tunable synchrotron radiation sources that made it a technically feasible method for protein structure determination. Hendrickson and colleagues (Hendrickson et al., 1988; Krishna Murthy et al., 1988) were the first to take advantage of this method and to use it for solving the structure of a protein (see also Guss et al., 1988). Of course, the protein should contain an element that gives a sufficiently strong anomalous signal. Therefore, the elements in the upper rows of the periodic system are not suitable. Hendrickson showed that the presence of one Se atom (atomic number 34) in a protein of not more than  $\sim 150$  amino acid residues is sufficient for a successful application of MAD (Hendrickson et al., 1990; Leahy et al., 1992); however, this depends very much on the quality of the data. With more Se atoms, the size of the protein can, of course, be larger. One way to introduce Se into a protein is by growing a micro-organism on a Se-methionine-containing substrate instead of a methionine-containing substrate. Condition for application of the method is that the wavelengths are carefully chosen to optimize the difference in intensity between Bijvoet pairs and between the diffraction at the selected wavelengths. In

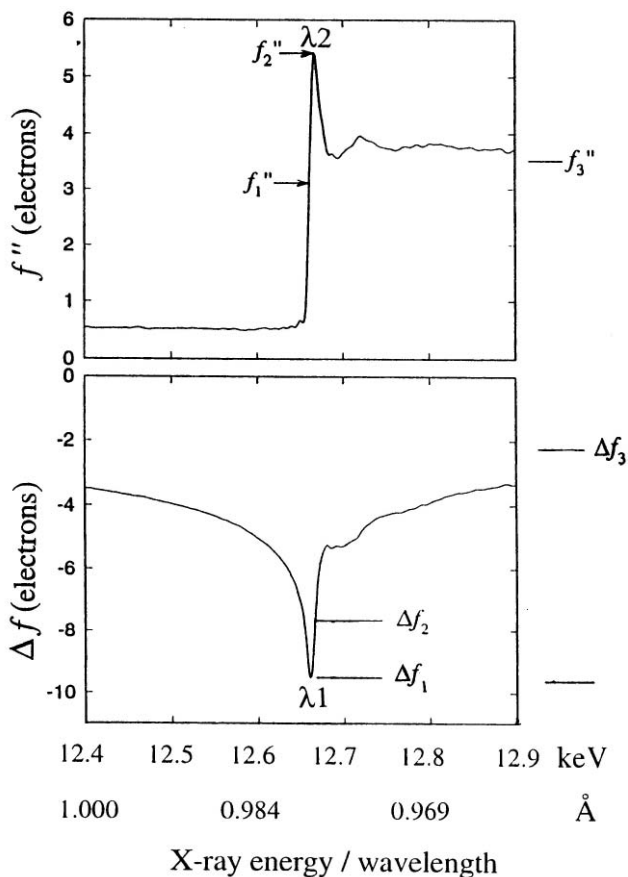


Figure 9.4. The curves for the real ( $\Delta f$ ) and imaginary ( $f''$ ) components of the anomalous scattering around the K-edge of selenium as a function of the wavelength. The minimum of  $\Delta f$  is at  $\lambda_1$ ;  $f''$  has the value  $f_1''$  at this wavelength. The maximum of  $f''$  is at  $\lambda_2$ ;  $\Delta f$  has the value  $\Delta f_2$ . The third wavelength,  $\lambda_3$ , is far to the right, at 0.93 Å. At this remote wavelength,  $\Delta f$  has the value  $\Delta f_3$ , and  $f''$  has the value  $f_3''$ . (Reproduced in a slightly modified form from: Ramakrishnan, V. and Biou, V. in *Methods in Enzymology*, Vol. 276, published by Academic Press Inc. Permission obtained.)

Figure 9.4, the anomalous scattering contributions  $\Delta f$  (the real part) and  $f''$  (the imaginary part) for Se are presented at three different wavelengths<sup>1</sup>: The position of the extremes in the curves is slightly affected by the chemical environment. To obtain optimal results, the curves must be determined for the protein crystal under investigation. See Note 1 in Section 9.5.3.

<sup>1</sup> Note that we indicate the real part of the anomalous signal by  $\Delta f$ , whereas in the literature, it is often called  $f'$ .

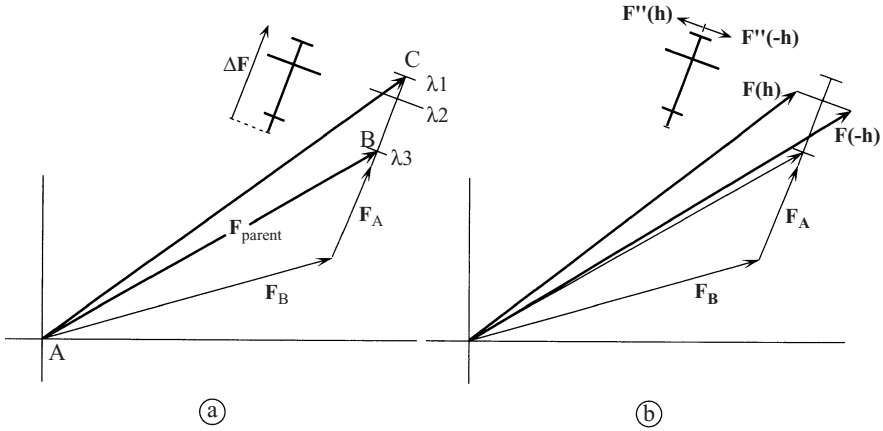


Figure 9.5. MAD as isomorphous replacement.  $F_B$  is the contribution to the structure factor by the nonanomalously scattering atoms,  $F_A$  is the nonanomalous contribution of the anomalously scattering atoms. The parent structure factor  $F_{parent} = F_B + F_A + \Delta F$ . The anomalous scattering contributions  $\Delta F$  and  $F''$  have been exaggerated. Moreover, the sign of  $\Delta F$  is taken as positive for easier drawing. (a) The processing of the data as isomorphous (dispersive) information.  $\Delta F_1 - \Delta F_3$  is comparable with the heavy atom contribution in real isomorphous replacement. (b) The processing of the data from anomalous information by exploiting the difference between  $|F(\mathbf{h})|$  and  $|F(-\mathbf{h})|$ . As usual, the structure factor  $F(-\mathbf{h})$  in the figure is the mirror image of the actual  $F(-\mathbf{h})$  with respect to the horizontal axis in the Argand diagram.

Usually, diffraction data are collected at three different wavelengths (Figure 9.4):

- $\lambda_1$  (also called the “edge”), where  $\Delta f$  has its minimum.
- $\lambda_2$  (also called the “white line”), where  $f''$  has its maximum and where the Bijvoet difference (between  $|F(\mathbf{h})|$  and  $|F(-\mathbf{h})|$ ) is largest.
- $\lambda_3$ , remote from the edge, on the left or right, where  $\Delta f$  and  $f''$  are small.

The position of the minimum of  $\Delta f$  (at  $\lambda_1$ ) corresponds to the position of the inflection point ( $f''_1$ ) in the  $f''$  curve.

The physical effect of anomalous scattering is not different from isomorphous replacement. In the latter method, a change in scattering is produced by introducing a sufficiently heavy atom, and in MAD, it is produced by changing the scattering of an existing atom (Ramakrishnan and Biou, 1997). The real and imaginary contributions to atomic scattering are wavelength dependent, and this effect is exploited in MAD (Figure 9.5). A typical strategy for data collection and processing is presented here. It is assumed that there is only one type of anomalously scattering atoms. We will call the real contribution to the atomic scattering by all anomalous scatterers in the crystal  $\Delta F$ . For the data collected with  $\lambda_1$ , this is  $\Delta F_1$ , and for the other datasets, they are  $\Delta F_2$  and  $\Delta F_3$ . The imaginary contribution is  $F''_1$  for the  $\lambda_1$  dataset,  $F''_2$  for the  $\lambda_2$  dataset, and  $F''_3$  for the  $\lambda_3$  dataset. The wavelengths are

chosen as in Figure 9.4 with the  $\lambda_3$  dataset as the parent; the other two datasets are scaled to the parent set. We distinguish two processes: isomorphous or dispersive MAD<sup>2</sup> (Figure 9.5a) and anomalous MAD (Figure 9.5b).

In isomorphous MAD the large difference between  $\Delta\mathbf{F}_3$  and  $\Delta\mathbf{F}_1$  is exploited as the major change in the structure factor by the anomalous scatterers. To remove the relatively small  $\mathbf{F}''$  contribution, the Bijvoet pairs in the  $\lambda_1$  and  $\lambda_3$  sets are averaged. In fact,  $\mathbf{F}_{\text{parent}}$  is taken as  $\mathbf{F}_B + \mathbf{F}_A + \Delta\mathbf{F}_3$  and triangle  $ABC$  in Figure 9.5a is comparable to triangle  $ABC$  in Figure 7.8 of Chapter 7. The processing is exactly as in isomorphous replacement.

In anomalous MAD, the  $\lambda_2$  set is chosen, the reason being that it has relatively strong differences between the Bijvoet pairs because of the large  $\mathbf{F}''^2$ .

In processing MAD data, the first step is locating the anomalous scatterers (the substructure) in the unit cell. This can be done with an anomalous difference Patterson (Section 7.9 of Chapter 7) or with a direct method [e.g., SHELXD (Schneider and Sheldrick, 2002; Usón et al. 2003), SnB (Hauptman, 1997a, 1997b)] (see Chapter 11) or a matrix method (Graaff et al., 2001). After refinement of the substructure, preliminary protein phase angles can be found with single isomorphous replacement (Section 7.14 of Chapter 7). The combined information from anomalous and isomorphous MAD is the input into a refinement procedure.

### 9.5.2. SAD

The disadvantage of MAD is the collection of data at three different wavelengths, the inherently long exposure time, and the danger of radiation damage to the crystal. These disadvantages are much less serious if the crystal structure could be solved by data collection on a single crystal with one wavelength only. A single wavelength is also sufficient in isomorphous replacement, but native and derivative crystals are required. For a structure determination with SAD, the crystal must contain an anomalous scatterer that provides a sufficiently strong anomalous signal. Already in 1981, Hendrickson and Teeter (1981) determined the structure of the small protein crambin with sulfur as the anomalous scatterer, but technological advances were required for a revival of the technique, which is now gradually overtaking MAD (Brodersen et al., 2000; Dauter, 2002; Dauter et al., 2002; Leonard et al., 2005; Rice et al., 2000).

The C, N, and O atoms in protein molecules do not show an anomalous diffraction effect sufficiently strong for the determination of phase angles. Sulfur atoms do so and this can be employed for proteins if the molecular weight is not too high. The K-absorption edge of S is near 5.02 Å, too far from the window with suitable synchrotron X-ray wavelengths between 0.8 and 2 Å. This is the reason that S is not a useful anomalous scatterer for MAD. For SAD with S as anomalous scatterer, a longer wavelength, for instance, synchrotron radiation or an X-ray generator with Cr anode ( $\lambda = 2.29$  Å) (Kitago et al., 2005; Mueller-Dieckmann et al., 2005).

<sup>2</sup> Dispersive means wavelength dependent.

Any anomalous scatterer can be used for SAD. With anomalous scatterers stronger than S (e.g., Se or a metal atom), it is now a routine procedure, becoming more popular than MAD.

The principle of SAD is easily understood with the Figures 9.6a and 9.6b. In Figure 9.6a, the Argand diagram is drawn with the assumption that we know all relevant structure factors. The origin is at  $O$ . Note that in this figure, the contributions to the structure factor for the  $\bar{h} \bar{k} \bar{l}$  reflection have been reflected with respect to the horizontal axis in the Argand diagram, as is done in Section 7.9 of Chapter 7 (represented as its complex conjugate). This allows easy combination with the contributions by the  $h k l$  reflection.

- $\mathbf{F}_P$  is the structure factor of the light protein atoms, C, N, and O.
- $\mathbf{F}_A$  the nonanomalous part of the anomalous scatterers (the substructure); + the real part of their anomalous scattering,  $\mathbf{F}'_A$ , consisting of the  $\Delta f$  values of the anomalous scattering atoms.
- $\mathbf{F}_{PA}$  is the sum of  $\mathbf{F}_P$  and  $\mathbf{F}_A$ .
- $\mathbf{F}''_A(+)$  is the imaginary part of the anomalous scattering for reflection  $hkl$ .
- $\mathbf{F}''_A(-)$  is the same for reflection  $\bar{h}\bar{k}\bar{l}$ .
- The observed amplitudes are  $|F_{\text{obs}}^{(+)}|$  for  $hkl$  and  $|F_{\text{obs}}^{(-)}|$  for  $\bar{h}\bar{k}\bar{l}$ .

$\mathbf{F}_{\text{obs}}^{(+)}$  is equal to the sum of vectors  $\mathbf{F}_P$ ,  $\mathbf{F}_A$  and  $\mathbf{F}''_A(+)$ .

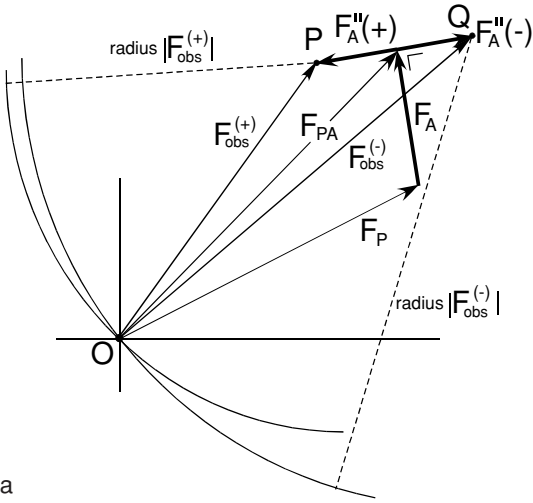
$\mathbf{F}_{\text{obs}}^{(-)}$  is equal to the sum of vectors  $\mathbf{F}_P$ ,  $\mathbf{F}_A$  and  $\mathbf{F}''_A(-)$

In applying SAD, the first step is the same as in MAD: the location of the anomalous scatterers from an anomalous Patterson map with coefficients  $||F(h k l)| - |F(\bar{h} \bar{k} \bar{l})||^2$  (Section 7.9 of Chapter 7) or by a direct method [e.g., SHELXD (Schneider and Sheldrick, 2002; Usón et al. 2003) or SnB (Hauptman, 1997a, 1997b)] (Section 11.2 of Chapter 11). This known information has been indicated as heavy vectors in Figure 9.6a. Moreover, the amplitudes but not the phase angles are known for  $\mathbf{F}_{\text{obs}}^{(+)}$  and  $\mathbf{F}_{\text{obs}}^{(-)}$ . With point  $P$  as its center, a circle can be drawn with radius  $|F_{\text{obs}}^{(+)}|$ . In the same way, a second circle can be drawn with radius  $|F_{\text{obs}}^{(-)}|$  and center at point  $Q$ . Their point of intersection is at  $O$  from where vector  $\mathbf{F}_P$  is drawn. It is clear that knowledge of the point of intersection in

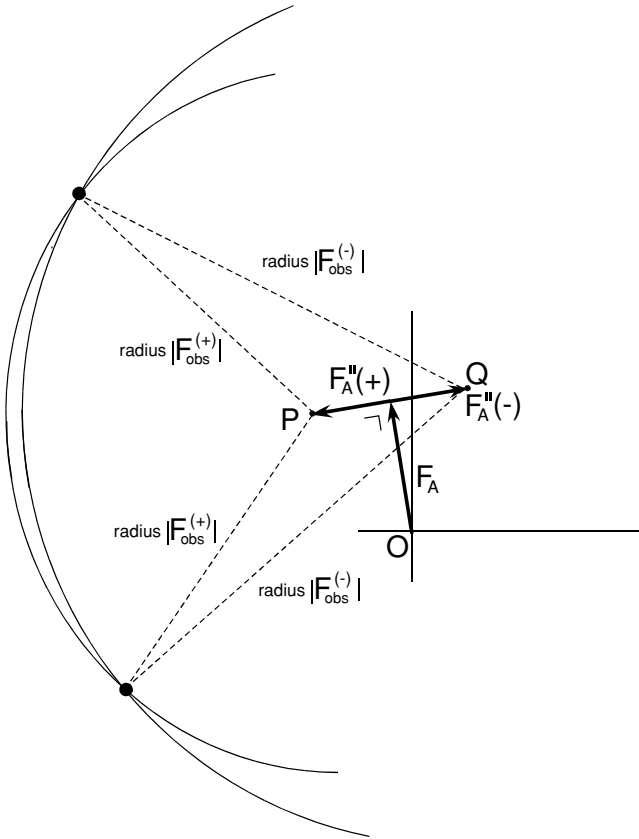
---

Figure 9.6. Argand diagram with the relevant vectors for application of SAD. (a) The origin of the Argand diagram is at the intersection of the two circles; (b) the origin has moved to the starting point of vector  $\mathbf{F}_A$ . This vector  $\mathbf{F}_A$  is the sum of the nonanomalous scattering by the substructure and the real part of its anomalous scattering. The anomalous part is  $\mathbf{F}''_A(+)$  for the  $h k l$  reflection and  $\mathbf{F}''_A(-)$  for  $\bar{h} \bar{k} \bar{l}$ . Note that in Figure 9.6, the contributions to the structure factor for the  $\bar{h} \bar{k} \bar{l}$  reflection have been reflected with respect to the horizontal axis in the Argand diagram as is done in Section 7.9 of Chapter 7. In this way,  $\mathbf{F}_P$  for the protein and  $\mathbf{F}_A$  for the substructure, are in this figure the same for  $h k l$  and  $\bar{h} \bar{k} \bar{l}$ . The amplitudes of the observed structure factors  $\mathbf{F}_{\text{obs}}^{(+)}$  for  $h k l$  and  $\mathbf{F}_{\text{obs}}^{(-)}$  for  $\bar{h} \bar{k} \bar{l}$  are known but not their phase angles. In this figure, the scattering by the substructure is exaggerated with respect to the protein scattering.





a



b

combination with structure factor contribution by the substructure (triangle  $OPQ$ ) is the clue to finding the structure factor  $\mathbf{F}_P$ . Now go to Figure 9.6b. The origin point  $O$  has been moved to the starting point of vector  $\mathbf{F}_A$  but otherwise nothing has changed, except that the figure shows only the known information. Moreover, the two circles do not have one but two points of intersection and two triangles present themselves for the phase angles of  $\mathbf{F}_{\text{obs}}^{(+)}$ , of  $\mathbf{F}_{\text{obs}}^{(-)}$ , and of  $\mathbf{F}_{\text{PA}}$ . In proceeding, one must first realize that although the substructure has been determined, its correct enantiomorph is not yet known. The usual way is to continue after refinement of the substructure, with both enantiomorphs, and select the better of the two resulting protein electron density maps.

How to choose between the two alternatives for  $\mathbf{F}_{\text{PA}}$ ? The way to proceed is by giving equal weight to the two alternatives. The phase angle is then chosen along the line  $PQ$ . The larger the difference between  $|\mathbf{F}_{\text{obs}}^{(+)}|$  and  $|\mathbf{F}_{\text{obs}}^{(-)}|$  is, the closer  $PQ$  approaches the direction of  $\mathbf{F}_{\text{PA}}$  and the more accurate the phase choice for  $\mathbf{F}_{\text{PA}}$  is. For  $|\mathbf{F}_{\text{obs}}^{(+)}| \ll |\mathbf{F}_{\text{obs}}^{(-)}|$ , the direction along  $PQ$  should be chosen from  $P$  to  $Q$ , or the phase angle is equal to that of  $\mathbf{F}_A + 270^\circ$ . If  $|\mathbf{F}_{\text{obs}}^{(+)}| \gg |\mathbf{F}_{\text{obs}}^{(-)}|$ , the opposite direction ( $Q \rightarrow P$ ) or the phase angle of  $\mathbf{F}_A + 90^\circ$  must be chosen. In this way, a reasonably reliable phase angle can be chosen for  $\mathbf{F}_{\text{PA}}$  if  $|\mathbf{F}_{\text{obs}}^{(+)}|$  and  $|\mathbf{F}_{\text{obs}}^{(-)}|$  are appreciably different. If, on the other hand, the difference between  $|\mathbf{F}_{\text{obs}}^{(+)}|$  and  $|\mathbf{F}_{\text{obs}}^{(-)}|$  is small, the choice is much less reliable. If  $|\mathbf{F}_{\text{obs}}^{(+)}|$  and  $|\mathbf{F}_{\text{obs}}^{(-)}|$  have the same length, the phase angle of  $\mathbf{F}_{\text{PA}}$  is equal to that of  $\mathbf{F}_A$  or has the opposite direction. The choice cannot be made. This is also true for centric reflections, for which  $|\mathbf{F}_{\text{obs}}^{(+)}| = |\mathbf{F}_{\text{obs}}^{(-)}|$ .

The resulting electron density map will then be a mixture of the correct structure and noise. If the polypeptide chain can be identified, the map can be improved by density modification. In principle, there is a slight preference for the alternative that has the phase angle of  $\mathbf{F}_{\text{PA}}$  closest to the phase angle of  $\mathbf{F}_A$ . The reason is that the anomalous scatterer contributes with  $\mathbf{F}_A$  to the total scattering, represented by  $\mathbf{F}_{\text{PA}}$ . Therefore, the phase angle of  $\mathbf{F}_{\text{PA}}$  is slightly biased toward  $\mathbf{F}_A$ . This is stronger if the substructure constitutes a larger fraction of the total structure.

The probability curve  $P_{\text{ano}}(\alpha)$  derived from anomalous scattering for the protein phase angle  $\alpha$  (Section 9.3 and Section 14.3 of Chapter 14) does not help in making the choice because it has the same value for both alternatives. A curve that does differentiate between the two alternatives is provided by the Sim probability curve for partial structures (Chapter 8). If the substructure is regarded as the partial structure, the equation becomes

$$P_{\text{Sim, ano}} = N^* \times \exp \left[ \frac{2 |F_{\text{PA}}| |F_A|}{\sum_1^n f_i^2} \cos(\alpha_{\text{PA}} - \alpha_A) \right]$$

The amplitude of  $\mathbf{F}_{\text{PA}}$  is the same for both alternatives (Figure 9.6a). This vector is comparable with vector  $\mathbf{F}$  in Figure 8.1 of Chapter 8.  $\mathbf{F}_A$  represents the known part

of the structure. The angle ( $\alpha_{PA} - \alpha_A$ ) is comparable with the angle ( $\alpha_{PH} - \alpha_H$ ) in Figure 7.13 of Chapter 7. It is different for the two alternatives.

It is customary to use the product of  $P_{\text{ano}}$  and  $P_{\text{Sim, ano}}$  as the final probability curve (Chapter 14). A similar method but taking errors into account has been published by Giacovazzo et al. (2003).

### 9.5.3. Notes

1. Anomalous contributions to the structure factor are small and, therefore, it is important to select the three wavelengths near an absorption edge of the anomalous scatterer: more precisely,  $\lambda_1$  for the dispersive difference exactly at the dip in the  $\Delta f$  curve and  $\lambda_3$  for the anomalous difference on the sharp peak in the  $f''$  curve. Moreover, the synchrotron beam must be highly stable.

The anomalous contribution to the atomic scattering factor is a function of the atomic absorption coefficient for the anomalously scattering element and can be derived from the experimental values of this coefficient. The absorption coefficient must be measured at the absorption edge of the element and at some distance from the edge. Because the precise position of the absorption edge depends on the chemical environment of the element, the spectrum of the atomic absorption coefficient as a function of the X-ray wavelength (or photon energy) should be measured on the crystal itself. This can conveniently be done by measuring the fluorescence from the element when radiated by an incident beam. Fluorescence is a product of the absorption, because in absorption, an electron is removed from its atomic orbital and fluorescent radiation is emitted when the empty position is filled up by another electron. The wavelength of the fluorescent radiation is characteristic for the irradiated element. In converting the fluorescence spectrum to the atomic absorption spectrum, background and scaling corrections are made in such a way that the experimental values for the atomic absorption coefficient fit their theoretical values. The latter cannot be calculated accurately inside the edge region, but it can be done outside of the edge region.

$$\mu_a = s \times R - (a + b\Delta + c\Delta^2),$$

where  $\mu_a$  is the atomic absorption coefficient and  $R$  is the fluorescence ratio  $I_{f1}(E)/I_0(E)$ , in which  $I_{f1}(E)$  is the fluorescent intensity and  $I_0(E)$  is the intensity of the incident beam.  $E$  is the energy of the incident photons.  $\Delta = E - E_0$ , where  $E_0$  corresponds with the photon energy at the absorption edge.  $s$  is a scale factor that is assumed to be independent of  $E$ .  $s$ ,  $a$ ,  $b$ , and  $c$  are chosen such that the experimental and theoretical curves fit as closely as possible to each other.

The atomic absorption curve ( $\mu_a$  as a function of  $\lambda$ ) is directly related to the wavelength dependence of the imaginary part of the anomalous scattering, and the position of the peak in the absorption curve corresponds exactly with the position of the peak in the  $f''$  curve (for an explanation, see the end of

this section). The real part,  $\Delta f$ , can be derived from the imaginary part by the Kramers–Kronig transformation (Hendrickson et al., 1988). The mathematical relationships are derived in James (1965). It turns out that the dip in the  $\Delta f$  curve corresponds with the inflection point in the  $f''$  curve, as indicated in Figure 9.4.

2. Bijvoet differences are most accurately measured if the corresponding reflections,  $hkl$  and  $\bar{h}\bar{k}\bar{l}$ , or a symmetry-related one, are measured close together in time, for instance by the inverse beam geometry: measure  $hkl$ , rotate the crystal  $180^\circ$ , and measure  $\bar{h}\bar{k}\bar{l}$  (see Figure 4.20 of Chapter 4). By measuring them close together, differences because of beam instability, radiation damage of the crystal, or absorption by ice growing on the specimen in a cryo experiment can be avoided.
3.  $f''$  is always positive.  $\Delta f$  can be either positive or negative.
4. The great advantage of MAD is ideal isomorphism. Data collection for all wavelengths is on the same crystal or the same type of crystal.
5. Anomalous scattering is the result of tightly bound electrons close to the atomic nucleus. Because this inner region is small in size, the anomalous effect stays rather constant up to the resolution edge for proteins. It means that the relative contribution by the anomalous scattering increases with resolution.
6. An overview of a typical MAD experiment is given by Walsh et al. (1999).
7. Lanthanide ions have the advantage of a strong anomalous signal. Girard et al. (2003) have developed a number of gadolinium complexes with excellent protein-binding properties. In Table 9.1, a number of edge wave lengths are listed.
8. The effect of anomalous scattering on the electron density. The density is calculated with the coefficients

$$|F(hkl)| \exp[ia(hkl)]$$

and

$$|F(\bar{h}\bar{k}\bar{l})| \exp[ia(\bar{h}\bar{k}\bar{l})].$$

Table 9.1. X-ray Absorption Edges for a Number of Elements

K-edges in Å						
Fe	Cu	Zn	Se	Br		
1.7436	1.3806	1.2834	0.9796	0.9202		
L <sub>III</sub> -edges in Å						
I	Gd	Sa	Ir	Pt	Au	Hg
2.7207	1.7109	1.8452	1.1054	1.0720	1.0401	1.0093

More data are found in the *International Tables for Crystallography, Volume C*, 2nd ed., Wilson, A.J.C. and Prince, E., eds, Kluwer Academic, Dordrecht, 1999.

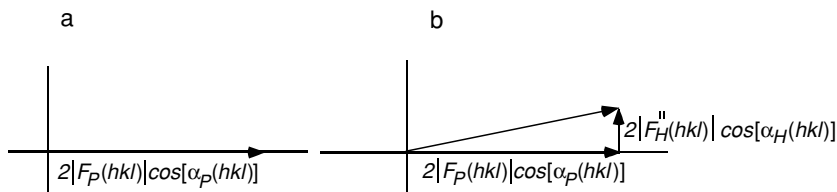


Figure 9.7. The sum of structure factors  $\mathbf{F}(hkl)$  and  $\mathbf{F}(\bar{h}\bar{k}\bar{l})$  (a) if an anomalous scatterer is absent and (b) when it is present.

If an anomalous scatterer is absent,  $|F(hkl)| = |F(\bar{h}\bar{k}\bar{l})|$  and  $\alpha(hkl) = -\alpha(\bar{h}\bar{k}\bar{l})$ . The coefficients can be combined to (Section 4.11 of Chapter 4)

$$2 |F(hkl)| \cos[\alpha(hkl)].$$

These combinations are vectors along the real axis in the Argand diagram and the electron density calculated with them is also real.

With an anomalous scatterer in the structure,

$$|F(hkl)| \neq |F(\bar{h}\bar{k}\bar{l})|$$

and

$$\alpha(hkl) \neq -\alpha(\bar{h}\bar{k}\bar{l})$$

The sum of  $\mathbf{F}(hkl)$  and  $\mathbf{F}(\bar{h}\bar{k}\bar{l})$  is a vector not directed along the real axis but slightly off (Figure 9.7). However, for the calculation of the electron density, this is often neglected, and for  $\mathbf{F}(hkl)$  and  $\mathbf{F}(\bar{h}\bar{k}\bar{l})$ , the average value is taken with the result of a slightly wrong electron density. Of course, this can be avoided by processing the structure factors for  $hkl$  and  $\bar{h}\bar{k}\bar{l}$  separately.

---

### The Relation Between Absorption and the Imaginary Part of Anomalous Scattering

The direct relationship between absorption and the imaginary part of anomalous scattering can easily be understood with the Argand diagram in Figure 9.8. The phase of the incident beam is indicated by a vector on the real axis, pointing to the right. A free electron scatters the X-ray beam with a phase angle of  $\pi$  with respect to the incident beam; its vector is pointing to the left, opposite to the incident beam vector (Section 4.14 of Chapter 14). In Section 4.15 of Chapter 4, we have seen that a plane of free electrons (or atoms with free electrons) scatters  $\pi/2$  behind a free electron. If the electrons are not completely free, there is an anomalous contribution to the scattering. The imaginary part of it has a phase angle  $\pi/2$  ahead of the scattering by free electrons; this is also true for a plane of electrons. The consequence is that a plane of anomalously scattering electrons has a phase angle just opposite to the incident beam. This expresses itself as absorption.

---

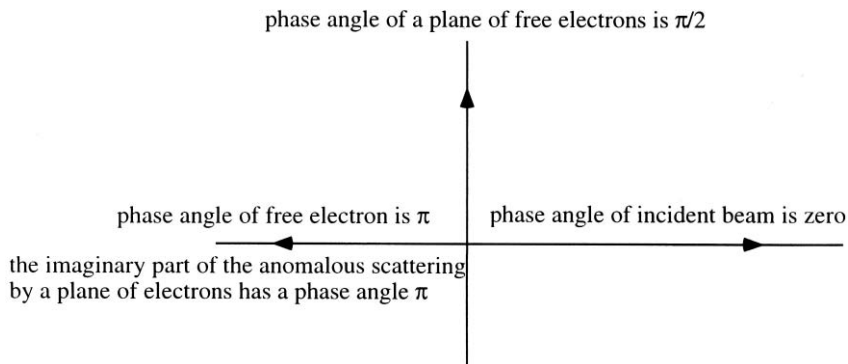


Figure 9.8. Vectors indicating phase angles in the Argand diagram. The vector for the incident beam is on the real axis, pointing to the right, because it is given phase angle 0. A free electron scatters the X-ray beam with a phase angle of  $\pi$  with respect to the incident beam; its vector is pointing to the left. A plane of free electrons (or atoms with free electrons) scatters  $\frac{1}{2}$  behind a free electron and the arrow is pointing upward. If the electrons are not completely free, the imaginary part of anomalous scattering by a plane of nonfree electrons has a phase angle  $\frac{1}{2}$  ahead of the scattering by free electrons, and its vector is pointing along the real axis to the left. The consequence is that a plane of anomalously scattering electrons has a phase angle component just opposite to the incident beam and that diminishes its intensity; in other words: absorption. This is true because in an absorption experiment, the incident beam and the scattered beam go in the same direction and interfere.

## Summary

Tightly bound electrons in an atom cause measurable anomalous scattering of X-rays. For light atoms (C, N, and O), the effect is negligible, but for heavier atoms (from S onward for the commonly used X-ray wavelengths) a measurable effect does occur and this causes a difference in intensity between Friedel pairs of reflection (anomalous effect). Moreover, anomalous scattering is wavelength dependent (dispersive effect).

Anomalous scattering is exploited for the improvement of phase angles as determined by isomorphous replacement. If sufficiently strong anomalously scattering atoms are present in, or introduced into, the native structure MAD or SAD can profitably be applied without the need for an isomorphous structure. MAD and SAD have become very popular phase-determination techniques. SAD is the preferable choice for high-throughput experiments because it has the advantage over MAD in that it is faster and better suited for automatic structure determination procedures by X-ray diffraction.

# Chapter 10

## Molecular Replacement

### 10.1. Introduction

With the isomorphous replacement method or with one of the anomalous diffraction techniques, a preliminary set of protein phase angles and a first model of the protein structure can be obtained. As we will see in Chapter 13, such a model can be refined by minimizing the difference between the observed  $|F|$  values and the  $|F|$  values calculated from the model. An easier way to obtain a first model can be followed if the structure of a protein with a homologous amino acid sequence has already been established. The structure of this homologous protein is—as it were—borrowed by the protein for which the structure must be determined and serves as a very first model that can subsequently be refined. This procedure is based on the observation that proteins, homologous in their amino acid sequence, have a very similar folding of their polypeptide chain. Also, if, for another reason, two structure can be expected to be similar, one known and the other unknown, the procedure can be applied.

The problem is to transfer the known protein molecular structure from its crystalline arrangement to the crystal of the protein for which the structure is not yet known. The solution is the molecular replacement method, which was initiated in pioneering studies by Rossmann and Blow (1962). Placement of the molecule in the target unit cell requires its proper orientation and precise position. In short, it involves two steps: rotation and translation. In the rotation step, the spatial orientation of the known and unknown molecule with respect to each other is determined, whereas in the next step, the translation needed to superimpose the now correctly oriented molecule onto the other molecule is calculated. The molecular replacement method can also serve another purpose: If a crystal structure has more than one protein molecule or a number of equal subunits in the asymmetric unit, then their relative position can be determined. This noncrystallographic symmetry is

useful information in the process of improving protein phase angles by molecular averaging (Section 8.4 of Chapter 8).

The basic principle of the molecular replacement method can be understood by regarding the Patterson function of a protein crystal structure. The Patterson map is a vector map: Vectors between atoms in the real structure show up as vectors from the origin to maxima in the Patterson map. If the pairs of atoms belong to the same molecule, then the corresponding vectors are relatively short and their end points are found not too far from the origin in the Patterson map; they are called *self-Patterson vectors*. If there were no intermolecular vectors (*cross-Patterson vectors*), this inner region of the Patterson map would be equal for the same molecule in different crystal structures, apart from a rotation difference. For homologous molecules, it is not exactly equal but very similar. Therefore, the self-Patterson vectors can supply us with the rotational relationship between the known and the unknown molecular structures. From the cross-Patterson vectors, the translation required for moving the molecules to their correct position can be derived. The principle of separating the Patterson vectors into these two groups and using them for orientation and translation determination was given by Hoppe (1957).

## 10.2. The Rotation Function

We will first consider how the angular relationship between identical units within one asymmetric unit (*self-rotation function*) or between equal or closely related molecules in two different crystal forms (*cross-rotation function*) can be derived from the X-ray data. This will be discussed following the original Rossmann and Blow procedure. It is true that in many of the software packages available to calculate the rotational orientation, the conventional Rossmann and Blow procedure is replaced by the mathematically more elegant Crowther's fast rotation function (Crowther, 1972). Even more advanced is the introduction of maximum likelihood techniques (Section 13.2.2 of Chapter 13) for the solution of the rotation and translation problem (McCoy et al., 2005; Storoni et al., 2004). However, the principle of the method can be best understood with the Rossmann and Blow procedure.

The self-Patterson peaks all lie in a volume around the origin with a radius equal to the dimension of the molecule (or subunit). If a number of identical molecules (or subunits) lie within one asymmetric unit, the self-Patterson vector distribution is exactly the same for all of these molecules, except for a rotation that is the same as their noncrystallographic rotational symmetry in real space. Therefore, if the Patterson function is superimposed on a correctly rotated version, maximum overlap between the two Patterson maps will occur. Similarly, for two different lattices, the two different Patterson maps must be superposed to maximum overlap by a rotation of one of the two maps.

We assume that the crystal system has orthogonal axes. An atom in one system is located at position  $\mathbf{x} = x_1\mathbf{a}_1 + x_2\mathbf{a}_2 + x_3\mathbf{a}_3$  in a crystallographic lattice with axes  $\mathbf{a}_1$ ,  $\mathbf{a}_2$ , and  $\mathbf{a}_3$ . Rotation of the axial system, keeping the same origin, leads



to a new set of axes:  $\mathbf{a}_{r,1}$ ,  $\mathbf{a}_{r,2}$  and  $\mathbf{a}_{r,3}$ . With respect to the new axes, the position of the particular atom in position  $\mathbf{x}$  is  $\mathbf{x}_r = x_{r,1}\mathbf{a}_{r,1} + x_{r,2}\mathbf{a}_{r,2} + x_{r,3}\mathbf{a}_{r,3}$  and the relationship between the two sets of coordinates is

$$\left. \begin{aligned} x_{r,1} &= c_{11}x_1 + c_{12}x_2 + c_{13}x_3 \\ x_{r,2} &= c_{21}x_1 + c_{22}x_2 + c_{23}x_3 \\ x_{r,3} &= c_{31}x_1 + c_{32}x_2 + c_{33}x_3 \end{aligned} \right\} \text{ or in matrix notation } \mathbf{x}_r = [C]\mathbf{x}.$$

A rotation of the axes has the same effect as a rotation of the structure in the opposite direction. If the structure rotates, its Patterson map rotates in the same way. Applying the rotation  $[C]$  to the Patterson function  $P(\mathbf{u})$  gives the rotated Patterson function  $P_r(\mathbf{u}_r)$ . An overlap function  $R$  of  $P(\mathbf{u})$  with the rotated version,  $P_r(\mathbf{u}_r)$ , of the same crystal lattice (self-rotation function) or a different crystal lattice (cross-rotation function) is defined as

$$R(\alpha, \beta, \gamma) = \int_U P(\mathbf{u}) \times P_r(\mathbf{u}_r) d\mathbf{u}. \quad (10.1)$$

$U$  is the volume in the Patterson map where the self-Patterson peaks are located. The product function  $R$  depends on the rotation angles (related to  $[C]$ ) and will have a maximum value for correct overlap.  $P(\mathbf{u})$  can be expanded in a Fourier series:

$$P(\mathbf{u}) = \frac{1}{V} \sum_{\mathbf{h}} |F(\mathbf{h})|^2 \exp[-2\pi i \mathbf{h}\mathbf{u}].$$

For  $P_r(\mathbf{u}_r)$  can be written

$$P_r(\mathbf{u}_r) = \frac{1}{V} \sum_{\mathbf{h}'} |F(\mathbf{h}')|^2 \exp[-2\pi i \mathbf{h}'\mathbf{u}_r].$$

Because  $\mathbf{u}_r = [C]\mathbf{u}$ ,

$$P_r(\mathbf{u}_r) = \frac{1}{V} \sum_{\mathbf{h}'} |F(\mathbf{h}')|^2 \exp[-2\pi i \mathbf{h}'[C]\mathbf{u}],$$

$\mathbf{h}'[C]$  is equal to  $[C^{-1}]\mathbf{h}'$ , and, therefore,

$$P_r(\mathbf{u}_r) = \frac{1}{V} \sum_{\mathbf{h}'} |F(\mathbf{h}')|^2 \exp[-2\pi i [C^{-1}]\mathbf{h}'\mathbf{u}],$$

which is equal to

$$\frac{1}{V} \sum_{\mathbf{h}'} |F([C]\mathbf{h}')|^2 \exp[-2\pi i \mathbf{h}'\mathbf{u}].$$

$P(\mathbf{u})$  and  $P_r(\mathbf{u}_r)$  must now be superimposed and  $P(\mathbf{u}) \times P_r(\mathbf{u}_r)$  calculated for every position  $\mathbf{u}$  within  $U$  and then the integral must be taken to obtain  $R(\alpha, \beta, \gamma)$ :

$$R(\alpha, \beta, \gamma) = \frac{1}{V^2} \sum_{\mathbf{h}} \sum_{\mathbf{h}'} |F(\mathbf{h})|^2 |F([C]\mathbf{h}')|^2 \times \int_U \exp[-2\pi i (\mathbf{h} + \mathbf{h}')\mathbf{u}] d\mathbf{u} \quad (10.2)$$

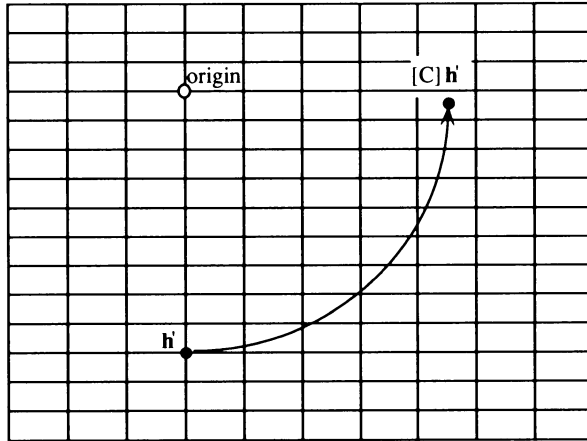


Figure 10.1. The effect of a rotation  $[C]$  in reciprocal space is that an integral lattice point  $\mathbf{h}'$  ends up at a nonintegral lattice position  $[C]\mathbf{h}'$ . This is illustrated here for a two-dimensional lattice.

A problem arises here: For the calculation of  $P_r(\mathbf{u}_r)$ , the coefficients must be sampled at positions  $[C]\mathbf{h}'$  in reciprocal space, which is impossible, because, in general,  $[C]\mathbf{h}'$  is at nonintegral reciprocal lattice positions (Figure 10.1). This problem can be solved together with another problem, namely that an enormous number of terms must be calculated, because a multiplication is required for each  $\mathbf{h}$  with all  $\mathbf{h}'$ . However, it is not as difficult as it looks like, because of the weighting term

$$\int_U \exp[-2\pi i(\mathbf{h} + \mathbf{h}')\mathbf{u}]d\mathbf{u}.$$

It limits the summation over  $\mathbf{h}'$  to only a restricted number of  $\mathbf{h}'$  terms. This can be understood in the following way. Suppose a crystalline lattice has a very special structure: It contains in each unit cell a body with the shape and the volume of  $U$ . The center of  $U$  is at the origin of the unit cell. The electron density inside  $U$  is flat  $[\rho(\mathbf{x}) = \rho]$ , and outside  $U$ , the unit cell is empty:  $\rho(\mathbf{x}) = 0$  (Figure 10.2). The structure factor of this special structure at reciprocal lattice position  $-(\mathbf{h} + \mathbf{h}')$  is

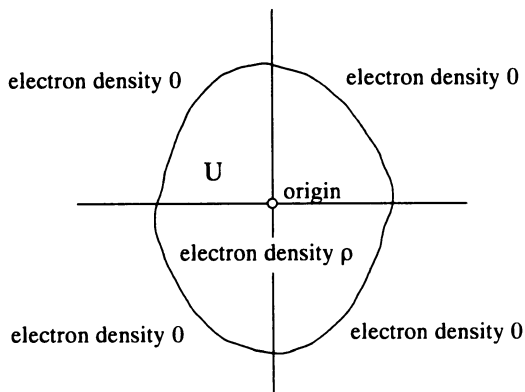
$$F[-(\mathbf{h} + \mathbf{h}')] = V \int_V \rho(x) \exp[-2\pi i(\mathbf{h} + \mathbf{h}')\mathbf{x}] dx.$$

Because of the special electron density distribution,

$$\mathbf{F}[-(\mathbf{h} + \mathbf{h}')] = V\rho \int_U \exp[-2\pi i(\mathbf{h} + \mathbf{h}')\mathbf{x}] d\mathbf{x}. \tag{10.3}$$

If the Fourier transform of the body with the shape and volume of  $U$  and unit electron density is  $\mathbf{G}$ , then the value of the transform for the body with uniform

Figure 10.2. The integral in Equation (10.2) is developed by using a special structure that has a flat electron density inside the three-dimensional body  $U$  [ $\rho(\mathbf{x}) = \rho$ ] and no electron density outside  $U$  [ $\rho(\mathbf{x}) = 0$ ]. The center of  $U$  is in the origin of the unit cell.



electron density  $\rho$  at reciprocal lattice position  $-(\mathbf{h} + \mathbf{h}')$  is

$$U \times \rho \times \mathbf{G}[-(\mathbf{h} + \mathbf{h}')]. \quad (10.4)$$

Comparing Equations (10.3) and (10.4) gives

$$\int_U \exp[-2\pi i(\mathbf{h} + \mathbf{h}')\mathbf{x}] d\mathbf{x} = \frac{U}{V} \times \mathbf{G}[-(\mathbf{h} + \mathbf{h}')]. \quad (10.5)$$

The rotation function can thus be written as

$$R(\alpha, \beta, \gamma) = \frac{U}{V^3} \sum_{\mathbf{h}} \sum_{\mathbf{h}'} |F(\mathbf{h})|^2 |F([\mathbf{C}]\mathbf{h}')|^2 \times \mathbf{G}[-(\mathbf{h} + \mathbf{h}')]. \quad (10.6)$$

The properties of  $\mathbf{G}[-(\mathbf{h} + \mathbf{h}')]$  allow us to solve the two problems mentioned earlier. Usually,  $U$  is assumed to be spherical and the transform of a sphere with radius  $\mathbf{r}$  at the origin of a unit cell is

$$G = \frac{3(\sin 2\pi x - 2\pi x \cos 2\pi x)}{(2\pi x)^3};$$

$x$  is in our case equal to  $(\mathbf{h} + \mathbf{h}') \cdot \mathbf{r}$ . The graphic representation of the function is shown in Figure 10.3.  $\mathbf{G}$  has its maximum value for  $\mathbf{h}' = -\mathbf{h}$  and falls off very rapidly for values of  $\mathbf{h}'$  differing from  $-\mathbf{h}$ . Therefore, the summation in Equation (10.2) can be performed for every  $\mathbf{h}$  with only a limited number of  $\mathbf{h}'$  terms, namely only those for which  $\mathbf{h}'$  is close to  $-\mathbf{h}$ . This solves the second problem.

The fall off of  $G$  can be illustrated with an example. Let the cell dimension be  $80 \text{ \AA}$  and the radius of the sphere  $r = 20 \text{ \AA}$ , then we obtain the following values

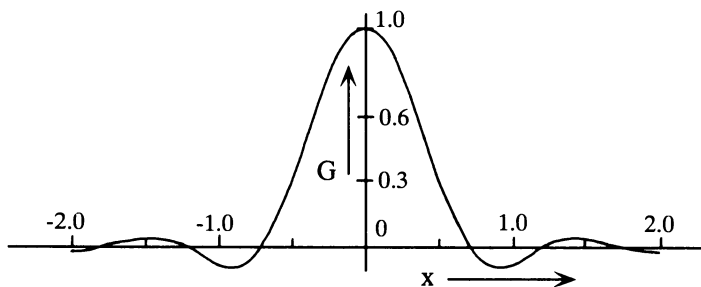


Figure 10.3. The function  $G = [3(\sin 2\pi x - 2\pi x \cos 2\pi x)]/(2\pi x)^3$  is plotted as a function of  $x$ . Note the rapid fading away for increasing  $x$ .

for  $G$ :

Distance from $-\mathbf{h}$ in reciprocal lattice units	$x$	$G$
1	0.25	0.78
2	0.50	0.30
3	0.75	-0.029

To solve the first problem,  $|F([\mathbf{C}]\mathbf{h}')|^2$  is calculated for a number of integral lattice points around  $([\mathbf{C}]\mathbf{h}')$  and the  $|F|^2$  value at  $([\mathbf{C}]\mathbf{h}')$  is obtained by interpolation, giving a weight  $G[(\mathbf{h} + \mathbf{h}')$  to the  $|F|^2$  values at the integral lattice points around  $([\mathbf{C}]\mathbf{h}')$ .

In the application of the rotation method, it is important that all strong reflections be present because the calculation of the rotation function basically depends on the rotation of a Patterson map, which is mainly determined by the strong reflections. Another point to consider is the resolution range of the data used in the calculation of the rotation function. Low-resolution data can be excluded because they are rather insensitive to rotation; moreover, they are determined to an appreciable extent by the solvent region. High-resolution data are more discriminating but are also more sensitive for the model. The best range is often found between 3 and 5 Å. Also, because of computational limitations, the integration is extended to a rather modest resolution.

Other parameters to choose are the shape and the size of the region  $U$ . For a matter of convenience, the region is assumed to be spherical. Its radius can be chosen equal to, or somewhat less than, the diameter of the molecule. In the calculation of the rotation function, the shorter intermolecular vectors confuse the situation. This can be improved if in the calculation of the rotation function, the known molecule is put into a large artificial unit cell having no crystallographic symmetry (space group  $P1$ ). The dimensions of the cell should be such that all cross-vectors are longer than the diameter of the molecule. Instead of working with the X-ray data from the crystal structure of the known molecule, the calculated

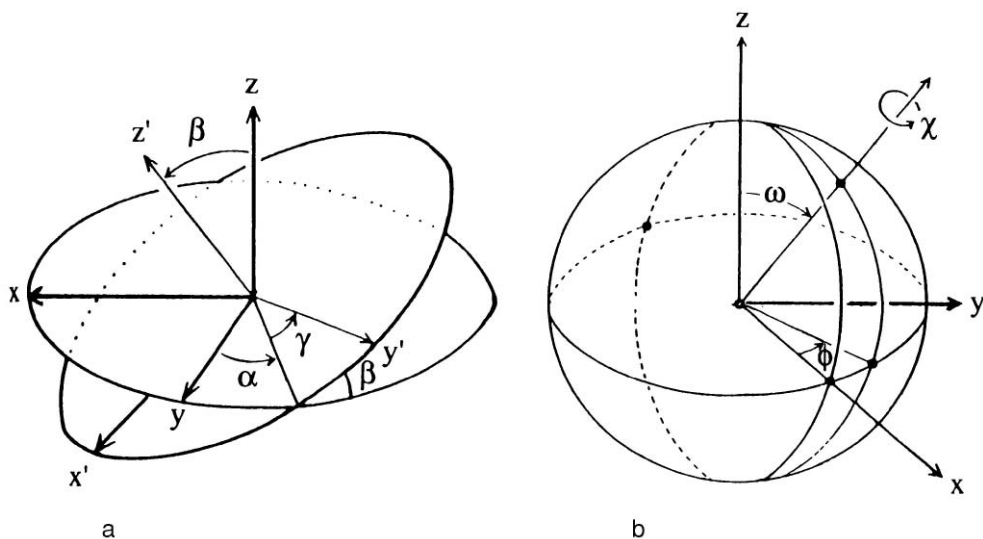


Figure 10.4. (a) Eulerian angles  $\alpha$ ,  $\beta$ , and  $\gamma$ ; (b) polar angles  $\chi$ ,  $\omega$ , and  $\phi$ . (Reproduced from the Proceedings of the Daresbury Study Weekend on Molecular Replacement, 15–16 February, 1985, with permission from the Daresbury Laboratory, Daresbury, Warrington, UK)

structure factors of the artificial lattice are used. It is not always easy to find the optimal model structure and different models must be tried if the first results are unsatisfactory. For instance, the original model can be truncated by deleting side chains (doubtful parts) using one monomer if the original model was an oligomer and using just one domain of the model molecule.

The magnitude of the rotation function is plotted in a three-dimensional space with the three angular rotations as the coordinates. Several alternatives and conventions for the directions, names, signs, and origins of the rotation angles exist. This can cause a great deal of confusion and it is extremely important to know the procedure in the available software package. The usual system works with Eulerian angles because then the symmetry of the rotation function shows up clearly. The system used by Rossmann and Blow in their original work (Rossmann and Blow, 1962) applies first a rotation by the angle  $\alpha$  around  $z$  of an orthogonal coordinate system, then around the new  $x$ -axis by an angle  $\beta$ , and, finally, a rotation by  $\gamma$  around the new  $z$ -axis. However, another convention is now generally used (Machin, 1985): Rotation by the angle  $\alpha$  around the  $z$ -axis, next a rotation by the angle  $\beta$  around the new  $y$ -axis, and, finally, a rotation by the angle  $\gamma$  around the new  $z$ -axis (Figure 10.4a). The sign for the rotation of the axes is positive for a clockwise rotation when looking from the origin along the positive rotation axis.

If one is searching for noncrystallographic symmetry in an asymmetric unit (self-rotation function), a zero rotation results in a high value for  $R$ , because it simply superposes the Patterson map on itself. An odd feature of  $R$  is the ridge in

the section  $\beta = 0$ . It represents the set of equivalent zero rotations ( $\alpha, 0, -\alpha$ ). This stems from the fact that for  $\beta = 0$ , the rotations  $\alpha$  and  $\gamma$  have the same effect on the rotation and, therefore, all rotations with the same  $\alpha + \gamma$  are identical. The same is also true for  $\beta = 180^\circ$ , where  $\alpha - \gamma$  rotations are equivalent. Equivalent effects can also be obtained for different combinations of the three angular coordinates, which causes symmetry in the rotation function. It depends on symmetry in the Patterson functions that are rotated with respect to each other and on the choice of the system of variables chosen for the rotation. Because of the symmetry in the rotation function, it needs to be calculated only for its asymmetric unit. Methods for deriving the asymmetric unit in the rotation function have been given by Tollin and Rossmann (1966), Narasinga Rao et al. (1980), and Moss (1985).

When searching for noncrystallographic symmetry, it is convenient to work with spherical polar rotation (Figure 10.4b).  $\omega$  and  $\phi$  determine the position of the rotation axis and  $\chi$  is the rotation around this axis. The advantage of this system derives from the fact that rotations of  $\chi = 180^\circ$  and  $120^\circ$  are very common and the search can be restricted to a fixed value for  $\chi$ . In Figure 10.4b,  $Z$  is the polar axis. However, when working in a monoclinic space group, it is convenient to have the unique  $y$ -axis as the polar axis.

From Equation (10.1) it is clear that the strong reflections will dominate the calculation of  $R$ . This is true to such an extent that it suffices to incorporate only a fraction of all reflections in the calculation—for instance, 10% with the highest intensities (Tollin and Rossmann, 1966). To obtain an impression of the quality of the rotation function it is advisable to give the ratio of the highest to the next highest peak in the rotation map.

In principle, a simpler way than the Rossmann and Blow method to solve the rotation problem was proposed by Huber and his colleagues (Huber, 1985). In their method, the Patterson map is also rotated and the rotated map is superimposed on the original map. However, now the operation is performed, not in reciprocal but in direct space. A number of high peaks (a few hundred to a few thousand) in the Patterson map are selected for a rough rotational search, which is done in steps of  $10^\circ$ . These peaks lie within a sphere around the origin where most of the self-Patterson peaks are located. However, the innermost region of this sphere, close to the high origin peak of the Patterson map, is neglected. As a fit criterion, the product of the map and its rotated version at corresponding grid points is used, as in the Rossmann and Blow procedure. After a highest peak or a few high peaks are found in the product function, the search can be continued in finer steps around these peaks.

### 10.3. The Translation Function

The rotation function is based on the rotation of a Patterson function around an axis through its origin. A translation is not incorporated. However, for the final solution of the molecular replacement method, the translation required to overlap one molecule (or subunit) onto the other in real space must be determined, after it

has been oriented in the correct way with the rotation function. The simplest way to do this is by trial and error. The known molecule is moved through the asymmetric unit and structure factors are calculated— $\mathbf{F}(\text{calc})$ —and compared with the observed structure factor by calculating an  $R$ -factor or the correlation coefficient as a function of the molecular position:

$$R = \frac{\sum_{hkl} \left| |F(\text{obs})| - k|F(\text{calc})| \right|}{\sum_{hkl} |F(\text{obs})|}.$$

The standard linear correlation coefficient  $C$  is

$$C = \frac{\sum_{hkl} (|F(\text{obs})|^2 - \overline{|F(\text{obs})|^2}) \times (|F(\text{calc})|^2 - \overline{|F(\text{calc})|^2})}{\left[ \sum_{hkl} (|F(\text{obs})|^2 - \overline{|F(\text{obs})|^2})^2 \sum_{hkl} (|F(\text{calc})|^2 - \overline{|F(\text{calc})|^2})^2 \right]^{1/2}}.$$

The advantage of this correlation coefficient over the  $R$ -factor is that it is scaling insensitive; replacement of  $|F(\text{obs})|^2$  by  $k|F(\text{obs})|^2$  ( $k$  is the scale factor for the intensities) gives the same value. During  $R$ -factor search calculations, one need not start to calculating the  $F(\text{calc})$  values from atomic coordinates every time the molecule is shifted; instead, one can calculate phase shifts for each set of the molecules related by crystallographic symmetry. This saves considerable computer time. The result from the rotation function can be refined by changing the rotation parameters in small steps. With increased computing power, it might be possible, instead of calculating the rotation and translation function, to carry out a six-dimensional search with the three rotation angles and the three translation components as parameters. It can also be helpful to exploit packing analysis; the protein molecules in the unit cell cannot penetrate each other and this limits the possible positions of the molecules. Although not necessarily giving a unique solution, it excludes parts of the unit cell, and in this way, it reduces the computer time (Harada et al., 1981; Hendrickson and Ward, 1976).

In a more straightforward method than the trial-and-error search, a translation function is calculated that gives the correlation between a set of cross-Patterson vectors for a model structure and the observed Patterson function. Cross-Patterson vectors in this context mean vectors in the Patterson map derived from vectors between atoms in two molecules in the model structure related by a crystallographic symmetry operation  $[C] + \mathbf{d}$ . In space group  $P1$ , in which no crystallographic symmetry exists, the origin can be chosen everywhere and this has no influence on the absolute value of the structure factor. The calculation of the translation function is then not necessary.

### 10.3.1. The Crowther and Blow Translation Function

Here, the translation function will be presented as derived by Crowther and Blow (1967) and we will do this for an unknown structure with crystals belonging to space

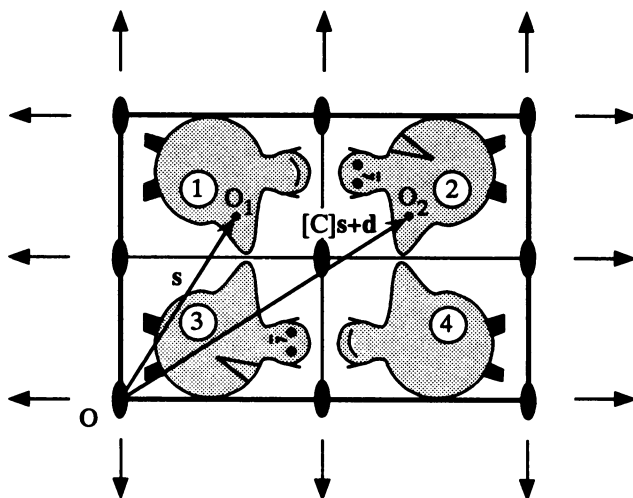


Figure 10.5. A unit cell for space group  $P222$ . It contains four molecules, 1–4. The origin of the unit cell is in  $O$ . Molecule 1 has its local origin in  $O_1$  at position  $s$ , and the origin of molecule 2 is in  $O_2$  at position  $[C]s + \mathbf{d}$ , where the matrix  $[C]$  transfers molecule 1 to molecule 2; see also Figure 10.6.

group  $P222$  (Figure 10.5). They have one molecule in the asymmetric unit and, therefore, four molecules (1–4) in the unit cell. We choose one pair of molecules (e.g., 1 and 2). Their orientation is known from the rotation function, but not their position in the unit cell. With the translation function we can determine the position of molecule 1 with respect to the symmetry related molecule 2 and, subsequently, for any other pair of symmetry-related molecules.

The local origin of molecule 1 is in  $O_1$  and that of molecule 2 in  $O_2$ . The origin of the unit cell is in  $O$ . Cross-Patterson vectors between the two molecules can then be calculated with (see Section 7.10 of Chapter 7)

$$P_{1,2}(\mathbf{u}) = \int_V \rho_1(\mathbf{x}) \times \rho_2(\mathbf{x} + \mathbf{u}) d\mathbf{x}. \quad (10.7)$$

If the electron density expressed with respect to the local origin of the first molecule, the model molecule  $M$ , is  $\rho_M$ , then (Figure 10.6)

$$\rho_1(\mathbf{x}) = \rho_M(\mathbf{x} - \mathbf{s})$$

and

$$\rho_2(\mathbf{x} + \mathbf{u}) = \rho(\mathbf{x} + \mathbf{u} - [C]s - \mathbf{d})$$

for the local origin in  $O_2$ . This is equal to the electron density in the model molecule (molecule 1) at the symmetry related position  $[C^{-1}](\mathbf{x} + \mathbf{u} - [C]s - \mathbf{d})$  and, therefore,

$$\rho_2(\mathbf{x} + \mathbf{u}) = \rho_M\{[C^{-1}](\mathbf{x} + \mathbf{u} - [C]s - \mathbf{d})\}.$$



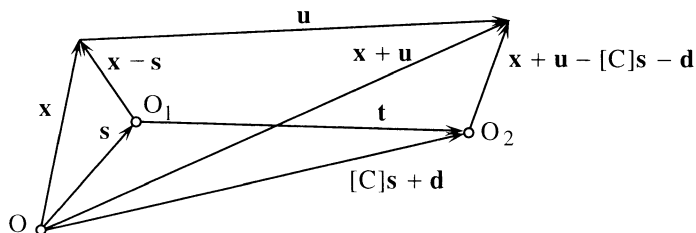


Figure 10.6. The position ( $\mathbf{x}$ ) in molecule 1 and ( $\mathbf{x} + \mathbf{u}$ ) in molecule 2.  $O_1$  and  $O_2$  are local origins.

Equation (10.7) becomes

$$P_{1,2}(\mathbf{u}, \mathbf{s}) = \int_V \rho_M(\mathbf{x} - \mathbf{s}) \times \rho_M\{[C^{-1}](\mathbf{x} + \mathbf{u} - [C]\mathbf{s} - \mathbf{d})\} d\mathbf{x}.$$

If  $\rho_M$  is written as a Fourier series in terms of the structure factors  $\mathbf{F}_M$ , we have

$$\begin{aligned} P_{1,2}(\mathbf{u}, \mathbf{s}) &= \int_V \sum_{\mathbf{h}} \mathbf{F}_M(\mathbf{h}) \exp[-2\pi i \mathbf{h} \cdot (\mathbf{x} - \mathbf{s})] \\ &\quad \times \sum_{\mathbf{p}} \mathbf{F}_M(\mathbf{p}) \exp[-2\pi i \mathbf{p}[C^{-1}](\mathbf{x} + \mathbf{u} - [C]\mathbf{s} - \mathbf{d})] d\mathbf{x} \\ &= \sum_{\mathbf{h}} \sum_{\mathbf{p}} \mathbf{F}_M(\mathbf{h}) \times \mathbf{F}_M(\mathbf{p}) \exp[2\pi i (\mathbf{h} \cdot \mathbf{s} + \mathbf{p}[C^{-1}]([C]\mathbf{s} + \mathbf{d}))] \\ &\quad \times \exp[-2\pi i \mathbf{p}[C^{-1}]\mathbf{u}] \int_V \exp[-2\pi i (\mathbf{h} + \mathbf{p}[C^{-1}])\mathbf{x}] d\mathbf{x}. \end{aligned}$$

Because  $[C]$  is a crystallographic rotation,  $\mathbf{p}[C^{-1}]$  is a reciprocal lattice point and, therefore,  $(\mathbf{h} + \mathbf{p}[C^{-1}])$  is an integral number, and as a consequence, the integral vanishes unless  $(\mathbf{h} + \mathbf{p}[C^{-1}]) = 0$  (see Figure 4.15 of Chapter 4). Then the integral is equal to  $V$ , with  $\mathbf{p} = -\mathbf{h}[C]$ . Deleting the constant  $V$ ,

$$P_{1,2}(\mathbf{u}, \mathbf{s}) = \sum_{\mathbf{h}} \mathbf{F}_M(\mathbf{h}) \cdot \mathbf{F}_M(-\mathbf{h}[C]) \exp[2\pi i \mathbf{h}(\mathbf{s} - [C]\mathbf{s} - \mathbf{d})] \exp[2\pi i \mathbf{h} \cdot \mathbf{u}].$$

If the intermolecular vector  $\mathbf{t}$  is between  $O_1$  and  $O_2$ , then

$$\mathbf{t} = -\mathbf{s} + [C]\mathbf{s} + \mathbf{d}.$$

Because  $\mathbf{F}_M(-\mathbf{h}[C]) = \mathbf{F}_M^*(\mathbf{h}[C])$  with  $\mathbf{F}_M^*$  the complex conjugate of  $\mathbf{F}_M$ ,

$$P_{1,2}(\mathbf{u}, \mathbf{t}) = \sum_{\mathbf{h}} \mathbf{F}_M(\mathbf{h}) \cdot \mathbf{F}_M^*(\mathbf{h}[C]) \exp[-2\pi i \mathbf{h} \cdot \mathbf{t}] \exp[2\pi i \mathbf{h} \cdot \mathbf{u}]. \quad (10.8)$$

This is the cross-Patterson function of the model structure in which two molecules are related by crystallographic symmetry. This should now be compared with the observed Patterson function  $P(\mathbf{u})$ . To this end, the translation function  $T(\mathbf{t})$  is

calculated:

$$T(\mathbf{t}) = \int_V P_{1,2}(\mathbf{u}, \mathbf{t}) \times P(\mathbf{u}) d\mathbf{u}. \quad (10.9)$$

When the intermolecular vector  $\mathbf{t}$  is equal to the true intermolecular vector  $\mathbf{t}_0$ , the function  $T(\mathbf{t})$  will reach a maximum value, because then the computed Patterson  $P_{1,2}(\mathbf{u}, \mathbf{t})$  fits correctly on the observed Patterson function  $P(\mathbf{u})$ . If  $P_{1,2}(\mathbf{u}, \mathbf{t})$  in Equation (10.9) is replaced by the right-hand side of Equation (10.8) and  $P(\mathbf{u})$  is replaced by  $\sum_{\mathbf{p}} |F_{\text{obs}}(\mathbf{p})|^2 \exp[-2\pi i \mathbf{p} \cdot \mathbf{u}] d\mathbf{u}$ , the translation function becomes

$$T(\mathbf{t}) = \int_V \sum_{\mathbf{h}} \mathbf{F}_M(\mathbf{h}) \cdot \mathbf{F}_M^*(\mathbf{h}[C]) \exp[-2\pi i \mathbf{h} \cdot \mathbf{t}] \exp[2\pi i \mathbf{h} \cdot \mathbf{u}] \\ \times \sum_{\mathbf{p}} |F_{\text{obs}}(\mathbf{p})|^2 \exp[-2\pi i \mathbf{p} \cdot \mathbf{u}] d\mathbf{u}$$

Because the integration is over  $\mathbf{u}$ , we can take all terms with  $\mathbf{u}$  together under the integral

$$T(\mathbf{t}) = \sum_{\mathbf{h}} \mathbf{F}_M(\mathbf{h}) \cdot \mathbf{F}_M^*(\mathbf{h}[C]) \exp[-2\pi i \mathbf{h} \cdot \mathbf{t}] \\ \times \sum_{\mathbf{p}} |F_{\text{obs}}(\mathbf{p})|^2 \int_V \exp[2\pi i (\mathbf{h} - \mathbf{p}) \cdot \mathbf{u}] d\mathbf{u}.$$

For the same reason as earlier, the integral vanishes unless  $\mathbf{h} - \mathbf{p} = 0$  or  $\mathbf{p} = \mathbf{h}$  and, therefore, apart from the constant  $V$ ,

$$T(\mathbf{t}) = \sum_{\mathbf{h}} |F_{\text{obs}}(\mathbf{h})|^2 \cdot \mathbf{F}_M(\mathbf{h}) \cdot \mathbf{F}_M^*(\mathbf{h} \cdot [C]) \exp[-2\pi i \mathbf{h} \cdot \mathbf{t}]. \quad (10.10)$$

This final form of the translation function is a Fourier summation in which the coefficients are known. Therefore, it can easily be calculated. Unwanted background in the translation function is caused by self-Patterson vectors (vectors between atoms within one molecule) and by ignoring the Patterson vectors between molecules other than those under consideration. Self-Patterson vectors can easily be eliminated from the observed Patterson map, assuming that the known and unknown molecules have the same structure and, therefore, the same self-Patterson vectors. As an example, we use again crystals with  $P222$  symmetry. The orientation of the four molecules in the unit cell is known from the rotation function. Therefore, self-Patterson functions for each of the molecules can be calculated with coefficients  $|F_{M(n)}(\mathbf{h})|^2$ , where  $n = 1 - 4$ . The self-Patterson-corrected translation function for the example of Figure 10.5 is then

$$T_1(\mathbf{t}) = \sum_{\mathbf{h}} \left\{ |F_{\text{obs}}(\mathbf{h})|^2 - \sum_{n=1}^4 |F_{M(n)}(\mathbf{h})|^2 \right\} \cdot \mathbf{F}_M(\mathbf{h}) \cdot \mathbf{F}_M^*(\mathbf{h} \cdot [C]) \\ \times \exp[-2\pi i \mathbf{h} \cdot \mathbf{t}]. \quad (10.11)$$

In addition, the intermolecular vectors for pairs of molecules that have already been solved could be subtracted.

The translation functions  $T(\mathbf{t})$  and  $T_1(\mathbf{t})$  are two dimensional with the intermolecular vectors  $\mathbf{t}$  perpendicular to the symmetry axis under consideration. For a complete solution of the unknown structure, the various two-dimensional translation functions must be combined. This is straightforward for the  $P222$  example discussed earlier, but more complicated in high-symmetry space groups. This is the reason that  $T_1(\mathbf{t})$  is no longer a very popular translation function. An improved translation function has been derived by Crowther and Blow (1967); it results in peaks corresponding to all possible intermolecular vectors in the unknown structure. The model structure now does not contain a pair of molecules, but the same number of molecules as the unknown crystal structure has in its unit cell.

Because of the large number of intermolecular vectors, it is now more convenient to use the position vector  $\mathbf{m}$  of the model molecule  $M$  as the variable. The positions and orientations of the other molecules ( $j = 2, \dots, n$ ) in the unit cell are derived from the model molecule by the operations  $[C_j]\mathbf{m} + \mathbf{d}_j$ . We must now derive an expression for the calculated Patterson function.

$$\mathbf{F}_{\text{calc}}(\mathbf{h}, \mathbf{m}) = \sum_{j=1}^n \mathbf{F}_M(\mathbf{h}[C_j]) \exp[-2\pi i \mathbf{h}([C_j]\mathbf{m} + \mathbf{d}_j)],$$

where  $\mathbf{F}_M(\mathbf{h}[C_j])$  is the contribution to the structure factor of reflection  $\mathbf{h}$  by the  $j$ th molecule with respect to its local origin in the orientation defined by  $[C_j]$ , and  $\exp[-2\pi i \mathbf{h}([C_j]\mathbf{m} + \mathbf{d}_j)]$  takes care of the fact that the origin of the molecule is at  $[C_j]\mathbf{m} + \mathbf{d}_j$ :

$$\mathbf{F}_{\text{calc}}(\mathbf{h}, \mathbf{m}) = \sum_{j=1}^n \mathbf{F}_M(\mathbf{h}[C_j]) \exp[-2\pi i \mathbf{h} \mathbf{d}_j] \exp[-2\pi i \mathbf{h}[C_j]\mathbf{m}].$$

Because  $|F_{\text{calc}}(\mathbf{h}, \mathbf{m})|^2 = \mathbf{F}_{\text{calc}}(\mathbf{h}, \mathbf{m}) \cdot \mathbf{F}_{\text{calc}}^*(\mathbf{h}, \mathbf{m})$ ,

$$\begin{aligned} |F_{\text{calc}}(\mathbf{h}, \mathbf{m})|^2 &= \sum_{j=1}^n \sum_{k=1}^n \mathbf{F}_M(\mathbf{h}[C_j]) \mathbf{F}_M^*(\mathbf{h}[C_k]) \times \exp[-2\pi i \mathbf{h}(\mathbf{d}_j - \mathbf{d}_k)] \\ &\quad \times \exp[-2\pi i \mathbf{h}([C_j] - [C_k])\mathbf{m}] = Q. \end{aligned}$$

The calculated Patterson function is then  $\mathbf{P}_{\text{calc}}(\mathbf{m}, \mathbf{u}) = \sum_{\mathbf{h}} Q \exp[-2\pi i \mathbf{h} \cdot \mathbf{u}]$ , and the new translation function is

$$\mathbf{T}_2(\mathbf{m}) = \int_V P_{\text{obs}}(\mathbf{u}) \times P_{\text{calc}}(\mathbf{m}, \mathbf{u}) d\mathbf{u}.$$

As earlier, this equation contains the integral

$$\int_V \exp[2\pi i (\mathbf{h} - \mathbf{p}) \cdot \mathbf{u}] d\mathbf{u},$$

which vanishes unless  $\mathbf{h} - \mathbf{p} = 0$ , and, therefore,

$$T_2(\mathbf{m}) = \sum_{\mathbf{h}} |\mathbf{F}_{\text{obs}}(\mathbf{h})|^2 \sum_{j=1}^n \sum_{k=1}^n \mathbf{F}_M(\mathbf{h}[C_j]) \mathbf{F}_M^*(\mathbf{h}[C_k]) \\ \times \exp[-2\pi i \mathbf{h}(\mathbf{d}_j - \mathbf{d}_k)] \times \exp[-2\pi i \mathbf{h}([C_j] - [C_k])\mathbf{m}].$$

This can be calculated as a Fourier summation if, instead of the normal index  $\mathbf{h}$ , the index is taken as  $\mathbf{h}([C_j] - [C_k])$ .

The name  $T_2(\mathbf{m})$  is confusing because it suggests a two-dimensional function, whereas, in fact, it is a three-dimensional function because it utilizes all symmetry operators simultaneously. So far, we have assumed that only one molecule is present in the asymmetric unit. Driessen et al. (1991) expanded this to asymmetric units containing more than one molecule (subunit) by associating each subunit in the asymmetric unit with an independent translation vector. An improvement of the signal-to-noise ratio can be obtained if the self-Patterson vectors are subtracted from both the observed and the calculated Pattersons. For further improvement, it is recommended that normalized structure factor amplitudes be used (Section 6.3 of Chapter 6) because this sharpens the Patterson map. Alternatively, a negative temperature factor parameter  $B$  can be applied.

In the two-step procedure, first one calculates the rotation function and, subsequently, the translation function, the latter usually causes more problems than the first; for example, the search model differs too much from the unknown structure or the highest peak in the rotation function does not correspond to the correct orientation. Several methods have been proposed to improve this situation:

- Combine the translation search with a limited systematic variation of the orientation parameters using the  $R$ -factor or the correlation coefficient as criterion.
- Refine the search model and its orientation after the rotation, but before the translation search (Patterson correlation refinement).
- Combine any existing phase information from isomorphous replacement with the translation function (phased translation function).
- Zhang and Matthews (1994) proposed a modified translation function if part of the structure is known (addition and subtraction strategy).

The first method has been described and successfully used by Fujinaga and Read (1987) in their program BRUTE. More recently, this was replaced by the program BEAST, applying a maximum-likelihood-based approach (Section 13.2.2 of Chapter 13) (Read, 2001). Inspired by previous work of Harada et al. (1981), they were the first to introduce the standard linear correlation coefficient as a criterion for solving the translation problem (Appendix 2):

$$C = \frac{\sum (|F_o|^2 - \overline{|F_o|^2}) \times (|F_c|^2 - \overline{|F_c|^2})}{\left[ \sum (|F_o|^2 - \overline{|F_o|^2}) \times \sum (|F_c|^2 - \overline{|F_c|^2})^2 \right]^{\frac{1}{2}}}.$$

This criterion was later also applied in the second improvement method by Brünger (Brünger, 1990, 1997a; Brünger and Nilges, 1993) but now in a form with normalized structure factors:

$$C_{\text{tr}} = \frac{|\overline{E_h(\text{obs})}|^2 \times |\overline{E_h(\text{calc})}|^2 - \overline{|E_h(\text{obs})|^2} \times \overline{|E_h(\text{calc})|^2}}{[\{|\overline{E_h(\text{obs})}|^4 - \overline{|E_h(\text{obs})|^2}^2\} \times \{|\overline{E_h(\text{calc})}|^4 - \overline{|E_h(\text{calc})|^2}^2\}]^{1/2}}.$$

In fact, Brünger introduced two techniques for increasing the success in finding the correct translation of the search model. First, he calculated a normal rotation function; peaks close together are clustered to a single peak. He selected not only the highest peak in the rotation function but a number of peaks (e.g., 200) and calculated the standard linear correlation coefficient,  $C_{\text{tr}}$ , between the squares of the normalized observed ( $E_{\text{obs}}$ )<sup>2</sup> and calculated ( $E_{\text{calc}}$ )<sup>2</sup> structure factors, as a function of the coordinates of the center of gravity of the search model and its symmetry mates. This three-dimensional search for the optimal coordinates is done for each of the selected orientations and the orientation that gave the highest value for the correlation coefficient is then chosen for the translation search.

If this search is unsuccessful, the highest peaks of the rotation function are again selected, but now, before a translation search is carried out, the search model and its orientation are adjusted by minimizing  $E_{\text{total}}(\mathbf{r})$  in Eq. (10.12). A single copy of this search model is put into a triclinic cell, identical in geometry to the crystal unit cell and in an orientation derived from the rotation function. The translation is then of no relevance because a change of the molecule's position with respect to the origin changes only the phases, not the magnitudes of the structure factors. The target function to be minimized in the refinement is the energy term:

$$E_{\text{total}}(\mathbf{r}) = E_{\text{PC}}(\mathbf{r}) + E_{\text{emp}}(\mathbf{r}). \quad (10.12)$$

$E_{\text{emp}}(\mathbf{r})$  is an empirical energy function (Section 13.4.4 of Chapter 13).  $E_{\text{PC}}(\mathbf{r})$  is a pseudoenergy term, related to the standard linear correlation coefficient,  $C(\mathbf{r}, \Omega)$ , which measures the correlation between the squares of the normalized observed ( $E_{\text{obs}}$ )<sup>2</sup> and calculated ( $E_{\text{calc}}$ )<sup>2</sup> structure factors:

$$E_{\text{PC}}(\mathbf{r}) = W_{\text{PC}}\{1 - C(\mathbf{r}, \Omega)\},$$

where  $\Omega$  is the rotation matrix defining the orientation,  $C$  is a function of  $E_{\text{calc}}$ , and  $E_{\text{calc}}$  is a function of  $\Omega$  and of the positional parameters of the atoms.

If the correlation is at its maximum,  $E_{\text{PC}}(\mathbf{r})$  has a minimum value.  $W_{\text{PC}}$  is a suitably chosen weighting factor that determines the relative weight of the empirical and the pseudoenergy term. In many applications, the minimization is carried out exclusively with  $E_{\text{PC}}(\mathbf{r})$ .

The refinement is particularly important if the protein molecule has flexible parts, which have different relative positions in the crystal structure to be solved, compared with the search model. This was, for example, true for the structure determination of the antigen-binding fragment of an immunoglobulin molecule (Brünger, 1991a). The orientation and translation of the individual domains of the search model (a homologous antigen-binding fragment) were appreciably modified

in the refinement. The combination of the adjusted search model and its orientation produced an unambiguous solution for the translation search.

For the third method, the phased translation function, any bit of phase information, even from a poor heavy atom derivative, can facilitate the resolution of the translation problem. The method is based on overlapping the electron density map computed with the prior phase information, with the electron density map of one copy of the search model correctly oriented in the unit cell (Bentley and Houdusse, 1992; Cygler and Desrochers, 1989; Read and Schierbeek, 1988; Zhang and Matthews, 1994). The variable is the translation vector  $\mathbf{t}$ , which moves the model away from its arbitrary position in the unit cell to its correct position. The criterion is the standard linear correlation coefficient  $\text{Corr.}(\mathbf{t})$  (Appendix 2):

$$\text{Corr.}(\mathbf{t}) = \frac{\int_V [\rho_P(\mathbf{x}) - \overline{\rho_P}] \times [\rho_M(\mathbf{x} - \mathbf{t}) - \overline{\rho_M}] d\mathbf{x}}{\left\{ \int_V [\rho_P(\mathbf{x}) - \overline{\rho_P}]^2 d\mathbf{x} \times \int_V [\rho_M(\mathbf{x} - \mathbf{t}) - \overline{\rho_M}]^2 d\mathbf{x} \right\}^{1/2}}. \quad (10.13)$$

Alternatively, the symmetry operations in the unit cell can be applied to the search model and this would improve the signal somewhat. However, it has been shown that the simple “one copy of search model” technique works satisfactorily.

Equation (10.13) can be simplified because the average electron densities  $\overline{\rho_P}$  and  $\overline{\rho_M}$  are zero if  $F(0\ 0\ 0)$  is omitted from the Fourier summation. Moreover, the integral  $\int_V [\rho_M(\mathbf{x} - \mathbf{t})]^2 d\mathbf{x}$  (with a single copy of the search model in the unit cell) is independent of the actual position of the model in the unit cell and, therefore, independent of  $\mathbf{t}$ ; the integral is equal to  $\int_V [\rho_M(\mathbf{x})]^2 d\mathbf{x}$ .

$$\begin{aligned} \rho_P(\mathbf{x}) &= \frac{1}{V} \sum_{\mathbf{h}} m_P |F_0(\mathbf{h})| \exp[i\alpha_P] \exp[-2\pi i(\mathbf{h} \cdot \mathbf{x})], \\ \rho_M(\mathbf{x}) &= \frac{1}{V} \sum_{\mathbf{h}'} \mathbf{F}_M(\mathbf{h}') \exp[-2\pi i(\mathbf{h}' \cdot \mathbf{x})] \\ &= \frac{1}{V} \sum_{\mathbf{h}'} \mathbf{F}_M^*(\mathbf{h}') \exp[2\pi i(\mathbf{h}' \cdot \mathbf{x})] \end{aligned}$$

because  $\mathbf{F}_M(-\mathbf{h}') = \mathbf{F}_M^*(\mathbf{h}')$ , the complex conjugate of  $\mathbf{F}_M(\mathbf{h}')$ .  $m_P$  is the figure of merit. In the integration in the numerator of Equation (10.13), all terms cancel except if  $\mathbf{h}' = \mathbf{h}$ , and it can easily be verified that the result is

$$\int_V \rho_P(\mathbf{x}) \times \rho_M(\mathbf{x} - \mathbf{t}) d\mathbf{x} = \frac{1}{V} \sum_{\mathbf{h}} m_P |F_0(\mathbf{h})| \exp[i\alpha_P] \mathbf{F}_M^*(\mathbf{h}) \exp[-2\pi i(\mathbf{h} \cdot \mathbf{t})].$$

It can be shown in a similar way for the denominator terms that

$$\int_V \{\rho_P(\mathbf{x})\}^2 d\mathbf{x} = \frac{1}{V} \sum_{\mathbf{h}} \{m_P |F_0(\mathbf{h})|\}^2$$

and

$$\int_V \{\rho_M(\mathbf{x})\}^2 d\mathbf{x} = \frac{1}{V} \sum_{\mathbf{h}} \{|F_M(\mathbf{h})|\}^2.$$

The final result for  $\text{Corr.}(\mathbf{t})$  is

$$\text{Corr.}(\mathbf{t}) = \frac{\frac{1}{V} \sum_{\mathbf{h}} m_P |F_0(\mathbf{h})| \exp[i\alpha_P] F_M^*(\mathbf{h}) \exp[-2\pi i(\mathbf{h} \cdot \mathbf{t})]}{\frac{1}{V} \left[ \sum_{\mathbf{h}} \{m_P |F_0(\mathbf{h})|\}^2 \times \sum_{\mathbf{h}} \{|F_M(\mathbf{h})|\}^2 \right]^{1/2}}. \quad (10.14)$$

Because  $\mathbf{F}_M^*(\mathbf{h}) = |F_M(\mathbf{h})| \exp[-i\alpha_M]$ , the correlation function can now straightforwardly be calculated as a Fourier summation with amplitudes  $m_P |F_0(\mathbf{h})| \times |F_M(\mathbf{h})|$  and phase angles  $(\alpha_P - \alpha_M)$ , multiplied by

$$V \left[ \sum_{\mathbf{h}} \{m_P |F_0(\mathbf{h})|\}^2 \times \sum_{\mathbf{h}} \{|F_M(\mathbf{h})|\}^2 \right]^{-1/2}.$$

The maximum of  $\text{Corr.}(\mathbf{t})$  should give the correct translation vector  $\mathbf{t}$ .

The addition and subtraction strategy of Zhang and Matthews (1994) can improve the quality of the rotation function as well as the translation function if part of the structure is known and another part is as yet unknown. For solving the rotation function of the unknown part with the addition strategy, the Patterson function of the known part is added in its correct orientation to the Patterson function of the search model for the unknown part:

$$\{P_{\text{known}} + [C]P_{\text{search}}\}.$$

This modified Patterson is calculated as a function of  $[C]$  and compared with the observed Patterson. In the subtraction method, the Patterson function of the known part is subtracted from the observed Patterson and  $[C]P_{\text{search}}$  is solved as a function of  $[C]$  by comparing it with  $\{P_{\text{obs}} - P_{\text{known}}\}$ . Of course, a normal rotation function must be calculated first. If then the orientation of the molecule or subunit or part of it is known, the rotation result can best be improved by incorporating the subtraction strategy, which will reduce noise in the map of the rotation function. Zhang and Matthews (1994) also proposed a modified translation function in which the addition and subtraction strategies are applied simultaneously.

In protein crystallography, the development of more powerful software is a continuous process. This is also true for molecular replacement. An examples of recent developments is the program QUEEN of SPADES (Glykos and Kokkinidis, 2001). In the Section 10.3.2 we will discuss the program AMoRE that has been very successful in molecular replacement.

### 10.3.2. AMoRe

Navaza (1994, 2001) has written a molecular replacement program AMoRe that incorporates several features, such as the exploration of many potential solutions and

already existing knowledge of the models. In fact, it is a combination of programs with three core programs: ROTING for orientation, TRAINING for translation, and FITING for refinement of the results (Navaza and Soludjian, 1997; Navaza and Vernoslova, 1995).

AMoRe has the following characteristics:

1. Fast computation of structure factors from the continuous Fourier transform of the model, produced by the program TABLING, in all stages of the process.
2. Many potential solutions are explored.
3. Correlation coefficients are the main criteria for selection.
4. Efficient links between the various programs allow a high degree of automation.

ROTING is a fast rotation function, defined as the overlap of observed and calculated Patterson functions [Equation (10.1)]. The Patterson functions are expanded in spherical harmonics, as in Crowther's fast rotation function (Crowther, 1972) but with an increased accuracy. The resulting peaks in the rotation function are tested and selected with the correlation coefficient between calculated and observed structure factor amplitudes.

The output of ROTING is the multiple input for the translation function TRAINING. However, this is not a single translation function but a collection of four different fast translation functions from which the user can choose:

1. A Patterson overlap function similar to  $T_2$  of Crowther and Blow (1967).
2. A phased translation function (Section 10.3.1 of Chapter 10).
3. A function similar to the one proposed by Harada et al. (1981); it incorporates packing considerations in the translation function and uses a modified correlation coefficient in terms of intensities as the target function. This function can be evaluated by fast Fourier techniques.
4. The fourth function uses the normal correlation coefficient in terms of intensities as the target function. The correlation coefficient in terms of intensities has the advantage that it can be rapidly evaluated using fast Fourier techniques, contrary to the coefficient in terms of amplitudes (Navaza and Vernoslova, 1995).

The highest peaks in the translation function(s) are tested with the correlation coefficient in terms of amplitudes because it is the most discriminating criterion. On this basis, acceptable solutions are selected. Molecular replacement solutions are usually followed by rigid-body refinement: the orientation and position of the search model in the target unit cell are refined (Section 13.4.1 of Chapter 13). In AMoRe, this is done using the program FITING (Castellano et al., 1992). The difference with other rigid-body refinement strategies is that FITING presents the search model as an electron density map, not as an atomic model. It is similar, although numerically improved, to a method previously proposed by Huber and Schneider (1985).



### Rigid-Body Refinement in AMoRe

If  $\rho(\mathbf{r})$  is the electron density in the unit cell of the target crystal structure (the structure to be refined), its structure factors are

$$\mathbf{F}_{\text{obs}}(\mathbf{h}) = \int_{\text{unit cell}} \rho(\mathbf{r}) \exp[2\pi i \mathbf{h} \cdot \mathbf{r}] d\mathbf{r}. \quad (10.15)$$

With  $s$  symmetry operators, each characterized by a crystallographic rotation matrix  $[C]_s$  and a translation  $\mathbf{t}_s$ , this is equal to

$$\sum_s \exp[2\pi i \mathbf{h} \mathbf{t}_s] \int_{\text{asym. unit}} \rho(\mathbf{r}) \exp[2\pi i \mathbf{h} [C]_s \mathbf{r}] d\mathbf{r}. \quad (10.16)$$

The search model (the known structure) is positioned in a suitable model box. Its electron density is  $\tilde{\rho}(\mathbf{u})$ , where  $\mathbf{u}$  are the coordinates in the box. For transferring this electron density  $\tilde{\rho}(\mathbf{u})$  to the crystal structure, we must apply the rotation matrix  $[C]_R$ , the translation vector  $\mathbf{x}$ , and, in addition, two transformation matrices:  $[O]$  for transforming fractional into orthogonal coordinates in the model box and  $[D]$  to transform orthogonal into fractional coordinates in the crystal. After the model is transferred into the crystal structure, its positional coordinates  $\mathbf{r}$  are related to its coordinates  $\mathbf{u}$  in the model box as  $\mathbf{r} = [D][C]_R[O]\mathbf{u} + \mathbf{x}$ .

The structure factors calculated for the model in the crystal structure are

$$\begin{aligned} \mathbf{F}_{\text{calc}}(\mathbf{h}) &= \sum_s \exp[2\pi i \mathbf{h} \mathbf{t}_s] \int_{\text{asym. unit}} \tilde{\rho}(\mathbf{u}) \exp[2\pi i \mathbf{h} [C]_s \mathbf{r}] d\mathbf{r} \\ &= \sum_s \exp[2\pi i \mathbf{h} \mathbf{t}_s] \int_{\text{model box}} \tilde{\rho}(\mathbf{u}) \exp[2\pi i \mathbf{h} [C]_s ([D][C]_R[O]\mathbf{u} + \mathbf{x})] d\mathbf{u} \\ &= \sum_s \exp[2\pi i \mathbf{h} \mathbf{t}_s] \exp[2\pi i \mathbf{h} [C]_s \mathbf{x}] \\ &\quad \times \int_{\text{model box}} \tilde{\rho}(\mathbf{u}) \exp[2\pi i \mathbf{h} [C]_s ([D][C]_R[O]\mathbf{u})] d\mathbf{u} \\ &= \sum_s \exp[2\pi i \mathbf{h} \mathbf{t}_s] \exp[2\pi i \mathbf{h} [C]_s \mathbf{x}] \times \mathbf{f}(\mathbf{h} [C]_s [D][C]_R[O]), \quad (10.17) \end{aligned}$$

where  $\mathbf{f}(\mathbf{h} [C]_s [D][C]_R[O])$  is the Fourier transform of the model in its box at reciprocal lattice position  $(\mathbf{h} [C]_s [D][C]_R[O])$ . In a least squares procedure, the difference between the amplitudes of  $\mathbf{F}_{\text{obs}}(\mathbf{h})$  [Equation (10.16)] and  $\mathbf{F}_{\text{calc}}(\mathbf{h})$

[Equation (10.17)] is minimized with respect to  $[C]_R$ ,  $\mathbf{x}$ , and the scale factor  $\lambda$ :

$$Q([C]_R, \mathbf{x}, \lambda) = w(\mathbf{h}) \sum_{\mathbf{h}} \{|F_{\text{obs}}(\mathbf{h})| - \lambda |F_{\text{calc}}(\mathbf{h})|\}^2,$$

where  $w(\mathbf{h})$  is any convenient weighting function.

### 10.3.3. Notes

1. A special translation case should be mentioned. If a crystal has noncrystallographic symmetry and a local axis is parallel to another local axis or a crystallographic axis, this is expressed in the Patterson map as cross-vectors between the subunits (or molecules) (Stubbs et al., 1996). A special case is illustrated in Figure 10.7 (Eagles et al., 1969; Epp et al., 1971). If there is a noncrystallographic 2-fold axis parallel to a crystallographic 2-fold, one can easily find the position of the noncrystallographic axis with respect to the crystallographic one from the Patterson map. It is clear that the Patterson map will show a high peak corresponding to the distance  $\Delta$  between the atoms in molecules 1 and 2 and their counterparts in molecules 3 and 4; this is equal to the distance between the local 2-fold axes.
2. An interesting application of the translation function has been reported by Antson et al. (1995). They expected to find 11 Br atoms in the heavy atom

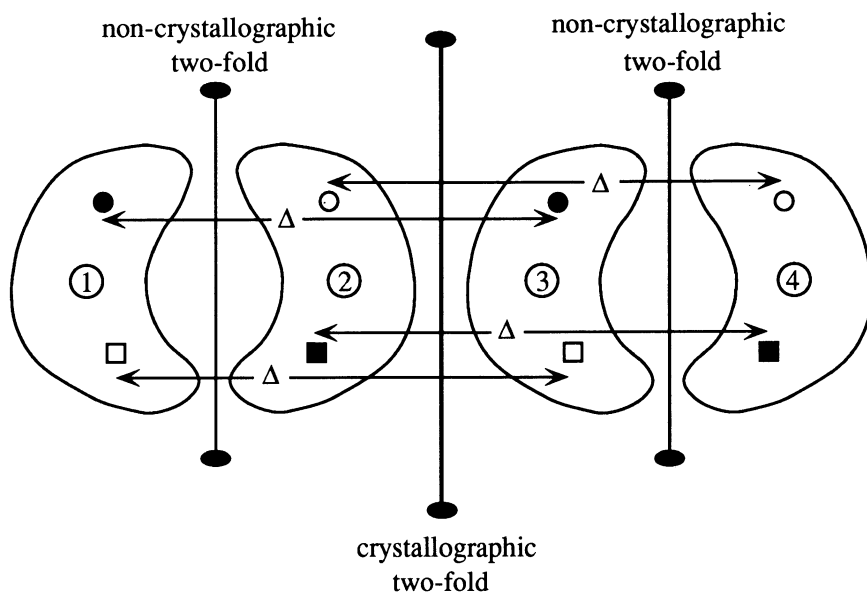


Figure 10.7.  $\Delta$  is the distance between corresponding atoms, which are above the plane of the figure (black) or below it (open circles and rectangles).

derivative of *trp* RNA-binding attenuation protein but were unable to locate them from an isomorphous or anomalous Patterson map. Because of 11-fold symmetry in the structure, it was expected that the 11 Br atoms would lie in one plane. The translation function (AMoRe) was successfully applied against the isomorphous and anomalous differences with a model structure consisting of a ring of 11 Br atoms. The radius of the ring was varied stepwise.

3. The cross-Patterson function  $P_{1,2}(\mathbf{u}, \mathbf{t})$  [Equation (10.8)] is a noncentrosymmetric function, just as the cross-Patterson function  $P(\mathbf{u})$  in Section 7.10 of Chapter 7. Therefore, the translation function is also noncentrosymmetric. This property can be helpful in determining the correct space group (e.g., making the choice between  $P3_121$  and  $P3_221$ ). Apply the translation function in both space groups and choose the one that gives the highest peak. Alternatively, look in the relevant Harker section to check whether the molecules at position  $\frac{1}{3}c$  higher are rotated with respect to the previous one by  $120^\circ$  ( $P3_121$ ) or  $240^\circ$  ( $P3_221$ ).
4. Issue 10 of *Acta Crystallographica* (2001), **D57** has been completely devoted to molecular replacement.

## Summary

For the molecular replacement technique, a known structure is required, which serves as a model for the unknown structure. Homology in the amino acid sequence is an indication of whether a model is suitable. The solutions of the rotation and translation functions are not always found in a straightforward way. It can be necessary to modify the model, for instance, by ignoring side chains and deletions/additions in the model and to play with the resolution range of the X-ray data. With the rapid increase in the number of successful protein structure determinations, molecular replacement has become an extremely useful technique for protein phase angle determination.

# Chapter 11

## Direct Methods

### 11.1. Introduction

The major problem in X-ray crystallography is to determine the phase angles of the X-ray reflections. In protein crystallography, this problem is solved by the application of either isomorphous replacement or molecular replacement or multiple-(MAD) or single-wavelength anomalous diffraction (SAD). In small-molecule crystallography, a completely different solution is applied. There, direct methods are the standard techniques for determining the phase angles of the structure factors. They use the principle that phase information is included in the intensities and this principle depends on the basic assumptions that the electron density is always positive [ $F(0\ 0\ 0)$  included in the Fourier summation] and the crystal consists of discrete atoms that are sometimes even considered to be equal. Phase relations based on probability theory have been formulated and these phase relations are applied to suitably chosen clusters of reflections. Although these direct methods work perfectly well for small-molecule crystals, it has thus far not been easy to apply them for the determination of a complete protein molecular structure. However, a number of direct methods have been developed for locating the substructure atoms in a protein crystal. We present two of them: Shake-and-Bake and SHELXD.

### 11.2. Shake-and-Bake

This is one of the few *ab initio* or direct methods that has been rather successful in the determination of protein phase angles. The basis of Shake-and-Bake is the triplet relation between phase angles and this relationship is derived in Section 11.2.1.

### 11.2.1. The Phase Triplet

Structure factors are not independent of each other; they are related through structure. A particular relation exists for the reflections from lattice planes that belong to one zone. A group of lattice planes forms a zone if they are all parallel to one axis—the zone axis. The relationship is the triplet

$$\phi(\mathbf{h}_1) + \phi(\mathbf{h}_2) + \phi(-\{\mathbf{h}_1 + \mathbf{h}_2\}) = 0. \quad (11.1)$$

The  $\phi$ 's are the phase angles of the reflections  $\mathbf{h}_1$ ,  $\mathbf{h}_2$ , and  $-\{\mathbf{h}_1 + \mathbf{h}_2\}$ . This triplet forms the basis of the Shake-and-Bake phase determination method and a simplified derivation will be presented.

In Section 4.7.2 of Chapter 4 it was mentioned that all atoms in a reflecting plane scatter in phase. Also, all member planes of a set of parallel reflecting planes scatter in phase. In the derivation, we assume that all atoms are identical and lie only on lattice planes, not in between. We will focus on three sets of planes: 1, 2, and 3 (Figure 11.1a) and choose the origin  $O$  of the system in an arbitrary position.

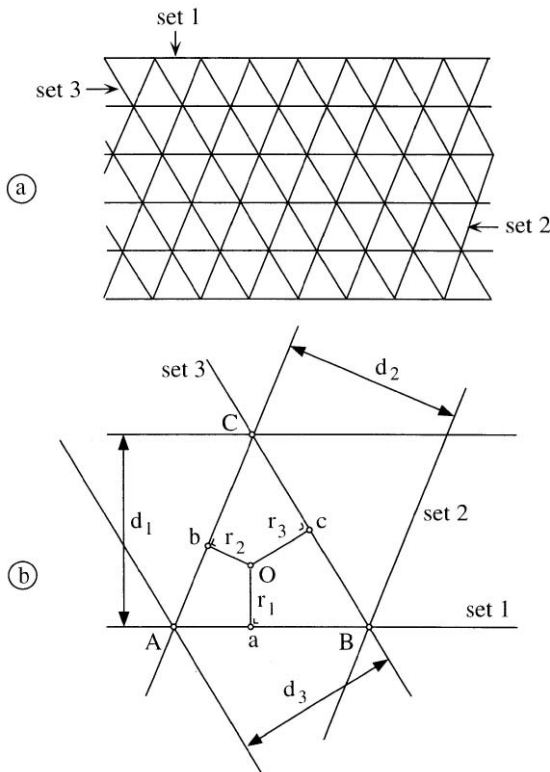


Figure 11.1. (a) Three sets of lattice planes belonging to one zone. The drawing is of a plane perpendicular to the zone axis. (b) A close-up of one of the triangles in (a).  $O$  is the origin of the system;  $d_1$ ,  $d_2$ , and  $d_3$  are interplanar spacings.

The phase angle of a reflection is determined by the distance of the origin  $O$  of the system to the nearest member of the set of reflecting planes. In Figures 11.1a and 11.1b, the plane perpendicular to the zone axis and through the origin  $O$  is drawn, and the phases of points  $a$ ,  $b$ , and  $c$  with respect to  $O$  are required.

The individual phase angles depend on the position of  $O$ , but there is a fixed phase relation among  $\phi_1$ ,  $\phi_2$ , and  $\phi_3$ , where  $\phi_1$  is the phase angle of the beam reflected against set 1,  $\phi_2$  is that for set 2, and  $\phi_3$  is that for set 3. It is easy to prove, with our assumption of atoms on lattice planes, that

$$\phi_1 + \phi_2 + \phi_3 = 0. \quad (11.2)$$

*Proof:*

Set 1: interplanar spacing  $d_1$ ; distance of origin to nearest member  $r_1$ .

Set 2: interplanar spacing  $d_2$ ; distance of origin to nearest member  $r_2$ .

Set 3: interplanar spacing  $d_3$ ; distance of origin to nearest member  $r_3$ .

The position of  $a$ ,  $b$ , and  $c$  in Figure 11.1b is comparable to the position of the atoms in the unit cell in Figure 4.12 of Chapter 4. Instead of atoms 1, 2, and 3 in that figure, we now have points  $a$ ,  $b$ , and  $c$ , with the only difference being that not all three points  $a$ ,  $b$ , and  $c$  can be located in one unit cell. Suppose that  $b$  and  $c$  are inside one unit cell and  $a$  is in another unit cell. This means that  $r_2$  and  $r_3$  have positive values and  $r_1$  has a negative value:

$$\phi_1 = \frac{r_1}{d_1} \times 2\pi; \quad \phi_2 = \frac{r_2}{d_2} \times 2\pi; \quad \phi_3 = \frac{r_3}{d_3} \times 2\pi. \quad (11.3)$$

The area,  $S$ , of the triangle  $ABC$  in Figure 11.1b is

$$S = \frac{1}{2}[-(r_1 \times AB) + (r_2 \times AC) + (r_3 \times BC)]. \quad (11.4)$$

Combining Equations (11.3) and (11.4) gives

$$2 \times S \times 2\pi = -(d_1 \times AB \times \phi_1) + (d_2 \times AC \times \phi_2) + (d_3 \times BC \times \phi_3). \quad (11.5)$$

$2 \times S$  is also equal to  $d_1 \times AB = d_2 \times AC = d_3 \times BC$ .

Divide both sides in Equation (11.5) by  $2 \times S$ :

$$2\pi = -\phi_1 + \phi_2 + \phi_3.$$

The full phase circle of  $2\pi$  can be subtracted and the result is that the sum of  $-\phi_1$ ,  $\phi_2$ , and  $\phi_3$  is equal to zero. This result is independent of the position of the origin  $O$ . The relation between the Miller indices of the lattice plane sets 1, 2, and 3 can be derived from the reciprocal lattice vectors of the reflections (Figure 11.2). Set 2 has indices  $\{h_2, k_2\}$  and set 3 has indices  $\{h_3, k_3\}$ . From Figure 11.2, it is clear that set 1 has the indexes  $\{h_1, k_1\} = \{(h_2 + h_3), (k_2 + k_3)\}$ . It follows that

$$-\phi\{(h_2 + h_3), (k_2 + k_3)\} + \phi\{h_2, k_2\} + \phi\{h_3, k_3\} = 0,$$

or if  $\{h_2, k_2\}$  is called  $\mathbf{h}_1$  and  $\{h_3, k_3\}$  is named  $\mathbf{h}_2$ ,

$$-\phi(\{\mathbf{h}_1 + \mathbf{h}_2\}) + \phi(\mathbf{h}_1) + \phi(\mathbf{h}_2) = 0,$$

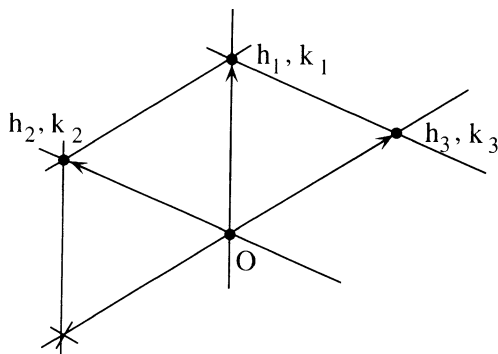


Figure 11.2. A reciprocal space representation of the sets of lattice planes 1, 2, and 3. Set 2 has indexes  $\{h_2, k_2\}$  and set 3 has indexes  $\{h_3, k_3\}$ . It is clear that set 1 has the indexes  $\{h_1, k_1\} = \{(h_2 + h_3), (k_2 + k_3)\}$ .

or because  $-\phi(\{h_1 + h_2\}) = \phi(-\{h_1 + h_2\})$ ,

$$\phi(-\{h_1 + h_2\}) + \phi(\mathbf{h}_1) + \phi(\mathbf{h}_2) = 0 \quad (= \text{Equation (11.1)}).$$

This is the triplet relation between phase angles. In the derivation, it was assumed that all atoms were located on lattice planes. In fact, this is not true and Equation (11.1) is only approximately valid. It is closer to the truth for strong reflections (large structure factor amplitudes), because then the lattice planes are heavily occupied with atoms and there are not many atoms in between.

### 11.2.2. Execution of Shake-and-Bake

Equation (11.1) is successfully used in the phase angle determination for crystal structures of small compounds by applying it to the strongest reflections only. For structures with more than 150 nonhydrogen atoms, the unit cell is so evenly filled with atoms that the method does not work. This is certainly true for proteins. Hauptman and coworkers have modified the method in such a way that it provides a fully automatic procedure for structures up to 1000 nonhydrogen atoms. A requirement is that  $\leq 1.2 \text{ \AA}$  resolution data are available (DeTitta et al., 1994; Hauptman, 1997a, 1997b; Weeks et al., 1994). The technique is called Shake-and-Bake and has been applied successfully to a number of small protein structures (Ealick, 1997; Weeks and Miller, 1999), as well as for the location of the anomalous scatterers (substructure) in the application of MAD and SAD or for the heavy atoms introduced in isomorphous replacement. For the location of a substructure, 3- $\text{\AA}$  data are sufficient because the distance between the contributing atoms is, in general, long compared with the resolution of the data. In working with Shake-and-Bake, normalized structure factors  $\mathbf{E}$  (Chapter 6) are used instead of the more familiar form  $\mathbf{F}$ .

The principle of the modification introduced by Hauptman et al. is that the triplet sum [Equation (11.1)] is no longer set to zero, but to a value  $\phi$ ; or,  $\cos \phi$  is no longer equal to 1. The value they do give to  $\cos \phi$  can be understood by comparison with the Sim weighting factor (Section 8.2 of Chapter 8). In the derivation of the

Sim weighting factor it was found that the probability distribution for the unknown phase angle  $\xi$ , given the observed structure factor amplitude  $|F|$  and the calculated amplitude  $|F_K|$ , depends on  $|F|$  and  $|F_K|$ . The optimal weighting factor,  $w = \cos \xi$ , for noncentric reflections, turned out to be

$$w = \frac{I_1(X)}{I_0(X)},$$

with

$$X = \frac{2|F| \times |F_K|}{\sum_i f_i^2}$$

and  $I_1$  and  $I_0$  are modified Bessel functions of order 1 and 0, respectively. This result is now transferred to Shake-and-Bake: Instead of putting  $\cos \phi$  equal to 1, a procedure has been developed to have  $\cos \phi$  approaching

$$\frac{I_1[X(\mathbf{h}_1, \mathbf{h}_2)]}{I_0[X(\mathbf{h}_1, \mathbf{h}_2)]},$$

where  $X(\mathbf{h}_1, \mathbf{h}_2)$  is now equal to

$$\frac{2}{\sqrt{N}} |E(\mathbf{h}_1)| \times |E(\mathbf{h}_2)| \times |E(\mathbf{h}_1 + \mathbf{h}_2)|.$$

The  $|E|$ 's are the normalized structure factor amplitudes for the reflections  $\mathbf{h}_1$ ,  $\mathbf{h}_2$ , and  $-(\mathbf{h}_1 + \mathbf{h}_2)$ .  $N$  is the number of identical atoms per unit cell. The actual function to be minimized with respect to  $\phi$  is  $\Re(\phi)$  (Debaerdemaeker and Woolfson, 1983). It comprises a chosen set of the stronger reflections and is the weighted mean square difference between the current cosine of the triplet sum,  $\cos\{\phi(\mathbf{h}_1, \mathbf{h}_2)\}$ , and the statistically expected cosine:

$$\Re(\phi) = \frac{\sum_{\mathbf{h}_1, \mathbf{h}_2} X(\mathbf{h}_1, \mathbf{h}_2) \left[ \cos\{\phi(\mathbf{h}_1, \mathbf{h}_2)\} - \frac{I_1\{X(\mathbf{h}_1, \mathbf{h}_2)\}}{I_0\{X(\mathbf{h}_1, \mathbf{h}_2)\}} \right]^2}{\sum_{\mathbf{h}_1, \mathbf{h}_2} X(\mathbf{h}_1, \mathbf{h}_2)}. \quad (11.6)$$

$X(\mathbf{h}_1, \mathbf{h}_2)$  is a weighting function that is large for large values of the  $|E|$ 's, giving more weight to

$$\left[ \cos\{\phi(\mathbf{h}_1, \mathbf{h}_2)\} - \frac{I_1\{X(\mathbf{h}_1, \mathbf{h}_2)\}}{I_0\{X(\mathbf{h}_1, \mathbf{h}_2)\}} \right]^2.$$

The denominator  $\sum_{\mathbf{h}_1, \mathbf{h}_2} X(\mathbf{h}_1, \mathbf{h}_2)$  normalizes the function.

It appears that minimization of  $\Re(\phi)$  does not necessarily lead to the correct solution of the phase angles. It does so only if constraints are introduced and this is done in real space. This constraint is a simple density-modification step: A number of the largest peaks are chosen, equal to the expected number of atoms in the asymmetric unit. They are all made equal in height. The rest of the electron



density map is given zero density. A minimum atomic distance constraint of 1 Å is applied.

According to Weeks et al. (1994), the number of peaks chosen should be equal to or less than the expected number of atoms in the asymmetric unit. It is important to use fewer peaks for protein structures, which are likely to have many disordered atoms or atoms with high thermal motion. Such atoms are unlikely to be found during the preliminary stages of a solution, and inclusion of an unnecessarily large number of incorrect peaks does more harm than good. In fact, if oxygen is the heaviest element present, it is good to choose the number of peaks to be ~80% of the expected number of atoms. If several sulfurs are present, it is better to use even fewer peaks (40% of expected atoms). For atoms heavier than oxygen, an appropriate number of the highest peaks are weighted by the appropriate atomic numbers. The remainder (identified as C, N, or O) are weighted as nitrogens. Good weighting can have a significant impact on the success of the procedure.

The computer program for executing Shake-and-Bake is called SnB (Miller et al., 1994). The steps in the procedure are given in the flowchart in Figure 11.3.

*Conclusion:* Shaking (of the phase angles) occurs in reciprocal space. In real space, baking is applied by removing low-density regions. Therefore, it is called a dual-space direct method. SnB is extremely useful in locating substructure atoms, where substructure means the collection of heavy atoms in isomorphous replacement or the anomalously scattering atoms in MAD or SAD. The reason is that the substructure is comparable with a small-molecule structure.

### 11.3. SHELXD

SHELXD (Schneider and Sheldrick, 2002) is also a dual-space direct method for substructure determination, equally useful as SnB. It uses normalized difference structure factors and X-ray data truncated to, for instance, 3 Å depending on the significance of the anomalous signal. The dataset for execution of the program is reduced by this truncation and is further reduced by restricting to the strongest normalized difference structure factors. This reduction speeds up the process considerably. It starts with several sets of  $N$  atoms, where  $N$  is equal to the expected number of substructure atoms. An interesting feature of SHELXD is that the positions of the  $N$  starting atoms are not chosen randomly but that they are consistent with the Patterson function of the substructure. This increases the efficiency of the program even further. It is achieved by applying an image-seeking function, the Patterson minimum function (PMF), originally introduced by Nordman (1966). The principle behind this function is that the experimental Patterson map has the real structure hidden in its wealth of peaks. If one knew the real structure and moved it over the Patterson, then if the structure coincided with the hidden structure, the average value of the overlapping points would be high. Two atoms are taken as the preliminary real structure with a vector between the two that corresponds to a high Patterson peak. This two-atom vector is put at an arbitrary position in the unit cell and the position of the symmetry-equivalent atoms and the PMF calculated. This is done for 10,000 to 100,000 random positions of the two-atom

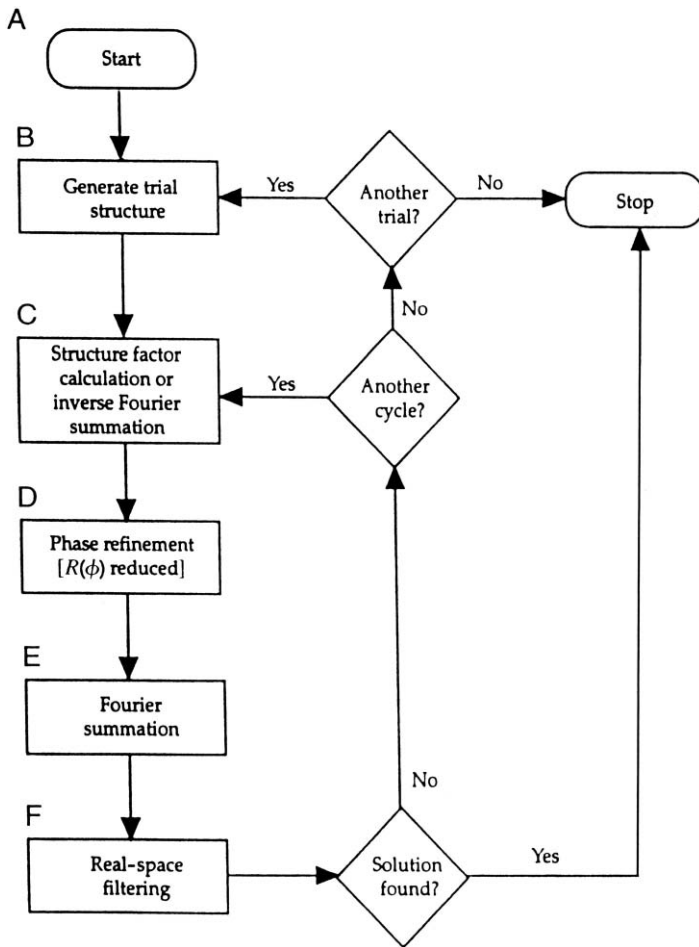


Figure 11.3. Flowchart for SnB. (Reproduced in a slightly modified form from: Hauptman H.A. in *Methods in Enzymology*, Vol. 277, published by Academic Press Inc. Permission obtained.)

vector. The one with the highest PMF is chosen. Further atoms are found from the two starting atoms by Patterson superposition before entering the dual-space refinement. Structure factors are calculated and phase angles refined, or extended to not yet phased reflections. SnB uses the minimum function for refinement, but SHELXD applies the tangent formula, one of the most useful direct methods for determining, refining, or extending phase angles of small-compound structures (Karle and Hauptman, 1956):

$$\tan(\varphi_{h_1}) = \frac{-\sum_{h_2} |E_{h_2} E_{-h_1-h_2}| \sin(\varphi_{h_2} + \varphi_{-h_1-h_2})}{\sum_{h_2} |E_{h_2} E_{-h_1-h_2}| \cos(\varphi_{h_2} + \varphi_{-h_1-h_2})}$$

SHELXD extends the phase set to the remaining reflections, keeping fixed values for the 40% highest calculated E values. In the next step, a switch to real space happens by calculating an electron density map. The top  $N$  peaks are chosen, but, optionally, some of them are deleted as in an OMIT map. The remaining atoms are used to calculate new phases and a new cycle of reciprocal space refinement is started. If the omitted atomic positions were correct, they will reappear. If they were incorrect, they will disappear. This iteration of steps continues until the correlation coefficient (Appendix 2) between observed and calculated normalized structure factors of the substructure identifies a potential solution. In the final dual-space cycles, the occupancies of the heavy atom sites are refined by least squares. This is especially important for derivatives prepared by soaking.

The process starts all over with another set of (almost) random starting atoms. The final solution is the one with the highest correlation coefficient. The number of cycles required is mainly a matter of experience. Meier et al. (2005) advised not stopping at the first acceptable correlation coefficient but continue the search for additional acceptable values.

## 11.4. The Principle of Maximum Entropy

A nonclassical approach in direct phase angle determination for proteins, which is mathematically very demanding, has been pioneered by Bricogne (1993). We will not go into detail here. A full explanation can be found in Bricogne (1997). The process from structure factor amplitudes to phase angles is a stepwise process under the control of the concepts of Bayesian statistics. Probabilities play a major role, as they do in classical direct methods. However, macromolecules require a more subtle treatment than small molecules. This is provided by maximum entropy distributions instead of random distributions for unknown atomic positions.

The maximum entropy principle originated in information theory. Skilling (1988) proposed that the entropy  $S(f, m)$  of an image  $f$  relative to a model  $m$  is

$$S(f, m) = - \int f(x) \log \frac{f(x)}{m(x)} dx. \quad (11.7)$$

This is true for both  $f(x)$  and  $m(x)$  normalized. Equation (11.7) cannot be proven, but it has been shown that it is the only one that gives correct results. In crystallography, the image  $f(x)$  is the normalized electron density distribution in the unit cell:  $q(\mathbf{x}) = \rho(\mathbf{x})/F(0\ 0\ 0)$ , with  $F(0\ 0\ 0) = \int_V \rho(\mathbf{x}) d\mathbf{x}$

The formula for the entropy is

$$S(q, m) = - \int q(\mathbf{x}) \log \frac{q(\mathbf{x})}{m(\mathbf{x})} d\mathbf{x},$$

or, for discrete grid points,

$$S(q, m) = - \sum_j q_j \log \frac{q_j}{m_j}.$$

The  $m_j$  distribution is the prior information that exists about the electron density distribution. If no other information (no structure factors) is available,  $q_j = m_j$  for all  $j$  and  $S(q, m)$  has a maximum value equal to zero. If besides  $m_j$ , extra information is available,  $S(q, m) < 0$ , because the experimental data impose restrictions on  $q_j$  and, therefore, the entropy is reduced.  $q_j$  is always  $\geq 0$  and  $q_j \geq m_j$ .

In the various maximum entropy methods,  $S(q, m)$  is maximized with respect to  $q$  under the restraints of the extra information. More specifically, the maximization of  $S(q, m)$  should occur under the condition that

$$(|F_{\text{obs}}(hkl)| - |F_{\text{calc}}(hkl)|)^2$$

or

$$(I_{\text{obs}}(hkl) - I_{\text{calc}}(hkl))^2$$

and any other X-ray terms (for instance, related to phase information) are minimized. In Figure 11.4, the procedure is expressed in a pictorial way. Maximizing  $S(q, m)$  is finding the shortest route (vector **A** in Figure 11.4) from the starting point to the region determined by the restraints. If, in a next step, more restraints can be added, the true solution can be approached in an iterative way. This is a formidable mathematical problem and the progress in the use of the maximum entropy formalism for the phase determination of a protein depends largely on

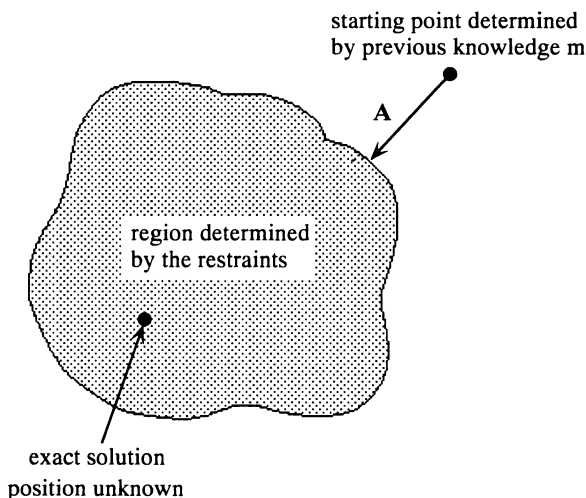


Figure 11.4. Simple schematic of the mathematical process in the application of the maximum entropy method.

solving these problems. A *de novo* structure determination of a protein by maximum entropy alone is not yet possible. However, a combination of maximum entropy with existing information from, for instance, MIR (multiple isomorphous replacement) or MAD, which by itself gives an uninterpretable map, does result in some cases in a successful solution of the protein structure. Also, knowledge of the molecular envelope could be useful.

## Summary

Direct methods for phase angle determination of a complete protein structure have, so far, been restricted to small protein structures combined with very high-resolution data. Direct methods are more successful in the elucidation of substructures in protein molecules—for instance, anomalously scattering atoms. These structures contain a more limited number of atoms and do not require high resolution. The success of the most popular techniques, Shake- and-Bake and SHELXD, is based on the “dual-space” principle: alternating refinement in real and in reciprocal space.

A completely different approach is by applying the maximum entropy principle, but this technique must be further developed before it is more generally applicable.

# Chapter 12

## Laue Diffraction

### 12.1. Introduction

When a stationary crystal is illuminated with X-rays from a continuous range of wavelengths (polychromatic or “white” radiation), a Laue diffraction pattern is produced. The very first X-ray diffraction pictures of a crystal were in fact obtained in this way by Friedrich, Knipping, and Laue in 1912. However, since then, monochromatic beams were used nearly exclusively in X-ray crystal structure determinations. This is due to the fundamental problem that a single Laue diffraction spot can contain reflections from a set of parallel planes with different  $d/n$ , where  $d$  is the interplanar distance and  $n$  is an integer. These spots are multiples instead of singles. This is easily explained by Bragg’s law:

$$2d \sin \theta = \lambda,$$
$$2 \sin \theta = \frac{\lambda}{d} = \frac{\lambda/2}{d/2} = \frac{\lambda/3}{d/3} = \dots$$

The reflection conditions are satisfied, not only for the interplanar spacing  $d$  and wavelength  $\lambda$  but also for  $d/2$  and wavelength  $\lambda/2$ , and  $d/3$  and wavelength  $\lambda/3$ , and so forth. Another problem with conventional X-ray sources is that their spectral properties with anode-specific lines are not very suitable for Laue diffraction.

The availability of synchrotrons as X-ray sources has changed this situation. Their fully polychromatic beam with a smooth spectral profile, having very high intensity and very small divergence, make them excellent sources for Laue diffraction of protein crystals. Moreover, the harmonics (or multiple) problem turned out not to be as serious as previously thought and not to be a limiting obstacle (Cruickshank et al., 1987). The extremely high intensity of synchrotron X-ray sources, combined with their broad effective spectrum, allows X-ray diffraction pictures

taken in times as short as 150 ps (Srajer et al., 1996). This opens perspectives for time-resolved X-ray structure determinations (Moffat, 1989). Major contributions to the application of the Laue method in the area of protein X-ray crystallography have been made in the Daresbury Laboratory of the Science and Engineering Research Council in the United Kingdom and in laboratories in the United States. The Laue method is extensively discussed in the book by Cruickshank et al. (1992); see also Hajdu and Johnson (1990), Pai (1992), Sweet et al. (1993), and Moffat (1997).

## 12.2. The Accessible Region of Reciprocal Space

The range of reflections registered on a Laue photograph depends on the minimum and maximum values of the wavelength region ( $\lambda_{\max} - \lambda_{\min}$ ). This is illustrated in Figure 12.1. Absorption and radiation damage increase with the wavelength and become very serious around 2 Å, which determines the useful maximum wavelength. These problems exist to a far lesser degree at a shorter wavelength, but here the weaker diffraction intensity is limiting because of its proportionality to  $\lambda^2$  (see Section 4.14 of Chapter 4). The efficiency of the detector as a function of the wavelength also plays a role.

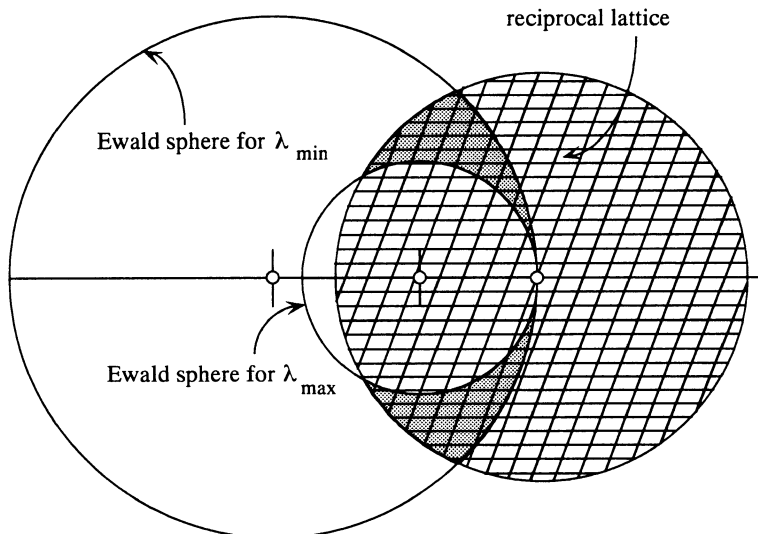


Figure 12.1. A reciprocal space representation of Laue diffraction by a stationary crystal (and thus a stationary reciprocal lattice). For the reciprocal lattice points in the shaded area, the reflection conditions are satisfied, at least if not truncated by a maximum diffraction angle.

### 12.3. The Multiple Problem

A Laue spot can contain the reflections from a set of planes that are “harmonics” of each other (e.g., 3 1 7; 6 2 14; 9 3 21, etc.) or in general a set of reflections  $nh\ nk\ nl$ , where  $n$  is an integer  $\geq 1$  and  $h\ k\ l$  is the first harmonic, which has 1 as the greatest common divisor of its indexes. In reciprocal space, such a set of reflections forms a line through the origin and the  $n$ th harmonic reflects in the same direction as  $h\ k\ l$ , but with a spacing  $d(nh\ nk\ nl) = (1/n) \times d(h\ k\ l)$  and for a wavelength  $\lambda(nh\ nk\ nl) = (1/n)\lambda(h\ k\ l)$  (Figure 12.2). The maximum multiplicity of a Laue spot is  $d(h\ k\ l)/d_{\min}$ , where  $d_{\min}$  is the resolution limit. However, due to the finite-wavelength region, the multiplicity might be lower (Figure 12.2).

For the processing of the data, one must know whether a spot is a single or a multiple. The intensities of the singles can be used directly, but the multiples must be unscrambled. Fortunately, a large fraction of the observed spots will be singles, as can be shown in the following way (Cruickshank et al., 1987). If the common divisor is  $p$ , then every index ( $h$  or  $k$  or  $l$ ) has the chance of  $1/p$  to have that divisor. For the three indexes together, it is  $1/p^3$ . The probability that  $p$  is not a common divisor is  $\{1 - 1/p^3\}$ ;  $p$  has one of the prime numbers 2, 3, 5, 7, ..., and the probability that the point is the first on an harmonics line is

$$\{1 - 1/(2^3)\} \times \{1 - 1/(3^3)\} \times \{1 - 1/(5^3)\} \times \{1 - 1/(7^3)\} \times \dots = 0.83.$$

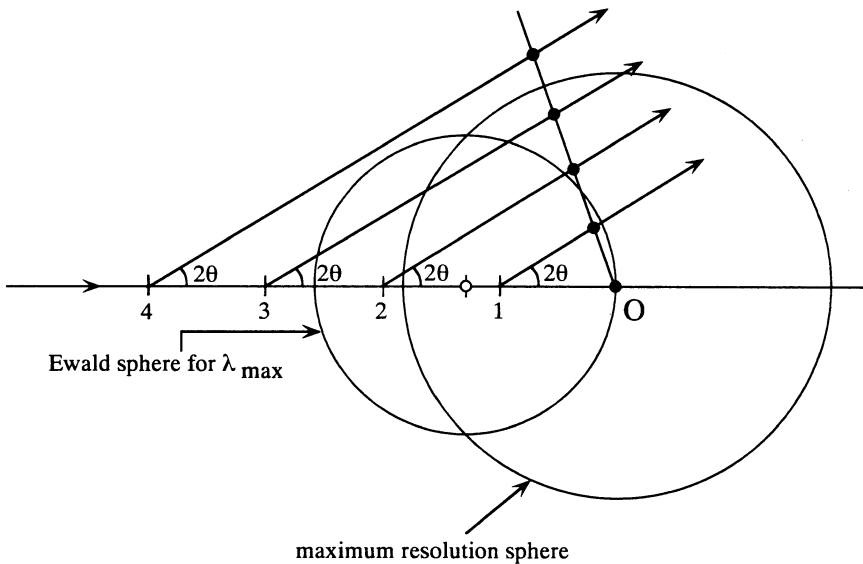


Figure 12.2. Reciprocal space construction for a double. In this example, the first harmonic does not diffract, because it falls inside the Ewald sphere for  $\lambda_{\max}$ , with radius  $1/\lambda_{\max}$ . The fourth and higher harmonics fall outside the resolution range. The origin of the reciprocal lattice is in  $O$ . The points 1, 2, 3, and 4 are the centers of the  $\lambda(h\ k\ l)$ , the  $\lambda(2h\ 2k\ 2l)$ , the  $\lambda(3h\ 3k\ 3l)$ , and the  $\lambda(4h\ 4k\ 4l)$  spheres, respectively.



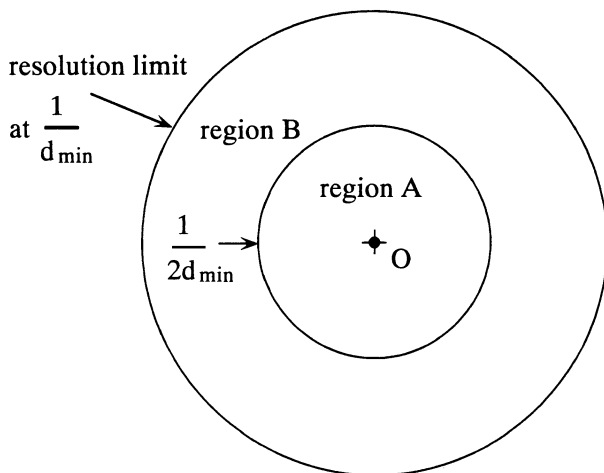


Figure 12.3. Region A in reciprocal space is within the sphere with radius  $1/2d_{\min}$  and region B is the shell between the two spheres. Of the reflections in region B, 83% are measured as singles, but all reflections in region A are—in principle—members of a multiple.

This gives the confidence that 83% of the reflections, corresponding with a spacing  $d$ , which is *smaller* than half of the resolution limit (reflections in region B in Figure 12.3) are measured as singles. However, all reflections corresponding with a spacing *larger* than half of the resolution limit (reflections in region A in Figure 12.3) are measured as multiples, unless all but one of the harmonics are excluded by the wavelength-limiting Ewald spheres. Therefore, the low-resolution reflections suffer most from harmonic overlaps. In addition, due to the Laue geometry, only relatively few low-resolution reflections are in a diffracting position (Figure 12.1).

## 12.4. Unscrambling of Multiple Intensities

The intensity of a multiple spot is the sum of the component intensities. For instance, in Figure 12.2, the reciprocal lattice points on the line radiating from the origin in reciprocal space form a double. Because of symmetry and Friedel's law, this spot is measured a number of times:  $K$ . Depending on the crystal orientation, the spots  $i$ , with  $i = 1$  to  $K$ , are either singles, doubles, triples, and so forth. This forms the basis for the unscrambling procedure (Ren and Moffat, 1995). Each measurement  $i$  is the sum of the intensities of the contributing Bragg reflections:

$$I(\text{spot } i) = \sum_{j_{\min}}^{j_{\max}} I(\text{Bragg refl. } j) = \sum_{j_{\min}}^{j_{\max}} \frac{|F|^2(\text{Bragg refl. } j)}{f(\text{Bragg refl. } j)}. \quad (12.1)$$

$j_{\min}$  and  $j_{\max}$  are integers, indicating the lowest order and the highest order, respectively, of the reciprocal lattice spots on the radial line that forms one Laue spot.

The function in the denominator “ $f$  (Bragg refl.  $j$ )” is a wavelength-dependent correction factor composed of many terms, such as Lorentz and polarization correction and wavelength-normalization factor  $g(\lambda)$  (Section 12.6). There are  $K$  observations of the spots  $i$ , giving  $K$  equations of type (12.1). Most spots  $i$  are singles ( $j_{\min} = j_{\max}$ ) (Section 12.3), and for those spots,  $f$  values can be obtained. The  $K$  equations can then be solved, and in a least squares refinement procedure, accurate values for the structure factor amplitudes of the separate Bragg reflections within each multiple can be obtained.

## 12.5. The Spatial Overlap Problem

Although the divergence of a synchrotron beam is small and the spots on the detector are sharp, there are so many spots on a typical protein Laue photograph (Figure 12.4) that spatial overlap of neighboring spots is a problem. To reduce this problem, the crystal-to-detector distance can be increased; one should, however, realize the effect of this increase on the resolution. Profile fitting also reduces the problem. Standard profiles should be derived from nonoverlapping spots in subregions of reciprocal space and applied to partially overlapping spots in the same region. Profile fitting also improves the accuracy of weak intensities, assuming that strong and weak reflections share a common profile.

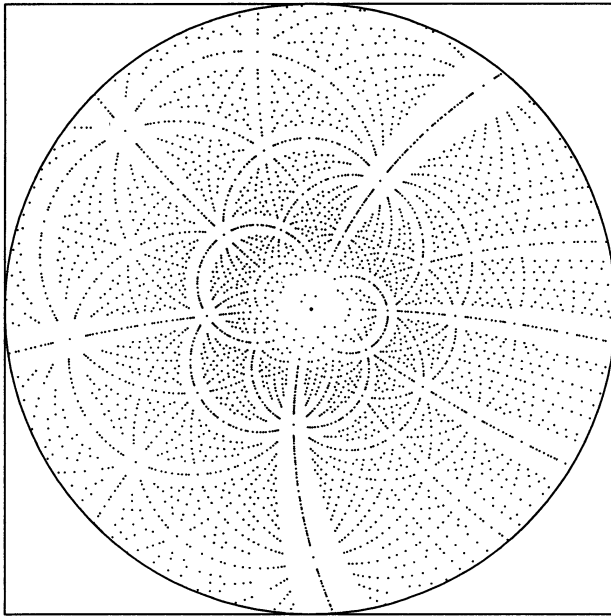


Figure 12.4. A calculated Laue diffraction pattern of a crystal of the human oncogene product Ha-*ras*-p21 (molecular weight = 21 kDa). (Courtesy of Dr. Axel J. Scheidig, Max-Planck-Institut für Medizinische Forschung, Heidelberg, Germany.)

## 12.6. Wavelength Normalization

One of the complexities in the evaluation of Laue diffraction data is to compensate for wavelength-dependent parameters influencing the intensities of the spots. They are numerous:

1. The spectral characteristics of the white radiation at the sample
2. Sample absorption, which is stronger for longer wavelength
3. Wavelength-dependent detector response, including absorption edges
4. Anomalous scattering if present
5. The crystal scattering dependence on  $\lambda^2$
6. Wavelength-dependent source polarization

All of these factors are corrected for by multiplying each reflection intensity with a wavelength-dependent factor  $1/g(\lambda)$ . This factor is determined empirically, either by using symmetry-related reflections, measured at different wavelengths within a single image, or by using the same reflections, measured at different wavelengths in different crystal orientations. In practice,  $g(\lambda)$  is represented by a suitable mathematical function such as a simple polynomial. The parameters of the function are adjusted to obtain the best agreement between the reflection intensities recorded at different wavelengths (Ren and Moffat, 1995).

## Summary

Advantages of the Laue method are as follows:

1. Extremely short data collection time with synchrotron radiation.
2. Consequently, structural changes in the 150 ps to 1s range can be observed.
3. One or only a few exposures at different angular settings cover a substantial portion of the reciprocal lattice. The higher the symmetry in the crystals, the fewer exposures needed.
4. Very small crystals can be used in principle, but the mosaicity of the crystal and background scattering might be unfavorably high.

The main problems are as follows:

1. An unbalanced coverage of reciprocal space with relatively few low-order reflections.
2. The crystal must withstand short exposures to extremely intense X-ray radiation.
3. Spatial overlap that requires a low mosaicity.

These problems can be addressed by careful experimental design (Moffat, 1997). However, because of the availability of extremely strong monochromatic radiation from synchrotron sources, which allows reduced exposure times, the interest in Laue diffraction as a routine, static data collection method has diminished. It remains the only technique that is appropriate to very rapid, time-resolved data

collection on timescales shorter than a few milliseconds. In such studies, it is important that the initiation of the structural and chemical reaction be synchronized in all unit cells, be uniform throughout the crystal, and be nondamaging. These conditions have been met in certain systems (Srajer et al., 1996; Stoddard et al., 1996) and have permitted the pulsed nature of the synchrotron beam to be utilized to reveal structural changes on the nanosecond timescale.

# Chapter 13

## Refinement of the Model Structure

### 13.1. Introduction

When the broad features of a protein molecular structure become known, structure factors calculated on the basis of this model are generally in rather poor agreement with the observed structure factors. The agreement index between calculated and observed structure factors is usually represented by an *R*-factor as defined in Equation (13.1). Thus an *R*-factor of 50% is not uncommon for the starting model, whereas for a random acentric structure it would be 59% (Wilson, 1950).

$$R = \frac{\sum_{hkl} \left| |F_{\text{obs}}| - k|F_{\text{calc}}| \right|}{\sum_{hkl} |F_{\text{obs}}|} \times 100\%. \quad (13.1)$$

Refinement is the process of adjusting the model to find a closer agreement between the calculated and observed structure factors. Several methods have been developed and, if applied, they lower the *R*-factor substantially, reaching values in the 10–20% range or even lower. The adjustment of the model consists of changing the positional parameters and the temperature factors for all atoms in the structure, except the hydrogen atoms. Because hydrogen atoms have one electron only, their influence on X-ray scattering is low and they are normally disregarded in the structure determination. However, the number of nonhydrogen atoms is very high. In the refinement of the papain crystal structure at 1.65 Å resolution, 25,000 independent X-ray reflections had been measured. The parameters to be refined were three positional parameters (*x*, *y*, and *z*) and one isotropic temperature factor parameter (*B*) for each of the 2000 nonhydrogen atoms, making a total of 8000 parameters. Therefore, the ratio of observations to parameters is only 3, and this is a poor overdetermination. This is the reason why as many as possible additional “observations” are incorporated in the refinement process (Brünger and Nilges,

1993). They are, in the first place, the stereochemical data from small molecular structures. Their bond lengths and angles have been determined with high precision and it can be safely assumed that these data for amino acids and small peptides are also valid in proteins (Engh and Huber, 1991). A further “observation” is that the bulk solvent that fills the channels between protein molecules in their crystalline arrangement is not ordered and should appear as a flat region in the electron density map. This “solvent flattening”—which has already been discussed in Section 8.3 of chapter 8—can, therefore, be imposed on the map. Finally, noncrystallographic symmetry (Section 8.4 of Chapter 8)—if it does exist and is detected by molecular replacement—makes an important contribution to the refinement of the protein structure by imposing the equality in structure of the noncrystallographically related molecules or subunits. One can apply the stereochemical information on bond lengths, bond angles, and so forth in two different ways:

- They are taken as rigid and only dihedral angles can be varied. In this case, the geometry and the refinement are called *constrained*. This effectively reduces the number of parameters to be refined. In the application of this method, it is difficult to move small parts of the structure to a “best fit” position because many angular motions are involved.
- If, on the other hand, the stereochemical parameters are allowed to vary around a standard value, controlled by an energy term, the refinement is called *restrained*. The atomic coordinates are the variables and the restraints are on bond lengths, bond angles, torsion angles, and van der Waals contacts. Restraints are “observations” because a penalty is included for disagreement with a restraint. This allows an easy movement of small parts of the structure, but it is difficult to move large parts (e.g., an entire molecule or domain).

Because protein structures are very complicated, their refinement is computationally a large project. It is, therefore, fair to say that only through the availability of fast computers has the thorough and at the same time rapid refinement of protein structures become possible. It is perhaps superfluous to state that it makes sense to refine a structure only if careful attention has been paid to the determination of the cell dimensions and the measurement and correction of the X-ray intensity data. It is preferable to measure intensities of the reflections more than once (e.g., in another symmetry-related position). Low-order reflections, having Bragg spacings longer than about 7 Å, are usually omitted in the refinement process because their intensities are rather seriously affected by the diffraction of the continuous solvent. Moreover, many data collection techniques for proteins are not designed to measure the low-order reflections accurately. That the diffraction by the solvent affects only the low-order reflections can be understood in the following way. Suppose that the unit cell in Figure 13.1 is homogeneously filled with the same electron density  $\rho$  in regions P and S. Region P has the size and shape of the protein molecule. The diffraction intensities will be zero; all structure factors are zero. For a structure in which region P only is filled with homogeneous density  $\rho$  and region S is empty, the structure factors are  $\mathbf{G}_P$ , where  $\mathbf{G}_P$  is the transform of the homogeneously filled particle P. If only region S is filled with homogeneous

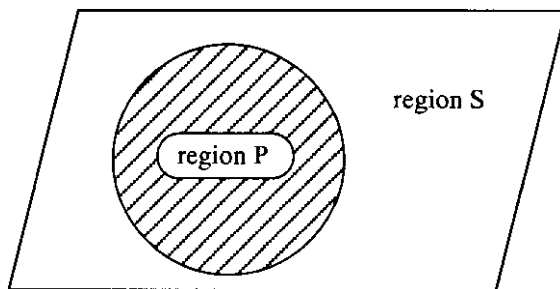


Figure 13.1. In this two-dimensional unit cell,  $e$  region P represents the size and shape of a protein molecule. Region S contains the disordered solvent.

density  $\rho$  and region P is empty, the structure factor must be  $-\mathbf{G}_P$ , because the sum of the two separate structures has diffraction zero. For diffraction by a particle of the type P, which is normally close to spherical, we can refer to Figure 10.3 of Chapter 10, in which the shape of the diffraction curve by a homogeneously filled, perfect sphere is given. For such particles, with the size of a protein molecule, the diffraction fades away rapidly with increasing diffraction angle. It has an appreciable contribution to lower-order reflections only and, therefore, this is also true for the disordered solvent in the crystal. As mentioned earlier, low-order reflections are usually omitted in the refinement because they are strongly affected by the disordered solvent. Inclusion of this disordered solvent effect improves the refinement and the  $R$ -factor drops a few percent. This can be done in the following way (Badger, 1997; Moews and Kretsinger, 1975).

$$\mathbf{F}(\text{disordered solvent}) = -\mathbf{K}\mathbf{G}_P$$

$$\mathbf{K} \text{ is a scale factor equal to } \frac{\text{average solvent density}}{\text{average protein density}}.$$

$\mathbf{G}_P$  is approximated by  $\mathbf{F}(\text{protein})$ , the structure factor calculated for the protein model. This is Babinet's principle: The structure factors of a mask have the same amplitudes but opposite phase angles as the structure factors of the rest of the unit cell.

An artificial temperature factor is applied to restrict the disordered solvent effect to low-order reflections:

$$\mathbf{F}(\text{disordered solvent}) = -\mathbf{K}\mathbf{F}(\text{protein}) \times \exp \left[ -\mathbf{B}(\text{solvent}) \frac{\sin^2 \theta}{\lambda^2} \right].$$

The calculated structure factor for the low-order reflections is then

$$\mathbf{F}(\text{calc}) = \left\{ 1 - \mathbf{K} \exp \left[ -\mathbf{B}(\text{solvent}) \frac{\sin^2 \theta}{\lambda^2} \right] \right\} \times \mathbf{F}(\text{protein}).$$

The inclusion of the disordered solvent is no more than a correction of the structure factors calculated for the protein model.

Ordered solvent molecules do contribute to the scattering up to a high resolution. They are located as electron density peak positions obeying H-bond geometry, and during refinement, they are usually introduced into the molecular model at a resolution better than 2.5 Å.

## 13.2. The Mathematics of Refinement

### 13.2.1. The Method of Least Squares

The refinement techniques in protein X-ray crystallography are based on the principle of least squares or maximum likelihood (Tronrud, 2004). An introduction to least squares has been given in Section 7.11 of Chapter 7, but it will now be treated more extensively. Before we do so, it must be stated that the method of least squares is a special case of the more general refinement method: “maximum likelihood.” In least squares, the observations have fixed values and the parameters are varied such that the calculated values approach the observations as closely as possible in the refinement. It can easily be shown that maximum likelihood gives the same result as least squares for the special case of a Gaussian distribution of the observations. However, for other probability distributions, the results are different.

We will first discuss the least squares method for the case in which the X-ray data are the only observations. Later, in the treatment of more specific refinement methods, constraints and restraints also play a role. Refinement by least squares is an iterative process. In each step (or cycle), the parameters to be refined change, or should change, toward their final value without reaching them right away. Usually, a great many refinement cycles are carried out before the changes in the parameters become small enough. The refinement has then converged to the final parameter set. The range of convergence is the maximum distance for the atoms to move to their final position. If they are further away, there is a good chance that the function to be minimized will be trapped in a local minimum that is not the true minimum. The progress of a refinement can be monitored by calculating after each cycle the crystallographic  $R$ -factor [Eq. (13.1)] or, better, the more reliable  $R_{\text{free}}$  (Section 15.2 of Chapter 15).

For a structure determination with data to 2.0 Å resolution, the final  $R$ -factor should be close to 20%, with  $R_{\text{free}}$  a few percent higher. In the least squares refinement,  $\sum_{hkl} (|F_{\text{obs}}| - |F_{\text{calc}}|)^2$  is minimized. More accurately, the function to be minimized is

$$Q = \sum_{hkl} w(hkl) (|F_{\text{obs}}(hkl)| - |F_{\text{calc}}(hkl)|)^2. \quad (13.2)$$

The summation is over all crystallographically independent reflections and  $w$  is the weight given to an observation. The usual weighting factor in small-molecule crystallography is  $w(hkl) = 1/\sigma^2(hkl)$ ;  $\sigma$  is the standard deviation. For proteins, some  $(\sin \theta)/\lambda$ -dependent function is more satisfactory. It is assumed that the  $|F_{\text{obs}}(hkl)|$  values are on absolute scale. The minimum of  $Q$  is found by varying the



atomic parameters  $u_j (j = 1, \dots, n)$  that determine  $|F_{\text{calc}}(hkl)|$ , and this is done by putting the differentials of  $Q$  with respect to all  $u_j$  equal to zero:  $\partial Q / \partial u_j = 0$  or

$$\sum_{hkl} w(hkl) (|F_{\text{obs}}(hkl)| - |F_{\text{calc}}(hkl)|) \frac{\partial |F_{\text{calc}}(hkl)|}{\partial u_j} = 0. \quad (13.3)$$

Each  $|F_{\text{obs}}(hkl)|$  is a constant and each  $|F_{\text{calc}}(hkl)|$  depends on the variables  $u_j$ . For the solution of these equations,  $|F_{\text{calc}}(hkl)|$  is expressed in a Taylor expansion:

$$\begin{aligned} |F_{\text{calc}}(hkl; u)| &= |F_{\text{calc}}(hkl; u_s)| + \sum_i \varepsilon_i \left[ \frac{\partial |F_{\text{calc}}(hkl; u)|}{\partial u_i} \right]_{u_s} \\ &+ \left[ \frac{1}{2} \sum_j \sum_i \varepsilon_j \varepsilon_i \frac{\partial^2 |F_{\text{calc}}(hkl; u)|}{\partial u_j \partial u_i} + \dots \right] \\ &\rightarrow \text{neglected} \end{aligned} \quad (13.4)$$

$|F_{\text{calc}}(hkl; u)|$  indicates that the  $|F_{\text{calc}}|$  depend on the parameters  $u$ . The starting values of  $u$  are  $u_s$  and are changed by a small amount  $\varepsilon$ . For parameter  $u_i$ , we have  $\varepsilon_i = u_i - u_{i,s}$ .  $[\partial |F_{\text{calc}}(hkl; u)| / \partial u_i]_{u_s}$  means that the differential of  $|F_{\text{calc}}(hkl; u)|$  with respect to  $u_i$  is calculated at the starting value  $u_s$ . Because the  $\varepsilon$  values are small, higher-order terms in  $\varepsilon$  can be neglected. Combination of equations (13.4) and (13.3) gives the so-called normal equations:

$$\begin{aligned} \sum_{hkl} w(hkl) (|F_{\text{obs}}(hkl)| - |F_{\text{calc}}(hkl; u_s)|) \times \left[ \frac{\partial |F_{\text{calc}}(hkl; u)|}{\partial u_j} \right]_{u_s} \\ - \sum_i \varepsilon_i \sum_{hkl} w(hkl) \left[ \frac{\partial |F_{\text{calc}}(hkl; u)|}{\partial u_i} \right]_{u_s} \times \left[ \frac{\partial |F_{\text{calc}}(hkl; u)|}{\partial u_j} \right]_{u_s} = 0. \end{aligned}$$

With these  $n$  equations ( $j = 1 \rightarrow n$ ), the  $\varepsilon$  values must be found and then applied to the variables  $u$ . Because of the truncation of higher-order terms in the Taylor series, the final values are approached by iteration. In other words, in the next cycle of refinement the process is repeated until convergence is reached. For each cycle, new values of  $|F_{\text{calc}}(hkl; u)|$  and its derivatives with respect to  $u_j$  must be calculated. This requires much computing power.

The principle of solving the normal equations is as follows. In abbreviated form they can be written as  $\sum_i (\varepsilon_i a_{ij}) - b_j = 0$  or  $\sum_i \varepsilon_i a_{ij} = b_j$ .

$$\begin{aligned} \text{For } j = 1: & a_{11}\varepsilon_1 + a_{21}\varepsilon_2 + a_{31}\varepsilon_3 + \dots = b_1, \\ j = 2: & a_{12}\varepsilon_1 + a_{22}\varepsilon_3 + a_{32}\varepsilon_3 + \dots = b_2. \end{aligned}$$

These equations can be expressed in matrix form:

$$\begin{bmatrix} a_{11} & a_{21} & a_{31} & \dots & \dots \\ a_{12} & a_{22} & a_{32} & \dots & \dots \\ \dots & \dots & \dots & \dots & \dots \\ \dots & \dots & \dots & \dots & \dots \end{bmatrix} \times \begin{bmatrix} \varepsilon_1 \\ \varepsilon_2 \\ \varepsilon_3 \\ \dots \\ \dots \end{bmatrix} = \begin{bmatrix} b_1 \\ b_2 \\ b_3 \\ \dots \\ \dots \end{bmatrix}$$

or  $[\mathbf{A}] \times [\boldsymbol{\varepsilon}] = [\mathbf{b}]$ .  $[\mathbf{A}]$  is called the normal matrix. Because  $j = 1, \dots, n$  and  $i = 1, \dots, n$ , it is a square matrix with  $n$  rows and columns; moreover, the matrix is symmetric. Its elements are

$$\sum_{hkl} w(hkl) \left[ \frac{\partial |F_{\text{calc}}(hkl; u)|}{\partial u_i} \right]_{u_s} \times \left[ \frac{\partial |F_{\text{calc}}(hkl; u)|}{\partial u_j} \right]_{u_s};$$

$[\boldsymbol{\varepsilon}]$  is the unknown vector and  $[\mathbf{b}]$  is the known gradient vector containing the elements

$$\sum_{hkl} w(hkl) (|F_{\text{obs}}(hkl)| - |F_{\text{calc}}(hkl; u_s)|) \times \left[ \frac{\partial |F_{\text{calc}}(hkl; u)|}{\partial u_j} \right]_{u_s}.$$

Because matrix  $[\mathbf{A}]$  is a square matrix, another matrix can be derived,  $[\mathbf{A}^{-1}]$ , which is the inverse or reciprocal of  $[\mathbf{A}]$ . Its property is  $[\mathbf{A}^{-1}] \times [\mathbf{A}] = [\mathbf{E}]$ , where  $[\mathbf{E}]$  is the unit matrix:

$$[\mathbf{E}] = \begin{bmatrix} 1 & 0 & 0 & - & - & - & - & - & - \\ 0 & 1 & 0 & - & - & - & - & - & - \\ - & - & - & - & - & - & - & - & - \\ - & - & - & - & - & - & - & - & - \end{bmatrix};$$

$[\mathbf{A}^{-1}] \times [\mathbf{A}] \times [\boldsymbol{\varepsilon}] = [\mathbf{A}^{-1}] \times [\mathbf{b}]$  or  $[\mathbf{E}] \times [\boldsymbol{\varepsilon}] = [\mathbf{A}^{-1}] \times [\mathbf{b}]$ . Because the property of a unit matrix is  $[\mathbf{E}] \times [\boldsymbol{\varepsilon}] = [\boldsymbol{\varepsilon}]$ , the solution of the normal equations is  $[\boldsymbol{\varepsilon}] = [\mathbf{A}^{-1}] \times [\mathbf{b}]$ . If  $[\mathbf{A}]$  is not a very large matrix, its inverse  $[\mathbf{A}^{-1}]$  can be calculated without too much effort and the problem of finding the parameter shifts  $[\boldsymbol{\varepsilon}]$  can easily be solved. However, in protein X-ray crystallography,  $[\mathbf{A}]$  is a huge matrix. Its number of rows and columns is equal to the number of parameters to be refined and this can easily be of the order of 10,000 or more. This prohibits the calculation of  $[\mathbf{A}^{-1}]$ . Fortunately, many elements of matrix  $[\mathbf{A}]$  are zero or close to zero for the following reason. The elements of matrix  $[\mathbf{A}]$  are

$$a_{ij} = \sum_{hkl} w(hkl) \left[ \frac{\partial |F_{\text{calc}}(hkl; u)|}{\partial u_i} \right]_{u_s} \times \left[ \frac{\partial |F_{\text{calc}}(hkl; u)|}{\partial u_j} \right]_{u_s}. \quad (13.5)$$

If  $u_i$  and  $u_j$  are positional parameters  $x$  or  $y$  or  $z$  of the same atom, then for an orthogonal system of axes, the derivatives are not correlated and the elements  $a_{ij}$  will have a low value. This is not true for  $i = j$ , when both derivatives are with respect to the same parameter for the same atom. If  $u_i$  and  $u_j$  concern different atoms and these atoms are well resolved, small changes in a parameter of one atom do not affect the other atom and the elements  $a_{ij}$  are again small. Correlation between positional parameters and temperature factors is also neglected, although some correlation usually does exist. It follows that the diagonal elements of matrix  $[\mathbf{A}]$  are, in general, larger than the off-diagonal elements and the simplification is that all off-diagonal elements are set to zero.

With a diagonal matrix (all off-diagonal elements zero), the calculation of  $[\mathbf{A}^{-1}]$  is trivial and a set of parameter shifts  $[\boldsymbol{\varepsilon}]$  can easily be calculated. However, because the diagonal matrix is not the ideal matrix and because of the neglect of higher-order terms in the Taylor expansion, this set of shifts is not the final one and

the procedure is continued as an iterative process: Recalculate  $[\mathbf{A}]$  with the new parameters, find a new set of shifts, and so on until convergence is reached. To increase the rate of convergence, the conjugate gradient method is applied, which is discussed below.

If, in addition to X-ray information, geometric or energy information is also incorporated in the refinement, the elements of matrix  $[\mathbf{A}]$  are

$$a_{ij} = \sum_{hkl} w(hkl) \left[ \frac{\partial |F_{\text{calc}}(hkl; u)|}{\partial u_i} \right]_{u_s} \times \left[ \frac{\partial |F_{\text{calc}}(hkl; u)|}{\partial u_j} \right]_{u_s}$$

+ terms to account for the extra observations. The elements of vector matrix  $[\mathbf{b}]$  also contain extra terms:

$$\sum_{hkl} w(hkl) (|F_{\text{obs}}(hkl)| - |F_{\text{calc}}(hkl; u_s)|) \times \left[ \frac{\partial |F_{\text{calc}}(hkl; u)|}{\partial u_j} \right]_{u_s}$$

+ extra terms. The extra terms contribute to off-diagonal elements and these elements can no longer be set to zero. As a consequence,  $[\mathbf{A}^{-1}]$  is not easy to calculate and the refinement must be carried out by some numerical method, approaching the final parameter set in a cyclic way.

The most popular numerical method in protein X-ray crystallography is the conjugate gradient technique (Tronrud, 1992). The method depends on matrix  $[\mathbf{A}]$  being symmetric. One starts with an initial estimate of the parameter shifts  $[\varepsilon_0]$ , which can be taken as zero if no other choice is available. Next, a residual vector matrix  $[\mathbf{r}_0] = [\mathbf{b}] - [\mathbf{A}] \times [\varepsilon_0]$  is calculated. A second new vector matrix required is the search direction vector  $[\mathbf{z}]$  along which the function  $Q$  [Equation (13.2)] is minimized. Choose the first  $[\mathbf{z}]$  (i.e.,  $[\mathbf{z}_0]$ ) equal to  $[\mathbf{r}_0]$ . In a number of iterative steps  $n = 0, 1, 2, \dots$ , the vectors  $[\varepsilon_{n+1}]$ ,  $[\mathbf{r}_{n+1}]$ , and  $[\mathbf{z}_{n+1}]$  are calculated with the following recipe:

$$\begin{aligned} [\varepsilon_{n+1}] &= [\varepsilon_n] + \alpha_n [\mathbf{z}_n] \quad \text{with} \quad \alpha_n = \frac{[\mathbf{r}_n] \cdot [\mathbf{r}_n]}{[\mathbf{z}_n] \cdot [\mathbf{A}] \times [\mathbf{z}_n]}, \\ [\mathbf{r}_{n+1}] &= [\mathbf{r}_n] - \alpha_n [\mathbf{A}] \times [\mathbf{z}_n], \\ [\mathbf{z}_{n+1}] &= [\mathbf{r}_{n+1}] + \beta_n [\mathbf{z}_n] \quad \text{with} \quad \beta_n = \frac{[\mathbf{r}_{n+1}] \cdot [\mathbf{r}_{n+1}]}{[\mathbf{r}_n] \cdot [\mathbf{r}_n]}. \end{aligned}$$

With  $\alpha_n$  and  $\beta_n$  chosen as indicated, it can be proven that the search directions  $[\mathbf{z}]$  are all conjugate to each other:  $[\mathbf{z}_{n+1}] \cdot [\mathbf{A}] \times [\mathbf{z}_j] = 0$  for all  $j = 0, 1, 2, \dots, n$ . This guarantees that an efficient path is followed in parameter space toward the minimum of function  $Q$  [Equation (13.2)]. It can also be shown that the residuals  $[\mathbf{r}]$  are independent of each other:  $[\mathbf{r}_{n+1}] \cdot [\mathbf{r}_j] = 0$ , for all  $j = 0, 1, 2, \dots, n$ .

The iteration process can be further accelerated by "preconditioning." A matrix  $[\mathbf{K}]$  is chosen that resembles  $[\mathbf{A}]$ , but that can easily be inverted to  $[\mathbf{K}^{-1}]$ . The expression  $[\mathbf{A}] \times [\varepsilon] = [\mathbf{b}]$  is now replaced by  $[\mathbf{K}^{-1}] \times [\mathbf{A}] \times [\varepsilon] = [\mathbf{K}^{-1}] \times [\mathbf{b}]$ . The more  $[\mathbf{K}]$  resembles  $[\mathbf{A}]$ , the better  $[\mathbf{K}^{-1}] \times [\mathbf{A}]$  resembles the unit matrix  $[\mathbf{E}]$  and the faster the convergence. During the procedure, matrix  $[\mathbf{A}]$  is retained unchanged. This is a great advantage because the nonzero elements can then be

stored for the matrix multiplications. After convergence has been reached,  $[\mathbf{A}]$  is recalculated and another cycle of refinement can be started. In the beginning of the refinement, only the X-ray data to moderate resolution are incorporated, and during the refinement process, the resolution is gradually extended. Structure factors and their derivatives can be conveniently calculated with a method proposed by Agarwal (1978) that uses the fast Fourier transform algorithm (see Section 13.3).

The inverse matrix  $[\mathbf{A}^{-1}]$  also serves another purpose. From its diagonal elements  $a_{jj}$ , the standard deviation  $\sigma$  of the parameter  $u_j$  at the end of the refinement can be estimated:

$$\sigma^2(u_j) = a_{jj} \left( \frac{\sum_{h=1}^p w_h (\Delta F_h)^2}{p - n} \right),$$

where  $p$  is the number of independent reflections,  $n$  is the number of parameters, and  $\Delta F_h = |F_{\text{obs}}(h\ k\ l)| - |F_{\text{calc}}(h\ k\ l)|$  calculated with the present parameter value (Cruickshank, 1965). However, this can only be done if the protein is small and the resolution of the diffraction pattern is extremely high. Stec et al. (1995) applied it to crambin, for which the data were collected to a resolution of 0.83 Å at 130 K, and Tickle et al. (1998) applied it to  $\gamma$ B-crystallin and  $\beta$ B2-crystallin. The protein was refined by a full matrix least squares refinement with limited use of restraints. For the majority of macromolecular structure determinations, this is impossible and root mean square deviations from dictionary values (Engh and Huber, 1991) for bond lengths and angles are listed.

### 13.2.2. The Formalism of Maximum Likelihood

“Maximum likelihood changes a world where measurements are values to a new world full of statistics”

*Eric de La Fortelle*

As mentioned earlier, the conditions for least squares refinement are not always fulfilled. These conditions are as follows (de La Fortelle and Bricogne, 1994; Pannu and Read, 1996):

1. The probability distribution of  $|F(\text{calc})|$  is a Gaussian centered on  $|F(\text{obs})|$ .
2. The standard deviation of the Gaussian is an observed quantity and independent of the parameters of the model.
3. Phase angles should be either known or treated as model parameters.

These limiting conditions are also discussed by Tickle et al. (1998). If these conditions are not fulfilled, least squares results are not necessarily the best estimates of the model parameters. One should apply the more general method of maximum likelihood (Fisher, 1912). The principle of this method is rather simple and is based on Bayesian statistics.

Let  $(x_1, \dots, x_n)$  be a set of observations and  $(r_1, \dots, r_m)$  a set of model parameters with a known relationship between the two sets. If there would be no errors at all, one could exactly calculate the observations  $(x_1, \dots, x_n)$  that corresponds to a set of model parameters  $(r_1, \dots, r_m)$ . Unfortunately, because of errors in the model and in the observations, only the *probability* that a set of observations corresponds to a set of given model parameters can be calculated. It should be realized that the probability of any set of (not necessarily existing) observations can be calculated if a particular set of model parameters is given. This is the very first step in setting up a maximum likelihood function.

$$p[(x_1, \dots, x_n); (r_1, \dots, r_m)] = p[\text{data}; \text{model}].$$

The semicolon means “given the known values of.” The crystallographer is not so much interested in the probability of the data, given the model,  $p[\text{data}; \text{model}]$ , but in the probability of the model given the data,  $p[\text{model}; \text{data}]$ , because the data are the fixed observations. These two probabilities are related through Bayes’ theorem:

$$p[\text{model}; \text{data}] = \frac{p[\text{model}] \cdot p[\text{data}; \text{model}]}{p[\text{data}]} \quad (13.6)$$

---

### Proof of Bayes’ Theorem

For convenience, we introduce  $A$  for model and  $B$  for data. Let  $p[A, B]$  be the joint probability of both  $A$  and  $B$  occurring and  $p[B; A]$  the conditional probability of  $B$  given  $A$ . By means of Figure 13.2, it can be shown that

$$p[A, B] = p[A] \cdot p[B; A], \text{ and also } p[A, B] = p[B] \cdot p[A; B].$$

It follows that  $p[A; B] = p[A] \cdot p[B; A]/p[B]$  and this proves Bayes’ theorem.

Bricogne pioneered the introduction of Bayesian statistics and maximum likelihood into crystallography (for a review, see Bricogne, 1997). In crystallography, the data are the structure factor amplitudes  $|F(\text{obs})|$  and the parameters are the parameters of the model. However, for convenience, the model parameters are replaced by  $\mathbf{F}(\text{calc})$  because the  $\mathbf{F}(\text{calc})$ ’s are directly related to the model parameters.<sup>1</sup> Because  $p[\mathbf{F}(\text{calc})]$  is based on all prior information about the model, including, constraints or restraints, and other types of information, we call it  $p^{\text{prior}}[\mathbf{F}(\text{calc})]$  Equation (13.6) transforms into

$$p[\mathbf{F}(\text{calc}); |F(\text{obs})|] = p^{\text{prior}}[\mathbf{F}(\text{calc})] \times \frac{p[|F(\text{obs})|; \mathbf{F}(\text{calc})]}{p[|F(\text{obs})|]} \quad (13.7)$$

The term in the denominator,  $p[|F(\text{obs})|]$ , can be regarded as a normalization constant and can, for our purposes, be deleted. If prior information, such as restraints, is absent  $p^{\text{prior}}[\mathbf{F}(\text{calc})]$  can be regarded as a constant function and can

---

<sup>1</sup> If the problem concerns the refinement of heavy atom parameters,  $\mathbf{F}(\text{calc})$  does not only depend on the model parameters but also on the not exactly known protein phase angles. In that case, integration over all possible phase angles (and preferably amplitudes) is the solution.

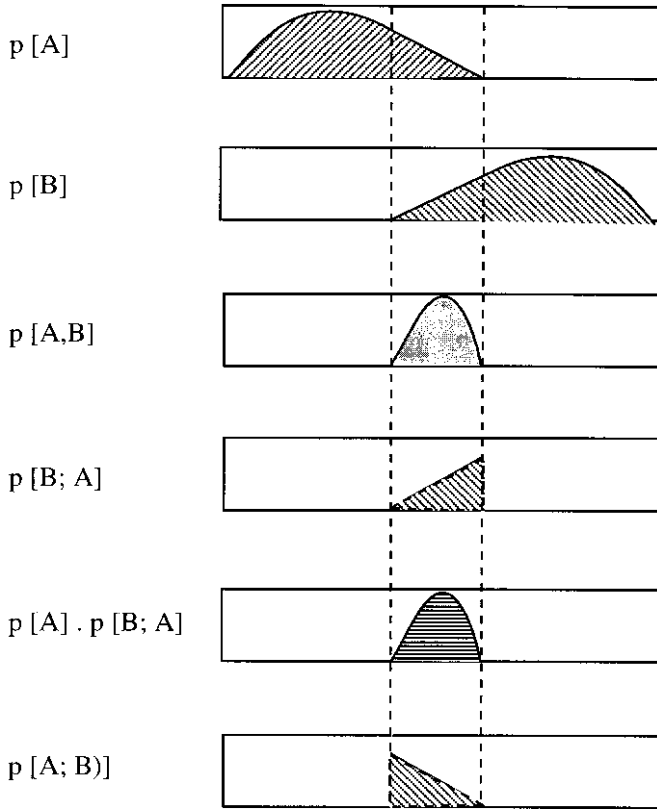


Figure 13.2. Bayes' theorem  $p[A; B] = [p] \cdot p[B; A] / p[B]$  explained by means of simple figures.  $p[A, B]$  is the joint probability of  $A$  and  $B$  occurring both.  $p[B; A]$  is the conditional probability of  $B$  given  $A$ , and  $p[A; B]$  the conditional probability of  $A$  given  $B$ .

be disregarded. What remains is

$$p[\mathbf{F}(\text{calc}); |F(\text{obs})|] = p[|F(\text{obs})|; \mathbf{F}(\text{calc})]. \tag{13.8}$$

The important result is that we have “inverted” the probability. We started with the probability of finding any set of observations, given the model:

$$p[|F(\text{obs})|; \mathbf{F}(\text{calc})]$$

and have inverted it into the probability of the model with the introduction of the actual observations:

$$p[\mathbf{F}(\text{calc}); |F(\text{obs})|]$$

Because we have disregarded normalization,  $p[\mathbf{F}(\text{calc}); |F(\text{obs})|]$  does not exactly obey the requirements for “probability” and is, therefore, given a different notation:

$L$  (likelihood) instead of  $p$ :

$$\mathcal{L} = [\mathbf{F}(\text{calc}); |F(\text{obs})|] = p[|F(\text{obs})|; \mathbf{F}(\text{calc})].$$

The problem now is to find the correct expression for  $p[|F(\text{obs})|; \mathbf{F}(\text{calc})]$ . This can be done for each reflection, and these probabilities must be combined to a joint probability for the entire set of reflections. To simplify this problem, we assume that the observations  $|F(\text{obs})|$  are independent of each other. The joint probability for all reflections is then  $\prod_h p[|F_h(\text{obs})|; \mathbf{F}_h(\text{calc})]$  and the required likelihood:

$$\mathcal{L}_{\text{total}} = \prod_h p[|F_h(\text{obs})|; \mathbf{F}_h(\text{calc})]. \quad (13.9)$$

*Note:* The mutual independence of the observations  $|F(\text{obs})|$  is a matter of debate. Because of their relationship via the structure, they are not independent. However, the issue is that the errors in the  $|F(\text{obs})|$ 's are to a great extent independent, and multiplication of their probabilities is perfectly valid. Weak correlations between errors do exist as a consequence of, for instance, detector inhomogeneities and poor absorption correction. Stronger correlations exist between the partners in a Bijvoet pair of reflections.

In the concept of maximum likelihood, the most reliable set of parameters is obtained if the likelihood  $\mathcal{L}_{\text{total}}$  in Equation (13.9) is maximized. Because it is easier to find the maximum of a sum than the maximum of a product, the log of the likelihood ( $\log \mathcal{L}_{\text{total}}$ ) is taken. Its maximum is at the same position as the maximum of  $\mathcal{L}_{\text{total}}$ . Also, it is still easier to minimize  $-\log \mathcal{L}_{\text{total}}$ :

$$-\sum \log [p|F_h(\text{obs})|; \mathbf{F}_h(\text{calc})].$$

The minimization is with respect to the parameters of the model structure. In Section 13.2.3, maximum likelihood will be illustrated as applied in the programs MLPHARE and SHARP for the refinement of the parameters of heavy atoms and anomalous scatterers in multiple isomorphous replacement (MIR) and multiple-wavelength anomalous diffraction (MAD).

---

### 13.2.3. The Refinement of the Parameters of Heavy Atoms and Anomalous Scatterers in MIR and MAD by MLPHARE and SHARP

#### 13.2.3.1. MLPHARE

Refinement of heavy atom parameters was discussed in Section 7.11 of Chapter 7, where the program MLPHARE (Otwinowski, 1991) was mentioned. In this program, the single value of the protein phase angle, as used in the least squares lack of closure error refinement, is replaced by an integrated value of all phase angles, weighted by their likelihood. The likelihood  $L$  in MLPHARE is a very simple one, assuming that errors in the measurements of the native amplitudes are smaller than

the combined errors of the measurements of heavy atom derivative amplitudes and nonisomorphism errors.

$$\mathcal{L}(\mathbf{F}_H) = \exp \left[ -\frac{\{k_j |F_{PH}|_{\text{obs}} - |F_{PH}|_{\text{calc}}\}^2}{2E^2} \right], \quad (13.10)$$

where  $\mathcal{L}(\mathbf{F}_H)$  is a Gaussian function and  $E^2$  is the average value of  $\{k_j |F_{PH}|_{\text{obs}} - |F_{PH}|_{\text{calc}}\}^2$ . The likelihood for one reflection is obtained by integrating over all phase angles. This likelihood for the individual reflections must then be multiplied to generate the global likelihood function for one derivative. Multiplying these global likelihood functions for all derivatives gives the total likelihood, and this must be maximized with respect to the adjustable parameters. As a general procedure, the protein phases resulting from MLPHARE are used as input for solvent flattening or other density modification procedures (Section 8.3 of Chapter 8). MLPHARE can be applied again after this procedure to give improved protein phase angles (Rould et al., 1992).

MLPHARE has no likelihood for the structure factor amplitudes incorporated, only for the phase angles. A more extensive implementation of the formalism of maximum likelihood is found in the program SHARP (de La Fortelle and Bricogne, 1997), also intended to refine heavy atom parameters. It is presented below.

### 13.2.3.2. SHARP

Another program, SHARP, for the refinement of heavy atom parameters was written by de La Fortelle and Bricogne (1997). This program is entirely based on the maximum likelihood formalism (Bricogne, 1988 and 1991). Therefore, the likelihood of the heavy atom parameters must be derived given the values of the observations and their distribution functions. The required likelihood is equal to the combined probabilities of the following:

- The measured values of  $|F_p|$  and  $|F_{PH}|$
- The scaling factors between native and derivative datasets
- Nonisomorphism
- Errors in the heavy atom model

A central role in their derivation of the likelihood is played by the unknown error-free native structure factor<sup>2</sup>  $\mathbf{F}_p^{\text{corr}}$ . For a reflection  $\mathbf{h}$ , which is, in general, acentric, the calculated value for  $\mathbf{F}_{PH,j}$  is, in the ideal case, equal to  $k_j(F_p^{\text{corr}} + \mathbf{F}_{H,j})$ , where  $k_j$  is a scaling factor. Because of errors in the native structure, this is not necessarily true and  $\mathbf{F}_{PH,j}$  is determined by a Gaussian distribution function,

<sup>2</sup>The actual value of  $\mathbf{F}_p^{\text{corr}}$  is unknown and at the start of the refinement an  $\mathbf{F}_p^{\text{trial}}$  is derived from the current native structure. It is removed from the likelihood by integrating over all possible values of  $\mathbf{F}_p^{\text{trial}}$  (i.e., over its amplitude and phase angle with suitable weighting factors. These weighting factors are derived from the values of the likelihood function at all points of the Harker diagram.



centered at

$$\langle \mathbf{F}_{\text{PH},j} \rangle = k_j (D_j \mathbf{F}_{\text{P}}^{\text{corr}} + \mathbf{F}_{\text{H},j}) \quad (13.11)$$

with a variance  $V_j^{\text{PH}}$ .

$D_j$  is related to coordinate errors in the native structure (Section 7.7 Of Chapter 7 and Equation (15.2) of Chapter 15 (Luzzati, 1952; Read, 1990b). In SHARP, it also includes deviations in atomic positions due to nonisomorphism.  $D_j$  has a value between 0 and 1. Because the phase angle of  $\mathbf{F}_{\text{PH},j}$  is not yet known, the Gaussian distribution must be integrated over the phase angle; the result is

$$p [ |F_{\text{PH},j}|; \mathbf{F}_{\text{P}}^{\text{corr}}, k_j, V_j^{\text{PH}} ] = \mathcal{R}_j = \frac{|F_{\text{PH},j}|}{V_j^{\text{PH}}} \exp \left[ -\frac{|F_{\text{PH},j}|^2 + |\langle F_{\text{PH},j} \rangle|^2}{2V_j^{\text{PH}}} \right] \\ \times I_0 \left[ \frac{|F_{\text{PH},j}| + |\langle F_{\text{PH},j} \rangle|}{V_j^{\text{PH}}} \right], \quad (13.12)$$

where  $I_0$  is a modified Bessel function of order 0 (see Section 8.2 of Chapter 8).  $\mathcal{R}_j$  is called a Rice distribution. Assuming that there are  $M$  derivatives and the  $M$  datasets are independent, the joint probability distribution of the  $M$  structure factor amplitudes is the following for one reflection  $\mathbf{h}$ :

$$p [ |F_{\text{PH},j=1 \dots M}|; \mathbf{F}_{\text{P}}^{\text{corr}}, k_{j=1 \dots M}, V_{j=1 \dots M}^{\text{PH}} ] = \prod_{j=1}^M \mathcal{R}_j. \quad (13.13)$$

Next, errors in the measurement of the data must be considered. Instead of being true values, they are assigned a Gaussian distribution function  $\mathcal{P}^{\text{obs}}$  with a mean value  $\langle |F_{\text{PH},j}^{\text{obs}}| \rangle$  and a standard deviation  $\sigma_j(\mathbf{h})$ . The probability in Equation (13.13) is now multiplied by  $\mathcal{P}^{\text{obs}} [ |F_{\text{PH},j}^{\text{obs}}|; \langle |F_{\text{PH},j}^{\text{obs}}| \rangle, \sigma_j(\mathbf{h}) ]$  and integrated over all possible values of  $|F_{\text{PH},j}^{\text{obs}}|$ , yielding the likelihood:

$$\prod_{j=1}^M \int_{|F_{\text{PH},j}^{\text{obs}}|=0}^{\infty} \mathcal{R}_j \times \mathcal{P}^{\text{obs}} d |F_{\text{PH},j}^{\text{obs}}| \cong \prod_{j=1}^M \mathcal{R}_j [ |F_{\text{PH},j}|, |\langle F_{\text{PH},j} \rangle|, V_j^{\text{total}} ] \quad (13.14)$$

with  $V_j^{\text{total}} = V_j^{\text{PH}} + \{ \sigma_j(\mathbf{h}) \}^2$ .

$|\langle F_{\text{PH},j} \rangle|$  contains  $|\mathbf{F}_{\text{P}}^{\text{corr}}|$ ,  $\mathbf{F}_{\text{H},j}$ , and  $k_j$ . Therefore,  $\mathcal{R}_j$  is a function of  $|\mathbf{F}_{\text{P}}^{\text{corr}}|$ ,  $\mathbf{F}_{\text{H},j}$ ,  $k_j$ ,  $V_j^{\text{PH}}$ , and  $\sigma_j(\mathbf{h})$ . The likelihood of the model parameters derived from one acentric reflection is then

$$\mathcal{L}_{\text{acentr.}(\mathbf{h})}^{\text{iso}} = \int_{\alpha_{\text{P}}=0}^{2\pi} \int_{|F_{\text{P}}|=0}^{\infty} \prod_{j=1}^M \mathcal{R}_j [ |F_{\text{PH},j}|, |\langle F_{\text{PH},j} \rangle|, V_j^{\text{total}} ] d\alpha_{\text{P}} d|F_{\text{P}}|. \quad (13.15)$$

In a similar way as for the isomorphous data, a likelihood can be derived from the anomalous differences:  $\Delta_j = |F_{\text{PH},j,+}| - |F_{\text{PH},j,-}|$ , where  $+$  stands for  $+\mathbf{h}$  and  $-$  for  $-\mathbf{h}$ . Because of errors,  $\Delta_j$  is distributed as a one-dimensional Gaussian function

$\mathcal{G}$  around a center  $\delta_j$  with variance  $V_j^\delta$ . Equation (13.11) for the isomorphous differences is here replaced by

$$\delta_j = k_j(|\mathbf{F}_P^{\text{corr}} + \mathbf{F}_{H,j,+}|) - (|\mathbf{F}_P^{\text{corr}} + \mathbf{F}_{H,j,-}|),$$

$$\mathcal{G}_j(\delta_j, \Delta_j, V_j^\delta) = \frac{1}{\sqrt{2\pi V_j^\delta}} \exp\left[-\frac{(\Delta_j - \delta_j)^2}{2V_j^\delta}\right]. \quad (13.16)$$

In a procedure similar to the one leading to Equation (13.15), the likelihood of the model parameters derived from anomalous diffraction is

$$\mathcal{L}_{\text{acentr.}(\mathbf{h})}^{\text{anom}} = \int_{\alpha_p=0}^{2\pi} \int_{|F_p|=0}^{\infty} \prod_{j=1}^M \mathcal{G}_j \, d\alpha_p d|F_p|. \quad (13.17)$$

The combined likelihood is

$$\mathcal{L}_{\text{acentr.}(\mathbf{h})}^{\text{iso+anom}} = \int_{\alpha_p=0}^{2\pi} \int_{|F_p|=0}^{\infty} \prod_{j=1}^M \mathcal{R}_j \times \mathcal{G}_j \, d\alpha_p d|F_p|. \quad (13.18)$$

It depends exclusively on the parameters to be refined:  $D_j$ , the heavy atom parameters incorporated in  $\mathbf{F}_{H,j}$ , scale factors, and variances.

A similar likelihood function can be derived for centric reflections. At the start of the refinement, the current values of the heavy atom parameters, the scale factors  $k_j$ , the variances, and  $\mathbf{F}_P^{\text{trial}}$  are introduced. The probability distribution according to Equation (13.12) is calculated for each reflection and each derivative. In the next step, measurement errors are taken into account, and the information from the various derivatives is combined. Finally, the integration over  $\mathbf{F}_P^{\text{trial}}$  is carried out.

So far, the likelihood of the model parameters was derived from the information of one reflection  $\mathbf{h}$ . Assuming independent nonisomorphism errors, the likelihood of all reflections can be multiplied or, easier, their logarithmic values are added:

$$\log \mathcal{L}_{\text{total}} = \sum_{\substack{\text{acentr.} \\ \text{reflect}}} \log \mathcal{L}_{\text{acentr.}} + \sum_{\substack{\text{centr.} \\ \text{reflect}}} \log \mathcal{L}_{\text{centr.}}. \quad (13.19)$$

$\log \mathcal{L}_{\text{total}}$  must be maximized or  $-\log \mathcal{L}_{\text{total}}$  minimized, with respect to the parameters of the heavy atom model, scale factors, and nonisomorphism until convergence is reached. The heavy atom parameters are as follows

- The heavy atom coordinates
- Occupancies
- Temperature factors

The scale factors  $k_j$  include, in addition to a constant  $K_j^{\text{sc}}$ , a relative temperature factor with parameter  $B_j^{\text{sc}}$

$$k_j(\mathbf{h}) = K_j^{\text{sc}} \exp \left[ -\frac{1}{4} B_j^{\text{sc}} \left( \frac{2 \sin \theta}{\lambda} \right)^2 \right]. \quad (13.20)$$

An anisotropic term can also be included.

As mentioned earlier, in SHARP,  $D_j$  is related to coordinate errors in the native structure and to nonisomorphism. Because the errors are assumed to be isotropic,  $D_j$  is expressed as an isotropic temperature factor:

$$D_j(\mathbf{h}) = \exp \left[ -\frac{1}{4} B_j^{\text{non-iso}} \left( \frac{2 \sin \theta}{\lambda} \right)^2 \right]. \quad (13.21)$$

In SHARP, the variance for nonisomorphism,  $V_j^{\text{PH}}$ , consists of two parts: a component  $V_j^{\text{glob}}$  that increases with resolution and a component that decreases with resolution,  $V_j^{\text{loc}}$ :

$$V_j^{\text{glob}}(\mathbf{h}) = \langle |F_p^{\text{trial}}|^2 \rangle \times \{1 - D_j^2(\mathbf{h})\}. \quad (13.22)$$

This is based on arguments by Read (1990b).

$\langle |F_p^{\text{trial}}|^2 \rangle$  is calculated in resolution bins at the start of the refinement.  $V_j^{\text{loc}}$  is related to specific local errors and is called the localized component. It decreases with resolution because of a temperature factor with parameter  $B_j^{\text{loc}}$ :

$$V_j^{\text{loc}}(\mathbf{h}) = C_j^{\text{loc}} \langle (|F_{j=1}^{\text{PH}}| - |F_{j \neq 1}^{\text{PH}}|)^2 \rangle \left\{ \exp \left[ -\frac{1}{2} B_j^{\text{loc}} \left( \frac{2 \sin \theta}{\lambda} \right)^2 \right] \right\};$$

$C_j^{\text{loc}}$  is a constant  $<1$  and the mean square isomorphous differences  $\langle (|F_{j=1}^{\text{PH}}| - |F_{j \neq 1}^{\text{PH}}|)^2 \rangle$  are estimated in resolution bins at the start of the refinement. The total nonisomorphous variance,  $V_j^{\text{PH}}$ , is a suitable combination of  $V_j^{\text{glob}}$  and  $V_j^{\text{loc}}$ .

### 13.3. The Principle of the Fast Fourier Transform Method

A very time-consuming step in the refinement procedure is the calculation of all structure factors and their derivatives from the new parameter set at the end of each cycle in the refinement. To speed up these calculations, fast Fourier algorithms are used. A detailed discussion of the application of the fast Fourier technique in crystallography is given by Ten Eyck (1973); see also Agarwal (1978). They enormously reduce the time needed for calculating structure factors from an electron density distribution or, the other way around, the calculation of the electron density map from a series of structure factors. The electron density is sampled at grid

points, usually at distances equal to one-third of the maximum resolution. The number of grid points is then

$$\frac{V}{\left(\frac{1}{3}d\right)^3} = 27\frac{V}{d^3},$$

where  $V$  is the unit cell volume and  $d$  is the maximum resolution. At this maximum resolution, the number of structure factors in the volume of a reciprocal space sphere is

$$\frac{\frac{4}{3}\pi(1/d)^3}{V^*} = \frac{4}{3}\pi\frac{V}{d^3}$$

because the volume of the unit cell in reciprocal space,  $V^*$ , is equal to  $1/V$  (Section 4.8 of Chapter 4).

The fast Fourier transform (FFT) technique requires that the number of structure factors and the number of grid points be the same. The former is usually smaller than the latter, but dummy structure factors can be added up to the number of grid points. For simplicity, we will deal with a one-dimensional case only. Let us write the Fourier inversion as

$$X(k) = \sum_{j=0}^{N-1} x(j)W_N^{jk}.$$

Suppose  $\mathbf{F}(h)$  is calculated from the  $\rho(x)$  map;  $j$  indicates the grid points:  $x = j/N$ ;  $k$  is the index for the structure factors and  $W_N^{jk}$  is the exponential term:  $W_N^{jk} = \exp[2\pi i(j \times k/N)]$ . To calculate the  $\rho(x)$  map from the structure factors, the form of the equation remains the same, but then  $W_N^{jk} = \exp[-2\pi i(j \times k/N)]$ .

The principle of the FFT method is to change the linear series of  $j$  terms into a two-dimensional series. To do this,  $N$  is written as the product of two numbers,  $N_1$  and  $N_2$ :  $N = N_1 \times N_2$ . Also,  $j$  and  $k$  are split up;  $j = j_2 + N_2 \times j_1$  and  $k = k_2 + N_2 \times k_1$ . If  $j_2$  ranges from 0 to  $N_2 - 1$  and  $j_1$  ranges from 1 to  $N_1$ , all of the integers in the range from 0 to  $N$  are generated once and only once. This is true because  $j = j_2 + N_2 \times j_1$ , in which the second term on the right-hand side covers the range  $N_2 \times (1, \dots, N_1) = N_2, \dots, N_2N_1 = N_2, \dots, N$  and the first term covers the range  $0, \dots, N_2 - 1$ . The same is true for  $k$ , if  $k_2$  ranges from 0 to  $N_2 - 1$  and  $k_1$  from 1 to  $N_1$ .

$$x(j) = x(j_2, j_1) = x(j_2 + j_1N_2)$$

and

$$\begin{aligned} X(k_1, k_2) &= \sum_{j_2=0}^{N_2} \sum_{j_1=1}^{N_1} x(j_2, j_1) \times W_N^{jk}, \\ W_N^{jk} &= W_N^{(j_2+j_1N_2)(k_1+k_2N_1)}, \\ &= W_N^{j_1k_1N_2} \times W_N^{j_2k_1} \times W_N^{j_2k_2N_1} \times W_N^{j_1k_2N}, \end{aligned}$$

$$\begin{aligned}
 W_N^{j_1 k_2 N} &= W_N^N = \exp \left[ 2\pi i \frac{N_2}{N} \right] = \cos 2\pi + i \sin 2\pi = 1, \\
 W_N^{jk} &= \exp \left[ 2\pi i \frac{N_2}{N} \right] = \exp \left[ 2\pi i \frac{1}{N_1} \right] = W_{N_1}^1, \\
 W_N^{jk} &= W_{N_1}^{j_1 k_1} \times W_{N_2}^{j_2 k_1} \times W_{N_2}^{j_2 k_2}, \\
 X(k_1, k_2) &= \sum_{j_1=1}^{N_1} \left( W_{N_1}^{j_1 k_1} \times \sum_{j_2=0}^{N_2} \{x(j_2, j_1) \times W_N^{j_2 k_1} \times W_{N_2}^{j_2 k_2}\} \right).
 \end{aligned}$$

Grouping the terms depending on  $j_1$  together, we have

$$X(k_1, k_2) = \sum_{j_2=0}^{N_2} \left( W_N^{j_2 k_1} \times W_{N_2}^{j_2 k_2} \times \sum_{j_1=1}^{N_1} \{x(j_2, j_1) \times W_{N_1}^{j_1 k_1}\} \right).$$

$\sum_{j_1=1}^{N_1} x(j_2, j_1) \times W_{N_1}^{j_1 k_1}$  is a Fourier transform of length  $N_1$  and must be done for each  $j_2$ , so  $N_2$  times. The outer summation over  $j_2$  is a Fourier transform of length  $N_2$ . To calculate all  $X(k)$ , it must be done  $N_1$  times.

The time needed for evaluating a Fourier summation is proportional to the number of terms ( $N$ ) and the number of grid points ( $N$ ). Therefore, the time needed for calculating a normal Fourier transform of length  $N$  would be proportional to  $N^2$ , and with FFT:

$$N_2 \times N_1^2 + N_1 \times N_2^2 = N \times (N_1 + N_2).$$

Suppose  $N = 2500$  and  $N_1 = N_2 = 50$ , then we must compare  $N^2 = (2500)^2 = 625 \times 10^4$  with  $2500 \times 100 = 25 \times 10^4$ , an appreciable reduction in time.

## 13.4. Specific Refinement Methods

### 13.4.1. Rigid-Body Refinement

Sussman and co-workers developed a constraint/restraint least squares refinement program, CORELS (Sussman, 1985). In this program, a rigid geometry is assigned to parts of the structure and the parameters of these constrained parts are refined rather than individual atomic parameters. Optionally, specified dihedral angles within a group can also be refined, which is then no longer completely rigid. It is possible to regard an entire molecule as a rigid entity and to refine its position and orientation in the unit cell. This is often done as a first step in a refinement procedure (for instance, after the molecular replacement procedure has given starting values for the position and orientation of the molecule). With CORELS, the molecule can then be more properly positioned. The rigid entity can also be of smaller size—for instance, a folding unit consisting of  $\beta$ -strands and  $\alpha$ -helices, or a prosthetic group, or, in nucleic acid structures, a nucleotide. The method increases the data/parameter ratio appreciably and is, therefore, applicable if only moderate resolution data are available.

Because CORELS is based on the conventional method of structure factor calculation and, therefore, is slow, rigid-body refinement is performed much faster with a number of other rigid-body refinement programs in which FFT techniques are employed (e.g., Brünger's XPLOR package, Tronrud's TNT program, or Navaza's AMoRe; Section 10.3.2 of Chapter 10). However, the principle is the same. In pure crystallographic refinement without adding stereochemical information, the quantity to be minimized is

$$Q = \sum_{hkl} w(hkl) \{ |F_{\text{obs}}(hkl)| - |F_{\text{calc}}(hkl)| \}^2.$$

In the CORELS program the constrained entities contribute as such to the calculation of the  $|F_{\text{calc}}(hkl)|$  values. Restraints modify the least squares criterion to the minimization of

$$\begin{aligned} Q = & \sum_{hkl} w(hkl) \{ |F_{\text{obs}}(hkl)| - |F_{\text{calc}}(hkl)| \}^2 \\ & + w_{\text{D}} \sum_d w_d \{ D_{\text{obs}}(d) - D_{\text{calc}}(d) \}^2 \\ & + w_{\text{T}} \sum_i w_{\mathbf{x}} \sum_{\mathbf{x}} \{ X_{\text{T}}(i, \mathbf{x}) - X(i, \mathbf{x}) \}^2. \end{aligned}$$

$D_{\text{obs}}(d)$  is the standard distance, corresponding not only to bond lengths but also to angles and van der Waals distances, because in CORELS, all restraints are introduced as distances: a bond length as the distance between nearest neighbors, a bond angle as the distance between next nearest neighbors, and a dihedral angle as the distance between a first and a fourth atom (Figure 13.3).  $D_{\text{calc}}(d)$  is the distance calculated from the current model.  $w_d = 1/\sigma_d$ , where  $\sigma_d$  is the standard deviation for distances of type  $d$  bonds as observed in small-molecule structures. The third term restrains the coordinate vectors  $\mathbf{x}$  ( $= x, y, z$ ) of a model atom to a corresponding target position. For crystallographic refinement, the third term is omitted by putting  $w_{\text{T}} = 0$ . It plays a role in model building for which  $w(hkl) = 0$ . By choosing the weighting factors  $w(hkl)$  and  $w_{\text{D}}$  properly, a relative weight can be given to the X-ray and the stereochemical restraints in the refinement process. The quantity  $Q$  is minimized with respect to all positional coordinates and thermal parameters in the usual way with the least squares method.

### 13.4.2. Stereochemically Restrained Least Squares Refinement

Stereochemical restraints are fully incorporated in this method. The occasional calculation of an electron density map, a difference electron density map, or OMIT map (Section 8.2 of Chapter 8) is useful for manually correcting major imperfections in the model. The Konnert–Hendrickson program, PROLSQ (Hendrickson, 1985), has found wide application in the accurate structure determination of protein molecules, but now more efficient and flexible programs, for instance, TNT, written by Tronrud et al. (1987) using the FFT algorithm, are mainly used for stereochemically restrained least squares refinement.

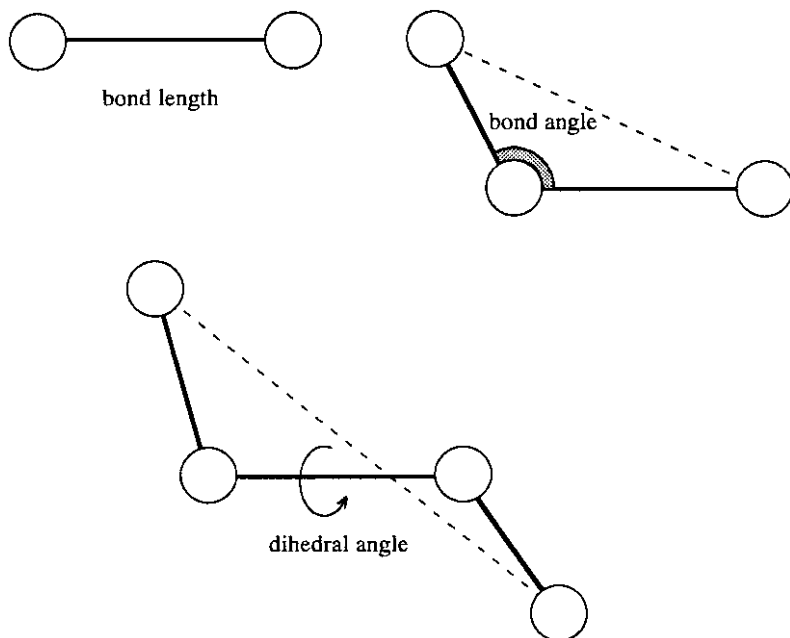


Figure 13.3. In the CORELS refinement method, all restraints are introduced as distances: a bond length as the distance between nearest neighbors, a bond angle as the distance between next nearest neighbors, and a dihedral angle as the distance between a first and a fourth atom.

The function to be minimized consists of a crystallographic term (a) and several stereochemical terms (b)–(f)

$$Q = \sum_{hkl} w(hkl) \{ |F_{\text{obs}}(hkl)| - |F_{\text{calc}}(hkl)| \}^2 \quad (\text{a})$$

$$+ \sum_{\text{dist. } j} w_D(j) (d_j^{\text{ideal}} - d_j^{\text{model}})^2 \quad (\text{b})$$

$$+ \sum_{\substack{\text{planes} \\ k}} \sum_{\substack{\text{coplanar} \\ \text{atoms } i}} w_P(i, k) (\mathbf{m}_k \cdot \mathbf{r}_{j,k} - d_k)^2 \quad (\text{c})$$

$$+ \sum_{\substack{\text{chiral} \\ \text{centers } l}} w_C(l) (V_l^{\text{ideal}} - V_l^{\text{model}})^2 \quad (\text{d})$$

$$+ \sum_{\text{nonbonded contacts } m} w_N(m) (d_m^{\text{min}} - d_m^{\text{model}})^4 \quad (\text{e})$$

$$+ \sum_{\text{torsion angles } t} w_T(t) (X_t^{\text{ideal}} - X_t^{\text{model}})^2; \quad (\text{f})$$

term (a) is the usual X-ray restraint. All other terms are stereochemical restraints. Term (b) restrains the distance between atoms, defining bond lengths, bond angles,

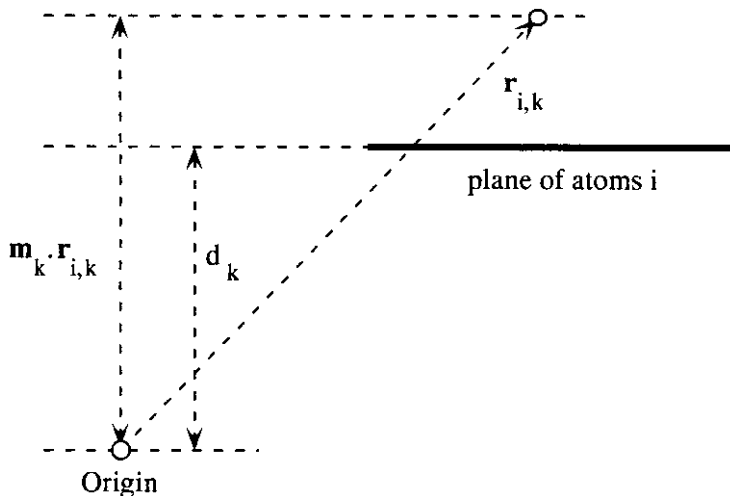


Figure 13.4. Planarity restraining in the Konnert–Hendrickson refinement method is on the deviation of the atoms from the least squares plane of the group.  $d_k$  is the distance from the origin to the current least squares plane. For an atom at position  $\mathbf{r}_{i,k}$ , the distance from the least squares plane is expressed by  $\mathbf{m}_k \cdot \mathbf{r}_{i,k} - d_k$ . Here,  $\mathbf{m}_k$  is the unit vector normal to the plane.

or dihedral angles. Term (c) imposes the planarity of aromatic rings. The same applies to the guanidyl part of arginine and to peptide planes. The actual restraining is on the deviation of the atoms from the least squares plane of the group (see Figure 13.4).  $d_k$  are the parameters of the current least square plane. For an atom at position  $\mathbf{r}_{i,k}$ , the distance from the least squares plane is expressed by  $\mathbf{m}_k \cdot \mathbf{r}_{i,k} - d_k$ . Here,  $\mathbf{m}_k$  is the unit vector normal to the plane and  $d_k$  is the distance from the origin to the plane.

Term (d) restrains the configuration to the correct enantiomer. A protein structure has many chiral centers: at the  $C\alpha$  atoms (except for glycine) and at the  $C\beta$  of threonine and isoleucine. Chirality can be expressed by a chiral volume, which is calculated as the scalar triple product of the vectors from a central atom O to three attached atoms 1, 2, and 3;  $\{(\mathbf{O} \rightarrow 1) \cdot [(\mathbf{O} \rightarrow 2) \times (\mathbf{O} \rightarrow 3)]\}$  or, shorter,  $\{\mathbf{1} \cdot [\mathbf{2} \times \mathbf{3}]\}$ . This is the scalar product of vector  $\mathbf{1}$  with a new vector  $\mathbf{4}$ , which is the vector product of vector  $\mathbf{2}$  and vector  $\mathbf{3}$  (Figure 13.5). The new vector  $\mathbf{4}$  is perpendicular to both vectors  $\mathbf{2}$  and  $\mathbf{3}$ ; its length equals the surface area of the parallelogram formed by  $\mathbf{2}$  and  $\mathbf{3}$ ; multiplied by  $\mathbf{1}$ , a scalar results that equals six times the volume of the pyramid that has O as top and triangle 1, 2, 3 as its base. For the enantiomeric configuration, two vectors are interchanged, and because  $\{\mathbf{1} \cdot [\mathbf{2} \times \mathbf{3}]\} = -\{\mathbf{3} \cdot [\mathbf{2} \times \mathbf{1}]\} = -\{\mathbf{1} \cdot [\mathbf{3} \times \mathbf{2}]\} = -\{\mathbf{2} \cdot [\mathbf{1} \times \mathbf{3}]\}$ , the triple product will have the opposite sign.

Term (e) introduces restraints for nonbonded or van der Waals contacts. They prevent the close approach of atoms not connected by a chemical bond and are stop



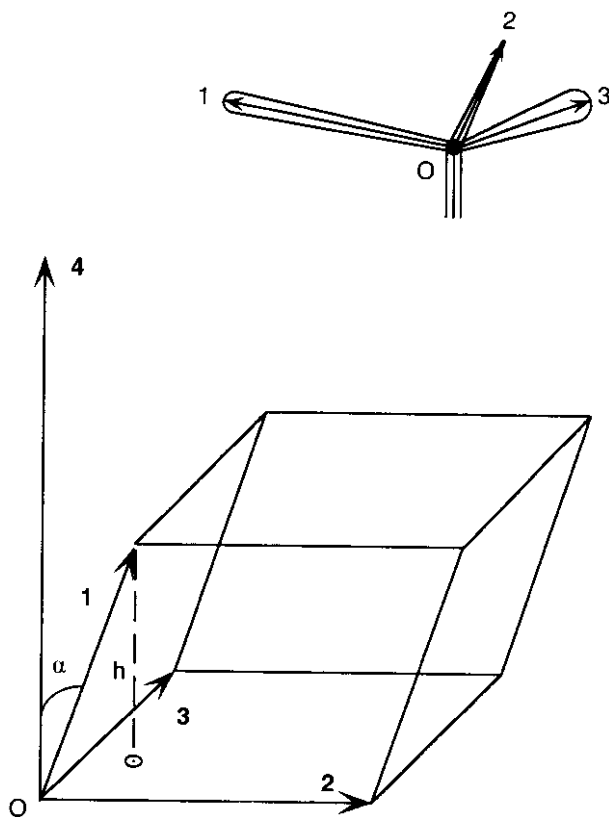


Figure 13.5. The chirality of an amino acid is expressed as a chiral volume, which is calculated as the scalar triple product of the vectors from a central atom  $O$  to three attached atoms  $1$ ,  $2$ , and  $3$ :  $\{\mathbf{1} \cdot [\mathbf{2} \times \mathbf{3}]\}$ . Vector  $\mathbf{4}$  is the vector product of vectors  $\mathbf{2}$  and  $\mathbf{3}$ . The area of the parallelogram formed by vectors  $\mathbf{2}$  and  $\mathbf{3}$  is  $|\mathbf{2} \times \mathbf{3}|$ . The volume of the parallelepiped formed by vectors  $\mathbf{1}$ ,  $\mathbf{2}$ , and  $\mathbf{3}$  is  $V = h \cdot |\mathbf{2} \times \mathbf{3}| = h \cdot |4|$ , where  $h$  is the altitude;  $h$  is parallel to  $\mathbf{4}$  and equals  $|\mathbf{1}| \cdot |\cos \alpha|$  (because  $0 < \alpha < 180^\circ$ ,  $\cos \alpha$  might be negative and, therefore, the absolute value of  $\cos \alpha$  is taken).  $V = |\mathbf{1}| \cdot |4| \cdot |\cos \alpha| = |\mathbf{1} \cdot \mathbf{4}| = |\mathbf{1} \cdot [\mathbf{2} \times \mathbf{3}]|$ . The volume of the pyramid with  $O$  as the top and triangle  $1$ ,  $2$ , and  $3$  as the base is  $\frac{1}{3} \cdot h \cdot \frac{1}{2} |\mathbf{2} \times \mathbf{3}| = \frac{1}{6} \cdot V$ .

signs for those atoms. As such, they play an important role in protein structures. Only the repulsive term of the van der Waals potential is taken into account:

$$E_{\text{repulsive}} = A \times r^{-12}.$$

For contacts between C, N, O, and S atoms and for  $d$  values near and shorter than the equilibrium distance  $d^{\text{min}}$ , the repulsive term can be approximated by

$$E(d) - E(d^{\text{min}}) = \frac{1}{\sigma^4} (d - d^{\text{min}})^4$$

and the function to be minimized becomes

$$\sum_{\substack{\text{nonbonded} \\ \text{contacts } m}} w_N(m)(d_m^{\text{min}} - d_m^{\text{model}})^4.$$

Term (f) restrains torsion angles. Although a free rotation is, in principle, possible around single bonds, there are certain restrictions imposed by nonbonded repulsion. For instance, the rotations around the  $C_\alpha \rightarrow N$  and the  $C_\alpha \rightarrow C = O$  bond in the peptide main chain are limited to certain combinations. Also, in aliphatic side chains, the staggered conformation is more stable than the eclipsed one.

All weighting factors  $w$  can be chosen with some freedom, although the normal choice is  $w = 1/\sigma^2$ , except for  $w_N$ , which is taken as  $1/\sigma^4$ ;  $\sigma$  is the standard deviation of the expected distribution. In addition to the restraints (a)–(f), several others can be added. For instance, it can be expected that the  $B$  parameters of the temperature factors of neighboring atoms are related because large temperature movements of an atom will cause its neighbors to also move over longer than average distances. On the other hand, rigid parts restrict the movement of their neighbors. This correlation can be introduced by restraining the  $B$  value of an atom to those of its neighbors.

In structural papers, the statistics of the refinement results are usually given in table form—for instance, as in Table 13.1.

### 13.4.3. SHELXL

Originally, this program was devised for the refinement of small molecules, but it has been adapted for macromolecule refinement (Sheldrick and Schneider, 1997). The condition is that the X-ray data have been collected to at least 2.5 Å resolution. The program applies a least squares strategy and refines against  $F^2$  values. It incorporates many features similar to those found in CORELS, PROLSQ, and TNT, such as constraints and geometric restraints with the exception of torsion angle and H-bonding restraints. If noncrystallographic symmetry (NCS) is present, it increases the refinement efficiency considerably. NCS is applied as a restraint in two ways:

1. Distances between atoms 1 and 4 in a connectivity chain 1, 2, 3, 4, ... are restrained to be equal in the NCS-related molecules.
2. Isotropic temperature factors of related atoms are restrained to be equal.

These restraints reduce the number of parameters appreciably. The power of SHELXL has been attributed to the following:

- A conventional structure factor calculation that is more precise than an FFT calculation. This causes the program to be relatively slow, but it improves the convergence properties.
- The inclusion of important off-diagonal terms in the least squares matrix.

Table 13.1. Statistics of Data Collection and Refinement for Hevamin at pH 2.0

Data processing	
Number of observations	109,372
Number of unique reflections	19,169
$R_{\text{merge}}$ (1.93–1.90 Å)	0.065 (0.213) <sup>a</sup>
Completeness (1.93–1.90 Å)	0.941 (0.414)
Refinement	
Resolution range (Å)	15.0–1.90
Completeness of working set	0.83
Completeness of test set	0.09
$R$ -factor	0.157
$R_{\text{free}}$	0.199
Number of protein atoms	2,087
Number of solvent atoms	140
RMS deviations from ideality	
Bond lengths (Å)	0.010
Bond angles (degrees)	1.48
Dihedrals (degrees)	23.0
$B$ -value correlations for bonded atoms (Å <sup>2</sup> )	2.1
Average $B$ values (Å <sup>2</sup> )	
All protein atoms	16.5
Main chain atoms	13.2
Side chain atoms	20.1
Solvent atoms	33.2

*Note:* The structure was refined with TNT against data from 15.0 to 1.9 Å resolution.

*Source:* From Terwisscha van Scheltinga, thesis, 1997, University of Groningen, with permission.

<sup>a</sup>Values in parentheses are for the high-resolution shell

Further advantages are the flexible treatment of disorder (e.g., more than one position for a side chain) and the feature of anisotropic refinement. Moreover, it can refine twinned crystals by fitting the sum of the calculated intensities for the individual components to the observed intensities. This is better than trying to “detwin” the data, which introduces systematic errors.

#### 13.4.4. Energy Refinement (EREF)

In the Konnert–Hendrickson refinement the least squares function

$$\sum_h w(h) (|F_{\text{obs}}(h)| - |F_{\text{calc}}(h)|)^2$$

is minimized simultaneously with a number of geometric terms related to bond lengths, angles, and so forth. In another refinement method—proposed by Jack and Levitt (1978)—the X-ray term is minimized together with a potential energy function including terms for bond stretching, bond angle bending, torsion potentials, and van der Waals interactions. Electrostatic interactions are usually ignored, because they act over rather long distances and are not sensitive to small changes in atomic position. Moreover, the calculations are performed assuming the molecule to be in a vacuum and the electrostatic energy to be extremely high, unless artificial dielectric constants are introduced. The function to be minimized is

$$Q = (1 - w_X) \times E + w_X \times \sum_h w(hkl) (|F_{\text{obs}}(hkl)| - |F_{\text{calc}}(hkl)|)^2$$

where  $E$  is the energy term and  $w_X$  controls the relative contribution of the energy and the X-ray term. Its choice, between  $w_X = 0$  (pure energy minimization) and  $w_X = 1$  (pure X-ray minimization) is rather arbitrary and depends on experience; however, a more objective way for determining  $w_X$  has been presented by Brünger (1993) by optimizing the free  $R$ -factor (Section 15.2 of Chapter 15). For the potential energy of a bond, the harmonic approximation is used:

$$E_{\text{bond}} = \frac{1}{2} K_{\text{bond}} (b - b_0)^2,$$

with  $b_0$  the minimum energy distance and  $b$  the actual distance between the atoms.  $K_{\text{bond}}$  and  $b_0$  can be derived from the vibration spectra of small molecules. The same assumption is made for the bond angles:

$$E_{\text{bond angle}} = \frac{1}{2} K_{\tau} (\tau - \tau_0)^2.$$

The torsion energy around a bond is expressed as

$$E_{\text{torsion}} = \frac{1}{2} K_{\xi} (\xi - \xi_0)^2.$$

The energy for a dihedral angle is

$$E_{\text{dihedral}} = K_{\theta} \{1 + \cos(m\theta + \delta)\}.$$

(see Figure 13.6).  $\theta$  is the rotation angle and  $\delta$  is a phase angle determining the zero point of rotation.  $m$  is the rotation frequency (3 for the C—C bond in ethane). This is a very simple presentation of the dihedral energy and it is only approximately true for bonds that have a large group on either side. For the van der Waals interaction energy, both the attractive term ( $B \times r^{-6}$ ) and the repulsive term ( $A \times r^{-12}$ ) are taken into account:

$$E_{\text{van der Waals}} = A \times r^{-12} + B \times r^{-6}.$$

Although EREF is somewhat less popular than stereochemically restrained refinement, it can play a useful role in minimizing the energy of a system before refining it with the molecular dynamics technique, which will be discussed in Section 13.4.5.

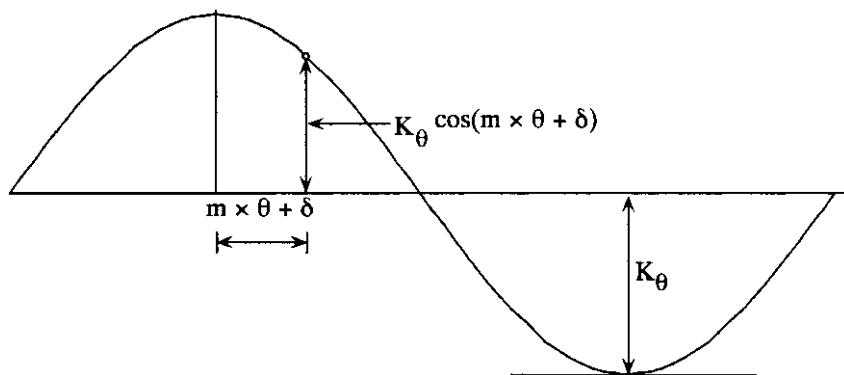


Figure 13.6. The energy for a dihedral angle.  $\theta$  is the rotation angle and  $\delta$  is a phase angle determining the zero point of rotation.  $m$  is the rotation frequency (for instance, 3 for the C—C bond in ethane).

### 13.4.5. Molecular Dynamics or Simulated Annealing

The refinement procedures described so far are based on the least squares method. The function to be minimized follows a downhill path toward its minimum value, and if the starting model is not too different from the real structure, the refinement easily converges to the correct solution. However, if the distance between the atoms in the model and in the real structure is rather large, the refinement might be trapped in a local minimum instead of reaching the global or true minimum. To avoid this situation, a refinement technique is required that allows uphill as well as downhill search directions to overcome barriers in the  $Q$ -function. This technique is supplied by molecular dynamics and was introduced by Brünger and incorporated in the X-PLOR package (Brünger and Nilges, 1993). In molecular dynamics, the behavior of a system of particles is simulated. This simulation yields an ensemble of structures that is energetically allowed for a given temperature and pressure: The energy distribution of the structures in the ensemble follows Boltzmann's law, which states that the number of structures with a potential energy  $\epsilon_{\text{pot}}$  is proportional to  $\exp[-\epsilon_{\text{pot}}/kT]$ ;  $k$  is Boltzmann's constant and  $T$  is the absolute temperature. The potential energy depends on the relative positions of the atoms and is calculated on the basis of known potential energy functions, which are always only approximately accurate. The potential energy terms are similar to those in EREF. However, in the molecular dynamics refinement, an electrostatic term is added. It is calculated as

$$\sum \frac{q_i \times q_j}{4\pi \epsilon_0 \epsilon_r r_{ij}}$$

$\epsilon_0$  is the permittivity constant:  $4\pi \epsilon_0 = 1.11264 \times 10^{-10} \text{ C}^2 \text{ N}^{-1} \text{ m}^{-2}$ .  $\epsilon_r$  is the local dielectric constant, which is given an estimated value between 1 and 80, depending

on the position of the atoms  $i$  and  $j$  with interatomic distance  $r_{ij}$  or, alternatively, instead of  $\epsilon_r > 1$ , the electric charges can be reduced.

A molecular dynamics calculation on a molecule starts with assigning to the atoms velocities derived from a Maxwellian distribution at an appropriate temperature. At time  $t = 0$ , the atoms are in a starting configuration that has a potential energy  $E_{\text{pot}}$  for the entire molecule. On each atom  $i$  at position  $\mathbf{r}_i$ , a force is acting that is the derivative of the potential energy:  $\text{force}(i) = -\partial E_{\text{pot}}/\partial \mathbf{r}_i$ . With the equation from Newtonian mechanics,  $\text{force}(i) = m_i(d^2\mathbf{r}_i/dt^2)$ , the acceleration  $d^2\mathbf{r}_i/dt^2$  for atom  $i$  with mass  $m_i$  can be calculated and then applied. After a short time step  $\Delta t$ , in the femtosecond range ( $1 \text{ fs} = 10^{-15} \text{ s}$ ), the process is repeated with the atoms in the new positions. If the number of steps is sufficient ( $10^3$ – $10^4$ ), the minimum of  $E_{\text{pot}}$  is reached and information about the dynamic behavior of the atoms in the molecule is obtained. If the temperature of the system is raised to a higher value, more atoms have a higher speed and a higher kinetic energy and can overcome higher-energy barriers. The basic idea of molecular dynamics as a superior refinement technique is to raise the temperature sufficiently high for the atoms to overcome energy barriers and then to cool slowly to approach the energy minimum. The method is called simulated annealing (SA) in comparison with, for instance, removing internal strain from glass by heating it first and then slowly cooling it down (Brünger, 1991b). In an alternative method, the temperature is kept constant, but all potential energy terms are scaled by an overall scale factor  $c$ , with  $0 \leq c \leq 1$ . This is based on Boltzmann's law. An increase in  $T$  with constant  $\epsilon_{\text{pot}}$  has the same effect as diminishing  $\epsilon_{\text{pot}}$  at constant  $T$ .

A typical example of a high-energy barrier occurs in the flipping of a peptide plane. It is impossible for the other refinement techniques to overcome this barrier, but not so for SA. In the application of molecular dynamics (MD) (or SA) to crystallographic refinement, the calculated structure factors of the system are restrained to the observed structure factors as target values, by adding a maximum likelihood target function

$$E_x = \sum_{hkl \in W} \left( \frac{1}{\sigma_{\text{ML}}^2} \right) (|F_{\text{obs}}(hkl)| - \langle |F_{\text{obs}}(hkl)| \rangle)^2 \quad (13.23)$$

as a pseudoenergy term to the potential energy  $E_{\text{pot}}$  of the system.  $W$  is the working set of reflections, containing 95–100% of the total number of reflections; it is explained in Section 15.2 of Chapter 15. The expected value  $\langle |F_{\text{obs}}(hkl)| \rangle$  as well as the variance ( $\sigma_{\text{ML}}^2$ ), can be derived (Pannu and Read, 1996) from  $|F_{\text{obs}}(hkl)|$ ,  $|F_{\text{calc}}(hkl)|$ , and  $\sigma_A$ , which is an error-related parameter (Section 15.6 of Chapter 15). Equation (13.23) replaces the original target function  $E_x$  based on least squares.

The total energy,  $E_x + E_{\text{pot}}$ , is minimized during the refinement. In principle,  $\mathbf{F}_{\text{calc}}$  must be calculated after each time step  $\Delta t$ . The same is true for the derivatives of  $|F_{\text{calc}}|$  with respect to atomic parameters. These derivatives are required for calculating the “force.” However, the atomic parameters change very little during  $\Delta t$  and, therefore, it is sufficient to calculate  $\mathbf{F}_{\text{calc}}$  and its derivatives only after a

preset change in the coordinates has been reached (e.g., one-tenth of the resolution). MD refinement is usually preceded by energy refinement (EREF) with or without X-ray restraints, to reduce possibly high energies in the system.

In Section 8.2 of Chapter 8, OMIT maps were discussed for improving or checking troublesome parts of the structure. An OMIT map is calculated with the observed structure factor amplitudes and phase angles calculated for the reliable part of the structure. The “missing” parts should then show up in the electron density map at half of their actual height. To reduce model bias, Sim weighting factors are applied.

OMIT maps are sometimes used to systematically check a molecular model by deleting parts of the structure, one after the other. The omitted part comprises 2–5% of the structure. Model bias can also be reduced by applying simulated annealing to the “known” parts. The atoms in the “known” part at the border of the omitted region are restrained to keep them from moving into the omitted region. The maps calculated in this way are called simulated annealing OMIT maps or composite annealed OMIT maps (Shah et al., 1997).

#### 13.4.5.1. Advantage of MD Refinement

An advantage of MD refinement is the large radius of convergence, which can be several angstrom units long. In other words, MD draws groups of atoms, originally several angstroms away from their final position, corresponding with the potential energy minimum, toward those final positions without any manual intervention. Large errors in the starting model can be corrected. This speeds up the refinement appreciably. The method is very demanding on computer time, but with modern high-speed computers, this is not a problem.

#### 13.4.5.2. The Time-Averaging MD Technique

In MD refinement, the dynamic system of moving atoms is restrained by the X-ray data of a static model, including isotropic temperature factors. This is, in principle, not correct because in fact the atomic movements are not necessarily isotropic, but can just as well be anisotropic and anharmonic. Gros et al. (1990) proposed improving the MD refinement technique by adding as a pseudoenergy term:

$$E_x = k_x \times \sum_{hkl} [|F_{\text{obs}}(hkl)| - k] \{F_{\text{calc}}(hkl)\}_{\text{average}}|^2.$$

$\{F_{\text{calc}}(hkl)\}_{\text{average}}$  is not the structure factor of a single model (based on the atomic coordinates  $x$ ,  $y$ ,  $z$  and the temperature factor parameter  $B$ ), but the ensemble average of calculated structure factors without the temperature factor:

$$\{F_{\text{calc}}(hkl)\}_{\text{average}} = \frac{\int_{t=0}^{t'} P_t F_{\text{calc}}^t(hkl) dt}{\int_{t=0}^{t'} P_t dt},$$

where  $t'$  is the total trajectory time (e.g., 1,000 time steps),  $t$  is any time in the trajectory,  $P_t$  is the weight given to the structure factor  $\mathbf{F}_{\text{calc}}^t(h k l)$ , calculated for the model at time  $t$ , and  $P_t$  is chosen as  $\exp[-(t' - t)/\tau_x]$ . The effect of this choice is that an exponentially decreasing weight is given to “older” structures (small  $t$ ) with a relaxation time  $\tau_x$ , which regulates the contribution from an “old” structure: the larger  $\tau_x$ , the more it contributes:

$$\int_{t=0}^{t'} P_t dt = \tau_x \left\{ 1 - \exp \left[ -\frac{t'}{\tau_x} \right] \right\} \approx \tau_x.$$

If  $t' \gg \tau_x$ , the factor  $\{1 - \exp[-t'/\tau_x]\}$  can be ignored:

$$\{\mathbf{F}_{\text{calc}}(h k l)\}_{\text{average}} = \frac{1}{\tau_x} \int_{t=0}^{t'} \exp \left[ -\frac{t' - t}{\tau_x} \right] \mathbf{F}_{\text{calc}}^t(h k l) dt.$$

The structure factor  $\mathbf{F}_{\text{calc}}^t(h k l)$  of an individual structure at time  $t$  in the trajectory depends on positional parameters only. No individual thermal parameters are assigned to the atoms; instead, their movement is now represented by their spatial distribution during the complete trajectory. This is not necessarily isotropic but can also be anisotropic and anharmonic.

In the execution of the method,  $\{\mathbf{F}_{\text{calc}}(h k l)\}_{\text{average}}$  at time  $t = 0$  is taken equal to the classical  $\mathbf{F}_{\text{calc}}(h k l)$ , including the temperature factor parameter  $B$ . In the course of the process, these  $B$  parameters are gradually lowered to  $1 \text{ \AA}^2$  and the relaxation time  $\tau$  increased from 0 to, for instance, 10 ps (1 ps =  $10^{-12}$  s). In this way, a gradual change from classical to time-averaging MD is accomplished. There is no need to calculate  $\mathbf{F}_{\text{calc}}(h k l)$  of the structure after each time step  $\Delta t$ . It is sufficient to do it for an ensemble of, for instance, 100 structures. The derivatives of  $|\mathbf{F}_{\text{calc}}|$ , as obtained by a FFT according to Agarwal (1978), must be recalculated more often because of the small but rapidly changing fluctuations in the atomic positions. It should be remarked that each individual structural model (i.e., a model calculated after a time step  $\Delta t$ ) is a poor representation of the actual structure: The atoms are not in their equilibrium position and no real  $B$  parameters are incorporated. It is the complete collection of the individual models that approaches the ideal one. Therefore, time-averaging MD is not a refinement technique in the pure sense, but a sampling technique that provides us with an excellent model of the structure, including a more complete description of the atomic fluctuations around the equilibrium positions, as the conventional X-ray structure does.

With this time-averaging MD technique remarkably low,  $R$ -factors—near 10%—can be reached. It will be clear that even more computer time is needed than for the molecular dynamics technique without time averaging, and still more if solvent molecules are to be included in the refinement.

Although the convergence range is large for MD refinement and manual intervention is less frequently required than with the previous refinement techniques, the electron density map should be checked occasionally for large errors, such as



side chains placed in the density of solvent molecules that are not included in the refinement.

### 13.4.5.3. Torsion Angle Refinement

In 1971, Diamond introduced a refinement technique for protein structures in which only the torsion angles were refined (Diamond, 1971). Peptide planes were kept planar, and bond distances and bond angles were kept constant. It was based on least squares refinement and turned out not to be a very effective refinement method. In the 1980s, it was replaced by more common refinement protocols. Rice and Brünger (1994) have reintroduced torsion angle refinement with more success by applying it in the context of simulated annealing. Restriction to torsion angles greatly increases the observation/parameter ratio. The method shows an increased convergence compared with conventional methods, but it does not replace them. It can precede them if the preliminary model is too far from the final solution for a conventional technique.

### 13.4.6. REFMAC

Murshudov et al. (1997) have written the refinement program REFMAC, which is entirely based on the maximum likelihood formalism. According to Equation (13.7),

$$p[\mathbf{F}(\text{calc}); |F(\text{obs})|] = p^{\text{prior}}[\mathbf{F}(\text{calc})] \times \frac{p[|F(\text{obs})|; \mathbf{F}(\text{calc})]}{p[|F(\text{obs})|]}.$$

Disregarding the normalization constant  $p[|F(\text{obs})|]$ ,

$$p[\mathbf{F}(\text{calc}); |F(\text{obs})|] = p^{\text{prior}}[\mathbf{F}(\text{calc})] \times p[|F(\text{obs})|; \mathbf{F}(\text{calc})];$$

$p^{\text{prior}}[\mathbf{F}(\text{calc})]$  expresses the prior information as stereochemical restraints. This information is known and will not be discussed here. We restrict ourselves to

$$p[|F(\text{obs})|; \mathbf{F}(\text{calc})].$$

The required likelihood is [Equation (13.9)]

$$\mathcal{L}_{\text{total}} = \prod_{\mathbf{h}} [p[|F_{\mathbf{h}}(\text{obs})|; \mathbf{F}_{\mathbf{h}}(\text{calc})].$$

We start from Equation (8.6a) and Figure 8.1 of Chapter 8 if vector  $\mathbf{F}_K$  is regarded as  $\mathbf{F}(\text{calc})$  and vector  $\mathbf{F}$  is regarded as  $\mathbf{F}(\text{obs})$ . The conditional probability  $p[\xi; |F|]$  is equal to the conditional probability

$$p[\mathbf{F}; \mathbf{F}_K] = p[\mathbf{F}(\text{obs}); \mathbf{F}(\text{calc})].$$

Because only the amplitudes of  $\mathbf{F}(\text{obs})$  are known, Equation (8.6a) of Chapter 8

must be integrated over  $\xi$  to obtain

$$\begin{aligned}
 p[|F(\text{obs})|; \mathbf{F}(\text{calc})] &= \\
 & \frac{|F(\text{obs})|}{\pi \times \sum_{j=1}^n f_j^2} \exp \left[ -\frac{|F(\text{obs})|^2 + |F(\text{calc})|^2}{\sum_{j=1}^n f_j^2} \right] \\
 & \int_{\xi=0}^{2\pi} \exp \left[ \frac{2|F(\text{obs})| \times |F(\text{calc})| \cos \xi}{\sum_{j=1}^n f_j^2} \right] d\xi \\
 &= 2 \times \frac{|F(\text{obs})|}{\sum_{j=1}^n f_j^2} \exp \left[ -\frac{|F(\text{obs})|^2 + |F(\text{calc})|^2}{\sum_{j=1}^n f_j^2} \right] \\
 & \times I_0 \left[ \frac{2|F(\text{obs})| + |F(\text{calc})|}{\sum_{j=1}^n f_j^2} \right]
 \end{aligned}$$

$I_0$  is a zero-order Bessel function [compare with Equation (8.7) of Chapter 8].

This probability function for  $p[\mathbf{F}(\text{obs}); \mathbf{F}(\text{calc})]$  was derived assuming no errors in atomic positions in the model. The effect of these errors is, as pointed out by Luzzati (1952) and Read (1990b), that  $|F(\text{calc})|$  must be replaced by

$$D \times |F(\text{calc})|, \quad \text{and} \quad \sum_{j=1}^n f_j^2 \text{ by } (1 - D^2) \times \sum_{j=1}^n f_j^2.$$

$D$  is the Fourier transform of the probability distribution  $p(\Delta \mathbf{r})$  of  $\Delta \mathbf{r}$  [see Equation (15.2)].

Experimental errors in the  $|F(\text{obs})|$  values can be incorporated by increasing the variance  $\sum_{j=1}^n f_j^2$  with the variance  $\sigma_e^2$  of the experimental error. We finally obtain

$$\begin{aligned}
 p[\mathbf{F}(\text{obs}); \mathbf{F}(\text{calc})] &= \\
 & 2 \times \frac{|F(\text{obs})|}{2\sigma_e^2 + \sum_{j=1}^n f_j^2} \exp \left[ -\frac{|F(\text{obs})|^2 + D^2|F(\text{calc})|^2}{2\sigma_e^2 + \sum_{j=1}^n f_j^2} \right] \\
 & \times I_0 \left( \frac{2|F(\text{obs})| + D|F(\text{calc})|}{2\sigma_e^2 + \sum_{j=1}^n f_j^2} \right)
 \end{aligned}$$

### 13.4.7. Crystallographic and NMR Systems (CNS)

The special feature of the program CNS (Brünger et al., 1998) is that it encompasses a large number of computational procedures for structure determination. The CNS capabilities for X-ray crystallography are as follows:

#### **Experimental phasing**

Heavy atom (Patterson) searches  
Patterson refinement  
Multiple isomorphous replacement phasing and refinement  
MAD phasing and refinement

#### **Molecular replacement**

Patterson real space and direct rotation searches  
Patterson correlation refinement  
FFT translation searches

#### **Density modification**

Creation of envelopes  
Solvent flattening  
Density averaging  
Histogram matching

#### **Refinement**

Maximum likelihood targets  
Torsion angle molecular dynamics  
Cartesian molecular dynamics  
Conjugate gradient minimization  
Composite annealed OMIT map

## Summary

From a first, nonrefined model of a protein structure (for instance, obtained with isomorphous replacement), important biological information can already be derived. However, for more reliable information and finer details, the structure must be refined. The poor overdetermination limits the refinement, in general, to the positional parameters and an isotropic, but not anisotropic, temperature factor for each atom. Existing stereochemical information from small molecules adds additional “observations” and changes the observation/parameter ratio favorably. The refinement methods use the least squares or maximum likelihood formalism for approaching the final solution, often after a great many cycles in which the fast Fourier transform method is essential.

Molecular dynamics or simulated annealing is one of the most popular refinement techniques. It combines real energy terms with restraints on the structure factor amplitudes as pseudoenergy terms. With the simulated annealing concept, the system can jump over local energy minima and, therefore, has a long radius of convergence.

In many refinement programs the least squares method is replaced by the maximum likelihood formalism.

Issue 12 (1) of Volume D60 of *Acta Crystallographica* (2004) has been entirely devoted to Model Building and Refinement.

# Chapter 14

## The Combination of Phase Information

### 14.1. Introduction

In the multiple isomorphous replacement method, the phase information from the various heavy atom derivatives and from anomalous scattering is combined by multiplying the individual phase probability curves. If the electron density map, which results from isomorphous replacement, can be fully interpreted, the crystallographer immediately starts with model refinement and the isomorphous phase information is left behind. However, if the electron density map is inadequate for complete interpretation, map improvement (i.e., phase refinement) should precede model refinement. Solvent flattening and the inclusion of molecular averaging are examples of map improvement techniques (Chapter 8). Another way to improve the existing model is by combining the isomorphous replacement phase information with phase information from the known part of the structure. It is clear that a general and convenient way of combining phase information from these various sources would be most useful. Such a method has been proposed by Hendrickson and Lattman (1970) and has been based on previous studies by Rossmann and Blow (1961). Hendrickson and Lattman proposed an exponential form for each individual probability curve of the following type:

$$P_s(\alpha) = N_s \exp [K_s + A_s \cos \alpha + B_s \sin \alpha + C_s \cos 2\alpha + D_s \sin 2\alpha];$$

$P_s(\alpha)$  is the probability for phase angle  $\alpha$  derived from source  $s$ ,  $K_s$  and the coefficients  $A_s$ ,  $B_s$ ,  $C_s$ , and  $D_s$  contain, for example, structure factor amplitudes but not the protein phase angles  $\alpha$ .  $N_s$  is a normalization factor. The multiplication of the available  $P_s(\alpha)$  functions to the overall probability function  $P(\alpha)$  is now simplified to an addition of all  $K_s$  and of the coefficients  $A_s$  to  $D_s$  in the exponential

term:

$$P(\alpha) = \prod_s P_s(\alpha) = N' \exp \left[ \sum_s K_s + \left( \sum_s A_s \right) \cos \alpha + \left( \sum_s B_s \right) \sin \alpha + \left( \sum_s C_s \right) \cos 2\alpha + \left( \sum_s D_s \right) \sin 2\alpha \right]$$

or, combining  $N'$  and  $\exp[\sum_s K_s]$ ,

$$P(\alpha) = N \exp [A \cos \alpha + B \sin \alpha + C \cos 2\alpha + D \sin 2\alpha]. \quad (14.1)$$

The value of  $N$  is not important. Moreover, it disappears if the “best” Fourier map is calculated with Equation (7.36) of Chapter 7:

$$\mathbf{F}_{hkl}(\text{best}) = \frac{\int_{\alpha} P_{hkl}(\alpha) \mathbf{F}_{hkl}(\alpha) d\alpha}{\int_{\alpha} P_{hkl}(\alpha) d\alpha}.$$

We will now derive the form of the coefficients  $A_s$  to  $D_s$  for the following:

- Isomorphous replacement
- Anomalous scattering
- Partial structures
- Solvent flattening
- Molecular averaging
- Single-wavelength anomalous replacement (SAD)

## 14.2. Phase Information from Isomorphous Replacement

In Section 7.12 of Chapter 7, the probability function  $[P(\alpha)]_j$  for one reflection and derivative  $j$  in the isomorphous replacement has been presented as

$$[P(\alpha)]_j = N \exp \left[ -\frac{\varepsilon_j^2(\alpha)}{2E_j^2} \right].$$

$\varepsilon_j(\alpha)$  is the “lack of closure error” for the structure factor amplitude  $|F_{\text{PH}}(\text{calc})|$  of derivative  $j$ :

$$\varepsilon_j(\alpha) = \{|F_{\text{PH}}(\text{obs})|_j - k_j |F_{\text{PH}}(\text{calc})|_j\}.$$

The derivation of a suitable form of the phase probability curve is easier if the error is redefined as an error in the derivative intensity instead of the structure factor amplitude. Assuming that  $|F_{\text{PH}}(\text{calc})|^2$  and  $|F_{\text{PH}}(\text{obs})|^2$  are on the same scale, we have

$$\begin{aligned} \varepsilon'_j(\alpha_P) &= |F_{\text{PH},j}(\text{calc})|^2 - |F_{\text{PH},j}(\text{obs})|^2, \\ |F_{\text{PH},j}(\text{calc})|^2 &= |\mathbf{F}_P + \mathbf{F}_{H,j}|^2 \\ &= |F_P|^2 + |F_{H,j}|^2 + 2|F_P| \times |F_{H,j}| \times \cos(\alpha_{H,j} - \alpha_P). \end{aligned}$$

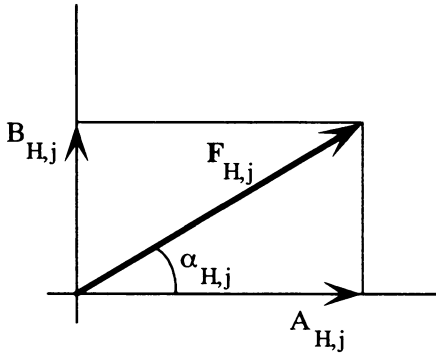


Figure 14.1. The separation of  $\mathbf{F}_{H,j}$  into its components:  $A_{H,j} = |F_{H,j}| \cos \alpha_{H,j}$  and  $B_{H,j} = |F_{H,j}| \sin \alpha_{H,j}$ .

(See Figure 7.15 of Chapter 7.)

$$\begin{aligned} \varepsilon'_j(\alpha_P) &= |F_P|^2 + |F_{H,j}|^2 - |F_{PH,j}(\text{obs})|^2 + 2|F_P| \times |F_{H,j}| \\ &\quad \times \cos(\alpha_{H,j} - \alpha_P). \end{aligned}$$

A Gaussian distribution for  $\varepsilon'_j(\alpha_P)$  is assumed:

$$[P_{\text{iso}}(\alpha_P)]_j = N_j \exp \left[ -\frac{\{\varepsilon'_j(\alpha_P)\}^2}{2(E'_j)^2} \right]. \quad (14.2)$$

$N_j$  is a normalizing factor and  $E'_j$  is the estimated standard deviation of the errors in the derivative intensity.

$$\begin{aligned} \{\varepsilon'_j(\alpha_P)\}^2 &= (|F_P|^2 + |F_{H,j}|^2 - |F_{PH,j}(\text{obs})|^2)^2 \\ &\quad + 4 \times (|F_P|^2 + |F_{H,j}|^2 - |F_{PH,j}(\text{obs})|^2) \\ &\quad \times |F_P| \times |F_{H,j}| \times \cos(\alpha_{H,j} - \alpha_P) \\ &\quad + 4 \times |F_P|^2 \times |F_{H,j}|^2 \times \cos^2(\alpha_{H,j} - \alpha_P) \end{aligned}$$

We want to separate functions with  $\alpha$  only from the rest. This can be done by writing

$$\begin{aligned} \cos^2(\alpha_{H,j} - \alpha_P) &\rightarrow \frac{1}{2} \{1 + \cos 2(\alpha_{H,j} - \alpha_P)\}, \\ \cos(\alpha_{H,j} - \alpha_P) &\rightarrow \cos \alpha_{H,j} \cos \alpha_P + \sin \alpha_{H,j} \sin \alpha_P. \end{aligned}$$

With the separation of  $\mathbf{F}_{H,j}$  into its components (Figure 14.1), this results in

$$\begin{aligned} \{\varepsilon'_j(\alpha_P)\}^2 &= (|F_P|^2 + |F_{H,j}|^2 - |F_{PH,j}(\text{obs})|^2)^2 + 2 \times |F_P|^2 \times |F_{H,j}|^2 \\ &\quad + 4 \times (|F_P|^2 + |F_{H,j}|^2 - |F_{PH,j}(\text{obs})|^2) \times |F_P| \times A_{H,j} \times \cos \alpha_P \\ &\quad + 4 \times (|F_P|^2 + |F_{H,j}|^2 - |F_{PH,j}(\text{obs})|^2) \times |F_P| \times B_{H,j} \times \sin \alpha_P \\ &\quad + 2 \times |F_P|^2 \times (A_{H,j}^2 - B_{H,j}^2) \cos 2\alpha_P \\ &\quad + 4 \times |F_P|^2 \times A_{H,j} \times B_{H,j} \times \sin 2\alpha_P. \end{aligned}$$

Comparison of this equation with Equations (14.1) and (14.2) gives

$$A_{\text{iso},j} = -\frac{2(|F_{\text{P}}|^2 + |F_{\text{H},j}|^2 - |F_{\text{PH},j}(\text{obs})|^2) \times |F_{\text{P}}|}{(E'_j)^2} \times A_{\text{H},j},$$

$$B_{\text{iso},j} = -\frac{2(|F_{\text{P}}|^2 + |F_{\text{H},j}|^2 - |F_{\text{PH},j}(\text{obs})|^2) \times |F_{\text{P}}|}{(E'_j)^2} \times B_{\text{H},j},$$

$$C_{\text{iso},j} = -\frac{|F_{\text{P}}|^2}{(E'_j)^2} \times (A_{\text{H},j}^2 - B_{\text{H},j}^2),$$

$$D_{\text{iso},j} = -\frac{2|F_{\text{P}}|^2}{(E'_j)^2} \times A_{\text{H},j} \times B_{\text{H},j}.$$

### 14.3. Phase Information from Anomalous Scattering

The improvement of protein phase angles by incorporating information from anomalous scattering has already been discussed in Section 9.3 of Chapter 9:

$$P_{\text{ano}}(\alpha_{\text{P}}) = N' \exp \left[ -\frac{\varepsilon_{\text{ano}}^2(\alpha_{\text{P}})}{2(E')^2} \right]$$

[see Equation (9.2)] with  $\varepsilon_{\text{ano}}(\alpha_{\text{P}}) = \Delta\text{PH}(\text{obs}) - \Delta\text{PH}(\text{calc})$  and

$$\Delta\text{PH}(\text{obs}) = |F_{\text{PH}}(+)| - |F_{\text{PH}}(-)|,$$

$$\Delta\text{PH}(\text{calc}) = -\frac{2 \times |F_{\text{P}}| \times |F_{\text{H}}|}{k \times |F_{\text{PH}}|} \sin(\alpha_{\text{H}} - \alpha_{\text{P}})$$

(Section 9.3),

$$\begin{aligned} \varepsilon_{\text{ano}}(\alpha_{\text{P}}) &= |F_{\text{PH}}(+)| - |F_{\text{PH}}(-)| + \frac{2|F_{\text{P}}| \times |F_{\text{H}}|}{k \times |F_{\text{PH}}|} \sin(\alpha_{\text{H}} - \alpha_{\text{P}}) \\ &= \underline{\hspace{2cm}} \Delta \underline{\hspace{2cm}} + k \sin(\alpha_{\text{H}} - \alpha_{\text{P}}) \end{aligned}$$

with

$$\begin{aligned} \Delta &= |F_{\text{PH}}(+)| - |F_{\text{PH}}(-)| \text{ and } k = \frac{2|F_{\text{P}}| \times |F_{\text{H}}|}{k \times |F_{\text{PH}}|}, \\ \varepsilon_{\text{ano}}^2(\alpha_{\text{P}}) &= \Delta^2 + 2 \times \Delta \times k \sin(\alpha_{\text{H}} - \alpha_{\text{P}}) + k^2 \sin^2(\alpha_{\text{H}} - \alpha_{\text{P}}). \end{aligned}$$

As earlier, terms with  $\alpha_{\text{P}}$  only should be separated:

$$\begin{aligned} \sin(\alpha_{\text{H}} - \alpha_{\text{P}}) &= \sin \alpha_{\text{H}} \cos \alpha_{\text{P}} - \cos \alpha_{\text{H}} \sin \alpha_{\text{P}}. \\ \sin^2(\alpha_{\text{H}} - \alpha_{\text{P}}) &= \frac{1}{2} \{-\cos 2(\alpha_{\text{H}} - \alpha_{\text{P}})\} \\ &= \frac{1}{2} - \frac{1}{2} \cos 2\alpha_{\text{H}} \cos 2\alpha_{\text{P}} - \frac{1}{2} \sin 2\alpha_{\text{H}} \sin 2\alpha_{\text{P}}. \end{aligned}$$

$$\begin{aligned}
\varepsilon_{\text{ano}}^2(\alpha_P) &= \Delta^2 + \frac{1}{2}k^2 + (2 \times \Delta \times k \sin \alpha_H) \cos \alpha_P \\
&\quad - 2 \times \Delta \times k \cos \alpha_H \sin \alpha_P \\
&\quad - \frac{1}{2} \times k^2 \cos 2\alpha_H \cos 2\alpha_P \\
&\quad - \frac{1}{2} \times k^2 \sin 2\alpha_H \sin 2\alpha_P \\
-\frac{\varepsilon_{\text{ano}}^2(\alpha_P)}{2(E')^2} &= -\frac{\Delta^2 + \frac{1}{2}k^2}{2(E')^2} \quad (= K_{\text{ano}}) \\
&\quad - \frac{\Delta \times k \sin \alpha_H}{(E')^2} \cos \alpha_P \quad (= A_{\text{ano}} \cos \alpha_P) \\
&\quad + \frac{\Delta \times k \cos \alpha_H}{(E')^2} \sin \alpha_P \quad (= B_{\text{ano}} \sin \alpha_P) \\
&\quad + \frac{k^2 \cos 2\alpha_H}{4(E')^2} \quad (= C_{\text{ano}} \cos 2\alpha_P) \\
&\quad + \frac{k^2 \sin 2\alpha_H}{4(E')^2} \sin 2\alpha_P \quad (= D_{\text{ano}} \sin 2\alpha_P)
\end{aligned}$$

#### 14.4. Phase Information from Partial Structure Data, Solvent Flattening, and Molecular Averaging

For partial structure information as well as for solvent flattening and molecular averaging, we encountered the same form of the phase probability function:

$$P_{\text{SF}}(\alpha_P) = P_{\text{average}}(\alpha) = N \exp[X' \cos(\alpha_P - \alpha_{\text{calc}})]$$

[see Equation (8.14) of Chapter 8],

$$P_{\text{partial}}(\alpha_P) = N \exp[X \cos(\alpha_P - \alpha_{\text{partial}})];$$

see Equation (8.9) in which  $(1/2)\pi I_0(X)$  is now replaced by the normalizing constant  $N$ .

The exponential term for phase combination is simply

$$\begin{aligned}
\frac{X \cos \alpha_{\text{partial}}}{= A_{\text{partial}}} \cos \alpha_P + \frac{X \sin \alpha_{\text{partial}}}{= B_{\text{partial}}} \sin \alpha_P
\end{aligned}$$

or

$$\begin{aligned}
\frac{X' \cos \alpha_{\text{SF}}}{= A_{\text{SF}}} \cos \alpha_P + \frac{X' \sin \alpha_{\text{SF}}}{= B_{\text{SF}}} \sin \alpha_P
\end{aligned}$$

or

$$\begin{aligned}
\frac{X \cos \alpha_{\text{average}}}{= A_{\text{average}}} \cos \alpha_P + \frac{X' \sin \alpha_{\text{average}}}{= B_{\text{average}}} \sin \alpha_P
\end{aligned}$$



## 14.5. Phase Information from SAD

$$P_{Sim, ano} = N^* \times \exp \left[ \frac{2 |F_{PA}| |F_A|}{\sum_1^n f_i^2} \cos(\alpha_{PA} - \alpha_A) \right];$$

$F_{PA}$  (Figure 9.6a of Chapter 9) is comparable with vector  $\mathbf{F}$  in Figure 8.7 of Chapter 8.  $F_A$  represents the known part of the structure. The angle  $(\alpha_{PA} - \alpha_A)$  is comparable with the angle  $(\alpha_{PH} - \alpha_H)$  in Figure 7.12 of Chapter 7. It is customary to use the product of  $P_{ano}$  (Section 14.3) and  $P_{Sim, ano}$  as the final probability curve.

### Summary

The major advantage of the Hendrickson and Lattman formalism is that one need not calculate phase probability distributions anew every time some new information is added to the protein phases. The new information can easily be combined with previous information by simple addition to the coefficients  $A$ ,  $B$ ,  $C$ , and  $D$  in the general phase probability distribution  $P(\alpha) = N \exp[A \cos \alpha + B \sin \alpha + C \cos 2\alpha + D \sin 2\alpha]$ .

## Chapter 15

# Checking for Gross Errors and Estimating the Accuracy of the Structural Model

### 15.1. Introduction

After the molecular model of the protein structure has been refined, it might still contain errors that have crept into the model during the interpretation of the electron density map, particularly in the regions where the electron density is weak. Some of the errors are obvious and should cause immediate suspicion; for instance, the presence of left-handed helices can almost always be ruled out. Most of the available modeling programs allow regularization of geometry, but do not guarantee overall good quality of the final model. A very qualitative impression of the accuracy of the structural model can be obtained by inspection of the electron density map:

- The connectivity of the main chain and the side chains
- The bulging out of the carbonyl oxygen atoms from the main chain
- The interpretation of the side chain electron density

### 15.2. *R*-Factors

A more quantitative impression of the accuracy of the structure is obtained from the various residual indices (see Appendix 2). The common crystallographic *R*-factor is

$$R = \frac{\sum_{hkl} ||F_{\text{obs}}| - k|F_{\text{calc}}||}{\sum_{hkl} |F_{\text{obs}}|},$$

where *k* is a scale factor. For acentric model structures with the atoms randomly distributed in the unit cell, *R* = 0.59. For structures refined to high resolution

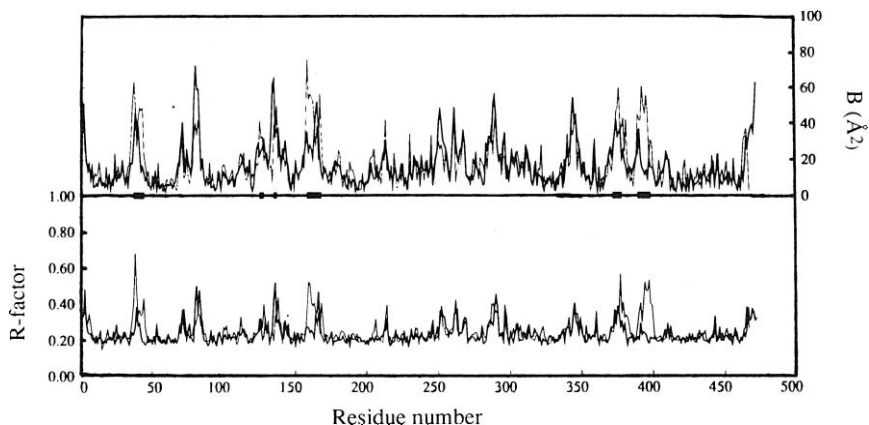


Figure 15.1. Real-space  $R$ -factor (lower panel) and average  $B$ -factor (upper panel) of the *Azotobacter vinelandii* lipoamide dehydrogenase. Misplaced loops are indicated by a thin line, and after their correction, they are indicated by a thick line. Note the correspondence between the  $R$ -factor and the  $B$ -factor at the problem sites. (Courtesy of Dr. Andrea Mattevi.)

(e.g., 1.6 Å), the  $R$ -factor should not be much higher than 0.16. This  $R$ -factor is an overall number and does not indicate major local errors. More useful in this respect is  $R_{\text{real space}}$  (Jones et al., 1991). It is obtained in the following way: The final electron density map is plotted on a grid  $G_1$  and a calculated map is plotted on an identical grid  $G_2$ . This calculated map is obtained by a Gaussian distribution of electron density around the average position for each atom in the model, with the same temperature factor for all atoms. The two density sets are scaled together. Now the electron densities of separate residues, or groups of atoms in a residue, are selected on both grids and built on a grid  $G_3(\text{obs})$  and a grid  $G_3(\text{calc})$ , respectively. For nonzero elements in the two  $G_3$  grids,  $R$  is calculated as

$$R_{\text{real space}} = \frac{\sum |\rho_{\text{obs}} - \rho_{\text{calc}}|}{\sum |\rho_{\text{obs}} + \rho_{\text{calc}}|}.$$

It is plotted as a function of the residues along the polypeptide chain (Figure 15.1). The fitting of the main chain alone can be obtained by incorporating just the N, C( $\alpha$ ), C( $\beta$ ), C, and O atoms in the calculation. The fitting of the side chains in the density can be checked by taking only the side chain atoms.

It has been shown that the normal crystallographic  $R$ -factor can reach surprisingly low values in the refinement of protein structural models that later appear to be incorrect, for instance, because the number of model parameters is taken too high. Brünger (1992, 1993) suggested improving this situation with the introduction of a free  $R$ -factor, which is unbiased by the refinement process. In this method, one divides the reflections into a “test set ( $T$ )” of unique reflections and a “working set ( $W$ ).” The test set is a random selection of 5–10% of the observed reflections. Noncrystallographic symmetry causes a correlation between certain reflections. It must be avoided that reflections in the test set are correlated with

reflections in the working set. To assure that correlated reflections are either in the working set or in the test set, the reflections in a number of very thin shells in reciprocal space are taken as the test set (Kleywegt and Jones, 1995; Kleywegt et al., 1996; Rees, 1983). The refinement is carried out with the working set only, and the free  $R$ -factor is calculated with the test set of reflections only:

$$R_{\text{free}} = \frac{\sum_{hkl \subset T} ||F_{\text{obs}}| - k|F_{\text{calc}}||}{\sum_{hkl \subset T} |F_{\text{obs}}|},$$

where  $h k l \subset T$  means all reflections belonging to test set  $T$ . Brünger could show that a high correlation exists between the free  $R$ -factor and the accuracy of the atomic model phases. Separating the working set and the test set is called “cross-validation” (Brünger, 1997b). The underlying principle is that if a structure is really improved in a refinement step, both  $R_{\text{working set}}$  and  $R_{\text{free}}$  will decrease. If, however,  $R_{\text{working set}}$  decreases as a result of fitting to noise,  $R_{\text{free}}$  will not decrease, but increase. For instance, it can happen that too many peaks in the electron density map are assigned to water molecules, whereas in fact they are noise peaks and should be removed in the refinement. Applications of  $R_{\text{free}}$  are reviewed by Kleywegt and Brünger (1996).

### 15.3. The Ramachandran Plot

The stereochemistry of the main chain folding can be investigated with a Ramachandran plot (Ramachandran et al., 1963), in which the dihedral angles  $\varphi$  and  $\Psi$  for each residue are plotted in a square matrix (Figure 15.2). It is customary to have the conformation of the fully extended chain in the corners of the square. Short contacts between atoms of adjacent residues prevent  $\varphi$  and  $\Psi$  from taking on all possible angles between  $-180^\circ$  and  $+180^\circ$ . They are clustered in regions in the Ramachandran matrix, with boundaries depending on the choice of the permitted van der Waals distances and tetrahedral angles. Usually, a conservative and a more relaxed boundary are given, as in Figure 15.2. For highly refined structures, almost all of the  $\varphi/\Psi$  values do lie within the allowed regions.

Due to the lack of a side chain, glycyl residues can adopt a larger range of  $\varphi$  and  $\Psi$  angles. The electron density for nonglycine residues lying outside the allowed region should be carefully checked.

### 15.4. Stereochemistry Check

Unusual  $\omega$  angles (Figure 15.3) and eclipsed dihedral angles in side chains should cause suspicion. Another feature to observe is whether the structure shows more than a few unsatisfied H-bonds. If it does, this would be energetically extremely

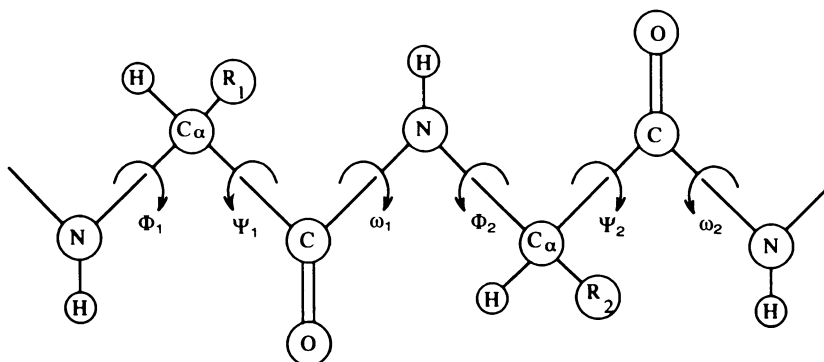


Figure 15.2. A schematic of a fully stretched polypeptide chain. The rotations around the  $C_{\alpha}$ -NH bonds are given by the angle  $\varphi$  and around the  $C_{\alpha}$ -C=O bonds by the angle  $\psi$ . The peptide planes are usually flat, with  $\omega = 180^\circ$ .

unfavorable. Attention should also be given to residues or parts of residues with conspicuously high  $B$  values as well as to unpaired charged residues in the interior of the molecule and to abnormally close van der Waals contacts. Cooperation among several laboratories resulted in a number of programs for the validation of macromolecular structures: PROCHECK (Laskowski et al., 1993a, 1993b; MacArthur et al., 1994; <http://www.biochem.ucl.ac.uk/~roman/procheck/manual/>), WHAT\_CHECK (Hooft et al., 1996; <http://www.cmbi.kun.nl/gv/whatcheck>), and PROVE (Pontius et al. 1996). The first two programs are now routinely used in the majority of all X-ray and NMR (nuclear magnetic resonance) laboratories. PROCHECK makes a very detailed analysis of all geometric aspects of proteins. Bond lengths, bond angles, planarities, and so on are compared with ideal values as determined from an analysis of peptide structures extracted from the Cambridge Crystallographic Data Centre (<http://www.ccdc.cam.ac.uk>). Torsion angles, such as  $\varphi$ ,  $\psi$ , and  $\omega$  (Figure 15.2), are compared with values observed in high-resolution protein structures in the Protein Data Bank (PDB; <http://rutgers.rcsb.org/pdb/>).

WHAT\_CHECK provides a whole battery of checks, ranging from administrative checks, as space groups,  $V_M$  (Section 3.9 of Chapter 3), and so on, via geometric checks similar to the ones in PROCHECK, to a series of normality determinations for rotamers, peptide flip likelihood, and so on. PROVE compares atomic volumes with a database of average atomic volumes determined from high-resolution PDB files.

## 15.5. The 3D-1D Profile Method

An interesting method for checking the quality of a protein molecular model has been developed by Eisenberg and co-workers (Bowie et al., 1991; Lüthy

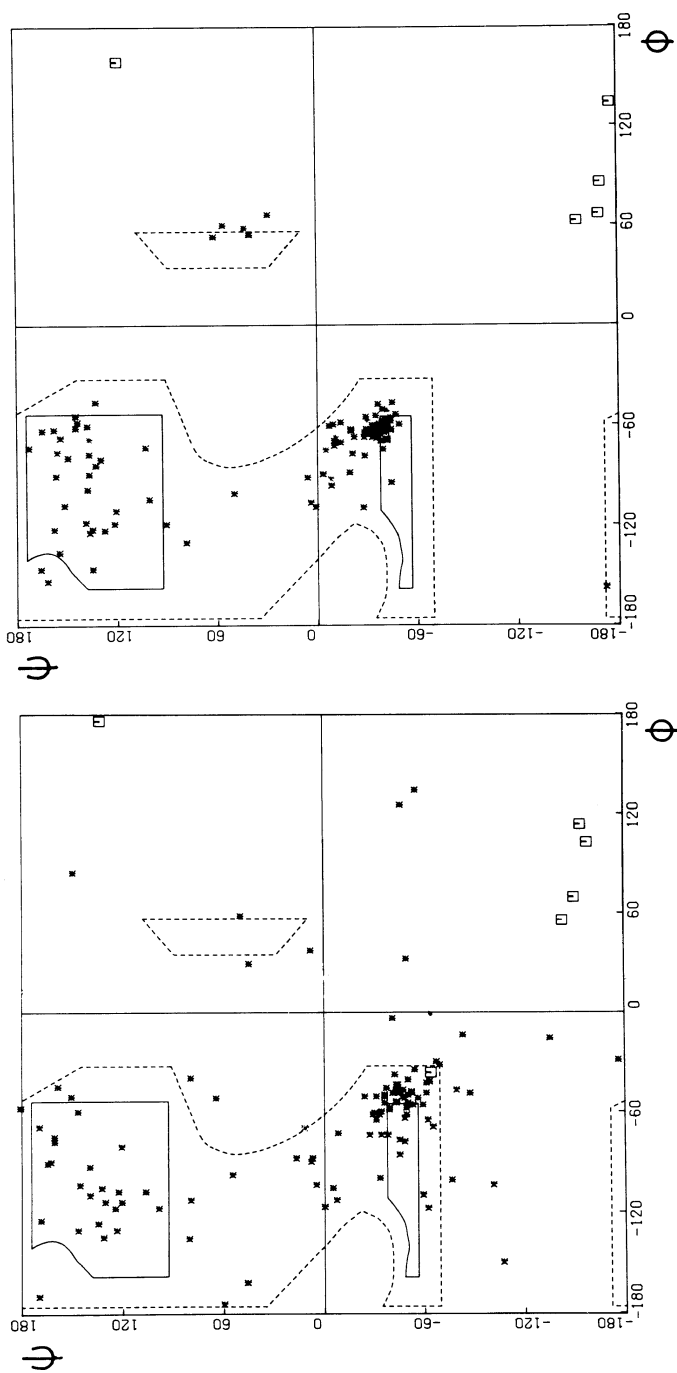


Figure 15.3. Ramachandran plot of the polypeptide chain conformation in phospholipase  $A_2$  at 1.7 Å resolution. Glycine is denoted by open squares, all other residues are denoted by asterisks. Continuous lines enclose regions in which the tetrahedral angle  $(N, C_\alpha, C) = 110^\circ$  and broken lines enclose regions with the angle  $(N, C_\alpha, C) = 115^\circ$ . The left-hand side is for the structural model before the refinement and the right-hand side is that after the refinement. The convention for the sense of the  $\phi$  and  $\psi$  angle rotation is the following: The angles are positive for a right-handed rotation: when looking along any bond from N to  $C_\alpha$  and from  $C_\alpha$  to C; the far end rotates clockwise relative to the near end, as is indicated by the arrows in Figure 15.2.

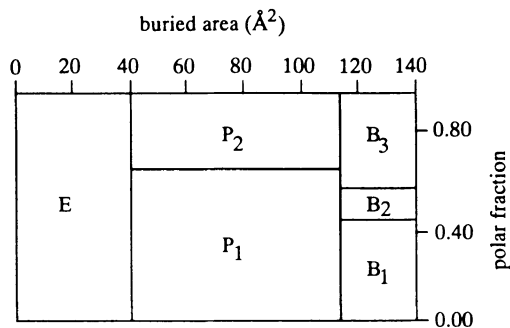


Figure 15.4. The six side chain environment categories in the Eisenberg profile method. A residue was assigned to category E (exposed) if less than  $40 \text{ \AA}^2$  of the side chain was buried. For a buried area between  $40$  and  $114 \text{ \AA}^2$ , the residue was placed in environment category  $P_1$  (polar) if the polar fraction was smaller than  $0.67$ , and in  $P_2$  if the polar fraction was  $0.67$  or larger, where the polar fraction is the fraction of the side chain area covered by polar atoms. For buried side chains, side chains with a buried area of more than  $114 \text{ \AA}^2$ , three classes were distinguished:  $B_1$  with a polar fraction smaller than  $0.45$ ,  $B_2$  with a polar fraction between  $0.45$  and  $0.58$ , and  $B_3$  with a polar fraction of  $0.58$  and larger.

et al., 1992; Wilmanns and Eisenberg, 1993). In this method, a so-called 3D (three-dimensional) profile is compared with the amino acid sequence of the protein. The 3D profile is obtained in the following way. Each residue in the chain is assigned to one of six classes of side chain environment. These classes are determined by two parameters (see Figure 15.4): (1) the area of the residue that is buried and (2) the fraction of side chain area that is covered by polar atoms (O and N). In addition to the six classes of the side chain environment, three classes of local secondary structure are distinguished:  $\alpha$ -helix,  $\beta$ -sheet, and others. Together, there are  $6 \times 3 = 18$  classes. On the basis of a number of well-refined 3D structures, a standard matrix has been constructed giving the 3D–1D (one-dimensional) score for every type of amino acid residue in each of the 18 classes. For each residue in the polypeptide chain, the 3D–1D score is read from the matrix. The overall 3D score  $S$  for the compatibility of the model with the sequence is the sum of the 3D–1D scores for all residues in the chain (Figure 15.5). A high score is found for a correct structure; a low one is found for an incorrect structure. A low score means that the residue is in a class where it is not frequently found. Because  $S$  depends on the length of the polypeptide chain, it should be compared for proteins with the same length. In addition to the overall 3D–1D score  $S$ , a profile score for each position in the polypeptide chain can be determined to locate improperly built segments in the 3D model. This score is calculated as the average of the 3D–1D scores for 21 residues in a window with the particular residue in the center of that window (Figure 15.6).

The weakness of the method is that the division into discrete classes means that because of sharp boundaries, the residue preferences can change dramatically with even extremely small changes in buried area ( $b$ ) or in polarity ( $p$ ) of the residue.

residue number	residue type	class	3D–1D score
.....	.....	.....	.....
46	T	E $\alpha$	-0.17
47	D	E	0.22
48	Y	P1	-1.31
49	L	B1	1.10
.....	.....	.....	.....

+ —————  
S = total score

Figure 15.5. Four residues of an arbitrary polypeptide chain. In column 3, the class to which each residue belongs is given, and in column 4, the 3D–1D score that is derived from the standard matrix is given. The total score  $S$  is obtained as the sum over all residues of the 3D–1D scores.

Therefore, a continuous representation of the residue preferences as a function of the buried area and the polar fraction was introduced (Kam and Eisenberg, 1994).

$P(i; j, b, p)$  is the conditional probability that a residue  $i$  in a secondary structure state  $j$  occurs in one of the six environment classes determined by  $b$  and  $p$ . They define an information value  $S_{i,j}^o(b, p)$  as

$$S_{i,j}^o(b, p) = \ln \left[ \frac{P(i; j, b, p)}{P(i)} \right];$$

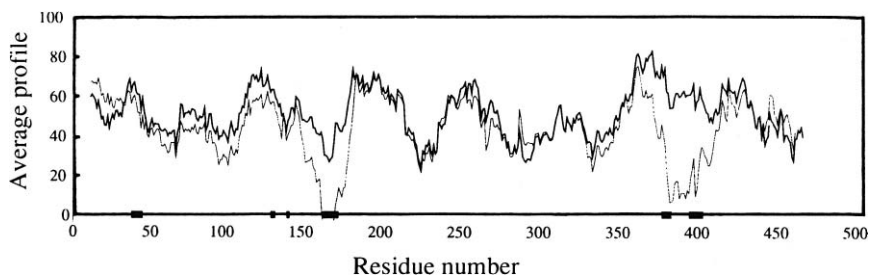


Figure 15.6. Plot of the average 3D–1D score of the first subunit in *Azotobacter vinelandii* lipoamide dehydrogenase before (thin line) and after (thick line) corrections to the model versus residue number (profile score). Because a 21 residue sliding window was used, the scores for the first and last 10 residues have no meaning and were omitted. A score below 0.20 indicates a bad part of the model. Note the improvement in the model after application of the corrections. (Source: Dr. Andrea Mattevi.)



$P(i)$  is the a priori probability of the occurrence of residue  $i$ .  $P(i)$  is known for each type of amino acid and  $P(i; j, b, p)$  can be read from the standard matrix. Therefore,  $S_{i,j}^o(b, p)$  is a function of the discrete values of  $b$  and  $p$ . This function is smoothed to a two-dimensional function  $S_{i,j}(b, p)$  that best represents the observed values  $S_{i,j}^o(b, p)$ . A 3D profile can be constructed from the continuous representation of residue preferences instead of the original discrete representation.

The advantage of the profile method is that it is completely independent of any assumption introduced into the model construction, because it depends exclusively on the compatibility of the model with its own amino acid sequence.

## 15.6. Quantitative Estimation of the Coordinate Error in the Final Model

The indicators so far mentioned do not give a value for the error in the atomic coordinates of the molecular model. An estimation of the average value of this error,  $|\overline{\Delta r}|$ , can be obtained by methods proposed by Luzzati (1952) and Read (1986, 1990b). Luzzati has derived a relationship between the average error  $|\overline{\Delta r}|$  in the atomic coordinates and the difference between  $|F_{\text{obs}}|$  and  $|F_{\text{calc}}|$ , as expressed in the crystallographic reliability factor  $R$ . The  $R$ -factor is plotted as a function of  $(\sin \theta)/\lambda$  and this curve is compared with a family of calculated lines, which are functions of  $|\overline{\Delta r}| \times (\sin \theta)/\lambda$ . The members of the family are calculated for different values of  $|\overline{\Delta r}|$  and from the line that is closest to the experimental curve,  $|\overline{\Delta r}|$  for the crystal structure is derived. The assumption is that the difference between  $|F_{\text{obs}}|$  and  $|F_{\text{calc}}|$  is due exclusively to errors in the positional coordinates of the atoms. The mathematics of the Luzzati method is rather complicated and we will not go into any detail. For an example, see Figure 15.7. Because the crystallographic  $R$ -factor is a less reliable indicator for the accuracy of the model than  $R_{\text{free}}$  of the test set, it has been suggested that  $R_{\text{free}}$  values be used instead of  $R$ -values in

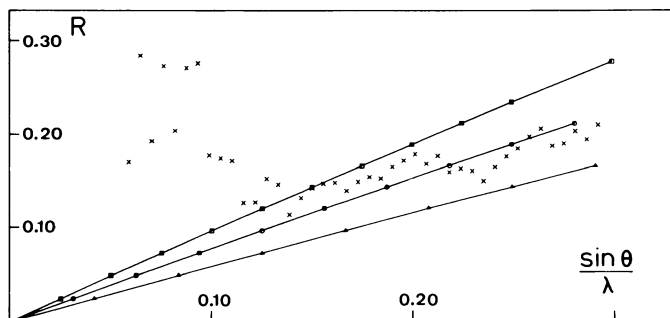


Figure 15.7. Plot of the crystallographic  $R$ -factor as a function of  $(\sin \theta)/\lambda$  (crosses). Superimposed are calculated Luzzati lines for a coordinate error  $|\overline{\Delta r}|$  of 0.08 Å (triangles), 0.12 Å (circles), and 0.16 Å (squares). [Reproduced with permission from Dijkstra et al. (1981).]

a Luzzati plot (Brünger, 1997b; Kleywegt et al., 1994; In the method proposed by Read (1986), which is based on previous work by Luzzati and others—for instance Srinivasan and Ramachandran (1965)—the root mean square value of the coordinate error  $\sqrt{(\Delta |r|)^2}$  is obtained in a graphic way; the difference is that now a single plot is sufficient, the  $\sigma_A$  plot, based on Equation (15.1):

$$\ln \sigma_A = \frac{1}{2} \ln \left( \frac{\sum_P}{\sum_N} \right) - \frac{8}{3} \pi^2 \overline{(\Delta |r|)^2} \left( \frac{\sin \theta}{\lambda} \right)^2. \quad (15.1)$$

$\sigma_A$  is defined as

$$\sigma_A = D \left( \frac{\sum_P}{\sum_N} \right)^{1/2},$$

where  $\sum_N = \sum_{j=1}^N f_j^2$ . The summation is over all  $N$  atoms in the structure for  $\sum_N$  and over all atoms in the partially known structure for  $\sum_P$ .  $\sum_P/\sum_N$  should be 1 if the structure is completely identified. However, this is never true because of rather disordered solvent atoms in the crystal. These atoms contribute appreciably to low-order reflections that should, therefore, be ignored.  $D$  is the Fourier transform of the probability distribution  $p(\Delta \mathbf{r})$  of  $\Delta \mathbf{r}$ :

$$D(\mathbf{S}) = \int p(\Delta \mathbf{r}) \exp [2\pi i(\Delta \mathbf{r}) \cdot \mathbf{S}] d\Delta \mathbf{r};$$

$D$  is, in general, complex, but a centrosymmetric distribution for  $p(\Delta \mathbf{r})$  is assumed and, therefore,  $D$  can be written as

$$D(\mathbf{S}) = \int p(\Delta \mathbf{r}) \cos [2\pi(\Delta \mathbf{r}) \cdot \mathbf{S}] d\Delta \mathbf{r}. \quad (15.2)$$

If  $\ln \sigma_A$  is plotted versus  $\{(\sin \theta)/\lambda\}^2$ , a straight line is obtained with slope  $\{-\frac{8}{3}\pi^2 \overline{(\Delta |r|)^2}\}$  and intercept of  $1/2 \ln(\sum_P/\sum_N)$  [see Equation (15.1)].  $\sigma_A$  is obtained from an independent estimate. Different methods are available. They are discussed by Read (1986). It can, for example, be done with a method suggested by Hauptman (1982). He regarded  $\sigma_A$  as the square root of the correlation coefficient between the observed and calculated normalized structure factors:

$$\sigma_A = \left[ \frac{\sum (|E(\text{obs})|^2 - \overline{|E(\text{obs})|^2})(|E(\text{calc})|^2 - \overline{|E(\text{calc})|^2})}{\left\{ \sum (|E(\text{obs})|^2 - \overline{|E(\text{obs})|^2})^2 \sum (|E(\text{calc})|^2 - \overline{|E(\text{calc})|^2})^2 \right\}^{1/2}} \right]^{1/2},$$

with  $\overline{|E(\text{obs})|^2} = \overline{|E(\text{calc})|^2} = 1$ . It was shown by Read that this estimated value of  $\sigma_A$  can be refined by finding the zero of the residual function:

$$R = \sum w(\sigma_A - m|E_N||E_P^c|),$$

where  $w$  is 1 for centric and 2 for noncentric reflections;  $m$  is the figure of merit. An alternative method is given by Srinivasan and Chandrasekaran (1966). They

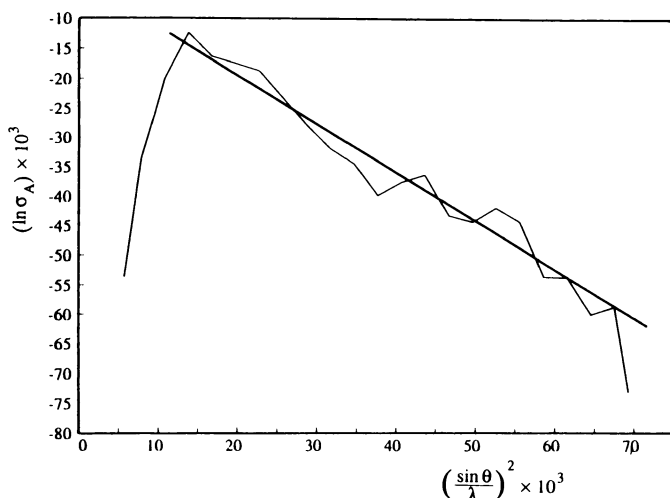


Figure 15.8.  $\sigma_A$  plot of haloalkane dehalogenase from *Xanthobacter autotrophicus*. The structure was determined to a resolution of 2.5 Å. (Courtesy of Dr. K.H.G. Verschueren.)

gave the following expression for  $\sigma_A$ :

$$\sigma_A = \frac{|E(\text{obs})||E(\text{calc})| \cos [\alpha(\text{obs}) - \alpha(\text{calc})]}{D}$$

Because  $D$ , and therefore also  $\Sigma_A$ , is a function of resolution,  $\sigma_A$  must be estimated in ranges of resolution. As the example in Figure 15.8 shows, the data points at lower resolution do not fit the line. The same is true for the points at high resolution, which is probably due to measurement errors.

For well-refined structures, the Luzzati method and the  $\sigma_A$  plot give nearly invariably estimated errors in the coordinates between 0.2 and 0.3 Å.

### The Derivation of the $\sigma_A$ Plot

We start with Equation (15.2) and must first of all find  $p(\Delta\mathbf{r})$  as a function of  $|\Delta r|$ . If the assumption is made that  $p(\Delta\mathbf{r})$  is spherically symmetric (does not depend on the direction of  $\Delta\mathbf{r}$ ) and, moreover, that  $|\Delta r|$  is distributed as a Gaussian function, then

$$p(\Delta\mathbf{r}) = N \exp \left[ -\frac{|\Delta r|^2}{2\sigma^2} \right],$$

in which  $N$  is the normalization constant and  $\sigma$  is the standard deviation.  $N$  can be obtained from

$$\int_0^\infty p(\Delta\mathbf{r}) d(\Delta\mathbf{r}) = 1,$$

$$N \int_0^\infty \exp \left[ -\frac{|\Delta r|^2}{2\sigma^2} \right] 4\pi |\Delta r|^2 d|\Delta r| = (2\pi\sigma^2)^{3/2} \times N = 1,$$

$$N = (2\pi\sigma^2)^{-3/2} \text{ and } p(\Delta\mathbf{r}) = (2\pi\sigma^2)^{-3/2} \exp\left[-\frac{|\Delta\mathbf{r}|^2}{2\sigma^2}\right], \quad (15.3)$$

$$\begin{aligned} D(\mathbf{S}) &= \int p(\Delta\mathbf{r}) \cos[2\pi(\Delta\mathbf{r}) \cdot \mathbf{S}] d\Delta\mathbf{r}, \\ &= (2\pi\sigma^2)^{-3/2} \int \exp\left[-\frac{|\Delta\mathbf{r}|^2}{2\sigma^2}\right] \cos[2\pi(\Delta\mathbf{r}) \cdot \mathbf{S}] d\Delta\mathbf{r}. \end{aligned}$$

Replace  $\Delta\mathbf{r}$  and  $\mathbf{S}$  by their orthogonal components:

$$\begin{aligned} \Delta\mathbf{r} &= \Delta x + \Delta y + \Delta z \quad \text{and} \quad \mathbf{S} = h + k + l \\ (\Delta\mathbf{r}) \cdot \mathbf{S} &= h \times \Delta x + k \times \Delta y + l \times \Delta z, \\ \cos 2\pi(\Delta\mathbf{r}) \cdot \mathbf{S} &= \cos 2\pi(h \times \Delta x + k \times \Delta y + l \times \Delta z), \\ &= \cos(2\pi h \times \Delta x) \cos(2\pi k \times \Delta y) \cos(2\pi l \times \Delta z). \end{aligned}$$

All sin terms have vanished because of the spherical symmetry of  $\Delta\mathbf{r}$ .

$$\begin{aligned} \int_{\text{all } \Delta\mathbf{r}} &= \int_{\Delta x=-\infty}^{+\infty} \int_{\Delta y=-\infty}^{+\infty} \int_{\Delta z=-\infty}^{+\infty} = 8 \times \int_{\Delta x=0}^{+\infty} \int_{\Delta y=0}^{+\infty} \int_{\Delta z=0}^{+\infty}, \\ D &= 8(2\pi\sigma^2)^{-3/2} \int_{\Delta x=0}^{\infty} \int_{\Delta y=0}^{\infty} \int_{\Delta z=0}^{\infty} \exp\left[-\frac{(\Delta x)^2 + (\Delta y)^2 + (\Delta z)^2}{2\sigma^2}\right], \\ &\quad \times \cos(2\pi h \times \Delta x) \cos(2\pi k \times \Delta y) \cos(2\pi l \times \Delta z) d(\Delta x) d(\Delta y) d(\Delta z). \end{aligned}$$

Using the fact that the definite integral

$$\int_0^{\infty} \exp[-a^2 x^2] \cos bx \, dx = \frac{\sqrt{\pi}}{2a} \exp\left[-\frac{b^2}{4a^2}\right],$$

it follows that

$$D = \exp[-2\pi^2 |S|^2 \sigma^2]. \quad (15.4)$$

Next the relation between  $\sigma^2$  and  $|\overline{\Delta r}|^2$  must be found.

$$\begin{aligned} |\overline{\Delta r}|^2 &= \int_0^{\infty} p(|\Delta r|) (|\Delta r|)^2 d|\Delta r| \\ &= (2\pi\sigma^2)^{-3/2} \times 4\pi \int_0^{\infty} (|\Delta r|)^2 \times (|\Delta r|)^2 \times \exp\left[-\frac{|\Delta r|^2}{2\sigma^2}\right] d|\Delta r| \\ &= (2\pi\sigma^2)^{-3/2} \times 4\pi \int_0^{\infty} (|\Delta r|)^4 \times \exp\left[-\frac{|\Delta r|^2}{2\sigma^2}\right] d|\Delta r|. \end{aligned}$$

Knowing that  $\int_0^{\infty} x^{2n} \exp[-ax^2] dx = \frac{1 \times 3 \times 5 \times \dots \times (2n-1)}{2^{n+1} a^n} \sqrt{\frac{\pi}{a}}$  we obtain

$$\sigma^2 = \frac{1}{3} \overline{|\Delta r|^2} \quad \text{and} \quad D = \exp \left[ -\frac{8}{3} \pi^2 \overline{|\Delta r|^2} \left( \frac{\sin \theta}{\lambda} \right)^2 \right]$$

$$\sigma_A = D \left( \frac{\sum_P}{\sum_N} \right)^{\frac{1}{2}} \quad \text{and} \quad \ln \sigma_A = \frac{1}{2} \ln \left( \frac{\sum_P}{\sum_N} \right) - \frac{8}{3} \pi^2 \overline{|\Delta r|^2} \left( \frac{\sin \theta}{\lambda} \right)^2 .$$

In a later article, Read (1990b) showed that his (and Luzzati's) assumption of a Gaussian  $\Delta \mathbf{r}$  distribution, equal for all atoms, is, in general, not allowed. As a consequence, the Luzzati plot and the  $\sigma_A$  plot can, in principle, be used only for comparative, rather than absolute, measures of the coordinate errors. However, from the comparison of independently determined structures, it seems that, somewhat surprisingly, the  $\sigma_A$  plot gives reasonable results although the actual errors might be somewhat larger. For instance, Daopin et al. (1994) compared two crystal structures of transforming growth factor (TGF- $\beta_2$ ) and found that the root mean square difference between the two structures was 0.33 Å, whereas 0.21 Å was obtained from the Luzzati plot and 0.18 Å from the  $\sigma_A$  plot.

Ohlendorf (1994) came to the conclusion that the "errors" derived from the comparison of four independently refined models of human interleukin-1 $\beta$  could be partly due to real differences in conformation.

For further information on the validation of protein structures, the reader is referred to the article by Kleywegt [Kleywegt (2000)].

---

## Summary

In the literature, a number of protein structures have been presented that later turned out to be entirely or partly wrong. Apparently, the density map was incorrectly interpreted. It is not guaranteed that interpretation errors will be removed in the refinement process and the best way to follow is to apply the methods presented in this chapter to check the accuracy of the model. If any suspicion is raised about part of the model, it should be carefully checked for alternative conformations. The Luzzati method and the  $\sigma_A$  plot give an estimate of the coordinate error. Because of underlying assumptions, which are not always true, they can, in principle, be used only for comparative, rather than absolute, measures of the coordinate errors. However, from the comparison of independently determined structures, it seems that the  $\sigma_A$  plot gives reasonable results. It is clear that a better method for the estimation of errors in a protein structure is needed, but as long as that is not available, the best that one can do is to use the  $\sigma_A$  plot.

# Chapter 16

## Practical Protein Crystallization

Jeroen R. Mesters

*Institute of Biochemistry, University of Lübeck, Germany*

### 16.1. Introduction

There are several excellent books that nicely cover the topic of macromolecular crystallization and we highly recommend consulting and studying these in depth. Therefore, with this chapter we do not provide a summary or overview of these books; rather, we take the reader on a journey from sequence to crystal.

---

#### **Books to consult (in alphabetic order)**

1. T.M. Bergfors (ed.), *Protein Crystallization: Techniques, Strategies, and Tips*, International University Line
2. A. Ducruix and R. Giegé (eds.), *Crystallization of Nucleic Acids and Proteins, a Practical Approach*, Oxford University Press
3. S. Iwata (ed.), *methods and results in crystallization of membrane proteins*, International University Line
4. A. McPherson, *Crystallization of Biological Macromolecules*, Cold Spring Harbor Laboratory Press

---

With all of the tools and kits currently available, it has become very fashionable to quickly set up several hundred crystallization experiments, even if this type of sampling of crystallization space is somewhat biased, redundant, and unsatisfactory. Disappointment spreads if no crystals grow in any of the droplets, and novices will ask how to continue. This question is not easy to answer because the crystallization of biological macromolecules is a multiparameter problem. In principle, you have to (re-)design the particular crystallization strategy from the beginning. The use of selected high-throughput methods as a first approach (i.e., one size fits all) is

definitely justifiable, but reality shows that many proteins require an individual approach.

In the ideal case, the protein of interest can be expressed in large amounts, is very soluble, can be easily purified, and possesses an ideal ball-shaped, non-floppy structure that favors packing into a crystal lattice. This is a somewhat unrealistic situation; nevertheless, the latter sentence impinges on several central themes that need to be addressed: amount, solubility, purity, flexibility, and surface properties.

## 16.2. Gene Cloning and Expression

It is highly recommended to study the amino acid residue and nucleotide sequence of the target of interest *in silico*. Ideally, a (structure-based) multiple-sequence alignment would be performed. Only the use of several structure prediction programs in combination with a variety of homologous sequences will enable you to get an initial, more correct, structural impression. One of the goals of such an investigation is to quickly reveal unstructured regions within the sequence. At this stage, you must decide whether to clone the whole gene into the expression vector, to truncate it, or to go for (single) domains. You need to take into consideration that unstructured regions within a protein can become structured upon oligomerization or the binding of ions, small ligands (cofactor, prosthetic group, substrate, or inhibitor), oligo-nucleotides (DNA or RNA molecule), or oligo-peptides (protein molecule). Actually, the *in silico* studies should help you to identify possible sequence motives and you should act accordingly.

### **Bio-informatic tools (a small selection for the novice)**

3D JURY: <http://bioinfo.pl/Meta/> (Ginalski et al., 2003)

DISOPRED2: <http://bioinf.cs.ucl.ac.uk/disopred> (Ward et al., 2004)

DomPred: <http://bioinf.cs.ucl.ac.uk/dompred> (Bryson et al., 2005)

FoldIndex: <http://bioportal.weizmann.ac.il/fldbin/findex> (Prilusky et al., 2005)

GLOBPLOT 2: <http://globplot.embl.de> (Linding et al., 2003)

Phyre: <http://www.sbg.bio.ic.ac.uk/phyre> (successor to 3D-PSSM, Kelley et al., 2000)

PSIPRED: <http://bioinf.cs.ucl.ac.uk/psipred> (Bryson et al., 2005)

SER: <http://nihserver.mbi.ucla.edu/SER> (after Derewenda, 2004)

The type of purification tag employed has a direct influence on protein purity and yield (Lichty et al., 2005). Attachment of a tag to either the N- or C-terminus of the protein might disturb the biological function and should be taken into consideration if it will not be cleaved off afterward. For example, the introduction of a so-called His<sub>6</sub> tag habitually adds more amino acids to the protein than just the six histidines alone. As a result, an unstructured terminus of up to 25 amino acids is introduced

that certainly can interfere with the packing of the macromolecules within a crystal lattice. A cleavable tag should be favored and it can add to increased sample purity if removed during a second affinity-purification chromatography step (e.g., cleavage on the column).

The best choice of vector-and-strain combination is difficult to predict and, like the purification tag, it directly influences the amount of soluble, pure protein obtained in the end. Quite a bit of thought should be spent on the design of the optimal promoter, polymerase- and ribosome-binding site. The sequence around the different binding sites directly influences the processivity of the polymerase and the efficiency of translation initiation by ribosomes (Baneyx, 1999); for example, the Shine-Dalgarno sequence or AUG start codon of your construct can be involved in base-pairing, thus preventing translation initiation. In practice, little attention is given to (further) optimization once a few milligrams of protein per liter of culture medium are obtained. Yet, the right combination of vector and strain, culture medium (including ligand or inhibitor), and culture temperature should and can be optimized in a relative short time—an investment that will pay off in the long run. The more soluble target protein present in the cell lysate, the easier it is to obtain a pure protein preparation and, as a result, the better the chances are in crystallizing it. In order to avoid entering a dead-end street from the beginning, diversify by testing more constructs in parallel on a small scale either *in vivo* (see, e.g., Knaust & Nordlund, 2001; Lesley, 2001; Stevens, 2000; Yokoyama, 2003) or cell-free (Betton, 2004; Sawasaki et al., 2002). Cell-free protein expression is often considered a last resort for producing sufficient amounts of the protein, although the method clearly deserves more attention by the crystallographers.

Not all proteins can be expressed in *Escherichia coli*. Reasons are, for example, problems regarding protein folding, the incorporation of certain prosthetic groups, and posttranslational modifications that are necessary for obtaining a correctly folded, functional protein: 15–20% of the proteins require chaperones, disulfide-isomerases, or prolyl-isomerases. The modifications affect the structural integrity and uniformity of the protein preparation and thereby directly influence its crystallizability. The formation of inclusion bodies might in fact be advantageous because pure protein without a purification tag can be obtained (Vallejo & Rinas, 2004). However, lipids might accumulate inside the inclusion bodies and they must be removed by binding the protein to an affinity column and washing (dialysis does not work) with Triton X-100 followed by *n*-octyl- $\beta$ -D-glucoside. For a more uniform glycosylation, expression in a specially engineered *Pichia pastoris* strain (Bobrowicz et al., 2004) or in *Leishmania tarentolae* (Kushnir et al., 2005) should be considered. In our experience, glycosylation does not *a priori* hinder crystallization.

### 16.3. Protein Purification

The use of modern molecular biology techniques and the availability of a large variety of purification tags and organisms for heterologous gene expression strongly



propelled the production and purification of proteins. Nevertheless, the disruption of the harvested cells and the purification of the target protein is not a trivial step. Not only should several different buffer compositions be tested over a wide pH range in order to maximize the retrieval of correctly folded and active protein (Collins et al., 2005; Jancarik et al., 2004; Lindwall et al., 2000), but also the method of disruption itself is not unimportant (Lopez de Heredia & Jansen, 2004). Sonifiers, French presses, and glass-bead mills are not really recommended because they introduce both heat and oxygen into the cell mash. More suitable are manual grinding (of the cell pellet with aluminum oxide, type A-5) or enzymatic disintegration methods. In addition, it is advisable to degas all solutions before use. Be aware that the commercially available kits and tags that you choose dictate specific conditions that might not be compatible with your protein; one easily tends to neglect the protein's needs, like its optimal pH range and demand for ligands. The solubility of partially hydrophobic proteins can often be improved by adding detergents like *n*-alkyl- $\beta$ -glucosides or *n*-alkyl- $\beta$ -maltoosides or something simple like glycerol. All ingredients used for preparing the different buffers should be tested carefully for their target compatibility. A 72-well Terasaki plate can be used for quickly testing potential ingredients by pipetting 0.5- $\mu$ l (protein-ingredient mixture) droplets under paraffin oil. It is often not a good sign if the protein precipitates quickly at low ingredient concentrations and, moreover, can no longer be redissolved by adding 0.5–1  $\mu$ l of buffer solution without the ingredient.

Crystallization itself can be used as a purification step. However, purification through crystallization can only work efficiently if the contaminants do not interact with the target of interest. Starting from a mixture of two proteins, it is, of course, possible to produce two different crystals in a single droplet, each containing only one of the two proteins. Reality though is that small contaminations are often detrimental to crystal growth because they poison the emerging nuclei. Purity and structural integrity/homogeneity are of utmost importance: The greatest enemy in crystallization is the protein stock solution itself. Therefore, protein preparations obtained by means of single-step purification strategies are not suitable for setting up crystallization trials. Once initial crystallization conditions have been identified, additional purification steps can be very effective in obtaining quality crystals. The actual concentration of the protein used in the screening should (initially) be as high as possible. The chances of the formation of large enough nuclei (within a certain time span) that will develop into crystals directly depend on the protein concentration used for setting up the droplets. The better way of concentrating a protein solution is by using a (nitrogen gas pressurized) stirred ultrafiltration cell. In this mode, very high protein concentrations near the ultrafiltration membrane are prevented that could otherwise lead to protein aggregation and precipitation. On the other hand, it is a good sign if a protein sample can be readily concentrated with centrifugal filter devices. Dynamic light scattering (DLS) measurements should be conducted during the concentration step, not only for determining the dispersity of the protein in solution but also for determining the maximum concentration limit above which protein aggregation will occur. Keep in mind that the protein-solubility phase diagram already applies to the solution

that you are concentrating; that is, even at low salt concentrations, the protein solution can arrive at a supersaturated state and the protein will start to precipitate. Therefore, it is not a good idea to directly concentrate the column eluent that often contains high concentrations of, for example, sodium chloride or imidazole.

The purity of the protein sample can be easily improved at the cost of recovery. It is much better not to try and pool together as many fractions as possible after each chromatography step; for example, less than 25% recovery but highly pure makes more sense than 75% recovery and not so pure. Actually, do not consider pooling column fractions together, but rather, use several fractions independently; the protein concentration in the peak fractions can already be sufficiently high in that they can be directly used for setting up trials. The purity of a protein preparation can be easily checked by sodium dodecyl sulfate polyacrylamide gel electrophoresis (SDS-PAGE) and subsequent Coomassie or silver staining. Either way, samples with both a small and a large amount of protein should be analyzed in parallel in order to correctly judge the quality of the sample. It is advisable to run an iso-electric focusing (IEF) gel of the protein in order to determine its pI and to evaluate the degree of microheterogeneity. If you suspect that the protein is partially unfolded or floppy (independently moving domains like pearls on a string), investigate the matter by conducting limited proteolytic digestion experiments using a variety of proteases (simple and cost-effective). Such experiments can help you to (1) determine the core of a protein, (2) correctly locate domain borders, and (3) reveal the influence of ligands on overall stability and fold. Floppy proteins are easily degraded and notoriously difficult to crystallize. At worst, other proteins need to be coexpressed in order to stabilize or fold parts of the target protein and the complexes must now somehow be isolated. In general, proteins should be handled with sufficient care: they are sensitive to temperature extremes, oxidation, and the presence of ligands and ions and are subject to degradation by metals and proteases. Protein (stock) solutions should not be diluted with pure water, unless the protein can stand such harsh treatment; pure water can remove essential (counter-)ions from the protein.

In addition to  $^1\text{H}$ -NMR (nuclear magnetic resonance) and circular dichroism (CD) spectroscopy, a simple DLS measurement can already reveal whether a protein is likely to be folded. People are often astounded by the outcome of a first DLS measurement of their precious sample. Indicative of a partially unfolded protein can be the apparent but unexplainable discrepancy in the molecular weight of the protein. Also, a broad peak is symptomatic of a badly behaved protein solution, as is a large distribution in apparent molecular weights (so-called polydisperse). Incubating the protein sample for some time at elevated temperatures can often cure local disorder and unfolding (e.g., arising from cold denaturation). A well-behaved monodisperse protein solution (D'Arcy, 1994) constitutes an excellent starting point but is not an absolute requirement for crystallization. Frequently, one of the oligomeric states of the protein is the true building block for the growing crystal, but it is often not possible (and not necessary) to purify a single state due to the dynamic equilibria between them. Other useful analytical methods for studying disorder/unfolding in proteins are calorimetry (Weber & Salemme, 2003), thermal shift assays (Lo et al., 2004),

deuterium-exchange mass spectroscopy (Spraggon et al., 2004), and simple two-dimensional gel electrophoresis (Csizmók et al., 2006).

## 16.4. Protein Crystallization

Growing a crystal is all about tampering with the protein's solubility. In principle, the phase diagram used in protein crystallization is the summation/interplay of many factors that influence the solubility, like pH, temperature, and precipitant and protein concentration. Modulation of temperature as an instrument in crystallization is not widely used as a technique. This might be due to the fact that proteins behave differently to changes in temperature: some become more soluble at elevated temperature, whereas others behave in the opposite way and, finally, some do not react at all. The pH of the solution has a much clearer and more profound effect on protein solubility. In fact, a gradual alteration of the pH (but also temperature) is a powerful technique for growing crystals.

A small inquiry in the author's laboratory showed an interesting tendency. If crystals grew at a pH near the pI of the protein, polyethylene glycol (PEG) was used more often, whereas salts were used more successfully at a pH value away from the pI of the protein. These observations underscore the importance of the physico-chemical mechanisms underlying the crystallization process (i.e., the pH-dependent choice of precipitating agent, known as the Hofmeister series; see Boström et al., 2005; Ries-Kautt & Ducruix, 1997). Conducting an initial screening at three different pH values—one chosen above the pI, one below the pI, and one at about the pI—seems worthwhile. It is therefore recommended to confirm the calculated pI value of your protein by IEF techniques. Needless to say, an analysis of the amino acid composition of the protein is very informative too. Depending on the pI of the protein, it is not always feasible to sample (extreme) pH values both above and below the pI.

Before starting any crystallization experiment, recall that all of the solution components are additives and that each single additive will either promote or hinder the crystallization process. As such, the choice of additives, be they buffers, salts, or small organic molecules, should be very carefully considered and investigated. Apparently innocent additives like chloride ions are easily introduced by a pH adjustment of the buffer or through column chromatography, despite the fact that low concentrations of chloride can sometimes be detrimental to crystal growth. The final concentration of any additive in the protein stock solution should be kept as low as possible, and screening with freshly prepared protein is highly recommended and circumvents the need for additional additives like glycerol or ethylene glycol as a cryogenic agent. At any pH value, proteins bear charges at their surface and, as a result, counterions must be supplied in order to neutralize the charges on the protein surface, thereby preventing protein aggregation. Thus, even at pH values near the pI (when screening with PEGs), small amounts of counterions are often needed in order to keep the protein in solution ("salting-in" effect). Removal of ions from the protein solution can lead to denaturation,

aggregation, or sometimes even crystallization (!), a technique not often used in daily practice (inverse “salting-in”).

The experimentation does not stop after the cover slide is placed over the reservoir, so to speak. Should precipitation occur within a few hours, water should be added to the reservoir(s) immediately. Why? First, Ostwald ripening is not often observed (crystal growth from precipitate). Second, clearly the system has surpassed the supersaturated zone of the phase diagram where nucleation and crystal growth normally occur. Third, the effective concentration of the protein in solution will now be very low, a nonfavorable situation for nucleation. Finally, you will be able to discriminate between a good (which will redissolve again) and a bad protein precipitate. A stereomicroscope, with sufficient magnification (140–180 $\times$ ), proper light source (bright- and dark-field transmitted light illumination), and plenty of space in between the lens and the large working platform, is a prerequisite for identifying potential crystalline material. If a protein possesses a propensity to crystallize, it can often be crystallized using several different conditions. Consequently, if a protein likes to crystallize, a more limited initial screening (48–96 conditions: see also Page and Stevens, 2004) should suffice whereas employing a much more elaborate screening for proteins that do not like to crystallize will often be fruitless. Should no crystalline material appear within a period of 2–3 weeks, as a last resort, add a small droplet of diluted ammonia to your crystallization drop (the pH shift might trigger crystal growth). Better yet, construct a simple phase diagram with, for example, ammonium sulfate or PEG, select a condition at which the protein solution is nearly supersaturated, and then screen (microbatch technique using Al’s oil) for additives like metal ions and small organic molecules [e.g., dioxane, 2-ethyl-2,4 pentanediol, phenol, glycerol, heptanetriol, magnesium, nickel, calcium, mercury, zinc, cadmium, organometallic compounds (to name a few) and cocktails thereof: see also McPherson & Cudney, 2006]. Divalent metal ions and certain alcohols are known to mediate intermolecular contacts, the basic nature of a crystal! Should the protein again refuse to produce crystalline material within a few weeks, more profound changes need to be introduced into the protein sample: (1) isolate the protein in a clearly modified way (introduce different buffer components and columns), (2) use a different construct (change or remove purification tag, truncate termini or loops, mutate large charged residues in loops), or (3) use a different protein source (homologous protein).

Initial crystal hits might be further improved by switching from the prevalent vapor-diffusion techniques to the less common, but very effective, microbatch (Chayen, 2005) or counterdiffusion methodologies (Garcia-Ruiz, 2003), which do not only tend to produce high-quality crystals, but both techniques are also valuable for proteins sensitive to oxidation.

## Summary

The protein itself poses the greatest hurdle in obtaining a crystal. A clever crystallization strategy would therefore start with a broad bio-informatics analysis,

followed by two simple, yet very effective, analytical methods for studying partially unfolded regions in proteins, which are limited proteolysis and two-dimensional gel electrophoresis. The availability of as much *in silico* and *in vitro/in vivo* information as possible is decisive and must not be underestimated. Similarly, invest more time in the cloning, overexpression, and purification of the protein. The investment will pay off in that a better, more intelligently prepared protein sample can be obtained for an initial screening. Needless to say, a DLS measurement is irreplaceable. Start crystallizing by using PEGs at about the pI and several salts two to four pH units away from the pI, implementing the Hofmeister series; the construction of simple phase diagrams is highly recommended and very informative. Swiftly proceed by testing (cocktails of) additives and have the nerve to change your construct quickly.

Taken together, although macromolecular crystallization has matured and rightly plays a key role in the structure based drug design process (Hogg & Hilgenfeld, 2006), it is only partly understood. There are many anecdotes about what to try and what not. The bottom line is that many tips and tricks only work for a few reported cases. However, (1) construct design (bio-informatics, limited proteolytic digestion, surface entropy reduction), (2) purity and concentration (solubility screening, ligand identification, less recovery but purer), and (3) structural homogeneity (well-behaved DLS spectrum) are vital requisites for a more successful crystallization strategy.

# Appendix 1

## A Compilation of Equations for Calculating Electron Density Maps

### Straightforward Electron Density Map

$$\begin{aligned}\rho(x\ y\ z) &= \frac{1}{V} \sum_{hkl} |F(hkl)| \exp[-2\pi i(hx + ky + lz) + i\alpha(hkl)] \\ &= \frac{1}{V} \sum_{hkl} |F(hkl)| \cos[2\pi(hx + ky + lz) - \alpha(hkl)].\end{aligned}$$

The  $|F(hkl)|$ 's are the structure factor amplitudes of the reflections  $(hkl)$ .

### Difference Electron Density Map

$$\begin{aligned}\Delta\rho(x\ y\ z) &= \frac{1}{V} \sum_{hkl} \Delta|F(hkl)|_{\text{iso}} \exp[-2\pi i(hx + ky + lz) + i\alpha_{\text{p}}(hkl)] \\ &= \frac{1}{V} \sum_{hkl} \Delta|F(hkl)|_{\text{iso}} \cos[2\pi(hx + ky + lz) - \alpha_{\text{p}}(hkl)].\end{aligned}$$

$\Delta|F(hkl)|_{\text{iso}}$  is the difference between the structure factor amplitudes for the protein and an isomorphous derivative of that protein. The phase angles  $\alpha_{\text{p}}(hkl)$  are those of the native protein. The map shows the electron density, which is extra (or which is missing) in the derivative at half the actual height.

### A $2F_{\text{obs}} - F_{\text{calc}}$ Map

$$\rho(x\ y\ z) = \frac{1}{V} \sum_{hkl} (2|F_{\text{obs}}| - |F_{\text{calc}}|) \exp[-2\pi i(hx + ky + lz) + i\alpha_{\text{calc}}].$$

This map can be regarded as the sum of the electron density of a model and of a difference electron density map at double height. It shows, in addition to the electron density of the model, the difference between the actual structure and the model at normal height. The phase angles are those calculated for the model.

## A Residual, or Double-Difference, Electron Density Map

$$\Delta\rho(x\ y\ z) = \frac{1}{V} \sum_{hkl} \{ |F_{\text{obs}}| - |\mathbf{F}_{\text{native}} + \mathbf{F}_{\text{attached}}| \} \\ \times \exp[-2\pi i(hx + ky + lz) + i\alpha_{\text{calc}}].$$

$|F_{\text{obs}}|$  is the structure factor amplitude for the derivative.  $\mathbf{F}_{\text{attached}}$  is the structure factor contribution by those attached atoms or groups of atoms for which the parameters are already known. The phase angles  $\alpha_{\text{calc}}$  are for the native protein and the attached heavy atoms. This is a useful Fourier summation for the detection of extra attached atoms or groups of atoms.

## An OMIT Map

$$\Delta\rho(x\ y\ z) = \frac{1}{V} \sum_{hkl} (|F_{\text{obs}}| - |F_{\text{calc}}|) \exp[-2\pi i(hx + ky + lz) + i\alpha_{\text{calc}}].$$

$|F_{\text{calc}}|$  is the structure factor amplitude of a partial model (i.e., a model from which a fragment has been deleted). The phase angles  $\alpha_{\text{calc}}$  are for the model with fragment deleted. It is a difference Fourier summation that is often used if part of the electron density map cannot be interpreted satisfactorily. This part is then deleted in the model and does not contribute to the phase angle calculation. The map should show the density corresponding to the fragment, at half the height. Alternatively, one can calculate

$$\rho(x\ y\ z) = \frac{1}{V} \sum_{hkl} |F_{\text{obs}}| \exp[-2\pi i(hx + ky + lz) + i\alpha_{\text{calc}}]$$

This map should show the entire model with the deleted fragment at half-height. Or a map with coefficients  $2|F_{\text{obs}}| - |F_{\text{calc}}|$ , which also shows the entire model but the deleted fragment at full height.

## A Simulated Annealing OMIT Map

This is an OMIT map with simulated annealing applied to the “known” part of the structure. It is also called the composite annealed OMIT map.

## An OMIT Map with Sim Weighting

$$\Delta\rho(x\ y\ z) = \frac{1}{V} \sum_{hkl} m(|F_{\text{obs}}| - |F_{\text{calc}}|) \exp[-2\pi i(hx + ky + lz) + i\alpha_{\text{calc}}],$$

where  $m = I_1(X)/I_0(X)$  for noncentric reflections and  $m = \tanh(X/2)$  for centric reflections, where

$$X = \frac{2|F_{\text{obs}}| \times |F_K|}{\sum_1^n f_i^2};$$

$I_0$  and  $I_1$  are modified Bessel functions of order 0 and 1, respectively,  $|F_{\text{obs}}|$  is the observed structure factor amplitude, and  $|F_K|$  is the amplitude for the known part of the structure. The  $f_i$ 's are the atomic scattering factors for the  $n$  missing atoms. It is assumed that the partial structure is error-free. In practice, this will not be true and then  $X$  must be taken as

$$X = \frac{2\sigma_A |E_{\text{obs}}| \times |E_K|}{1 - \sigma_A^2},$$

where  $|E|$  is the normalized structure factor amplitude and  $\sigma_A$  is defined in Section 15.6 of Chapter 15.

## A Weighted Electron Density Map Calculated with Phase Angles $\alpha_{\text{calc}}$ from the Partial Structure

$$\rho(x\ y\ z) = \frac{1}{V} \sum_{hkl} (2m|F_{\text{obs}}| - |F_{\text{calc}}|) \exp[-2\pi i(hx + ky + lz) + i\alpha_{\text{calc}}]$$

for noncentric reflections and

$$\rho(x\ y\ z) = \frac{1}{V} \sum_{hkl} m|F_{\text{obs}}| \exp[-2\pi i(hx + ky + lz) + i\alpha_{\text{calc}}]$$

for centric reflections. This map is an improvement over the  $2F_{\text{obs}} - F_{\text{calc}}$  map because it applies Sim weighting to the observed structure factor amplitudes (see above). Possible missing parts in the structure will show up more clearly in the electron density map than without Sim weighting. Sim assumed the partial structure to be error-free, but, in practice, this is never true. The effect of these errors is taken care of by defining  $X$  differently:

$$X = \frac{2\sigma_A |E_{\text{obs}}| \times |E_K|}{1 - \sigma_A^2}$$

and by weighting down  $|F_{\text{calc}}|$ :

$$\rho(x\ y\ z) = \frac{1}{V} \sum_{hkl} (2m|F_{\text{obs}}| - D|F_{\text{calc}}|) \exp[-2\pi i(hx + ky + lz) + i\alpha_{\text{calc}}],$$

with  $D = \sigma_A(\Sigma_P/\Sigma_N)^{-1/2}$  (Section 15.6 of Chapter 15).  $|E|$  is the normalized structure factor amplitude.



## Appendix 2

# A Compilation of Reliability Indexes

Common Crystallographic  $R$ -Factor for Indicating the Correctness of a Model Structure

$$R = \frac{\sum_{hkl} ||F_{\text{obs}}| - k|F_{\text{calc}}||}{\sum_{hkl} |F_{\text{obs}}|}.$$

The Free  $R$ -Factor

$$R_{\text{free}} = \frac{\sum_{hkl \subset T} ||F_{\text{obs}}| - k|F_{\text{calc}}||}{\sum_{hkl \subset T} |F_{\text{obs}}|},$$

where  $hkl \subset T$  means all reflections belonging to test set  $T$  of unique reflections. The refinement is carried out with the remaining reflections: the working set  $W$ . The advantage of using this  $R$ -factor over the regular crystallographic  $R$ -factor is that it is unbiased by the refinement process.

$R$ -Factor for Comparing the Intensity of Symmetry-Related Reflections

$$R_{\text{sym}}(I) = \frac{\sum_{hkl} \sum_i |I_i(hkl) - \overline{I(hkl)}|}{\sum_{hkl} \sum_i I_i(hkl)}$$

for  $n$  independent reflections and  $i$  observations of a given reflection.  $\overline{I(h\ k\ l)}$  is the average intensity of the  $i$  observations.

## R-Factor for Comparing the Structure Factor Amplitude for Symmetry-Related Reflections

$$R_{\text{sym}}(F) = \frac{\sum_{hkl} \sum_i ||F_i(h\ k\ l)| - |\overline{F(h\ k\ l)}||}{\sum_{hkl} \sum_i |F_i(h\ k\ l)|}$$

for  $i$  observations each of  $n$  independent reflections.  $|\overline{F(h\ k\ l)}|$  is the average value for the structure factor amplitude of the  $i$  observations of a given reflection.

## Precision Indicating Merging R-Factor for Determining the Precision of an Average Measurement

$$R_{p.i.m.} = \frac{\sum_{hkl} \frac{1}{(N-1)^{1/2}} \sum_i |I_i(h\ k\ l) - \overline{I(h\ k\ l)}|}{\sum_{hkl} \sum_i I(h\ k\ l)},$$

where  $N$  is the redundancy of the data and  $\overline{I(h\ k\ l)}$  the average intensity. This R-factor has the advantage over  $R_{\text{sym}}$ , which it is redundancy independent

## R-Factor for the Comparison of $N$ Datasets After Merging

On  $|F_{hkl}|$ :

$$R_{\text{merge}} = \frac{\sum_{hkl} \sum_{j=1}^N ||F_{hkl}| - |F_{hkl}(j)||}{\sum_{hkl} \sum_{j=1}^N |F_{hkl}(j)|},$$

where  $|F_{hkl}|$  is the final value of the structure factor amplitude.

On  $I_{hkl}$ :

$$R_{\text{merge}} = \frac{\sum_{hkl} \sum_{j=1}^N |I_{hkl} - I_{hkl}(j)|}{\sum_{hkl} \sum_{j=1}^N I_{hkl}(j)}.$$

## Real-Space $R$ -Factor

$$R_{\text{real space}} = \frac{\sum |\rho_{\text{obs}} - \rho_{\text{calc}}|}{\sum |\rho_{\text{obs}} + \rho_{\text{calc}}|}.$$

The function is calculated per residue for either all atoms, or the main chain atoms only, or the side chain atoms. The summation is over all grid points for which  $\rho_{\text{calc}}$  has a nonzero value for a particular residue. The function shows how good the fit is between the model and the electron density map.

## $R_{\text{Cullis}}$ for Centric Data

$$R_{\text{Cullis}}(\text{centric}) = \frac{\sum_{hkl} ||F_{\text{PH}} \pm F_{\text{P}}| - F_{\text{H}}(\text{calc})|}{\sum_{hkl} |F_{\text{PH}} \pm F_{\text{P}}|}$$

for centric reflections only.  $F_{\text{P}}$ ,  $F_{\text{PH}}$ , and  $F_{\text{H}}$  include their sign (+ or -):  $F_{\text{PH}} + F_{\text{P}}$  if the signs of  $F_{\text{PH}}$  and  $F_{\text{P}}$  are opposite and  $F_{\text{PH}} - F_{\text{P}}$  if they are equal.

## $R_{\text{Cullis}}$ for Noncentric Data

$$R_{\text{Cullis}}(\text{noncentric}) = \frac{\sum_{hkl} \int_{\alpha_{\text{P}}=0}^{2\pi} |F_{\text{PH}}(\text{obs})| - |\mathbf{F}_{\text{P}} + \mathbf{F}_{\text{H}}(\text{calc})| d\alpha_{\text{P}}}{\sum_{hkl} |F_{\text{PH}} - F_{\text{P}}|},$$

where the integration is over  $\alpha_{\text{P}}$ , the phase angle of the protein.

$R_{\text{Cullis}}(\text{ano})$

$$R_{\text{Cullis}}(\text{ano}) = \frac{\sum_{hkl} \left| |\Delta F_{\text{PH}}^{\pm}(\text{obs})| - |\Delta F_{\text{PH}}^{\pm}(\text{calc})| \right|}{\sum_{hkl} \Delta F_{\text{PH}}^{\pm}(\text{obs})},$$

where  $\Delta F_{\text{PH}}^{\pm}(\text{obs})$  is the structure factor amplitude difference between Bijvoet pairs and  $\Delta F_{\text{PH}}^{\pm}(\text{calc}) = 2(f''/\Delta f)|F_{\text{H}}| \sin(\alpha_{\text{PH}} - \alpha_{\text{H}})$ .

$R_{\text{Kraut}}$

$$R_{\text{Kraut}} = \frac{\sum_{hkl} \int_{\alpha_{\text{P}}=0}^{2\pi} \left| |F_{\text{PH}}| - |\mathbf{F}_{\text{P}} + \mathbf{F}_{\text{H}}(\text{calc})| \right|}{\sum_{hkl} |F_{\text{PH}}|},$$

where  $\alpha_{\text{P}}$  is the phase angle of the protein. This  $R$ -factor is used in isomorphous replacement methods to check the heavy atom refinement.

Derivative  $R$ -Factor

$$R_{\text{deriv}} = R_{\text{iso}} = \frac{\sum_{hkl} |I_{\text{deriv}}(h\ k\ l) - I_{\text{native}}(h\ k\ l)|}{\sum_{hkl} I_{\text{native}}(h\ k\ l)}.$$

This  $R$ -factor is used for checking the quality of an isomorphous derivative.

Anomalous  $R$ -factor  $R_{\text{ano}}$

$$R_{\text{ano}} = \frac{\sum_{hkl} (|I_{hkl} - \overline{I_{hkl}}|)}{\overline{I_{hkl}}},$$

where  $\overline{I_{hkl}}$  is the average value of  $I_{+h\ +k\ +l}$  and  $I_{-h\ -k\ -l}$ .

## Standard Linear Correlation Coefficient Between Observed and Calculated Structure Factor Amplitudes

$$C = \frac{\sum_h (|F_h(\text{obs})| - \overline{|F_h(\text{obs})|}) \times (|F_h(\text{calc})| - \overline{|F_h(\text{calc})|})}{\left[ \sum_h (|F_h(\text{obs})| - \overline{|F_h(\text{obs})|})^2 \times \sum_h (|F_h(\text{calc})| - \overline{|F_h(\text{calc})|})^2 \right]^{1/2}}$$

The same but in a different form:

$$C = \frac{\overline{|F_h(\text{obs})|} \times \overline{|F_h(\text{calc})|} - \overline{|F_h(\text{obs})|} \times \overline{|F_h(\text{calc})|}}{\left[ \{ \overline{|F_h(\text{obs})|^2} - (\overline{|F_h(\text{obs})|})^2 \} \times \{ \overline{|F_h(\text{calc})|^2} - (\overline{|F_h(\text{calc})|})^2 \} \right]^{1/2}}$$

## Standard Linear Correlation Coefficient Between Two Electron Density Maps, $\rho_1(xyz)$ and $\rho_2(xyz)$

$$C = \frac{\Sigma(\rho_1(xyz) - \overline{\rho_1(xyz)}) \times (\rho_2(xyz) - \overline{\rho_2(xyz)})}{\left[ \Sigma(\rho_1(xyz) - \overline{\rho_1(xyz)})^2 \times \Sigma(\rho_2(xyz) - \overline{\rho_2(xyz)})^2 \right]^{1/2}}$$

The same but in a different form:

$$C = \frac{\overline{\rho_1(xyz)} \times \overline{\rho_2(xyz)} - \overline{\rho_1(xyz)} \times \overline{\rho_2(xyz)}}{\left[ \{ \overline{(\rho_1(xyz))^2} - (\overline{\rho_1(xyz)})^2 \} \times \{ \overline{(\rho_2(xyz))^2} - (\overline{\rho_2(xyz)})^2 \} \right]^{1/2}}$$

## The Phasing Power of Heavy Atoms in an Isomorphous derivative

Isomorphous phasing power:

$$\left[ \frac{\sum_{hkl} |F_H(\text{calc})|^2}{\sum_{hkl} |E|^2} \right]^{1/2},$$

with

$$\sum_{hkl} |E|^2 = \sum_{hkl} \{ |F_{PH}(\text{obs})| - |F_{PH}(\text{calc})| \}^2.$$

An alternative expression is

$$\frac{\sum_{hkl} |F_H(\text{calc})|}{\sum_{hkl} |E|}.$$

## The Phasing Power of Anomally Scattering Atoms

Anomalous phasing power:

$$\left[ \frac{\sum_{hkl} |F_H(\text{imag.})|^2}{\sum_{hkl} ||\Delta F_{PH}^\pm(\text{obs})| - |\Delta F_{PH}^\pm(\text{calc})||^2} \right]^{1/2}$$

or, alternatively,

$$\frac{\sum_{hkl} |F_H(\text{imag.})|}{\sum_{hkl} ||\Delta F_{PH}^\pm(\text{obs})| - |\Delta F_{PH}^\pm(\text{calc})||},$$

where  $\Delta F^\pm$  is the structure factor amplitude difference between Bijvoet pairs and  $F_H(\text{imag.})$  is the imaginary component of the calculated structure factor contribution by the anomalously scattering atoms.

## Figure of Merit

The figure of merit for a given reflection ( $h k l$ ) is defined as

$$m = \frac{|F(h k l)_{\text{best}}|}{|F(h k l)|},$$

where

$$\mathbf{F}(h k l)_{\text{best}} = \frac{\sum_{\alpha} P(\alpha) \mathbf{F}_{hkl}(\alpha)}{\sum_{\alpha} P(\alpha)}.$$

It can be shown that the figure of merit is the weighted mean of the cosine of the deviation of the phase angle from  $\alpha_{\text{best}}$ :  $m = \overline{\cos\{\alpha - \alpha(\text{best})\}}$ . It is also equal to  $I_1(X)/I_0(X)$  for acentric reflections and to  $\tanh(X/2)$  for centric reflections. For the definition of  $X$ , see Section 8.2 of Chapter 8.

## Appendix 3

# The Variation in the Intensity of X-ray Radiation

When the anode of an X-ray tube is bombarded by electrons, their deceleration causes the emission of photons. One electron impact gives rise to a photon with a certain amount of energy. There is no relation between the photons, either in time or in energy. Therefore, the number of emitted photons with the same energy, if measured during a time  $t$ , is not a fixed number (Figure A3.1). If that number is measured  $n$  times (where  $n$  is very large) with an average value of  $N_0$ , the probability of measuring  $N$  photons is

$$P(N) = \frac{1}{N!} N_0^N \exp[-N_0] \text{ (Poisson distribution)}. \quad (\text{A3.1})$$

For sufficiently large  $N_0$  ( $N_0 \geq 9$ ), this distribution can be replaced by the Gauss distribution:

$$P(N) = \frac{1}{\sqrt{2\pi N_0}} \exp\left[-\frac{(N - N_0)^2}{2N_0}\right]. \quad (\text{A3.2})$$

The general form of the Gauss distribution is

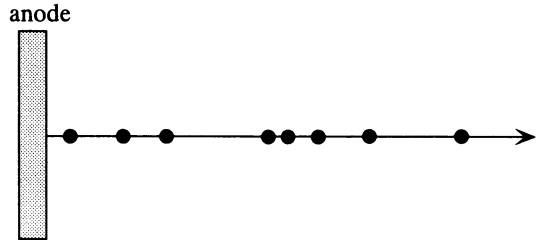
$$f(x) = \frac{1}{\sigma\sqrt{2\pi}} \exp\left[-\frac{(x - \bar{x})^2}{2\sigma^2}\right]. \quad (\text{A3.3})$$

The spread of the curve is usually expressed in the variance of  $x$ , which is defined as

$$\sigma^2 = \int_{x=-\infty}^{+\infty} (x - \bar{x})^2 f(x) dx \quad (\text{A3.4})$$

By comparing Equations (A3.2) and (A3.3), the standard deviation  $\sigma$  for the X-ray photon emission is found to be  $\sqrt{N_0}$ .

Figure A3.1. Photons with the same energy leaving the anode as a function of time.



In practice, the number of photons is usually measured only once and the value of  $N$  found in that single measurement is taken as the best value with a standard deviation  $\sigma = \sqrt{N}$ . This is also true for synchrotron radiation, because we do not have perfect control over the physical state of the charged particles.



# References

- Abrahams, J.P. *Acta Crystallogr.* (1997) **D53**, 371–376.
- Agarwal, R.C. *Acta Crystallogr.* (1978) **A34**, 791–809.
- Amemiya, Y. *Methods Enzymol.* (1997) **276**, 233–243.
- Antson, A.A., Otridge, J., Brzozowski, A.M., Dodson, E.J., Dodson, G.G., Wilson, K.S., Smith, T.M., Yang, M., Kurecki, T., and Gollnick, P. *Nature* (1995) **374**, 693–700.
- Azaroff, L. *Acta Crystallogr.* (1955) **8**, 701–704.
- Badger, J. *Methods Enzymol.* (1997) **277**, 344–352.
- Baneyx, F. *Curr. Opin. Biotechnol.* (1999) **10**, 411–421.
- Basavappa, R., Petri, E.T., and Tolbert, B.S. *J. Appl. Cryst.* (2003). **36**, 1297–1298.
- Bentley, G.A. and Houdusse, A. *Acta Crystallogr.* (1992) **A48**, 312–322.
- Bergfors, T.M., ed. *Protein Crystallization: Techniques, Strategies, and Tips*. International University Line, La Jolla, 1999.
- Betton, J.M. *Biochimie* (2004) **86**, 601–605.
- Bhat, T.N. *J. Appl. Cryst.* (1988) **21**, 279–281.
- Bhat, T.N. and Cohen, G.H. *J. Appl. Cryst.* (1984) **17**, 244–248. Blessing, R.H., Guo, D.Y., and Langs, D.A. *Acta Crystallogr.* (1996) **D52**, 257–266.
- Blow, D.M. and Crick, F.H.C. *Acta Crystallogr.* (1959) **12**, 794–802.
- Blow, D.M. and Matthews, B.W. *Acta Crystallogr.* (1973) **A29**, 56–62.
- Bobrowicz, P., Davidson, R.C., Li, H., Potgieter, T.I., Nett, J.H., Hamilton, S.R., Stadheim, T.A., Miele, R.G., Bobrowicz, B., Mitchell, T., Rausch, S., Renfer, E., and Wildt, S. *Glycobiology* (2004) **14**, 757–766.
- Boggon, T.J. and Shapiro, L. *Structure* (2000) **8**, R143–R149.
- Boström, M., Tavares, F.W., Finet, S., Skouri-Panet, F., Tardieu, A., and Ninham, B.W. *Biophys. Chem.* (2005) **117**, 217–224.
- Bowie, J.U., Lüthy, R., and Eisenberg, D. *Science* (1991) **253**, 164–170.
- Bricogne, G. *Acta Crystallogr.* (1974) **A30**, 395–405.
- Bricogne, G. *Acta Crystallogr.* (1976) **A32**, 832–847.
- Bricogne, G. *Acta Crystallogr.* (1988) **A44**, 517–545.

- Bricogne, G. in *Isomorphous Replacement and Anomalous Scattering*, Proceedings of the Daresbury Study Weekend, Wolf, W., Evans, P.R., and Leslie, A.G.W., eds. SERC Daresbury Laboratory, Warrington, UK, 1991, pp. 60–68.
- Bricogne, G. *Acta Crystallogr.* (1993) **D49**, 37–60.
- Bricogne, G. *Methods Enzymol.* (1997) **276**, 361–423.
- Brodersen, D.E., de La Fortelle, E., Vornrhein, C., Bricogne, G., Nyborg, J., and Kjeldgaard, M. *Acta Crystallogr.* (2000) **D56**, 431–441.
- Brünger, A.T. *Acta Crystallogr.* (1990) **A46**, 46–57.
- Brünger, A.T. *Acta Crystallogr.* (1991a) **A47**, 195–204.
- Brünger, A.T. *Annu. Rev. Phys. Chem.* (1991b) **42**, 197–223.
- Brünger, A.T. *Nature (London)* (1992) **355**, 472–475.
- Brünger, A.T. *Acta Crystallogr.* (1993) **D49**, 24–36.
- Brünger, A.T. *Methods Enzymol.* (1997a) **276**, 558–580.
- Brünger, A.T. *Methods Enzymol.* (1997b) **277**, 366–396.
- Brünger, A.T., Adams, P.D., Clore, G.M., DeLano, W.L., Gros, P., Grosse-Kunstleve, R.W., Jiang, J.-S., Kuszewski, J., Nilges, M., Pannu, N.S., Read, R.J., Rice, L.M., Simonson, T., and Warren, G.L. *Acta Crystallogr.* (1998) **D54**, 905–921.
- Brünger, A.T., and Nilges M., *Quarterly Review of Biophysics* (1993) **26**, 49–125.
- Brünger, A.T., Kuriyan, J., and Karplus, M. *Science* (1987) **235**, 458–460.
- Bryson, K., McGuffin, L.J., Marsden, R.L., Ward, J.J., Sodhi, J.S., and Jones, D.T. *Nucleic Acids Res.* (2005) **33**, W36–W38.
- Brzozowski, A., Derewenda, Z.S., Dodson, E.J., Dodson, G.G., and Turkenburg, J.P. *Acta Crystallogr.* (1992) **B48**, 307–319.
- Burla, M.C., Caliandro, R., Carrozzini, B., Cascarano, G.L., De Caro, L., Giacovazzo, C., and Polidori, G. *J. Appl. Cryst.* (2004) **37**, 258–264.
- Burmeister, W.P. *Acta Crystallogr.* (2000) **D56**, 328–341.
- Castellano, E.E., Oliva, G., and Navaza, J. *J. Appl. Cryst.* (1992) **25**, 281–284.
- CCP4 (Collaborative Computational Project, Number 4). *Acta Crystallogr.* (1994) **D50**, 760–763. Available from <http://www.dl.ac.uk/ccp/ccp4/main.html>.
- Chayen, N.E. *Structure* (1997) **5**, 1269–1274.
- Chayen, N.E. *Acta Crystallogr.* (1998) **D54**, 8–15.
- Chayen, N.E. *Prog. Biophys. Mol. Biol.* (2005) **88**, 329–337.
- Chayen, N.E., Shaw Stewart, P.D., Maeder, D.L., and Blow, D.M. *J. Appl. Crystallogr.* (1990) **23**, 297–302.
- Chayen, N.E., Show Stewart, P.D., and Blow, D.M. *J. Crystal Growth* (1992) **122**, 176–180.
- Collins, B., Stevens, R.C., and Page, R. *Acta Crystallogr.* (2005) **F61**, 1035–103.
- Cowtan, K.D. and Main, P. *Acta Crystallogr.* (1996) **D52**, 43–48.
- Crick, F.H.C. and Magdoff, B.S. *Acta Crystallogr.* (1956) **9**, 901–908.
- Crowther, R.A. *Acta Crystallogr.* (1969) **B25**, 2571–2580.
- Crowther, R.A. in *The Molecular Replacement Method*, Rossmann, M.G., ed. Gordon & Breach, New York, 1972, pp. 173–178.
- Crowther, R.A. and Blow, D.M. *Acta Crystallogr.* (1967) **23**, 544–548.
- Cruickshank, D.W.J. in *Computing Methods in Crystallography*, Rollett, J.S., ed. Pergamon Press, Oxford, 1965, p. 113.
- Cruickshank, D.W.J., Helliwell, J.R., and Johnson, L.N.: *Time resolved macromolecular crystallography*. Oxford Science Publications (Oxford University Press), Oxford, 1992. Cruickshank, D.W.J., Helliwell, J.R., and Moffat, K. *Acta Crystallogr.* (1987) **A43**, 656–647.

- Csizmók, V., Szollosi, E., Friedrich, P., and Tompa, P. *Mol. Cell. Proteomics* (2006) **5**, 265–273.
- Cyglér, M. and Desrochers, M. *Acta Crystallogr.* (1989) **A45**, 563–572.
- Cymborowski, M., Otwinowski, Z., Chruszcz, M., and Minor, W. *Acta Crystallogr.* (2006) **D62**, 859–866.
- Daopin, S., Davies, D.R., Schlunegger, M.P., and Grütter, M.G. *Acta Crystallogr.* (1994) **D50**, 85–92.
- D'Arcy, A. *Acta Crystallogr.* (1994) **D50**, 469–471.
- Dauter, Z. *Acta Crystallogr.* (1999) **D55**, 1703–1717.
- Dauter, Z. *Acta Crystallogr.* (2002) **D58**, 1958–1967.
- Dauter, Z., Dauter, M. and Dodson, E.J. *Acta Crystallogr.* (2002) **D58**, 494–506.
- Dauter, Z., Dauter, M. and Rajashankar, K.R., *Acta Crystallogr.* (2000) **D56**, 232–237.
- Debaeremaeker, T. and Woolfson, M.M. *Acta Crystallogr.* (1983) **A39**, 193–196.
- de La Fortelle, E. and Bricogne, G. *Trans. of the ACA Meeting, Likelihood, Bayesian Inference and their Application to the Solution of New Structures*, Bricogne, G. and Carter, C., eds., 1994. American Crystallographic Association, Buffalo.
- de La Fortelle, E. and Bricogne, G. *Methods Enzymol.* (1997) **276**, 472–494.
- Derewenda, U., Swenson, L., Green, R., Wei, Y., Morosoli, R., Sharek, F., Kluepfel, D., and Derewenda, Z.S. *J. Biol. Chem.* (1994) **269**, 20,811–20,814.
- Derewenda, Z.S. *Structure* (2004) **12**, 529–535.
- DeTitta, G.T., Weeks, C.M., Thuman, P., Miller, R., and Hauptman, H.A. *Acta Crystallogr.* (1994) **A50**, 203–210.
- Diamond, R. *Acta Crystallogr.* (1971) **27A**, 436–452.
- Dickerson, R.E., Weinzierl, J.E., and Palmer, R.A. *Acta Crystallogr.* (1968) **B24**, 997–1003.
- Diederichs, K., McSweeney, S., and Ravelli, R.B.G. *Acta Crystallogr.* (2003) **D59**, 903–909.
- Diederichs, K. *Acta Crystallogr.* (2006) **D62**, 96–101.
- Dijkstra, B.W., Kalk, K.H., Hol, W.G.J., and Drenth, J. *J. Mol. Biol.* (1981) **147**, 97–123.
- Driessen, H.P.C., Bax, B., Slingsby, C., Lindley, P.F., Mahadevan, D., Moss, D.S., and Tickle, I.J. *Acta Crystallogr.* (1991) **B47**, 987–997.
- Ducruix, A. and Giegé, R., eds. *Crystallization of Nucleic Acids and Proteins, a Practical Approach*. IRL Press, Oxford, 1999.
- Eagles, P.A.M., Johnson, L.N., Joynson, M.A., McMurray, C.H., and Gutfreund, H. *J. Mol. Biol.* (1969) **45**, 533–544.
- Ealick, S.E. *Structure* (1997) **5**, 469–472.
- Engh, R.A. and Huber, R. *Acta Crystallogr.* (1991) **A47**, 392–400.
- Epp, O., Steigemann, W., Formanek, H., and Huber, R. *Eur. J. Biochem.* (1971) **20**, 432–437.
- Evans, G. and Bricogne G. *Acta Crystallogr.* (2003) **D59**, 1923–1929.
- Ferré-d'Amaré, A.R. and Burley, S.K. *Structure* (1994) **2**, 357–359.
- Fisher, R.A. *The Messenger of Mathematics* (1912) **41**, 155–160.
- Foadi, J., Woolfson, M.M., Dodson, E.J., Wilson, K.S., Jia-xing, Y., and Chao-de, Z. *Acta Crystallogr.* (2000) **D56**, 1137–1147.
- Freund, A.K. *Structure* (1996) **4**, 121–125.
- Fujinaga, M. and Read, R.J. *J. Appl. Crystallogr.* (1987) **20**, 517–521.
- García, A.E., Krumhansl, J.A., and Frauenfelder, H. *Proteins: Structure, Function and Genetics* (1997) **29**, 153–160.
- García-Ruiz, J.M. *Methods Enzymol.* (2003) **368**, 130–154.
- García-Ruiz, J.M. and Moreno, A. *Acta Crystallogr.* (1994) **D50**, 484–490.
- Garman, E. *Acta Crystallogr.* (1999) **D55**, 1641–1653.

- Garman, E. *Curr. Opin. Struct. Biol.* (2003) **13**, 545–551.
- Garman, E. and Murray, J.W. *Acta Crystallogr.* (2003) **D59**, 1903–1913.
- Garman, E.F. and Owen, R.L. *Acta Crystallogr.* (2006) **D62**, 32–47.
- Garman, E.F. and Schneider, T.R. *J. Appl. Cryst.* (1997) **30**, 211–237.
- George, A. and Wilson, W.W. *Acta Crystallogr.* (1994) **D50**, 361–365.
- Gewirth, D.T. (2003) *HKL-2000 Manual*. p. 68. Published by HKL Research. Available from HKL Research, Charlottesville, VA, US or online at [www.hkl-xray.com](http://www.hkl-xray.com).
- Ghosh, M., Meerts, I.A.T.M., Cook, A., Bergman, A., Brouwer, A., and Johnson, L.N. *Acta Crystallographica* (2000) **D56**, 1085–1095.
- Giacovazzo, C., Ladisa, M., and Siliqi, D. *Acta Crystallogr.* (2003) **A59**, 262–265.
- Ginalski, K., Elofsson, A., Fischer, D., and Rychlewski, L. *Bioinformatics* (2003) **19**, 1015–1018.
- Girard, É., Stelter, M., Vicat, J., and Kahn, R. *Acta Crystallogr.* (2003) **D59**, 1914–1922.
- Glykos, N.M. and Kokkinidis, M. *Acta Crystallogr.* (2001) **D57**, 1462–1473.
- Gonzalez, A., Denny, R., and Nave, C. *Acta Crystallogr.* (1994) **D50**, 276–282.
- Gosh, D., Erman, M., Sawicki, M., Lala, P., Weeks, D.R., Li, N., Pangborn, W., Thiel, D.J., Jörnvall, H., Gutierrez, R., and Eyzaguirre, J. *Acta Crystallogr.* (1999) **D55**, 779–784.
- Gouaux, E. *Structure* (1998) **6**, 5–10.
- Graaff, R.A.G., Hilge, M., Plas van der J.L., and Abrahams, J.P. (2001) *Acta Crystallogr.* **D57**, 1857–1862.
- Gros, P., van Gunsteren, W.F., and Hol, W.G.J. *Science* (1990) **249**, 1149–1153.
- Gruener, S.M. *Curr. Opin. Struct. Biol.* (1994) **4**, 765–769.
- Guss, J.M., Merritt, E.A., Phizackerley, R.P., Hedman, B., Murata, M., Hodgson, K.O., and Freeman, H.C. *Science* (1988) **241**, 806–811.
- Hahn, T., ed. *International Tables for Crystallography, Vol. A*. 5th ed. Kluwer, Dordrecht, 2002.
- Hajdu, J. and Johnson, L.N. *Biochemistry* (1990) **29**, 1669–1678.
- Harada, Y., Lifchitz, A., Berthou, J., and Jolles, P. *Acta Crystallogr.* (1981) **A37**, 398–406.
- Harker, D. *Acta Crystallogr.* (1956) **9**, 1–9.
- Harp, J.M., Timm, D.E., and Bunick, G.J. *Acta Crystallogr.* (1998) **D54**, 622–628.
- Hauptman, H.A. *Acta Crystallogr.* (1982) **A38**, 289–294.
- Hauptman, H.A. *Methods Enzymol.* (1997a) **277**, 3–13.
- Hauptman, H.A. *Current Opin. Struct. Biology* (1997b) **7**, 672–680.
- Heitler, W.G. *The Quantum Theory of Radiation*, 3rd ed. Oxford University Press, London, 1966.
- Helliwell, J.R. *Macromolecular Crystallography with Synchrotron Radiation*. Cambridge University Press, Cambridge, 1992.
- Helliwell, J.R., Ealick, S., Doing, P., Irving, T., and Szebenyi, M. *Acta Crystallogr.* (1993) **D49**, 120–128.
- Hendrickson, W.A. *Methods Enzymol.* (1985) **115**, 252–270.
- Hendrickson, W.A. *Trends Biochem. Sci.* (2000) **25**, 637–643.
- Hendrickson, W.A. and Lattman, E.E. *Acta Crystallogr.* (1970) **B26**, 136–143.
- Hendrickson, W.A. and Teeter, M.M., *Nature* (1981) **290**, 107–113.
- Hendrickson, W.A. and Ward, K.B. *Acta Crystallogr.* (1976) **A32**, 778–780.
- Hendrickson, W.A., Horton, J.R., and LeMaster, D.M. *EMBO J.* (1990) **5**, 1665–1672.
- Hendrickson, W.A., Love, W.E., and Murray, G.C. *J. Mol. Biol.* (1968) **33**, 829–842.
- Hendrickson, W.A., Smith J.L., Phizackerley, R.P., and Merritt, E.A. *Proteins* (1988) **4**, 77–88.

- Hodel, A., Kim, S.-H., and Brünger, A.T. *Acta Crystallogr.* (1992) **A48**, 851–858.
- Hogg, T. and Hilgenfeld, R. *Comprehens. Med. Chem. II* (2006) Chapter 3.38, in press.
- Hönl, H. *Ann. Phys. 5. Folge* (1933) **18**, 625–655.
- Hooft, R.W.W., Vriend, G., Sander, C., and Abola, E.E. *Nature* (1996) **381**, 272.
- Hoppe, W.Z. *Elektrochemie* (1957) **61**, 1076–1083.
- Huber, R. in *Molecular Replacement. Proceedings of the Daresbury Study Weekend, 15–16 February*, Machin, P.A., ed. SERC Daresbury Laboratory, Warrington, UK, 1985, pp. 59–61.
- Huber, R. and Schneider, M.J. *Appl. Cryst.* (1985) **18**, 165–169.
- International Tables for Crystallography*, published for the International Union of Crystallography by Kluwer Academic Publishers, Dordrecht, 1995.
- Jack, A. and Levitt, M. *Acta Crystallogr.* (1978) **A34**, 931–935.
- Jacobson, R.H., Zhang, X.-J., DuBose, R.F., and Matthews, B.W. *Nature* (1994) **369**, 761–766.
- James, R.W. *The Optical Principles of the Diffraction of X-Rays*. Bell, London, 1965, Chapter 4.
- Jancarik, J. and Kim, S.-H. *J. Appl. Cryst.* (1991) **24**, 409–411.
- Jancarik, J., Pufan, R., Hong, C., Kim, S.H., and Kim, R. *Acta Crystallogr.* (2004) **D60**, 1670–1673.
- Jones, T.A., Zou, J.-Y., and Cowan, S.W. *Acta Crystallogr.* (1991) **A47**, 110–119.
- Kahn, R., Fourme, R., Gadet, A., Janin, J., Dumas, C., and André, D. *J. Appl. Cryst.* (1982) **15**, 330–337.
- Kalinin, Y., Kmetko, J., Bartnik, A., Steward, A., Gillilan, R., Lobkovsky, E., and Thorne, R.J. *J. Appl. Cryst.* (2005) **38**, 333–339.
- Kalinin, Y. and Thorne, R.J. *Acta Crystallogr.* (2005) **D61**, 1528–1532.
- Kam, Y.J.Z. and Eisenberg, D. *Protein Sci.* (1994) **3**, 687–695.
- Karle, J. and Hauptman, H. *Acta Crystallogr* (1956) **9**, 635–651.
- Kauzmann, W. *Quantum Chemistry*. Academic Press, New York, 1957.
- Kelley, L.A., MacCallum, R.M., and Sternberg, M.J. *J. Mol. Biol.* (2000) **299**, 499–520.
- Kitago, Y., Watanabe, N., and Tanaka, I. *Acta Crystallogr.* (2005). **D61**, 1013–1021.
- Klein, O. and Nishina, Y. *Z. Phys.* (1929) **52**, 853–868.
- Kleywegt, G.J. *Acta Crystallogr.* (2002) **D56**, 249–265.
- Kleywegt, G.J. and Brünger, A.T. *Structure* (1996) **4**, 897–904.
- Kleywegt, G.J. and Jones, T.A. *Structure* (1995) **3**, 535–540.
- Kleywegt, G.J. and Read, R.J. *Structure* (1997) **5**, 1557–1569.
- Kleywegt, G.J., Bergfors, T., Senn, H., Le Motte, P., Gsell, B., Shudo, K., and Jones, T.A. *Structure* (1994) **2**, 1241–1258.
- Kleywegt, G.J., Hoier, H., and Jones, T.A. *Acta Crystallogr.* (1996) **D52**, 858–863.
- Knaust, R.K., and Nordlund, P. *Anal. Biochem.* (2001) **297**, 79–85.
- Krishna Murthy, H.M., Hendrickson, W.A., Orme-Johnson, W.H., Merritt, E.A., and Phizackerley, R.P. *J. Biol. Chem.* (1988) **263**, 18,430–18,436.
- Kundrot, C.E., Judge, R.A., Pusey, M.L. and Snell E.H. *Crystal Growth Des.* (2001) **1**, 87–99
- Kushnir, S., Gase, K., Breitling, R., and Alexandrov, K. *Protein Express. Purif.* (2005) **42**, 37–46.
- Lamzin, V.S. and Wilson, K.S. *Acta Crystallogr.* (1993) **D49**, 129–147.
- Lamzin, V.S. and Wilson, K.S. *Methods Enzymol.* (1997) **277**, 269–305.
- Landau, E.M. and Rosenbusch, J.P. *Proc. Natl. Acad. Sci. USA* (1996) **93**, 14,532–14,535.

- Landau, E.M., Rummel, G., Cowan-Jacob, S.W., and Rosenbusch, J.P. *J. Phys. Chem.* (1997) **101**, 1935–1937.
- Laskowski, R.A., MacArthur, M.W., Moss, D.S., and Thornton, J.M. *J. Appl. Crystallogr.* (1993a) **26**, 283–291.
- Laskowski, R.A., Moss, D.S., and Thornton, J.M. *J. Mol. Biol.* (1993b) **231**, 1049–1067.
- Leahy, D.J., Hendrickson, W.A., Aukhil, I., and Erickson, H.P. *Science* (1992) **258**, 987–991.
- Leonard, G.A., Sainz, G., de Backer, M.M.E., and Mc Sweeney, S. *Acta Crystallogr.* (2005) **D61**, 388–396.
- Leslie, A.G.W. *Acta Crystallogr.* (1987) **A43**, 134–136.
- Lesley, S.A. *Protein Express. Purif.* (2001) **22**, 159–164.
- Leung, A.K.W., Park, M.M.V., and Borhani, D.W. *J. Appl. Cryst.* (1999) **32**, 1006–1009.
- Lichty, J.J., Malecki, J.L., Agnew, H.D., Michelson-Horowitz, D.J., and Tan, S. *Protein Express. Purif.* (2005) **41**, 98–105.
- Lindblom, G. and Rilfors, L. *Biochim. Biophys. Acta* (1989) **988**, 221–256.
- Linding, R., Russell, R.B., Neduva, V., and Gibson, T.J. *Nucleic Acids Res.* (2003) **31**, 3701–3708.
- Lindley, P.F. *Acta Crystallogr.* (1999) **D55**, 1654–1662.
- Lindwall, G., Chau, M., Gardner, S.R., and Kohlstaedt, L.A. *Protein Eng.* (2000) **13**, 67–71.
- Lopez de Heredia, M. and Jansen, R.P. *BMC Biochem.* (2004) **5**, 14.
- Lo, M.C., Culabaugh, A., Jin, G., Cowling, R., Bard, J., Malamas, M., and Ellestad, G. *Anal. Biochem.* (2004) **332**, 153–159.
- Lunin, V.Y. *Acta Crystallogr.* (1988) **A44**, 144–150.
- Lunin, V.Y. and Skovoroda, T.P. *Acta Crystallogr.* (1991) **A47**, 45–52.
- Lunin, V.Y. and Vernoslova, E.A. *Acta Crystallogr.* (1991) **A47**, 238–243.
- Lunin, V.Y., Urzhumtsev, A.G., and Skovoroda, T.P. *Acta Crystallogr.* (1990) **A46**, 540–544.
- Lüthy, R., Bowie, J.U., and Eisenberg, D. *Nature (London)* (1992) **356**, 83–85.
- Luzzati, V. *Acta Crystallogr.* (1952) **5**, 802–810.
- MacArthur, M.W., Laskowski, R.A., and Thornton, J.M. *Curr. Opin. Struct. Biol.* (1994) **4**, 731–737.
- Machin, P.A. ed., *Molecular Replacement. Proceedings of the Daresbury Study Weekend, 15–16 February*. SERC Daresbury Laboratory, Warrington, UK, 1985.
- Mac Sweeney, A., D'Arcy, A. *J. Appl. Cryst.* (2003) **36**, 165–166.
- Main, P. *Acta Crystallogr.* (1967) **23**, 50–54.
- Matthews, B.W. *J. Mol. Biol.* (1968) **33**, 491–497.
- Matthews, B.W. and Czerwinski, E.W. *Acta Crystallogr.* (1975) **A31**, 480–487.
- McCoy, A.J., Grosse-Kunstleve, R.W., Storoni, L.C., and Read, R.J. *Acta Crystallogr.* (2005) **D61**, 458–464.
- McPherson, A., *Methods Biochem. Anal.* (1976) **23**, 249–345.
- McPherson, A. *Crystallization of Biological Macromolecules*. Cold Spring Harbor Laboratory Press; Cold Spring Harbor, NY, 1999.
- McPherson, A., Malkin, A.J., and Kuznetsov, Y.G. *Structure* (1995) **3**, 759–768.
- McPherson, A., and Cudney, B. *J. Struct. Biol.* (2006), in press.
- Meier, C., Mancini, D.H., Bamford, M.A., Walsh, M.A., Stuart, D.I. and Grimes, J.M. *Acta Crystallogr.* (2005) **D61**, 1238–1244.
- Michel, H. *Crystallization of Membrane Proteins*. CRC Press, London, 1990.
- Miller, R., Gallo, S.M., Khalak, H.G., and Weeks, C.M. *J. Appl. Cryst.* (1994) **27**, 613–621.
- Minor, W., Symborowski, M., Otwinouski, Z., and Chruszcz, M. *Acta Crystallographica* (2006) **D62**, 859–866.
- Mitchell, E., Kuhn, P. and Garman, E. *Structure* (1999) **7**, R111–R121.

- Moews, P.C. and Kretsinger, R.H. *J. Mol. Biol.* (1975) **91**, 201–228.
- Moffat, K. *Annu. Rev. Biophys. Biophys. Chem.* (1989) **18**, 309–332.
- Moffat, K. *Methods Enzymol.* (1997) **277**, 433–447.
- Morris, R.J., Perrakis, A. and Lamzin, V. *Methods Enzymol.* (2003) **374**, 229–244.
- Moss, D.S. *Acta Crystallogr.* (1985) **A41**, 470–475.
- Mueller-Dieckmann, C., Panjikar, S., Tucker, P.A., and M. S. Weiss M.S. *Acta Crystallogr.* (2005) **D61**, 1263–1272.
- Murshudov, G.N., Vagin, A.A., and Dodson, E.J., *Acta Crystallogr.* (1997) **D53**, 240–255.
- Nagai, K., Evans, P.R., Li, J., and Oubridge, Ch. *Proceedings of the CCP4 Study Weekend, January, Daresbury Laboratory, Warrington, UK, 1991*, pp. 141–149.
- Nagai, K., Oubridge, C., Jessen, T.-H., Li, J., and Evans, P.R. *Nature (London)* (1990) **348**, 515–520.
- Narasimha Rao, S., Jyh-Hwang J., and Hartsuck, J.A. *Acta Crystallogr.* (1980) **A36**, 878–884.
- Narten, A.H. and Levy, H.A. in *Water; a Comprehensive Treatise, Vol. I*, Frank, F., ed. Plenum Press, New York, 1972< pp. 311–332.
- Navaza, J. *Acta Crystallogr.* (1994) **A50**, 157–163.
- Navaza, J. *Acta Crystallogr.* (2001) **D57**, 1367–1372.
- Navaza, J. and Soludjian, P. *Methods Enzymol.* (1997) **276**, 581–594.
- Navaza, J. and Vernoslova, E. *Acta Crystallogr.* (1995) **A51**, 445–449.
- Nieh, Y.-P. and Zhang, K.Y.J. *Acta Crystallogr.* (1999) **D55**, 1893–1900.
- Nordman, C.E. *Trans. Am. Cryst. Assoc.* (1966) **2**, 29–38.
- Ohlendorf, D.H. *Acta Crystallogr.* (1994) **D50**, 805–812.
- Otwinowski, Z. *Proceedings of the CCP4 Study Weekend, 25–26 January*, pp. 80–86, Wolf, W., Evans, P.R., and Leslie, A.G.W., eds. 1991. CLRC Daresbury Laboratory, Warrington UK.
- Page, R., and Stevens, R.C. *Methods* (2004) **34**, 373–389.
- Pähler, A., Smith, J.L., and Hendrickson, W.A. *Acta Crystallogr.* (1990) **A46**, 537–540.
- Pai, E.F. *Curr. Opin. Struct. Biol.* (1992) **2**, 821–827.
- Pannu, N.S. and Read, R.J. *Acta Crystallogr.* (1996) **A52**, 659–668.
- Pantazatos, D., Kim, J.S., Klock, H.E., Stevens, R.C., Wilson, I.A., Lesley, S.A., and Woods, V.L. *Proc. Natl. Acad. Sci. USA* (2004) **101**, 751–756.
- Parsons, S., *Acta Crystallogr.* (2003) **D59**, 1995–2003.
- Perrakis, A., Sixma, T.K., Wilson, K.S., and Lamzin, V.S. *Acta Crystallogr.* (1997) **D53**, 448–455.
- Podjarny, A.D., Bhat, T.N., and Zwick, M. *Annu. Rev. Biophys. Chem.* (1987) **16**, 351–373.
- Polikarpov, I. and Sawyer, L. *Joint CCP4 and ESF-EACBM Newsletter on Protein Crystallography, Daresbury Laboratory*, (1995) **31**, 5–11. CLRC Daresbury Laboratory, Warrington UK.
- Polikarpov, I., Teplyakov, A., and Oliva, G. *Acta Crystallogr.* (1997) **D53**, 734–737.
- Pontius, J., Richelle, J. and Wodak, S.J. *J. Mol. Biol.* (1996) **264**(1), 121–136
- Potier, N., Lamour, V., Poterszman, A., Thierry, J.C., Moras, D., and Van Dorsseleer, A. *Acta Crystallogr.* (2000) **D56**, 1583–1590.
- Ramachandran, G.N., Ramakrishnan, C., and Sasisekharan, V. *J. Mol. Biol.* (1963) **7**, 95–99.
- Ramakrishnan, V. and Biou, V. *Methods Enzymol.* (1997) **276**, 538–557.
- Read, R.J. *Acta Crystallogr.* (1986) **A42**, 140–149.
- Read, R.J. *Acta Crystallogr.* (1990) **A46**, 900–912.

- Read, R.J. *Methods Enzymol.* (1997) **277**, 110–128.
- Read, R.J. *Acta Crystallogr.* (2001) **D57**, 1373–1382.
- Read, R.J. and Schierbeek, A.J. *J. Appl. Cryst.* (1988) **21**, 490–495.
- Rees, D.C. *Acta Crystallogr.* (1983) **A39**, 916–920.
- Ren, Z. and Moffat, K. *J. Appl. Cryst.* (1995) **28**, 482–493.
- Rice, L.M. and Brünger, A.T. *Proteins* (1994) **19**, 277–290.
- Rice, L.M., Earnest, T.N., and Brünger, A.T. *Acta Crystallogr.* (2000) **D56**, 1413–1420.
- Ries-Kautt, M. and Ducruix, A. in *Crystallization of Nucleic Acids and Proteins: A Practical Approach*, Ducruix, A. and Giegé, R. eds. Oxford University Press, Oxford, 1999.
- Rosenbaum, G., Holmes, K.G., and Witz, J. *Nature (London)* (1971) **230**, 434–437.
- Rossmann, M.G. and Blow, D.M. *Acta Crystallogr.* (1961) **14**, 641–647.
- Rossmann, M.G. and Blow, D.M. *Acta Crystallogr.* (1962) **15**, 24–31.
- Rossmann, M.G. and Blow, D.M. *Acta Crystallogr.* (1963) **16**, 39–45.
- Rould, M.A., Perona, J.J., and Steitz, T.A. *Acta Crystallogr.* (1992) **A48**, 751–756.
- Sakabe, N. *J. Appl. Cryst.* (1983) **16**, 542–547.
- Sakabe, N. *Nucl. Instrum. Methods Phys. Res.* (1991) **A103**, 448–463.
- Sauer, O., Schmidt, A., and Kratky, C. *J. Appl. Cryst.* (1997) **30**, 476–486.
- Sawasaki, T., Ogasawara, T., Morishita, R., and Endo, Y. *Proc. Natl. Acad. Sci. USA* (2002) **99**, 14,652–14,657.
- Schneider, T.R. and Sheldrick, G.M. *Acta Crystallogr.* (2002) **D58**, 1772–1779.
- Schröder Leiros, H.-K., McSweeney, S.M. and Smalås, A.O. *Acta Crystallogr.* (2001) **D57**, 488–497.
- Shah, S.A., Shen, B.W., and Brünger, A.T. *Structure* (1997) **5**, 1067–1075.
- Sheldrick, G.M. and Schneider, T.R. *Methods Enzymol.* (1997) **277**, 319–343.
- Sheldrick, G.M., Hauptman, H.A., Weeks, C.M., Miller, R., and Usón, I. *International Tables for Crystallography, Vol. F*, edited by E. Arnold and M. Rossmann, Dordrecht: Kluwer Academic Publisher (2001), pp. 333–351.
- Sigler, P.B. *Biochemistry* (1970) **9**, 3609–3617.
- Sim, G.A. *Acta Crystallogr.* (1959) **12**, 813–815.
- Sim, G.A. *Acta Crystallogr.* (1960) **13**, 511–512.
- Skilling, J. in *Maximum Entropy and Bayesian Methods*, Skilling, J., ed. Kluwer Academic Publishers, Dordrecht, 1988, pp. 45–52.
- Sowadski, J.M. *Curr. Opin. Struct. Biol.* (1994) **4**, 761–764.
- Spraggon, G., Pantazatos, D., Klock, H.E., Wilson, I.A., Woods, V.L., Jr, and Lesley, S.A. *Protein Sci.* (2004) **13**, 3187–3199.
- Spurlino, J.C., Smallwood, A.M., Carlton, D.D., Banks, T.M., Vavra, K.J., Johnson, J.S., Cook, E.R., Falvo, J., Wahl, R.C., Pulvino, T.A., Wendoloski, J.J., and Smith, D.L. *Proteins* (1994) **19**, 98–109.
- Srajer, V., Teng, T.-Y., Ursby, T., Pradervand, C., Ren, Z., Adachi, S., Bourgeois, D., Wulff, M., and Moffat, K. *Science* (1996) **274**, 1726–1729.
- Srinivasan, R. *Acta Crystallogr.* (1966) **20**, 143–144.
- Srinivasan, R. and Chandrasekaran, R. *Indian J. Pure Appl. Phys.* (1966) **4**, 178–186.
- Srinivasan, R. and Ramachandran, G.N. *Acta Crystallogr.* (1965) **19**, 1008–1014.
- Stec, B., Zhou, R., and Teeter, M.M. *Acta Crystallogr.* (1995) **D51**, 663–681.
- Stevens, R.C. *Curr. Opin. Struct. Biol.* (2000) **10**, 558–563.
- Stewart, J.M. and Karle, J. *Acta Crystallogr.* (1976) **A32**, 1005–1007.
- Stoddard, B.L., Dean, A., and Bash, P.A. *Nature Struct. Biol.* (1996) **3**, 590–595.
- Storoni, L.C., McCoy, A.J. and Read, R.J. *Acta Crystallogr.* (2004) **D60**, 432–438



- Strijtveen, B. and Kellogg, R.M. *Tetrahedron* (1987) **43**(21), 5045.
- Stuart, D.I. and Jones, E.Y. *Curr. Opin. Struct. Biol.* (1993) **3**, 737–740.
- Stubbs, M.T., Nar, H., Lowe, J., Huber, R., Ladenstein, R., Spangfort, M.D., and Svensson, L.A. *Acta Crystallogr.* (1996) **D52**, 447–452.
- Sussman, J.L. *Methods Enzymol.* (1985) **115B**, 271–303.
- Sweet, R.M., Singer, P.T., and Smalås, A. *Acta Crystallogr.* (1993) **D49**, 305–307.
- Templeton, D.H. and Templeton, L.K. *Acta Crystallogr.* (1991) **A47**, 414–420.
- Ten Eyck, L.F. *Acta Crystallogr.* (1973) **A29**, 183–191.
- Teng, T.Y. *J. Appl. Cryst.* (1990) **23**, 387–391.
- Terwilliger, T.C. *Acta Crystallogr.* (2000) **D56**, 965–972.
- Terwilliger, T.C. *Acta Crystallogr.* (2002) **D58**, 2082–2086.
- Terwisscha van Scheltinga, A.C., Valegård, K., Ramaswamy, S., Hajdu, J., and Andersson, I. *Acta Crystallogr.* (2001) **D57**, 1776–1785.
- Terwisscha van Scheltinga, A.C., Valegård, K., Hajdu, J. and Andersson, I. *Acta Crystall.* (2003) **D59**, 2017–2022.
- Tickle, I.J., Laskowski, R.A., and Moss, D.S. *Acta Crystallogr.* (1998) **D54**, 243–252.
- Tollin, P. and Rossmann, M.G. *Acta Crystallogr.* (1966) **21**, 872–876.
- Tollin, P., Main, P., and Rossmann, M.G. *Acta Crystallogr.* (1966) **20**, 404–407.
- Tronrud, D.E. *Acta Crystallogr.* (1992) **A48**, 912–916.
- Tronrud, D.E. *Acta Crystallogr.* (2004) **D60**, 2156–2168.
- Tronrud, D.E., Ten Eyck, L.F., and Matthews, B.W. *Acta Crystallogr.* (1987) **A43**, 489–501.
- Tucker, A.D., Baty, D., Parker, M.W., Pattus, F., Lazdunski, C., and Tsernoglou, D. *Protein Eng.* (1989) **2**, 399–405.
- Usón, I., Schmidt, B., Bülow, R. von, Grimme, S., Figura, K. von, Dauter, M., Rajashankar, K.R., Dauter, Z., and Sheldrick, G.M. *Acta Crystallogr.* (2003) **D59**, 57–66.
- Vallejo, L.F. and Rinas, U. *Microb. Cell Fact.* (2004) **3**, 11.
- Van Asselt, E.J., Perrakis, A., Kalk, K.H., Lamzin, V.S., and Dijkstra, B.W. *Acta Crystallogr.* (1998) **D54**, 58–73.
- Vellieux, F.M.D. and Read, R.J. *Methods Enzymol.* (1997) **277**, 18–53.
- Walsh, M.A., Evans, G., Sanishvili, R., Dementieva, I., and Joachimiak, A. *Acta Crystallogr.* (1999) **D55**, 1726–1732.
- Walter, R.L., Thiel, D.J., Barna, S.L., Tate, M.W., Wall, M.E., Eikenberry, E.F., Gruner, S.M., and Ealick, S.E. *Structure* (1995) **3**, 835–844.
- Wang, B.-C. *Methods Enzymol.* (1985) **115**, 90–112.
- Ward, J.J., McGuffin, L.J., Bryson, K., Buxton, B.F., and Jones, D.T. *Bioinformatics* (2004) **20**, 2138–2139.
- Weber, P.C., and Salemme, F.R. *Curr. Opin. Struct. Biol.* (2003) **13**, 115–121.
- Weeks, C.M. and Miller, R. *J. Appl. Cryst.* (1999) **32**, 120–124.
- Weeks, C.M., DeTitta, G.T., Hauptman, H.A., Thuman, P., and Miller, R. *Acta Crystallogr.* (1994) **A50**, 210–220.
- Weilk, M., Ravelli, R.B.G., Silman, I., Sussman, J.L., Gros, P., and Kroon, J. *Protein Sci.* (2001) **10**, 1953–1961.
- Weiss, M.S., Mander, G., Hedderich, R., Diederichs, K. Ermler, U., and Warkentin, E. *Acta Crystallogr.* (2004) **D60**, 686–695.
- Weiss, M.S., Sicker, T., Djinnovt-Carugo, K., and Hilgenfeld, R. *Acta Crystallogr.* (2001) **D57**, 689–695.
- Westbrook, E.M. *Methods Enzymol.* (1985) **114**, 187–196.
- Wilmanns, M. and Eisenberg, D. *Proc. Natl. Acad. Sci. USA* (1993) **90**, 1379–1383.
- Wilson, A.J.C. *Nature* (1942) **150**, 151–152.

- Wilson, A.J.C. *Acta Crystallogr.* (1950) **3**, 397–398.
- Wilson, A.J.C. and Prince, E., eds, *International Tables for Crystallography, Vol. C*, 2nd ed. Kluwer, Dordrecht, 1999.
- Yeates, T.O. *Methods Enzymology* (1997) **276**, 344–358
- Yeates, T.O. and Fam, B.C. *Structure* (1999) **7**, R25–R29.
- Yokoyama, S. *Curr. Opin. Chem. Biol.* (2003) **7**, 39–43.
- Zhang, K.Y.J. and Main, P. *Acta Crystallogr.* (1990a) **A46**, 41–46.
- Zhang, K.Y.J. and Main, P. *Acta Crystallogr.* (1990b) **A46**, 377–381.
- Zhang, K.Y.J., Cowtan, K., and Main, P. *Methods Enzymol.* (1997) **277**, 53–64.
- Zhang, K.Y.J. and Matthews, B.W. *Acta Crystallogr.* (1994) **D50**, 675–686.

# Index

## A

- absolute configuration, determination of, 198–199
  - absorption coefficients, 101, 148, 206
  - ACORN, 133, 145
  - acupuncture method, 6
  - alcohol, 15
  - amino acid, 56
  - ammonium sulfate, 3, 5, 139
  - Amore, 226–229
  - Ångström units, 19
  - anisotropic substances, 9
  - anisotropic vibration, 83
  - annealing, 17, 145, 148–152
    - phase information from, 282–283
    - in protein phase angle determination, 194–198
  - area detectors, 35–38
  - Argand diagram, 67, 70–71, 88, 94, 103–104, 106, 114–115, 139, 149–150, 152, 160, 167
  - asymmetric units, 57–58
  - atomic scattering, 71–72
  - atomic vibration, 82–83
  - average reflection intensity, 111–114
- ## B
- Babinet's principle, 250
  - bacteriorhodopsin, 4
  - batch crystallization, 4
  - Bayesian statistics, 255
  - Bayes' theorem, 256
  - BEAST program, 224
  - bending magnets, 27
  - Bessel function, 173, 177, 235, 277
  - best Fourier, 163, 164, 170
  - Bijvoet mate, 169, 194
  - Bijvoet J.M., 91
  - Bijvoet pairs, 91, 151, 194, 197–198
  - blind region, 40
  - Boltzmann's constant, 272
  - Boltzmann's law, 273
  - borosilicate glass, 11
  - Bragg planes, 76
  - Bragg reflections, 102, 245
  - Bragg reflectors, 31
  - Bragg's law, 14, 19, 31, 61, 76–77, 80, 84, 99, 241
  - Bragg spacings, 113
  - Bremsstrahlung, *see* electromagnetic radiation
  - brilliance, 25
  - Brownian motion, 106, 112
  - Brünger techniques, 224
  - BRUTE program, 224
  - button, 6

**C**

capillary, 5, 7, 11  
carboxylic acids, 61  
CCD detectors, 35, 37–38  
CCP4 library, 189  
centered lattices, integral reflection  
    conditions for, 95–96  
centrosymmetric projections, 142  
choice of unit cell, 49  
choice of wavelength, 105  
circular dichroism (CD) spectroscopy, 301  
classical dispersion theory, 149  
cocrySTALLIZATION, 135  
common origin of derivatives, 154–157  
complex plane, 67  
compton scattering, 102  
computer-controlled diffractometer, 32  
convolution, 129, 131  
coordinate triplets, 56–57  
copper anode, 24, 30  
CORELS program, 264–265  
correction of diffracted intensity, 106  
cosine rule, 169, 176  
Crick and Magdoff's estimation, of X-ray  
    reflection intensity changes, 139–140  
cross-Patterson peaks, 155  
cross-Patterson vectors, 211  
CRUNCH, 145  
cryocooling, 15–17  
cryocrystallography, 27  
    advantages of, 17  
cryogenic temperature, 15  
cryoloop, 16  
cryonozzle, 17  
cryoprotectants, 15–16  
crystallization  
    of lysozyme, 8–9  
    of proteins, *see* protein crystallization  
crystallization nuclei, 1  
*Crystallization of Biological  
    Macromolecules*, 297  
*Crystallization of Nucleic Acids and  
    Proteins, a Practical Approach*, 297  
crystallization techniques  
    batch crystallization, 4  
    dialysis technique, 6–7  
    liquid-liquid diffusion technique, 4–5  
    vapor diffusion technique, 5–6

crystallographic symmetry, 57  
crystals, 9–11  
    asymmetric unit, 57–58  
    characterization, 61–63  
    characterization of, 61–63  
    coordinate triplets, 56–57  
    crystal systems, 58–60  
    mercury derivative, 15  
    mounting the, 18  
    point groups, 58  
    quasicrystalline protein, 56  
    radiation damage, 60–61  
    symmetry of, 49–56  
    of trimethylammonium bromide, 46  
crystal lattice, 47, 49  
crystal systems, 58–60  
Cs-sulfate, 139  
Cu radiation, 101  
Curie, 42

**D**

Daresbury Laboratory of the Science and  
    Engineering Research Council, 242  
delta function, 89–90  
3D-1D profile method, 288–292  
density maps, 305–307  
density modification procedures, 192–193  
deoxyhemoglobin, 45  
dialysis technique, 6–7  
diffraction spots, 13–14  
difference Fourier, 146–148  
direct lattice, 78  
disulfide bonds, 61  
dynamic disorder, 84

**E**

electromagnetic field strength, 65  
electromagnetic radiation, 22  
electromagnetic waves, 65  
    imaginary part of, 67  
    real part of, 67  
electron density, calculation of, 84–85,  
    87  
electron density map, 171, 179  
electronic area detectors, 42–43  
electron microscopy, 2  
ellipsoid of vibration, 83  
energy refinement (EREF), 270–272

Eppendorf tube, 7  
 error in Fourier map, 167–170  
*Escherichia coli*, 299  
 ethyleneglycol, 15  
 European Synchrotron Radiation Facility (ESRF), 26–27  
 Ewald, P.P., 19  
 Ewald sphere, 19, 38, 64, 77, 79, 99, 244  
 exponential terms, properties of, 68

**F**

fast Fourier transform method (FFT)  
 principle of, 262–264  
 Ficoll, 62  
 figure of merit, 164, 313  
 FITING program, 227  
 flash-cooled crystal, 17  
 flash freezing, 15  
 floppy proteins, 301  
 fluorescence, 206  
 fluorescence depolarization, 2  
 Fourier inversion, 87–88  
 Fourier maps, 167, 169  
 remaining error in, 167–170  
 Fourier program, 185  
 Fourier summation, 123, 146–148, 155, 157, 223, 225–226  
 Fourier transform, 88–89, 131, 181–182, 213, 293  
 algorithm, 255  
 Fourier transformation, 85–86, 180  
 freely traveling electrons, 27  
 Fresnel zones, 103, 105  
 Friedel mate, 174  
 Friedel pairs, 91, 151  
 Friedel's law, 244  
 Friedrieich, 45

**G**

Gauss error curve, 158  
 Gauss error function, 109, 111  
 Gaussian distribution function, 109, 286  
 Gaussian probability distribution, 161, 197  
 gene cloning, 298–299  
 gene expression, 298–299  
 glycerol, 15  
 goniometer, 12–13, 16

**H**

Hampton Research, 8  
 heavy atom  
 effect on x-ray intensities, 139–142  
 Patterson map of, 142  
 phasing power of, 312  
 scattering factor of, 153  
 heavy atom parameters  
 from acentric reflections, 144–148  
 from centro symmetric projection, 142–144  
 refinement of, using preliminary protein phase angles, 157–160  
 heavy atom parameters from centro symmetric projections, determination of, 142–144  
 heavy atom refinement, using preliminary protein phase angles, 157–160  
 hemoglobin, 133  
 histogram matching, 187–190

**I**

image plates, 34–35  
 disadvantages of rotation method with, 41  
 rotation instruments with, 40–42  
 integral reflection conditions, 95  
*International Tables for Crystallography*, 52  
 iso electric focusing (IEF) gel, 301  
 isomorphous replacement method, 133–139, 167, 196, 198  
 attachment of heavy atoms, 134–136  
 chemical modification of protein, 137–138  
 genetic modification of protein, 138  
 phase information from, 280–282  
 problems encountered in searching heavy atom derivative, 138–139  
 single, 170–171, 195, 199  
 site of attachment of heavy atoms, 136–137  
 steps in, 134  
 isotropic vibration, 82

**J**

Jena Bioscience, 8  
*Journal of Synchrotron Radiation*, 35

**K**

- K-absorption edges, 148, 202
- Knipping, 45
- Konnert–Hendrickson program, 265
- $K_{\alpha}$  radiation, 24

**L**

- “lack of closure” method, 159
- lasso technique, 16
- Laue conditions, 75–76
- Laue diffraction
  - accessible region of reciprocal space, 242–243
  - multiple problem, 243–244
  - spatial overlap problem, 245
  - unscrambling of multiple intensities, 244–245
  - wavelength normalization, 245–246
- least square method, 158–159, 251–255
- least squares criterion, 163
- least squares refinement, of heavy atoms, 160
- Leishmania tarentolae*, 299
- light scattering, 2
- linear correlation coefficients, 312
- lipidic cubic phases, 4
- liquid-liquid diffusion technique, 4–5, 17
- liquid nitrogen, 16
- Li-sulfate, 139
- loop technique, 12
- Lorentz factor, 98–99, 108
- Luzzati method, 292, 294
- Luzzati plot, 296
- lysozyme crystallization, 8–9

**M**

- magnetic devices, in storage rings, 27
- Mar Research instrument, 35
- Mass spectrometry, 2
- maximum entropy, 236–240
- maximum entropy principle, 238–240
- maximum likelihood, principle of, 160, 255–258
- membrane proteins, 2, 4
- mercury derivative crystals, 15
- merohedrally twinned crystal, 117
- methods and results in crystallization of membrane proteins*, 297
- 2-methyl-2,4-pentanediol, 2–3, 5, 15

- microbatch method, *see* batch crystallization
- microdialysis procedure, *see* dialysis technique
- microgravity, 1
- Miller indices, 233
- MIRAS method, 197
- MLPHARE program, 160, 258–259
- molecular averaging, 185–187
  - phase information from, 283
- Molecular Dimensions, 8
- molecular dynamics, 272–276
- molecular replacement
  - rotation functions, 211–217
  - translation function, 217–230
- monochromators, 30–31
- mosaic blocks, 61, 96–97, 99
- MPD, *see* 2-methyl-2,4-pentanediol
- multiple intensities, 244–245
- multiple isomorphous replacement (MIR), 161
- multiple problem, 243–244
- multiple wavelength anomalous diffraction (MAD), 199–202
- Mylar film, 16

**N**

- nitrogen gas, 15
- noncrystallographic symmetry (NCS), 185–187, 286
- nonisomorphism, 133–134, 159
- normal equations, 252–253
- normalization constant, 176
- normalized structure factor, 120–121

**O**

- OMIT maps, 173–179, 238, 274, 306–307
- organic solvents, 3
- oscillation angle, 41

**P**

- Panulirus interruptus*, 10
- paraffin oil, 4
- partial structure data
  - phase information from, 283
- Patterson automatic search procedure, 133
- Patterson function, 124–133, 212

- Patterson maps, 187, 198, 215, 224  
 anomalous, 151  
 of centrosymmetric projection, 143  
 of heavy atom, 142  
 peaks in, 155–157
- Patterson minimum function (PMF), 236
- Patterson summation, 142, 145, 152–154, 157
- p*-chloromercuriphenyl sulfonate (PCMS), 8
- PEG, *see* polyethylene glycol
- Perutz, Max Ferdinand, 133
- Petromyzon marinus*, 45
- phase improvement  
 density modification, 192–193  
 histogram matching, 187–190  
 non crystallographic symmetry and  
 molecular averaging, 185–187  
 OMIT map with and without Sim  
 weighting, 173–179  
 solvent flattening, 179–185
- phase information  
 from anomalous scattering, 282–283  
 from isomorphous replacement,  
 280–282  
 from molecular averaging, 283–284  
 from partial structure data, 283–284  
 from SAD, 284  
 from solvent flattening, 283–284
- photoelectric absorption, 102
- photographic film, 34
- photon energy, 22  
 critical, 27
- point groups, 58
- polarization factor, 99–101
- polyethylene glycol, 2–3, 5, 139, 302
- position-sensitive detectors, 35
- primary extinction, 102
- PROCHECK program, 288
- PROLSQ, *see* Konnert–Hendrickson  
 program
- propane gas, 16
- protein crystallization, 18, 302–303  
 detergents, use of, 4  
 practical application of, 298–303  
 principles of, 1–4  
 steps in, 2  
 techniques in, *see* crystallization  
 techniques
- Protein Crystallization: Techniques,  
 Strategies, and Tips*, 297
- protein crystallography, 105
- protein phase angles, 160–167
- protein phase angle, determination of  
 with anomalous scattering, 194–198
- protein phase angle, determination of,  
 194–198
- protein precipitation, 2
- protein purification, 299–302
- protein salt concentration, 3
- protein X-ray crystallography, 33, 38,  
 42–43, 115, 253
- pseudoprotein models, 191
- purity requirements, 1
- Pyrex glass, 18
- Q**
- quasicrystals, 56
- QUEEN of SPADES program,  
 226
- R**
- radiation absorbed dose, 43
- radiation damage, 60
- radiation protection, 42–43
- Raleigh scattering, 102
- Ramachandran Plot, 287
- random acentric structure, 248
- rayon fibers, 16
- RBE, *see* relative biological effect
- reciprocal lattice, 77–81  
 conclusions related to, 79–81  
 construction of, 77–79
- reciprocal space, 242
- refinement  
 mathematics of, 251–262  
 specific methods, 264–278
- reflections, 19
- REFMAC program, 276–278
- relative biological effect, 43
- reliability indices, 308–313
- resin, 12
- reverse osmosis, 8
- R*-factors, 285–287  
 anomalous, 311  
 for comparing intensity of symmetry  
 related reflections, 308–309  
 for comparing *N* data sets, 309

- for comparing structure factor
  - amplitude, 309
  - derivative, 311
  - free, 308
  - real-space, 310–311
- rhombohedral unit cell, 59
- robots, 18
- Roentgen, 21
- rotating anode tubes, 25
- rotation camera, 32
- rotation functions, 211–217
- rotation (oscillation) instrument, 38–43
- ROTING function, 227
- rubber ring, 6
- S**
- “salting in” effect, 3
- scalar products, 69
- scattering equation, 97
- scattering process
  - by atom, 71–72
  - by crystal, 74–75
  - by unit cell, 73
- secondary extinction, 103
- seed model, 190
- selenomethionine, 138, 199
- self-Patterson vectors, 211, 223
- serendipity, 18
- serial reflection conditions, 95
- Shake-and-Bake phase determination
  - method, 231–236
- SHARP program, 258–262
- SHELXD methods, 133, 145, 203, 231, 236–238
- SHELXL program, 269–270
- Shine-Dalgarno sequence, 299
- shock cooling, 15
- Sievert, 43
- siliconized microscope glass cover slip, 6
- Sim conception, 183, 187
- Sim’s phase probability function, 187
- simulated annealing (SA), 272–276
- single-photon counters, 33–34
- single isomorphous replacement method (SIRAS), 170–171, 195
- single wavelength anomalous diffraction (SAD), 202–206
  - phase information from, 284
- single isomorphous replacement (SIR), 133, 145
- small-bore capillary, 4
- SnB, 133, 145, *see also* Shake-and-Bake
  - phase determination method
  - soaking procedure, 135
- sodium acetate buffer solution, preparation of, 8
- sodium chloride solution preparation of, 8–9
- sodium dodecyl sulfate polyacrylamide gel electrophoresis (SDS-PAGE), 301
- soldering iron, 12
- solvent flattening, 179–185
  - phase information from, 283
- sparse matrix sampling, 8
- spatial overlap problem, 245
- spatula technique, 16
- SQUASH program, 189
- standard deviation, 110–111
- static disorder, 84
- statistical density modification, 185
- Steno, Nicolaus, 45
- stereochemistry check, 287–288
- structure factor data, 74
  - distribution of, 114–116
  - normalized form of, 120–122
  - unitary form of, 119–120
- surface tension energy, 2, 12
- symmetry
  - graphic symbols of elements, 53–55
  - for protein crystals, 56
  - of diffraction pattern
    - three-dimensional translational, 49
- synchrotron radiation, 35
  - properties of, 29–30
- synchrotrons, 25
- T**
- Taylor expansion, 252–253
- Teaching Edition, of Volume A, 52
- temperature factor, 81–84
- Thomson scattering, 98
- three-dimensional grid, 180
- three-dimensional translational symmetry, 49
- torsion angle refinement, 276



- translation function, 217–218  
 AMoRe program, 226–229  
 Crowther and Blow, 218–226
- triclinic lattice, 79
- triplet, 232–234
- two-dimensional histogram matching, 190
- twinning, 116–118
- U**
- undulators, 27, 29
- unitary structure factor, 119–120
- V**
- Van der Waals distance, 31
- vapor diffusion technique  
 hanging drop method, 5–6  
 sitting drop method, 6
- vector products, 69–70
- von Laue, 45  
 diffraction theory of, 21
- W**
- Wang's real space method, 184
- wARP models, *see* weighted averaging of multi-refined dummy atomic models
- water–buffer solution, 2
- water–organic solvent, 2
- wavelength normalization, 246
- wavelength shifter, 27–28
- weighted averaging of multi-refined dummy atomic models, 190–192
- weighted reciprocal lattice, 79
- Weissenberg cameras, 42
- WHAT\_CHECK program, 288
- wiggler, 27  
 multipole, 29
- Wilson plots, 111–114, 142–143
- X**
- x*-axis of the lattice, 46
- X-PLOR package, 272
- X-ray beam, 19, 31, 33, 35, 64, 101  
 absorption of, 102–103  
 as electromagnetic waves, 65  
 and human body, 12  
 radiation damages to, 60–61
- X-ray crystallographer, 22, 27, 29
- X-ray crystallography, 63–64, 85
- X-ray detectors, 33, 36, 60
- X-ray diffraction  
 equipment, 31  
 experiment, preparation of, 11–15  
 patterns of, 19, 45, 62  
 diffraction, by crystal, 105  
 diffraction conditions, 76–77  
 electron density, calculation of, 84–90  
 Ewald construction, 77–81  
 integral reflection conditions, for central lattices, 95–96  
 intensity diffracted, by crystal, 96–103
- X-ray film, 32, 35
- X-ray generator, 21
- X-ray photons, 34, 60, 105
- X-ray radiation, variation of, 314–315
- X-ray sources, 21–30  
 rotating anode tubes, 25  
 sealed X-ray tubes, 22–25  
 synchrotron radiation, 25–30  
 synchrotrons as, 241–242
- X-ray wavelength, 18, 24, 30
- Z**
- Zeppezauer method, 6